Variable Stars in the SuperWASP All-Sky Survey

Thesis

Variable Stars in the SuperWASP All-Sky Survey

Heidi Budd Thiemann

School of Physical Sciences

The Open University

Submitted for the degree of

Doctor of Philosophy in Astrophysics

14 May 2021

Per ardua ad astra.

Acknowledgements

All men have stars, but they are not the same things for different people. For some, who are travelers, the stars are guides. For others they are no more than little lights in the sky. For others, who are scholars, they are problems... But all these stars are silent. You-You alone will have stars as no one else has them...

– Antoine de Saint-Exupéry, The Little Prince

There are so many people to whom I owe a huge debt of gratitude. Ever since I was young, I've been obsessed with space and I can't begin to thank enough everyone who has helped me in my career so far. Each person mentioned here has, in some way or another, helped to realise the dreams of a young girl who looked up at the night sky and fell in love with the stars.

My amazing and patient supervisors, Andrew Norton and Ulrich Kolb, deserve the first mention for their teaching, support, encouragement, and for always pushing me to do better. I have genuinely enjoyed every moment of working with them and I will always value the opportunity they gave me to work on such a fantastic project and travel the world for the sake of astronomy. For their advice and contributions to my work, I would like to thank a few colleagues, especially Marcus Lohr and Hugh Dickinson. They have always been generous in their help, whether it be wrestling with the PIRATE telescope or tackling some obscure astronomy software.

A huge thank you also goes out to all my friends in the astronomy office and the wider Astronomy Research Group at The Open University. They all made my time there so much

fun, even in the unique situation of being socially distanced during a global pandemic. A particular thanks goes to my friends Joe Cooper, Dean Roberts, Mark Parker, and Meredith Morrell. We made a great team.

Thank you to my family, not just for the obvious reasons but also for putting up with years of me talking about space and astronomy non-stop. And I do really mean non-stop. To my parents for their unwavering love and support; to my siblings for keeping me down to Earth; to my gran for sending me newspaper cuttings of the latest space news. And a special thank you to Terry for all his love and selfless support over the years. I couldn't have done it without him.

This doctoral research was supported by The Open University and the Science and Technology Facilities Council [grant number ST/P006760/1] through the DISCnet Centre for Doctoral Training. The SuperWASP project is currently funded and operated by Warwick University and Keele University, and was originally set up by Queen's University Belfast, the Universities of Keele, St. Andrews and Leicester, the Open University, the Isaac Newton Group, the Instituto de Astrofisica de Canarias, the South African Astronomical Observatory and by STFC.

Some parts of this work were previously published in the following journal papers:

Heidi B. Thiemann, Andrew J. Norton, Ulrich C. Kolb, Hugh J. Dickinson, Adam McMaster, (2021), SuperWASP Variable Stars: Classifying Light Curves Using Citizen Science, *MNRAS*, 502, 1

Heidi B. Thiemann, Andrew J. Norton, Ulrich C. Kolb (2020), The stellar rotation–activity relation for a sample of SuperWASP and ASAS-SN field stars, *PASA*, 37, e042

Abstract

The SuperWASP project has a vast archive of stellar variables still to be exploited. In this work, I explored three aspects of stellar variability using this archive: rotational variation, contact binaries, and citizen science.

In the first part of my research, I used the SuperWASP archive and ASAS-SN Catalogue of Variable Stars to identify rotationally modulated stellar variables with a coincident X-ray source. These results were used to characterise the rotation-activity relation for a sample of field stars. For the SuperWASP targets, I found a slope of the power-law fit to the unsaturated regime of $\beta = -1.84 \pm 0.18$, in line with the canonical value of $\beta = -2$, and evidence of the supersaturated regime.

In the second part of my research, a candidate near contact red giant eclipsing binary was discovered, thought to be the progenitor of the rare transient, red novae. I characterised 27 candidates both photometrically and spectroscopically. The observational data fed directly into component modelling and evolutionary modelling, confirming their existence and identifying component masses of $\sim$0.3–3 $M_{\odot}$, semi-major axes of $\sim$13–70 $R_{\odot}$, temperatures of $\sim$3600-5600 K, and radii of 3–25 $R_{\odot}$. For such unusual binaries to form, I identified that they must have evolved from detached binaries with mass ratios of q=1$\pm$0.01, and are on the brink of experiencing a rapid inspiralling event which will likely occur within just 5,000 years to 29 Myr (0.03 Gyr). It is, however, uncertain whether the death of near contact red giant eclipsing binaries will form white dwarf binaries, red novae, or something else entirely.

In the third part of my research, I analysed the results of 2 years of engagement with members of the public through *SuperWASP Variable Stars*. I identified over 300 new stellar variables and laid the groundwork for future exploitation of the SuperWASP archive.

Table of contents

List of figures

List of tables

Chapter 1

Introduction

In this chapter, I will introduce the research done for my PhD. I will summarise the key goals and what was done to achieve those goals, and then outline the structure of the thesis and the content of each chapter.

1.1 Project summary

Searching for "variables stars in the SuperWASP all-sky survey" was a wide and open project brief in which almost any path of research could be explored. For this reason, this PhD project came to be shaped by serendipitous discoveries and deep dives into archives of astronomical data.

The SuperWASP (Wide Angle Search for Planets) survey was designed to hunt for transiting exoplanets, and remains the most successful ground based search for such exoplanets to date. However, this is not where this project has focused. During the decade over which SuperWASP surveyed the night sky, night after night, year after year, a vast archive of stellar variability was created. This archival data forms a valuable source through which populations and individual stellar variables can be discovered, explored, and characterised.

In this work, the exploitation of this archive became focused around three main aspects of stellar variability in SuperWASP data. The first goal was to investigate and characterise rotational modulation using SuperWASP data, in which star spots on the surface of a star are dragged along the surface causing periodic sinusoidal changes in the brightness. This variability was combined with X-ray detections to characterise the relationship between the rotational period of late-type stars, and their X-ray activity, known as the rotation-activity relation. The study of the rotation-activity relation is key to improving our understanding of the underlying stellar dynamo, and this research provides the first analysis using photometrically defined periods using SuperWASP and ASAS-SN field star data.

The second aspect of stellar variability explored came quite by chance, and is the most exciting part of this work. During the creation of SuperWASP Variable Stars, a new configuration of binary star was serendipitously discovered. This new binary was identified as a near contact red giant eclipsing binary, a long period binary system comprised of two late-type giants, in, or almost in contact. These systems have never been recognised before, and defy previous knowledge of binary evolution. We postulated that, based on possible instability within the system and the late-type classification, this new binary could be the progenitor of the rare transient, red novae. The goal quickly became to identify similar candidate binaries, conduct photometric and spectroscopic follow-up, and model the systems and their evolution. If these binaries are red novae progenitors, this is a golden opportunity to identify and characterise merger candidates before the merger event itself, furthering our understanding of these rare transients.

This discovery of a new type of binary spurred on the analysis of the SuperWASP Variable Stars project, which makes up the third aspect of research. SuperWASP Variable Stars is a citizen science project running on the Zooniverse platform. The aim of this project is to use the power of "the wisdom of the crowd" to classify variable stars into broad variable types for the purpose of population studies and studies of unique and extreme stellar variables. A

first analysis aimed to understand the accuracy of citizen science classifications and identify new stellar variables discovered by citizen scientists.

1.2 Thesis outline

In this thesis, I will be telling the story of how SuperWASP has become a valuable archive for the field of stellar variability, with serendipitous discoveries and new ideas leading down exciting pathways of research. The thesis is split roughly into four parts to align with the pathways described above.

The first part provides the background to stellar variability and the second summarises my research on the rotation-activity relation. The third part is by far the longest, describing the serendipitous discovery of a set of near contact red giant eclipsing binaries, thought to be the progenitors of red novae, the follow-up, and modelling. The fourth part focuses on the future of the SuperWASP archive for further studies of stellar variability through citizen science.

This chapter has outlined the research goals and achievements. In Chapter 2, I introduce the field of stellar variability, with a particular focus on binary stars. In Chapter 3, the focus moves to introducing the SuperWASP project, from the telescopes themselves to the data archives exploited during the work. I also introduce other relevant surveys and catalogues used in this research, from the ASAS-SN Catalogue of Variable Stars to the Variable Stars Index.

Chapter 4 provides an in-depth background to the rotation-activity relation and summary of the unanswered questions of the field, whilst in Chapter 5 I describe my work on characterising the rotation-activity relation using the SuperWASP all-sky survey and ASAS-SN Catalogue of Variable Stars. The bulk of this Chapter is from Thiemann et al. (2020), my first published paper.

In Chapter 6, I outline the background to red novae, and in Chapters 7, 8, and 9, I summarise the serendipitous discovery of a near contact red giant eclipsing binary, J001521, during the creation of SuperWASP Variable Stars. These chapters describe and provide the results of the subsequent hunt for and follow-up of a set of similar candidate binaries. In Chapter 10, I combine the photometric and spectroscopic follow-up to model the components of the binaries using the binary star modelling software, PHOEBE. This chapter also includes the modelling and evaluation of their evolutionary pathways, from birth to death, to assess whether they are progenitors of red novae. In Chapter 11, I briefly summarise the candidates which, after follow-up, were found not to be binaries. These failed candidates in and of themselves are interesting, with multiple Be/shell stars identified, but have not been modelled in any more detail.

In Chapter 12, I provide the first analysis of SuperWASP Variable Stars. This chapter is taken from Thiemann et al. (2021), and describes the project, analysis, and results, including the discovery of over 300 new stellar variables and the future of the project.

Finally, in Chapter 13, I summarise and conclude my story of research with SuperWASP and leave the book open for future research using a combination of citizen science, machine learning, and chance discoveries.

Chapter 2

Background to Variable Stars

Variable stars are key to investigating and testing stellar astrophysics, and the dynamics and structure of stellar systems. The detection, classification, and study of classes of variable stars is therefore an important pursuit. The magnitude of a variable star can vary over huge ranges, from fractions of a magnitude to over 20 magnitudes for cataclysmic events, and the time periods over which this change occurs can also span many orders of magnitude. Typically, variable stars are detected through amplitude and period variations in their photometric light curve, and whilst classifications of periodic variables based on their light curve are not always conclusive, it does give a strong indication of variable type.

In this chapter, I will provide an introduction to stellar variability and the classification of variable stars. There will be a particular focus on binary stars (especially contact binaries), rotationally modulated stars, and Cepheid variables, which reflect the main topics of this research. The method of measuring period change in binary systems, known as O–C diagrams, will also be introduced.

2.1 History of stellar variability

For millennia, humans viewed stars as eternal and unchanging celestial spheres in the night sky. Only in the past few hundred years have we really known that stars are, in fact, changing constantly and in many varied ways.

The oldest known artefact to document stellar variability is that of an ancient Egyptian Cairo Calendar of lucky and unlucky days dating back to 1244–1163 BC (Porceddu et al., 2008). Figure 2.1 shows a section of the calendar, in which lucky days are based on a lunar cycle. Time series analysis of this calendar found a significant period of $P \sim$2.85 d, remarkably close to the period of Algol (also known as β Persei), a bright eclipsing triple star system with a period of $P \sim$2.86 d. In the passing millennia, Algol has had many evil-sounding names, including the pre-classical Greek 'Demon Star' (Wilk, 1996), the Arabic *ra's al-ghūl* meaning the head (ra's) of the ogre (al-ghūl) (Smart, 1986), and the Chinese *Tseih She* (pronounced Zhi Shi) meaning 'piled up corpses' (Ridpath, 2018).

Jumping from ancient times to the renaissance, the study of the changing brightness of stars really began. Omicron Ceti (now known as Mira) was observed in 1596 by German pastor David Fabricius (Gaspani, 1998). The star appeared to increase then decrease in brightness, and it was assumed that o Ceti was a nova. In 1638, after multiple cycles of brightening and fading, Johannes Holwarda determined the period of variability of o Ceti, and Johannes Hevelius, who was also observing it, named it Mira in 1662[1] (Hoffleit, 1997). In 1669, Algol was discovered by Geminiano Montanari (E. Baiada 1995; Montanari 1671), and the variability was characterised by John Goodricke over 100 years later, in 1784 (Goodricke, 1784). By that time, approximately ten variable stars were known (Hoffleit, 1993), and by the mid 19th century, the field had taken off.

During the late 19th and early 20th century, variable stars were regularly being discovered and studied. A particularly famous example is that of Henrietta Swan Leavitt, who was

[1] Fabricius sadly did not live long enough to celebrate his discovery of the first variable star. After denouncing a local goose thief from the pulpit in 1617, the accused murdered him with a shovel.

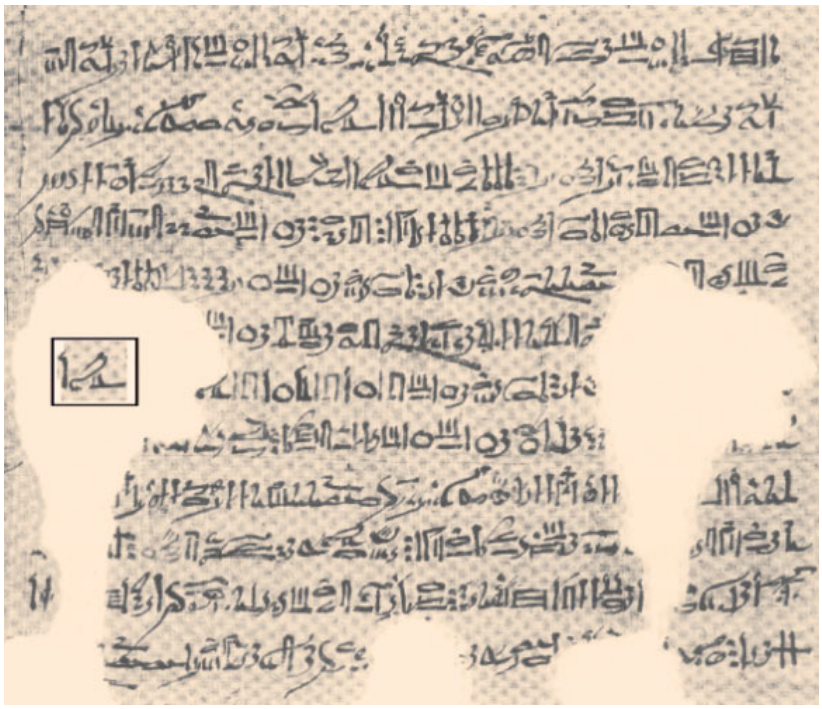

Fig. 2.1 A section of the Cairo Calendar of lucky and unlucky days, dating to the reign of Ramses II (Porceddu et al., 2008)

employed as a "computer", examining hundreds of photographic plates in order to catalogue the brightness of thousands of stars. Leavitt discovered ∼2,400 variables and discovered the luminosity-period relationship in Cepheid variables (Leavitt 1908; Leavitt and Pickering 1912), paving the way for distance calculations in modern astronomy. By 1959, women had discovered over 75% of all 14,708 named variable stars (Hoffleit, 1993), many having been employed, like Leavitt, as computers.

Today, the International Variable Stars Index (VSX)[2] (Watson et al., 2020), maintained by the American Association of Variable Star Observers (AAVSO), is a catalogue comprised of over 2 million variable stars and counting.

[2]www.aavso.org/vsx/index.php

2.2 Stellar variability

Over 200 variability types and sub-types are listed in VSX, making the task of categorising variable stars a challenging one. Thankfully, we can categorise stellar variability broadly into two categories: 'intrinsic variability' (variability caused by physical changes within the system) and 'extrinsic variability' (variability caused by external factors). We can go into a little more detail and provide seven sub-categories, which are now widely recognised, as listed below:

- Intrinsic variables:
  - Cataclysmic - variability due to explosions of a star or an accretion disc
  - Eruptive - variability due to chromospheric activity, flaring, or shell ejections
  - Pulsating - variability due to the radial or non-radial stellar pulsations
  - X-ray - variability of X-ray and optical emission, typically from a neutron star or black hole component in a binary system
- Extrinsic variables:
  - Eclipsing - variability caused by the eclipse of one star by another along an orbital plane coincident with our line of sight
  - Microlensing - variability due to the brightening of a background source by a foreground lens
  - Rotating - variability caused by the rotation of a star, either through a star spot, reflection, or changing shape

Work by Eyer and Mowlavi (2008) provides a grouping of variable sources present in the Universe, as shown in Figure 2.2. Here, variables are grouped on the first level according to the physical origin of their variability. The second level groups variability by type of

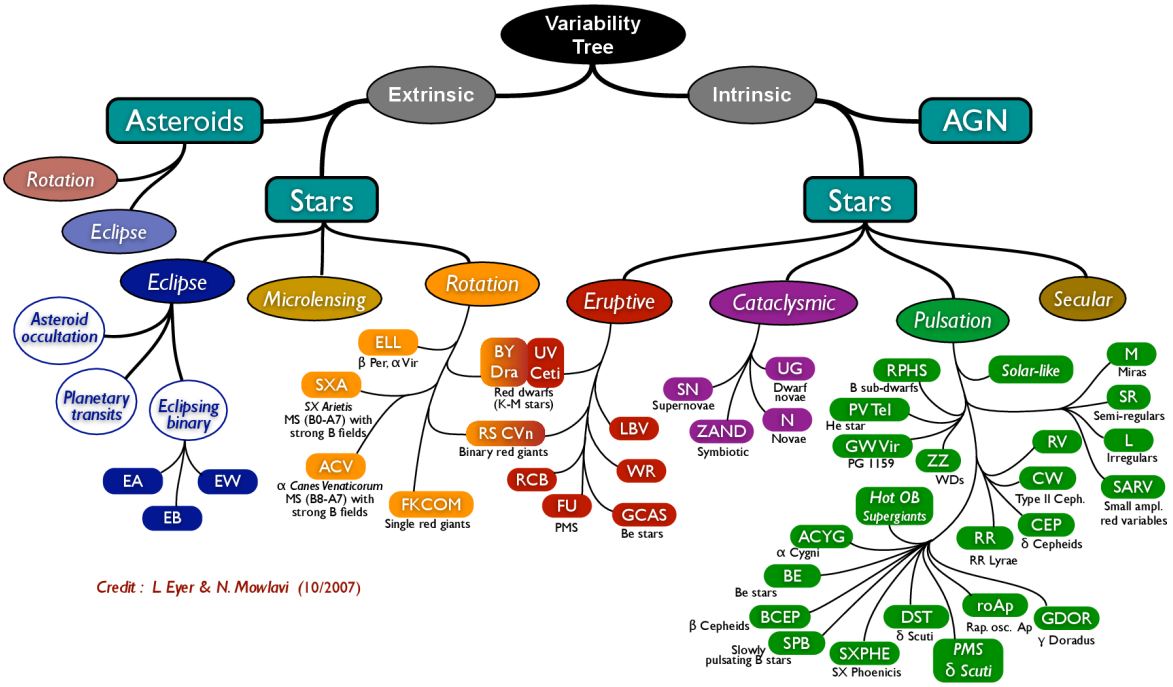

Fig. 2.2 The "variability tree" as organised by Eyer and Mowlavi (2008).

object, and the third level identifies the phenomena causing the variability itself. However, some stellar variables are more complex than just falling into a single variable type. In some instances, a system can fall into two categories, for example, a pulsating variable in a binary system. Despite this, the variability tree and VSX classifications generally provide a good method of categorising stellar variables.

A selection of different types of variability will be detailed in the following sections, with a particular focus on binaries, rotationally modulated variables, and Cepheids. Where relevant, light curves and models are included. Descriptions have been adapted from the General Catalogue of Variable Stars (GCVS) (Samus et al., 2017), VSX (Watson et al., 2020), and Eyer and Mowlavi (2008).

2.2.1 Intrinsic variables

Intrinsic variability is caused by physical changes within the star itself, such as eruptions or pulsations. In the following section, types of intrinsic variability are categorised into four

main classes: cataclysmic, eruptive, pulsating, and X-ray. Each category contains numerous sub-categories, and where relevant, these are discussed.

Cataclysmic variables and novae

Cataclysmic variables stars are a class of interacting binary stars with a white dwarf accreting from a red dwarf via Roche lobe overflow, with orbital periods of 1–12 hours. These are systems which experience a dramatic change in brightness due to a violent and energetic astrophysical event. They are not necessarily periodic variables, but instead are transients such as supernovae or novae of various different kinds (Samus et al., 2017). Similarly energetic transients include novae, with some examples described below.

Classical/recurrent novae are cataclysmic variables in which the white dwarf accretes enough matter to undergo runaway thermonuclear burning on the surface. This system is not destroyed in the outburst, since the outburst occurs on the surfaces. It is thought that classical novae may be recurrent novae if observed over a long enough time, with estimates of the recurrence of a classical novae with a 1.3 $M_{\odot}$ white dwarf being $\sim$0.3 Myr.

Typically, novae are a result of the interactions of a close binary system comprised of at least one evolved star. These outbursts are driven by thermonuclear processes either deep within the star or occurring on the surface. An example of this is the accretion induced collapse (or thermonuclear destruction) of a white dwarf in a semi-detached binary system (resulting in a Type Ia supernova), which is visible as a dramatic increase in magnitude over a few days, followed by a slow decrease in brightness over the following months to years (Warner, 2003).

Another example is the core collapse of a massive star (resulting in a Type Ib/c, or II supernova), visible as a brightness increase of up 20 magnitudes for massive progenitor stars, and can outshine the rest of its galaxy across the electromagnetic spectrum. The brightest supernova detected to date is SN2016aps (Nicholl et al., 2020), reaching an apparent

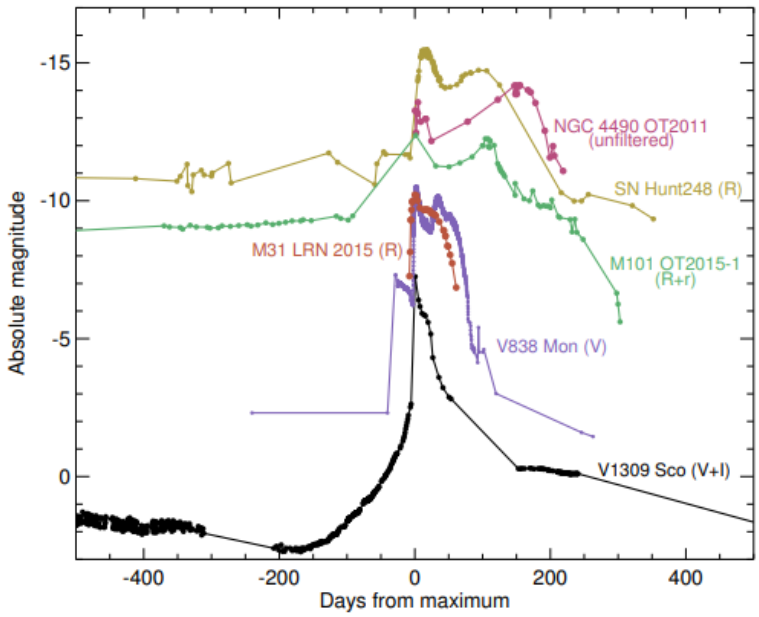

Fig. 2.3 Double-peaked light curves of several luminous red novae candidates (Metzger and Pejcha, 2017).

magnitude of -22.35 (Chornock et al. 2016; Guillochon et al. 2017). Although such bright events are rare, nova are relatively common, with a Galactic rate of $\sim$34 yr^{-1} (Darnley et al., 2006).

Red novae are newly identified type of novae (also known as a V838 Mon type event, or luminous red nova). A red nova is thought to be caused the merger of a close binary where one component is a giant and the other is main sequence. This rare optical transient has a double peaked light curve, as shown in Figure 2.3, and will be introduced in detail in Chapter 6.

Eruptive

Eruptive variables are stars which exhibit irregular outbursts, flaring, and brightness variations due to violent processes occurring in the chromosphere and coronae. These changes in luminosity often coincide with interactions with the interstellar medium, mass outflows, and interactions with a disc or ejections of shells.

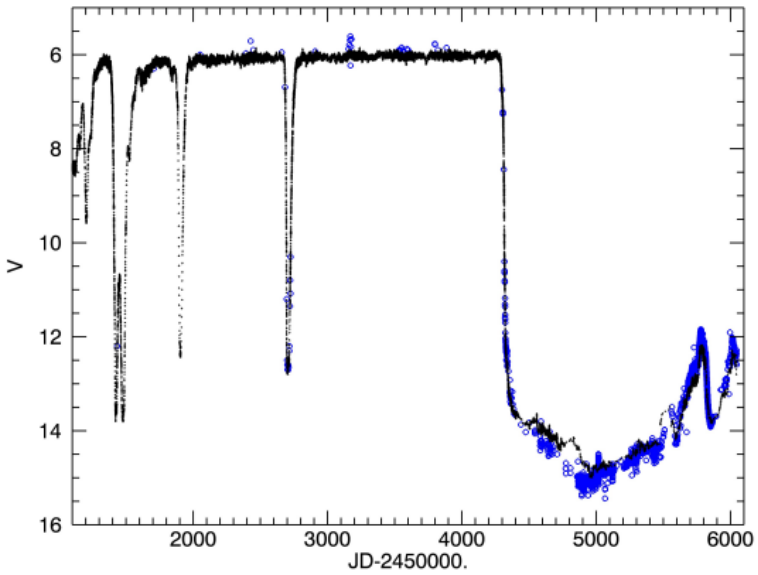

Fig. 2.4 Light curve of R CrB between 1998–2012 using AASVO data. Black dots indicate visual magnitudes, blue circles indicate Johnson V data (Clayton, 2012).

Types of eruptive variables include Orion variables, primarily evolving protostellar objects including FU Orionis type (FU) and T Tauri stars. These systems are thought to flare due to sudden mass transfer from an accretion disc onto a young star (Bertout 1989; Reipurth 1990). Other flare stars are common, and include UV Ceti type (UV) stars. These stars experience unpredictable and dramatic increases in brightness for just a few minutes at a time. UV type stars appear to be low mass, late main sequence stars experiencing magnetic reconnection, similar to solar flares at higher energy (Gershberg and Shakhovskaia, 1983). By contrast, R Corona Borealis type stars (R CrB) are rare hydrogen-deficient and carbon rich supergiants which experience irregular dimming events due to dust shrouding the system (Clayton, 2012). A light curve showing the irregular dimming and brightening of R CrB is shown in Figure 2.4.

Shell stars are characterised by broad absorption lines due to a rapidly rotating photosphere, and emission lines (including Hα) from the motion of an ionised equatorial circumstellar disc of gas, as shown in Fig 2.5. Shell stars experience a rapid rotation, with

radial velocities of 200–300 km^{-1}, nearing the point at which the rotational acceleration would disrupt the star itself (Saad et al. 2012; Silaj et al. 2014; Slettebak 1982).

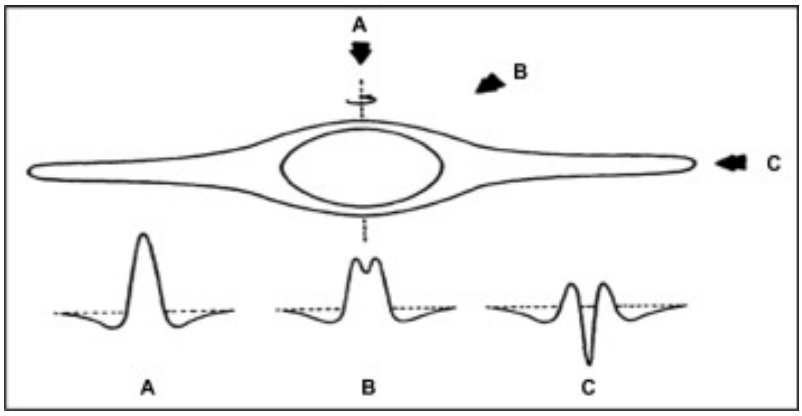

Fig. 2.5 How the observed Hα line profile of a shell star depends on the viewing angle as the disc structure rotates. This model was proposed by Struve (1931) and this diagram is taken from Saad et al. (2012).

Pulsating

Pulsating variables are stars which exhibit periodic expansion and contraction of their surface layers. These pulsations can be either radial, in which the star pulsates around a central point and remains spherical, or non-radial, in which the star does not pulsate around a central point and does not remain spherical. Such pulsations can either occur periodically or irregularly, but often pulsating variables have a single well-defined period. Depending on the type of pulsation and the location of the pulsation within the star, this type of variable may pulsate with a harmonic or overtone, and two or more periods may be detected for a single star.

These stars pulsate because they are not in hydrostatic equilibrium, and the force of gravity pulling mass together is not balanced with the internal radiation pressure. As the star is compressed, ionisation within the star increases, forcing the layers to expand outward. At this stage, the star becomes 'transparent' and photons escape, a phenomena known as the κ-mechanism. Once gravitational force becomes dominant, the star starts cooling and contracting, ionised material recombines, and the outward pressure decreases. The star's

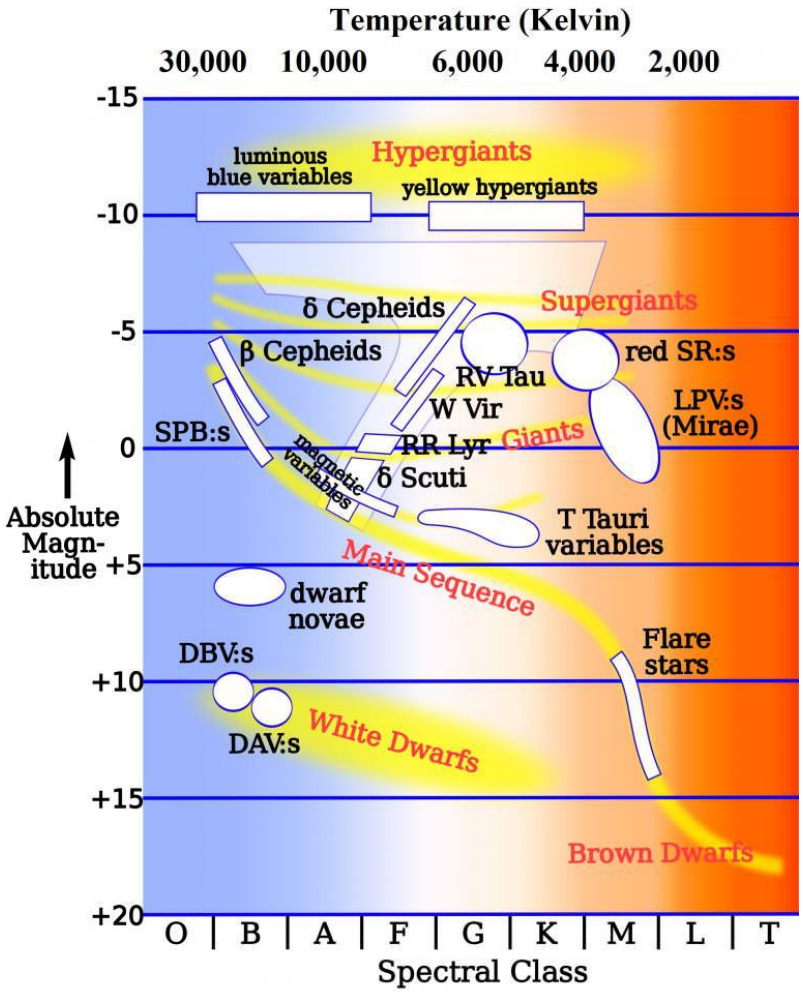

Fig. 2.6 The Hertzsprung-Russell diagram showing the location of types of pulsating variable stars and the instability strip. [Credit: Wikipedia; Rursus (2007)]

opacity increases and photons become trapped. This cycle continues and is visible as a periodic, often sharp, asymmetric pulse profile in the light curve.

Pulsating stars do not fall randomly on the Hertzsprung-Russell diagram. Instead, they are mostly found along a narrow zone called the instability strip. As subgiants with masses of $\sim 2M_{\odot}$ evolve off the main sequence, they pass through the instability strip where they experience a short phase of pulsation (Gautschy and Saio 1996; Ryan and Norton 2010a).

Some common types of pulsating variable star include δ Scuti stars, Cepheid variables, RR Lyrae stars, Mira variables, and semi-regular variables, as seen in Figure 2.6. δ Scuti

stars lie close to RR Lyrae stars, and Mira and semi-regular variables lie off the instability strip between giants and supergiants.

δ Scuti stars are the shortest period pulsating variables (Sterken and Jaschek, 1996) and are main-sequence or sub-giant stars which lie along the instability strip. They typically display low amplitude pulsations (pulsations of $>$0.15 V mag are known as High Amplitude δ Scuti stars), periods from 0.01–0.2 d, and spectral types of A5 to F2. Pulsations can be either radial or non-radial so whilst their light curves can vary in shape each cycle, they typically appear to be nearly symmetrical.

Cepheid variables are yellow giant or supergiant pulsating variables which lie along a narrow instability strip. Their pulsation periods can range from days to months, with surface temperature of 6000–8000 K, and are broadly categorised into two classes: Type I or classical Cepheids (young stars with masses greater than that of the Sun) and population II Cepheids (also known as W Virginis type stars, older, less massive stars). Discovered by Henrietta Swan Leavitt whilst studying variables in the Magellanic Clouds, the relationship between the period and luminosity of Cepheids was a milestone in distance determination (Leavitt and Pickering, 1912). The change in size and shape of Cepheid variables are observed as a resulting change in the apparent magnitude, radius, period, and radial velocity, as shown in Figure 2.7 (Percy, 2007).

RR Lyrae stars are post main-sequence giant stars which lie along the horizontal branch of the Hertzsprung-Russell diagram. These stars typically have a period of 0.1–1 d, temperatures of 6000–7500 K, spectral types of A5 to F5, and amplitudes in V mag of $\sim$1.5 (Percy, 2007)). These stars have exhausted hydrogen burning and have begun to burn helium in their core, and have a narrow range of luminosities, making them valuable standard candles.

A significant proportion of RR Lyrae stars display the Blazhko effect, a long-term modulation of the period, amplitude, and shape of the light and radial velocity curves. An example of a RR Lyrae experiencing the Blazhko effect is shown in Figure 2.8. The cause of

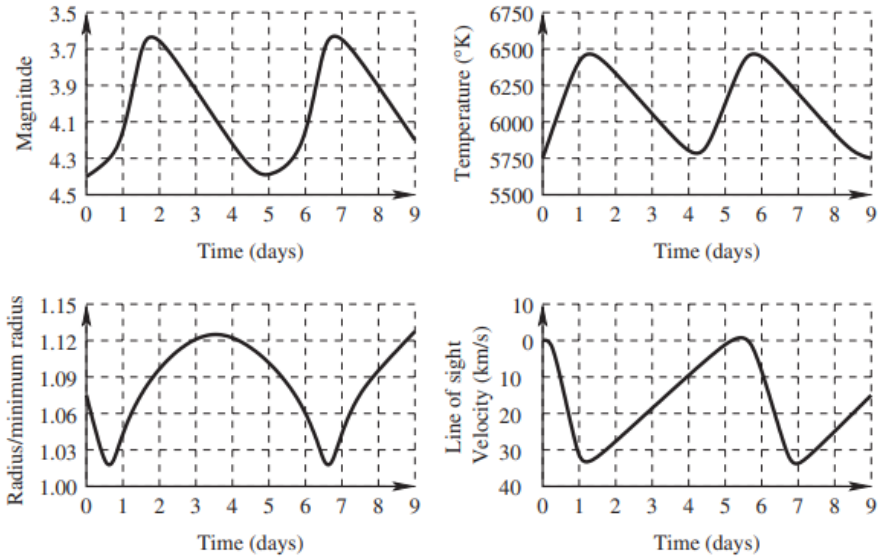

Fig. 2.7 The magnitude, temperature, radius, and radial velocity of the prototype Cepheid, δ Cephei (Percy, 2007).

the Blazhko effect is still unexplained, and correlations between parameters such as period and amplitude have not been found (Greer et al., 2017).

Other types of pulsating variables include Mira variables, which are red giant stars on the asymptotic giant branch. They typically experience pulsation periods of 80–1000 days (Samus et al., 2017) due to pulsations and contractions of the entire star. The light curve of the prototype variable, Mira, is shown in Figure 2.9. A similar type is the semi-regular variable (shown in Figure 2.10), which, as their name would suggest, are stars which show some periodicity in their light curves, but are often interrupted by irregularities. They have periods of 20 to >2,000 days and amplitudes ranging from hundredths of a magnitude to several magnitudes. The difference between Mira variables and semi-regular variables is, on the whole, rather arbitrary, with a gradation of properties between one and the other. However, some defining differences lie in the fact that semi-regular variables typically have smaller amplitudes, low mass loss, and no shock waves.

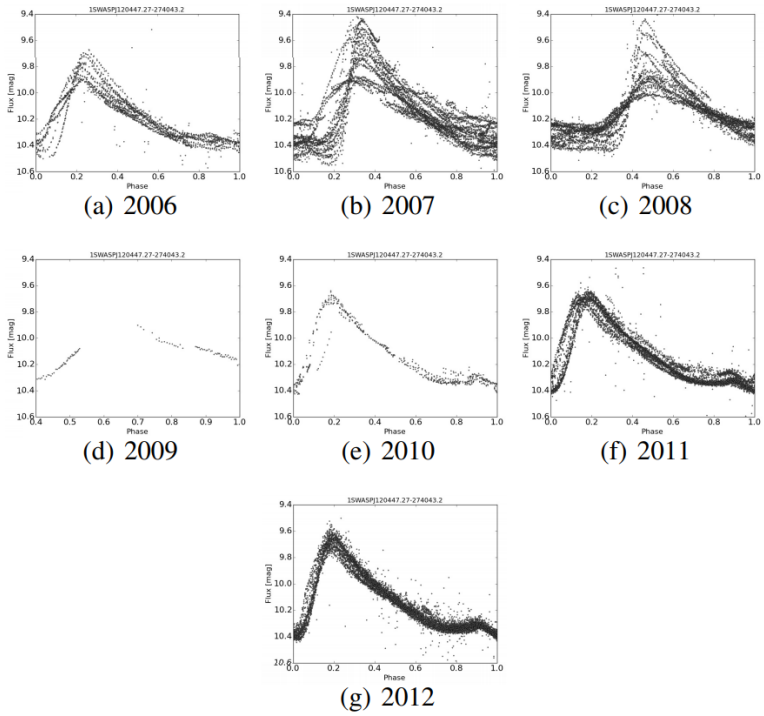

Fig. 2.8 The yearly light curves of 1SWASPJ120447.27-274043.2 showing amplitude changes characteristic of the Blazhko effect (Greer et al., 2017).

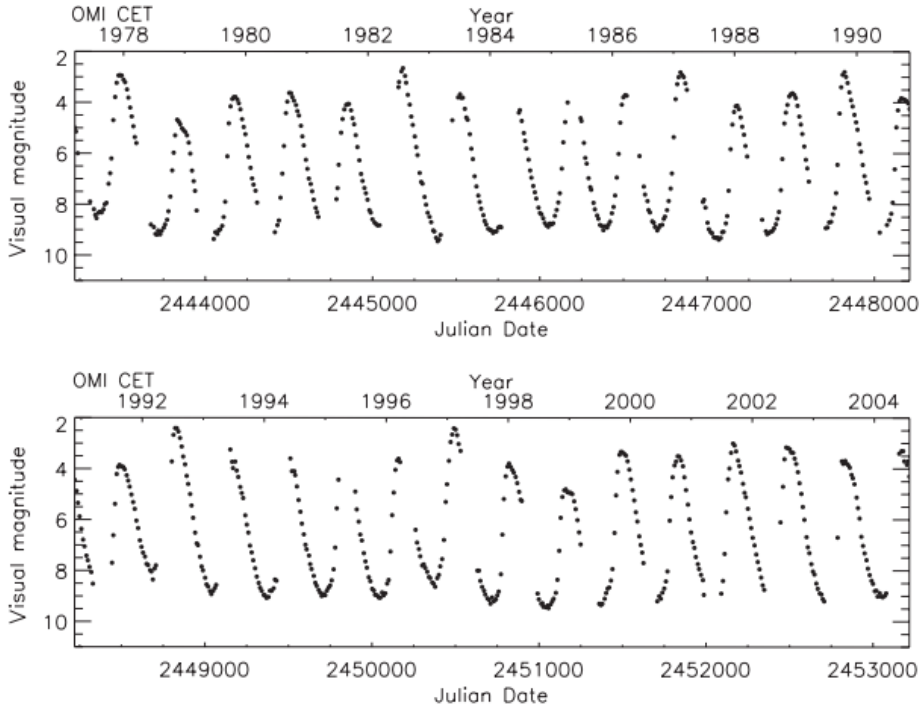

Fig. 2.9 The light curve of Mira between 1978–2004 based on measurements from AAVSO. [Credit: AAVSO]

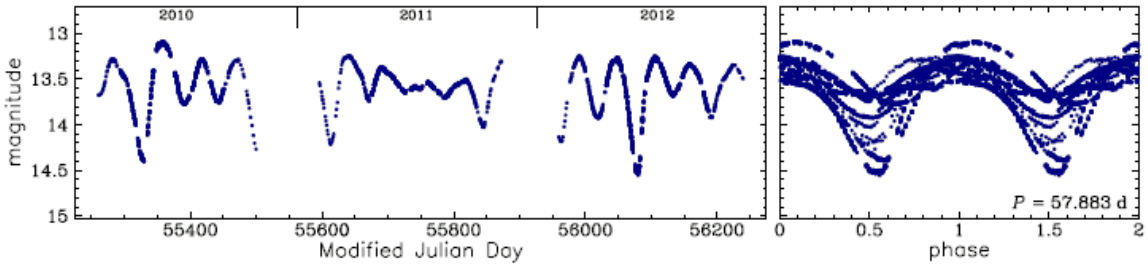

Fig. 2.10 Light curve of a yellow semi-regular variable (SRd star) between 2010–2012. [Credit: OGLE]

X-ray

It is up for debate as to whether X-ray variables deserve a class of their own since they really belong to the class of binary systems, however, they are briefly described here, although not so relevant to this research.

X-ray variables are binary systems characterised by a significant X-ray emission which is not attributed to any other mechanism for variability. Typically, one component is a compact object such as a black hole, neutron star, or white dwarf, and X-ray emission is caused by the infalling of matter onto this compact object or the accretion disc surrounding the compact object. Examples of X-ray variables include microquasars, high-, intermediate-, and low-mass X-ray binaries, and X-ray bursters.

One example, a low-mass X-ray binary (LMXB), is comprised of a solar mass star and a neutron star or black hole. Mass from the donor is pulled into the accretion disc and heated, releasing gravitational potential energy as a X-rays (e.g. (Tauris and van den Heuvel, 2006)). Figure 2.11 shows the optical light curve of V1408 Aql with a period of $\sim$9.3 hr, a system with a black hole component (Bayless et al., 2011).

2.2.2 Extrinsic variables

Extrinsic variability is caused by an external physical factor such as rotation, orbital motion, or an eclipse of the star. The causes of extrinsic variability can be categorised into three main subgroups: eclipses, rotations, and microlensing events.

Eclipsing

Binary stars are systems in which two gravitationally bound stars orbit a common centre of mass. Although a significant number of stars belong to binary or multiple star systems, photometrically, these systems can often appear to be non-variable single stars. Should these stars have the right orbital inclination, the orbiting companion will pass in front of the other

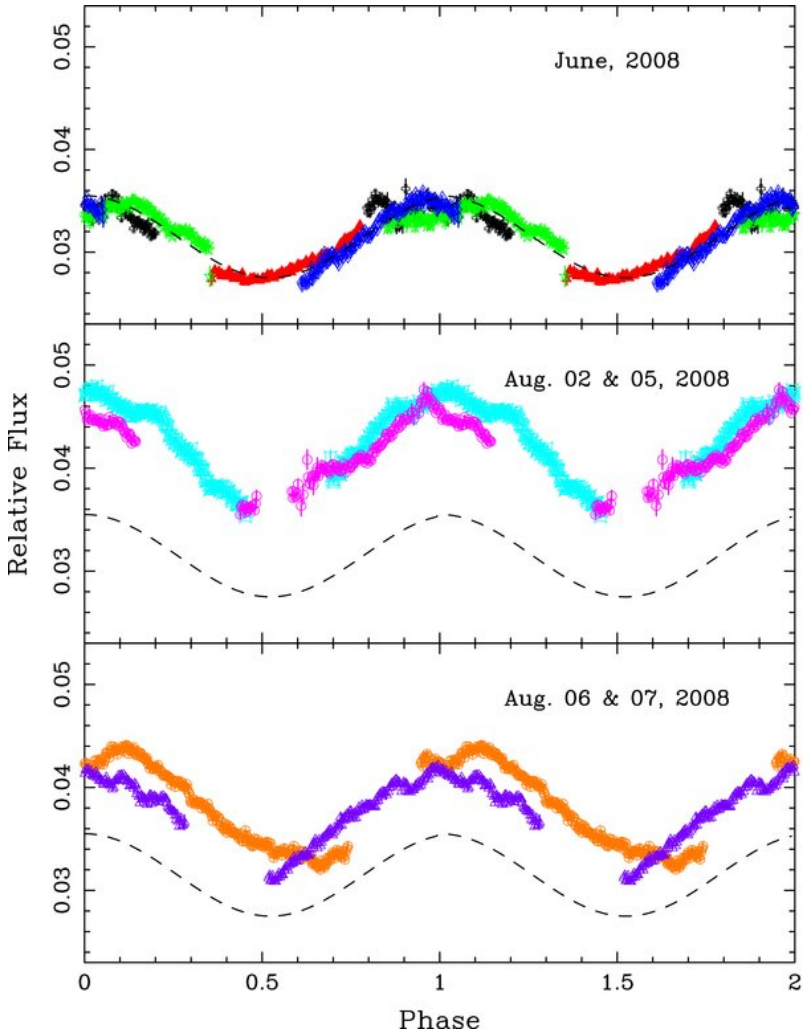

Fig. 2.11 Phase-folded light curve of V1408 Aql, a LMXB with a black hole component. Each colour indicates an individual night of observations (Bayless et al., 2011).

star, producing periodic dips in the flux, twice per orbital period. Therefore, in the case of an eclipsing binary star, the period of variability corresponds to the components' orbital motion, and the shape of the light curve depends on the separation of the components.

Eclipsing binary stars are classified into three classes based on the distinctive shape of their light curves: Algol-type (EA) - stars in this system are detached (neither star fills its Roche lobe) or semi-detached (one star fills its Roche lobe); Beta Lyrae-type (EB) - stars in this system are close enough to gravitationally distort one another, i.e. one star fills its Roche lobe whilst the other is distorted to an ellipsoidal shape; and W UMa-type (EW) systems - eclipsing binary systems in which the stars are in or almost in contact and there is a common envelope. Figure 2.12 shows the three distinctive classes of binary light curve, and Figure 2.13 shows an illustration of the three corresponding configurations of the stellar components.

EA type binaries are well separated, detached systems, and can be identified by sharp and narrow V-shaped eclipses separated by 0.5 in phase (unless the orbit is significantly elliptical). Outside of eclipse, there is typically a uniform brightness. Should the stars be closer, one of the stellar components may become distorted due to tidal effects and rotation and fill its equipotential surface, or Roche Lobe. The stars in this system are now known as semi-detached, EB type binaries, and the light curve becomes smoothly varying, making the beginning and end of eclipses challenging to identify. The primary and secondary eclipses, like EA type binaries, are usually different depths (Hall and Duerbeck, 1996). It is worth noting that there is not a distinct point at which an EA becomes an EB, and there is a continuous distribution between the two. EA and EB type binaries typically have periods between 0.3 d$\leq P \leq$10 d (e.g. (Stepien, 1995)), ranging up to years for some detached binaries (e.g. (Jayasinghe et al., 2018)).

Should the stars be even closer, they are classed as W Ursae Majoris (W UMa) type eclipsing binaries, EW type, contact, or overcontact binaries. EW type binaries typically

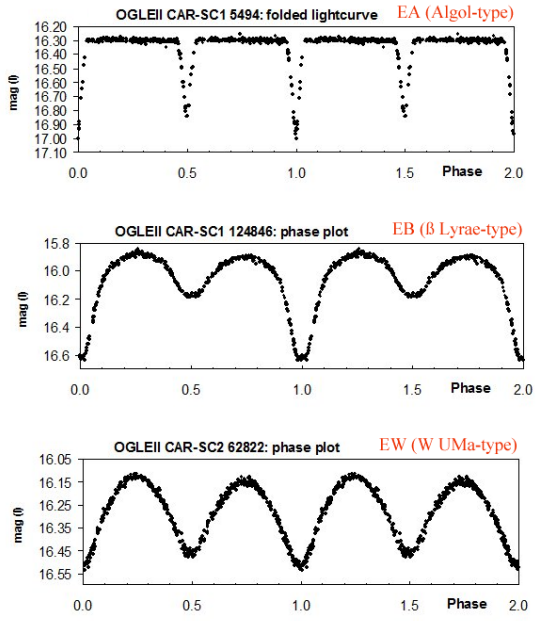

Fig. 2.12 Example light curves of different types of eclipsing binary stars, EA, EB, and EW (Huemmerich and Bernhard 2012; Szymanski 2005).

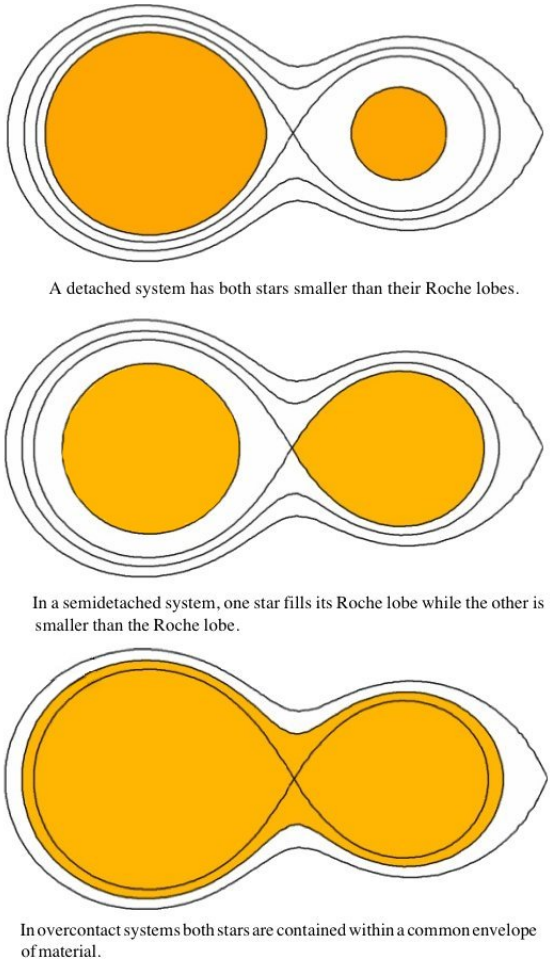

Fig. 2.13 Diagram of EA (detached), EB (semi-detached), and EW (contact) systems (Terrell, 2001).

have periods between 0.22 d$\leq P \leq$1 d (e.g. (Rucinski, 1992)), and orbit so close that they both fill their Roche lobe. Due to their close orbit, the stellar components are in contact with one another, and share a common envelope of stellar material. Within this common envelope, mass loss via angular momentum transfer is significant, often causing period change.

Orbital period change is common within binary systems, especially contact binaries, with almost 46% of binaries experiencing period change in one study by Kim et al. (2003). These physical processes causing period change via mass transfer and angular momentum loss include gravitational wave radiation, stellar winds, magnetic braking, and Roche lobe overflow (eg. Eggleton 2006; Hilditch 2001). Methods of period change via these methods are detailed further in Chapter 10.

The common envelope also equalises the temperatures, which contributes to the smoothly varying light curve and minima of near-equal depths (Duerbeck, 1996). In both EB and EW type systems, there can be a difference in the heights of the maxima due to the presence of star spots on one of the binary components, known as the O'Connell effect (O'Connell, 1951). Due to the proximity of the stellar components, their orbit is circularised, so eclipses will be separated by 0.5 in phase.

From photometric observations and the period of the system, we can deduce much about the physical properties of the star, such as the radii, luminosities, and temperatures of the stellar components. Combined with spectroscopic observations, even more can be deduced.

If the orbital motion of a binary has a component along the line of sight, and the period of the system is not too long, a periodic shift in spectral lines and a splitting of strong spectral lines should be observed. By observing the Doppler shifts of the spectral lines as the binary components move around their common centre of mass, it is possible to determine a number of characteristics about the binary through the radial velocity of the system. This includes the masses of the components, inclination, and Roche potentials of the system. Such parameters are not possible to determine through photometric light curves alone.

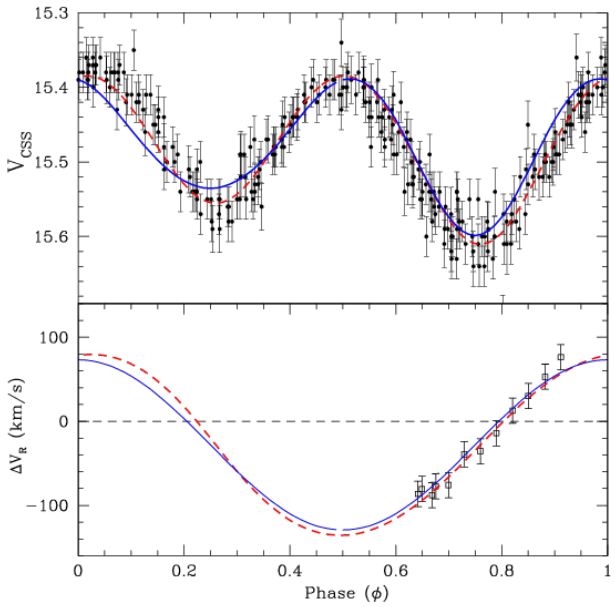

Fig. 2.14 The radial velocity curve and photometric light curve of the ultra-short period binary, CSS J001242.4+130809 (Drake et al., 2014).

Should both stars be of a similar luminosity, both components are visible in the spectrum, but should one star be significantly more luminous than the other, then a single periodically varying set of spectral lines will be seen. These are known as double-lined binaries (SB2) and single-lined binaries (SB1) respectively. The radial velocity of each component of the binary system is determined by the observed Doppler shift in wavelength:

$$\frac{\Delta\lambda}{\lambda_0} = \frac{\Delta v}{c}, \tag{2.1}$$

where λ_0 is the wavelength of the spectral line at rest, c is the speed of light, and v is the radial velocity. An example of a radial velocity curve is shown in Figure 2.14 (Drake et al., 2014). It is important to note that while the photometric light curves of eclipsing binaries show two maxima and two minima per cycle, the radial velocity curves of each component star will show only a single maximum and a single minimum per orbital period (Figure 2.14). This is in contrast to pulsating stars whose photometric light curves and radial velocity curves will each show single a single maximum and a single minimum per cycle (Figure 2.7). This

fact can help distinguish between competing models for a given system, as will be shown in Chapter 10.

Rotating Variables

Variability due to rotation can occur through a number of methods, and is often seen in conjunction with another type of variability, including binary eclipses or pulsations. Rotational variability is due to either a non-uniform surface brightness or a non-spherical shape.

Non-uniform surface brightness typically occurs due to the presence of spots or chromospheric activity on the stellar surface. These darker and brighter areas of the stellar surface typically move with the axial rotation of the star from the observers point of view, producing a continuous, often sinusoidal, light curve. Since star spots can change in size over time, the light curve may not be the same from one year to the next. An example of a light curve of a rotationally modulated star is shown in Figure 2.15 (Frasca et al., 2005). There is currently a fairly poorly understood relationship between the rotation period of a star and its activity, so rotational variables are a valuable probe for understanding this relationship.

Rotational variables can also take the form of non-eclipsing close binary stars which are distorted by gravity due to the proximity of the components. The visible component (often an evolved star) is distorted by an unseen component (often a lower mass main sequence star), and will appear as an ellipsoidally shaped star. As the stars orbit one another, the visible component presents a varying surface area. This is known as ellipsoidal modulation and often also appears as a sinusoidal light curve with two maxima and two minima per orbital cycle. The amplitude of ellipsoidal light curves typically does not exceed 0.1 mag in the V band (Samus et al., 2017). Several studies have focused specifically on ellipsoidal red giant binaries in the Large Magellanic Cloud (LMC) (shown in Figure 2.16) since they have a well-defined period-luminosity relationship (Nie et al. 2017; Soszynski et al. 2005; Wood 2000; Wood et al. 1999).

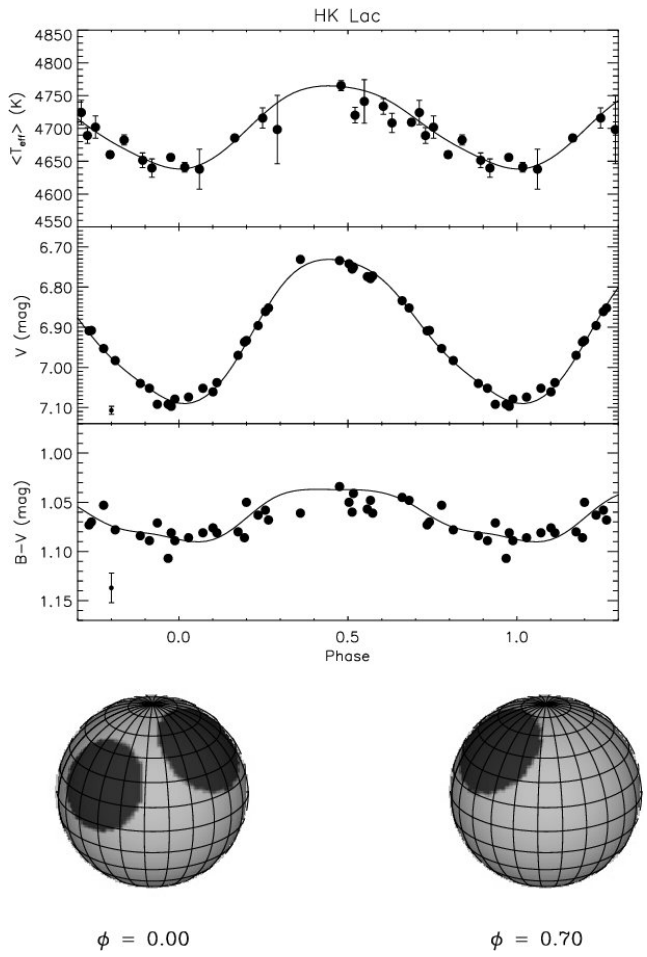

Fig. 2.15 The temperature, V band, and B-V light curves for HK Lac, and the spot model during two phases of its rotation (Frasca et al., 2005).

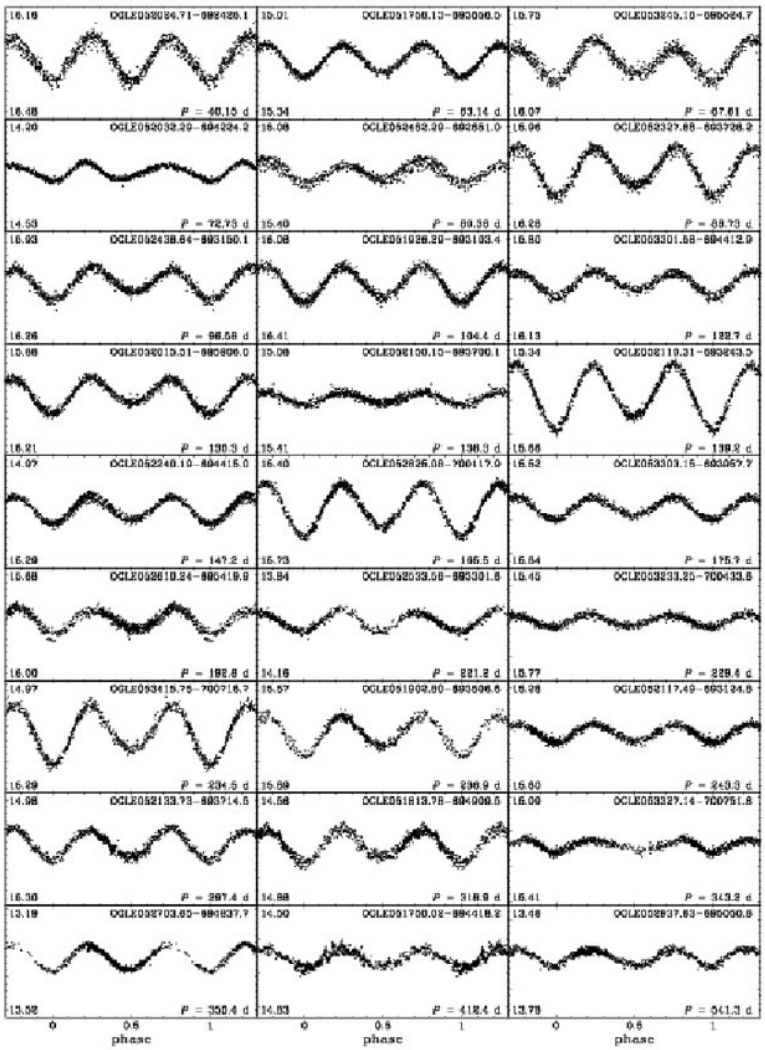

Fig. 2.16 Light curves of ellipsoidal red giants in the LMC (Soszynski et al., 2005).

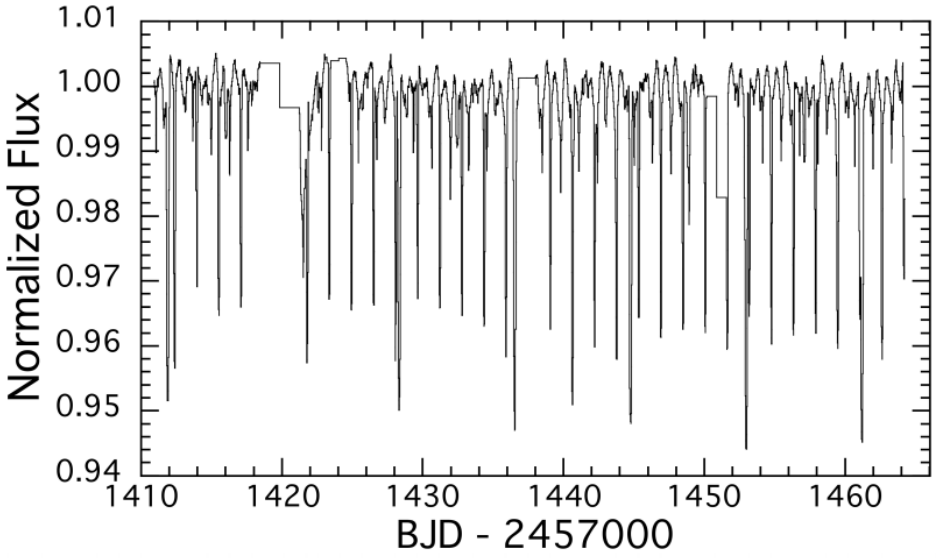

Fig. 2.17 The TESS light curve of TIC 168789840 showing multiple eclipses (Powell et al., 2021).

Multiply periodic stars

Multiply periodic stars are variables which display two or more coherent periodic modulations in their light curve, hence appearing to belong to two or more classes of variable types. Stars displaying two or more real periodic modulations in their light curve are of great interest, and multiply periodic systems can act as stellar laboratories. This might include hierarchical multiple stellar systems in which one point of light comprises a system of multiple binaries orbiting a common centre of mass. Two recent examples of such systems are the doubly eclipsing quintuple low-mass star system, 1SWASP J093010.78+533859.5 (Lohr et al., 2015a), and a sextuply eclipsing sextuple star system, TIC 168789840 (Powell et al., 2021), shown in Figure 2.17. Such systems have complex light curves which require careful disentangling but can play an important role in the investigation of the formation of stellar binaries and multiple systems.

Other multiply periodic systems include pulsating stars in eclipsing binaries, such that the light curve displays modulation at both a pulsation period and an eclipsing binary period. Such systems act as stellar laboratories, and allow us to measure stellar masses and radii,

and compare observations with predictions of stellar pulsation models. There are detections of only ∼100 δ Scuti stars in eclipsing binaries (Kahraman Aliçavuş et al., 2017), and no known Galactic Cepheids in eclipsing binaries with orbital periods of less than 1 year (Evans et al., 2011). Previous work with SuperWASP identified a bright δ Scuti in a semi-detached eclipsing binary (Norton et al., 2016); as of yet there are no detections of RR Lyrae stars in eclipsing binaries.

2.3 O–C diagrams

As the description of types of variable stars has indicated, the period of variability is not always constant from cycle to cycle or year to year. In order to understand the period change that a variable star might experience, a diagnostic tool known as an O–C diagram, or *Observed–Calculated*, can be used. O–C diagrams compare the actual, or observed, timing of a given event and compares it to when that event is expected to occur, assuming a constant period (Sterken, 2005). Examples of this might be the eclipse of a component in a binary system, the transit of an exoplanet, or the peak in the light curve of a pulsating star.

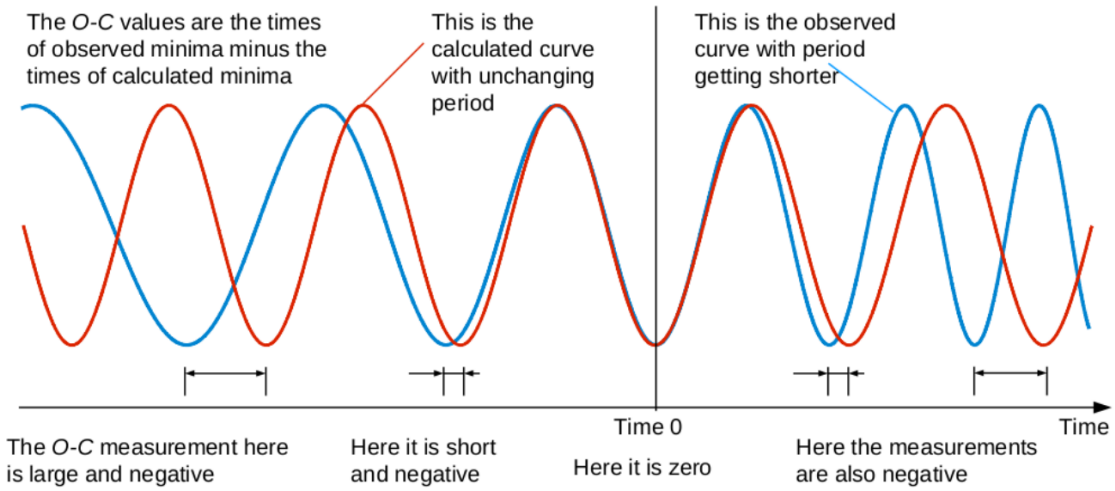

Fig. 2.18 A visual explanation of the determination of O–C values of a light curve when the period is known (Lohr, 2015).

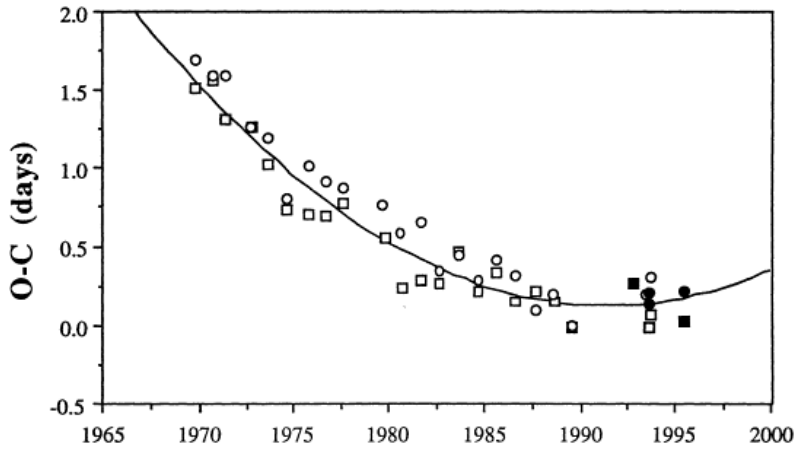

Fig. 2.19 The quadratic curve fitted to the O–C diagram for β Lyrae (Bruton et al., 1996).

In an O–C diagram, the horizontal axis is usually time, and the vertical is the O–C value (observed time minus calculated time). The shape of this diagram indicates the period change, or lack of, in the system. For a system with a linearly decreasing period, the O-C diagram will display a downwards opening parabola, and for a system with a linearly increasing period, the opposite parabola would be expected. If the period is not changing and the calculated period is correct, the O–C diagram will follow a straight, horizontal line, if the period is not changing but the period calculated is incorrect then the line will be sloping. The process of deriving a quadratic curve is illustrated clearly in Figure 2.18 (Lohr, 2015), and an example of the actual O–C diagram is shown in Figure 2.19 (Bruton et al., 1996).

For binary stars, understanding the period change identified in O–C diagrams is crucial for understanding the underlying physics of the system. If the period of the binary system is increasing, the separation between the stars is increasing; if the period is decreasing, the stars are moving close and a merger event may be on the horizon. Alternatively, periodic period decreases and increases can indicated the presence of an unseen third body, such as an exoplanet or third star.

2.4 Summary

This chapter has provided an overview of the field of stellar variables, including the types of variables, examples of light curves, and the underlying astrophysical mechanisms. In this thesis, whilst I research various aspects of stellar variability, I particularly focus on rotational variability and extreme long-period binary stars, and begin to explore the use of citizen science in classifying stellar variables. For each of these focus areas, photometric variability underpins the basis of the research. In Chapter 3 I provide an overview of the detection and analysis of stellar variables through all-sky surveys including the SuperWASP all-sky survey and the newly created catalogue of SuperWASP variable stars.

Chapter 3

Background to the SuperWASP All-Sky Survey and Other Relevant Surveys

In this chapter I will provide background information to the SuperWASP project, the archive, and the subsequent reduction and resulting periodicity catalogue. This chapter also includes details of the SuperWASP telescope and set up, and briefly introduces other relevant surveys used throughout this research: the ASAS-SN Catalogue of Variable Stars, Gaia-DR2, and XMM-DR9. Some of this chapter was published in Thiemann et al. (2020) and Thiemann et al. (2021).

3.1 The SuperWASP all-sky survey

The Wide Angle Search for Planets, SuperWASP, is the most successful ground-based search for transiting exoplanets (Pollacco et al., 2006), having discovered $\sim$200 hot Jupiters since 2004. SuperWASP is made up of two identical robotic observatories and a consortium of eight academic institutions.

SuperWASP (Pollacco et al., 2006) surveyed almost the entire night sky using two identical observatories, SuperWASP-North in La Palma, Canary Islands, and SuperWASP-

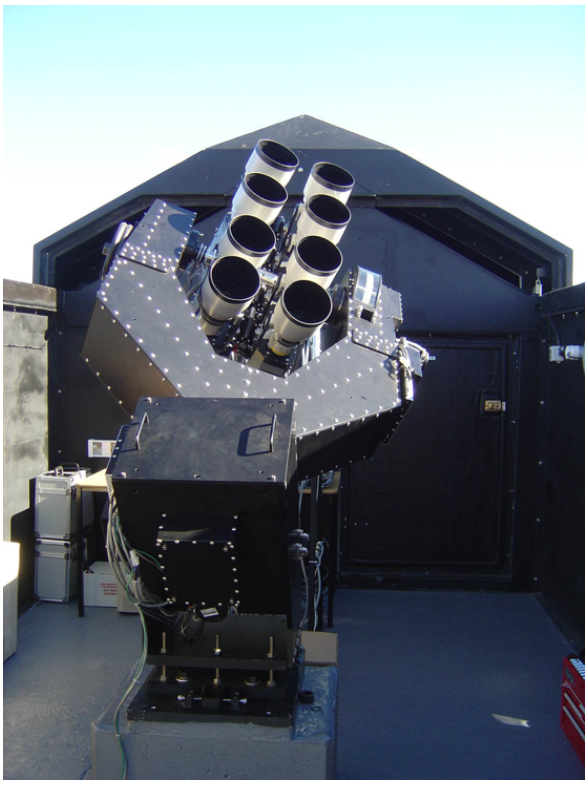

Fig. 3.1 SuperWASP-South cameras on the equatorial mount [Credit: David Anderson]

South in Sutherland, South Africa. SuperWASP-South is shown in Figure 3.1. Each robotic observatory consisted of 8 cameras each with a 14 cm aperture and a 7.8 $\times$ 7.8 square degree field of view, allowing for a total sky coverage of $\sim$500 square degrees per exposure through 16 cameras in total. The survey excludes the Galactic Plane where the large pixel scale of 16.7 arcsecond per pixel prevents separation of signals from individual stars in this dense stellar region. SuperWASP observations were reduced using the pipeline described in Pollacco et al. (2006). Over the course of $\sim$2800 nights between 2004–2013, SuperWASP accumulated $\sim$16 million images containing $\sim$580 billion data points corresponding to $\sim$31 million unique stars (Norton, 2018). The SuperWASP data set therefore provides high cadence and long baseline of observations for more than 30 million stars with magnitudes between $V = 8 - 15$.

For SuperWASP observations, 1 count s^{-1} after background subtraction is roughly equivalent to V$\sim$15. Therefore the mean SuperWASP magnitude is defined as V = -2.5

$\log_{10}(\frac{F}{10^6})$ where F is the mean SuperWASP flux and the pseudo-V magnitude is comparable to the Tycho V magnitude. A typical object in the SuperWASP archive will have ∼20,000 observations in its light curve. While the SuperWASP data can contain a significant level of noise, the long baseline of observations can often compensate for this in phase folded light curves.

SuperWASP photometry is carried out by placing apertures of sizes 2.5, 3.5 and 4.5 pixels on the images at pre-defined positions identified using the USNO catalogue as an input (Pollacco et al., 2006). However, the large pixel size of the individual cameras means that it is possible that a single star can be associated with two or more different identifiers in the SuperWASP archive, and that light from multiple stars can appear within the same photometric aperture.

Objects in the SuperWASP archive are named according to IAU conventions, and are named based on the best-measured co-ordinates[1]. The form of the SuperWASP catalogue name is:

1SWASP Jhhmmss.ss±ddmmss.s

The SuperWASP archive contains multiple entries for many single objects, and as such, duplicates must be removed before working with this data.

3.1.1 SuperWASP Discoveries

The full SuperWASP photometric archive contains >30 million light curves of relatively bright stars (V≤15), observed with a high cadence (as short as 30 seconds) and long baseline (∼11 years). A previous period search using the first few years of the SuperWASP archive enabled a significant amount of research in the field of stellar variability.

Previous work with SuperWASP stellar variables includes: the identification of 140 short-period eclipsing binaries close to the period cut-off (Lohr et al., 2013); the identification of

[1] wasp.warwick.ac.uk/archive/docs/structure.shtml

period change in post common-envelope eclipsing binary systems to search for circumbinary planets (Lohr et al., 2014); the discovery of a doubly eclipsing quintuple system (Lohr et al., 2015b); the identification of period change in ∼1400 eclipsing binaries (Lohr et al., 2015a); the discovery of a δ Scuti star in an eclipsing binary (Norton et al., 2016); the study of ∼5000 RR Lyrae stars and identification of ∼800 Blazhko effect systems (Greer et al., 2017); and the study of rotationally modulated variables (Thiemann et al., 2020). A more recent re-analysis of this archive detected ∼8 million potential periods in ∼3 million unique objects (Norton, 2018).

3.1.2 SuperWASP Periodicity Catalogue

Norton (2018) recently performed a re-analysis of the entire SuperWASP archive with the aim of detecting all periodic variables. The re-analysis comprised a one-dimensional CLEAN power spectrum analysis (based on the technique outlined by Roberts et al. (1987)) as well as a phase dispersion minimisation and folding analysis (following the method of Davies (1990)). Only periods that were significantly detected using *both* methods were considered to be plausible. For each light curve, all periods that passed these criteria were recorded, with a significance value recorded from both the folding analysis and the Fourier analysis. The periods identified have an average uncertainty of $\sim \pm 0.1\%$.

This re-analysis detected ∼8 million candidate periods of stellar variables in ∼3 million unique objects (∼10% of objects in the SuperWASP archive), shown in the left portion of Figure 3.2. There are significant numbers of excess periods close to integer multiples or fractions of a sidereal day or lunar month, indicated by coloured vertical lines (red lines correspond to fractions of a day; light blue corresponds to multiples of a day; dark blue corresponds to the monthly and longer cycles). All such periods are flagged and may be discarded. The upper panel shows the cumulative period histogram while the lower one, whose vertical axis is truncated, shows the regular histogram.

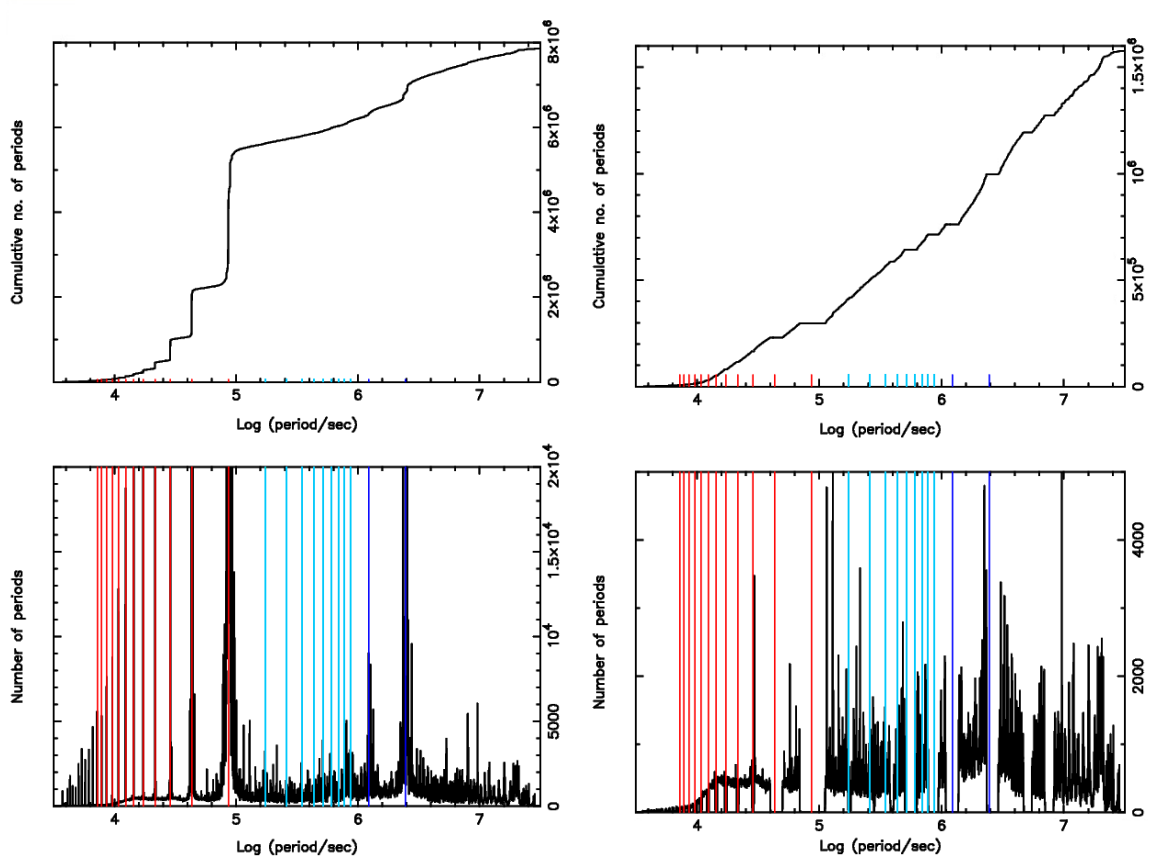

Fig. 3.2 **Left:** Histogram of the identified periods in all objects in the *SuperWASP Periodicity Catalogue*.
Right: Histogram of all unflagged periods corresponding to objects in the *SuperWASP Periodicity Catalogue*.

A significant number of period detections result from systematic effects in the SuperWASP photometric data, resulting in the detection of periods close to integer fractions or multiples of a sidereal day or lunar month (i.e. 1 day, 1/2 day, 1/4 day, etc.). Periods flagged as affected by one of these effects were removed from the data set, leaving 1,569,061 candidate periods in 767,199 unique objects, shown in right portion of Figure 3.2. The upper panel shows the cumulative period histogram while the lower one shows the regular histogram.

Clearly some genuine periods will have been rejected by this method, but if we extrapolate across the gaps, the rejected genuine periods should amount to no more than 5% of the total.

The *SuperWASP periodicity catalogue* is available in the Warwick SuperWASP archive[2] as the table *period_ajn5*.

As a result of these systematic effects, any object "flagged" as having a period close to these values was rejected from this work. All "unflagged" objects are the subject of a citizen science Zooniverse project aiming to classify 1,569,061 periods in 767,199 objects ($\sim$2.5% of objects in the SuperWASP archive), resulting in the construction of catalogues of types of stellar variable (Norton, 2018) (see Chapter 12).

3.1.3 Details of the SuperWASP periodicity catalogue

The *SuperWASP periodicity catalogue* has a number of key parameters worth noting, used in this work. These parameters are: CAMERA_ID - a dummy camera ID indicating "all cameras"; *OBJ_ID* - the unique SuperWASP ID; *IDX* - the sequence number for periods in a given object; *PERIOD* - the period in seconds; *SIGMA* - the significance measure from the power spectrum using the σ parameter; *CHI* - the measure of the goodness of the folded light curve using the χ^2 parameter; *FLAG* - the period flag where "0" indicates a good period.

In addition to the most useful parameters, *OBJ_ID* and the period, the other parameters can be useful in characterising the most likely 'best' period, by taking, for example, the highest $\chi \times \sigma$ value for an object with multiple period detections. As a general rule, the lower the value of *IDX*, the higher the $\chi \times \sigma$ value.

To gain additional parameters through which to characterise SuperWASP objects, the *period_ajn5* file can be combined with other tables in the SuperWASP archive. Such tables include *photsummary* which contains photometric measurements of objects, *nomad* which includes columns from the NOMAD 1.0 catalogue, *hunterdet* which contains output from runs of the hunter transit detection code, and the *default* table which represents the root catalogue[3]. The most commonly used additional tables and parameters include: *photsummary*: *npts* - the

[2]http://wasp.warwick.ac.uk/archive/docs/index.shtml
[3]http://wasp.warwick.ac.uk/archive/docs/tables.shtml

number of data points for an object; *photsummary*: *flux_mean* - the mean flux of the object in the observed interval; *hunderdet*: *teff_vk*, *teff_jh* - the stellar temperatures in K derived from $V-K$ and $J-H$ colour; *nomad*: *bmag*, *vmag*, *jmag*, *hmag*, *kmag* - the B, V, J, H, K magnitudes derived from NOMAD 1.0; *default*: *ra*, *declination* - the RA and declination in degrees.

3.2 ASAS-SN

The All-Sky Automated Survey for Supernovae (ASAS-SN) is an optical survey which has monitored the entire sky since 2014 (Jayasinghe et al., 2019). ASAS-SN is currently comprised of 24 telescopes based in Hawaii, Chile, Texas, South Africa, and China. Each camera has a field of view of 4.5 deg^2, and a pixel scale of $8''$. Despite the relatively large pixel scale, the typical astrometric error is $\sim 1''$.

Like SuperWASP, this survey did not aim to study stellar variability, instead focusing on bright supernovae, but given the cadence of $\sim$2-3 days, and a limiting magnitude of V$\leq$17 mag, ASAS-SN has been able to study $>$ 50 million bright sources. Light curves of variable stars are classified using a random forest classifier, and verified against other catalogues, as described in Jayasinghe et al. (2018). Cross-correlated with other catalogues, e.g. NOMAD, 99% of ASAS-SN variables detected are within $5.2''$ of a previously catalogued star. It is worth noting that ASAS-SN uses APASS (Henden et al., 2015) magnitudes, which tend to deviate from the V-band ASAS-SN magnitudes for V$>$14 due to blended sources where multiple APASS sources are detected by a single ASAS-SN pixel.

Each object in the ASAS-SN Catalogue of Variable Stars contains information about the variability type, classification probability, period, and magnitude, amongst other values. The ASAS-SN Catalogue of Variable Stars contains 666,502 light curves, and all light curves are available to the public. The catalogue contains $\sim$150,000 eclipsing binaries, of which $\sim$48,000 are EAs, $\sim$25,000 are EBs, and $\sim$76,000 are EWs.

3.3 XMM-Newton

XMM-Newton[4] (Rosen et al., 2016) is the European Space Agency's X-ray Multi-Mirror satellite. It is the most powerful X-ray telescope placed in orbit and has detected hundreds of thousands of X-ray sources thanks to its wide field of view (30′ across) and resolution of 5" (full width half-maximum) at all wavelengths. XMM-Newton consists of over 170 'Wolter-type I' wafer-thin concentric cylindrical mirrors contained within three mirror modules, giving a large collecting area to detect X-rays over a spectral range of 1–120 Å (12–0.2 keV). By following a highly eccentric orbit which has varied between an apogee altitude of 99,000–115,000 km and perigee altitude of 6,000–22,000 km, XMM-Newton is able to make long, uninterrupted observations.

The 4XMM-DR9 catalogue contains detections of 550,124 unique X-ray sources from 11,204 observations made by the XMM-Newton EPIC cameras covering 1089 square degrees. The detections cover the energy range 0.2–12 keV and span 19 years between 3 February 2000 and 26 February 2019. 4XMM-DR9 objects are named according to IAU conventions, and the form is taken from the right ascension (RA) and declination (DEC) of the catalogue[5]. In this work, 4XMM-DR9 is used in the characterisation of the rotation-activity relation (see Chapters 4 and 5).

3.4 Gaia

Gaia[6] is an ESA space-based observatory operating at the Sun-Earth L_2 Lagrangian point. The Gaia payload is composed of three main instruments: astrometry (Astro) instrument, photometric (BP/RP) instrument, and Radial-Velocity spectrometer (RVS) (Gaia Collaboration 2016, 2018).

[4]http://sci.esa.int/xmm-newton/
[5]https://www.cosmos.esa.int/web/xmm-newton/source-naming-convention
[6]http://sci.esa.int/gaia/

The second all-sky Gaia catalogue, Gaia Data Release 2 (Gaia-DR2), was released on 25 April 2018. It contains positions on the sky, parallaxes, and proper motions for more than 1.3 billion sources. There is a limiting magnitude of G = 21, and a bright limit of $\sim$ 3. It also contains classifications for more than 550,000 variable sources, with almost 364,000 objects with an estimated variable type.

The naming convention for sources within the Gaia-DR2 catalogue differ from that of SuperWASP and XMM-Newton, and are instead identified using the Gaia Source Identifier. Gaia objects are named using a level 12 HEALPix index encoded in their upper bits[7]. In this work, Gaia-DR2 is used in the characterisation of the rotation-activity relation (see Chapters 4 and 5) and to assess luminosity and stellar type in work on near contact red giant eclipsing binaries (see Chapters 7, 8, and 9).

3.5 Summary

In this chapter, I detailed the relevant all-sky surveys that are particularly useful for the study of stellar variability in this research. The SuperWASP all-sky survey's photometric archive containing $>$30 million light curves serves at the basis and starting point for this thesis, and whilst it is a huge archive, the initial cut to $\sim$1.6 million light curves of stellar variables makes the data exploration more manageable. In future chapters, SuperWASP will be used to explore rotational variability, binary stars, and the intersection of stellar variability and citizen science.

[7]https://www.cosmos.esa.int/web/gaia/dr2

Chapter 4

Background to the Rotation-Activity Relation

My first foray into the SuperWASP data came in the form of investigating rotational variability, something barely touched upon in previous explorations of the archive. In this first section of the thesis, I take a dive into rotational variability. In this chapter, I introduce the background to the relationship between the stellar rotation period and the X-ray to bolometric flux ratio, known as the rotation-activity relation. This chapter will cover the history of the relationship, and provide the scientific context as to why this relationship is key for understanding the internal stellar astrophysics. I also detail some of the previous work on this relationship, and briefly discuss how this relationship can impact on work on exoplanet habitability. Some of this chapter was published in Thiemann et al. (2020).

4.1 History

The rotation-activity relation is the relationship between the rotation period and the X-ray flux, or coronal activity, of stars. It was described by Wilson (1966) as "one of the older, but

still troublesome, problems of astrophysics", and "one of the most intriguing unexplained phenomena of stellar astronomy" by Kraft (1967).

Pioneering work on the rotation-activity relation by Kraft (1967) noted that rotational velocity is greater in stars with a Ca II emission. From the strong link between Ca II emission and stellar age, it followed that rotational velocity declines with age. It was also proposed that magnetically coupled winds are responsible for the deceleration of a star's rotation, even during the main sequence. Skumanich (1972) confirmed this link between chromospheric Ca II & K emission and the decrease in rotation rate, suggesting that the rotation-activity relation was a causal consequence of the internal dynamo action.

The first correlation between X-ray luminosity and rotation was first discovered for RS Canum Venaticorum (RS CVn) systems by Walter and Bowyer (1981) and generalised by Pallavicini et al. (1981). RS CVns have very active chromospheres and large star spots which are believe to be the main cause of luminosity variations, with star spots covering 10–20% of the surface (Solanki, 2018).

Further work by Pallavicini et al. (1981) found that X-ray luminosity scaled as $L_X \propto (v \sin i)^{1.9}$, and was the first to provide evidence for dynamo-induced coronal activity. Pallavicini et al. (1981) went on to describe the dependence of X-ray luminosity on rotation, and found that whilst X-ray luminosity scales with bolometric luminosity for early-type stars (O3-A5), the X-ray luminosity of late-type stars (G–M) shows no dependence on bolometric luminosity. Building on this, and utilising the Mt. Wilson survey, Noyes et al. (1984) quantified the rotation-activity relation using chromospheric Ca II & K emission. It was shown that the chromospheric–bolometric flux ratio correlates to the rotation period–colour ratio.

Although Noyes et al. (1984) characterised the rotation-activity relation from observations of chromospheric Ca II & K emission, other activity diagnostics can be used to determine the relation, including Hα emission (Douglas et al., 2014; Newton et al., 2017; Soderblom et al., 1993), surface averaged magnetic field strengths (Vidotto et al., 2014), magnetic flux

B_f (Reiners et al., 2009), and flare activity (Audard et al., 2000). Noyes et al. (1984) also was the first to determine a single parameter, the Rossby number, as the ratio of rotational period to convective turnover time of internal stellar gas cells.

In 2003, the rotation-activity relation was revisited by Pizzolato et al. (2003), using a sample of 259 observations of late-type MS stars, empirically deriving a timescale to investigate the relationship between X-ray flux and an X-ray-based Rossby number, $Ro = P_{rot}/\tau_e$, as the ratio of stellar rotation period, P_{rot}, to the convective turnover time, τ, of plasma covering a certain distance in the convective envelope, and which acts as a parameter for the stellar dynamo (Landin et al., 2010). More recently, magnetic mapping studies by Vidotto et al. (2014) have investigated dynamo theory, concluding that dynamos are linear with magnetic fields and that X-ray rotation scales with magnetic energy density. To date, the size of samples of MS stars used to study the rotation-activity relation has been in the hundreds.

4.2 Overview

The history of the rotation-activity relation is a fascinating one. In this next section, I will briefly introduce the relevant scientific context to the relationship. This will cover the X-ray emission process and stellar dynamo theory, before moving into an overview of the different regimes of the rotation-activity relation.

4.3 X-ray emission processes

Every star has a magnetic field, and an important product of such a field is X-ray emission. The majority of X-ray emissions originate from active regions - concentrated areas of magnetic fields on the stellar surface such as star spots, collisions between the wind and

circumstellar material (Parkin et al., 2009), and small-scale wind shocks (Lucy and White, 1980).

In solar and late-type stars, the stellar magnetic field is generated in a magnetically confined plasma (Vaiana et al., 1981). This plasma is driven by the stellar magnetic dynamo, which is in turn driven by the internal stellar differential rotation (Parker (1955); Wilson (1966); Kraft (1967)). This process was confirmed in the Sun through helioseismology (Duvall et al., 1984), and is exhibited in the Sun through solar activity cycles. Cool late-type stars (G–M) emit X-rays primarily through coronal activity and flares. Whilst these late-type stars can be highly variable in their emission, many saturate at $L_X/L_{bol} \sim 10^{-3}$ (Testa et al., 2015). Thanks to the proximity of the Sun, we have been able to characterise this type of X-ray emission, the 11 year solar cycle, and rotational modulation due to star spots in detail.

For early-type stars, shocks produced by instabilities in the radiatively driven stellar winds of massive stars are the main causes of X-ray emission (Lucy and White, 1980). These stars exhibit low levels of X-ray variability, where $L_X/L_{bol} \sim 10^{-7}$ (Owocki et al., 1988). In the PMS phase, stars appear to be moderate emitters of X-rays, through powerful coronal activity, accretion, jets, magnetic fields, and stellar winds (Testa et al., 2015).

A few exceptions to this are late B-type to mid-A-type stars, which are weak emitters or are X-ray dark (Czesla and Schmitt, 2007). Most late-type stars are X-ray emitters, and often exhibit variability over four orders of magnitude or more (Testa, 2010). Recent studies by X-ray observatories, Chandra and XMM-Newton, have been integral to understanding X-ray emission processes in stars.

Over the lifetime of a star, the rotation rate and X-ray activity changes significantly. Protostars grow through the accretion of gas and dust from a molecular cloud and begin the PMS phase as they contract under gravity. PMS stars are stellar objects which have not yet initiated hydrogen burning in the core. Their luminosity is a result of the release of

gravitational potential energy as they contract. PMS stars can be many times more X-ray luminous than the Sun, due to their comparably large surface area (Gregory et al., 2016).

Such stars in the youngest star forming regions do not abide by the rotation-activity relation, and can exhibit signs of saturation regardless of rotation rate, albeit with a greater scatter in L_X/L_{bol} (Preibisch and Feigelson, 2005).

As a star ages and moves from the Pre-Main Sequence (PMS) to the Main Sequence (MS), it experiences spin-down, the internal dynamo weakens, and as a result, the coronal X-ray emission decreases (Wright et al., 2011). Magnetic braking is active in PMS phase, but opposed by collapse/contraction which would speed up the star, and continues on the MS. Spin-down is driven primarily by mass loss through the magnetised stellar winds steadily transferring angular momentum away from the star. For MS stars, this decline in rotation can be approximated by Skumanich's law, $\Omega_e \propto t^{-1/2}$ (Skumanich, 1972), where Ω_e is the angular velocity of the star's equator, and t is the age of the star.

4.4 Stellar dynamo theory and the tachocline

Like many stars, the Sun's magnetic field drives all solar activity, and is generated internally by a hydromagnetic dynamo (Ryan and Norton, 2010b). This dynamo is thought to be partly driven by interior differential rotation, which itself is generated in the rotating convective envelope by the Coriolis force, although the exact method is not yet fully understood (Wright and Drake, 2016).

In solar-type stars, magnetic fields generate atmospheric and coronal emission in the UV to X-ray wavelengths, flares, star-spots and other phenomena. These phenomena act as a reliable method of studying the stellar dynamo (Charbonneau, 2014). Using Skumanich's law and work by Vidotto et al. (2014), and assuming that stellar magnetic fields scale linearly with rotation rate of the star, Gregory (2016) shows that X-ray luminosity scales with magnetic energy density, $L_X \propto B^2$, and coronal activity of a star scales with rotation. This is to be

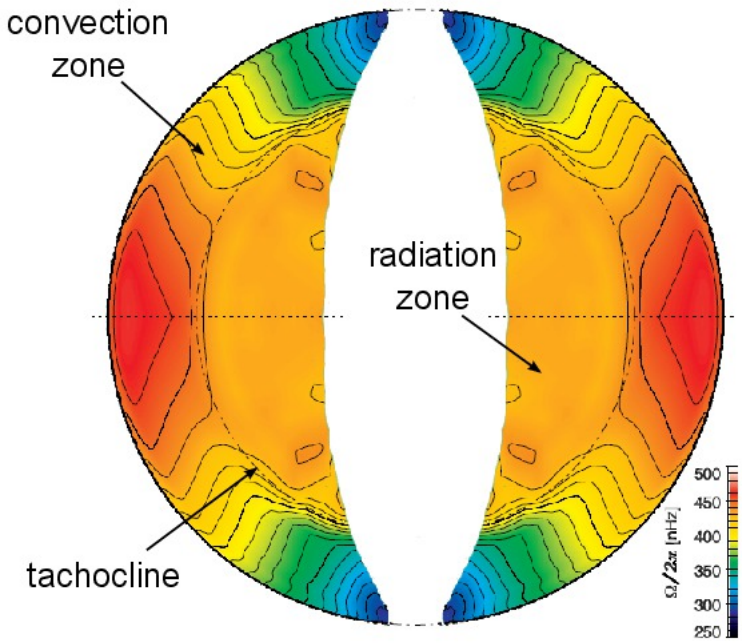

Fig. 4.1 The shear layer between areas of different angular velocity in the solar interior is known as the tachocline. Adapted from Korzennik and Eff-Darwich (2011).

expected, since magnetic activity and reconnection produces X-ray emission. Whilst the internal dynamos of stars are not yet fully understood, the rotation-activity relation acts as an important probe of the stellar dynamo.

Within the stellar dynamo, the tachocline is a boundary layer in solar-type stars between the radiative core and the convective envelope. Differential rotation in these layers generates the magnetic field, and has long been thought to be dependent on the shearing of internal magnetic fields in these regions (Spiegel and Zahn, 1992). The tachocline is of particular interest to dynamo theorists. In the Sun, the tachocline is located in the outer third of the Sun by radius (Charbonneau et al., 1999). At this location, differential rotation is high, causing a large shear profile. In turn, this generates large scale magnetic fields. Figure 4.1 shows the tachocline produced when such shearing occurs.

Fully convective stars (MS stars of spectral type later than M3-3.5) do not have a tachocline, and although the exact form is yet unknown, it is expected that their internal

dynamo mechanism is very different from solar-type stars (Wright and Drake, 2016). For these reasons, the role of tachoclines in the stellar dynamo is debated. Wright and Drake (2016) suggest that since the rotation-activity relationship is a strong proxy for the magnetic dynamo, observations of the rotation-activity relation in fully convective stars suggest that tachoclines are not a critical ingredient in the solar dynamo. Instead, support is shown for models in which the dynamo is present throughout the convection zone.

4.5 Rossby number

In order to analytically investigate the aspects of the stellar dynamo, a numerical method is required. For this reason, the rotation-activity relation is often interpreted through the Rossby number, *Ro*, or Coriolis number, which describes the strength of the rotational effect on convective flows. The Rossby number was first defined by Noyes et al. (1984) as $Ro = P_{rot}/\tau$, the ratio of rotational period to convective turnover time of gas cells within a star, and acts as a parameter for the stellar dynamo (Landin et al., 2010). There is debate as to its definition, and to the influence of the convective turnover time.

The Rossby number is commonly used when visualising the rotation-activity relation. By plotting L_X/L_{bol} against *Ro*, the scatter on rotation-activity diagrams is greatly reduced compared to plots against P_{rot}, especially for solar-type stars (Stepien, 1994). Figure 4.2 indicates the reduction in scatter clearly. The use of the Rossby number in plotting also allows for comparison of the rotation-activity relation across different spectral types.

There is some debate as to the most accurate way of calculating the Rossby number due to the parameter τ. The most common methods use either the empirical convective timescale, τ_e, the local convective turnover time, τ_c, or the global convective turnover time, τ_g. Each has their advantages and disadvantages, discussed in Section 4.6. This debate around which value of τ to use primarily stems from the need to minimise scatter. Another source of debate lies in the dependence of the Rossby number on stellar mass, with some methods having no

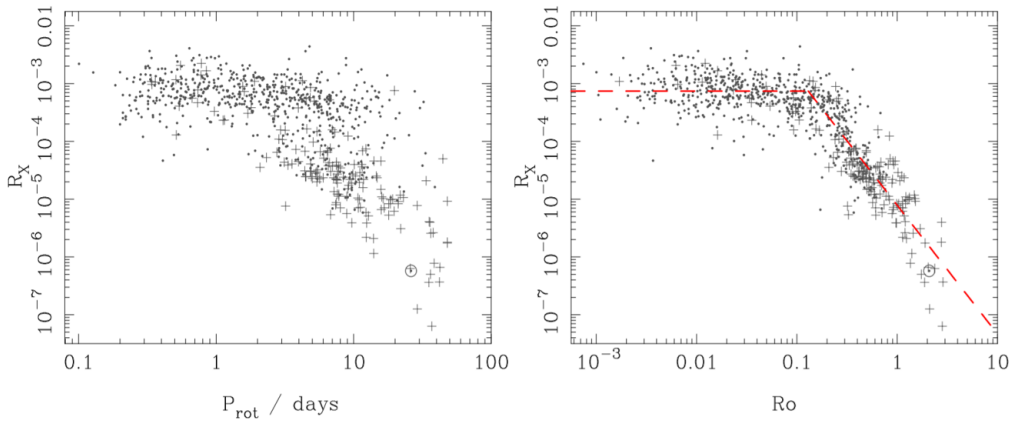

Fig. 4.2 Left: A plot of P_{rot} against the bolometric flux ratio for a sample of 824 stars. Right: A plot of Ro against the bolometric flux ratio for the same sample. The red line indicates the fits for the saturated and unsaturated regimes (Wright et al., 2011).

dependence of mass. For such methods, there is the concern that this removes dependence on other parameters that may be important.

There is also debate as to whether the Rossby number is even necessary. Reiners et al. (2014) states that scatter can be more efficiently reduced by ignoring the Rossby number, and instead plotting against rotational period, P, and stellar radius, R: L_X/L_{bol} against $P^{-2}R^{-4}$. This study suggests that only the rotation period determines the total X-ray emission. Studies of a greater number of stars, plus in-depth modelling of the stellar dynamo may help determine an answer to this.

4.6 Convective turnover time

Used in the calculation of the Rossby number, $Ro = P_{rot}/\tau$, τ is the convective turnover time of gas cells within the star. It can be calculated using a number of different routes, each deriving a variation of τ. Landin et al. (2010) builds on a body of previous work, using the local convective turnover time, τ_c, to calculate Ro. To calculate τ_c, one must make an assumption about the location of the convection zone in the stellar dynamo. Since τ_c is strongly dependent on depth, the value can vary significantly. Following work by L. Gilliland

(1985), Landin et al. (2010) calculates τ_c at a distance of halfway down the mixing depth above the convection zone. The local convective turnover time has the relationship:

$$\tau_c = \alpha \frac{H_P}{v} \tag{4.1}$$

where $\alpha \frac{H_P}{2}$ is half the mixing depth, and v is the convective velocity.

Alternative methods to calculate the Rossby number use either the global convective timescale, τ_g, or the empirical convective timescale, τ_e (Pizzolato et al., 2003). τ_g has the advantage that there is less reliance on an arbitrary mixing depth (Landin et al., 2010). The global convective turnover time has the relationship:

$$\tau_g = \int_{R_b}^{R_*} \frac{dr}{v} \tag{4.2}$$

where R_b is the radius as the base of the convective zone and R_* is the stellar radius.

The empirical convective turnover time, τ_e, was first calculated by Pizzolato et al. (2003) and improved by Landin et al. (2010) by first considering the power law:

$$L_x/L_{bol} = A_k P_{rot}^{-2} \tag{4.3}$$

where A_k is dependent on their mass range. This relationship describes the unsaturated regime. Landin et al. (2010) then considers a single relationship for all stars by scaling:

$$P_{rot} \Rightarrow \frac{P_{rot}}{\tau_e(M)} \tag{4.4}$$

where $\tau_e(M)$ is a mass dependent function which can be obtained from $(A_k/C)^{1/2}$ with $C = const$, such that:

$$L_X/L_{bol} = C \frac{P_{rot}}{\tau_e(M)} \tag{4.5}$$

where $\frac{P_{rot}}{\tau_e(M)}$ is described at the 'X-ray empirical Rossby number'. From this, τ_e can be empirically defined.

A simpler method is used by Wright et al. (2011) and Wright et al. (2018), who derive an alternative method for calculating τ, also briefly covered in Chapter 5. This form of the relationship relies on stellar colour, $V - K_s$ and takes the form of:

$$\log \tau = 0.64(\pm^{0.10}_{0.12}) + 0.25(\pm^{0.08}_{0.07})[V - K_s] \tag{4.6}$$

Each method has their advantages and disadvantages. τ_e has problems in that overturn time varies with depth, and it is not known at which depth the dynamo is most efficient. Other issues are that convective turnover time varies with parameters such as metallicity and age (Landin et al. 2010; Spada et al. 2013). On the other hand, τ_e has the advantage of calculating the Rossby number independent of stellar mass, for both saturated and non-saturated stars (Pizzolato et al., 2003). As such, Landin et al. (2010) concludes that τ_c is superior to τ_e. τ_g has a low reliance on mixing depth, but provides a lower accuracy, and τ (Wright et al., 2018) is derived empirically from previous work, so may provide a self consistent result.

4.7 Saturation regimes

Having calculated $Ro = P_{rot}/\tau$, and with L_x/L_{bol} available from observational data, the rotation-activity relation can be visualised. Numerous studies of late-type MS stars (e.g., Pizzolato et al. (2003), Wright et al. (2011)) have characterised the relationship between stellar activity and rotation period, dividing the rotation activity into two main regimes for rotation periods of $\sim$ 1–10 d: the unsaturated and saturated regimes, and a third possible regime, the supersaturated regime. The two main regimes can be seen in Figures 4.2 and 4.3. However, it is thought that MS stars with fully convective interiors can follow three, possibly four, regimes: the unsaturated, saturated, supersaturated regimes, and regime of anti-solar

differential rotation. This fourth regime is not yet well understood, or even confirmed to exist. This section will briefly describe each regime, as well as the saturation points, and stars which are understood not to follow the regimes.

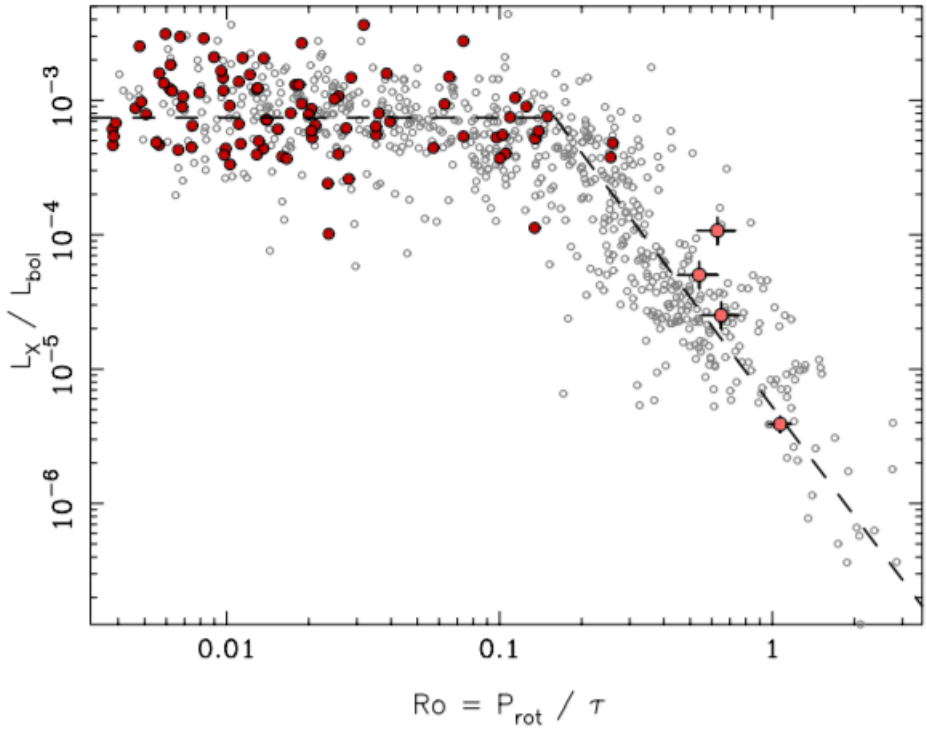

Fig. 4.3 The rotation-activity relation for MS stars: Fractional X-ray luminosity against Rossby number. Red and light red points indicate fully convective stars; grey points indicate partially convective stars. The dashed black line indicates the fits of the saturated and unsaturated regimes (Wright and Drake, 2016).

4.7.1 The unsaturated regime

The unsaturated regime in the rotation-activity relation lies in the region where $Ro > 0.13$. In this regime, the fractional X-ray luminosity, L_x/L_{bol}, anticorrelates with Ro. In the unsaturated regime, for $Ro > 0.13$, Wright et al. (2011) finds a power-law slope of $\beta \sim -2.7$ for F- to M- type MS stars. This strong rotation-activity relation indicates that the dynamo is responsible for stellar activity levels.

The unsaturated regime has been investigated in many studies using photometric observations and chromospheric activity. It is believed to be a good probe for the efficiency of heating of the corona by the internal stellar dynamo, and has been interpreted by authors including Pizzolato et al. (2003) as good evidence for an underlying physical relationship. It has been found that slow rotating early-type stars have partially convective interiors and follow the unsaturated regime. A study by Wright and Drake (2016) found that fully convective M-dwarfs, if spun-down enough, also follow this regime.

Saturation occurs at $Ro_{sat} \sim 0.13$ for all fast-rotating solar and late-type stars, regardless of spectral type (Vilhu, 1984). The saturation threshold, Ro_{sat} scales with the convective turnover time, τ, such that Ro is constant. Although the exact value of Ro_{sat} is not agreed on, studies of the saturation point agree that the value is $Ro_{sat} \sim 0.1$.

4.7.2 The saturated regime

For fast rotating solar and late-type MS stars, the relationship is found to break down (Micela et al., 1985), and saturation of L_x/L_{bol} occurs at $Ro \sim 0.13$, regardless of spectral type (Vilhu, 1984), with L_x/L_{bol} saturating at $L_x/L_{bol} \sim 10^{-3}$. At this point X-ray emission becomes a function of bolometric luminosity alone (Pizzolato et al., 2003), i.e. the colour, mass, or radius of the star. The saturation threshold, Ro_{sat}, scales with the convective turnover time, τ, such that Ro is constant. The cause of saturation is still debated. Theories include centrifugal stripping of the corona at high rotation rates (Jardine and Unruh, 1999), saturation of the filling factor of active regions on the stellar surface, or a saturation of the dynamo itself (Vilhu, 1984).

To date, studies have found that nearly all fully convective, fast-rotating solar and late-type stars exhibit saturation of coronal X-rays (Wright et al., 2011). The rotation period at which saturation occurs is longer for later spectral type stars, due to larger convective turnover times (Landin et al. 2010; Wright et al. 2011). It has also been found that fully

convective slow rotators show a solar-type rotation-activity relation (Wright et al., 2018). Despite this, a comprehensive and satisfactory dynamo theory that explains both the saturated and unsaturated regimes is yet to be found (Brandenburg et al., 2011; Weiss, 2005). It is not yet fully understood what causes saturation; a number of possible causes are discussed in Section 4.8.

4.7.3 The supersaturated regime

In addition to these two regimes, studies have indicated that a third regime, supersaturation, may exist for the very fastest rotating MS stars. It may occur at $Ro \leq 0.01$ for fast rotators at very high rotational velocities. Supersaturation has been detected in PMS stars, M-dwarfs, and W UMa contact binaries (Argiroffi et al., 2016; Jeffries et al., 2011; Randich, 1998; Stępień et al., 2001). In this regime, the X-ray to bolometric luminosity ratio has been observed to decrease slightly below the saturation level (Jardine, 2004; Jardine and Unruh, 1999; Jeffries et al., 2011). Although very scarcely observed, supersaturation has been seen to occur in young ($<$ 100 Myr) G- and K-type stars in young clusters (Randich et al., 1996). Whilst Argiroffi et al. (2016) has found evidence for supersaturation in pre-main-sequence (PMS) stars, studies such as Wright et al. (2011) have found no statistically significant evidence for supersaturation in MS stars, or any decline in luminosity ratio for fast rotators.

4.7.4 Anti-solar differential rotation

A fourth newly-identified regime, known as anti-solar differential rotation, is also thought to exist for the oldest slowest rotating stars, however, evidence for its existence has not yet been convincingly seen. At $Ro > 1$, solar-like differential rotation, with faster rotation at the equator and slower rotation at the poles, switches to anti-solar differential rotation, with slower equatorial rotation and faster polar rotation (Gastine et al., 2014).

Differential rotation is key for the generation of stellar magnetic fields, and two main regimes of stellar differential rotation exist, solar-like, with faster rotation at the equator and slower rotation at the poles, and anti-solar, with slower equatorial rotation and faster polar rotation (Gastine et al., 2014). Difficulties in observing slowly rotating stars which may exhibit anti-solar differential rotation (ASDR) means it is unclear as to how common it is in MS stars. Previously, ASDR had only been reported in a small number of K giants (Kővári et al., 2017; Özdarcan et al., 2016; Strassmeier et al., 2003) but not in dwarfs. However theoretical work by Gastine et al. (2014) provides evidence of ASDR in cool MS stars with large Rossby numbers. For cool MS stars, the change in regimes between the main solar-like and anti-solar regimes occurs when a $Ro \sim 1$ is reached (Gastine et al., 2014), which corresponds to a transition at $Ro \sim 2$ identified by van Saders et al. (2016). More recently, Brandenburg and Giampapa (2018) identified enhanced activity in solar-like stars in the open cluster M67, attributing this phenomena to a transition in differential rotation from solar-like to ASDR. As stars reach the critical Rossby number, differential rotation switches from solar-like to anti-solar. At this point, shear induced by differential rotation increases as a result of conservation of angular momentum, resulting in enhanced activity levels (Karak et al., 2015).

Brandenburg and Giampapa (2018) observed that the oldest slowest rotating stars exhibit evidence for anti-solar differential rotation in the form of enhanced activity levels at slower than expected rotation periods. This poses a problem for using rotation periods as a predictor of stellar age. Based on the relationship found by Skumanich (1972), 'gyrochronology' is a technique of using the stellar rotation period to calculate its age based on the Sun and young clusters (Barnes, 2007), and uses rotation periods and $B-V$ colour to derive the age of low-mass MS stars. The technique of gyrochronology is underpinned by reliable angular momentum loss through the stellar wind as a result of the stellar dynamo, however observational evidence suggests that global dynamo shut down may begin towards the middle

of a MS star's lifetime (Metcalfe and van Saders, 2017). A shut down of the dynamo reduces angular momentum loss, and as such, the relationships that gyrochronology relies on breaks down.

As a result, the rotation-age relationship may not be useful for MS stars late in their life (Metcalfe and Egeland, 2019). Whilst it appears that rotation may not be a valid age predictor for all MS stars, the Skumanich chromospheric activity-age relationship should still prove to be a good predictor of age.

4.7.5 Stars which do not follow the regimes

PMS stars do not follow the rotation-activity relation, showing saturation regardless of rotation rate but with a greater scatter in L_X/L_{bol} compared to MS stars (Preibisch and Feigelson, 2005). PMS stars evolve to form MS stars, and thus must begin to exhibit signs of following the rotation-activity relation regimes. Promisingly, observations by Argiroffi et al. (2016) found PMS beginning to display activity regimes similar to MS stars. OBA and F-type stars are also known not to follow the rotation-activity relation (Wright et al., 2018).

4.8 Causes of saturation

It is generally accepted that chromospheric and coronal activity saturates at high rotation rates, and saturation is observed in stars up to spectral type M8.5 (Mohanty and Basri, 2003). However, the processes which causes saturation of X-ray activity is still debated.

Saturation may be related to the efficiency of the stellar dynamo, hence intrinsic changes in the behaviour of the dynamo may be the cause (Gilman, 1983). This has been supported by observations by Reiners et al. (2009) of saturation in M-dwarfs. Jardine and Unruh (1999) argue that saturation of the underlying dynamo is not necessarily proven, and instead the cause may be centrifugal stripping of the corona. Wright et al. (2011) suggest that a change

in dynamo configuration itself is actually the cause of saturation, and as such, the unsaturated and saturated regimes should be treated as separate dynamo configurations.

Others have suggested that saturation of the filling factor of active areas of the stars are the cause (Vilhu, 1984). Saturation may simply occur because the star runs out of available surface area to host more active regions, limiting coronal emission (Jardine and Unruh, 1999). However, Reiners et al. (2009) argues that since magnetic flux shows the same saturation as activity saturation, activity cannot reach saturation purely because the surface area of the star has been filled by fields. Observations of rotationally modulated X-ray emissions of saturated stars by Flaccomio et al. (2005) are in accordance with this. Wright and Drake (2016) suggest that coronal X-ray emission may just become insensitive to the strength of the magnetic field, so energy is dissipated via other mechanisms. It is most likely that some form of change in the dynamo is the cause of saturation, however investigation of the filling factor would still make for a relevant study.

4.9 Scale of existing studies

To date, studies of the rotation-activity relation have used samples of MS stars in the hundreds, and the largest study as of 2017 for PMS stars is that of Gregory et al. (2016) using ~ 1000 stars, and for MS, the study by Reiners et al. (2014) using 821 stars, based on Pizzolato et al. (2003) and Wright et al. (2011) using 824 stars. More recently, (Fang et al., 2018) have studied a sample of 741 stars within 4 clusters, and Arkhypov et al. (2018) have used a sample of 1729 Kepler objects to study star spots, although without a focus on the rotation-activity relation. A number of studies focusing specifically on a few hundred M dwarfs include West et al. (2015) (238 stars), Stelzer et al. (2016) (134 stars), Newton et al. (2017) (386 stars), and Raetz et al. (2020) (430 stars). Studies of M-dwarfs are key, since the long rotation periods and low X-ray activity makes the rotation-activity relation hard to define.

The majority of existing studies have focused purely on stars within clusters which are relatively homogeneous in terms of age and chemical composition. This is advantageous for such existing studies as they focus on chromospheric activity as an indicator of rotational modulation, however, they lack the all-sky coverage that photometrically defined rotation periods can provide.

Future surveys and new data releases from current surveys will add to our understanding of stellar magnetism, coronal X-ray emission, and the internal stellar structure. Specific studies on PMS stars are needed to understand why these stars do not obey the rotation-activity relation, which will add to our understanding of the evolution of stellar dynamos and magnetism. Such studies will also help to better determine the Rossby number, and whether it should be determined by the scaling of L_X/L_{bol}, or by the rotational scaling of L_X, independent of stellar conditions.

4.10 Implications for exoplanet habitability

Just as the activity of the Sun affects Earth's magnetosphere and habitability, exoplanets are affected by their host star. Stellar X-ray emission is commonly used as an indicator of stellar magnetic activity, and surface X-ray flux is a good proxy for stellar wind for MS stars (Wright et al., 2011). In the field of exoplanet studies, stellar X-ray emission can also be a strong proxy for the prediction of extreme UV (EUV) flux since it impacts strongly on the planetary ionosphere, upper atmosphere, and potentially on (pre)biological evolution, since the stellar wind can constrain planetary magnetospheres (Vidotto, 2017). Understanding the dynamo mechanism for slow rotators especially will be important for uncovering the particle and photon radiation environments of exoplanets (Wright and Drake, 2016).

However, of the known stars up to ~ 25 pc from the Sun, only 32.9% have a detectable X-ray counterpart, which stifles the usefulness of X-ray emission as a proxy. It has been suggested that instead of the use of direct X-ray detections, star spot variability observed in

optical wavelengths could act as the X-ray proxy. Arkhypov et al. (2018) have developed a successful method of using star spot variability as an X-ray radiation proxy. Through the analysis of 1,729 MS stars observed by the Kepler mission, they found that the squared amplitude of the first harmonic, A_1^2, of a rotationally modulated star can be used as an activity indicator. Interestingly it gives almost the same relation to the L_x/L_{bol} as the Rossby number does.

Using observable X-ray radiation as a proxy for EUV flux and EUV luminosity, and the empirical relationship between L_x/L_{bol} and A_1^2, they found a relationship for the EUV luminosity as a function of period and temperate, $L_{EUV}(P, T_{eff})$. This relationship allows for the characterising of X-ray and EUV radiation of very distant objects which fall below the usual sensitivity levels of X-ray detectors. This may provide a useful tool for the statistical investigations of exoplanetary atmospheres. For example, the rotation-activity-age relationship has already been used in studies of of M-dwarf planets and host star properties (Muirhead et al., 2019; Pineda et al., 2020), direct imaging planet searching (Desidera et al., 2021), and how exoplanets can even trigger changes in the magnetic activity of cool host stars (Poppenhaeger, 2018).

4.11 Summary

In this chapter I briefly summarised the background to the rotation-activity relation, from the history to the implications the relationship can have on future work on exoplanet detection. The rotation-activity relation is still not well constrained, with questions surrounding the existence of the supersaturated regime and the possible regime of anti-solar differential rotation, however recent work has worked on better constraining each regime with larger and larger samples. In the next chapter, I will investigate the rotation-activity relation using photometrically defined rotation periods in the SuperWASP archive and ASAS-SN Catalogue of Variable Stars.

Chapter 5

Data Reduction and Results of the Rotation-Activity Relation

In this chapter, I characterise the rotation-activity relation described previously in Chapter 4. To do this, I combine new measurements of photometric rotation periods of stars in the SuperWASP periodicity catalogue and ASAS-SN Catalogue of Variable Stars, with XMM-Newton X-ray observations to produce a large sample of field stars with photometrically defined rotation periods and coincident X-ray luminosities. Only unique objects displaying a rotational modulation with photometric, X-ray, and parallax data are used in this work. This sample is used to study and characterise the rotation-activity relation, and investigate various regimes of the rotation-activity relation. Some of this chapter was published in Thiemann et al. (2020).

5.1 Data

In this short section, I outline the pre-processing done on each catalogue in order to select stellar objects to characterise the rotation-activity relation. The data sets themselves are described in detail in Chapter 3.

5.1.1 Photometric observations

Photometric observations serve two main purposes in the characterisation of the rotation-activity relation. Firstly, they provide a photometrically defined rotation period, and secondly, they provide magnitudes which can be used to calculate the bolometric flux. Candidate rotational variables were sourced from two catalogues: the SuperWASP periodicity catalogue and the ASAS-SN Catalogue of Variable Stars. Both catalogues were chosen for their ease of access, similar limiting magnitudes, and full sky coverage. However, each catalogue requires some pre-processing before use in the form of removal of duplicated objects and removal of non-rotational objects.

The *SuperWASP periodicity* catalogue contains duplicated objects, arising from the detection of multiple periods for a single object. The most likely period for each object was found through identifying the most significant period, and any duplicates were removed. Any remaining duplicated objects were removed by performing an internal positional cross-match, removing objects within a $2'$ radius of each other ($>$ 4 times the photometric aperture radius, 34"). The remaining 767,199 ($\sim$2.5% of objects in the SuperWASP archive) genuine objects with detectable periodic variability on timescales from hours to years are ready to be cross-matched with X-ray data. Following a cross-match with X-ray data, the next step is to identify only rotationally variable stellar objects, as described in Section 5.2.1.

The ASAS-SN Catalogue of Variable Stars requires less pre-processing. This catalogue contains 666,502 light curves of stellar variables with existing classifications, periods, and classification probabilities. For this work, only rotational variables were used, leaving 90,712 stellar objects. Of these, only stars with a classification probability of $>$0.75 were selected. There are likely to be duplicates of stellar objects identified in both SuperWASP and ASAS-SN, and these are removed later in the work.

5.1.2 X-ray observations

X-ray observations are used in the characterisation of the rotation-activity relation in order to determine the X-ray to bolometric flux ratio. Previous work by Norton et al. (2007) used ROSAT observations, and this research updates that work through the use of XMM-Newton observations in the form of the 4XMM-DR9 catalogue, which contains detections of 550,124 unique X-ray sources. This work uses *SC_EP_9_FLUX* in the broad energy band, corresponding to 0.2 – 4.5 keV.

As with the *SuperWASP periodicity* catalogue, some pre-processing is required. Possible duplicated objects were removed by performing an internal positional cross-match, removing objects within a $24''$ radius of each other ($\sim$4 times the uncertainty in the EPIC extent radius). The remaining objects are assumed to be unique and can be used for cross-matching. The second form of pre-processing removes uncertain objects from the catalogue. 4XMM-DR9 catalogue contains a summary flag for each source, from 0-11. For example, a flag of 0 indicates a 'good' source, a flag of 1 indicates that parameters may be affected, a flag of 2 indicates a possibly spurious source, and a flag of 3 indicates that the source is located in an area where there may be a spurious detection. 95.7% of the sources in this catalogue have a flag ≤ 1. All unique sources with a flag ≥ 2 are removed from the catalogue.

One form of pre-processing which is preferable but not possible is the removal of flares detected in X-ray. Low-mass stellar X-ray sources are known to show high levels of variability due to magnetic flares (Caramazza et al., 2007) and rotational modulation. Bright flares can significantly increase the X-ray flux from a source over the course of a short observation. Short-lived increases in X-ray flux should be removed through multiple observations of the same source, however the majority ($\sim$80%) of objects in the 4XMM-DR9 catalogue contain only one detection of the source, with only $\sim$41% of these objects having an uncertainty in the soft X-ray band of $\leq 20\%$ in flux. $\sim$71% have an uncertainty of $\leq 30\%$ in flux. This is expected to be one of the most significant sources of uncertainty in this work.

5.1.3 Additional catalogues

For the calculation of bolometric luminosity, photometric colour and parallax are required. The majority of previous studies of the rotation-activity relation have used either the $B-V$ or $V-K_s$ colour as various proxies, i.e. for effective temperature. B, V, R, J, H, K photometric magnitudes were taken from the Two Micron All Sky Survey (2MASS) (Skrutskie et al., 2006) and NOMAD (Zacharias et al., 2004) catalogues, supplemented by USNOB1.0 (Monet et al., 2003), APASS (Henden et al., 2015), and GCS2.3 (Lasker et al., 2008), and used to derive $V-K_s$ for all stars. $V-K_s$ was used as a proxy for effective temperature and used to derive bolometric corrections. For each star, estimated spectral types were based on Mamajek et al. (2015).

The conversion of observed to absolute magnitude requires stellar distance. Due to well-known problems with the use of non-corrected Gaia-DR2 parallaxes for distance calculation, the Bailer-Jones et al. (2018) catalogue was used, which provides corrected distances. A $10''$ cross-match was used between the Bailer-Jones et al. (2018) catalogue and *SuperWASP periodicity* catalogue and ASAS-SN Catalogue of Variable Stars. Both the bolometric luminosity and the X-ray luminosity scale with d^2, hence the distance value cancels in the bolometric flux ratio. In this work, distances are instead used to identify main sequence stars and correct for interstellar reddening.

Such a spatial cross-match is likely to pick up non-stellar and non-rotational stellar objects in the process, hence the final cross-match is a $10''$ search of SIMBAD tables to identify such objects. Non-stellar and non-rotational stellar objects were removed based on the SIMBAD object type. The catalogue V magnitudes and the observed V magnitudes of the remaining objects were plotted, as shown in Figure 5.1, and objects with a difference in V magnitude of >0.85 (or 1 σ) were removed. Stars with a V magnitude difference of greater than 1σ are removed from the catalogue.

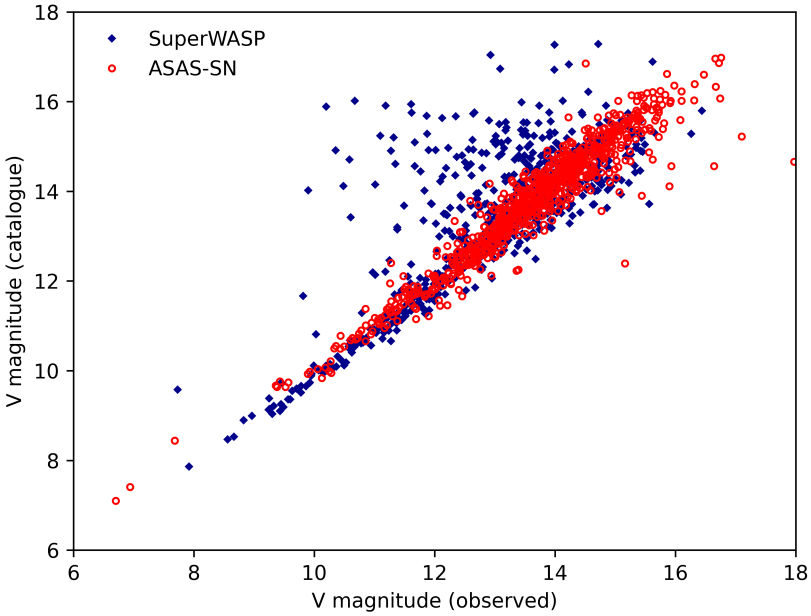

Fig. 5.1 V magnitude (observed) against V magnitude (catalogue).

5.2 Data reduction

This section describes the process of data reduction of the SuperWASP and ASAS-SN data in order to identify rotationally modulated variables with a coincident X-ray source with which to calculate the rotation-activity relation.

5.2.1 Cross-matching

Through a $2'$ cross-match of unique objects in both *SuperWASP periodicity* and 4XMM-DR9 objects using TOPCAT, 39,367 possibly coincident objects with both periodic photometric variability and an X-ray flux were identified. The large cross-match radius of $2'$ between the SuperWASP and 4XMM-DR9 catalogues is due to the large ($34''$) photometric aperture radius of SuperWASP, and accounts for $\sim$4 times this radius.

Of these, 16,827 were flagged as not having a period close to 1 day. Phase-folded light curves were plotted for 16,827 objects and were visually classified. 12,509 were rejected as

not convincingly variable, 1,232 displayed rotational modulation, and 2,131 were categorised as binaries and pulsators. Of these rotators, 990 had corresponding colours, and positive, real Gaia-DR2 parallaxes in the Bailer-Jones et al. (2018) catalogue. Of these 990 objects, 106 were found to be non-stellar or non-rotational stellar objects, and 303 were found to be giant or supergiant stars. Such stars do not follow a rotation-activity relation and are known to experience a sharp decrease in X-ray emission at spectral type K1. Giant and supergiant stars were identified using stellar luminosity by spectral class from Cox (2000). Removing giant stars from the catalogue leaves 581 SuperWASP stars.

The ASAS-SN rotational variable stars were cross-matched with 4XMM-DR9 with a $10''$ cross-match radius, giving 1,921 objects. Of these, 75 appeared in the SuperWASP catalogue and were removed as duplicates. For objects which occurred in both catalogues with a period detection, 72% of the objects had a period difference of $<2\%$, and 80% agreed to within $<10\%$. For objects with periods which differed by $>2\%$, each was assessed by eye to determine which was the most likely true period. Of the 1,846 remaining objects, 882 contain information on both period and colour. Of these, 786 have an ASAS-SN classification probability of > 0.75. The ASAS-SN Catalogue of Variable Stars has already been cross-matched with catalogues of variable stars (e.g. VSX and GCVS) and all 786 objects are confirmed as main sequence stars. 115 SuperWASP and ASAS-SN objects with an observed to catalogue V magnitude difference of $> 1\sigma$ were removed. Finally, all ASAS-SN stars were visually inspected, and 173 stars not displaying a clear rotational modulation were discarded. Combined, this gives a full catalogue of 1,079 stars from the SuperWASP and ASAS-SN catalogues.

Figure 5.2 gives an example of the light curve of a rotationally modulated star in the SuperWASP archive, and figure 5.3 gives an example of the light curve of a rotationally modulated star in the ASAS-SN Catalogue of Variable Stars.

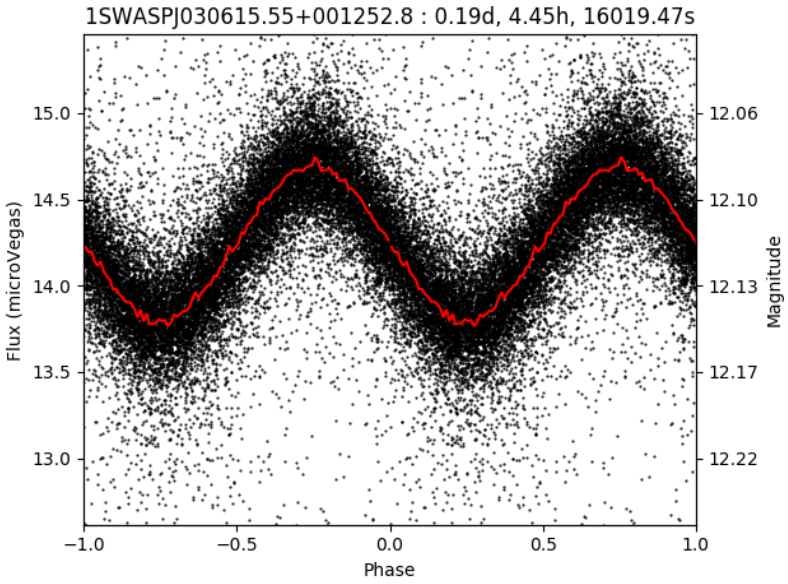

Fig. 5.2 Example of a light curve of a rotator with a period of 16,019 seconds (∼0.19 days) in the SuperWASP archive.

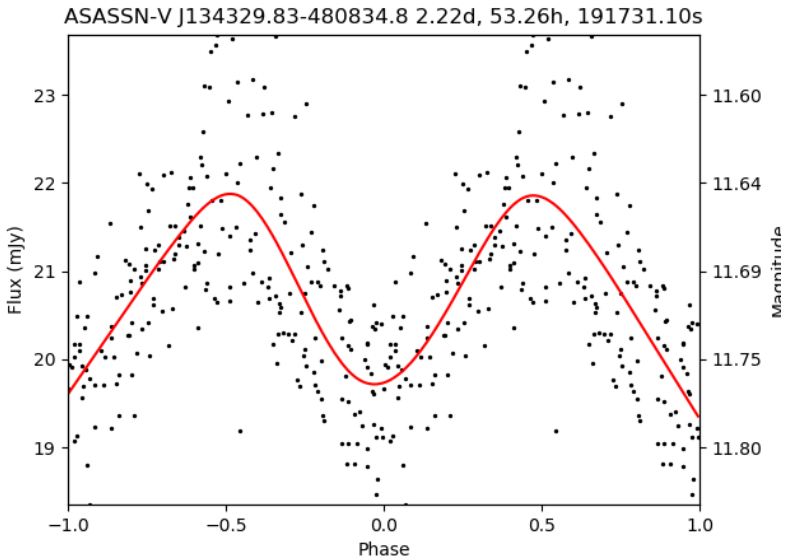

Fig. 5.3 Example of a light curve of a rotator with a period of 191,731 seconds (∼2.22 days) in the ASAS-SN variable stars database.

5.2.2 Positional coincidence

Much of this work relies on spatial cross-matching, but this raises the question: *how many of these cross-matches are likely to be the result of genuine X-ray emission from photometric sources?* In order to answer this, some simple calculations can be performed.

SuperWASP has a large pixel size of $13.7''$ pixel^{-1}. When combined with the 2.5 pixel extraction aperture for photometry, the error radius is $34''$. Although XMM-Newton sources have low positional uncertainties, there is still the possibility of chance positional coincidences between the photometric data and X-ray sources. The SuperWASP all-sky survey is comprised of 2×8 cameras in the Northern and Southern hemisphere, covering 7712 square degrees. In this survey, there are light curves of 3,091,808 unique objects with detectable photometric periods from the *SuperWASP periodicity* catalogue. Therefore, the mean linear separation between nearest neighbours is $180''$ for SuperWASP objects. The 4XMM-DR9 catalogue contains 550,124 unique X-ray sources covering 1089 square degrees, overlapping the SuperWASP sky area. The mean error radius of XMM-Newton positions is $<2''$. This corresponds to a 0.6% chance of an XMM-Newton source and a SuperWASP source coinciding at random. It is, however, possible that some fractino of the X-ray point source detections originate from an object too optically faint for SuperWASP to detect, hence the true chance of coincidence is likely to be greater than 0.6%. 39,367 positional matches are found (of which 581 are used to characterise the rotation-activity relation), rather than $\sim$2316 matches expected as a result of chance, suggesting that (39,367-2316)/39,367 = 94% of the positional coincidences are the result of genuine X-ray emissions from SuperWASP sources.

Using the same method, the mean linear separation between nearest neighbours for ASAS-SN sources is $103''$, and a 2% chance that XMM-Newton and ASAS-SN sources coincide at random. Therefore, 80% of the positional coincidences are the result of genuine X-ray emissions from ASAS-SN sources.

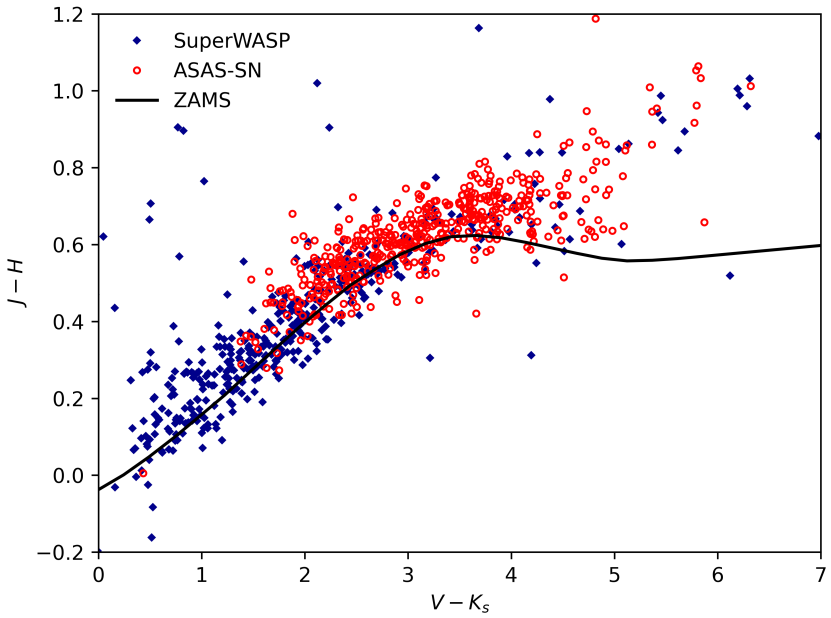

Fig. 5.4 The $V-K_s$, $J-H$ colour-colour plot of 900 stars in the full catalogue. The black line indicates the locus of the zero age main sequence for zero reddening.

5.2.3 Colours and reddening

For these same objects, colour and reddening was assessed in order to understand the data set further. Figure 5.4 shows the $V-K_s$ vs $J-H$ colour-colour plot of the catalogue, and the solid black line shows the locus of the Main Sequence for zero reddening. Extinction will move the line upwards in $J-H$ and right in $V-K_s$ according to Wegner (1994). There is a very slight offset shifting $J-H$ upwards, which may be due to the non-standard V magnitude calculated by SuperWASP (Norton et al., 2007), however since the majority of the objects are close to the zero-reddening MS, all objects are relatively close by. Although these objects are close by, extinction correction will be performed to be on the safe side.

5.2.4 Bolometric flux ratio

In order to characterise the rotation-activity relation, the bolometric flux ratio must be calculated. To first calculate bolometric luminosities, all objects were converted from observational magnitudes to absolute magnitudes, and extinction corrected using Equation 5.1. The extinction for each star was synthesised using the Binary and Stellar Evolution and Population Synthesis (BiSEPS) implementation of extinction given by Drimmel et al. (2003), using Bailer-Jones et al. (2018) Gaia-DR2 distances. For more details of BiSEPS, see Chapter 10.

$$M_v = m - 5\log\left(\frac{d}{10}\right) + A \tag{5.1}$$

where $A = 3.2[E(B-V)]$ and distance, d, is measured in parsecs.

Using this, bolometric corrections were then calculated from $V - K_s$ colour and Bailer-Jones et al. (2018) Gaia-DR2 distances, allowing for the calculation of bolometric luminosities using $M_{bol} = BC_v - M_v$. The bolometric luminosity was calculated using:

$$L_{bol} = L_0 \times 10^{-0.4 M_{bol}} \tag{5.2}$$

where L_0 is the zero point luminosity 3.0128×10^{28} W. X-ray fluxes were converted to X-ray luminosities using soft X-rays and Gaia-DR2 Bailer-Jones et al. (2018) distances using $L_x = 4\pi D^2 F_x$. Finally, the X-ray-to-bolometric luminosity ratios, $R_x = L_x/L_{bol}$, were determined.

5.2.5 Rossby number

The next step is to characterise the convective turnover time, then the Rossby number. For the remaining catalogue of 1,079 stars from SuperWASP and ASAS-SN, the convective turnover time, τ, was calculated using the $V - K_s$ colour relation derived by Wright et al. (2018).

Previous empirically derived relationships have been found, e.g. Pizzolato et al. (2003) and Wright et al. (2011), however these relationships have small $V-K_s$ ranges. Wright et al. (2018) extended this relationship, and as such, it is well constrained for $1.1 < V-K_s < 7.0$. It is worth noting that to derive this empirical form of the relation, Wright et al. (2018) assumes a rotation-activity relation as the input, hence it might be reasonable to assume that the output will be self-consistent and will show a rotation-activity relation in line with canonical values. This relationship has the form:

$$\log\tau = 0.64(\pm^{0.10}_{0.12}) + 0.25(\pm^{0.08}_{0.07})[V-K_s] \tag{5.3}$$

where τ is the convective turnover time. From this, Rossby numbers, $Ro = P_{rot}/\tau$, were calculated for all objects.

5.3 The full catalogue

Having characterised Ro and L_x/L_{bol}, cuts were made to the catalogue of 1,079 stars to make it suitable for use for the rotation-activity relation. Any stars with a period of $\geq$50 days were removed, since long period photometric variability is difficult to correctly define for long periods. Late-type stars with a bolometric luminosity of $L_{bol} \geq 10L_{\odot}$ were discarded as giants. The 4XMM-DR9 variability flag, *VAR_FLAG* was used to remove the 34 GKM-type sources detected as X-ray variable.

The full catalogue contains 900 X-ray visible unique objects displaying rotational modulation in their photometric variability. The spatial distribution of the full catalogue is shown in Figure 5.5, indicating SuperWASP stars lying away from the Galactic Plane, and ASAS-SN stars lying mostly along the Galactic Plane.

Figure 5.6 and Figure 5.7 show the distribution of period and $V-K_s$ colour in the full catalogue. The catalogue is concentrated around objects with a rotation period of 3-10 days.

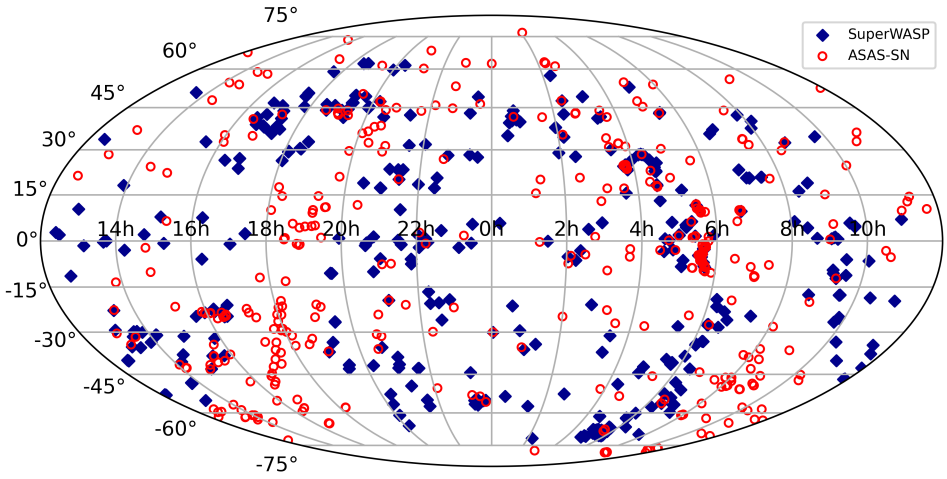

Fig. 5.5 The spatial distribution of the 900 objects in the full catalogue coincident with 4XMM-Newton sources.

Like the ASAS-SN Catalogue of Variable Stars, the *SuperWASP periodicity catalogue* reports the rotation period derived for each target. The periods given in this catalogue are therefore the "best guess" rotation period, and may not be the actual rotation periods of the stars. However, given that both the ASAS-SN Catalogue of Variable Stars and the *SuperWASP periodicity catalogue* have independently derived almost identical rotation periods through different methods, we can be confident enough in their accuracy to use this new catalogue to probe the rotation-activity relation. Table 5.1 and Table 5.2 show a sample of the full catalogue. Splitting the catalogue into spectral types based on $V - K_s$ colour and tables by Mamajek et al. (2015), gives 431 OBA-type, 33 F-type, and 402 GKM-type stars.

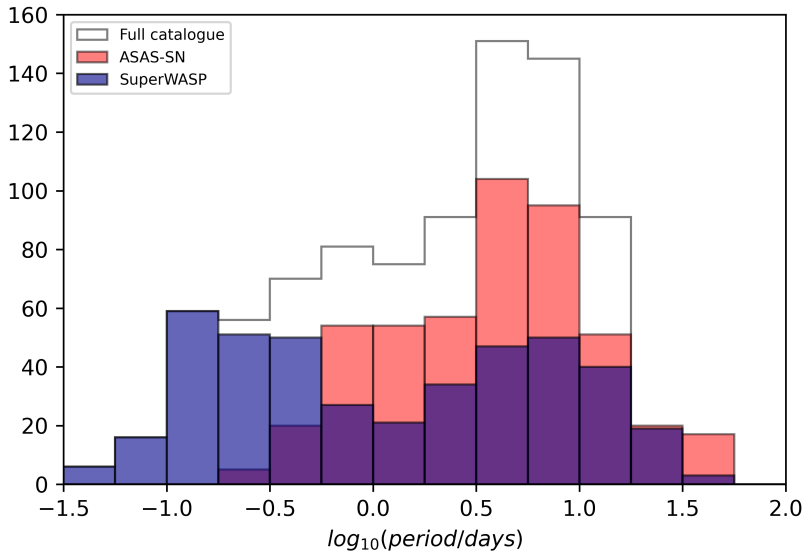

Fig. 5.6 The period distribution of 900 stars in the full catalogue coincident with 4XMM-Newton sources.

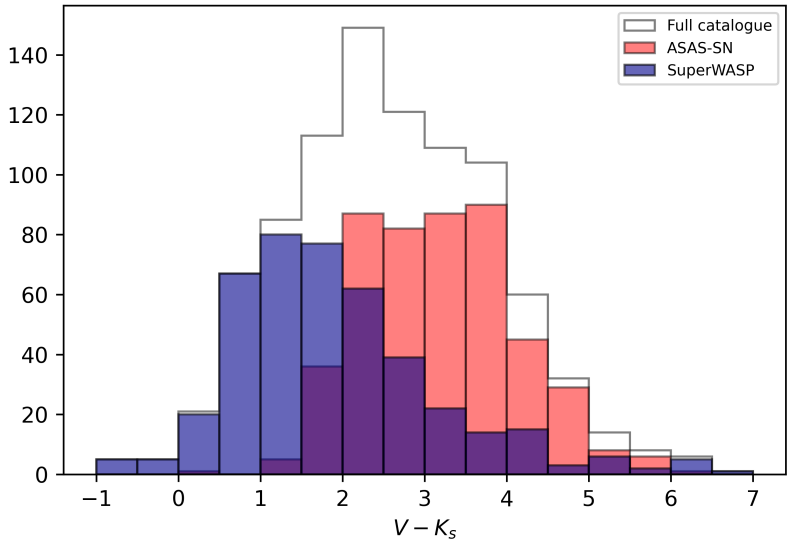

Fig. 5.7 The $V - K_s$ colour distribution of 900 stars in the full catalogue coincident with 4XMM-Newton sources.

The columns of the tables are as follows: 1. IAUNAME: The XMM-Newton identifier in the form 4XMM Jhhmmss.ss+ddmmss.s; with the position encoded in this identifier. 2. WASP ID: The SuperWASP identifier in the form 1SWASP Jhhmmss.ss+ddmmss.s; the position encoded in this identifier is identical to the position of the corresponding object in the USNO B1 catalogue, or ASAS-SN ID: The ASAS-SN identifying in the form ASASSN-V Jhhmmss.ss+ddmmss.s. 3. Spectral Type: Spectral type taken from Mamajek et al. (2015) based on $V-K_s$ colour. 4. V magnitude: V is the mean SuperWASP magnitude defined as $-2.5\log_{10}(\frac{F}{10^6})$ where F is the mean SuperWASP flux in microVegas - a pseudo-V magnitude which is comparable to the Tycho V magnitude, or V magnitude: ASAS-SN V magnitude. 5. Period: The SuperWASP photometric period in days identified by the *SuperWASP periodicity* period search, or Period: The ASAS-SN photometric period in days. 6. Distance: Distance in parsec taken from Bailer-Jones et al. (2018). 7. $V-K$: $V-K$ calculated using 2MASS and USNOB1 catalogue magnitudes. 7. Fx: Soft X-ray flux taken from *SC_EP_9_FLUX* in the broad energy band, corresponding to 0.2–4.5 keV. 12. $\log Ro$: Rossby number calculated using relationship derived in Wright et al. (2018)). 13. $\log Rx$: Logarithm of the ratio of X-ray to bolometric luminosity. The full catalogue of both SuperWASP and ASAS-SN can be found in Appendix A.

5.4 Calculating the rotation-activity relation

To characterise the rotation-activity relation for each spectral type, a power-law function is fitted in order to plot $\log(L_x/L_{bol})$ to $\log Ro$ for the unsaturated and supersaturated regimes, where applicable, and to find a mean for the saturated regime. The saturation point, Ro_{sat} is initially taken to be $Ro_{sat} = 0.13$ based on canonical values (e.g. Wright et al. (2011)). Points for the supersaturated regime fit are based on literature values. The fits for each regime and spectral type are based on Equation 5.4 and an initial fit using Ordinary Least Squares (OLS) was done to identify the saturation point as $Ro_{sat} = 0.14 \pm 0.03$. Each regime's fit is improved

Table 5.1 Subset of the 180 G- to M-type SuperWASP objects from the full catalogue containing 900 X-ray visible unique objects displaying rotational modulation in their photometric variability.

XMM ID	WASP ID	SpT	Period [d]	V [mag]	V-K	Distance [pc]	F_x [10^{-14}] [erg/cm^2/s]	log Ro	log R_x
4XMM J000234.8-300525	1SWASPJ000234.82-300525.3	K4.5V	0.71	13.81	2.78	23.25	5.46E+29 ± 1.40E+28	-1.49 ± 0.07	-4.63 ± 0.15
4XMM J001321.2+054505	1SWASPJ001321.26+054505.8	G8V	13.39	11.63	1.73	62.56	1.02E+30 ± 6.81E+28	0.05 ± 0.00	-5.24 ± 0.49
4XMM J002847.8+345355	1SWASPJ002841.59+345358.9	G2V	27.94	14.73	1.47	104.25	4.81E+29 ± 1.56E+29	0.44 ± 0.02	-4.22 ± 1.42
4XMM J002914.0+345133	1SWASPJ002918.85+345102.9	K1V	27.83	12.83	2.06	41.83	3.42E+29 ± 3.99E+28	0.29 ± 0.01	-4.83 ± 0.62
4XMM J003823.9+401250	1SWASPJ003823.99+401250.2	K2V	4.66	12.40	2.15	92.82	2.37E+31 ± 2.57E+29	-0.51 ± 0.03	-4.05 ± 0.44
4XMM J005305.0+394730	1SWASPJ005310.20+394834.0	G7V	25.88	13.00	1.68	51.32	2.61E+29 ± 5.99E+28	0.35 ± 0.02	-4.87 ± 1.13
4XMM J011858.9-341427	1SWASPJ011858.94-341428.5	K1V	15.78	12.98	2.06	68.63	7.94E+30 ± 1.18E+29	0.04 ± 0.00	-4.44 ± 0.21
4XMM J015636.6+285643	1SWASPJ015636.65+285643.7	K3.5V	5.27	12.94	2.63	22.16	6.72E+29 ± 3.02E+28	-0.58 ± 0.03	-4.59 ± 0.23
4XMM J020930.9+342421	1SWASPJ020930.99+342421.0	K2V	3.85	13.08	2.14	129.04	2.06E+31 ± 9.67E+29	-0.59 ± 0.03	-4.04 ± 0.55
4XMM J020953.8+342309	1SWASPJ020957.38+342412.6	K4V	0.40	13.91	2.69	19.93	8.60E+28 ± 1.51E+28	-1.71 ± 0.09	-4.51 ± 0.79
4XMM J021442.0-061635	1SWASPJ021442.07-061635.7	K3V	18.97	12.48	2.44	56.72	7.57E+30 ± 2.31E+29	0.03 ± 0.00	-4.40 ± 0.24
4XMM J022216.2-031036	1SWASPJ022215.35-031031.8	K3.5V	0.20	13.89	2.58	20.74	1.44E+28 ± 5.58E+27	-1.98 ± 0.10	-4.95 ± 1.92
4XMM J022319.5+472720	1SWASPJ022319.50+472722.1	G4V	3.16	11.45	1.53	18.33	3.63E+29 ± 3.94E+28	-0.52 ± 0.03	-4.84 ± 0.53
4XMM J022413.5+274136	1SWASPJ022413.54+274136.1	K2.5V	0.16	11.72	2.28	32.26	1.24E+30 ± 1.59E+29	-2.02 ± 0.10	-4.40 ± 1.00
4XMM J023507.6+034357	1SWASPJ023507.59+034356.7	K1.5V	4.23	12.38	2.10	7.88	2.95E+28 ± 2.16E+27	-0.54 ± 0.03	-5.06 ± 0.37
4XMM J023732.1-522331	1SWASPJ023732.16-522332.5	K5V	0.13	14.51	2.90	46.08	4.32E+29 ± 4.08E+28	-2.27 ± 0.11	-4.63 ± 0.45
4XMM J024614.4-205011	1SWASPJ024622.47-205004.5	G8V	0.18	14.70	1.81	177.96	1.05E+32 ± 6.18E+30	-1.85 ± 0.09	-2.97 ± 0.36
4XMM J025700.4+055415	1SWASPJ025702.21+055338.2	G0V	0.35	13.56	1.34	141.66	2.22E+30 ± 4.03E+29	-1.43 ± 0.07	-4.41 ± 0.88
4XMM J030816.4+490050	1SWASPJ030816.46+490051.0	K4V	1.73	12.50	2.72	24.83	2.26E+30 ± 7.57E+28	-1.08 ± 0.05	-4.54 ± 0.17
4XMM J030846.5+485946	1SWASPJ030846.52+485946.5	K5V	0.14	12.67	2.94	25.76	4.30E+29 ± 3.25E+28	-2.24 ± 0.11	-4.95 ± 0.38
4XMM J032240.3-365917	1SWASPJ032246.95-370025.9	G3V	0.36	11.84	1.48	43.99	3.48E+29 ± 5.32E+28	-1.46 ± 0.07	-5.31 ± 0.82
4XMM J032807.4-311826	1SWASPJ032807.62-311826.7	K3.5V	21.14	10.78	2.61	5.27	4.77E+28 ± 6.14E+27	0.03 ± 0.00	-4.99 ± 0.64
4XMM J032814.9+300119	1SWASPJ032814.96+300119.1	G8V	0.16	11.61	1.78	22.64	6.59E+29 ± 3.65E+28	-1.89 ± 0.09	-4.95 ± 0.32
4XMM J033939.5+152954	1SWASPJ033939.49+152954.9	K2V	4.37	11.82	2.16	15.54	2.98E+29 ± 2.28E+28	-0.54 ± 0.03	-4.83 ± 0.40
4XMM J034322.4+242910	1SWASPJ034322.39+242910.6	K1V	4.49	12.58	2.08	23.6	3.43E+29 ± 3.16E+28	-0.51 ± 0.03	-4.76 ± 0.45
4XMM J034403.5+243015	1SWASPJ034403.55+243015.2	K0.5V	1.48	10.93	1.98	13.5	1.99E+30 ± 1.58E+28	-0.97 ± 0.05	-4.93 ± 0.08
4XMM J034638.7+245734	1SWASPJ034638.77+245734.7	G4V	2.32	10.39	1.56	13.63	2.72E+29 ± 9.97E+27	-0.66 ± 0.03	-5.60 ± 0.22
4XMM J034902.4+231607	1SWASPJ034902.32+231509.0	K2V	6.15	11.85	2.16	13.99	2.11E+28 ± 4.78E+27	-0.39 ± 0.02	-5.45 ± 1.24
4XMM J042041.1-483736	1SWASPJ042041.16-483735.7	K5.5V	0.38	13.98	3.04	37.53	1.17E+30 ± 7.02E+28	-1.82 ± 0.09	-4.43 ± 0.27
4XMM J043356.3-612916	1SWASPJ043356.50-612916.5	K0.5V	3.39	10.57	1.98	9.29	9.51E+29 ± 1.29E+28	-0.61 ± 0.03	-5.14 ± 0.07
4XMM J043454.5+240512	1SWASPJ043456.17+240543.5	M2V	0.65	13.68	4.24	22.73	2.16E+28 ± 4.25E+27	-1.89 ± 0.09	-5.73 ± 1.13

Table 5.2 Subset of the 222 G- to M-type ASAS-SN objects from the full catalogue containing 900 X-ray visible unique objects displaying rotational modulation in their photometric variability.

XMM ID	ASAS-SN ID	SpT	Period [d]	V [mag]	V-K	Distance [pc]	F_x [10^{-14}] [erg/cm^2/s]	$\log Ro$	$\log R_x$
4XMM J000228.1-300442	ASASSN-V J000228.21-300443.4	K5V	5.46	13.02	2.89	24.66	6.41E-14	-0.62 ± 0.03	-3.61 ± 0.17
4XMM J004154.9+413332	ASASSN-V J004154.90+413332.3	K4V	7.71	15.81	2.76	164.18	2.86E-14	-0.44 ± 0.02	-2.74 ± 0.57
4XMM J005414.1-351713	ASASSN-V J005414.09-351712.6	K4V	3.40	13.74	2.68	20.38	9.53E-14	-0.79 ± 0.04	-3.12 ± 0.26
4XMM J011226.8+152751	ASASSN-V J011226.86+152752.4	K5.5V	1.16	14.65	3.06	24.94	1.64E-13	-1.33 ± 0.07	-2.45 ± 0.12
4XMM J011648.3-002104	ASASSN-V J011648.31-002103.5	K2.5V	25.10	11.63	2.23	60.99	2.46E-13	0.19 ± 0.01	-3.35 ± 0.22
4XMM J012106.0+195953	ASASSN-V J012106.02+195952.8	K3.5V	1.33	15.38	2.54	142.70	2.98E-14	-1.16 ± 0.06	-2.59 ± 0.53
4XMM J020656.2-044905	ASASSN-V J020656.27-044906.1	G9V	6.01	14.83	1.87	62.00	7.13E-15	-0.33 ± 0.02	-3.52 ± 0.78
4XMM J020841.2+351243	ASASSN-V J020841.29+351243.6	K5V	4.17	14.97	2.92	27.02	2.84E-14	-0.74 ± 0.04	-3.18 ± 0.18
4XMM J021802.8+625416	ASASSN-V J021803.03+625418.1	K4.5V	0.55	14.26	2.84	24.31	3.29E-14	-1.60 ± 0.08	-3.39 ± 0.41
4XMM J023000.7-042536	ASASSN-V J023000.79-042536.7	K8V	1.07	13.68	3.47	12.66	4.47E-13	-1.48 ± 0.07	-2.67 ± 0.08
4XMM J025805.9+125446	ASASSN-V J025806.02+125446.9	K5.5V	1.16	14.47	3.08	27.19	2.88E-14	-1.33 ± 0.07	-3.37 ± 0.39
4XMM J030654.5-775740	ASASSN-V J030654.80-775740.6	K4.5V	3.18	15.36	2.78	141.89	2.31E-14	-0.83 ± 0.04	-3.12 ± 0.36
4XMM J031331.7-223658	ASASSN-V J031331.73-223656.8	K4V	5.36	15.38	2.71	177.06	1.87E-14	-0.59 ± 0.03	-3.11 ± 0.60
4XMM J033046.8+435159	ASASSN-V J033046.92+435157.6	K5V	5.22	15.08	2.98	266.72	4.97E-14	-0.64 ± 0.03	-2.92 ± 0.77
4XMM J033202.1-270251	ASASSN-V J033202.12-270251.9	K5.5V	0.66	12.54	3.06	14.35	4.52E-13	-1.58 ± 0.08	-2.99 ± 0.07
4XMM J033735.1+170515	ASASSN-V J033735.10+170516.0	K6.5V	0.46	13.57	3.32	15.81	4.81E-14	-1.80 ± 0.09	-3.63 ± 0.30
4XMM J034008.5+412846	ASASSN-V J034008.44+412847.0	K3V	13.70	13.15	2.45	65.84	5.81E-14	-0.10 ± 0.00	-3.52 ± 0.30
4XMM J034112.0-050914	ASASSN-V J034112.02-050914.5	K3.5V	5.12	12.08	2.58	13.12	1.77E-13	-0.58 ± 0.03	-3.48 ± 0.16
4XMM J034351.2+321309	ASASSN-V J034351.24+321309.2	K6.5V	0.79	12.98	3.28	33.93	3.58E-13	-1.56 ± 0.08	-2.99 ± 0.12
4XMM J034425.5+321229	ASASSN-V J034425.57+321230.0	M3.5V	8.38	16.19	4.85	33.27	3.94E-14	-0.97 ± 0.05	-3.20 ± 0.25
4XMM J034703.6+240935	ASASSN-V J034703.58+240935.0	K7V	0.30	14.44	3.32	13.44	9.06E-14	-1.99 ± 0.10	-3.03 ± 0.10
4XMM J034737.9+232805	ASASSN-V J034737.76+232805.2	K4.5V	8.33	13.67	2.82	13.75	5.42E-14	-0.41 ± 0.02	-3.42 ± 0.13
4XMM J034741.3+235818	ASASSN-V J034741.44+235819.0	K5V	0.48	13.50	2.97	13.55	1.16E-13	-1.68 ± 0.08	-3.19 ± 0.13
4XMM J034810.9+233025	ASASSN-V J034810.98+233025.3	K5.5V	7.69	14.36	3.03	13.57	6.35E-14	-0.51 ± 0.03	-3.14 ± 0.12
4XMM J035017.8-502950	ASASSN-V J035017.98-502949.8	K6.5V	0.42	14.42	3.26	25.28	6.10E-14	-1.84 ± 0.09	-3.17 ± 0.34
4XMM J042208.1+191520	ASASSN-V J042208.27+191521.8	M2V	5.12	12.91	4.22	3.58	8.49E-13	-0.99 ± 0.05	-2.96 ± 0.06
4XMM J042318.2-275912	ASASSN-V J042318.14-275910.3	K6.5V	1.26	14.35	3.26	174.85	4.87E-14	-1.36 ± 0.07	-3.24 ± 2.53
4XMM J042923.2-030146	ASASSN-V J042923.22-030146.4	G8V	10.47	13.67	1.76	140.62	4.46E-14	-0.06 ± 0.00	-2.78 ± 0.22
4XMM J044056.3-531412	ASASSN-V J044056.45-531413.1	G9V	5.92	13.48	1.86	168.96	4.39E-14	-0.33 ± 0.02	-3.38 ± 0.70
4XMM J045635.3+543505	ASASSN-V J045635.17+543506.1	K5.5V	0.69	15.13	3.02	33.53	5.01E-14	-1.56 ± 0.08	-2.93 ± 0.29
4XMM J052951.5+114030	ASASSN-V J052951.62+114031.6	M1V	3.24	14.87	3.97	47.21	1.59E-13	-1.13 ± 0.06	-2.77 ± 0.26

using the Python package `emcee`, a Markov chain Monte Carlo (MCMC) implementation of the affine-invariant ensemble sampler created by Foreman-Mackey et al. (2013), which takes both uncertainties in Ro and (L_x/L_{bol}) into account.

The commonly used two-part power-law for the unsaturated and saturated regime (e.g. Pizzolato et al. (2003), Wright et al. (2011), Wright et al. (2018)) has the form:

$$\frac{L_x}{L_{bol}} = \begin{cases} CRo^{\beta} & \text{if } Ro > Ro_{sat} \\ (\frac{L_x}{L_{bol}})_{sat} & \text{if } Ro \leq Ro_{sat} \end{cases} \tag{5.4}$$

It is assumed that the supersaturated regime will have a similar, but positive, power-law form, β_s.

The final catalogue is split into OBA, F-, and GKM-type to identify observational differences between spectral types, and split between ASAS-SN and SuperWASP catalogues to identify further differences.

5.5 Results

Plots of the Rossby number, $Ro = P_{rot}/\tau$, against bolometric flux ratio, L_x/L_{bol}, for the full SuperWASP and ASAS-SN catalogue are shown in Figures 5.8 and 5.9 and 5.10. Regime thresholds are as follows: supersaturated regime ($0.03 > Ro$), saturated regime ($0.03 < Ro < 0.14$), and unsaturated regime ($0.14 < Ro < 2.00$).

OBA-type stars are known to not display the rotation-activity relation, as shown in Figure 5.8. A-type stars are typically X-ray dark, whereas O- and B-type stars generate X-rays via wind shocks or for binaries, shocks between colliding winds. Any X-ray emission from A-type stars is most likely the emission from an unresolved companion star.

The full catalogue was separated into the component ASAS-SN and SuperWASP catalogues and fitted separately, shown in Figure 5.9 and Figure 5.10. This demonstrates the

Table 5.3 Parameters for the GKM-type regime, separated by catalogues and period ranges. nWasp and nASAS-SN indicate the number of stars in each regime.

Regime	nWASP	WASP	nASAS-SN	ASAS-SN
Supersaturated (β)	60	1.42±0.22	21	0.43±0.24
Saturated (Rx)	31	-3.14	76	-2.81
Unsaturated (β_s)	89	-1.84±0.18	125	-0.33±0.11

significant difference between each subset of stars in the full catalogue. A fit to the SuperWASP catalogue shows the classical two-part power-law fit of unsaturated and saturated regime, and a third supersaturated regime, whereas the fitting to the ASAS-SN catalogue is extremely unconvincing and is shown purely to demonstrate this fact. The breakdown of fitting parameters for each regime and catalogue subset are shown in Table 5.3.

The unsaturated regime typically lies between $\sim 0.10 < Ro <\sim 2.00$. For this catalogue, the unsaturated regime is found to be in the range $0.14 < Ro < 2.00$. In the unsaturated regime there is an anti-correlation between the Rossby number, Ro, and X-ray luminosity ratio, L_x/L_{bol}. 89 SuperWASP G- to M-type stars were used to fit find a power-law fit of $\beta = -1.84 \pm 0.18$, matching the canonical value $\beta = -2$, within uncertainty ranges.

The saturated regime exists for fast rotating solar and late-type stars with $0.03 < Ro < 0.14$, independent of spectral type. The SuperWASP subset contains 31 saturated stars. Previous studies have found the value of the saturation point to be between $Ro_{sat} \sim 0.08$ (Marsden et al., 2009) and $Ro_{sat} \sim 0.16 \pm 0.02$ (Wright et al., 2011). A Rossby number of $Ro_{sat} = 0.14 \pm 0.03$, and a mean saturation of $\log(L_x/L_{bol}) = -3.14$ was found.

The supersaturated regime occurs for the very fastest rotating stars with $Ro < 0.03$. For the fastest rotating stars, L_x/L_{bol} has been observed to decrease below the saturation level. This SuperWASP GKM-type sample clearly displays evidence of a supersaturated regime, with a power-law slope fit of $\beta_s = 1.42 \pm 0.26$, with 60 stars in this subset.

The scatter in L_x/L_{bol} in the saturated regime is likely to arise from a number of factors: X-ray luminosity varying over a stellar cycle (sometimes up to an order of magnitude in our

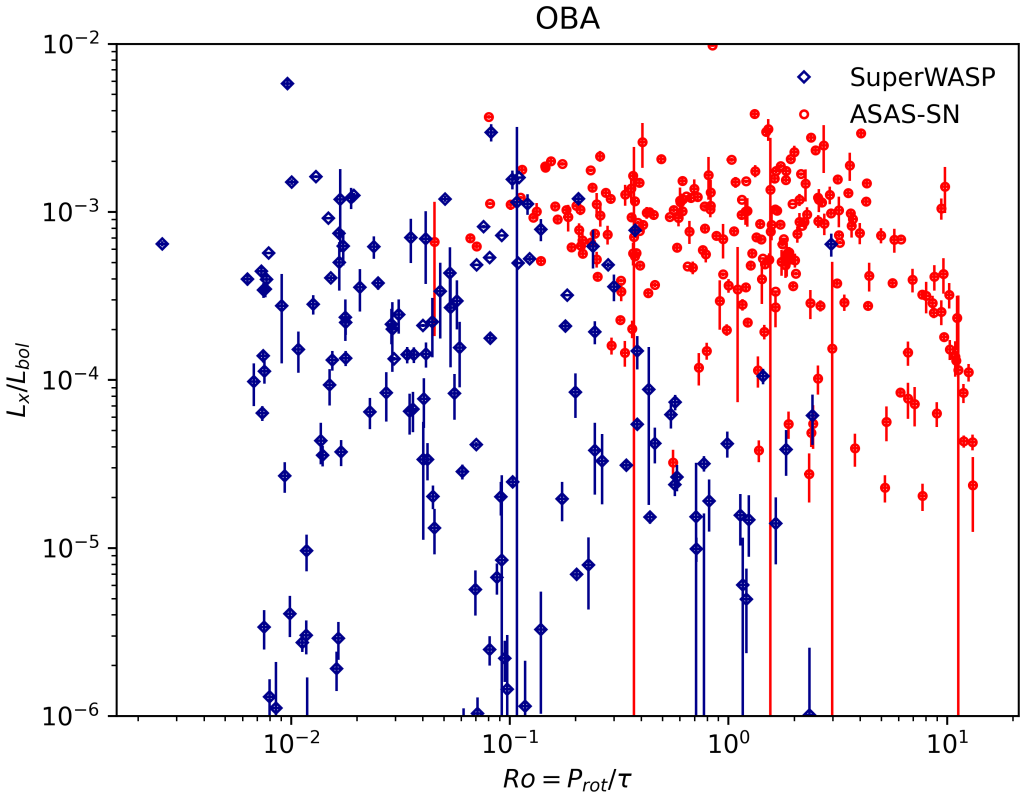

Fig. 5.8 The 431 OBA-type stars in the catalogue do not display the rotation-activity relation.

Sun (Peres et al., 2000), and with a significant portion of X-ray sources having only one detection, varying star spot coverage may change the measured activity of the star.

In $V - K_s$ space, the stars used to characterise the rotation-activity relation are distributed across the range $1.1 \leq V - K_s \leq 5.7$, with K-type stars dominating. Uncertainties in V magnitudes are generally small ($\sim 3\%$) compared to the measured X-ray fluxes, which have a typical uncertainty of $\sim 20\%$. Distance uncertainties are also typically small ($\sim 5\%$). As such, in L_x/L_{bol}, the X-ray uncertainty dominates. The rotation periods for the SuperWASP archive, P_{rot} are derived empirically, and the typical uncertainty is $\sim 0.1\%$. It is assumed that ASAS-SN periods have an equivalent uncertainty. Additionally, the SuperWASP subset has marginally smaller uncertainties, with a mean uncertainty of $\pm 6.05 \times 10^{-5}$ in L_x/L_{bol} compared to $\pm 9.88 \times 10^{-5}$ for the ASAS-SN subset. Similarly, in Ro, the SuperWASP

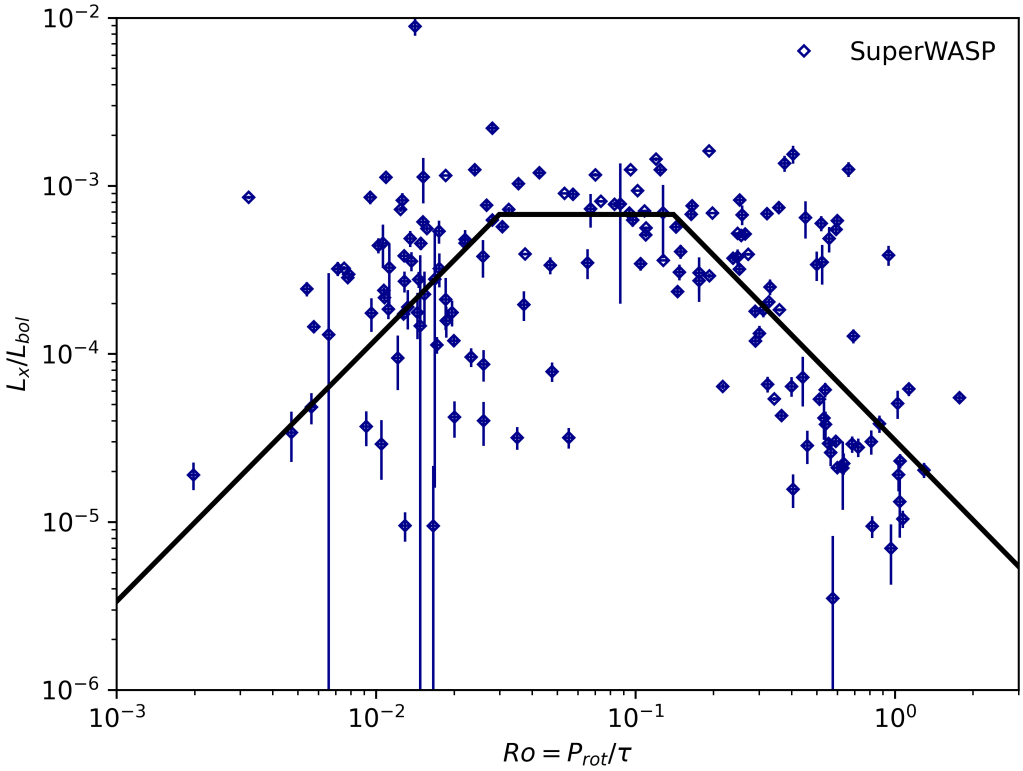

Fig. 5.9 Fractional X-ray luminosity, L_x/L_{bol}, plotted against the Rossby number, Ro, for 192 G- to M-type SuperWASP stars.

catalogue has a mean uncertainty of ± 0.06, whereas the ASAS-SN catalogue has a mean uncertainty of ± 0.15.

5.6 Discussion

Somewhat unexpectedly, the ASAS-SN and SuperWASP catalogues show very different results. Notably, the SuperWASP catalogue shows convincing evidence for the unsaturated and supersaturated regimes, and with a higher saturation point, whereas the ASAS-SN catalogue shows no convincing evidence for the unsaturated or supersaturated regimes.

It is likely even after cleaning the data, both subsets still have some level of contamination. Jayasinghe et al. (2018) states that rotational variables are "usually the most difficult to

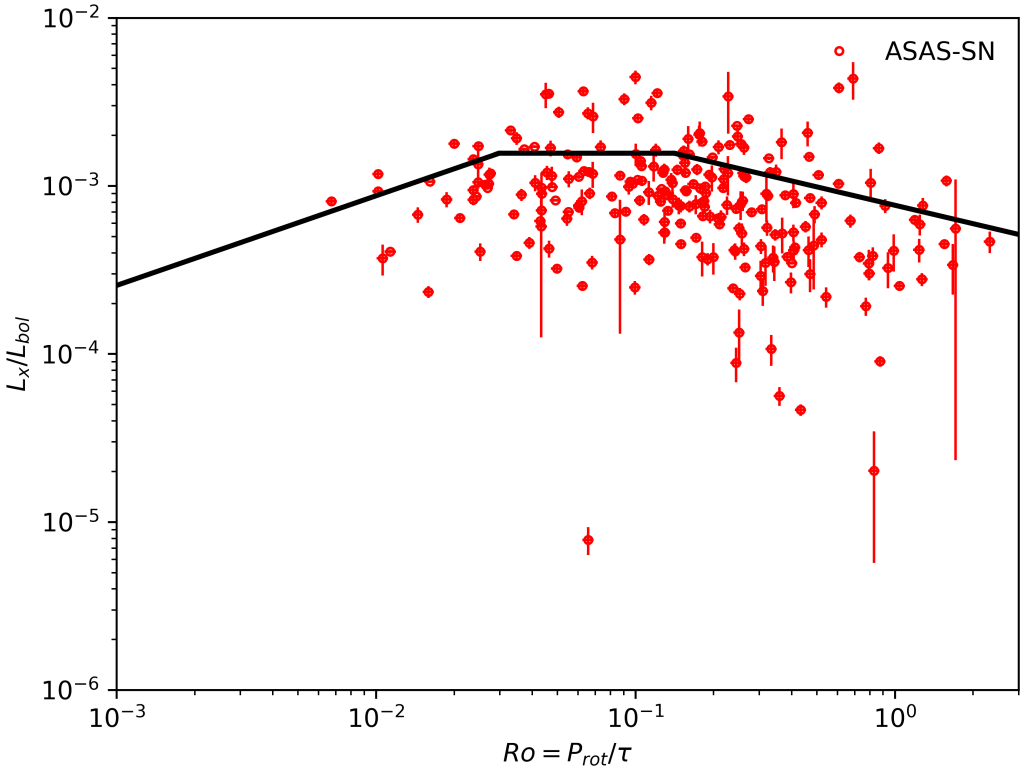

Fig. 5.10 Fractional X-ray luminosity, L_x/L_{bol}, plotted against the Rossby number, Ro, for 244 G- to M-type ASAS-SN stars.

precisely classify," and as such rotational variables in the ASAS-SN Catalogue of Variable Stars and the SuperWASP periodicity catalogue may be unclassified binaries or low amplitude Cepheids, especially for fast rotating objects with periods of ≤ 1 day, or for longer period objects. Jayasinghe et al. (2018) notes that the majority of rotational variables in the catalogue overlap with pulsators in both colour and period space. Without spectroscopic measurements for this study, these light curves can still be open to interpretation. However, since both catalogues have been classified by eye using the same method (for initial selection of the SuperWASP objects, and for final verification of the ASAS-SN objects), contamination alone cannot account for the inter-catalogue variation.

Investigating the differences between the two catalogues shows that the data sets show similar distributions of X-ray flux, however the ASAS-SN catalogue shows a distribution towards redder, fainter objects, shown in Figure 5.11. This is unsurprising, since the limiting magnitude of ASAS-SN is V = 17 mag, whereas SuperWASP is V = 15 mag, however such objects would still be expected to follow the relationship.

Figure 5.12 shows that the ASAS-SN catalogue contains no GKM-type objects with a period $\leq$0.3 days, whereas almost 25% of the SuperWASP catalogue contains objects within that period range. All flagged SuperWASP objects were removed from the catalogue to avoid the inclusion of spurious periods, hence there is a lack of SuperWASP objects with a period of close to 1 day. The SuperWASP data set includes a larger proportion of short period objects, made very clear by Figure 5.8 which shows a significant difference between *Ro*, and hence period range, of the two catalogues. As a test, removing all ASAS-SN objects with a period of $\geq$ 10 days does improve the power-law fit slightly, to $\beta = -0.87 \pm 0.18$. It is likely that the detection and automated classification methods used by ASAS-SN struggles with the period detection and classification of faint, long period rotational objects. There appears to be no other conclusive reason why the ASAS-SN sample appears to not follow the rotation-activity relation.

It is likely that misclassification of rotationally-modulated objects is also the primary reason for the small difference for the unsaturated regime power-law fit between the canonical value of $\beta = -2$ and for the SuperWASP value, which finds $\beta = -1.84 \pm 0.18$. Another, less likely possibility is that field stars may follow a marginally different rotation-activity relation than stars in clusters. Stars in clusters will have a similar age, metallicity, composition, and formation, and would experience magnetic braking and activity decline at similar rates, whereas field stars may not, however this is beyond the scope of this study.

It should also be acknowledged that, given the large pixel scales of both SuperWASP and ASAS-SN, there is a risk that some of these objects consist of blended multiple sources.

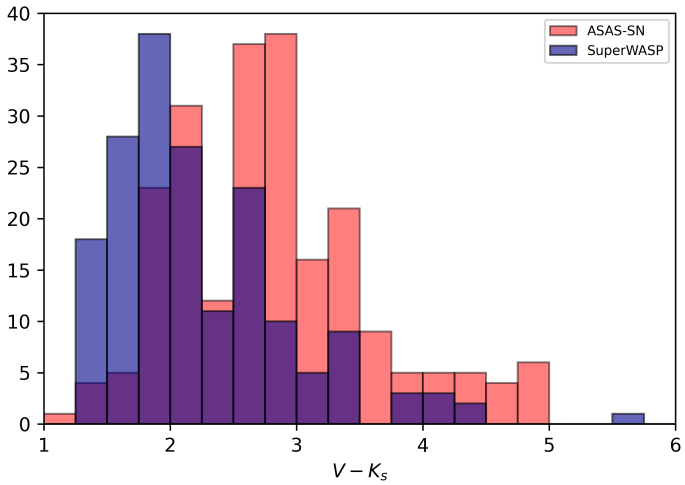

Fig. 5.11 The $V - K_s$ colour distribution of GKM-type stars.

Whilst every effort has been made to remove objects within a 2′ radius, is is possible that blended sources remain which artifically elevate the luminosities of some targets.

5.7 Summary

The study of the rotation-activity relation has so far been limited by the availability of deep observations over long baselines, and accuracy of stellar rotation periods. I tackled this through the use of the SuperWASP archive, which contains ∼10 years of high-cadence, long baseline observations, and a period search of the resulting $>$ 30 million light curves, and the automatically classified light curves in the ASAS-SN Catalogue of Variable Stars.

Through cross-matches of SuperWASP and ASAS-SN photometric data and XMM-Newton X-ray data, I updated the work by Norton et al. (2007), and characterised 900 rotationally modulated stars with photometric rotation periods from the *SuperWASP periodicity* period search and ASAS-SN Catalogue of Variable Stars, of which 402 late-type main-sequence field stars are used to study the rotation-activity relation.

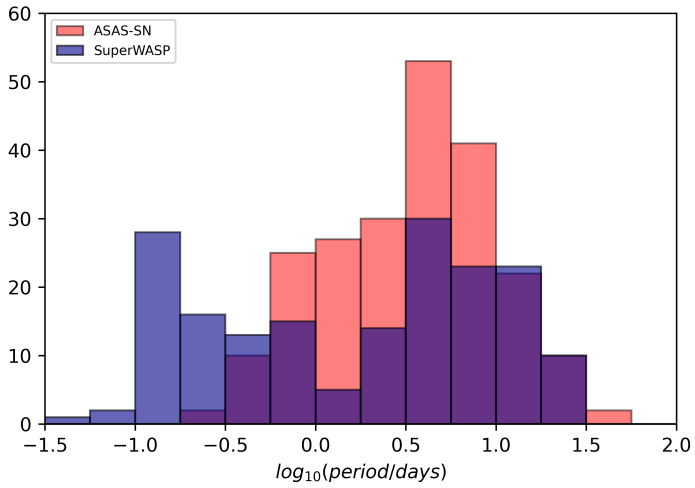

Fig. 5.12 The period distribution of GKM-type stars.

I find that while the ASAS-SN Catalogue of Variable stars provides a large catalogue of stars classified as rotationally modulated, using the catalogue without visually inspecting each light curve means that automatically classified data cannot be used to characterise the rotation-activity relation, and even after visual inspection, there may still be issues with the period detection for long period rotational objects in ASAS-SN. Having classified the SuperWASP light curves by eye, I find that late-type stars follow the rotation-activity relation, and the slope of the power-law fit of $\beta = -1.84 \pm 0.18$ is in line with the canonical value of $\beta = -2$. I also find a third supersaturation regime for the fastest rotating stars, and fit a power-law slope of $\beta_s = 1.42 \pm 0.26$. I suggest that the inclusion of indistinguishable non-rotational objects is the main reason for the lower β value.

Since the rotation-activity relation is believed to be a proxy for the stellar magnetic dynamo, and most dynamo models cannot yet reliably predict a match between rotation and activity indicators such as X-ray activity, all-sky observational studies prove vital for understanding the stellar dynamo, however I would advise that automatically classified rotationally modulated light curves are first thoroughly vetted by eye prior to avoid contamination of the sample.

Chapter 6

Background to Red Giant Binaries and Red Novae

In this second section of the thesis, I move from rotational variability to contact binaries. Whilst it might seem like a sudden switch, the beauty of the SuperWASP data are that serendipitous discoveries led me down intruiging paths of research. Having spent weeks visually classifying rotational variables, we realised that there was too much data to go through for a single person, leading us to set up the SuperWASP Variable Stars citizen science project (this will be tackled in later chapters). During this, an exciting discovery was made...

In the chapters following this one, I will detail the discovery and follow-up of a new configuration of binary star, a near contact red giant eclipsing binary. The prototype object is a Northern hemisphere object, TYC-3251-903-1, which is a relatively bright object (V=11.3) which has previously not been identified as a binary system. Although the light curve of TYC-3251-903-1 is characteristic of a W UMa (or EW) type eclipsing binary, the period is $\sim$42 d, notably longer than the characteristic contact binary period of $<$1 d. I suggest that this object, and others like it, could be the progenitors of red novae.

However, before I detail the discovery, follow-up, and modelling, it is helpful to understand the background and context to red giants, contact eclipsing binaries, and the predicted resulting rare transient, red novae. I will first provide the background to red giants, both in single and binary systems, followed by the relevant background to common envelope events (CEE) and red novae. These transients are extremely rare, with few confirmed observations and only one well-studied progenitor system, all listed in Table 6.1.

6.1 Red giants

Red giants are typically characterised by a luminosity of up to $\sim$3000 $L_{\odot}$, a radius of up to $\sim$200 $R_{\odot}$, a surface temperature of $\sim$3000–4000 K, a mass of $\sim$0.3–8 $M_{\odot}$, a spectral type of K or M, and a red-orange colour. Because of the low mass density of the envelope of a red giant, the outer layers have few but large cells, which often accounts for brightness variations. Much of this background has been adapted from Ryan and Norton (2010a).

Red giants are evolved stars which have left the main sequence. After billions of years on the main sequence, experiencing nuclear fusion in the core, red giants have depleted their supply of Hydrogen and can no longer generate energy through core Hydrogen burning. At this point, there is nothing to counter the force of gravity, and the degenerate Helium core begins to collapse. Heat is produced as a result of the sudden compression of the gas layers. In these layers, Hydrogen shell burning starts, increasing radiation pressure. The core temperature increases, and the diffuse outer layer of the star expands to hundreds of times greater than a solar radius. This increase in radius counters the increase in luminosity, and as such, the temperature of the star decreases and it reddens, moving onto the red-giant branch of the Hertzsprung-Russell diagram (Ryan and Norton, 2010a).

At this stage, the mass of the star determines its evolutionary path. For stars between 1–2 $M_{\odot}$ the density of the core prevents further collapse through electron degeneracy pressure. The degenerate core continues to heat up to around 10^8 K, at which point a Helium flash

occurs, where the entire core begins Helium fusion almost simultaneously. The triple-α process now begins fusing Helium to Carbon. A star of $\sim$1 $M_{\odot}$ will follow an evolutionary track similar to the one shown in Figure 6.1.

For star more massive than 2 $M_{\odot}$ the core is more diffuse and the core reaches 10^8 K before degeneracy occurs. Helium fusion begins in a more gentle fashion, and a Helium flash does not occur. In metal-poor stars, the core Helium fusing phase is known as the Horizontal Branch (HB). Metal-rich stars fusing Helium to Carbon lie on the red clump.

When the core Helium is depleted, the star collapses again until a new Helium shell reaches the core and ignites fusion, resulting in a degenerate Carbon-Oxygen core. At this point, outer shells of Hydrogen start fusion. This second red giant phase is known at the Asymptotic Giant Branch (AGB). For stars with a mass of less than 8 $M_{\odot}$ fusion does not occur for the degenerate Carbon-Oxygen core, and instead, the outer layers of the star are blown off as a planetary nebula, leaving a white dwarf, ending the evolution of the star. For a star with a mass greater than 8 $M_{\odot}$ the core continues to heat and fuse heavier and heavier elements, up until Iron. At a critical mass, the Iron core collapses and a supernova occurs. For very low mass red giants (0.2–0.5 $M_{\odot}$), the star is not massive enough to initiate Helium fusion. Whilst these stars cool and become more luminous, they never achieve a Helium flash, and instead lose their outer layers and become a white dwarf.

Stars are thought to spend on about 1% of their life in the red-giant phase, and evolution through the HB and AGB phases is a factor of ten times faster than the RGB phase.

6.2 Red giant binaries

For early spectral types, more than 50% of stars are in binary or multiple systems, and so massive stars are commonly found in a binary system (Duquennoy and Mayor 1991; Lada 2006), however, red giant binary systems are rare since these evolve from low mass stars of late spectral types.

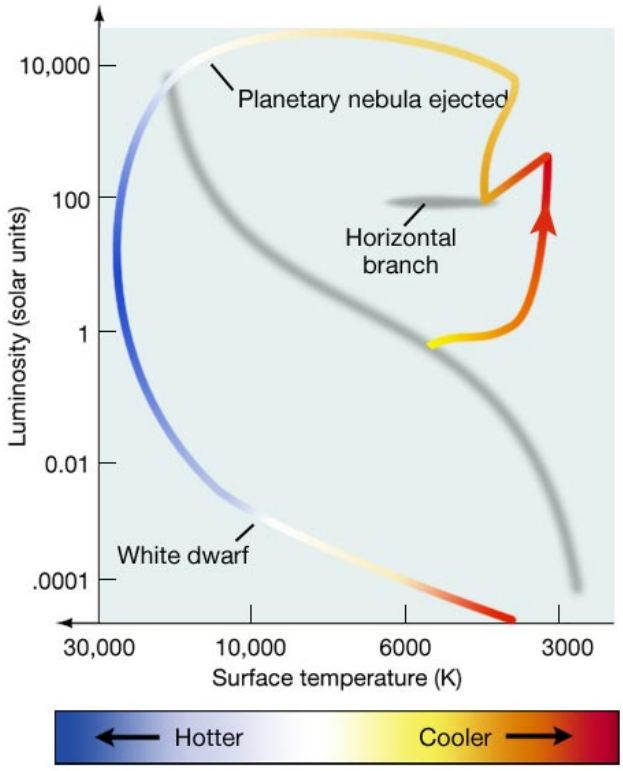

Fig. 6.1 The evolutionary track of a solar mass star [Credit: Penn State Astronomy & Astrophysics].

Red giant binaries typically refer to binary systems with one red giant component and an often unseen component, for example, a smaller main sequence star. Periodic variations in the light curve from this type of system occur due to the distorted shape of the red giant filling a significant portion of its Roche Lobe, often seen as an ellipsoidal variation in the light curve. These types of binaries have been well-studied, for example by the OGLE team who studied 34 long period twin red giant detached eclipsing binaries (Nataf et al., 2012), and Gaulme et al. (2013), who detected 19 ellipsoidal red giant binaries (for example KIC 9246715) through a cross correlation of Kepler $\sim$14,000 red giants and 2,500+ eclipsing binaries (Gaulme 2013; Gaulme et al. 2014, 2013; Hekker et al. 2010; Rawls 2016; Rawls et al. 2016), and Benbakoura et al. (2021) who studied 16 further red giants in eclipsing binaries. These discoveries have allowed astronomers to probe stellar mass, radius, temperature, metallicity, and evolutionary state through the study of global pulsations of the binary red giants, known as asteroseismology. Despite knowledge of these systems, red giant binaries are rare, and there previously appeared to be no known twin red giants in an eclipsing near-contact binary configuration.

The only exception appears to be work by Wood et al. (1999), who studied red giants in eclipsing binaries. Whilst most appeared to have light curves more typical of a red giant and a smaller main sequence companion, 4 red giant binaries along the sequence E branch of the period-luminosity relationship appeared to have light curves which resembled contact eclipsing binaries. These light curves can be seen in Figure 6.2, labelled as 7430.104 E, 7672.98 E, 7788.98 E, and 7673.79 E. Wood et al. (1999) could not find an explanation for the shape of this light curve, except that these must be eclipsing binaries made up of two giant stars in, or near contact with one another. They state that these binaries may be the progenitors of bipolar planetary nebulae, but *"if the existence of these red giant contact and semi-detached binaries is confirmed, then extant theories of binary star evolution will require substantial modification."*

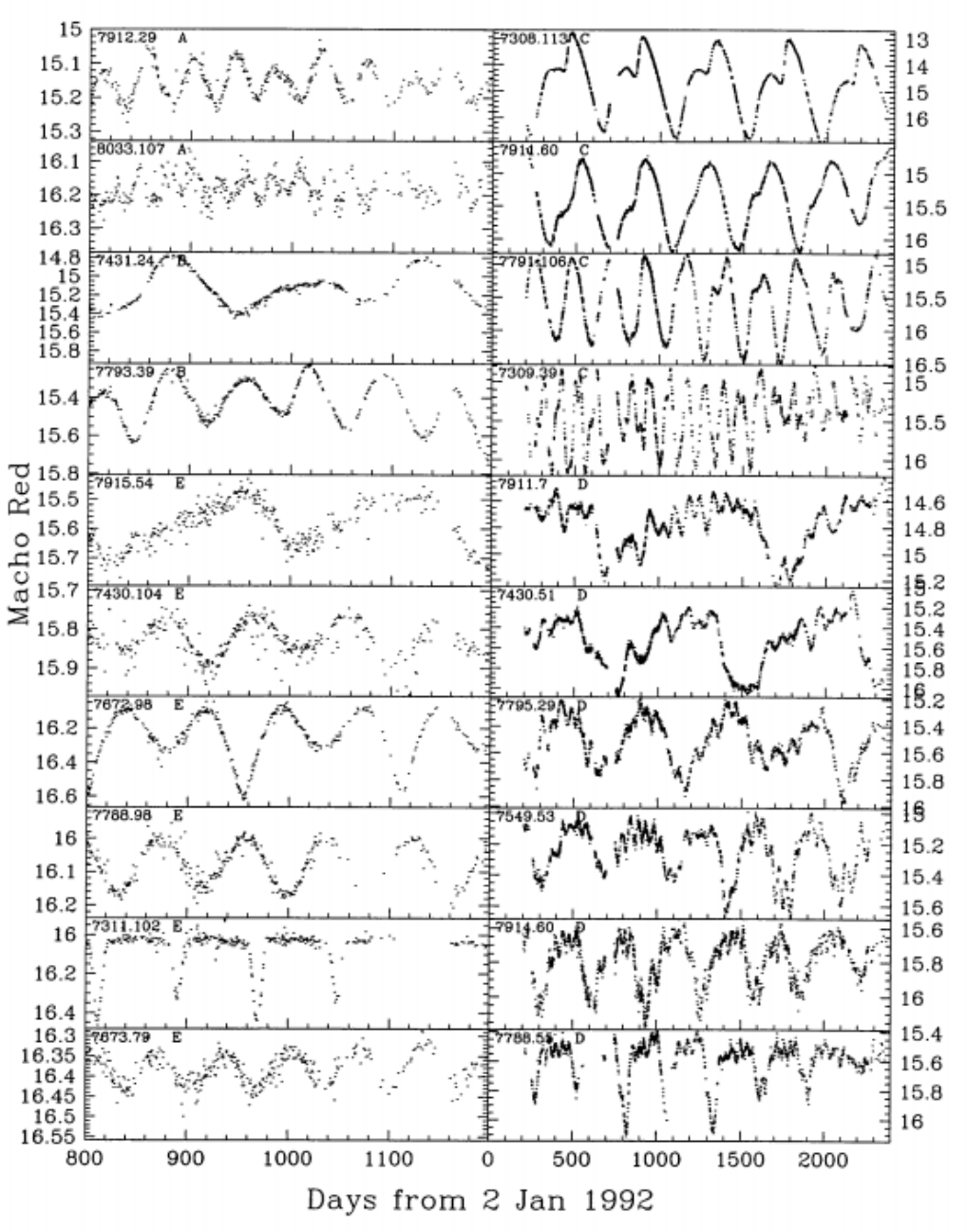

Fig. 6.2 Light curves of red giant binaries from Wood et al. (1999). Note the sequence E light curves which appear to resemble contact eclipsing binaries.

However, Soszynski et al. (2004) modelled these red giant binaries as ellipsoidal variables, a result accepted by the original authors. Wood (2007) responded to this further work on the sequence E red giant binaries, saying "eclipsing pairs of similar-size red giant stars, [are] an unlikely situation for a pair of independently evolving stars unless the masses are almost identical." Therefore, the existence of contact red giant eclipsing binaries is not ruled out.

Making the assumption that contact or near contact red giant eclipsing binaries do exist, there are some fascinating questions surrounding their formation and death. In future chapters, I suggest that near contact red giant eclipsing binaries are likely to be progenitors of stellar mergers known as 'red novae'. Hence, in the following sections, I present a summary of knowledge on red novae and their formation.

6.3 Common envelope events

In a binary system, the interactions between component stars is a common process (e.g. (Sana et al., 2012)). A common envelope is formed when orbital separation of the binary decreases or one of the stars overflows its Roche lobe (e.g. (Iben and Livio, 1993)). In the case of Roche lobe overflow for one star, it triggers dynamically unstable mass transfer, causing the orbital separation to decrease further and the donor star to expand more. This runaway process results in both stars becoming engulfed by a non-rotating common envelope (e.g. Benson 1970; Livio and Soker 1988; Paczynski 1976; Podsiadlowski 2001; Yungel'Son 1973).

The components of the binary (the core of the donor and the full companion) continue to rotate inside the common envelope. If the common envelope rotates more slowly than the binary, the hydrodynamical draw extracts angular momentum, reducing the orbital separation and increasing the orbital velocities, causing the stars to merge (e.g. Ivanova et al. 2013; MacLeod et al. 2017a) or end in a binary with a significantly reduced orbital separation (if the common envelope is ejected). The process of reducing the binary orbit is known as a

spiral-in (Ivanova et al., 2013). Whether the process produces a closer system or a merged star depends on the initial energy available, and the energy expense (Livio and Soker, 1988).

For systems with an envelope with low inertia, co-rotation could be maintained for a short period of time (Ivanova et al., 2013). Mass loss and angular momentum loss can also occur through the outer Lagrange points (e.g. Flannery 1977; Lombardi et al. 2011; Pejcha 2014; Shu et al. 1979). The loss of energy from the binary heats and expands the envelope. The common envelope phase ends when either the component stars merge, or the envelope is ejected. A common envelope event is usually expected to be accompanied by a rise in luminosity.

As of yet, models cannot fully explain the initial instability that leads to the eventual merger. Tidal instabilities (e.g. Lai et al. (1993)), for example, the Darwin instability (Rasio, 1995), and gravitational radiation, are processes which on their own might be too slow. Even though the timescales over which this whole process occurs are short, and it is challenging to observe a binary undergoing this process, modelling and observing common envelope events is important in understanding the underlying processes for objects including double black holes, X-ray binaries, close neutron stars, and Gamma Ray Bursts (Ivanova, 2016). Common envelope events can also take the form of even more rare transient events, such as red novae.

6.4 Red novae

A red nova (RN, plural RNe), or luminous red nova (LRN, plural LRNe) is a recently recognised class of stellar transient thought to be a stellar explosion caused by the merger of a non-compact massive binary system. Red novae are characterised by a red colour, a luminosity between that of classical novae and supernovae, and long outbursts and a slow expansion rate compared to other high energy novae, as shown in Figure 6.3. The light curves of red novae appear to show a double peaked light curve and are brightest in the infrared. Red novae are sometimes referred to as "luminous red variables", "red variables",

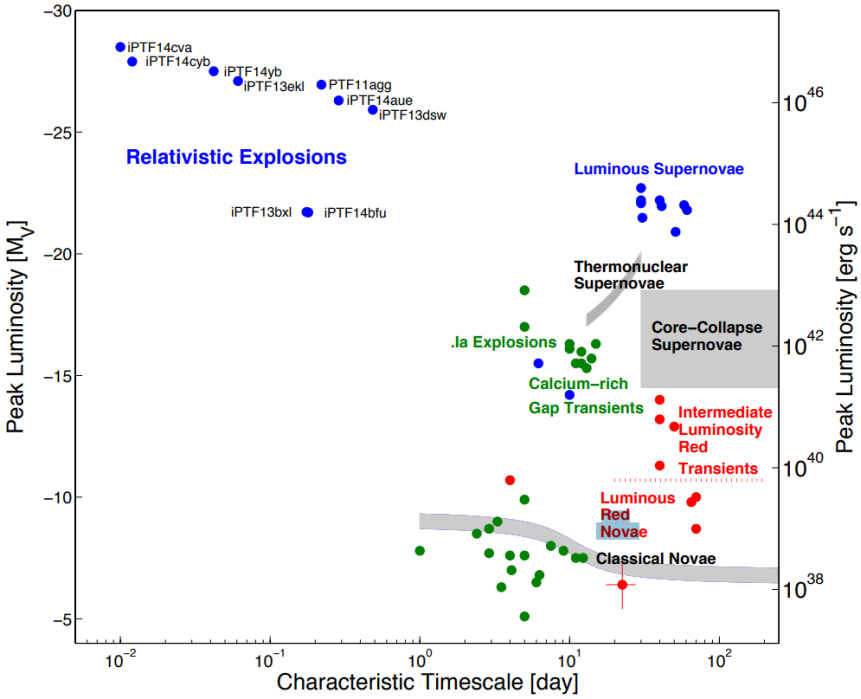

Fig. 6.3 Peak luminosity-decay timescale for explosive transients (Kasliwal, 2011).

"red transients", "Intermediate-luminosity red transients (ILRTs)", "V838 Mon type objects", or "mergerbursts". The following section will discuss their discovery and highlight notable LRNe, characteristics and evolution, predictions for future LRNe, and summarise knowledge of all LRNe detected to date.

6.4.1 Discovery

The importance of stellar mergers has long been recognised as an important part of stellar evolution. The unusually bright and red nova detected in M31 in 1988 (Bond and Siegel 2006; Mould et al. 1989; Rich et al. 1988) sparked interest in intermediate luminosity novae. Several unusual novae were detected over the following years, including the outburst of V4332 Sgr in 1994 (Martini et al., 1999). The outburst in V838 Mon in 2002 and subsequent light echo famously imaged by the Hubble Space Telescope is now thought to have been a LRNe (Bond et al. 2003; Brown et al. 2002).

The first confirmed LRNe was M85 OT2006-1 in the M85 galaxy, which was discovered during the Lick Observatory Supernova Search and followed up by (Kulkarni et al., 2007), who determined that the likely progenitor was a stellar merger rather than a stellar eruption. The outburst of V1309 Sco finally confirmed the hypothesis of Soker and Tylenda (2003) that LRNe are formed via the merger of contact binary stars. A number of subsequent possible LRNe have been detected and progenitors have been suggested, shown in Table 6.1. I discuss two important LRNe below, the eruptions of V838 Mon and V1309 Sco.

6.4.2 V838 Mon

V838 Mon temporarily became the most luminous star in the Milky Way in January 2002 as it experienced outburst and reached a magnitude of 6.75 in early February, discovered by Brown et al. (2002) and famously imaged by the Hubble Space Telescope, shown in Figure 6.4. This eruption was mysterious. Initially it was thought to be a nova, but the evolution did not follow typical nova behaviour. A number of mechanisms were suggested, including planetary capture, a thermonuclear event with a massive supergiant, an atypical nova, the death of the star itself, or a mergeburst, the merger of a binary and subsequent ejection of a common envelope. Following the in-depth study of V1309 Sco, this latter theory is thought to be the most likely scenario.

The eruption was characterised by a fast rise, and experienced three separate maxima over the following $\sim$3 months (Munari et al., 2002). By April 2002, V838 Mon had become extremely cool and red, and the central star had almost vanished in the optical in April 2002, but remained incredibly bright in the infrared. Post-eruption, V838 Mon became one of the coolest M-type supergiants ever observed (Munari et al., 2002). The light echo produced was well documented by the Hubble Space Telescope, but it is not yet clear whether the dust which caused the echo was associated with the progenitor itself.

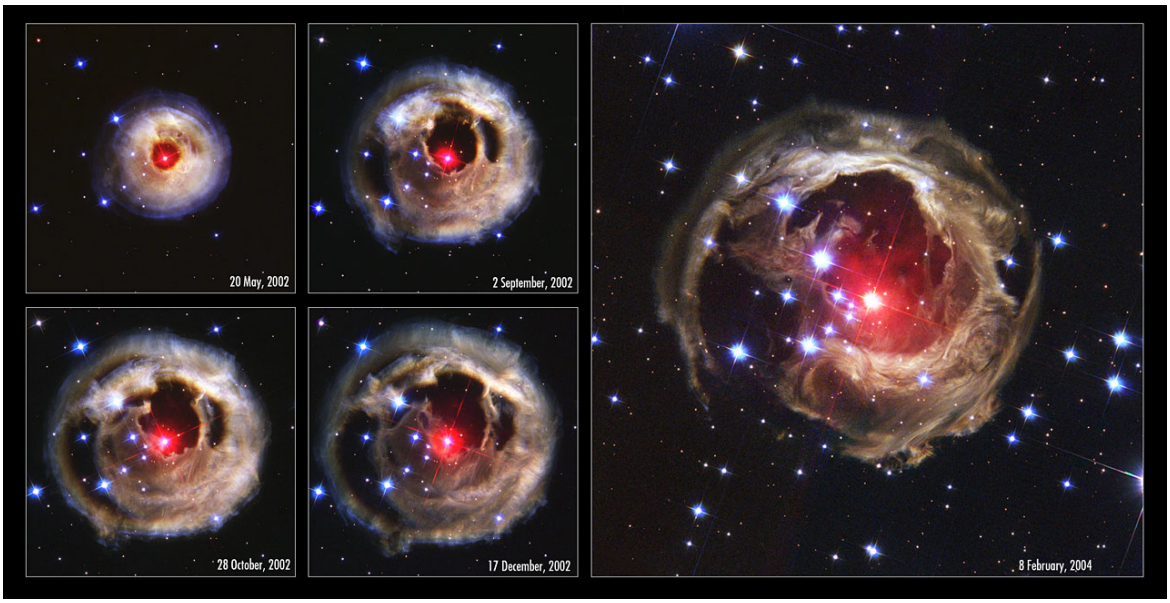

Fig. 6.4 The evolution of the light echo of V838 Mon [Credit: ESA/Hubble].

The progenitor of V838 Mon was originally thought to be an under-luminous F-type main sequence star, which was later revised to an early B-type star with an early A- or B-type companion (Tylenda et al., 2005). It has also been suggested that the progenitor was a $\sim 65 M_{\odot}$ massive supergiant, however this has been debated by Tylenda et al. (2005) and Tylenda and Soker (2006), who model the progenitor as the accretion of a low mass star onto a main sequence star. The unusual behaviour of V838 Mon mirrored that of M31 RV and V4332 Sgr. Both events were discovered in the late phases of their eruptions, and both showed an excess in the infrared and a strong emission-line spectra. Both objects begun as K- or early M-type objects at the start of eruption, evolving to cool late-type objects.

6.4.3 V1309 Sco

A "red nova" or "V838 Mon-type eruption" was detected in early September 2008 and was followed up using VLT/UVES observations by Nakano et al. (2008). This new nova, V1309 Sco, also known as Nova Sco 2008, seemed to be very out of the ordinary (Mason et al. 2010; Tylenda et al. 2011).

Luckily, V1309 Sco lies close to the Galactic centre in a field that was monitored by the OGLE project (Udalski, 2003a), so had been photometrically observed since 2001, with $\sim$1,340 observations in the Cousins I band. This allowed Tylenda et al. (2011) to identify the progenitor as an eclipsing contact binary containing an F-type giant (Rudy et al., 2008), with a slowly decreasing orbital period of $\sim$1.4 days.

Between 2002–2008, the period decreased by 1.2%. Between 2002–2006, the light curve showed a classic W UMa shape, with two maxima and two minima per cycle. By 2007, only one maximum and minimum was observed, and the brightness in the I band increased and decreased by $\sim$1 magnitude over the course of a year. In March 2008, the brightness rose exponentially until the merger in September 2008, shown in Figure 6.5. At this point, V1309 Sco was $\sim$6 magnitudes brighter than pre-outburst (Tylenda et al., 2011). Over the month post-outburst, the F-type giant progenitor evolved to a K- then early M-type giant (Mason et al. 2010; Rudy et al. 2008). After 8 months, the remnant was observed to have evolved to a late M-type giant (Mason et al., 2010). This evolution is similar to that of V838 Mon (e.g. Tylenda et al. (2005)). V1309 Sco has since become known as a Rosetta stone for the study of red novae, for the first time identifying the progenitor and full evolution of the system.

6.4.4 Pre-outburst characteristics

The progenitors of LRNe are now thought to be late-type giant contact binary systems, however other types of progenitors have been suggested, including intermediate mass yellow supergiants (Pastorello et al., 2019), massive OB-type binaries (Goranskij et al., 2016), the ejection of a common envelope from a massive binary (Blagorodnova et al., 2017), and even the merger of a giant planet with a parent star (Kashi et al., 2019).

Soker and Tylenda (2003) first proposed LRNe to be binary mergers, based on the stellar eruption of V838 Mon, a prediction that was confirmed by the LRNe of V1309 Sco (Tylenda et al., 2011). The light curve of the progenitor of V1309 Sco evolved from a typical W

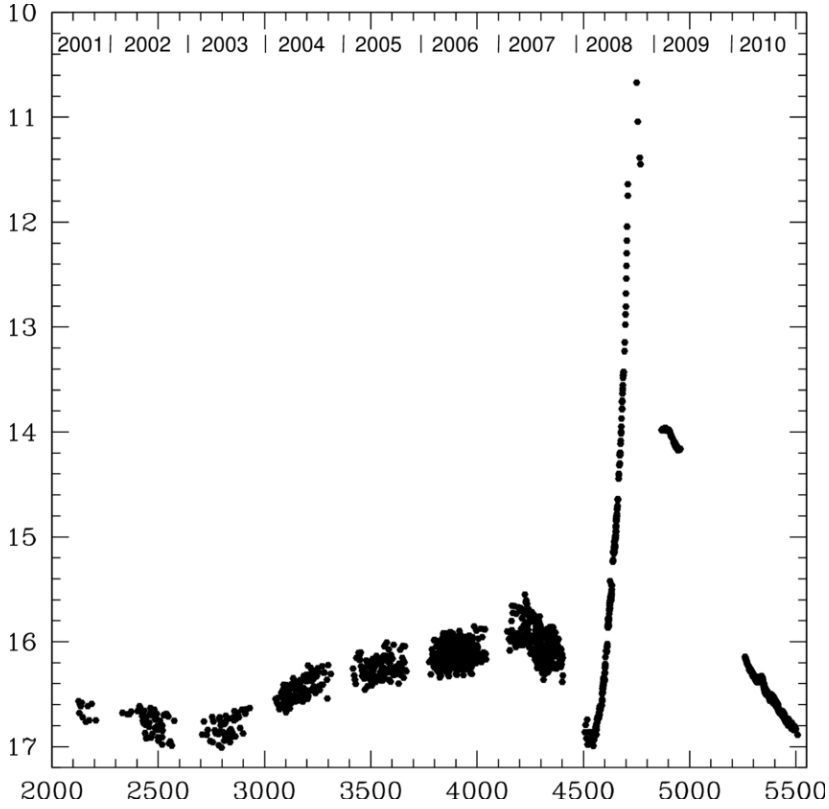

Fig. 6.5 The light curve of the merger of V1309 Sco from the OGLE-III and OGLE-IV projects (Tylenda et al., 2011).

UMa shape to just a single peak, possibly due to an obscuration of the binary by mass loss (Metzger and Pejcha, 2017). In the year before the merger, no periodic variability was detectable, but there was a slow brightening of up to 10 magnitudes, possibly due to mass loss again during the final orbital decay. The system experienced a rapid brightening of approximately 1 magnitude per day, likely due to the merger event, orbital energy dissipation, and expulsion of the common envelope (e.g. Blagorodnova et al. 2017; Ivanova et al. 2013; Metzger 2017; Nandez et al. 2014; Pejcha 2014). Similarly, the outburst of V4332 Sgr appeared to have a variable progenitor, and archival data suggests that it also experienced a slow rise in brightness over decades pre-outburst (Goranskij et al. 2007; Kimeswenger 2007). Pejcha (2014) suggests that this pre-outburst brightening, observed in other LRNe, is due to L2 mass-loss during the spiralling in phase (Tylenda and Kamiński, 2016). However, Metzger and Pejcha (2017) disagree with the model of giant star progenitors, and believe that progenitors of LRNe are actually relatively compact MS stars and not red (super)giants.

Tylenda et al. (2011) suggests that the onset of the Darwin instability is the mechanism that triggers outburst, which happens when the mass ratio is so low that the secondary star cannot keep the primary star synchronously rotating via tidal interaction. As angular momentum is transferred from the binary orbit to the primary, a runaway effect occurs. The mass ratio has been found to be q=0.09 for a radiative MS primary, and between q=0.04–0.15 for a giant (Molnar et al. 2017; Tylenda et al. 2011). LRNe progenitors range in mass, from 1–5 $M_{\odot}$ for the faintest objects, to up to a few tens of $M_{\odot}$. For context, V838 Mon was an intermediate mass object at 5–10 $M_{\odot}$.

The nova events themselves are characterised by a distinct red colour and a slow expansion rate compared to novae and supernovae. With so few confirmed detections of LRNe, detailed models and theoretical understanding are hard to achieve, so it is important to characterise the property of the progenitor, or the proposed common envelope phase (e.g. Iaconi and De Marco (2019)).

6.4.5 Outburst and evolution

Whilst the majority of the literature refers to red novae and luminous red novae as RNe and LRNe interchangeably, Pastorello et al. (2019) propose that there are actually two separate classes of objects, Galactic RNe and extra-Galactic LRNe. This interpretation states LRNe are scaled up versions of RNe, and that there are different possible evolutionary paths depending on the initial mass of the system. They classify LRNe as events with a progenitor system of a few tens of $M_{\odot}$, and peak magnitude brighter than $M_v = -10$, typically M_v=-12–-15, and RNe as events with a progenitor system of $< 10M_{\odot}$ with a peak magnitude fainter than $M_v = -10$. The possible evolutionary paths for LRNe and RNe are shown in Figure 6.6. Throughout this chapter, red novae will typically be referred to as LRNe, unless otherwise necessary.

As the binary components merge, the system expands extremely rapidly, reaching up to tens of thousands of solar radii in just a few months. During this time, the system initially brightens by approximately 1 magnitude per day and then plateaus in the visible for months, often experiencing a secondary maxima. As the visible light fades over the following months post-outburst, LRNe brighten in the infrared, and experience a number of resurgences in infrared brightness over time.

LRNe reach a maximum luminosity of $\sim 10^6 L_{\odot}$ (Tylenda et al., 2011), and the luminosity lies between supernovae (brighter) and nova (fainter). The energy involved in a LRNe is likely to be comparable to the orbital energy released from a common envelope event ($\sim 10^{47}$ erg) (Bond et al. 2009; Kulkarni et al. 2007). Since outburst, V1309 Sco has faded by a factor of ~ 50 (Tylenda and Kamiński, 2016), V838 Mon was a factor of ~ 60 fainter in 2009 than at outburst in 2002 (Tylenda et al., 2011), and V4332 Sgr has faded by factor of ~ 30 between 2003–2014.

The optical emission from LRNe was originally thought to be a result of hydrogen recombination in multiple shells of ejecta created during the dynamical stage of the merger

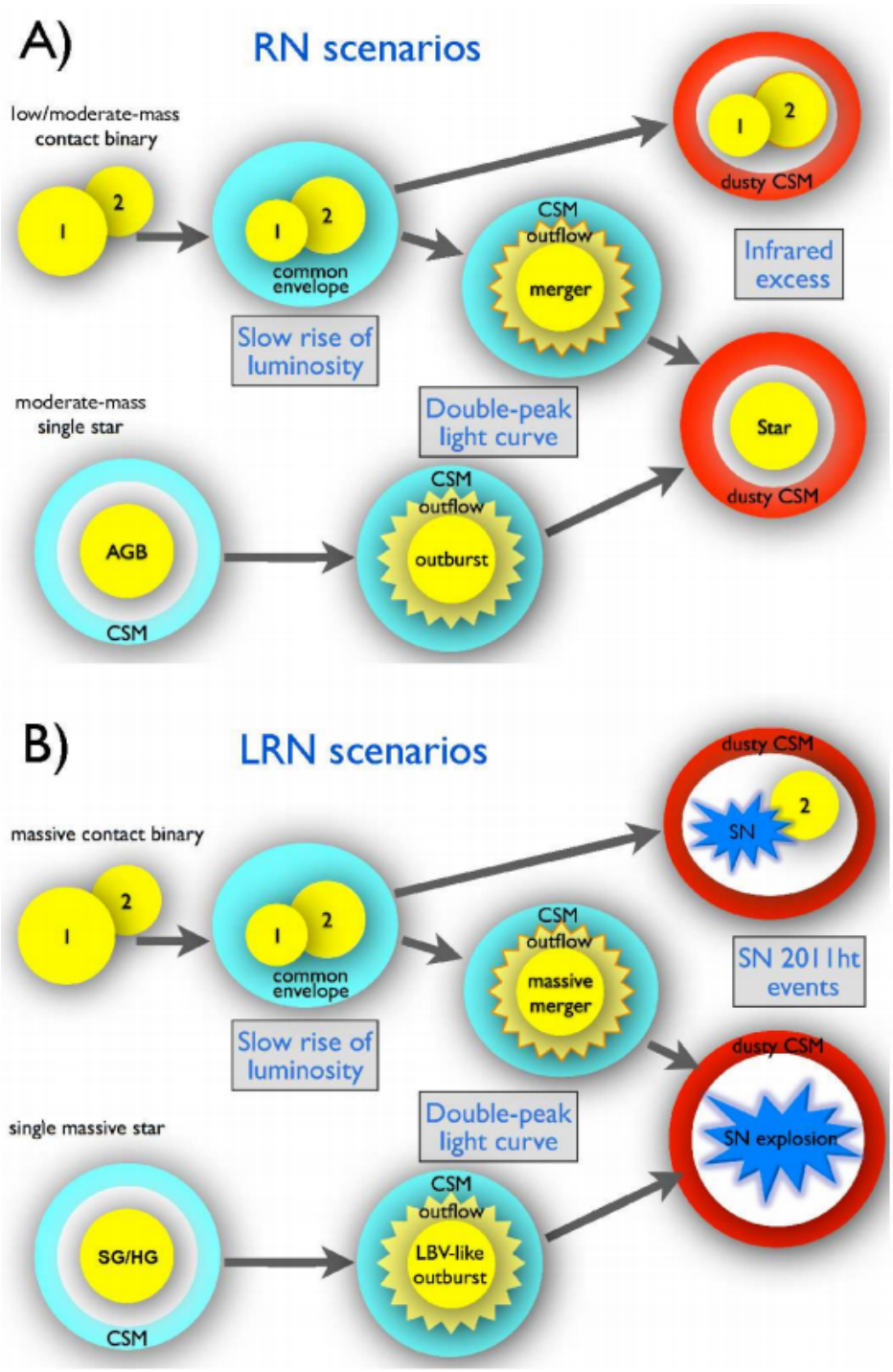

Fig. 6.6 Sketch from Pastorello et al. (2019) showing possible evolutionary paths for RNe (top) and LRNe (bottom).

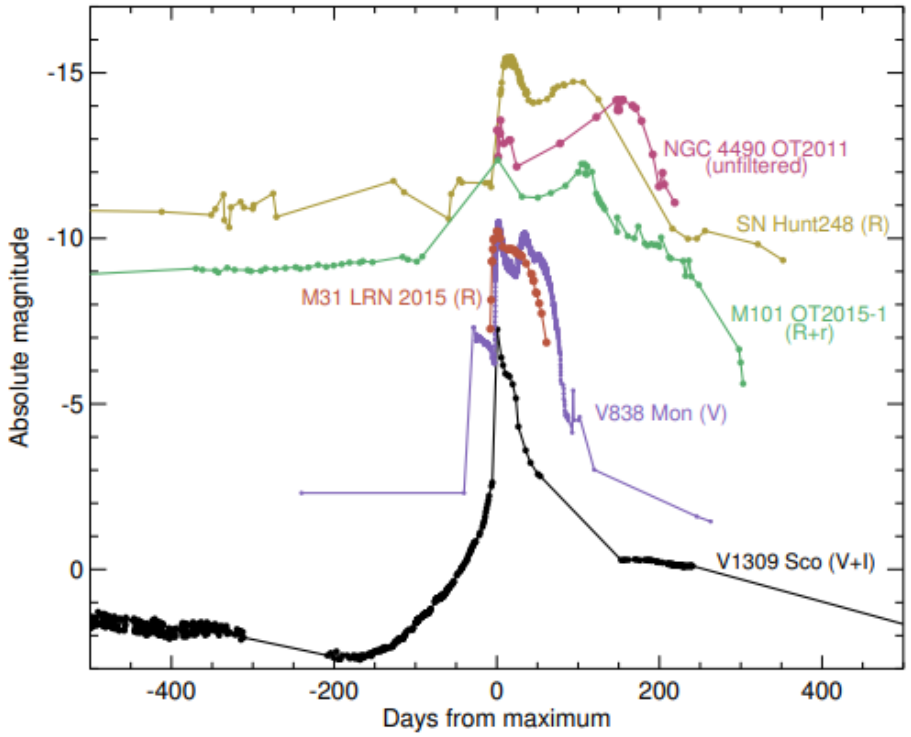

Fig. 6.7 Double-peaked light curves of several luminous red novae candidates (Metzger and Pejcha, 2017).

process (Ivanova et al. 2013; Lipunov et al. 2017). However, based on observations of M31 LRN 2015, MacLeod et al. (2017b) argue that this model does not account for the short duration and high luminosity of the initial peak, and it instead results from the release of thermal emission from the hot ejecta, similar to early supernova emission (e.g. Nakar and Sari (2010)). This single source of energy does not explain the secondary maximum unless multiple ejection events occur separated by multiple orbital periods. An alternative explanation from Lipunov et al. (2017) is that the secondary maximum is actually the remnant shining through the transparent ejecta. However, the luminosity of the second peak is usually above the Eddington limit, so may not be a fully correct model.

Metzger and Pejcha (2017) explains the double peaked light curve of LRNe, shown in Figure 6.7, by a modest mass ejection following merger. The early peak is the result of the release of thermal energy from fast ejecta, and the second peak is he result of shock-powered

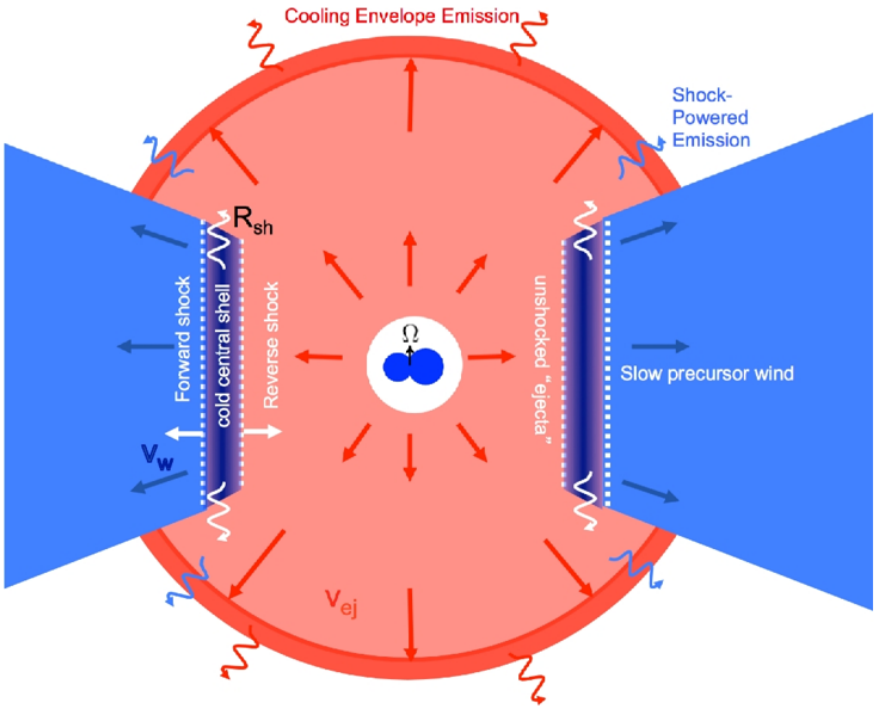

Fig. 6.8 A schematic of the shocks in stellar mergers, thought to be the power source of LRNe (Metzger and Pejcha, 2017).

emission in the collision between the fast shell and pre-existing material in the equatorial plane, shown in Figure 6.8. This would create a cooler, denser shell; an ideal place for late dust formation, as observed in the extra-galactic LRNe AT 2017jfs (Pastorello et al., 2019). Other models by Barsukova et al. (2014) suggest that the rapid merger generates a violent forward shock, increasing the photospheric temperature, producing the initial blue light curve peak. This is followed by a fast adiabatic expansion of the envelope which carries out thermal energy to the delayed outer layers which produces the broad red maximum.

Kochanek et al. (2014) suggests that the wider range in peak luminosities is connected to the total mass of the binary progenitor, with faint LRNe being $\sim 1M_{\odot}$, intermediate luminosity events such as V838 Mon being $< 10M_{\odot}$, and massive binaries up to 50–60 $M_{\odot}$ e.g. for AT2017jfs, SNhunt248 (Kankare et al. 2015; Mauerhan et al. 2015), and NGC 4490-2011OT1 (Pastorello et al. 2019; Smith et al. 2016). Mauerhan et al. (2018)

suggests a possible correlation between outflow velocities and light curve peak luminosities. Observations of the brightest LRNe might provide indirect evidence for the existence of massive ($> 40M_{\odot}$) red supergiants, and may be markers along the evolutionary pathway leading to the formation of double compact objects (Howitt et al., 2020).

The ejecta velocities of LRNe match expected merger or common envelope event velocities. Kasliwal et al. (2011) measured expansion velocities of ~ 1000 kms^{-1} for the possible LRNe, PTF 10fqs. The values for NGC300 OT 2008 vary greatly from $\sim$75 kms^{-1} (Bond et al., 2009) to $\sim$1000 kms^{-1} (Berger et al., 2009). Low velocities are compatible with the merger of a primary giant star or common envelope event models, and higher velocities suggest that the primary would be a less extended star such as an early giant, similar to V1309 Sco.

LRNe also have very distinct spectra. Spectroscopic observations of V4432 Sgr in 2005 show a $\sim$3600 K M3-type spectrum dominated by atomic and molecular emission features (Tylenda et al., 2019). Over 70 atomic lines from 11 elements have been detected, including Na, Mg, Al, K, Ca, Cr, Mn, Fe, Rb, Sr, and Ba, and $\sim$140 bands from AlO, ScO, TiO, VO, CrO, and YO. This is the richest and most intense emission spectra detected. Spectra taken in 2009 show an M5- to M6-type spectra, with a decrease in temperature by 300–350 K. This decrease in temperature is responsible for optical fading (Kamiński et al. 2010; Nicholls et al. 2013).

Following the eruption of V1309 Sco, the object became very faint in the optical (Kamiński et al., 2015). Since V1309 Sco lies in a crowded field, as the object faded, ground-based observations were hampered by nearby stars. But Kamiński et al. (2015) has shown that V1309 Sco is now spectrally similar to V4332 Sgr a few years after the 1994 eruption. Like V4332 Sgr, V1309 Sco now dominated by emission features from neutral atoms and molecules (Kamiński et al. 2015; Tylenda et al. 2015). Whilst the object remains bright in the infrared (Nicholls et al., 2013), the main remnant is almost completely shrouded

in dust, and the spectrum likely arises from scattering of central star radiation by circumstellar material.

Dust is a common factor amongst LRNe, shown brilliantly by the Hubble Space Telescope images of V838 Mon, and detected around V1309 Sco, which quickly became enshrouded in dust post-eruption (Tylenda and Kamiński, 2016). Observations of V4332 Sgr and CK Vul tell us that the remnant may remain hidden for decades or hundreds of years by a dusty thick disc. The V1309 Sco progenitor system likely already contained circumstellar material, and the increased rate of mass loss from the outer Lagrange point may have caused the pre-outburst optical fading, hiding $\sim$70% of the photosphere. However, this dust was most likely lost in the eruption, and the high temperature (900–1000 K) dust now visible must have formed during outburst. New infrared data from Herschel has detected cold dust ($\sim$30 K) at a few thousand AU from the central object, which suggests that prior to the outburst, the progenitor already experienced a period of intense mass loss (Tylenda and Kamiński, 2016). The mass of the V1309 dust envelope has been estimated to be at least $10^{-3} M_{\odot}$ (Tylenda and Kamiński, 2016).

In summary, remnants of LRNe have been observed to be either late-type giants and/or luminous infrared objects (Tylenda et al., 2013). This indicates that LRNe events can only be accounted for by a merger, and not classical novae or late He-shell flashes (Soker and Tylenda 2003; Tylenda and Soker 2006).

6.4.6 Detections of red novae

As previously noted, red novae are rare, despite increasing detections over the last 10 years. All detected LRNe, rejected LRNe, failed LRNe, and predicted progenitors of LRNe are listed in Table 6.1, and selected interesting LRNe candidates are detailed below.

Name	Date	Location	References
CK Vul	1670		Shara et al. (1985)
V1148 Sgr	1943		Mayall (1949)
M31 RV	1988	NGC 224	Rich et al. (1988)
V4332 Sgr	1994		Martini et al. (1999)
SN 1997bs*	1997	NGC 3627	Van Dyk et al. (2000)
OGLE-2002-BLG-360	2002		Tylenda et al. (2013)
V838 Mon	2002		Brown et al. (2002)
M85 OT2006-1$^{\diamond\star}$	2006	NGC 4382	Kulkarni et al. (2007)
SN2008S$^{\diamond\star}$	2008	NGC 6946	Prieto et al. (2009)
NGC300 OT-2008$^{\diamond\star}$	2008	NGC300	Berger et al. (2009)
V1309 Sco	2008		Tylenda et al. (2011)
PTF 10fqs$^{\diamond\star}$	2010	NGC 4254	Kasliwal et al. (2011)
PFT 10acbp$^{\diamond\star}$	2010	UGC 11973	Kasliwal (2011)
2011OT1*	2011	NGC 3437	Howerton et al. (2011)
OT2011*	2011	NGC 4490	Magill et al. (2011)
2013OT1*	2013	UGC 12307	Pastorello et al. (2019)
AT 2014ej*	2014	NGC 7552	Stritzinger et al. (2020)
SNhunt248*	2014	NGC 5806	Mauerhan et al. (2015)
ASASSN-13db$^{\diamond}$	2014		Kashi et al. (2019)
Sn2015bh$^{\diamond\star}$	2015	NGC 2770	Goranskij et al. (2016)
M31 LRN 2015*	2015	NGC 224	Dong et al. (2015)
M101 OT2015-1*	2015	NGC 5457	Blagorodnova et al. (2017)
AT 2017jfs*	2017	NGC 4470	Pastorello et al. (2019)
AT 2018hso*	2018	NGC 3729	Cai et al. (2019)
AT 2018bwo*	2019	NGC 45	Blagorodnova et al. (2021)
AT 2019zhd*	2019	NGC 224	Pastorello et al. (2021a)
M51 OT2019-1$^{\diamond\star}$	2019	NGC 5194	Jencson et al. (2019)
AT 2020hat*	2020	NGC 5068	Pastorello et al. (2021b)
AT 2020kog*	2020	NGC 6106	Pastorello et al. (2021b)
KIC 9832227*† (Progenitor)	2022		Molnar et al. (2017)
TY Pup (Progenitor)			Sarotsakulchai et al. (2018)
V1187 Her (Progenitor)			Samec et al. (2018)
ZZ PsA (Progenitor)			Wadhwa et al. (2021)
V857 Her (Progenitor)			Wadhwa et al. (2021)

Table 6.1 Table of red novae detected to date and candidate progenitors. $^{\diamond}$ indicates that the object was thought to be an LRNe but is likely another transient; * indicates that the object is extragalactic; † KIC 9832227 was later proved not to be a likely merger candidate.

Fig. 6.9 The chart of the position of the nova in CK Vul recorded by Hevelius and published by the Royal Society.

Selected historical detections

CK Vulpeculae (also Nova Vulpeculae 1670) is the oldest reliably-documented nova (Shara et al., 1985), but may have actually been the first LRNe on record. A new star appeared near the head of Cygnus the Swan on 20 June 1670 and was detected by French monk and astronomer Père Com Anthelme, see Fig. 6.9. It later faded in the autumn and brightened again in March 1671. By October 1671 it had faded once more. It shone faintly once more in 1672, then faded for good in the following months. Kamiński et al. (2015) observed the remnant spectroscopically, finding similarities between it and other LRNe.

Another historical object, V1148, was inferred to be a LRNe from its spectral evolution described by Mayall (1949) and Tylenda and Kamiński (2016). Although there was no accurate photometric motoring, the description of the spectra matches other double-peaked LRNe and appears to be a convincing LRNe candidate.

Selected red novae

OGLE-2002-BLG-360 has an interesting history. It was originally discovered as a microlensing candidate by the OGLE-III project, but investigations of the light curve show that it could not have been a gravitational lensing event. Tylenda et al. (2013) suggested it was a red nova due to similarities in spectral energy distribution and the appearance of a dusty shroud. It is likely to be a LRNe produced from the merger of low mass binaries (1–2 $M_{\odot}$) (Lipunov et al. 2017; MacLeod et al. 2017b).

Observations and analyses of M31 LRN 2015 reported by Dong et al. (2015), Wagner et al. (2015), and Adams et al. (2015), showed that the light curve and spectra closely resembled the double-peaked light curve of other LRNe caused by a binary merger (Williams et al., 2015). AT 2017jfs is another object showing that characteristic double-peaked light curve following by a spectrum cooling from a K-type to an M-type star. This is event is thought to be a common envelope event with a merger of a massive binary (Pastorello et al., 2019).

M101 OT2015-1 also has a clear double peaked light curve, however, the progenitor is thought to be a binary system with a primary F-type yellow supergiant (16–18 $M_{\odot}$) and a moderate mass secondary (Blagorodnova et al., 2017). This method of eruption is debated, and Pastorello et al. (2019) finds that common envelope ejection is the more favoured origin.

Selected discounted red novae

Some LRNe have been discounted since their original detection. For example, the classification of M85 OT2006-1, a "peculiar red nova", was proposed by Kulkarni et al. (2007), but subsequently debated by Pastorello et al. (2007) and (Thompson et al., 2009). The spectra of M85 OT2006-1 looks more similar to ILRTs (Kasliwal, 2011) and is now discounted in many LRNe lists.

NGC 4490-OT2011 erupted in 2011 was quickly identified as a SN imposter (Magill et al., 2011), and was proposed as an LRNe. It is now thought to have been a merger involving a massive blue progenitor or an intermediate mass yellow supergiant (Smith et al., 2016). Interestingly it also appears to closely resemble SN 2008s, so unclear if it is a real LRNe (Howitt et al., 2020).

It was thought that ASASSN-13db could be the least luminous LRNe discovered because the decline of the light curve is very similar to V8383 Mon, however this classification has been debated. It is more likely that the eruption was the result of the rare collision of a proto-planet of a few Earth masses with its host star (Kashi et al., 2019).

Selected candidate progenitors

As well as confirmed LRNe events, astronomers are monitoring binary systems which appear to be twins of V1309 Sco and other LRNe eruptions. An example of this is TY Pup (Sarotsakulchai et al., 2018). This object is a short period contact eclipsing low mass ratio and deep contact binary which is predicted to eventually merge and form a LRNe. Samec et al. (2018) and Wadhwa et al. (2021) list a further three candidate progenitors, including V1187 Her, a short period contact eclipsing extreme mass ratio binary, with continuous period decrease, which they predict will also eventually merge and form a LRNe.

6.4.7 Predictions

So far, nearly all discoveries of LRNe have been serendipitous, many being found by supernovae surveys or by searches of archival data after the merger event. However, it should be possible to predict which systems might merge, and predict the number of LRNe that will be detected.

By constraining observational and physical parameters, and improving models, it is expected that the Large Synoptic Survey Telescope (LSST) (Ivezić et al., 2019) will observe

a large number of LRNe per year. Estimates range from 80–3400 (Nandez and Ivanova, 2016) to 20–750 LRNe per year (Howitt et al., 2020). The increased numbers of observed LRNe will allow us to constrain the luminosity function and probe the physics of these common-envelope events.

Additionally, the rate of LRNe and LRNe-like events in our Galaxy can be estimated by using nearby galaxies as proxies (Kochanek et al., 2014). By assuming that M31 is a twin of our Galaxy, Kochanek et al. (2014) estimates that we should see a V1309 Sco or V838 Mon type event roughly every 20 years. In theory, these nearby galaxies should be ideal laboratories for better estimating merger rates because the extinction corrections become smaller and simpler.

Binary population synthesis models have also been used to estimate merger rates. In 1995, a binary population synthesis done by Han (1995) shows that 1–2 stellar mergers are expected in our Galaxy every decade. This result considers only binaries with stellar components having masses >0.8 $M_{\odot}$. Thus if multiple systems, lower mass stars, brown dwarfs and massive planets were also considered, two events in our Galaxy in a time span of 8 years are not surprising. A more recent estimate by Howitt et al. (2020) used the population synthesis code COMPAS to model Galactic rate of LRNe, finding it to be ~ 0.1 yr^{-1} in the Milky Way, in close agreement to the estimate by Kochanek et al. (2014) who found it to be ~ 0.2 yr^{-1}. For more extreme systems, such as very massive binary collisions, Pastorello et al. (2019) state that rare AT2017jfs-like events might occur once every 1000 years within 1 Mpc, so in a volume of 40 Mpc radius, we should see three events per year, consistent with observations. Howitt et al. (2020) provide a similar estimate, finding that the local average Galactic volumetric rate of LRNe is $\sim 8 \times 10^{-4}$ $Mpc^{-3}yr^{-1}$ (or ~ 5 yr^{-1}). Whilst LRNe are not common occurrences, Howitt et al. (2020) predict that LRNe are $\sim 10^4$ times more common than black hole-black hole binary mergers. The universal rate for LRNe has been

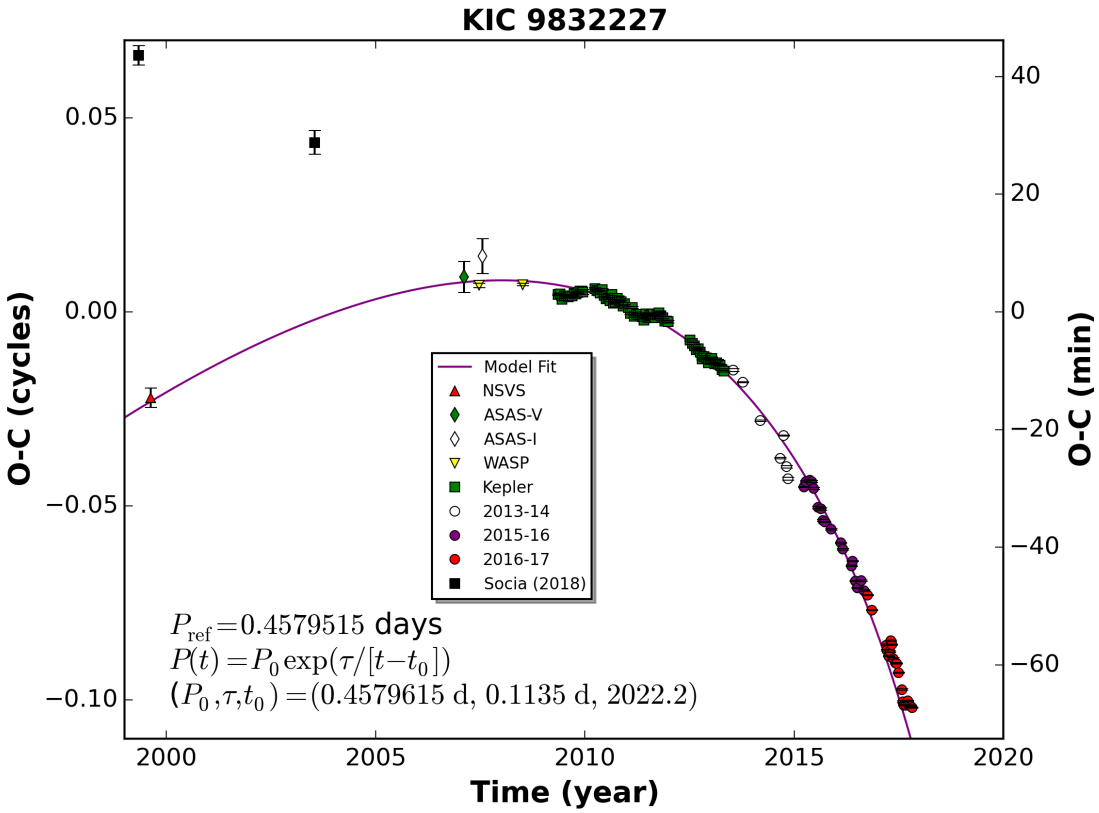

Fig. 6.10 The O-C diagram of KIC 9832227 (Molnar et al. 2017; Socia et al. 2018). The curve shows the exponentially decaying period fit from Molnar et al. (2017), based on the NSVS data point (red triangle). The corrected values (black squares) show the corrected data set, fundamentally changing the period decay model.

estimated by Rau et al. (2007) to be 1-10$\times10^{-13}$ yr^{-1}L$^{-1}_{\odot,K}$, where subscript K indicates the number per unit K-band light.

6.4.8 Progenitors

To date, a LRNe merger event has not yet been successfully predicted, though there have been attempts. The most famous example of a predicted LRNe merger event was by Molnar et al. (2017), who predicted that the binary star system KIC 9832227 would merger and produce a naked-eye visible red nova in early 2022 based on changes in the orbital period between 1999–2016.

However, the prediction was negated by Socia et al. (2018), who noticed a typo in the published Modified Julian Date of the NSVS data set, causing the 1999 data point to differ from the true time by 12 hours, shown in Figure 6.10. The binary system had a period of 11 hours, causing a 1 hour difference in data points and negating the period decay model. To test this, Molnar et al. (2017) computed the true elevation of the star with both times, and found that the original time would have meant that the star was apparently below the horizon at time of observation, therefore the corrected values must be correct and a merger event would now not occur. Although up for debate, it is thought that a third companion may be responsible for period change (Jordan et al., 2019).

Archival data have proven to be a valuable resource for those looking for LRNe progenitors. Identifying unusually long period W UMa-type binaries will be key to finding possible merger candidates. Kurtenkov (2017) used the Kepler eclipsing binary catalogue search for twins of the V1309 progenitor by identifying eclipsing timing variations. They investigated 128 long period W UMa systems (P=1.1–1.8 d), and found 14 systems with $P >$0.8 d and a statistically significant steady period decrease, but recognise that it is unlikely that any of the systems will merge in the coming decades. Similarly, Pietrukowicz et al. (2017) used the OGLE survey of 22,462 short-period ($P \leq$4 d) eclipsing binary systems to investigate 108 systems with period decrease and increase. They identified 22 systems which may merge in tens to hundreds of years, although some of the observed period changes may have been due to a tertiary star or slow moving star spots on the binary component. Others have identified possible individual merger candidates, including TY Pup (Sarotsakulchai et al., 2018), a low mass ratio, deep contact binary, with a possible third companion, and V1187 Her (Samec et al., 2018), the most extreme mass ratio binary known.

As Molnar et al. (2017) noted, to identify merger candidates, it will be key for surveys to quickly identify contact binaries and follow up those with notable period derivatives. Sifting through the vast data sets will inevitably give an exciting reward.

6.5 Summary

This chapter has reviewed the current status of the field of red novae, including existing detections, predicted progenitors, characteristics pre- and post-outburst. Little is known about LRNe, but as surveys like LSST come online, it should be possible to detect hundreds per year, constraining our understanding of their progenitors and evolution. Near contact red giant eclipsing binaries are proposed as a possible progenitor of LRNe, and the detection of red giant contact and semi-detached binaries might change existing theories of binary star evolution.

In the following chapters I summarise the detection, follow-up, and modelling, of a sample of 27 candidate near contact red giant eclipsing binary stars, the possible progenitors of red novae.

Chapter 7

Search for Near Contact Red Giant Eclipsing Binaries

Whilst setting up the SuperWASP Variable Stars Zooniverse project, a serendipitous discovery was made: the first near contact red giant eclipsing binary, TYC 3251-903-1. This spurred me on to search for similar objects in catalogue data.

This short chapter will detail the serendipitous discovery of, and subsequent search for candidate near-contact red-giant eclipsing binaries (NCRGEB), and hence candidate red novae progenitors. This includes: a summary of the data sets used; the cross correlation and identification techniques; full table of NCRGEB candidates; and initial assessment of the likelihood that the candidates are real based on O–C and phase-folding analysis.

7.1 Initial target TYC 3251-903-1

Whilst setting up the SuperWASP Variable Stars Zooniverse project in summer 2018, a serendipitous discovery of the first possible near contact red giant eclipsing binary was made. This Northern hemisphere object, TYC 3251-903-1, is a relatively bright object (Johnson V magnitude 11.3, corresponding to SuperWASP flux $\sim$25 counts s^{-1}) which had previously

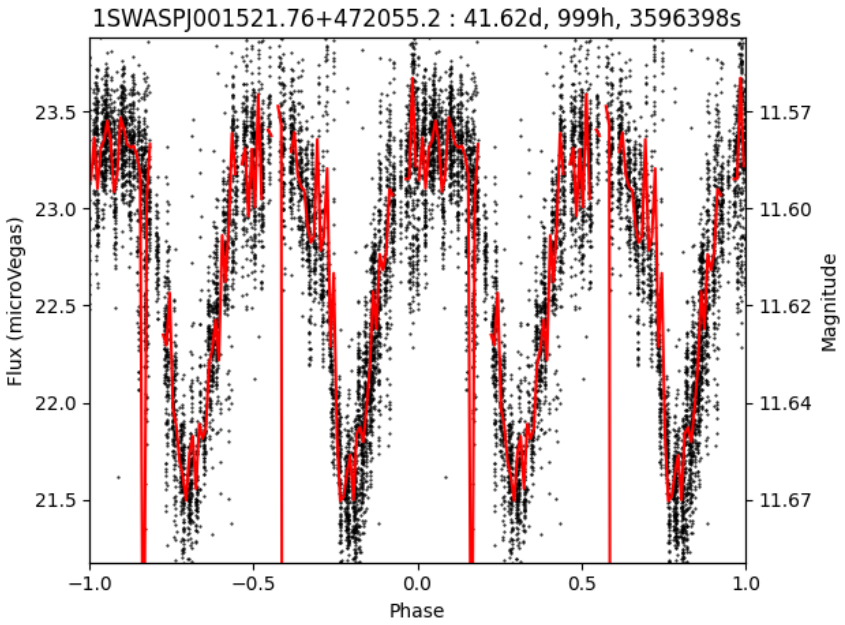

Fig. 7.1 SuperWASP light curve of TYC 3251-903-1 with a period of 41.62 days.

not been observed or identified as a binary system. By summer 2019, it had been classified as an eclipsing binary in the ASAS-SN Catalogue of Variable stars[1]. Although the light curve is characteristic of a W UMa type eclipsing binary, the period is ∼42 d. Figure 7.1 shows the SuperWASP light curve of this object, folded with a period of 41.62 days, and with an amplitude of ∼0.1 V magnitudes. Whilst Gaia-D2 data are known to not be accurate for unresolved binary systems (Andrae et al., 2018), the estimated temperature for TYC 3251-903-1 is ∼6750 K with a luminosity of ∼17 $M_{\odot}$, and a radius of of ∼3 $R_{\odot}$, giving it an estimated spectral type as an early K giant. The question arose, *what is this object?*

Eclipsing contact binaries stars typically have periods between ∼6 hours and ∼1 day, so for TYC 3251-903-1 to be in contact, or near contact, at such long periods requires the both stellar components to be giants. This appears to be the first example of a near-contact red-giant eclipsing binary. Red giants in binary systems are not uncommon, and typically exist in the form of a red giant and a dwarf, or two red giants with large separations of

[1]https://asas-sn.osu.edu/variables/4a0aac1a-6f91-5816-b9cb-3de86e31bc23

hundreds of AU, as detailed in Chapter 6. However, this configuration of near-contact red giant eclipsing binaries has not previously been observed.

A single spectrum of this target was obtained using LIRIS on the William Herschel Telescope, which appeared to show Paschen lines and evidence for it being a double lined object, hence a binary star with one red stellar component. Further details of this spectroscopic follow-up can be found in Chapter 10, and this first spectrum is shown in Figure 7.2. Without a series of spectra, hence, radial velocity measurements, it is impossible to fully model the system, however the stellar radii and separation range based on the period and estimated mass of the stars can be estimated, simply by using Kepler's third law:

$$\frac{P^2}{a^3} = \frac{4\pi^2}{G(m_1+m_2)}, \tag{7.1}$$

where P = period in years, a = semi-major axis in astronomical units, G = the gravitational constant, and m_1, m_2 = the stellar masses in $M_\odot$. Assuming a range of total mass of 1–10 $M_\odot$, where $M = m_1 + m_2$, a period of 41.62 days, and approximately equal stellar masses, radii, and temperatures, a binary of between 1–10 $M_\odot$ will have a semi-major axis range from 51–109 $R_\odot$. A simplistic model using the binary star modelling programme, PHOEBE (explained in depth in Chapter 9), can provide estimates for the radii and radial velocity amplitudes expected. Using these same parameters, for the same mass range of 1–10 $M_\odot$, the radii range is 7.5–37.5 $R_\odot$, and radial velocity amplitudes range from 60–100 kms^{-1}.

Therefore, based on the late type stellar components, temperatures, and assumed instability of a binary comprised of two contact, or near contact, red giants, it is thought that this new type of binary may be a candidate progenitor of red novae.

Long period contact binaries have been proposed as the progenitors of red novae, but none have been conclusively identified pre-nova, and red novae are believed to be formed through contact binary mergers, as detailed in Chapter 6. However, only one progenitor has been well-studied, V1309 Sco (Tylenda et al., 2011), and this was only recognised after the merger

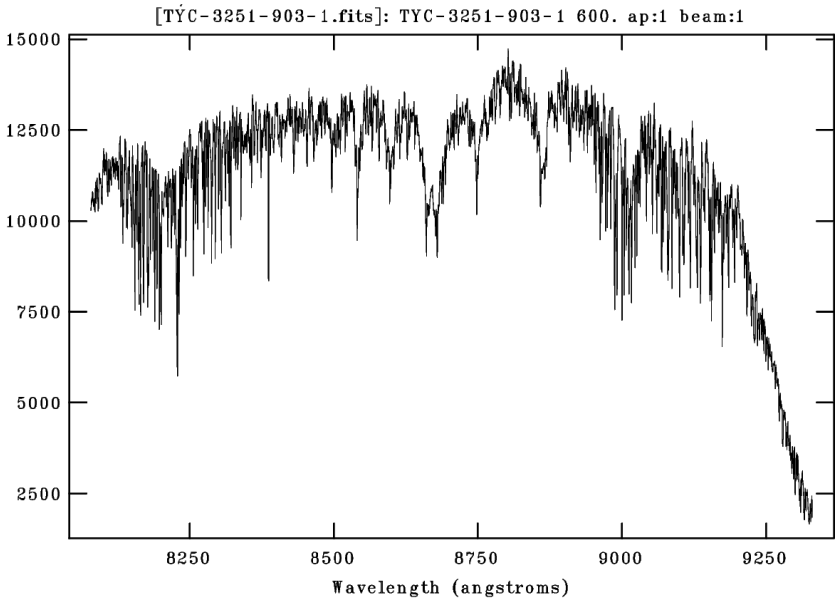

Fig. 7.2 Initial uncalibrated spectra of TYC 3251-903-1 from the WHT.

event itself. Searches for twins of the V1309 Sco progenitor by (Kurtenkov, 2017) identified a few potential systems with decreasing orbital periods. Rucinski (1998) previously identified similar binaries with periods of greater than 1.5 days, all with red colours, however these are all too faint for detailed spectroscopic follow-up. Therefore, this is a golden opportunity to identify merger candidates before the merger event itself, and constrain the parameters of the progenitors of red novae.

Spurred on by this discovery of a candidate near-contact red giant eclipsing binary, similar long period eclipsing binary objects were searched for in archival data. As a result of this, a set of candidates have been identified, all appearing to be long-period examples of near-contact eclipsing binaries, with orbital periods of up to a month or more.

7.2 Finding binary candidates in catalogue data

Finding similar targets in archival data was made simpler by making use of the ASAS-SN Catalogue of Variable Stars. The advantage of the ASAS-SN Catalogue of Variable Stars over

most other catalogues is that it is possible to easily use a web interface to sort by preliminary classification, and by period, allowing one to probe the extremes of each class.

The catalogue of ASAS-SN EW-type binaries was downloaded and a $10''$ cross-match with the *SuperWASP periodicity catalogue* was performed. All light curves with a period of $\geq$4 days were selected, leaving >100 EW-types. Each light curve from both catalogues was visually inspected to determine whether the objects truly looked like EW-types, and whether the period was similar or folded at half or double the SuperWASP period.

Through this, a further 16 candidate NCRGEB candidates were identified with periods of 4–42 d. Where possible, each of these objects had an ASAS-SN and a SuperWASP light curve showing the same modulation period and shape, characteristic of a contact, or near-contact eclipsing system. A further 10 long period EW-type objects were identified by Zooniverse volunteers, bringing the total number of candidates to 27. An in-depth analysis of the SuperWASP Variable Stars Zooniverse project is available in Chapter 12.

This catalogue of 27 NCRGEB candidates was complemented by data from SIMBAD (Wegner, 1994); the initial spectral type and multi-colour magnitudes of each object are found using the astronomical catalogue search tool VizieR (Ochsenbein et al., 2000), and are taken from NOMAD (Zacharias et al., 2004) and USNO B1.0 (Monet et al., 2003).

7.3 Candidate near contact red giant eclipsing binaries

Table 7.1 contains basic information the 27 candidate NCRGEB identified through the cross-match of SuperWASP and ASAS-SN, and through the SuperWASP Variable Stars project. The table of candidates includes the WASP IDs, ASAS-SN IDs, period, existing classifications, and B, V, and R magnitudes. The codes for each previous classification types can be found on the following websites: SIMBAD[2], VSX[3], and ASAS-SN[4]. Throughout the

[2]https://simbad.u-strasbg.fr/simbad/sim-display?data=otypes
[3]https://www.aavso.org/vsx/index.php?view=about.vartypes
[4]https://asas-sn.osu.edu/variables

remainder of this thesis, a shortened WASP ID will be used. For example, J231800 will refer to 1SWASPJ231800.38-031131.4.

Of the 27 candidates, 10 were identified by Zooniverse volunteers, denoted by the † symbol. These targets are primarily classified as rotators in ASAS-SN, so from the very start, have a lower probability of being successful NCRGEB candidates. By contrast, all non-Zooniverse candidates are classified as EW-type binaries in ASAS-SN, with the exception of J001521, which was only classified as an EB-type binary by ASAS-SN in 2019, the year following the discovery.

Of the non-Zooniverse candidates, the previous classifications from VSX and SIMBAD are varied, ranging from WV* (W Virginis type) variables, a subclass of classical Cepheids with periods of $\sim$17 days, to bL*, β Lyrae type eclipsing binaries. Of the 16 candidates with a classification in SIMBAD, only 1 is classified as a binary; of the 23 candidates with a classification in VSX, 8 are classified as binaries. At this stage, it is too early to discount any candidate based only on previous classifications.

7.3.1 Photometric light curves

Phase-folded photometric light curves were used to visually identify NCRGEB candidates. For brevity, the SuperWASP and ASAS-SN light curves of the 27 candidates are not shown here, but can be found in Appendix B. Instead, the SuperWASP and ASAS-SN light curves of the original target, J001521, and J035259 are displayed in Figure 7.3 and Figure 7.4 respectively. The SuperWASP light curves that appear to be the most convincing as binaries include: J231800, J204317, J190114, J183357, J165656, J035259, J002952, and J000927, whilst many others often have discrepancies between the ASAS-SN and SuperWASP light curves, or appear to more closely resemble pulsators (with asymmetric pulse profiles) than binaries.

Table 7.1 Table of near contact red giant eclipsing binary candidates and their previous classifications. † indicates that the NCRGEB was identified by Zooniverse volunteers.

WASP ID	ASAS-SN ID	*P*	Classification			B	V	R
		d	SIMBAD	VSX	ASAS-SN			
1SWASPJ231800.38-031131.4	ASASSN-V J231800.48-031131.1	23.84	WV*	CWA	EW	14.28	13.81	13.12
1SWASPJ204317.92-251850.0	ASASSN-V J204317.85-251850.9	4.92		ROT	EW	14.95	14.03	13.89
1SWASPJ194733.51-471201.4	ASASSN-V J194733.45-471159.8	35.08		ROT	EW	13.64	13.18	13.43
1SWASPJ194231.22-251605.5	ASASSN-V J194231.21-251605.0	23.18		CWA	EW	14.76	14.73	14.11
1SWASPJ192628.96-233856.1	ASASSN-V J192628.96-233856.1	28.54		ROT	EW	14.33	13.75	14.22
1SWASPJ192311.66-423244.5	ASASSN-V J192311.61-423244.8	16.64		ROT	EW	13.50	13.03	12.26
1SWASPJ191910.42-414050.9	ASASSN-V J191910.44-414050.5	16.60		CWA	EW	13.31	12.86	12.44
1SWASPJ190114.91-380729.0†	ASASSN-V J190114.84-380728.2	11.09	*	EC	ROT	13.33	11.28	10.45
1SWASPJ183357.87+423725.2	ASASSN-V J183357.78+423725.2	8.72	cC*	CEP	EW	15.36	12.38	12.22
1SWASPJ165656.26-040414.3	ASASSN-V J165655.96-040416.4	15.68	Ce*	CWB	EW	13.37	12.40	12.51
1SWASPJ165241.24+203224.7	ASASSN-V J165241.18+203224.4	15.13	WV*	CWB	EW	14.79	14.17	14.19
1SWASPJ154828.29+201442.8	ASASSN-V J154828.23+201441.8	7.47	cC*	EC	EW	11.63	10.57	9.92
1SWASPJ154607.55-191711.4	ASASSN-V J154607.43-191712.8	29.14	PM*	SR	EW	11.97	11.53	10.67
1SWASPJ135703.85-474817.9†	ASASSN-V J135701.95-474810.0	10.71		EA	EB	14.15	13.82	14.07
1SWASPJ132156.04-010742.8	ASASSN-V J132156.11-010742.8	32.09	WV*	EB	EW	15.47	14.63	14.19
1SWASPJ103327.40-304931.6	ASASSN-V J103327.32-304932.2	17.87		EB	EW	16.89	15.58	14.85
1SWASPJ093610.20-283847.2	ASASSN-V J093610.10-283846.4	6.92	*	ROT	EW	13.38	12.50	12.44
1SWASPJ035259.67+091717.1	ASASSN-V J035259.67+091717.4	24.61	WV*	EB	EW	13.35	12.52	11.45
1SWASPJ022953.03+041420.9†	ASASSN-V J022953.05+041420.9	6.66			ROT	13.78	13.01	13.34
1SWASPJ003544.75+495450.0†	ASASSN-V J003544.87+495449.2	17.86			ROT	13.45	12.70	11.41
1SWASPJ003414.72-291038.4†		11.32		CEP		15.75	15.23	14.88
1SWASPJ002952.96+475034.3†	ASASSN-V J002952.99+475034.9	20.33	bL*	EB	SR	11.23	10.16	9.50
1SWASPJ002349.66+483114.5†	ASASSN-V J002349.64+483114.4	17.15	X		ROT	13.50	12.60	11.83
1SWASPJ001545.50-622237.8†	ASASSN-V J001545.47-622238.0	44.90	*		ROT	12.27	11.28	10.66
1SWASPJ001521.76+472055.2	ASASSN-V J001521.75+472055.4	41.62	*	EB	EB	11.90	11.32	10.93
1SWASPJ000927.89+014542.1†		32.72	RG*	RRAB		14.84	14.15	14.30
1SWASPJ000018.09+091923.9†	ASASSN-V J000018.12+091922.7	85.76	*	MISC	ROT	11.81	10.91	10.37

Nearly all light curves have a period and shape that closely matches between each catalogue. Where there is a discrepancy between periods, for example, if a candidate from one catalogue shows a period of half the other catalogue, each light curve was assessed by eye, and the most realistic period was chosen for further analysis. Both SuperWASP and ASAS-SN observe only in the V band, hence further multicolour photometric follow-up is required to analyse the candidates further.

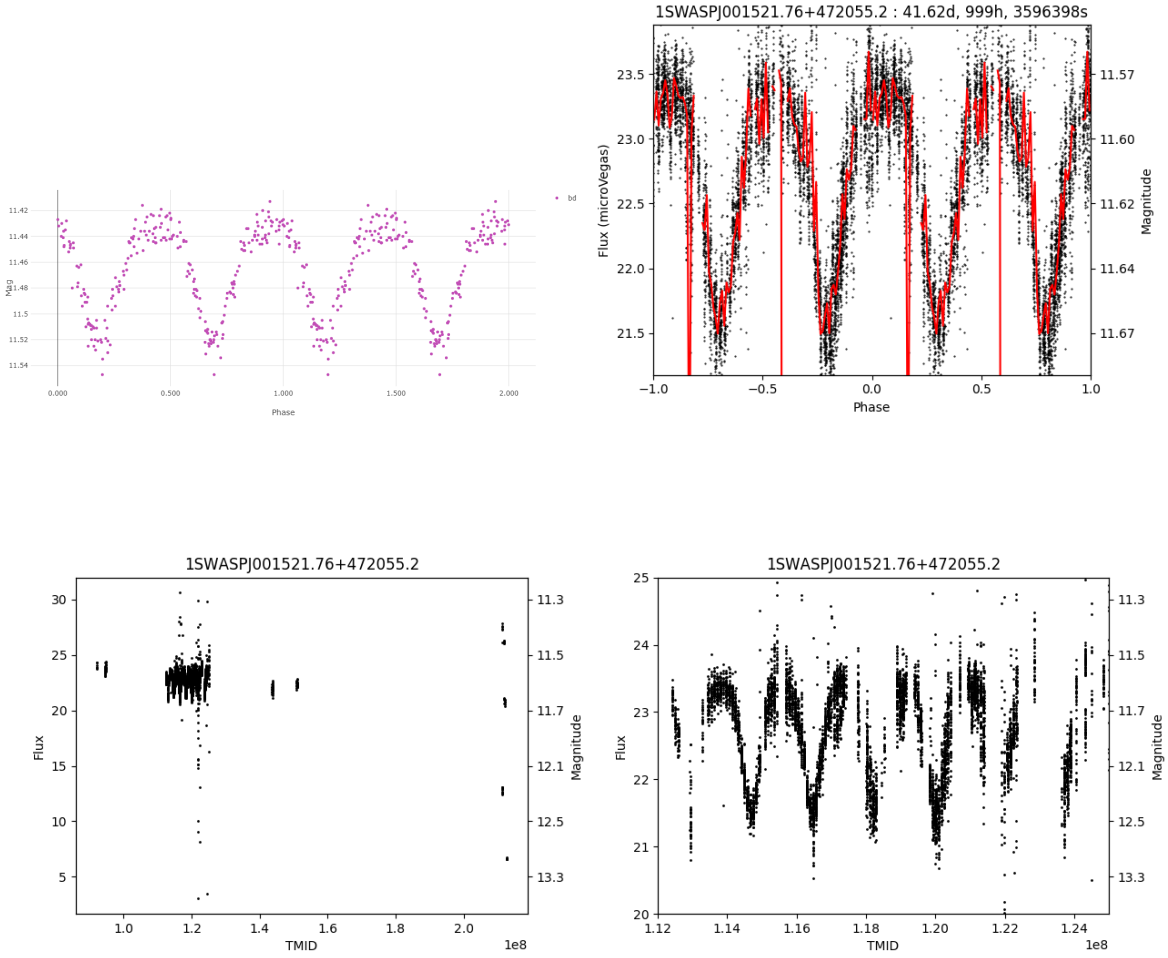

Fig. 7.3 Phase-folded light curves for J001521. **Top left:** phase-folded ASAS-SN; **top right:** phase-folded SuperWASP; **bottom left:** unfolded SuperWASP; **bottom right:** zoom in of unfolded SuperWASP.

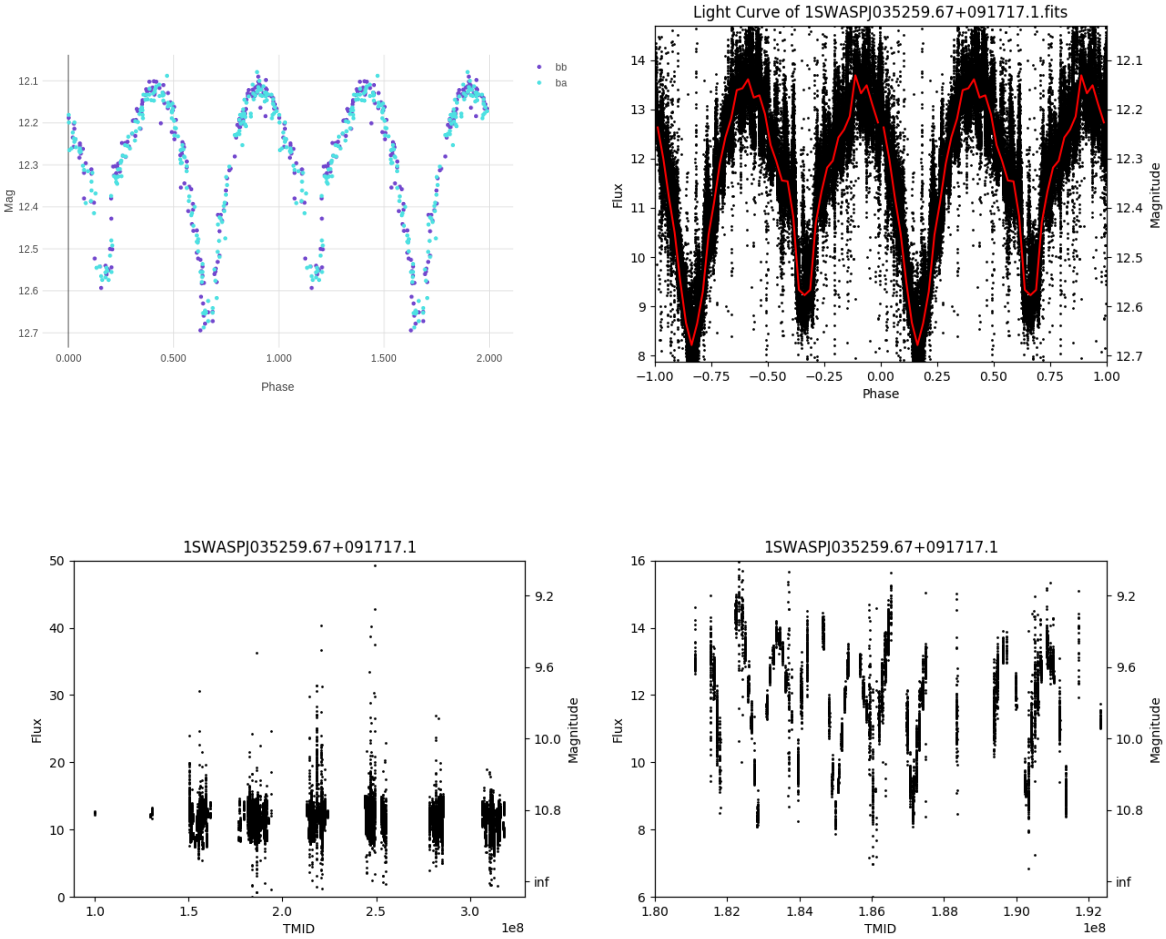

Fig. 7.4 Phase-folded light curves for J035259. **Top left:** phase-folded ASAS-SN; **top right:** phase-folded SuperWASP; **bottom left:** unfolded SuperWASP; **bottom right:** zoom in of unfolded SuperWASP.

7.3.2 Position on the HR diagram

A second initial check to identify whether these objects are likely to be binaries or another variable type can be done by simply plotting the candidates on an Hertzsprung-Russell (HR) diagram. This can identify which are more likely to be giant stars rather than main sequence stars.

Figure 7.5 shows the position of the binary candidates (for the 18 NCRGEB candidates with Gaia-DR2 luminosity and temperature estimates) on an HR diagram using a sample of 100,000 Gaia-DR2 targets. Whilst the majority appear to lie above the main sequence

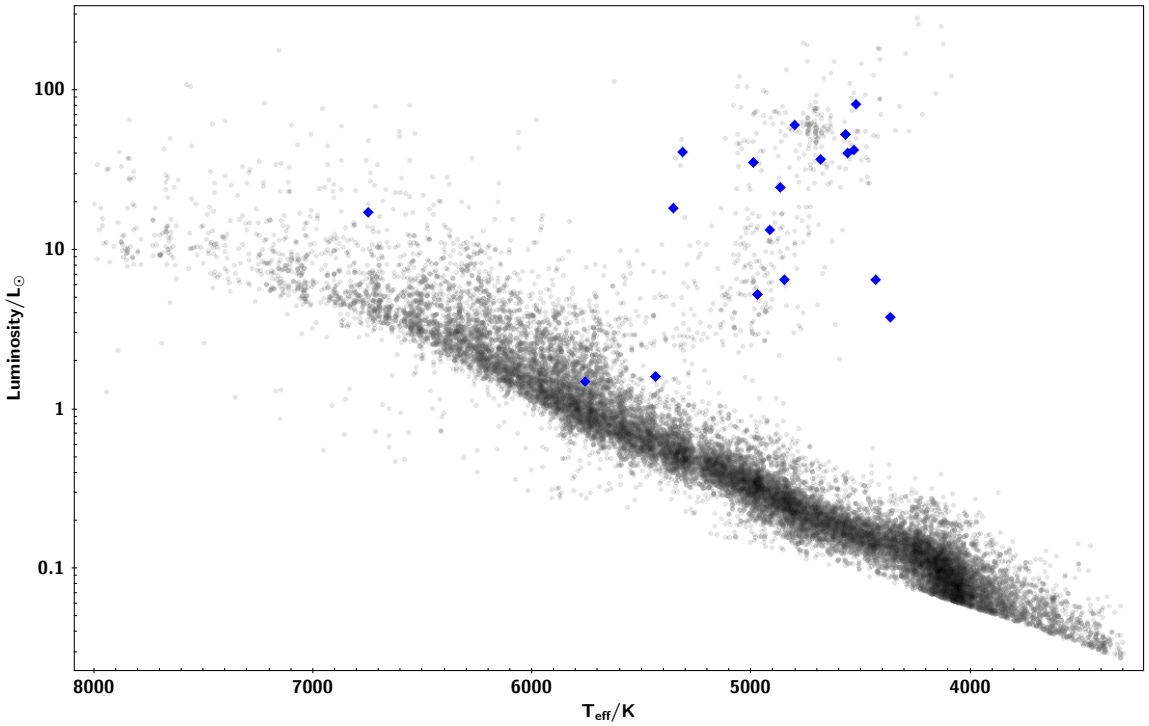

Fig. 7.5 18 NCRGEB candidates (blue diamonds) plotted on an HR diagram using a sample of 100,000 Gaia-DR2 targets.

towards the giant branch, J135703 and J00145 appear to lie along the main sequence and will likely be discounted as NCRGEB through the course of this research. J001521, the original target, has the highest temperature at ∼6750 K, lying close to the main sequence, and as a result of this, may be discounted as a NCRGEB.

Although this simple test has identified that J135703, J003414, and J001521 may actually lie along the main sequence rather than being giant stars, again, no candidates will be discounted at this stage. Since the overall sample of NCRGEB candidates is small, each candidate will be followed up, both photometrically and spectroscopically, in order to confirm the variable type. Additionally, Gaia-DR2 is known to be inaccurate for unresolved binaries (since unresolved binaries are treated as single stars (Andrae et al., 2018), so discounting any targets at this stage may remove genuine NCRGEB.

7.3.3 O–C assessment

A third initial test for the NCRGEB candidates is the assessment of period change, using O–C diagrams constructed using `ah3` by March Lohr (private communications 2018–19; (Lohr, 2015)). However, although `ah3` is known to work well for eclipsing binaries with periods $\leq$5 days, since the fitting algorithm assesses a single night of data at a time, it struggles to fit eclipses for binary periods $\geq$5 days which may have eclipses which last for longer than one night.

`ah3` was trialed on 10 NCRGEB systems in order to attempt to assess both whether the light curve looks like it belongs to a contact eclipsing binary, and whether the period change is realistic for a contact eclipsing binary. An example of the result of the O–C analysis can be seen in Figure 7.6 for J183357. O–C diagrams generated by `ah3` typically display 6 panels. The top left panel is a periodogram which finds the 'best' period; the top right shows the SuperWASP light curve, phases folded on the found 'best' period; the centre left panel shows the phase-aligned light curve, fitted with a binned average line; the centre right panel shows the O–C diagram fitted with both a linear and quadratic fit; the bottom left panel shows a plot of relative depths of the primary eclipse over time; the bottom right panel shows the out-of-eclipse flux level over time.

However, of the 10 systems analysed with `ah3`, 2 failed the analysis, and the period change estimated for the remainder was unrealistic. An example of the unrealistic O–C analysis is that of J165241, which shows a period change of $\sim$12,000 s yr^{-1}. Therefore, since no realistic period change could be analysed through `ah3`, analysis was not continued using this method. Therefore, other methods of assessing period change and evolutionary pathways will be explored in detail in Chapter 10.

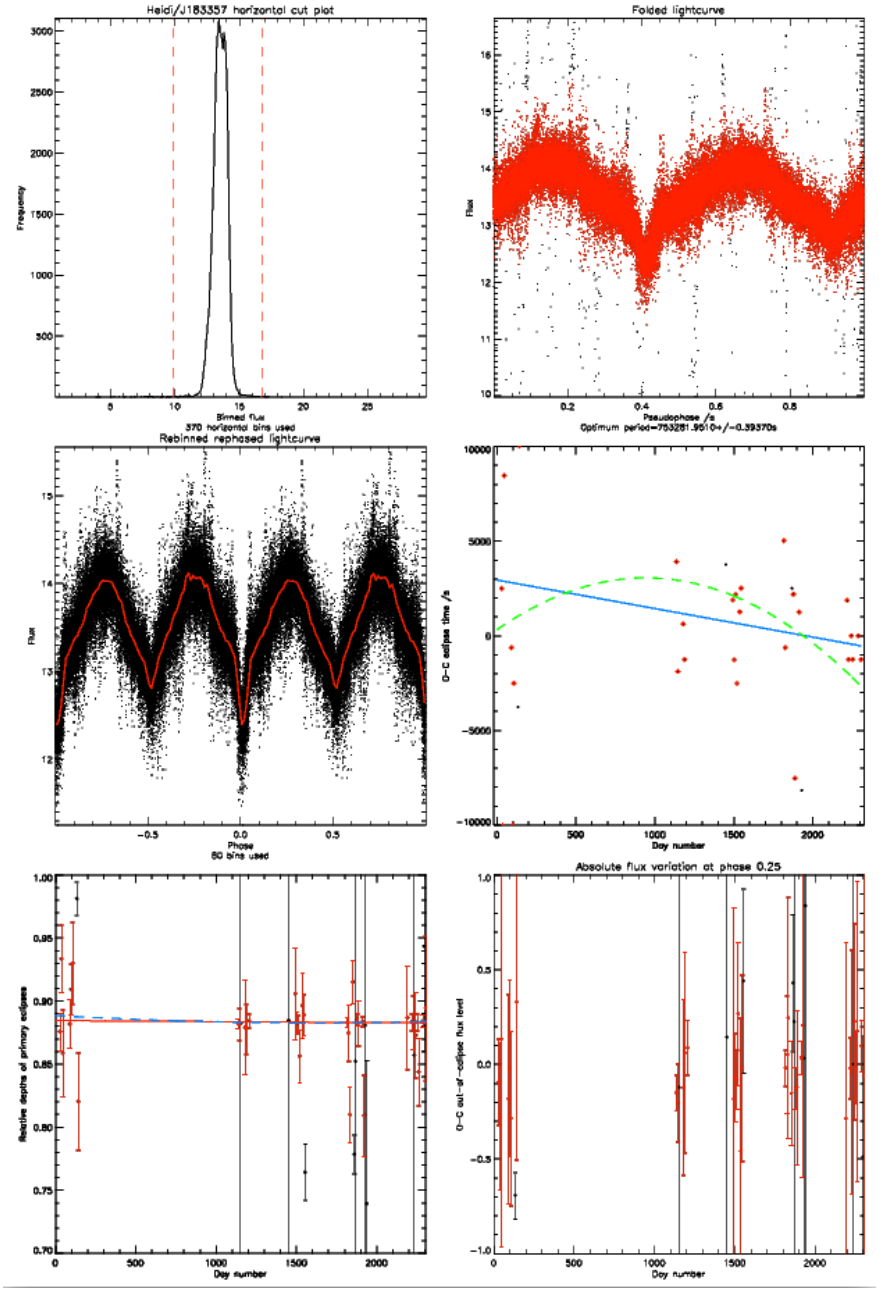

Fig. 7.6 Example of an `ah3` output for J183357.

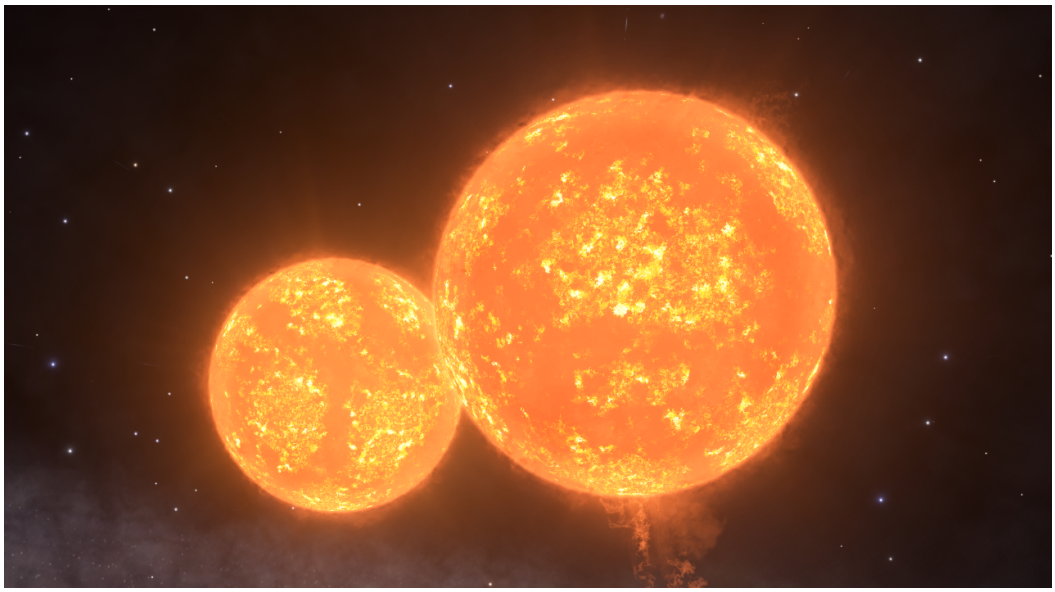

Fig. 7.7 What a near-contact red giant eclipsing binary system might look like. Visualisation taken from the video game Elite Dangerous. [Credit: Elite Dangerous/yum_raw_carrots]

7.4 Summary

The serendipitous discovery of the unusual binary, TYC 3251-903-1, had shown that there is the possibility of the existence of near-contact red-giant eclipsing binary stars, which may be the progenitors of the rare transient, red novae. This discovery led me to identify 26 additional candidates binaries through searches of the SuperWASP and ASAS-SN catalogues, and through classifications by citizen scientist volunteers. An visualisation of what a near-contact red giant eclipsing binary system might look like is displayed in Figure 7.7.

Of these 27 candidates, at the time of discovery, 19 had no previously published light curves, and 7 were classified as pulsating variables. In total, the NCRGEB candidates cover a period range of 5–90 days, far greater than the expected maximum period of a contact binary system. The colour and temperatures from Gaia-DR2 support the hypothesis that these binaries are made up of late-type giant stars, with the exception of 3 (J135703, J001521, and J00145). A visual assessment of the photometric V band phase-folded light curves complemented O–C analysis using `ah3`, providing an initial assessment as to whether the

27 targets are likely NCRGEB candidates. Whilst the O–C analysis is only rough (since `ah3` is intended for analysis of short period binaries), it has identified that J165241 and J154607 may not be NCRGEB. Although some targets do not look like strong NCRGEB candidates, all targets will be followed up to provide a thorough analysis of this new and exciting configuration of binary stars. For such a small sample size and for such an interesting configuration of binary stars, it is not worth discarding any candidates at this stage.

In the following chapters, I detail the photometric and spectroscopic follow-up, and the modelling of these systems using PHOEBE and 1D stellar evolution models, in order to assess, first, whether these NCRGEB candidates are real, and second, whether they could be the progenitors of red novae.

Chapter 8

Photometric Follow-Up of Near Contact Red Giant Eclipsing Binaries

The section will focus on the photometric follow-up observations of the candidate near-contact red giant eclipsing binaries identified in Chapter 7. This includes a summary of the telescopes and instrument set-ups, and the reduction pipelines implemented to extract light curves from the images, regardless of whether the targets are confirmed as binaries or not.

The majority of the multi-colour photometric data for this thesis was collected over 24 months using The Open University's own PIRATE telescope and reduced using a pipeline written by Morrell (2021). A complimentary set of observations were taken using a range of telescopes in the Las Cumbres Observatory (LCO) global network. These observations were taken as part of an educational proposal, and the observations themselves were taken by schools and students, and reduced using the LCO `BANZAI` pipeline.

Although it may not seem necessary to collect more photometric data, given the good V band coverage of each target by SuperWASP and ASAS-SN, the purpose of the collection of further photometric data is twofold. It provides an increased baseline to the SuperWASP and ASAS-SN data sets, allowing for possible period or variability change to be identified, and it also allows for the collection of multi-colour photometry which can be used in modelling

the temperatures of stellar components. The photometric follow-up ran in parallel with the spectroscopic follow-up, both of which are used in Chapter 9 to assess whether the NCRGEB candidates are real binaries.

8.1 Photometric follow-up

This section will detail the instrumentation and set-up of the PIRATE and the Las Cumbres Observatory telescopes, and discuss capabilities and limitations of the instruments. Each section will also include details on the observations themselves, including the filters, dates of observations, and lengths of exposures.

8.2 PIRATE

The Physics Innovations Robotic Astronomical Telescope Explorer (PIRATE) [1] telescope is a 17 inch robotic telescope owned and run by The Open University, shown in Figure 8.1. PIRATE has two primary aims. For 30% of the year, it operates as a distance learning telescope for undergraduate students at The Open University, giving them real-time access to research-level facilities. For the remainder of the time, it is primarily a research telescope for photometry used by researchers at The Open University (Holmes et al. 2011; Kolb et al. 2018).

PIRATE is located in the Observatio del Tiede on the Island of Tenerife in the Canary Islands. Observatio del Tiede is located 2,390m above sea level, and the observatory is above the cloud base for most of the year. The observatory also benefits from a low level of light pollution and excellent seeing conditions.

The telescope itself is a 17 inch robotic telescope with Cassegrain optics and a ProLine camera. The camera houses a 4096×4096 pixel CCD, with a 0.63″ per pixel resolution, a

[1] http://pirate.open.ac.uk/

Fig. 8.1 The PIRATE telescope (left) and COAST telescope (right) [Credit: Elena Mora (IAC)].

$43' \times 43'$ field of view (FoV). There are seven filters options: Baader R, G, B, Hα, OIII, SII, and Clear. This is all housed within a Baader Planetarium all-sky clamshell dome with a diameter of 4.5m, which, when opened, does not restrict movement or view of the telescope. The only restrictions on observing an object is that it must be above an altitude of 20 degrees, and must not be within 20 degrees of the Moon.

PIRATE is run by ABOT, an observatory control software (Sybilski et al., 2014), and observations are scheduled using the OpenScience Observatories (OSO) Scheduler (Kolb et al., 2018), software created by The Open University's OpenScience Laboratory team. The OSO scheduler was used to queue schedule all observations for this thesis. Each object was initially scheduled for a test night of observations to determine the best exposure time. The "best" exposure is one in which the target star and candidate comparison stars are not saturated (i.e. the counts is less than 65,000), but also have a suitable count rate (i.e. greater than 10,000) in order to have a good signal-to-noise ratio. Once the best exposure time had been found, the targets were then left in the OSO scheduler queue. All PIRATE observations

are reduced using the pipeline written by Morrell (2021). For a description of this pipeline, see section 8.2.2.

PIRATE was a natural choice of telescope for photometric follow-up for three reasons. Firstly, the almost year-round unrestricted access gives good coverage of each phase of the binary system. Secondly, PIRATE has some overlap with the fields of view of telescopes used for spectroscopic follow-up, meaning almost simultaneous photometry and spectroscopy can be acquired. Thirdly, PIRATE provides high quality, high resolution photometry which can resolve the maxima and minima of each binary system. PIRATE has a limiting V magnitude of $\sim$17.5; the faintest binary target has a V magnitude of $\sim$15.7.

The initial nightly set up for the OSO scheduler was: a 2$\times$2 binning, 4 observations of each of B, V, R, I filters, and 2 revisits per night (maximum). In September 2019, the binning was changed to binning 1 on the advice of another PIRATE astronomer. During the 24 months of observation, some issues were encountered with PIRATE. These issues will be discussed further in Section 8.2.2. Despite these issues, PIRATE has provided $\sim$400 nights of data, over 630 hours of data, and over 23,000 images for this thesis.

8.2.1 Observations

This section details the number of observations made with PIRATE. The first observing season started in September 2018 and ended in September 2019, taking observations using binning 2$\times$2. The second observing season started in September 2019 and ended in March 2020, with binning 1$\times$1. Table 8.1 lists the targets observed by PIRATE and their corresponding exposure time and number of good observations.

Of the 27 candidate binaries, 21 were visible by PIRATE, some more so than others, depending on coordinates and moon altitude. Targets with fewer observations were those that did not have year-round visibility from PIRATE, mostly the very southern hemisphere objects.

A significant number of observations of each target were discarded as "bad" observations during the reduction process.

8.2.2 Data reduction

This section describes the reduction pipeline written by and described in Morrell (2021), specifically for PIRATE data. It follows a standard calibration procedure to convert raw PIRATE images into usable science data. The process is outlined below:

1. Overscan removal: remove 40 pixels from each side of the image to remove overscan region.
2. Master bias: Create a master bias by stacking all bias frames.
3. Dark de-bias: De-bias each dark frame to remove readout noise.
4. Master dark: Scale each dark frame to 1 second and stack, creating a master dark.
5. Flat de-bias: De-bias each flat frame.
6. Scaling: Scale up the master dark frame to each flat and subtract.
7. Flat fielding: Create a master flat for each filter by stacking flats for each filter and dividing by the median counts. Flat fields are taken from 10 days before and after the observation date to create a master flat.
8. Final calibration: Use the three master calibration frames to perform the final calibration.
9. Plate solve: The process science files can be plate solved and aligned to obtain WCS coordinate. This is done using local version of Astrometry.net[2] source catalogues.

[2]http://nova.astrometry.net/

Target	M_v	Dates	Exposure Time (s)	Number of good observations
1SWASPJ231800.38-031131.4	13.81	07-11-2018–19-02-2020	B:200; V:200; R:200; I:200	B:55; V:44; R:46; I:79
1SWASPJ204317.92-251850.0	14.03	11-11-2018–03-10-2019	B:300; V:300; R:300; I:300	B:148; V:146; R:145; I:152
1SWASPJ194231.22-251605.5	14.73	10-11-2018–10-08-2020	B:300; V:300; R:300; I:300	B:113; V:138; R:131; I:134
1SWASPJ192628.96-233856.1	13.75	08-11-2018–18-09-2019	B:300; V:300; R:300; I:300	B:; V:37; R:31; I:
1SWASPJ183357.87+423725.2	12.38	10-11-2018–03-03-2020	B:300; V:100; R:100; I:100	B:230; V:224; R:202; I:192
1SWASPJ165656.26-040414.3	12.40	10-01-2019–03-03-2020	B:60; V:60; R:60; I:60	B:230; V:224; R:213; I:192
1SWASPJ165241.24+203224.7	14.17	28-12-2018–09-03-2020	B:300; V:300; R:300; I:300	B:197; V:199; R:163; I:168
1SWASPJ154828.29+201442.8	10.57	12-12-2018–03-03-2020	B:15; V:14; R:13; I:12	B:274; V:263; R:314; I:348
1SWASPJ154607.55-191711.4	11.53	09-03-2019–03-03-2020	B:17; V:16; R:15; I:14	B:255; V:264; R:266; I:258
1SWASPJ132156.04-010742.8	14.63	26-11-2018–03-03-2020	B:250; V:250; R:250; I:250	B:98; V:97; R:104; I:7
1SWASPJ103327.40-304931.6	15.58	26-11-2018–21-01-2019	B:300; V:300; R:300; I:300	B:62; V:50; R:53; I:59
1SWASPJ093610.20-283847.2	12.50	06-11-2018–11-05-2019	B:60; V:60; R:60; I:60	B:123; V:74; R:48; I:60
1SWASPJ035259.67+091717.1	12.52	06-11-2018–29-02-2020	B:70; V:70; R:70; I:70	B:335; V:322; R:375; I:422
1SWASPJ022953.03+041420.9	13.01	17-11-2019–04-12-2019	BB:60; V:60; R:60; I:60	B:60; V:59; R:85; I:89
1SWASPJ003544.75+495450.0	12.70	20-06-2019–02-03-2020	B:60; V:50; R:30; I:30	B:314; V:293; R:382; I:381
1SWASPJ003414.72-291038.4	15.23	29-11-2019–03-12-2019	B:300; V:300; R:300; I:300	B:20; V:20; R:45; I:44
1SWASPJ002952.96+475034.3	10.16	29-06-2019–02-12-2019	B:12; V:12; R:11; I:10	B:160; V:161; R:172; I:169
1SWASPJ002349.66+483114.5	12.60	17-11-2019–04-12-2019	B:60; V:60; R:60; I:60	B:0; V:47; R:63; I:64
1SWASPJ001521.76+472055.2	11.32	05-09-2018–20-02-2020	B:15; V:14; R:13; I:12	B:272; V:300; R:298; I:283
1SWASPJ000927.89+014542.1	14.15	22-11-2019–27-01-2020	B:300; V:300; R:300; I:300	B:29; V:25; R:71; I:71
1SWASPJ000018.09+091923.9	10.91	17-11-2019–12-02-2019	B:12; V:12; R:11; I:10	B:165; V:162; R:225; I:236

Table 8.1 Candidate NCRGEB observed using PIRATE. V-mag is taken from NOMAD. The exposure times and number of observations for each filter are liste d.

Aperture photometry can now be performed on the processed and aligned stack of science images, or alternative programmes can be used, such a `VaST`, detailed below. Although PIRATE provided good quality observations on the whole, some bad images had to be removed during the reduction and analysis process. Some of the issues encountered with PIRATE included software incorrectly calculating moon distance, the dome closing during images leaving a ghost-dome in the reduced images, wind shudder, incorrect focusing, filters being out of action for long periods of time, and working with a pipeline that was currently under development. An example of a "good" PIRATE image is shown in Figure 8.2 (left) and a "bad" image which has been majorly affected by wind shudder is shown in Figure 8.2 (right). Bad images were removed from the data set before light curve extraction.

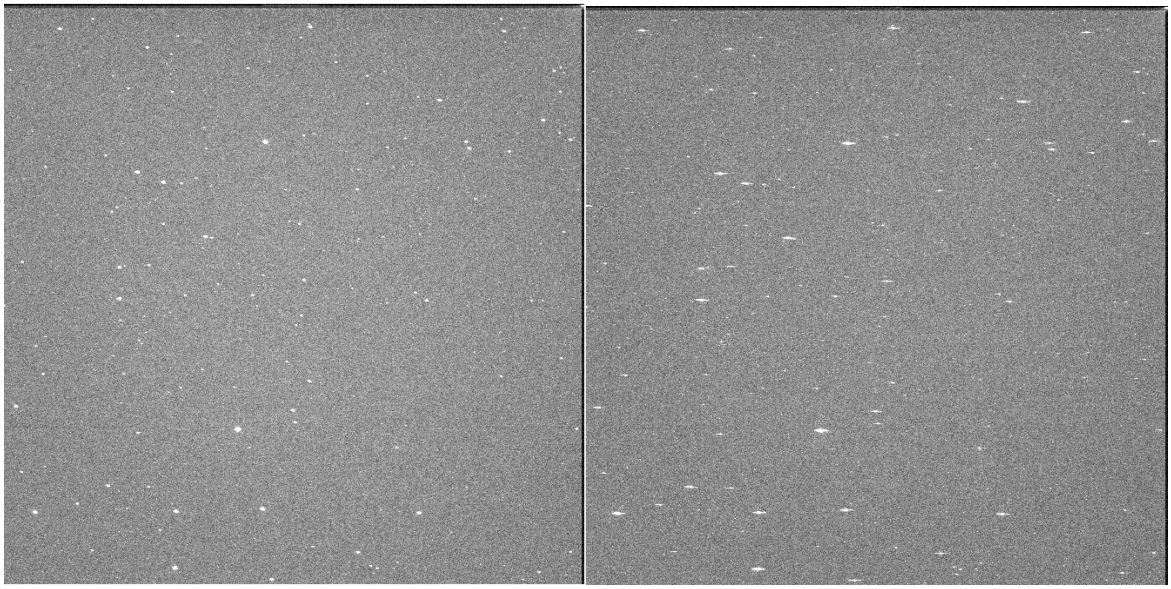

Fig. 8.2 **Left:** Example of a typical "good" PIRATE observation, with minor wind shudder. **Right:** Example of a typical "bad" PIRATE observation, with significant wind shudder and tracking issues.

Fig. 8.3 The LCO 80 cm telescope enclosure at the Sedgwick Reserve [Credit: LCO]

8.3 Las Cumbres Observatory

The Las Cumbres Observatory (LCO) (Figure 8.3) is a global network of robotic observatories covering both northern and southern hemispheres, allowing, in some instances, for continuous observations of a target for several days (Brown et al., 2013). The continuous coverage, rapid response, and possibility for high cadence observations means that LCO is an excellent follow-up facility.

LCO currently consists of two 2m telescopes, nine 1m telescopes, and seven 0.4m telescopes which can be centrally controlled to act as a single instrument. An observation requested by a user is scheduled to provide optimum observing for all telescopes and users. The sites of the network are currently Cerro Tolodo Interamerican Observatory (Chile), South African Astronomical Observatory (South Africa), Siding Spring Observatory (Australia), McDonald Observatory (USA), Haleakala Observatory (Hawaii), Teide Observatory (Canary Islands). It is expected that an additional telescope will soon be operational at the Ali Observatory (Tibet).

The 2m telescopes have a field of view of $10\times10''$ and a pixel scale of $0.3'$/pixel with a 2×2 binning and 18 filter options; the 1m telescopes have a $26\times26''$ field of view and a pixel scale of $0.389'$ /pixel with a 1×1 binning and 21 filter options; and the 0.4m telescopes have a $29\times29''$ field of view and a pixel scale of $0.571'$/pixel with a 1×1 binning and 9 filter options.

Education is a core mission of LCO, and to this extent, an educational observing programme including time on LCO was conducted. This programme, called "Hunting Giants", involved working with international schools on a series of observations. This programme has focused on teaching astronomical skills to secondary-school age children (planning an observation, using a telescope, reducing the data), allowing the number of observations of NCRGEB targets to be increased. Schools were encouraged to produce their own light curves, although access to the `BANZAI` reduced data were used to re-calibrate their light curves for this research. 10 hours of photometric observing time on the LCO network were awarded, and schools were able to use their own allocated time, vastly increasing the overall observing time. All observations were queue scheduled through the LCO website.

Unlike PIRATE, no issues were encountered with the LCO data. One reason for this is that unless an observation is taken successfully the pipeline classes it as a failed image and no reduced data are received. With PIRATE, where you might see a dome-ghost, this would be a failed image in LCO.

8.3.1 Observations

This section details the number of observations made with LCO. The observing season started on 21 November 2018 and ended on 30 September 2019. The students' observing season started on 29 January 2019 and ended on 23 November 2019. Table 8.2 and 8.3 lists the targets observed by LCO and their corresponding exposure time and number of good

observations. All three LCO telescope sizes were used in the observations, in Johnson B, V, R filters.

Of the 27 candidate binaries, 9 were observed by LCO, some more so than others depending on visibility. Table 8.2 details the observations taken during the non-educational programme. The 10 hours from the proposal were taken up mainly by the observation of 4 targets, and approximately 50% of the 10 hours were taken up by failed observations. Table 8.3 details the observations taken by the students as part of the educational programme. This clearly shows the sizeable increased in successful observations, however the failure rate for the students observations is not known.

8.3.2 Data reduction

For LCOGT, data from the science imagers are processed through the `BANZAI` pipeline[3], a generic pipeline for all users of the telescopes (McCully et al., 2018). `BANZAI` processes frames from the Spectral cameras on the 2m telescopes, the Sinistro cameras on the 1m telescopes, and the SBIG cameras on the 0.4m telescopes. `BANZAI` is coded in Python and runs automatically on every image as soon as it reaches the LCOGT's cloud archive, allowing users to access reduced data in under 10 minutes. This pipeline performs the following calibrations:

1. Bad-pixel masking
2. Bias subtraction
3. Dark subtraction
4. Flat field correction
5. Source extraction (using SEP, Source Extraction and Photometry in Python)

[3]https://lco.global/documentation/data/BANZAIpipeline/

Target	M_v	Dates	Exp Time	N good observations
1SWASPJ231800.38-031131.4	13.81	28-12-2018–14-01-2019	B:80; V:80; R:80	B:17; V:17; R:16
1SWASPJ204317.92-251850.0	14.03	26-11-2018–26-11-2018	B:150; V:150; R:150	B:4; V:4; R:4
1SWASPJ183357.87+423725.2	12.38	26-11-2018–26-11-2018	B:25; V:25; R:25	B:4; V:116; R:4
1SWASPJ103327.40-304931.6	15.58	29-11-2018–29-11-2018	B:420; V:420; R:420	B:4; V:4; R:4
1SWASPJ093610.20-283847.2	12.50	23-11-2018–29-11-2018	B:30; V:30; R:30	B:36; V:34; R:33
1SWASPJ035259.67+091717.1	12.52	25-11-2018–13-01-2019	B:25; V:25; R:25	B:25; V:25; R:25
1SWASPJ001521.76+472055.2	11.32	21-11-2018–26-11-2018	B:10; V:10; R:10	B:4; V:4; R:4

Table 8.2 Candidate NCRGEB observed using LCO. V-mag is taken from NOMAD. The exposure times and number of observations for each filter are liste d.

Target	M_v	Dates	Exp Time	N good observations
1SWASPJ204317.92-251850.0	14.03	04-10-2019–21-10-2019	B:150; V:150; R:150	B:26; V:26; R:26
1SWASPJ194733.51-471201.4	13.18	23-10-2019–01-11-2019	B:80; V:80; R:80	B:18; V:19; R:19
1SWASPJ183357.87+423725.2	12.38	26-07-2019–25-09-2019	B:25; V:25; R:25	B:4; V:4; R:116
1SWASPJ154828.29+201442.8	10.57	06-07-2019–23-04-2019	B:5; V:5; R:5	B:32; V:167; R:32
1SWASPJ093610.20-283847.2	12.50	24-01-2019–02-04-2019	B:30; V:30; R:30	B:19; V:194; R:15

Table 8.3 Candidate NCRGEB observed using LCO through the educational programme. V-mag is taken from NOMAD. The exposure times and number of observations for each filter are liste d.

6. Astrometric solution (using astrometry.net)

The processed science images are exported as multi-extension FITS files which include the science data, bad pixel mask, pixel uncertainties, catalogue of all sources positions, fluxes, and errors in the image. Raw images are also available for users to perform their own calibrations, however reducing the data separately seems to provide no notable reduction in photometric errors. Therefore the `BANZAI` reduced images are suitable for immediate aperture photometry, through `VaST` or `AIJ`.

8.4 Analysis of photometric observations

Although two sets of observations were obtained and reduced using different methods and different observers, the final stage of reduction (from image to light curve) follows the same general process. This section will discuss the extraction of light curves from the PIRATE and Las Cumbres Observatory observations, and the analysis used for each data set. It will also briefly detail the two programmes used to extract the light curves, `VaST` and `AIJ`.

8.4.1 Light curve extraction with `AstroImageJ`

`AstroImageJ` (`AIJ`) (Collins et al., 2017) is a general purpose tool for astronomical image analysis, commonly used for reducing raw observations and for extracting light curves from photometric observations via aperture photometry. The software has been optimised for time series analysis for a large number of images. Collins et al. (2017) discusses the programme and its usage, and the full user guide can be found online[4].

Whilst `AIJ` has the reduction suite which can perform bias subtraction, dark subtraction, and flat field division in one go, it was not used in favour of PIRATE and LCO pipelines, written specifically for PIRATE and LCO multi-colour photometry. Instead, `AIJ` is used to

[4]https://www.astro.louisville.edu/software/astroimagej/

plate solve any which the pipeline has missed, visually inspect all images for bad images, and perform aperture photometry.

A user can load up a series of images which allows them to manually check for and remove bad images (i.e. removing images which are too noisy, with satellite trails close to targets, dome lighting). Aperture photometry can be performed on the aligned and fully processed stack of science images. It is possible to vary the aperture size based on the full width at half maximum (FWHM) of the point spread function of the star, and different aperture sizes can be chosen for each of the target and comparison stars, or just the target star. The aperture photometry can be run automatically on the entire stack of images, and it outputs the flux, or magnitude if chosen, of the selected stars in the stack. An example of multi-aperture photometry being performed in `AIJ` is shown in Figure 8.4.

Difference photometry can be performed, if desired, by dividing the flux of the target star by the flux of selected non-variable companion stars. It is possible to choose the companion stars based on the root mean squre (RMS), and the lowest RMS stars are used in the process. The light curve is now ready to be analysed and phase-folded. The light curve can be imported directly into modelling programmes (such as PHOEBE, see Chapter 10) or can be immediately plotted as a phase-folded light curve.

8.4.2 Light curve extraction with `VaST`

Another programme used to extract light curves is the Variability Search Toolkit (`VaST`)[5], software designed for variable star detection in a stack of astronomical images (Sokolovsky and Lebedev 2017; Sokolovsky and Lebedev 2018). `VaST` is written in C and has a simple GUI in UNIX. `VaST` detects variability through source list matching, rather than image subtraction. SExtractor (Bertin and Arnouts, 1996) is used to create source lists and perform aperture photometry. `VaST` takes the first image in the stack as a detection image, and

[5]http://scan.sai.msu.ru/vast/

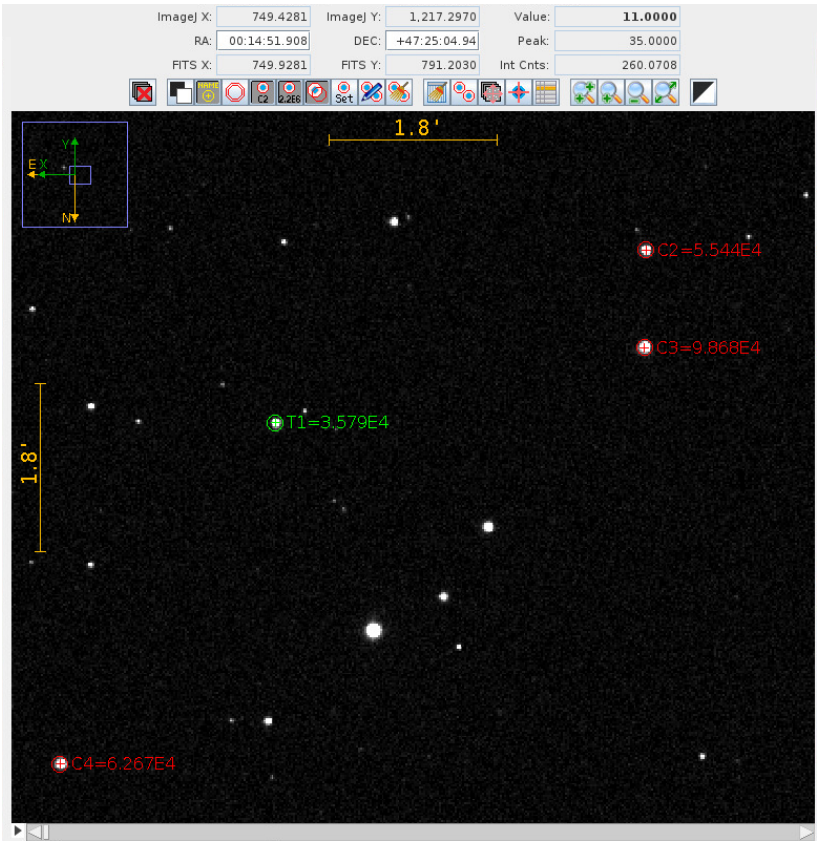

Fig. 8.4 An example of multi-aperture photometry being performed with `AIJ` on a stack of 318 V band PIRATE observations of J001521.

generates light curves for objects detected in this image. This assumes that the first image is good quality, has a good airmass, and the target star has been detected, which requires manual checking.

VaST automatically filters out bad images and generates a light curve for each object in the image, as well as scatter and smoothness of the light curve. The smoothness of the light curve is given as a variability index, and the higher the variability index of an object compared to other objects of similar brightness in the stack, the more likely the object is to be variable.

VaST performs a magnitude calibration by converting instrumental magnitudes produced by SEXtractor and calibrating them against a star catalogue. It takes the nearest star of a similar magnitude in order to calibrate it, however it is sometimes necessary to use many thousands of stars for this step for images with a large field of view. VaST then plots a best fit line between instrumental magnitude and APASS catalogue magnitude, creating a magnitude scale which can be used to convert the input instrumental magnitudes to apparent magnitudes. The corrected apparent magnitude is the final output.

VaST employs a variability search method, however since the targets are known, this is an unnecessary step. Instead, it is possible to search for the target star and save time. VaST also calculates the standard deviation of the data points from each light curve. This can be used to put a statistical value on the variability observed.

VaST is able to perform high accuracy aperture photometry on reduced images, and is able to handle image distortions, and rotated or shifted images, however it cannot be run on images with a different binning, hence a difference scale (arcsec/pixel). Unfortunately the binning was changed in PIRATE due to advice from a colleague on September 2019 which means that VaST has to be run separately on each binning and the results combined. VaST outputs a file of HJD, magnitude, and photometric error which, like AIJ, can be imported

directly into modelling programmes or plotted as a phase-folded light curve. An example of the VaST output is shown in Figure 8.5.

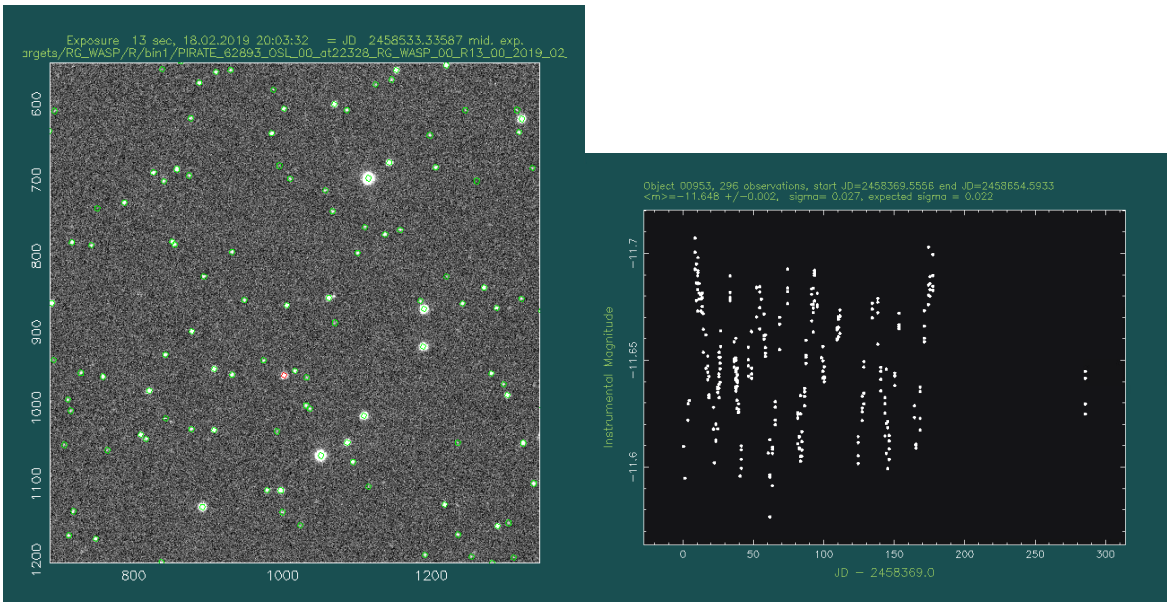

Fig. 8.5 An example of multi-aperture photometry being performed with VaST on a stack of 310 R band PIRATE observations of J001521. **Left:** Selecting the target star (red circle) in VaST from the field stars (green circles). **Right:** The light curve produced by VaST.

VaST and AIJ were both used to extract light curves from PIRATE and LCO data. Due to the set up of the Open University's ThinLinc Linux system, if a light curve was not plate solved by the PIRATE pipeline, it was not possible to plate solve it using AIJ. For targets with many hundreds of image frames, the process of moving the data to a different system and back became laborious. However, VaST can operate without plate solve frames, so in these instances, it was used to reduce light curves. Additionally, VaST is able to automatically detect bad images, which sped up the process of identifying and removing bad images from large data sets.

Conversely, VaST also faced two main issues, meaning that AIJ was the best option for certain targets. For targets where the binning changed from binning 1×1 to binning 2×2, VaST had to be run in two stages. If there were too few images in either binning, it became

advantageous to use AIJ. VaST also encountered unknown errors for some data sets, in which it would become stuck at the initial stage of reading the data, or would successfully read the data but be unable to produce a light curve for the target star. Again, in these situations, AIJ would be used. Rebinning the data would have been a suitable fix to this problem, but this was only realised after the data reduction had occured.

To assess whether VaST and AIJ reduced data can be used together, a comparison by Sokolovsky and Lebedev (2018) looked initially at the error bars of a light curve of a cataclysmic variable in VaST and in AIJ. They report that the error bars in AIJ are three times larger than those reported by VaST, due to different sources of error being taken into account. Errors in VaST are derived from a combination of background and photon noise, and scale with magnitude calibration function. In their test, errors in AIJ include background and photon noise from a single comparison star, slightly fainter than the target star. They do not take into account the error bars if multiple comparison stars are used, hence another reason to test the two methods.

VaST has functions for both PSF fitting and aperture photometry. Aperture photometry was chosen because it gives more similar plots to AIJ. There is only a notable difference between aperture photometry and PSF fitting for targets with a magnitude fainter than V=17. Since all of our targets have magnitudes brighter than V=16, this did not pose a problem.

8.5 Photometric Results

In total, 22 targets have been observed using PIRATE and LCO and their light curves extracted using the methods described above. On the whole, each target has a good level of coverage across all phases, and across B, V, R, and I. Even though some light curves are noisy and some are under sampled, the overall data set is good, and the multi-colour photometry will be valuable for modelling the temperatures of the binary components. The average number of observations of each target is $\sim$725, spread across 4 filters.

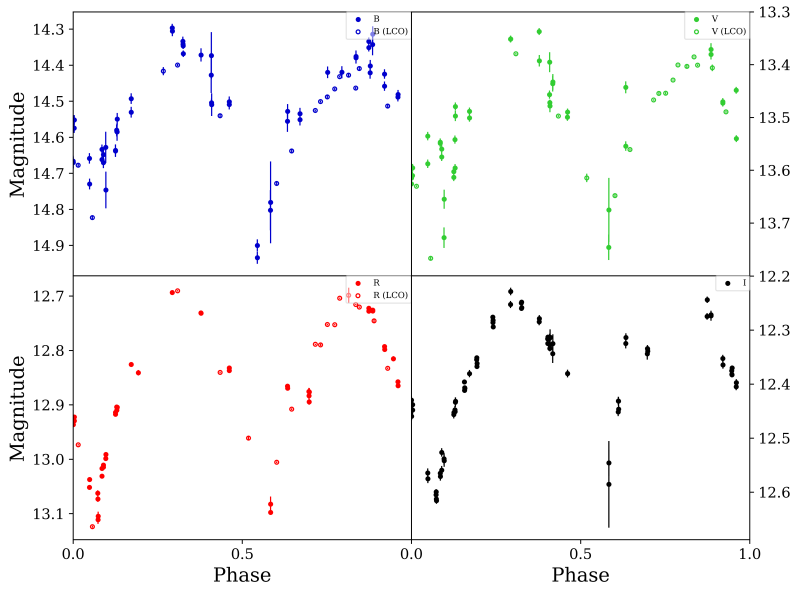

Fig. 8.6 Light curve of J231800 phase-folded with a period of 23.84 d.

Typically, photometric errors for both LCO and PIRATE are ∼0.01 mag, and the light curves have not been extinction corrected since the objects are Galactic and lie away from the Galactic Plane. In extreme cases, PIRATE photometric errors are as much as ∼0.1 mag. The photometric errors are greatest for objects low on the horizon, fainter objects, and objects closer to the Moon. Each phase-folded photometric light curve is displayed below, and a summary of each target is given in Table 8.5.

1SWASPJ231800.38-031131.4

J231800 has a SuperWASP period of 23.84d and was observed in BVRI with PIRATE and BVR with LCO, shown in Figure 8.6. The light curve is sparse due to a mistake in the original queue scheduling which was only rectified after ∼50 nights of observations were made of the wrong target. Although the multi-colour light curve of J231800 is relatively sparse, there are clear eclipses visible in each band with almost equal depths, and the target is a clear binary and is a prime candidate for spectroscopic follow-up.

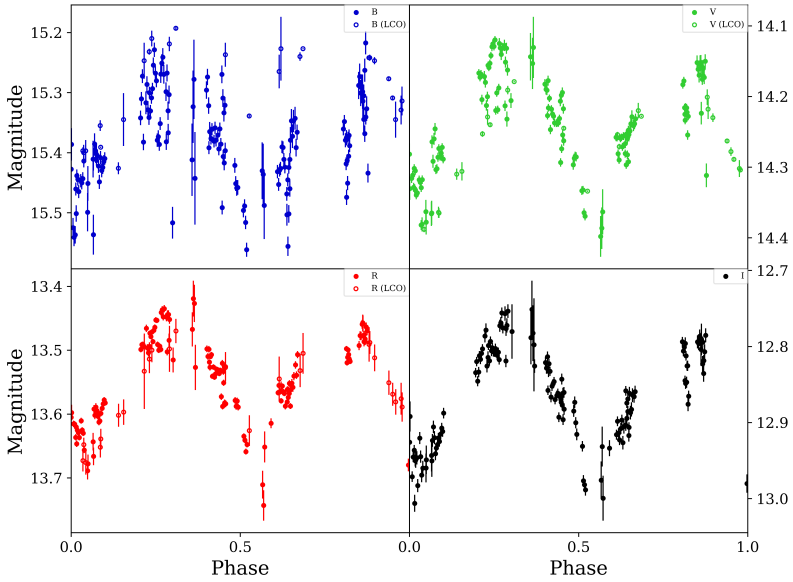

Fig. 8.7 Light curve of J204317 phase-folded with a period of 4.92 d.

1SWASPJ204317.92-251850.0

J204317 has a SuperWASP period of 4.92d and was observed in BVRI with PIRATE and BVR with LCO, shown in Figure 8.7. This light curve has good phase coverage, although the B band light curve has more noise. It is unclear as to whether this target has eclipses or if it is a rotational variable. Spectroscopic follow-up will be required to determine the variable type.

1SWASPJ194733.51-471201.4

J194733 was observed with LCO, and has very poor phase coverage due to the declination of the target, shown in Figure 8.8. It has a SuperWASP period of 35.08d, and the variation between the observations could be viewed as an eclipse, although that is very tenuous. Very little else can be deduced about this target from the observations.

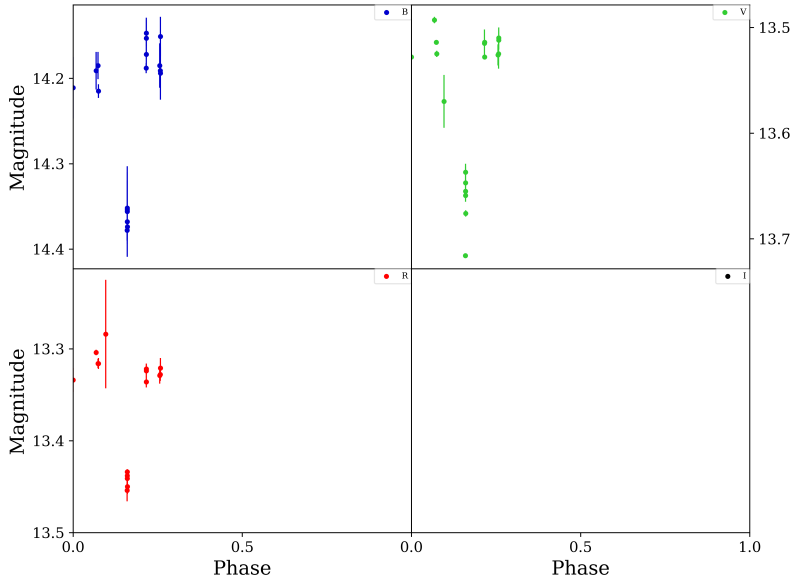

Fig. 8.8 Light curve of J194733 phase-folded with a period of 35.08 d.

1SWASPJ194231.22-251605.5

J192628 has a SuperWASP period of 23.18d and was observed with PIRATE in BVRI, shown in Figure 8.9. It has good phase coverage and shows beautifully clear eclipses of nearly equal depth in all bands. This system has low photometric error and will be followed up spectroscopically.

1SWASPJ192628.96-233856.1

J192628 has a SuperWASP period of 28.54 d and was observed with PIRATE in BVRI, shown in Figure 8.10. Despite the sparse observations, the phase coverage is good and the photometric error is extremely low. The light curve appears to show a pulsating variable, possible a long period Cepheid, so is unlikely to be a NCRGEB.

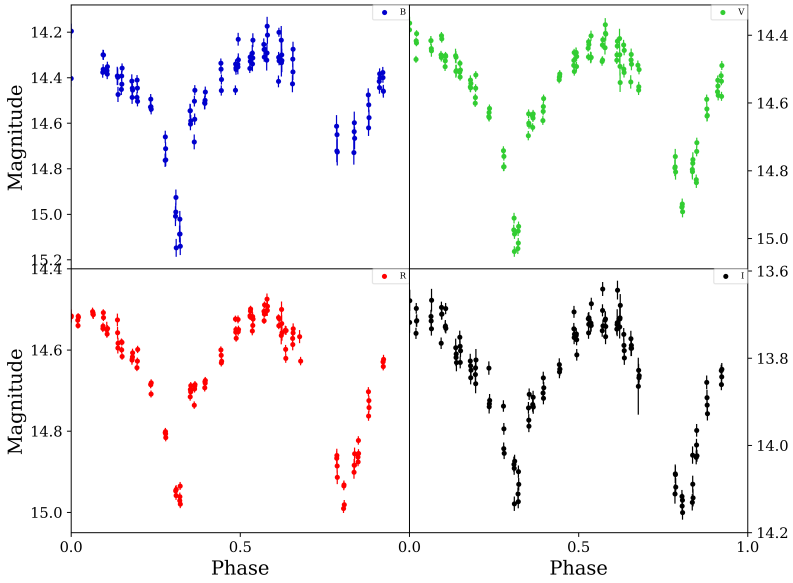

Fig. 8.9 Light curve of J194231 phase-folded with a period of 23.18 d.

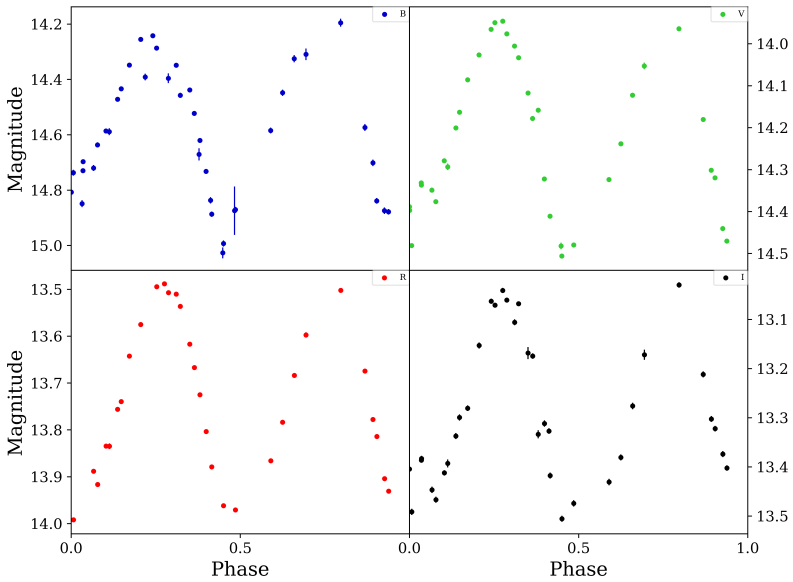

Fig. 8.10 Light curve of J192628 phase-folded with a period of 28.54 d.

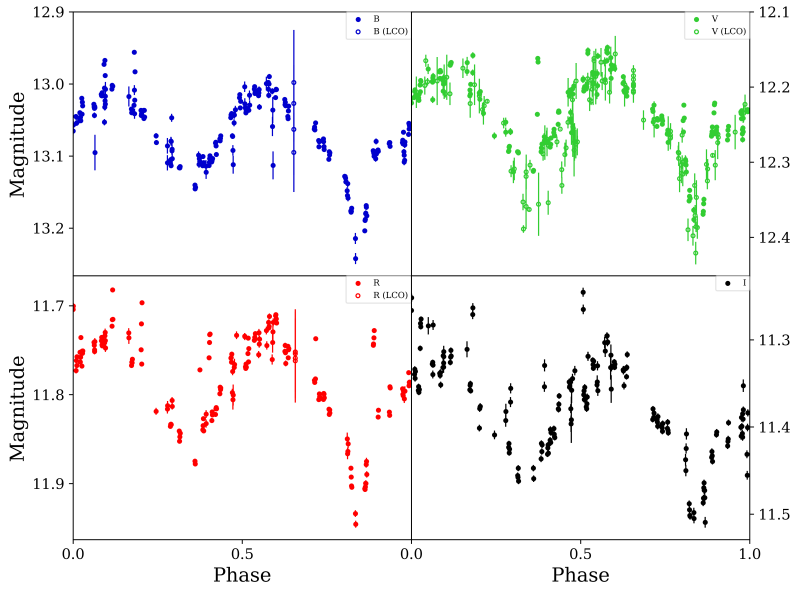

Fig. 8.11 Light curve of J183357 phase-folded with a period of 8.72 d.

1SWASPJ192311.66-423244.5

No multi-colour photometric follow-up was possible for J192311 due to the declination of the target.

1SWASPJ191910.42-414050.9

No multi-colour photometric follow-up was possible for J191910 due to the declination of the target.

1SWASPJ190114.91-380729.0

No multi-colour photometric follow-up was possible for J190114 due to the declination of the target.

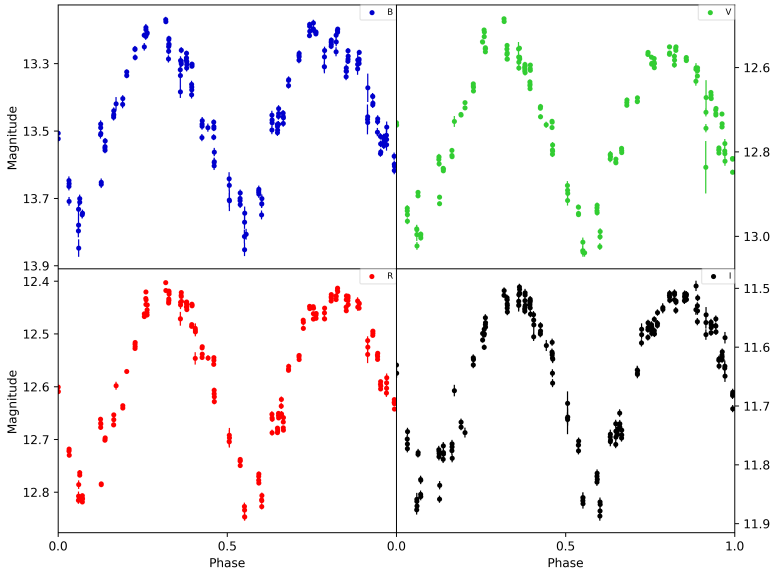

Fig. 8.12 Light curve of J165656 phase-folded with a period of 15.68 d.

1SWASPJ183357.87+423725.2

J183357 has excellent phase coverage from both PIRATE (BVRI) and LCO (BVR), shown in Figure 8.11. This target has a SuperWASP period of 8.72d, and shows clear eclipses in each band. Despite the spurious data points in each band, the overall light curve is sharp and the photometric errors are low. This target will be followed up spectroscopically.

1SWASPJ165656.26-040414.3

J165656 has a period of 15.68 d and was observed in BVRI with PIRATE, shown in Figure 8.12. The light curve has good phase coverage and low photometric noise, however, it is difficult to tell whether it is that of a pulsator or a binary. There are possible eclipses, however the system appears to have a pulse profile, indicating that this may not be a binary.

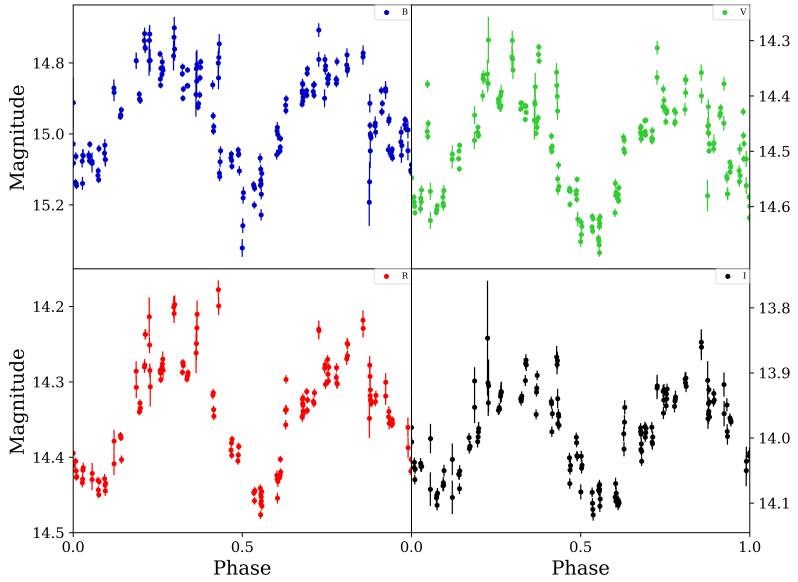

Fig. 8.13 Light curve of J165241 phase-folded with a period of 15.13 d.

1SWASPJ165241.24+203224.7

J164231 has an ASAS-SN period of 15.13 d and was observed in BVRI with PIRATE, shown in Figure 8.13. The light curve itself has good phase coverage, but has high photometric noise for some observations. The light curve is unconvincing as a binary, and appears to be more likely to be a pulsating variable due to the asymmetric pulse profile.

1SWASPJ154828.29+201442.8

J154828 has a period of 7.47d and was observed in BVRI with PIRATE and BVR with LCO, shown in Figure 8.14. The phase coverage is excellent despite the relatively high photometric noise. This target could be a binary, or it could be a pulsating or rotating variable. Further spectroscopic follow-up is required to determine the variable type.

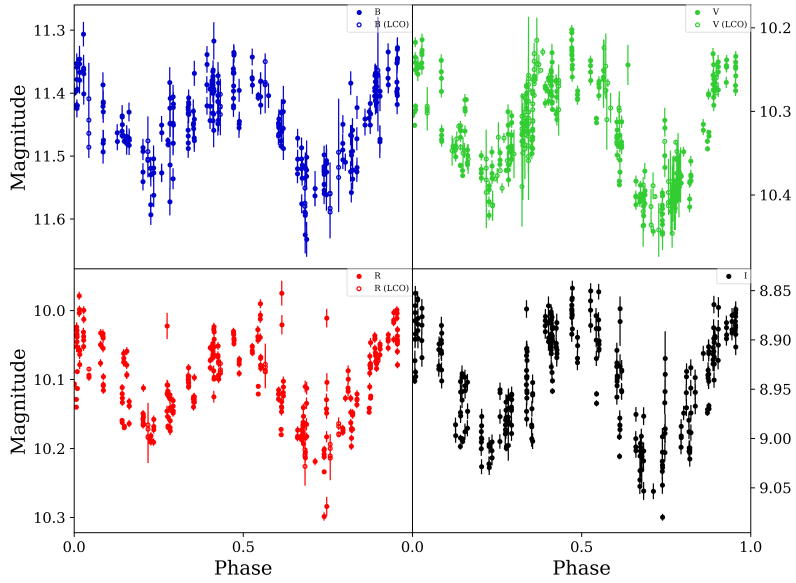

Fig. 8.14 Light curve of J154828 phase-folded with a period of 7.47 d.

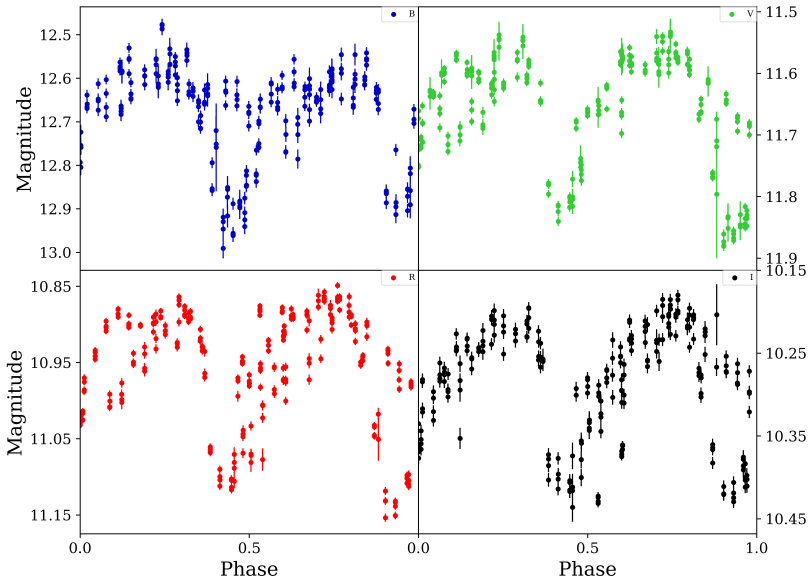

Fig. 8.15 Light curve of J154607 phase-folded with a period of 29.14 d.

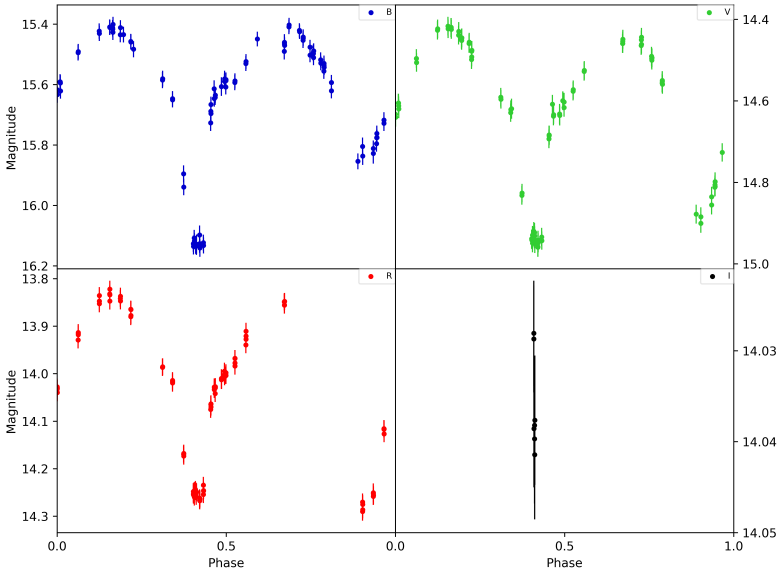

Fig. 8.16 Light curve of J132156 phase-folded with a period of 32.09 d.

1SWASPJ154607.55-191711.4

J154607 has a period of 29.14d and was observed in BVRI with PIRATE, shown in Figure 8.15. As seen in the ASAS-SN and SuperWASP light curves, the photometric phase-folded light curve appears to either be comprised of two sources or of a semi-periodic signal. This system is highly unlikely to be a NCRGEB.

1SWASPJ135703.85-474817.9

No multi-colour photometric follow-up was possible for J135703 due to the declination of the target.

1SWASPJ132156.04-010742.8

J132156, shown in Figure 8.16, has a SuperWASP period of 32.09d and was observed in BVRI with PIRATE, although due to a fault with PIRATE data reduction pipeline, it was not

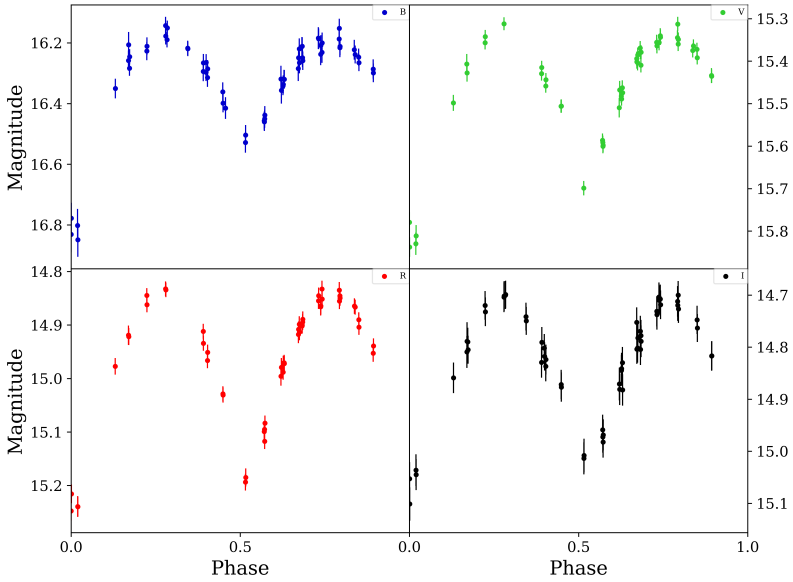

Fig. 8.17 Light curve of J103327 phase-folded with a period of 17.87 d.

possible to reduce I band observations with a binning of 1×1. Despite this, the remaining BVR light curves provide mostly good phase coverage and demonstrate that the system is indeed an eclipsing binary. The eclipse depths appear to be almost equal in R and of different depths in B, indicating that the components are late-type. This target is a high priority for spectroscopic follow-up.

1SWASPJ103327.40-304931.6

J103327 has a SuperWASP period of 17.87d and was observed in BVRI with PIRATE, shown in Figure 8.17. Whilst the light curve is relatively sparse, the phase coverage is good, photometric errors are low, and there appears to be clear eclipses visible in each band. This target is high priority for further spectroscopic follow-up.

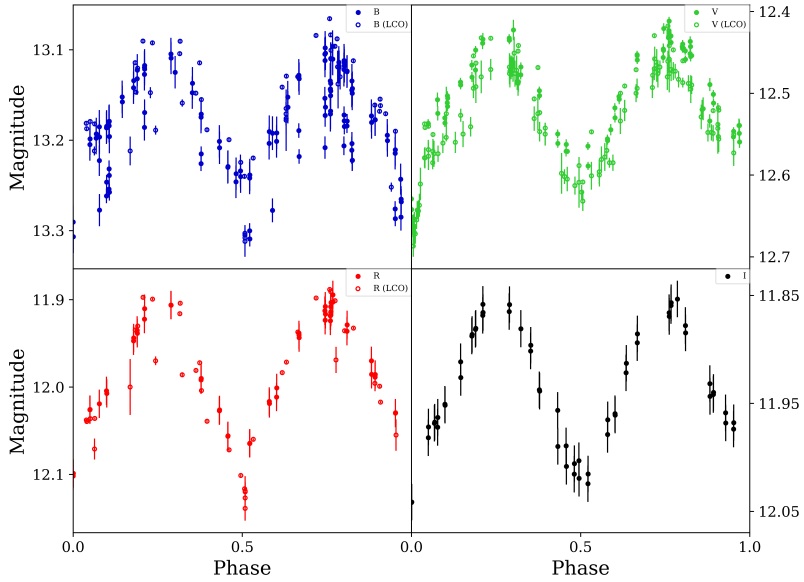

Fig. 8.18 Light curve of J093610 phase-folded with a period of 6.92 d.

1SWASPJ093610.20-283847.2

J093610, shown in Figure 8.18, has a SuperWASP period of 6.92d and was observed in BVRI with PIRATE and BVR with LCO. This target has good phase coverage, but high photometric uncertainty, particularly in the B band. The system appears to be shows eclipses, especially in V and R, however, this light curve could also feasibly be that of a pulsating variable if plotted at half the period. Spectroscopic follow-up will be key in determining the variability type.

1SWASPJ035259.67+091717.1

J035259 has a SuperWASP period of 24.61d and was observed in BVRI with PIRATE, shown in Figure 8.19. It is a beautiful example of an eclipsing binary system, with clear eclipses of different depths, low photometric uncertainty, and continuous variation. This system is

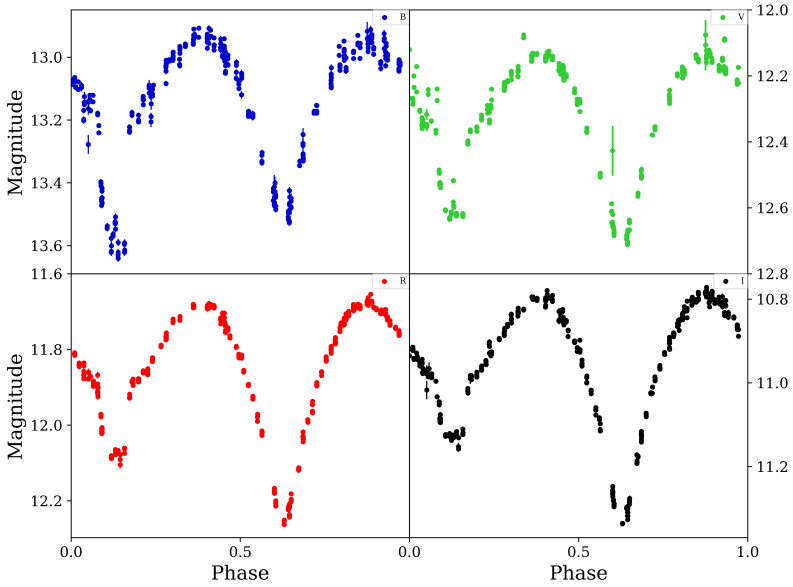

Fig. 8.19 Light curve of J035259 phase-folded with a period of 24.61 d.

definitely a binary system, but spectroscopic follow-up will determine if it is a NCRGEB system.

1SWASPJ022953.03+041420.9

J022953, shown in Figure 8.20, has a SuperWASP period of 6.66d and was observed in BVRI with PIRATE. Even with the sparse phase coverage, it is very clearly not a binary, and instead appears to be a pulsating variable folded at twice the period. This system is highly unlikely to be a NCRGEB, but spectroscopic follow-up will be used to confirm this.

1SWASPJ003544.75+495450.0

J003544 has a period of 17.86d and was observed in BVRI with PIRATE, which provided excellent phase coverage and low photometric uncertainties, shown in Figure 8.21. This target is very clearly a binary, with one eclipse slightly sharper and deeper than the other. This is a high priority target for spectroscopic follow-up.

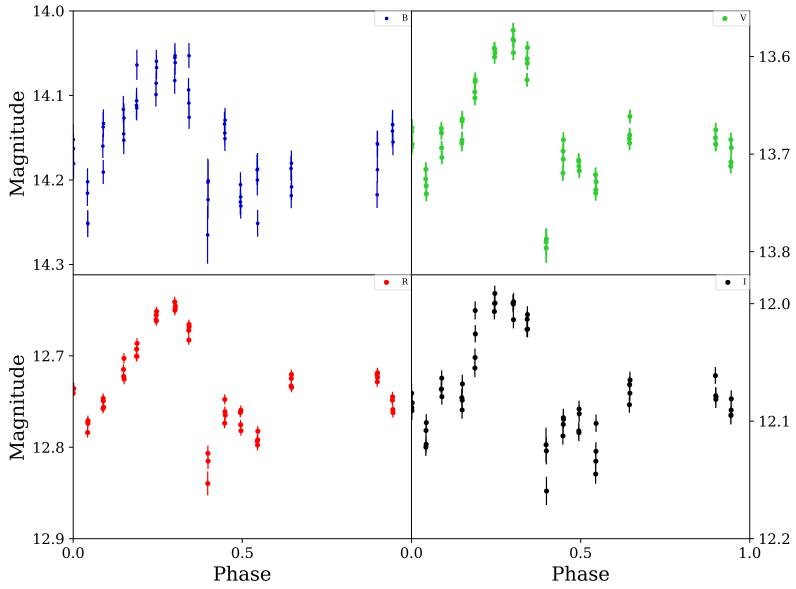

Fig. 8.20 Light curve of J022953 phase-folded with a period of 6.66 d.

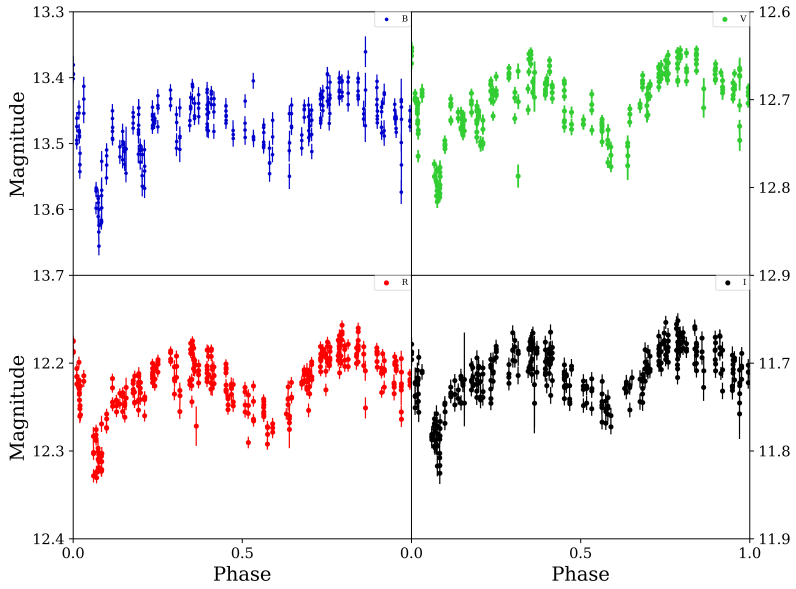

Fig. 8.21 Light curve of J003544 phase-folded with a period of 17.86 d.

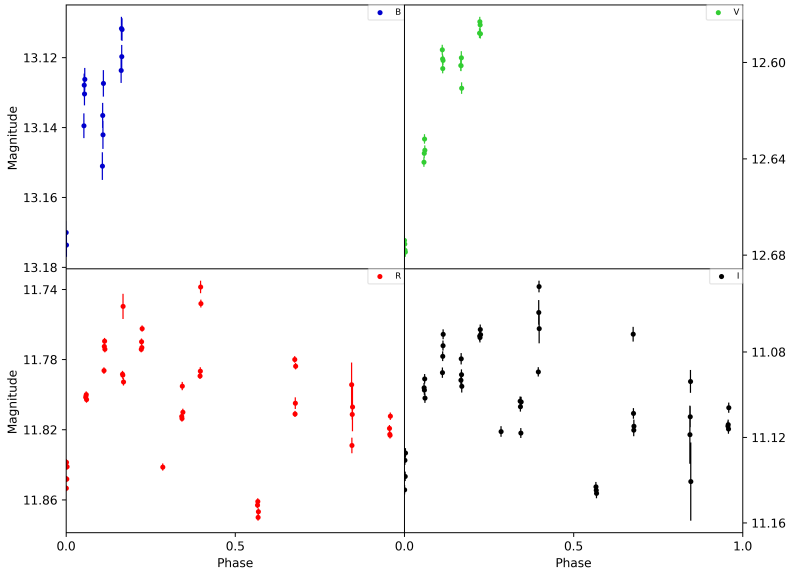

Fig. 8.22 Light curve of J003544 phase-folded with a period of 17.86 d.

1SWASPJ003414.72-291038.4

J003414 has a SuperWASP period of 11.32d and was observed in BVRI with PIRATE, shown in Figure 8.22. However very little multi-colour photometric follow-up was possible due to the declination of the target.

1SWASPJ002952.96+475034.3

J002952 has a SuperWASP period of 20.33d and was observed with PIRATE in BVRI, with good phase coverage, shown in Figure 8.23. The light curve appears to be smoothly varying, with marginally different depth minima. It is likely that this target is a NCRGEB.

1SWASPJ002349.66+483114.5

J002349, shown in Figure 8.24, has a SuperWASP period of 17.15d and was also observed only with PIRATE in BVRI, however an error in the PIRATE data reduction pipeline rendered

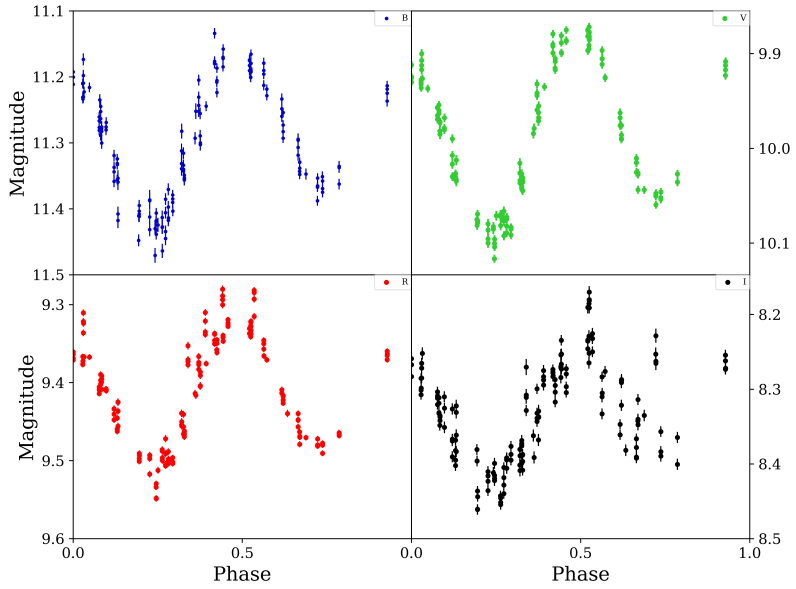

Fig. 8.23 Light curve of J002952 phase-folded with a period of 20.33 d.

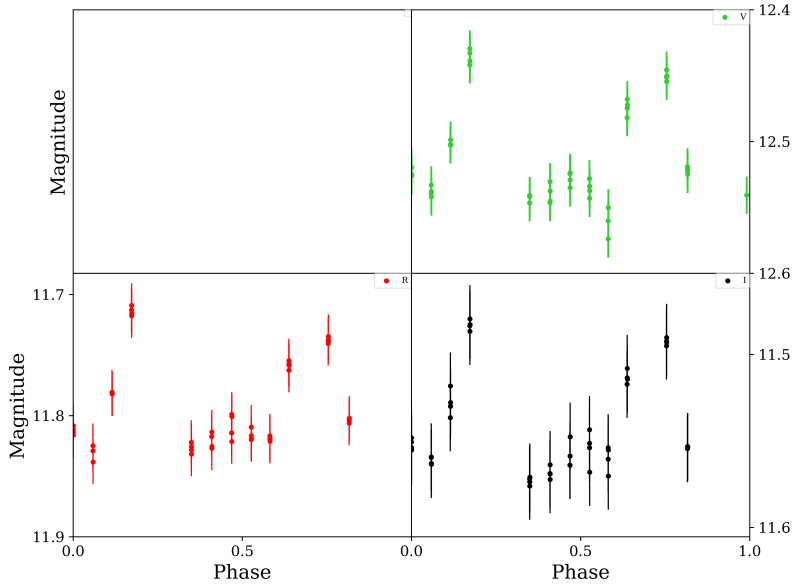

Fig. 8.24 Light curve of J002349 phase-folded with a period of 17.15 d.

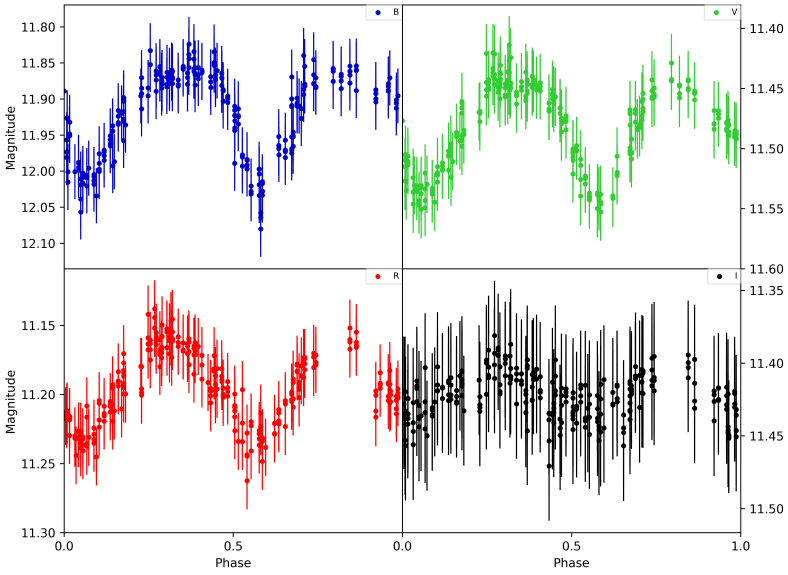

Fig. 8.25 Light curve of J001521 phase-folded with a period of 41.62 d.

B band data unusable. Despite this, the target has good phase coverage and low photometric errors, however it is likely that this system is actually that of a rotating or pulsating variable. The light curve lacks eclipses and appears to be slightly asymmetric, so is unlikely to be a NCRGEB system.

1SWASPJ001545.50-622237.8

No multi-colour photometric follow-up was possible for J001545 due to the declination of the target.

1SWASPJ001521.76+472055.2

J001521 has a SuperWASP period of 41.62d and was observed in BVRI with PIRATE, shown in Figure 8.25. This target received the highest number of observations, spanning almost 2 years, although the light curve here shows only half the observations gained due to an error in the PIRATE data reduction pipeline. The light curve has excellent phase coverage and low

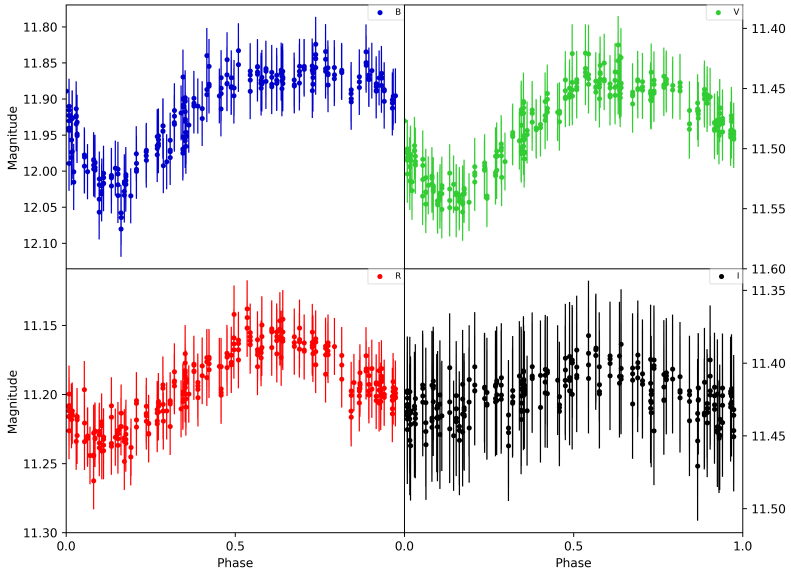

Fig. 8.26 Light curve of J001521 phase-folded with a period of 20.81 d.

photometric errors, however, it is difficult to conclude that J001521 is a binary system, let alone a NCRGEB. The shape of the light curve is notably different between B, V and R, and I, with B showing what appears to be eclipses, and V and R appearing to show pulsations. If plotted at half the period of 20.81d, however, J001521 appears to show a light curve of a Cepheid variable, shown in Figure 8.26. Since this target started off the path of research, but appears not to be a binary, it is one is the highest priority for spectroscopic follow-up. Spectroscopic follow-up will be key in determining the variable type.

1SWASPJ000927.89+014542.1

J000927, shown in Figure 8.27, has a SuperWASP period of 32.72d, but due to observing constraints, received only sparse observations from PIRATE in BVRI. Despite the sparse phase coverage in B and V, the R and I band appear to show a pulsating stellar variable with a low amplitude, rather than a binary system.

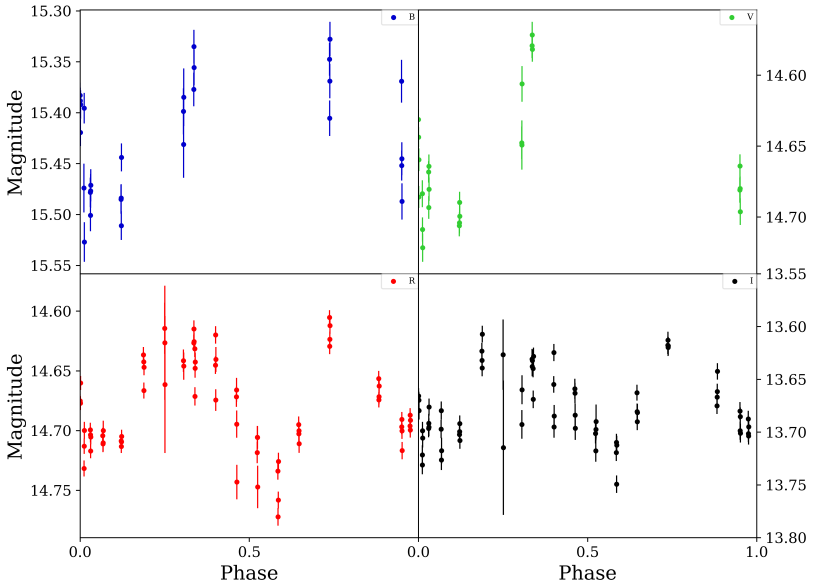

Fig. 8.27 Light curve of J000927 phase-folded with a period of 32.72 d.

1SWASPJ000018.09+091923.9

J000018 has a SuperWASP period of 85.76d, and an ASAS-SN period of 869.28d, shown in Figure 8.28. This target was observed in BVRI with PIRATE and received good phase coverage. From the light curve, J000018 appears to be a pulsating variable or a semiregular variable, which is why such significantly different periods were detected. The target is low priority for spectroscopic follow-up.

8.6 Summary

Over 24 months we completed a successful multi-colour photometric follow-up campaign of 22 candidate binary stars, the majority of which are in the northern hemisphere and mid-latitudes.

Approximately 23,000 observations were obtained through PIRATE, of which 15,000 were good images, and were reduced using the PIRATE pipeline written by Morrell (2021).

Table 8.4 NCRGEB candidates

WASP ID	Telescope	Filters	Comment
1SWASPJ231800.38-031131.4	PIRATE and LCO	B, V, R, I	Low photometric error, convincing binary
1SWASPJ204317.92-251850.0	PIRATE and LCO	B, V, R, I	High photometric error, convincing binary
1SWASPJ194733.51-471201.4	LCO	B, V, R	Low photometric error, too few observations
1SWASPJ194231.22-251605.5	PIRATE	B, V, R, I	Low photometric error, convincing binary
1SWASPJ192628.96-233856.1	PIRATE	B, V, R, I	Low photometric error, possible pulsator
1SWASPJ192311.66-423244.5	-	-	No photometric observations
1SWASPJ191910.42-414050.9	-	-	No photometric observations
1SWASPJ190114.91-380729.0	-	-	No photometric observations
1SWASPJ183357.87+423725.2	PIRATE and LCO	B, V, R, I	Low photometric error except in B, convincing binary
1SWASPJ165656.26-040414.3	PIRATE	B, V, R, I	Low photometric error, possible pulsator
1SWASPJ165241.24+203224.7	PIRATE	B, V, R, I	High photometric error, convincing binary
1SWASPJ154828.29+201442.8	PIRATE and LCO	B, V, R, I	Low photometric error except in B, unconvincing binary
1SWASPJ154607.55-191711.4	PIRATE	B, V, R, I	Low photometric error, semi-regular variable
1SWASPJ135703.85-474817.9	-	-	No photometric observations
1SWASPJ132156.04-010742.8	PIRATE	B, V, R, I	Low photometric error, convincing binary
1SWASPJ103327.40-304931.6	PIRATE and LCO	B, V, R, I	Low photometric error, convincing binary
1SWASPJ093610.20-283847.2	PIRATE and LCO	B, V, R, I	Low photometric error except in B, convincing binary
1SWASPJ035259.67+091717.1	PIRATE and LCO	B, V, R, I	Low photometric error, convincing binary
1SWASPJ022953.03+041420.9	PIRATE	B, V, R, I	High photometric error, possible pulsator
1SWASPJ003544.75+495450.0	PIRATE	B, V, R, I	High photometric error, convincing binary
1SWASPJ003414.72-291038.4	PIRATE	B, V, R, I	High photometric error, too few observations
1SWASPJ002952.96+475034.3	PIRATE	B, V, R, I	Low photometric error, convincing binary
1SWASPJ002349.66+483114.5	PIRATE	B, V, R, I	High photometric error, too few observations
1SWASPJ001545.50-622237.8	-	-	No photometric observations
1SWASPJ001521.76+472055.2	PIRATE and LCO	B, V, R, I	Low photometric error, possible binary
1SWASPJ000927.89+014542.1	PIRATE	B, V, R, I	High photometric error, not binary
1SWASPJ000018.09+091923.9	PIRATE	B, V, R, I	High photometric error, not binary

Table 8.5 Table of observations of NCRGEB candidates, including the telescopes each target was observed with, the photometric bands, and a brief assessment of the observations.

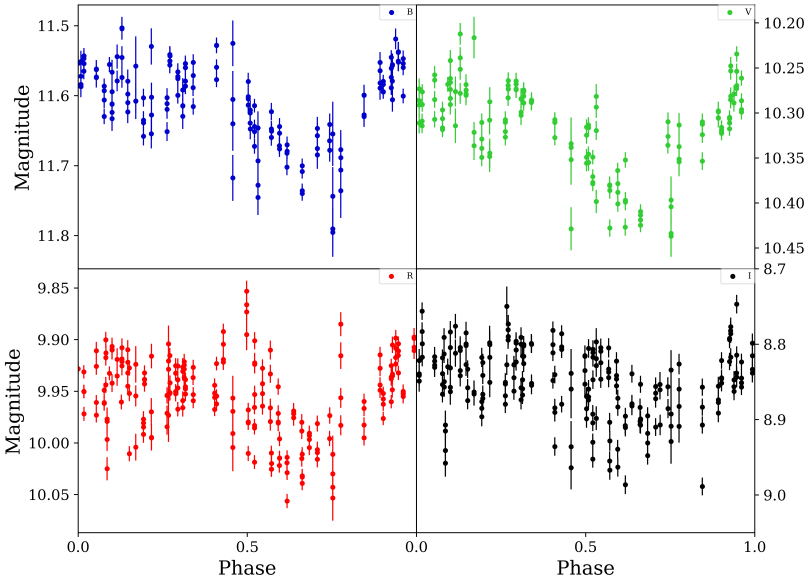

Fig. 8.28 Light curve of J000018 phase-folded with a period of 85.76 d.

Approximately 1,000 observations were obtained through LCO, both as part of an observing campaign and as part of an educational programme. LCO observations, whilst collected by different groups using different telescopes in the network, were all reduced using the automatic `BANZAI` pipeline, to ensure the output was reproducible. The educational programme allowed for a ten-fold increase our telescope time on LCO, as well as providing opportunities for students.

Some areas of improvement might include the adjustment of exposure times for some targets. Although an exposure test was done before observing with PIRATE, it was found that some targets were marginally underexposed in the reduced images, which increased the signal-to-noise ratio. Unfortunately, the OSO scheduler limits the exposure time of targets to 300 seconds, so for targets that required a longer exposure time, this was not possible. Another improvement could have been to increase the baseline of the observations. Some targets had under sampled light curves, despite the thousands of observations. A longer follow-up campaign would have benefited some targets.

This follow-up campaign produced high quality multi-colour light curves of 22 targets, which will feed into modelling in PHOEBE, allowing me to better constrain the temperatures and configurations of the binary systems. Of the candidates which received multi-colour photometric follow-up with PIRATE and LCO, 13 appear to be contact or near contact binary stars. The remainder are possible pulsating variables and semi-regular variables, or did not received enough observations for a decision to be made.

The next step to this follow-up campaign is the collection and reduction of spectroscopic data to complement the photometric data. Since the spectroscopic follow-up campaign ran mostly in parallel with the photometric follow-up, candidates are not discounted in this chapter. The spectroscopic follow-up and decision on whether objects are NCRGEB candidates will be detailed in Chapter 9.

Chapter 9

Spectroscopic Follow-Up of Near Contact Red Giant Eclipsing Binaries

This chapter will focus on the spectroscopic follow-up observations of the candidate near-contact red giant eclipsing binaries identified in Chapter 7 and followed up photometrically in Chapter 8. I include a summary of the telescopes and instrument set-ups, and the reduction pipelines implemented to extract the spectra and radial velocities from the observations, regardless of whether the targets are confirmed as binaries or not. This is followed by a discussion of the extracted radial velocities and spectra. Based on the combination of photometric and spectroscopic follow-up, I decide which candidate NCRGEB appear to be binaries, hence which are suitable for component modelling and evolutionary modelling.

The majority of the spectroscopic data were collected by three telescopes, the South African Large Telescope (SALT), the $74''$ telescope, and the Liverpool Telescope (LT). Additional spectra were taken using the William Herschel Telescope (WHT) and the Las Cumbres Observatory (LCO) global network. Unlike the photometric observations, LCO spectroscopic observations (see Chapter 8) were not taken as part of an educational programme, and are stand-alone observations.

Prior to this observing campaign, no time-series spectroscopic observations had been obtained for any of the binary targets. Therefore, the purpose of this work was to create the first set of spectroscopic observations for candidate near-contact red giant eclipsing binaries, allowing not only for extraction of radial velocities, but also spectral typing and spectral synthesis, constraining parameters to feed into modelling the stellar components in Chapter 10.

9.1 Spectroscopic follow-up

This section will detail the instrumentation, set-up, and data reduction for SALT, 74″, Liverpool Telescope, LCO, and WHT, and will discuss the capabilities and limitations of the instruments. Each section will also include details on the observations themselves, including comments on the observing conditions where necessary.

9.2 SALT

The South African Large Telescope (SALT) (Buckley et al., 2006), shown in Figure 9.1, is a 10 m class spectroscopic telescope with a primary mirror measuring 11.1×9.8 m. It has a fixed elevation of 53° and moves along the azimuth only, which means that although a target may be above the horizon, it may not be observable. SALT is located at the Sutherland site in South Africa, close to the 74″ and SuperWASP, which has an altitude of ∼1,768m, excellent seeing conditions, and very low light pollution.

To perform spectroscopy of the NCRGEB targets, the Robert Stobie Spectrograph (RSS) (Burgh et al. 2003; Kobulnicky et al. 2003) was used with the RSS in long-slit spectroscopy mode on the pg1800 grating, with a grating angle of 32.75°, and a camera angle of 65.50°, and a pc04600 filter (blocking blue light). This gives a dispersion of 0.21 Å/pixel in the range of 5300–6600 Å. The typical dispersion per binned pixel is therefore around 0.43

Fig. 9.1 SALT [Credit: Adele De Witte/Fotolia]

Å/pixel, corresponding to a velocity resolution of $\sim$21 km s^{-1} at this wavelength. This provides a spectral resolution of $R = \lambda/\Delta\lambda$ = 2890.

With a sufficient number of lines, sub-pixel cross-correlation techniques can measure velocity differences of the order of one-tenth of this, or about 2 km s^{-1}. Assuming the stars in each system have masses of 1–5 $M_{\odot}$, to be in contact at orbital periods of 4 – 42 d implies orbital separations of around 13–110 $R_{\odot}$. Such configurations would give rise to radial velocities in the range approximately 40 – 150 km s^{-1} for each star. As a result, the spectral resolution would be adequate to measure radial velocity curves of the targets. The RSS itself is made up of three CCD chips with a small separation between each. These gaps are positioned at $\sim$5757–5777Å and $\sim$6214–6232Å, meaning there is a small gap in wavelength coverage, however these do not impact on any strong lines. To provide wavelength calibration, Argon arc-lamp exposures were taken after each observation of the targets.

This instrumental set-up was chosen to capture a suitably large range of the red end of the spectrum in order to perform spectral typing; and in order to complete cross-correlation and

extract radial velocities. The chosen wavelength range just covers the Hα line at 6562.8Å , and comfortably includes the Na doublet at 5890Å and 5896Å . Depending on calibration, both sets of strong lines should be detected and possible to use for radial velocity extraction, although the Hα may experience distortion during the curvature correction and may not be reliable. Unfortunately this wavelength range does not cover the Ca triplet at 8498Å , 8542Å and 8662Å , which are typically stronger in giants than main sequence stars, however overall this range satisfies the needs of the study. With sampling across the full period of each target, with no more than one observation per night, it is possible to obtain a radial velocity curve suitable for modelling.

Several targets that were observed by SALT were also been observed by 74″, LCO, and PIRATE, in some cases almost simultaneously. The combination of photometric and spectroscopic follow-up allows for more accurate measurement of eclipses, and the simultaneous spectroscopic observations provide an opportunity for calibration between instruments and telescopes.

9.2.1 Observations

This section details the SALT observations of targets identified as candidate NCRGEB in Chapter 7. Observations of these targets were made with SALT over 4 observing semesters between 2019–2020. Targets were selected based on their magnitude, giving a suitable S/N, and visibility during the SALT observing semesters. All targets have corresponding photometric observations, and some targets have spectroscopic observations from other telescopes. Details of observations made with SALT can be found in Table 9.1.

9.2.2 Data reduction

SALT observations are provided in raw and reduced formats, using the `PySALT` reduction package (Crawford et al., 2010). This reduction routine accounts for CCD bias, gain, and

Target	M_v	Date range	Exposure time (s)	N observations
1SWASPJ231800.38-031131.4	13.81	2020-05-19–2020-10-12	915	7
1SWASPJ204317.92-251850.0	14.03	2019-06-16–2019-10-25	1013	5
1SWASPJ194231.22-251605.5	14.73	2019-04-27–2019-10-13	940	12
1SWASPJ190114.91-380729.0	11.28	2020-05-08–2020-09-03	875	7
1SWASPJ132156.04-010742.8	14.63	2019-04-29–2019-07-04	1013	8
1SWASPJ103327.40-304931.6	15.58	2019-11-24–2020-01-10	1039	5
1SWASPJ093610.20-283847.2	12.50	2019-11-22–2020-01-02	905	5

Table 9.1 List of NCRGEB candidate targets observed using SALT. A minimum of 8 observations is preferred to extract a radial velocity curve.

crosstalk between the CCD amplifiers, however this automated reduction does not correct for flat-fielding and cosmic-ray cleaning. Science images require correction for these, followed by wavelength calibration and background subtraction and extraction of the spectra, hence all SALT observations were recalibrated using a combination of `PySALT` and `IRAF/PyRAF` (Tody, 1986).

Each observation is ideally accompanied by one or more flat-fields, however this is not always the case, and many of my observations were not provided with accompanying flat-fields. However, according to the SALT team, flat-fields are stable over several weeks. Since these observations often take place within a week of one another, a single flat-field can be used for multiple calibrations, should flat-fields not be taken or the flat-field be unsuitable for use.

The SALT data reduction is done through a combination of `PySALT` and `IRAF/PyRAF`, following the reduction process of `PySALT`[1] and then the processes based on Staab (2018) and Cooper (2020).

[1]https://github.com/saltastro/pysalt/wiki/Long-Slit-Reductions

The initial stages of reduction were completed using `PySALT`, detailed below.

1. Prepare the data using `saltprepare`. This checks for keywords in the FITS headers and can create a variance and bap pixel map, should it be needed.

2. Correct for gain using `saltgain`. This uses gain levels recorded in the FITS headers to correct for gain of the difference CCDs.

3. Correct for cross-talk using `saltxtalk`. This corrects for the cross-talk between amplifiers which occurs during readout.

4. Correct for CCD bias using `saltbias`. This uses the overscan regions only for bias correction.

5. Correcting for cosmic rays using `saltcrclean`. This corrects for cosmic rays, but is currently not included in the automated SALT reduction pipeline, so this command is explicitly needed to ensure cosmic ray correction.

6. Create master flat using `saltcombine`. If multiple flat-field images have been taken, they are median combined to create a master flat.

7. Apply illumination correction to master flat using `saltillum`.

8. Flat field the data using `saltflat`. This flat field corrects the observations using the illumination corrected master flat.

9. Make mosaic from single frames using `saltmosaic`. The images from the different FITS extensions are mosaicked into a single usable frame.

The next steps in `PySALT` would be to carry out wavelength calibrations, sky subtractions, aperture calibration, and spectra extraction. However, after the mosaic step, `PySALT` failed on the Open University's `ThinLinc` Linux system and could not be fixed, so the remainder of

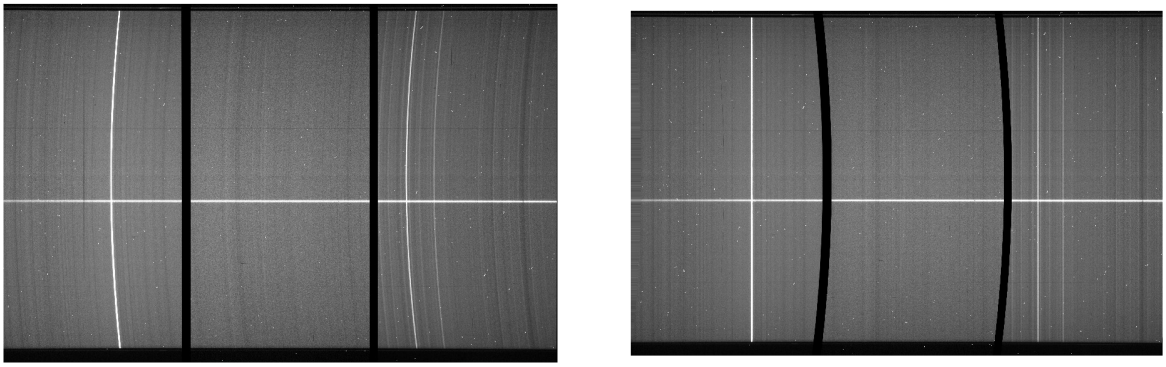

Fig. 9.2 Transformation of a science frame using arc lamp wavelength solution. The gaps across the CCD chip can be see at about a third and two thirds of the way across the x-axis. **Left:** before transformation, **right:** after transformation.

the data reduction and spectra extraction was done using `PyRAF/IRAF`. The following stages of reduction are detailed below.

1. Identify wavelengths in arc image using `identify`. This step identifies emission lines in the arc lamp spectrum using known strong lines using SALT Ar coordinate lists and finds the best fit for the arc images. This allows for wavelength calibration in future steps. Wavelength calibration is performed using the `twodspec.longslit IRAF` package.

2. Apply wavelength solution across the 2D spectrum using `reidentify`. This propagates the wavelength solution found using `identify` across the entire arc spectrum.

3. Create final 2D wavelength solution to apply to science image using `fitcoords`. This fits the best wavelength solution to the curved science image and relates the pixels to the wavelength.

4. Transform the science image using `transform`. Using the 2D wavelength solution, this transforms the science image and finds the dispersion. This outputs a science image with straight vertical sky lines, shown in Figure 9.2.

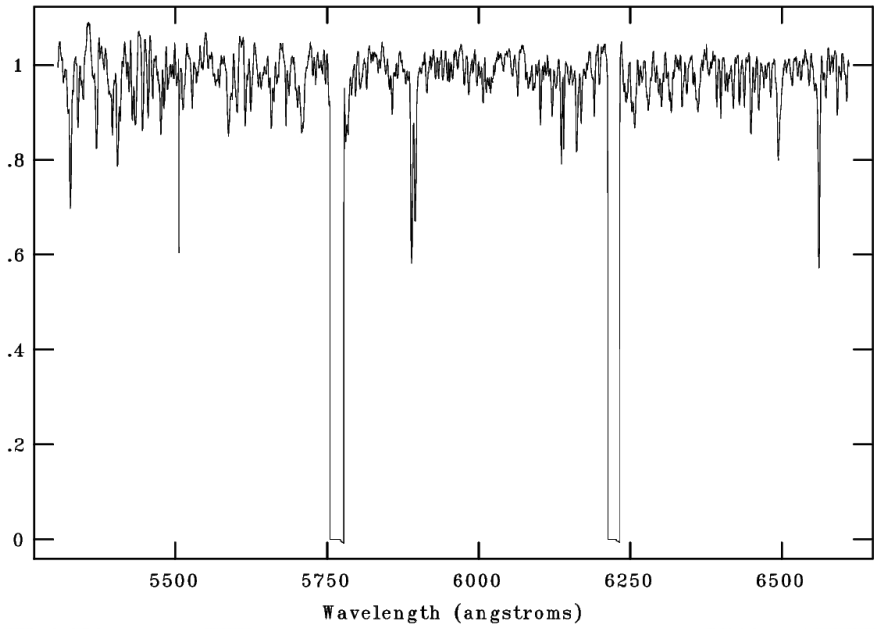

Fig. 9.3 The normalised, corrected SALT spectrum of 1SWASPJ190114. The gaps across the CCD chip can be see at about a third and two thirds of the way across the x-axis, and the Na doublet at ∼5890 Å and Hα at ∼6563 Å are visible.

5. Perform background subtraction using `background`. This step performs linear background fitting and removes the sky lines and residual sky background flux.

6. Extinction correct using `extinction`. This step performs extinction correction based on airmass using information from the FITS headers.

7. Extract 1D spectrum using `apall`. This step extracts the 1D spectrum using a suitable aperture, and calculates uncertainties using the photon noise and detector readout noise.

8. Calculate heliocentric correction using `rvcorrect`. This corrects for the motion of the Earth around the Sun which is important for accurately determining radial velocity.

9. Apply helicentric correction using `dopcor`.

10. Normalise the 1D spectrum using `continuum`. This step is not required for spectral fitting, but is required for radial velocity extraction. The output of this can be seen in Figure 9.3.

9.3 74″

The 1.9m or 74-inch (74″) Radcliffe Telescope, shown in Figure 9.4, is the oldest telescope at SAAO Sutherland facility, built between 1938–1948 due to delays caused by World War II, and transported to the Karoo in 1974 (Glass, 1989). From 1951–2004 it was the largest telescope in South Africa, surpassed only by SALT. The 74″ is on the same site as SALT and SuperWASP and has the same altitude of ∼1768m and excellent seeing conditions. The primary instrument for the 74″ is a Cassegrain spectrograph, SpUpNIC (Spectrograph Upgrade - Newly Improved Cassegrain) (Crause et al., 2016), which has a range of gratings, blocking filters, and CuAr and CuNe arc lamps.

To perform spectroscopic follow-up, SpUpNIC with the high resolution Grating 5 (G5) was used, which has 1200 lines/mm, providing a dispersion of 0.525 Å/pixel in the range 6400–7400 Å (blaze of 6800 Å). The FWHM of lines observed with G5 is ∼2 Å, and the dispersion is 0.525 Å/pixel. This spectral resolution corresponds to a velocity resolution of ∼85 km s^{-1}. With a sufficient number of lines, sub-pixel cross-correlation techniques can measure velocity differences of the order of one-tenth of this. This allows radial velocity curves with predicted amplitudes in the range 40–130 km s^{-1} to be successfully monitored. Using a 2.1″ slit in 1.2″ seeing, an angle of -4.1, Grating 5 gives a S/N∼40 per CCD pixel in 600 s, adequate for extracting highly accurate radial velocities. The Copper Neon (CuNe) arc lamp was used for calibration, and were taken before and after each observation. Dark frames were not required, and flat and bias frames were taken at the start and end of each night where possible. When this was not possible, arc frames appeared to be stable over the time span of a week so were suitable for use on another night.

Fig. 9.4 74″ telescope [Credit: Heidi B. Thiemann]

The NCRGEB candidate targets suitable for observations with 74″ have magnitudes of V = 10.6–15.6 and R = 9.9–14.9. Targets in this magnitude range typically require an exposure time of 100-200 s for 10th–12th mag, and 600–900 s for 13th–15th mag, dependent on observing conditions.

9.3.1 Observations

Observations of these targets were made with the 74″ telescope over 14 nights in August 2019. Targets were selected based on their magnitude, giving a suitable S/N, and visibility during the South African winter. All targets have corresponding photometric observations, and some targets have spectroscopic observations from multiple telescopes.

Ideally, observations with 74″ would have taken place with a one week on, one week off, one week on schedule, to provide significant period coverage for the longest period NCRGEB candidates. However the telescope time awarded was 2 weeks of continuous observing time, which still provided good coverage. 8 candidates were originally proposed for observing,

however a further 4 candidates were visible, and another 4 were discovered both after the accepted proposal and during the run itself, making the observing run more successful than originally planned.

This observing run was conducted in-person at Sutherland, where the weather and seeing was largely good. High humidity and ice forced an early dome closure on 3 nights, affecting 50% of observations on 26-08-2019 and 27-08-2019, and 25% of observations on 18-08-2019. I was too ill to observe on 24-08-2019. Unfortunately, on this night, the 74″ was used by another observer using a different instrumental set up. It is generally recommended that the same instrumental set up is kept and not changed during a run. However, there appears to have been no negative effects on the observations.

During the run, repairs had to be done to the dome (unrelated to my observing). This meant the dome could not be closed fully on 22-08-2019 and 23-08-2019 and as such dome flats could not be taken.

On 21-08-19, one week into the run, it was noticed that a few of the strongest arc lines were saturated with an arc exposure time of 10 seconds. On 22-08-19, the arc lamp exposure was reduced to 5 seconds to combat this. It was also noticed that the slit was marginally off centre which had the potential to cause issues with sky line subtraction. For full details of the observing run, see Tables 9.2 and 9.3.

9.3.2 Data reduction

The initial data reduction was done in `PyRAF/IRAF` following established long slit spectroscopy reduction routines (Tody, 1986). These standard routines perform bias corrections and flat fielding, and the remaining reduction and spectra extraction is done following the same routine as for SALT data. Spectra were also reduced using PAMELA (Marsh, 2014) (Pierre Maxted, private communications). These spectra were used to verify that the

Dates	Notes
14-08-2019	Good seeing, bright moon.
15-08-2019	Good seeing, bright moon, windy.
16-08-2019	Good seeing until 2am, bright moon, bad seeing and high humidity 2-6am.
17-08-2019	Unknown seeing due to observatory fault.
18-08-2019	High wind speed and high humidity forced early dome closure.
19-08-2019	Good seeing.
20-08-2019	Good seeing.
21-08-2019	Good seeing.
22-08-2019	Good seeing.
23-08-2019	Good seeing.
24-08-2019	No observations due to illness.
25-08-2019	High wind, light cloud.
26-08-2019	High humidity, ice, forced early dome closure.
27-08-2019	High humidity, ice, forced early dome closure.

Table 9.2 Condensed observing log for the 2 week run on 74″.

Target	M_v	Dates	Exp Time	N observations
1SWASPJ231800.38-031131.4	13.81	14-08-2019–26-08-19	900	11
1SWASPJ204317.92-251850.0	14.03	14-08-2019–26-08-19	1200	10
1SWASPJ194733.51-471201.4	13.18	15-08-2019–26-08-19	900	11
1SWASPJ194231.22-251605.5	14.73	15-08-2019–26-08-19	1200	10
1SWASPJ192628.96-233856.1	13.75	14-08-2019–27-08-19	1200	13
1SWASPJ192311.66-423244.5	13.03	14-08-2019–27-08-19	600	13
1SWASPJ191910.42-414050.9	12.86	14-08-2019–27-08-19	600	13
1SWASPJ190114.91-380729.0	11.28	19-08-2019–27-08-19	300	8
1SWASPJ165656.26-040414.3	12.40	15-08-2019–27-08-19	600	12
1SWASPJ154607.55-191711.4	11.53	15-08-2019–27-08-19	300	12
1SWASPJ135703.85-474817.9	13.82	16-08-2019–27-08-19	1200	10
1SWASPJ035259.67+091717.1	12.52	17-08-2019–22-08-19	600	3
1SWASPJ003414.72-291038.4	15.23	19-08-2019–25-08-19	1200	6
1SWASPJ001545.50-622237.8	11.28	19-08-2019–25-08-19	300	5
1SWASPJ000927.89+014542.1	14.15	14-08-2019–25-08-19	1200	7
1SWASPJ000018.09+091923.9	10.91	15-08-2019–25-08-19	200	9

Table 9.3 List of NCRGEB candidate targets observed using 74″. A minimum of 8 observations is preferred to extract a radial velocity curve.

`PyRAF/IRAF` extracted spectra gave similar outputs, and spectral synthesis provided the same spectral type.

There were two potential issues with observations prior to 22-08-2019: unfortunately the original positioning of the slit was slightly off-centred and slight saturation of the arc line had occurred, as well as an unauthorised instrument change on 24-08-2019.

An off-centre slit can cause issues with sky line background subtraction. This issue was investigated during data reduction using `PyRAF/IRAF`, and it was found that sky lines were not fully subtracted from the edges of the science frames. To combat this issue, careful trimming was performed and each science frame was examined to ensure that there was no increase in noise around sky line subtracted regions of the spectra.

Arc line saturation can make it harder to accurately determine emission lines in the arc lamp spectrum, creating a less accurate 2D wavelength solution to apply to science image. On average, only 2 lines were saturated in the saturated arc lamp images, and these lines were therefore not used to create the 2D wavelength solution. As a second check, the science images with corresponding saturated arc lamp images were also reduced using non-saturated arc lamp images following identical reduction routines. The 2D wavelength solution was found to be the same and the final extracted spectra were also the same.

The instrumental set up was changed by another astronomer on 24-08-2019. The original instrumental set up was restored prior to observations continuing on 25-08-2019 and appears to have made no impact on observations taken before and after.

9.4 Liverpool Telescope

The Liverpool Telescope (LT), shown in Figure 9.5, is a 2.0m robotic telescope owned by the Liverpool John Moores University and based at the Observatorio del Roque de Los Muchachos on La Palma, with an altitude of 2,363m (Steele et al., 2004).

For NCREGB candidate targets suitable for observations with the LT, FRODOSpec (Fibre-fed RObotic Dual-beam Optical Spectrograph) (Morales-Rueda et al., 2004) was used, an integral-field input spectrograph (IFS) with dual beams. The beams are split and there are two resolutions, low and high, available for each the blue arm and the red arm. For these targets, FRODOSpec was used with the IFU fibre bundle with the High Resolution (VPH) red arm, which has a wavelength range of 5900–8000 Å . This has a resolution of 5300, a dispersion of 0.8 Å /pixel, and a FWHM of 2Å which limits the resolution. At the middle of the range ($\sim$7000 Å), the spectral resolution corresponds to a velocity resolution of $\sim$85 km s^{-1}.

With a sufficient number of lines, sub-pixel cross-correlation techniques can measure velocity differences of the order of one-tenth of this, achieving a 8.5 km s^{-1} velocity resolution. This allows for identifying radial velocity curves with predicted amplitudes in the range 40-110 km s^{-1}. The NCRGEB targets have magnitudes of V = 10.6–12.7. A SNR = 100 and a FWHM of 2 Å is required, but 'dark' sky was not required, since these targets could be observed in 'astronomical twilight'. FRODOspec contains two calibration lamps, xenon and tungsten. The xenon arc lamp calibrations was used, and an arc exposure is obtained after every science image. Unlike SALT, no arc frames were missing from any observations.

9.4.1 Observations

Observations of these targets were made with LT in 2019. Targets were selected based on their magnitude, giving a suitable S/N, and visibility during the LT observing semesters. All targets have corresponding photometric observations, and some targets have spectroscopic observations from multiple telescopes. 15 observations of each target were requested in the observing proposal, with a maximum of 1 observation per night, although objects with a

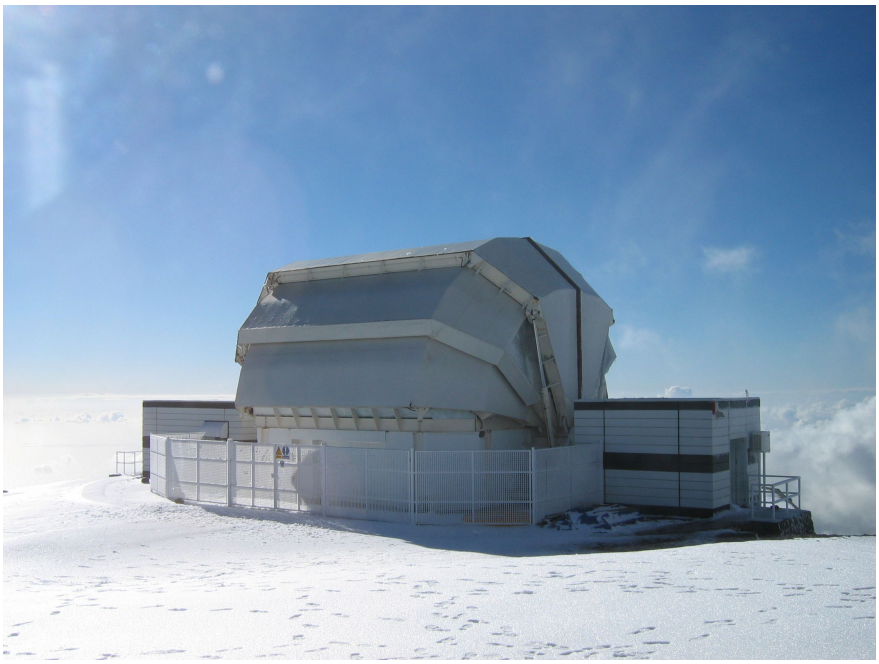

Fig. 9.5 The Liverpool Telescope in the snow [Credit: J. Marchant]

priority Z (filler time) received fewer observations. Typically, observations were taken over a 2 week period, and full details of observations can be found in Table 9.4.

9.4.2 Data reduction

The FRODOspec data are reduced fully by the automated `L1` and `L2` reduction pipelines (Barnsley et al., 2012). The `L1` pipeline performs CCD processing which includes bias subtraction, overscan trimming, and flat fielding. The `L2` pipeline performs the IFS reductions, including flux extraction, arc fitting, throughput correction, wavelength transformation, and sky subtraction.

Similar to the `PySALT` pipeline, the `L2` pipeline does not apply a flux calibration, telluric correction, or cosmic-ray removal, since automated cosmic ray removal can be unreliable (Barnsley et al., 2012). Cosmic rays are visible in the final stack, and provided that cosmic rays do not lie near strong lines required for radial velocity analysis, manual removal of cosmic rays through visual inspection of each fibre suffices. For observations where cosmic

Target	M_v	Date range	Exposure time	N observations
1SWASPJ183357.87+423725.2	12.38	2019-07-01–2019-07-19	600	15
1SWASPJ165656.26-040414.3	12.40	2019-07-01–2019-07-21	600	15
1SWASPJ165241.24+203224.7	14.17	2020-03-05–2020-04-02	1200	5
1SWASPJ154828.29+201442.8	10.57	2019-07-01–2019-07-21	100	16
1SWASPJ035259.67+091717.1	12.52	2019-07-21–2019-08-18	600	15
1SWASPJ003544.75+495450.0	12.70	2019-07-02–2019-07-27	600	15
1SWASPJ002952.96+475034.3	10.16	2020-07-11–2019-08-08	100	15
1SWASPJ002349.66+483114.5	12.60	2020-07-07–2019-07-30	600	15
1SWASPJ001521.76+472055.2	11.32	2019-07-02–2019-07-22	300	15

Table 9.4 List of NCRGEB candidate targets observed using LT. A minimum of 8 observations is preferred to extract a radial velocity curve.

rays lie close to strong lines, a combination of the spectral version of the `L.A.Cosmic` algorithm (van Dokkum, 2001) and manual visual removal were used to remove cosmic rays. Following the automated `L1` and `L2` reduction, and cosmic-ray removal, the final stages of reduction and spectra extraction are similar to routines for SALT and the 74″, from `extinction` to `continuum`.

9.5 Las Cumbres Observatory

The Las Cumbres Observatory (LCO) is a global network of robotic, queue-scheduled telescopes made up of two 2-metre telescopes, 16 1-metre telescopes (of which 2 will come online in 2021), and 11 0.4-metre telescopes. LCO has a Network of Robotic Echelle Spectrographs (NRES) (Siverd et al., 2018), four identical high-resolution, precise, optical, echelle spectrographs, fibre-fed by a ThAr lamp for calibration and two 1-metre telescopes.

Target	M_v	Dates	Exp Time	N observations
1SWASPJ022953.03+041420.9	13.01	2019-10-26–2019-10-30	900	4
1SWASPJ002952.96+475034.3	10.16	2019-10-17–2019-10-18	200	2
1SWASPJ002349.66+483114.5	12.60	2019-10-17	600	1

Table 9.5 List of NCRGEB candidate targets observed using LCO. A minimum of 8 observations is preferred to extract a radial velocity curve; no target achieved this.

Unlike photometric LCO follow-up, this spectroscopic follow-up has not involved schools as part of an educational programme, due to the complexity of working with spectroscopy, and the experimental nature of NRES.

The resolution of the spectrograph is much greater than the needs of these targets, with a resolution of R$\sim$53,000 at the centre of the wavelength range of 3800–8600 Å . The current precision is approximately 50 ms^{-1} to 100 ms^{-1}, with the long term accuracy goal being 3 ms^{-1} for a star brighter than V$\sim$11 to allow for spectroscopic follow-up of transiting exoplanets.

9.5.1 Observations and data reduction

Queue-scheduled observations of these targets were made with LCO in October 2019. Targets were selected based on their magnitude, giving a suitable S/N, and visibility from LCO. Although a total of 26 observations were requested across 3 targets, detailed in Table 9.5, only 7 were successful, due to reasons similar to that for the photometric follow-up with LCO.

All LCO NRES observations are reduced by the automated NRES reduction pipeline, detailed on the LCO website[2]. The reduced data are provided as a PDF of diagnostic plots and corresponding FITS files. Briefly, the reduction performed is:

1. Bias and dark subtraction.

[2]https://lco.global/documentation/data/nres-pipeline/

2. Fitting a model for the background light.

3. Iterative extraction and cross-dispersion centroid computation.

4. Computing an optimally-extracted spectrum and a noise model.

5. Examining residuals to identify radiation events. If any are found, the fit is recomputed.

6. Exporting the spectrum.

However, as noted above, no single target received enough good quality observations in order to extract a radial velocity curve, hence further reduction was not necessary. The observations are detailed here for completeness only.

9.6 WHT

LIRIS (Long-slit Intermediate Resolution Infrared Spectrograph) (Acosta-Pulido et al., 2002) is a near-IR imager and spectrograph on the William Herschel Telescope (WHT), shown in Figure 9.6, located at the Roque de los Muchachos Observatory on La Palma. The WHT has an altitude of 2,344m. LIRIS has a field of view of $4.27' \times 4.27'$ and a pixel scale of $0.25''$/pixel.

To obtain a spectrum of the original NCRGEB target, 1SWASPJ001521, a service night on LIRIS was used. LIRIS was used in long slit spectroscopy mode, using the hr_k grism providing a resolution of 2500 in the range 2.05–2.42 micron. This spectral resolution corresponds to a velocity resolution of 120 km s^{-1}. If a sufficiently large number of lines is used, cross-correlation techniques can measure velocity differences of the order one-tenth of this (i.e. 12 km s^{-1}). The target has magnitudes V=11.3 and K=10.7. The exposure time calculator showed that for a star of this magnitude with a blackbody spectrum at T=4000 K, assuming $0.8''$ seeing, an airmass of 1, and a $0.75''$ slit, then a pair of 120 s exposures (240 s exposure time total) will give a signal-to-noise ratio of 120–180 across the K band spectrum.

Fig. 9.6 The WHT telescope [Credit: IAC]

A single spectrum of this target was obtained during a scheduled observing run for other targets. That spectrum shows Paschen lines and clear evidence for being a double lined (hence binary) object, so supporting the preliminary identification that at least one component was a red giant. To gain further spectra, the same set up was used, aiming to gain up to 15 visits spread across the year, in order to aim to capture the spectrum at a range of orbital phases around the 40 d orbit and so generate a complete radial velocity curve using service time. Unfortunately, only 2 further observations were taken of this target, of which 1 was unusable due to an observing fault.

9.6.1 Observations and data reduction

Queue-scheduled observations of the original NCRGEB candidate were made with WHT, detailed in Table 9.6. Only 3 observations were made using service time, of which 1 was unusable due to negative pixel values. Since only 1 night of useful data was taken by the WHT, a radial velocity curve could not be extracted from LIRIS spectra, and hence

Target	M_v	Dates	Exp Time	N observations
1SWASPJ001521.76+472055.2	11.32	2018-10-21–2019-07-10	600	3

Table 9.6 NCRGEB candidate target observed using WHT. A minimum of 8 observations is preferred to extract a radial velocity curve.

further reduction was not necessary. The observations and spectrum are detailed here for completeness only.

The LIRIS data are reduced using a combination of the standard `IRAF` reduction routines and the `lirisdr IRAF` package described on the LIRIS data reduction website[3]. However, as has already been noted, only one night of data was available for reduction.

The initial data reduction routine is unlike the routines require by SALT, 74″, LT, and LCO, due to the set-up of the instrument to acquire 2-point nodding (dithered) spectra which requires the `lirisdir` package. The dithered spectra are acquired to ensure that LIRIS can create a proper sky background model. To correctly reduce LIRIS data, sky subtraction is done before wavelength calibration and curvature correction, but after flat-field correction. The extraction of the spectra uses the standard `apall` package, without the `background` parameter, since the spectra have already been subtracted. The final stages of data reduction and spectra extraction are similar to routines for SALT and the 74″, from `extinction` to `continuum`.

9.7 Spectral typing and synthesis

A process called spectral typing, as the name suggests, allows the spectral type of each component in the binary to be identified based on observational spectra. This in turn allows us to more accurately determine the metallicity and stellar temperature and provides a sanity check on the radial velocity identified through spectral line cross-correlation. Spectral

[3]http://research.iac.es/galeria/jap//lirisdr/LIRIS_DATA_REDUCTION.html

synthesis accomplishes a similar outcome through creating a synthetic spectrum based on a set of best guess input parameters and iterating through a series of parameters to find the closest match. Spectral synthesis can identify metal abundance (useful for estimating the age of the star), temperature, $\log(g)$, and abundances. Spectral synthesis does not provide a spectral type, but the extracted parameters can be used to estimate a spectral type. Used in combination, they are powerful tools for fully characterising the stellar components. Having found the spectral type of each stellar component, or system as a whole, parallax data from Gaia-DR2 can be used to identify the luminosity class of each target, taking into account the distance and absolute magnitude. To find the spectral type of each target, the method is as follows:

1. Spectra are fitted using least-square fitting to template spectra from SDSS.
2. Spectra are fitted to corresponding synthetic spectra using least-square fitting.
3. Gaia data are used to verify the luminosity class.

9.7.1 Spectral typing

The spectral type of each target was found by matching spectra from SALT, LT, 74″, and LCO to template spectra. This was done using a python-based tool called `PyHammer` V2 (Kesseli et al. 2017; Roulston et al. 2020), an automated spectral typing tool which uses the `IDL` code "Hammer" (Covey et al., 2007) in a python wrapper. `PyHammer` matches spectral lines in the observed spectra and least-square fits the lines to a catalogue of template spectra for O–L type stars, determines the stellar metallicity, and radial velocity shifts. `PyHammer` provides a user interface in which the user can visually assess the automatically identified spectral type.

`PyHammer` can identify SB1 and SB2 binaries to a high degree of accuracy, with 95% of SB2 correctly classified in `PyHammer` V2 (Roulston et al., 2020). However, whilst the

original paper highlights that both main sequence (dwarf) stars and giant stars can be spectral typed using `PyHammer`, no giant templates are provided in the programme itself. `PyHammer` uses spectral standards from the Sloan Digital Sky Survey's (SDSS) Baryon Oscillation Spectroscopic Survey (BOSS) for dwarf templates, so to rectify the lack of giant templates, a series of giant template spectra were sourced from SDSS BOSS (Kesseli et al., 2017), the same sample from which the dwarf spectral templates were sources. This allowed for spectral typing against giant template spectra.

Most observational spectra from this follow-up cover a wavelength range of a couple of thousand Å , however the BOSS template spectra used in `PyHammer` covers a wavelength range of 3,650–10,200 Å with a R$\sim$2,000. Despite the observational spectra covering a small section of the template spectra, the fitted results closely match the observational spectra.

Each un-normalised observational spectrum was run through `PyHammer` to automatically identify the spectral type, metallicity, and radial velocity shift. The spectral type was verified by eye and adjusted to improve the fit if necessary. An example of the fit spectra is shown in Figure 9.7 with the observed spectrum in red and the template spectrum in black. The result of spectral typing each target with `PyHammer` is shown in Table 9.7.

9.7.2 Spectral synthesis

Spectral synthesis was performed on each target using the programme `iSpec` (Blanco-Cuaresma et al., 2014), a python-based tool for analysing and synthesising stellar spectra. `iSpec` integrates the MARCS (Gustafsson et al., 2008) and ATLAS (Kurucz, 2014) model stellar atmospheres with radiative transfer codes, including SPECTRUM (Gray and Corbally, 1994), Turbospectrum (Plez, 2012), SME (Valenti and Piskunov, 2012), MOOG (Sneden et al., 2012), and Synthe/WIDTH9 (Kurucz, 2005). The SPECTRUM code and MARCS model atmosphere are the default in `iSpec` and these perform spectral synthesis faster than other available codes and models.

Fig. 9.7 Using `PyHammer` to spectral type the target 1SWASP231800. This shows only a short section of the spectrum.

The aim of using `iSpec` is to identify the spectral type and compare it to that found with `PyHammer`, as well as other parameters including metallicity, temperature, surface gravity, rotational velocity shift, limb darkening, and more. Characterising these parameters is important for modelling the stellar components and stellar evolution, and can be used the radial velocities identified in the cross-correlation method. Like `PyHammer`, `iSpec` can be used to analyse SB1 and SB2, however the capabilities of SB2 analysis are limited by the luminosity differences between each component in the binary. NCRGEB targets typically have similar luminosities and spectral type, and often appear to be SB1 throughout most of the orbit, making spectral disentanglement for spectral typing and synthesis difficult or impossible. To combat this issue for NCRGEB which appear to be SB1, either only the primary star was synthesised, or where possible, synthesis was done at the most extreme radial velocity shifts where the visual separation was at its maximum.

Detailed instructions for using `iSpec` can be found on the website[4]. `iSpec` takes unnormalised spectra as the input. First, spectra are typically corrected for the radial velocity of the target and barycentric velocity, accounting for the motion of the Earth in the direction of the target. These spectra have already been corrected for barycentric velocity, so a correction of 0 km s^{-1} was made for each spectrum. Should this not have been corrected for, it can be calculated by `iSpec` by simply inputting the position and velocity at the time of the observation. `iSpec` can either calculate the radial velocity through a cross-correlation of telluric lines within the spectrum and fitting a Gaussian, or it can take a value determined by cross-correlation of strong lines. Having done these initial corrections, a 3 spline fit is used to normalise the spectrum, shown in Figure 9.8.

The next step is to locate spectral lines using an input line list, as shown in Figure 9.9. The GES (Gaia ESO Survey (Gaia-ESO Survey Team, 2012)) line list for 4200–9000 Å was used for the targets, with the aim of identifying strong spectral lines including Na II, Hα, K, Fe 1 and Fe2. Lines are automatically located by `iSpec`, with each line being fitted at the

[4]https://www.blancocuaresma.com/s/iSpec/manual/introduction

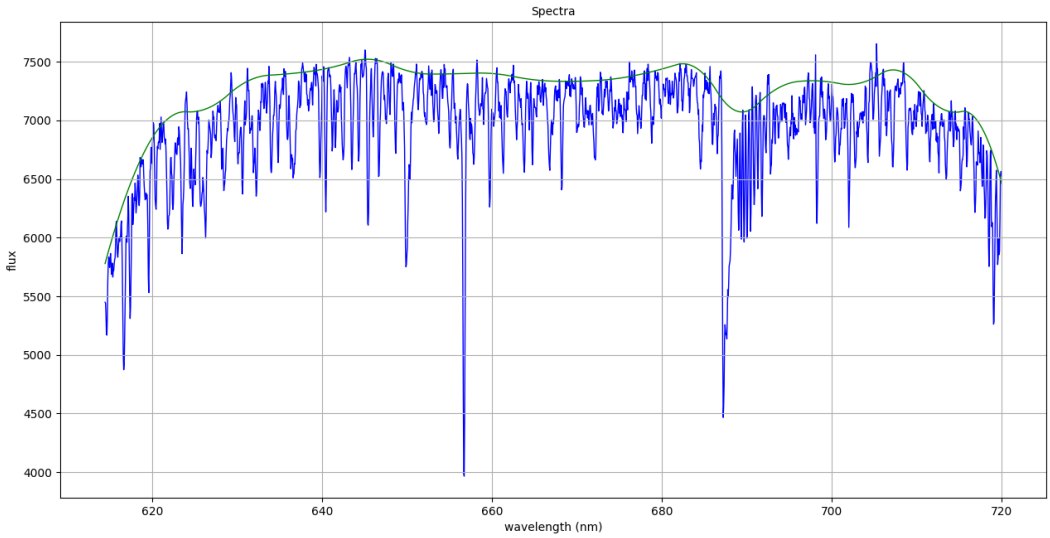

Fig. 9.8 Using `iSpec` to normalise the spectrum of J190114. The blue line shows the input spectra for J190114 and the green line shows the fitted spline.

base of the continuum level with a Gaussian, however to correctly identify all the strong lines, the fit must be iteratively and interactively improved. Should lines be incorrectly identified, this can cause a misalignment of the synthetic spectrum.

After line fitting, spectral synthesis can take place. To do this correctly, a set of initial best guess stellar parameters must be input, some of which are provided by the spectral typing process of `PyHammer`. Input parameters include effective temperature, surface gravity, metallicity, microturbulent velocity, macroturbulent velocity, rotational velocity, and the linear limb darkening coefficient. Having input these parameters, synthesis can be performed.

`iSpec` uses the best guess input parameters to create a synthetic spectrum and calculates a χ^2 value based on the input spectrum and the new synthetic spectrum, shown in Figure 9.10 and 9.11. `iSpec` then follows a process of χ^2 minimisation to iteratively improve the fit, stopping once there is no significant change in χ^2 between one iteration and the next, or the programme reaches the maximum number of iterations determined by the user. It is possible to fix input parameters to identify which parameter effects the χ^2 value the most.

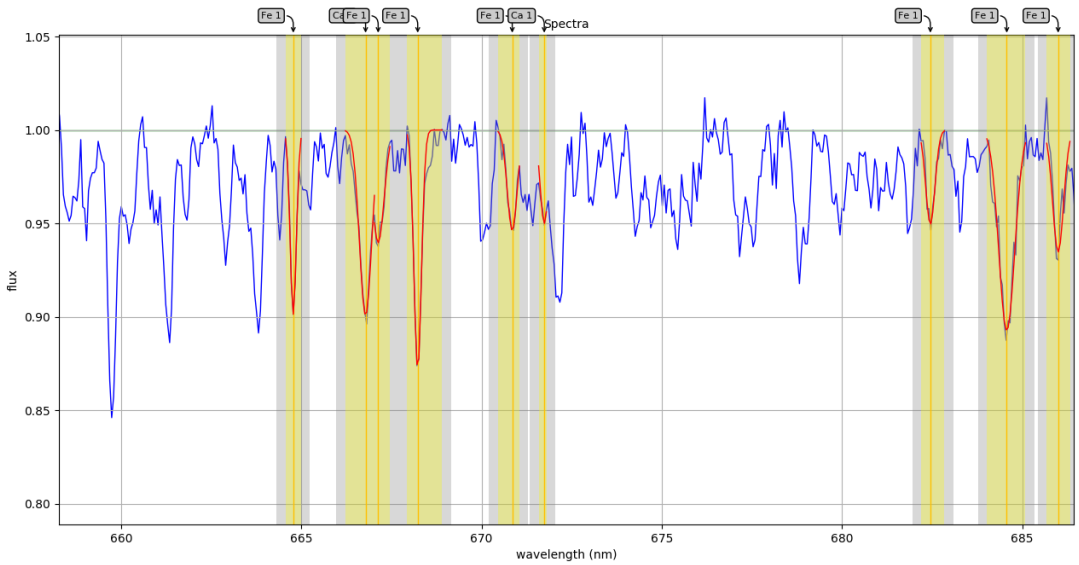

Fig. 9.9 Using `iSpec` to fit line segments to the spectrum of J190114. In this example, Fe and Ca lines have been identified. The blue line shows the input spectrum for J190114 and the red line shows the spectral lines identified. The yellow regions show the line masks for each spectral line.

The temperature was found to have the most significant effect on the χ^2 value, so I minimised χ^2 adjusting the temperature only, then adjusted for the remaining parameters.

For the NCRGEB spectra it takes fewer than 15 iterations on average. `iSpec` outputs the best fit spectrum as well as the stellar parameters from the best synthetic spectrum. The spectral type is not specified, but using the output parameters, a stellar spectral type can be identified. The output parameters are used for modelling the stellar components in `PHOEBE` and the metal abundance [M/H] can be used in stellar evolution modelling to estimate the age of the stellar components.

9.7.3 Results

The result of spectral typing each target with `iSpec` and `PyHammer` is shown in Table 9.7. Luminosity class is estimated from the Gaia-DR2 luminosity, absolute magnitude, and

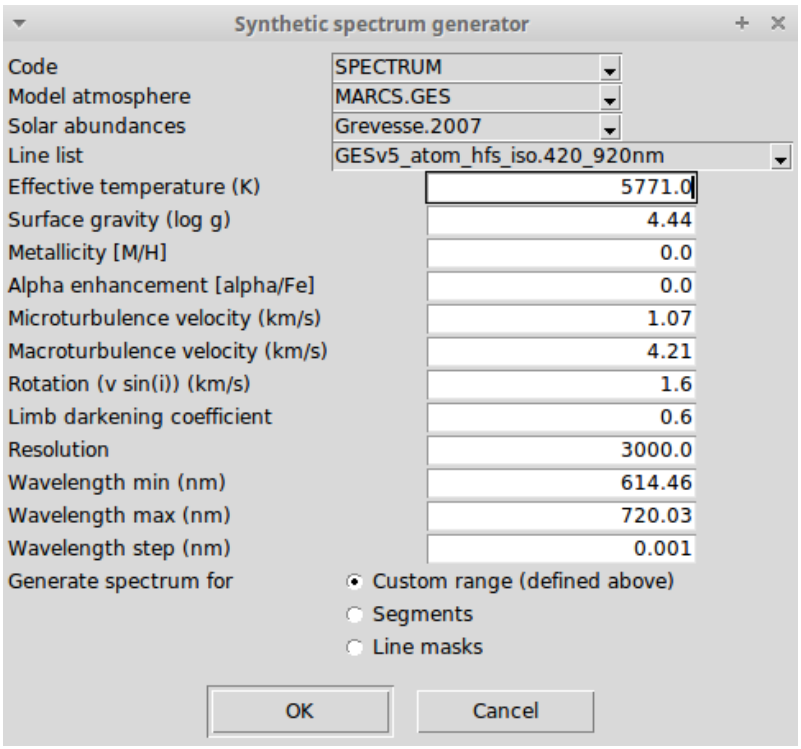

Fig. 9.10 Using `iSpec` to create a synthetic spectrum using parameters identified through a combination of spectral typing from `PyHammer` and best guess input parameters from `iSpec` for J190114.

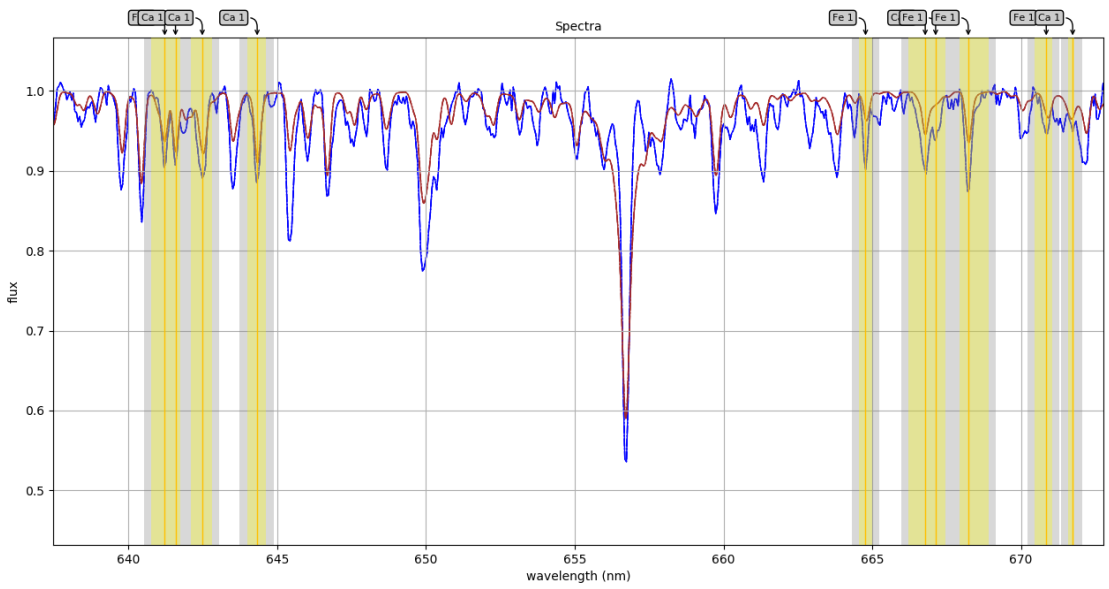

Fig. 9.11 The initial synthetic spectrum created by `iSpec` using the best guess input parameters. Once an initial synthetic spectrum has been created, the fit can be iteratively improved. The blue line shows the input spectrum for J190114 and the red line shows the initial synthesised spectrum.

estimated spectral type, using the method described in Cooper (2019). Absolute magnitude, M_v, takes the equation:

$$M_v = m_v + 5(\log_{10}(d_{pc}) - 1), \tag{9.1}$$

where m_v is the apparent V band magnitude and d_{pc} is the distance each star in parsecs. The distance is determined by Bayesian inference, taken from Luri et al. (2018), since the Gaia-DR2 parallaxes are often unreliable. The Gaia-DR2 luminosity class of each target is used here to distinguish dwarfs from giants. This finds that 25 of the 27 candidates are subgiant or giant stars (IV, III), with J003414 and J135703 appearing to be dwarfs (V).

Spectral typing and spectral synthesis found that the majority of the systems are comprised of late-type (G- and K-) giants with temperatures of 3500–5500 K. `PyHammer` provides a general spectral type, through which the temperature can be derived, whilst `iSpec` provides an exact temperature. `iSpec` and `PyHammer` generally find agreement on temperature, metallicity, and spectral type, however, there are some candidates which differ in temperature significantly. One such example is J190114, which has an `iSpec` temperature of ∼4,000 K and a `PyHammer` temperature of ∼5,500 K. Interestingly, the Gaia-DR2 temperature of ∼4,500 falls between the two. Additionally, the temperatures found through `iSpec` and `PyHammer` are lower than the Gaia-DR2 temperatures, although in some cases, for example J191910 and J093610, temperature differs by ∼1,000 K between `iSpec`/`PyHammer` and Gaia-DR2.

The reasons for the temperature difference are unknown, and may be down to manual fitting of spectral lines in `iSpec` compared to automated fitting with `PyHammer`. It is also possible that the different temperatures correspond to the influence of the two components in the binary being detected by each programme. Gaia-DR2 temperatures may differ from `iSpec` and `PyHammer` temperatures due to the way they are derived. Gaia-DR2 temperatures are derived from three broad photometric bands, and Andrae et al. (2018) estimate an accuracy

of $\sim$324 K over the temperature range of 3,000–10,000 K, although the disparity is greater in this sample for many candidates. Additionally, single-line binaries are treated as single stars in Gaia-DR2 and variable stars have not been classified in detail, hence parameters such as temperature, radial velocity, luminosity, and radius may not always be provided or accurate.

Therefore, the temperatures in Table 9.7 should be taken as a sensible range and a good starting point for modelling the stellar components using multi-colour photometry in `PHOEBE`, discussed in Chapter 10.

9.8 Radial velocity curves

Another primary aim of spectroscopic follow-up of NCRGEB is to observe strong absorption lines in the spectra which can ultimately be used to extract radial velocities of the binary components in order to model the system itself. In the spectrum of a red giant binary, depending on the wavelength range, one would expect to use the Na doublet, Hα, or Ca triplet, to identify spectral line splitting (which would confirm whether or not there are two binary components in the spectrum), or use these strong lines to carry out cross-correlation to characterise the radial velocity of each binary component. Not only does radial velocity extraction allow the motion and mass of the binary components to be characterised, as well as the angle of inclination and the Roche potentials, which will be explored in Chapter 10, but it also allows us to differentiate between true binary systems and impostor systems such as Cepheid variables.

As previously covered, the photometric light curves of eclipsing binaries show two maxima and two minima per cycle, the radial velocity curves of each component shows a single maximum and a single minimum per orbital period (Figure 9.12). This can be used to differentiate binaries from pulsating stars, whose photometric light curves and radial velocity curves will each show single a single maximum and a single minimum per cycle (Figure 9.13).

WASP ID	PyHammer SpT	PyHammer Temp (K)	iSpec Temp (K)	Gaia-DR2 Temp (K)	Gaia-DR2 Luminosity Class
1SWASPJ231800.38-031131.4	K5	3980	4618	4801	III
1SWASPJ204317.92-251850.0	K4	4080	4054	4916	III
1SWASPJ194733.51-471201.4	K4	4080	4186	5274	III
1SWASPJ194231.22-251605.5	G1	5200	5145	4840	III
1SWASPJ192628.96-233856.1	K4	4080	5087	5162	III
1SWASPJ192311.66-423244.5	K0	4810	4856	5348	III
1SWASPJ191910.42-414050.9	K4	4080	5089	5215	III
1SWASPJ190114.91-380729.0	K5	3980	5521	4569	III
1SWASPJ183357.87+423725.2	G8	4960	5529	5312	III
1SWASPJ165656.26-040414.3	G8	4960	4953	4918	III
1SWASPJ165241.24+203224.7	K0	4810	5000	5149	III
1SWASPJ154828.29+201442.8	G8	4960	4687	4870	III
1SWASPJ154607.55-191711.4	K4	4080	4394	4432	IV
1SWASPJ135703.85-474817.9	G8	4960	5369	5439	V
1SWASPJ132156.04-010742.8	K5	3980	3230	4629	III
1SWASPJ103327.40-304931.6	K3	4320	4335	4931	III
1SWASPJ093610.20-283847.2	K3	4320	3904	5356	III
1SWASPJ035259.67+091717.1	K5	3980	3572	4535	III
1SWASPJ022953.03+041420.9	K0	4810	4896	4975	IV
1SWASPJ003544.75+495450.0	G8	4960	4867	4993	III
1SWASPJ003414.72-291038.4	G8	4960	5673	5760	V
1SWASPJ002952.96+475034.3	K0	4810	4702	4523	III
1SWASPJ002349.66+483114.5	K3	4320	4354	4368	III
1SWASPJ001545.50-622237.8	K5	3980	4128	4560	III
1SWASPJ001521.76+472055.2	K0	4810	5918	6750	III
1SWASPJ000927.89+014542.1	K5	3980	4806	4850	IV
1SWASPJ000018.09+091923.9	K4	4080	4153	4684	III

Table 9.7 The temperatures and spectral types of NCRGEB candidates from spectral synthesis, spectral typing, and luminosity classes from Gaia-DR2 (where V = dwarf, IV = subgiant, II = giant).

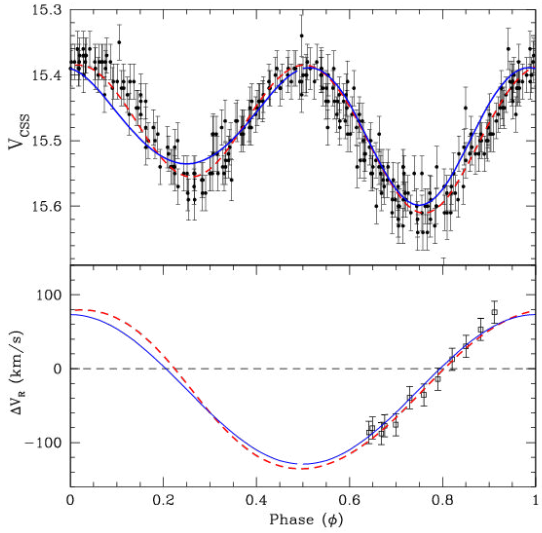

Fig. 9.12 The radial velocity curve and photometric light curve of the ultra-short period binary, CSS J001242.4+130809 (Drake et al., 2014).

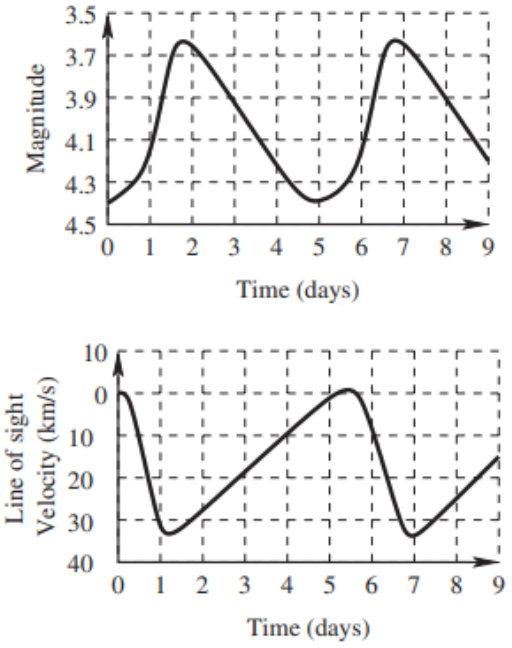

Fig. 9.13 The magnitude and radial velocity of the prototype Cepheid, δ Cephei (Percy, 2007).

Another method of differentiation comes from the amplitude of the radial velocity curve. A typical Cepheid variable will experience a radius change of 10–20% (e.g. Madore and Freedman 1985; Rodgers 1957). This corresponds to a maximum radial velocity amplitude of $\sim$60 km s^{-1}. Many of the NCRGEB display a radial velocity amplitude of up to $\sim$200km s^{-1}, which would require a Cepheid to experience a change in radius of $\sim$90%, a physically unrealistic scenario.

9.8.1 Cross-correlation

To calculate the radial velocities of each target, the `IRAF` cross-correlation package `fxcor` was used. `fxcor` is short for Fourier cross-correlation, and is a commonly used package which is based on the method developed by Tonry and Davis (1979). This method correlates a series of "object" (observed) spectra of unknown redshift (or velocity) and velocity dispersion, with a "template" (either observed at zero point phase or synthesised) spectrum of zero redshift and known velocity dispersion (usually zero for stellar objects). `fxcor` can use either strong lines within a spectrum, or the entire spectrum, for cross-correlation and returns a value for the redshift (or radial velocity in km s^{-1}) of the object spectrum. A comprehensive description of the method can be found in (Alpaslan, 2009).

The aim of matching an object to a template spectrum is to find the best cross-correlation fit, and can be quantified in two ways: the height of the fit on the y-axis shown in Figure 9.14, and the Tonry and Davis (1979) (TD) R-value. According to TD, the fit is "excellent" if the peak is above 0.8, and "good" if the peak is above 0.5. Alternatively, the R-value is defined as the ratio between the height of the real peak and the rest of the cross-correlation function (CCF), where $R = h/\sqrt{2}\sigma_a$, where h corresponds to the height of the true peak and $\sqrt{2}\sigma_a$ corresponds to the average peak in the rest of the CCF. A fit can be adjusted and improved by sampling only sections of the CCF peak, or only certain strong lines in the spectrum. Both methods are used to assess whether the cross-correlation performed is "good". The `fxcor`

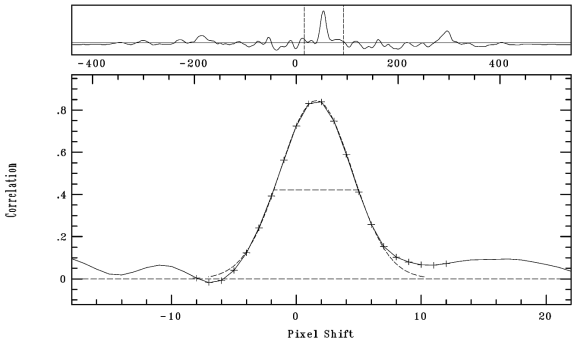

Fig. 9.14 Performing cross-correlation on J231800 using the `IRAF fxcor` package. This cross-correlation has a cross-correlation function of 0.82, implying an excellent fit. The observed spectra is shifted by ∼2 pixels, corresponding to a radial velocity of ∼40 km s^{-1}.

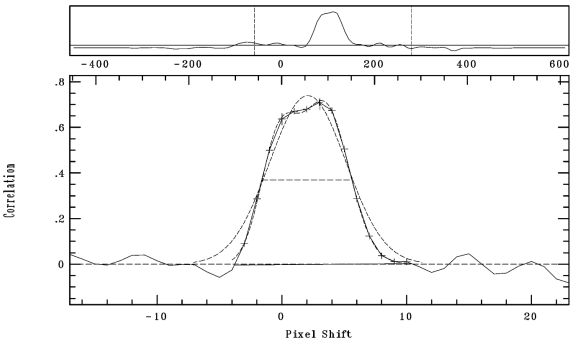

Fig. 9.15 Performing cross-correlation on J183357 using the `IRAF fxcor` package. This cross-correlation shows a double peaked cross-correlation with cross-correlation functions of ∼0.72 and ∼0.75, implying a good fit. Two peaks have been fitted, each with a different radial velocity shift.

process performs optimally if the object and template spectra have the same resolution and wavelength range, so where necessary, the higher resolution template spectrum was rebinned to match the resolution of the observed (object) spectrum, and trimmed the template spectrum to a suitable wavelength range.

For a system in which the secondary is behind the primary from the point of view of an observer, only one spectral line will be visible, giving a single CCF peak. When the primary and secondary are side-by-side, from the point of view of an observer, strong lines appear to be split. This allows two CCFs to be fitted, finding radial velocities for both components of the binary.

To calculate the radial velocities of the NCRGEB, the 1D reduced spectra were cross-correlated with a binned, trimmed template synthesis spectra created using the MILES library of spectral templates (Falcón-Barroso et al. 2011; Sánchez-Blázquez et al. 2006) and the PHOENIX library of stellar atmospheres and synthetic spectra (Husser et al., 2013). As a secondary measure, the observed spectra are also cross-correlated with the "best" (lowest noise) spectrum of each observing run for that target. These methods provide the same radial velocity curve but with a different zero-point.

Cross-correlation techniques are very effective for spectra with a high density of lines, however for NCRGEB, the spectra are fairly continuum dominated and strong lines are relatively sparse. Therefore, it is more effective to perform cross-correlation on strong spectral lines towards to centre of the spectrum. Cross-correlation is more accurate on lines towards the centre compared to those at the edge of the spectrum, since the edge of the spectrum receives significantly more distortion correction. Using these strong lines in the spectra including Hα and the Na doublet, radial velocities were calculated for each binary system, and are fed into the `PHOEBE` binary modelling programme, in Chapter 10.

9.8.2 SB1 and SB2 binaries

Eclipsing binaries either present double-lined spectra (SB2), in which spectral lines from both components are visible in the spectrum, or single-lined spectra (SB1), in which the spectral lines from only one component is visible.

For eclipsing binary stars, we would expect to see SB2, due to the binary components being of similar mass, size, spectral type, and luminosity. However, only 4 candidate NCRGEB show strong evidence of visible line splitting, an example of which is shown in Figure 9.16. However the remaining 23 targets appear to be SB1, where either line splitting was not clearly visible, an example of which is shown in Figure 9.17, or line broadening was visible.

For SB1 systems, `fxcor` struggled to determined a good fit (i.e. a low CCF value is achieved). However, despite no clear line splitting, strong lines are visibly red and blue shifted periodically, and as such, can be used for radial velocity extraction. The question is, *why would NCRGEB appear to be SB1s rather than SB2s?*

Visual inspection of the spectra appears to show that the SB1 are likely to be SB2 but with tangled spectra, which `fxcor` struggles to detect as two separate components. These lines also appear to change in line width (or equivalent width) and intensity. Targets which

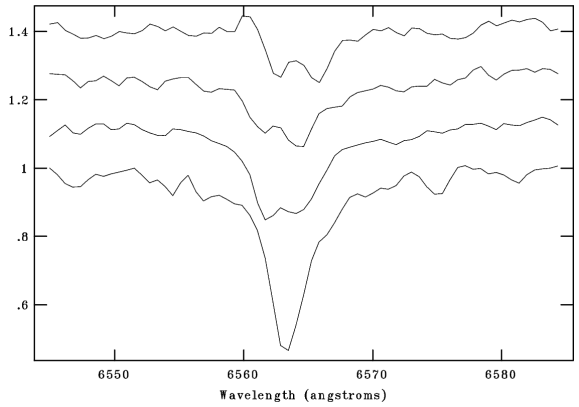

Fig. 9.16 Spectra of J183357 showing clear splitting of the Hα line (laboratory wavelength 6562.8Å).

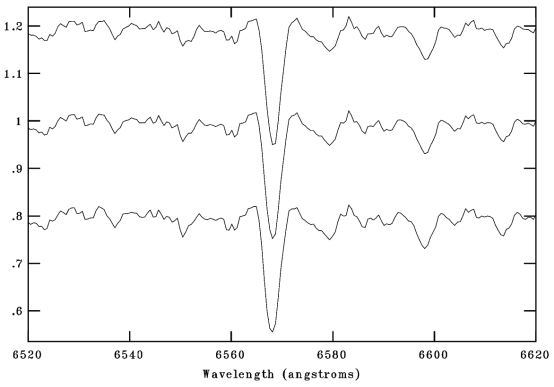

Fig. 9.17 Spectra of J231800 showing no clear splitting of the Hα line (laboratory wavelength 6562.8Å).

do appear to be SB2 are those in which the mass ratio is lower, the luminosity difference between both the component vary greatest, and the separation between the components is greatest. This implies that if the targets were observed at a higher resolution, or in some cases, more favourable phases (i.e. the extremes of the period where the binary components are at the maximum separation from an observer's point of view), then the spectra would show clear SB2. The solution to this is simply that the parameters of the secondary component can be inferred from the orbital parameters based on the primary using `PHOEBE`.

While `fxcor` cannot confidently pick up these SB1s and SB2s, other techniques to prove that a system is a binary rather than a Cepheid includes phase-folding line intensity and phase-folding equivalent width. As shown in Figure 9.18, equivalent width and the radial velocity amplitude are at their maximum when line intensity is at its minimum (when both stellar components are side-by-side), and line intensity is at maximum when equivalent with and radial velocity amplitude are at their minimum (when one stellar component eclipses the other). This technique was used to verify candidates with SB1-type systems as binaries.

To further investigate the question of *why would NCRGEB appear to be SB1s rather than SB2s?*, blended spectra were synthesised of all SB1 NCRGEB across a grid of resolution, phases, binary separations, and radial velocities. This was repeated using observed spectra at

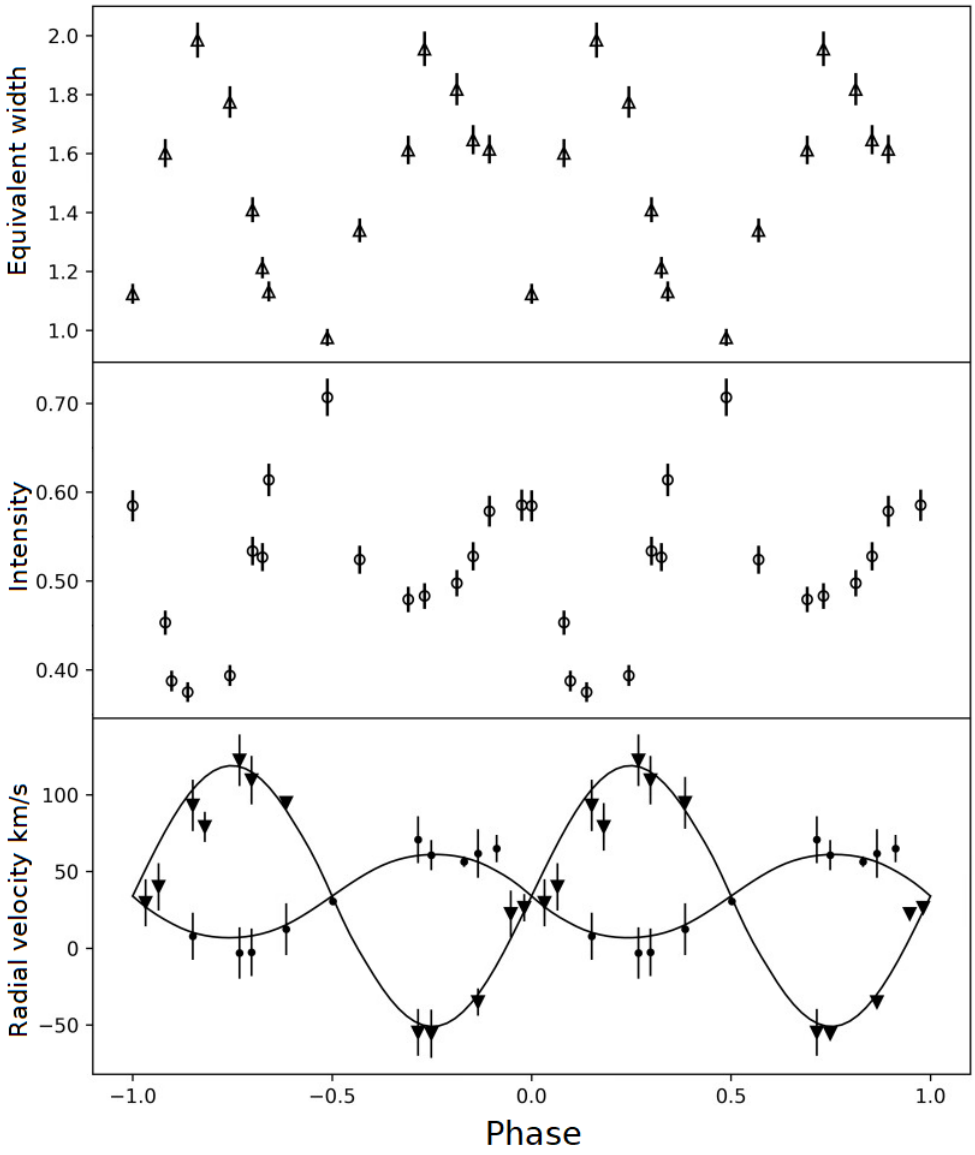

Fig. 9.18 **Top:** Plot of equivalent width of J183357, phase-folded with a period of 8.72 d. **Middle:** Plot of intensity of the Hα of J183357, phase-folded with a period of 8.72 d. Line intensity and equivalent width both show periodic variability on the same timescale as the system, confirming that this target is a NCRGEB. **Bottom:** Plot of radial velocity curve of J183357, phase-folded with a period of 8.72 d.

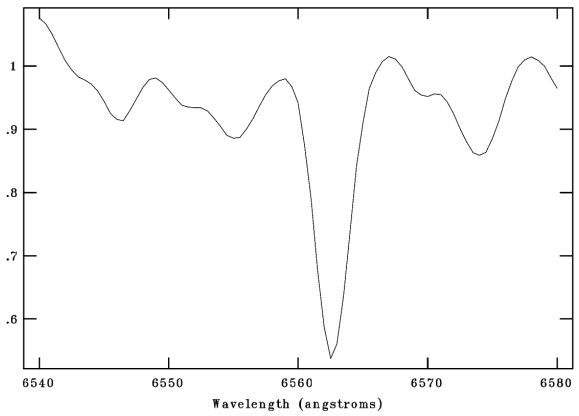

Fig. 9.19 Synthetic spectrum of a red giant (T_{eff}=3958 K) focused on the Hα line.

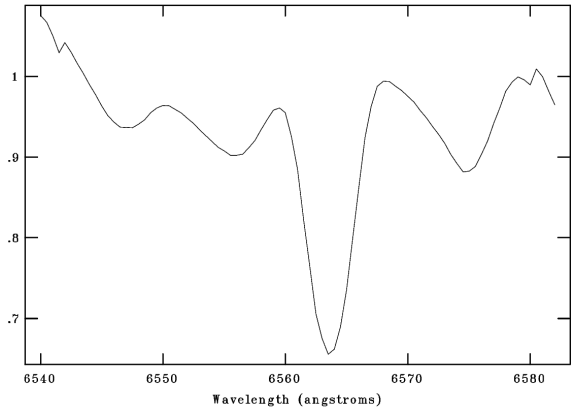

Fig. 9.20 Synthetic blended spectrum comprised of two identical red giant spectra (T_{eff}=3958 K, R$\sim$3100 in line with the resolution of the 74$''$) combined at maximum radial velocity amplitude of ($\sim$60 km s^{-1}).

zero-point phase in which only one component should be visible. The aim was to understand the cause of SB1 when two components should be visible. An example of this is the comparison between a synthetic spectrum (Figure 9.19) and a synthesised SB1 spectrum (Figure 9.20), which has been synthesised by blending synthetic spectra of two identical red giants at a maximum radial velocity amplitude of $\sim$60 km s^{-1} (i.e. where the separation between the binary components is the greatest). At this resolution and separation, the Hα line is broadened (hence the equivalent width is increased) and the line intensity is reduced.

At resolutions of R$\sim$20,000, or radial velocity amplitudes of $>\sim$80 km s^{-1}, blended synthetic spectra were clearly SB2, however at the resolution of the spectra were reduced, strong lines in the spectra became blended. At a resolution of $\sim$6,000, blended synthetic spectra were only visible as SB1. It is therefore likely that the SB1 spectra are blended SB2, and higher resolution spectra would be required to accurately constrain radial velocities. The intensity ratio (or the ratio of contribution from each stellar component) was estimated, finding that NCRGEB have a average ratio of 55:45–50:50. Therefore, each component of the binary provides a roughly equal luminosity contribution.

Additionally, observed SB1 spectra were deblended in order to estimate the radial velocities of each component. `IRAF`'s `deblend` capability was used to initial estimate the line fitting, and `PySpecKit`'s *fitting line profile* capability to iterate over a number of fits to find the best fit for each spectrum using Gaussian profiles. Using the pixel shift identified, the radial velocity of each component in each spectrum was estimated. However, since the accuracy of deblended spectra depends on initial positioning of the Gaussian profiles, errors on estimated radial velocities are significantly greater than those measured for SB1s. Therefore, these systems are presented as SB1s, and orbital parameters are measured from the primary component only.

9.8.3 Results

From spectroscopic follow-up and radial velocity extraction, a decision was made for each candidate NCRGEB, the results of which are displayed in Table 9.8. Of the 27 candidates, 12 have been confirmed to be binary systems, and the remainder appear to be Cepheids or shell stars. In this section, the radial velocity curves are discussed for each NCRGEB candidate found to be binaries. For NCRGEB candidates which were found not to be binaries, plots are displayed in Chapter 11.

1SWASPJ231800.38-031131.4

J231800 has a SuperWASP period of 23.84 d, and is classified as an EW-type binary in ASAS-SN also with a period of 23.84 d. The light curves of this target both show clear eclipses, although Drake et al. (2014) classify it as a Cepheid with a period of 11.92 d. Little else is known about this target.

The target was followed up using both SALT and the $74''$, providing 13 observations and good phase coverage for half of the phase. Only 2 observations were taken in the second half

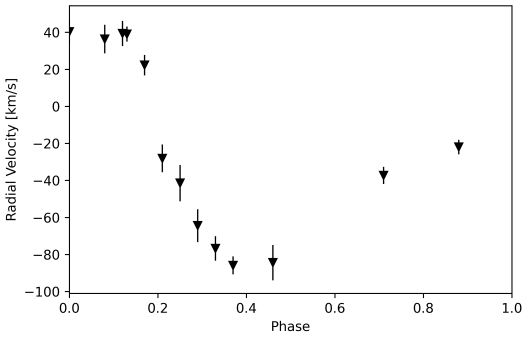

Fig. 9.21 Radial velocity curve for J231800 phase-folded with a period of 23.84 d.

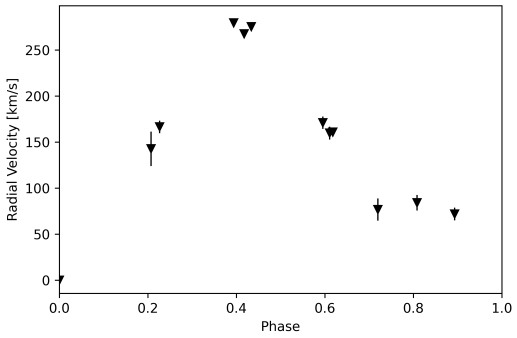

Fig. 9.22 Radial velocity curve for J204317 phase-folded with a period of 4.92 d.

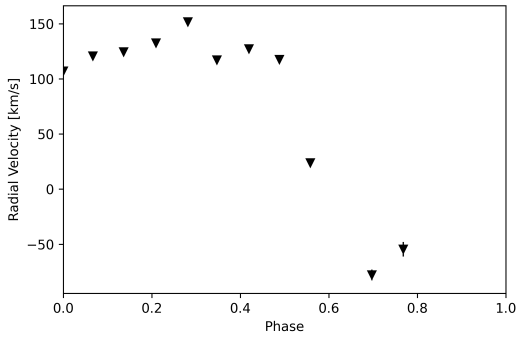

Fig. 9.23 Radial velocity curve for J194733 phase-folded with a period of 35.08 d.

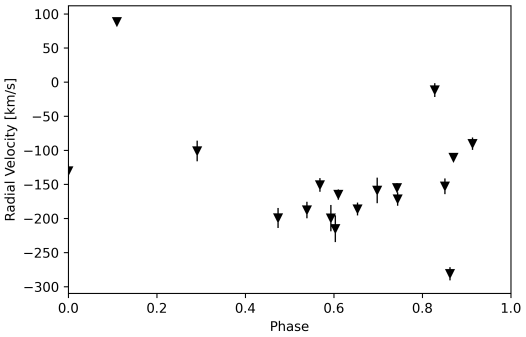

Fig. 9.24 Radial velocity curve for J194231 phase-folded with a period of 23.19 d.

of the phase, and although no line splitting was observed, the radial velocity curve (Figure 9.21) shows a clear periodic variation on the same timescale as the photometric variability.

1SWASPJ204317.92-251850.0

J204317 has a SuperWASP period of 4.92 d, and is classified as an EW-type binary in ASAS-SN with the same period. Drake et al. (2017) classifies it as a rotational variable with a period of 4.92 d, although the ASAS-SN and SuperWASP light curves appears to show eclipses. Little else is known about this target.

J204317 was followed up using the 74″ and SALT, gaining 12 good quality observations with good phase coverage. The extracted radial velocity curve (Figure 9.22) shows variability

which aligns with the period of the target, although two observations between phase 0.8–1 do not appear to follow the expected curve. The reason for this is unknown. This target appears to be a good candidate for further binary component modelling.

1SWASPJ194733.51-471201.4

J194733 was identified through a search of the SuperWASP archive and ASAS-SN Catalogue of Variable Stars. The SuperWASP object has a period of 35.08 d, and two ASAS-SN object lie within a 2″ radius of the SuperWASP object, ASASSN-V J194733.45-471159.8, an EW-type binary with a period of 14.33 d, and ASASSN-V J194736.75-471226.9, a brighter (V=10.7) semiregular star. Drake et al. (2017) categorises it as a rotational variable with a period of 14.34 d. Little else is known about this target.

The SuperWASP phase-folded light curve appeared to be unconvincing as a binary, and no further photometric follow-up was done. However, spectroscopic follow-up was done on the 74″ over 11 nights. Through spectral typing and synthesis, the target was found to be a K4-type star with T_{eff} ∼3980 K. No binary line splitting was observed, but the extracted radial velocity curve (Figure 9.23) appears to show that the radial velocity varies on the same periodic timescales. J194733 is unlikely to be a real NCRGEB, but is kept in the catalogue for confirmation through binary component modelling.

1SWASPJ194231.22-251605.5

J194231 has a SuperWASP period of 23.18 d, and a classification of EW-type binary with a period of 23.19 d in ASAS-SN. Drake et al. (2017) classifies it as a Cepheid variable with a period of 23.19 d. Little else is known about this target, however the phase-folded light curve appears to show clear eclipses.

J194231 was followed up with both SALT and the 74″, providing phase coverage primarily in only half of the full phase. From the extracted radial velocity curve (Figure 9.24), it is

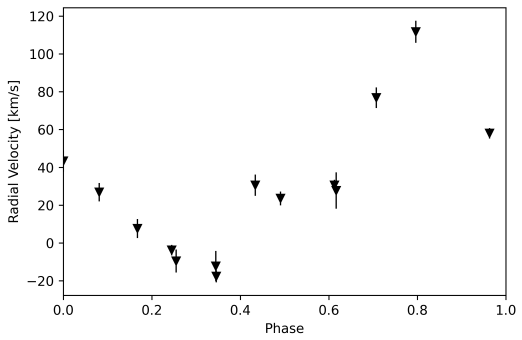

Fig. 9.25 Radial velocity curve for J190114 phase-folded with a period of 11.09 d.

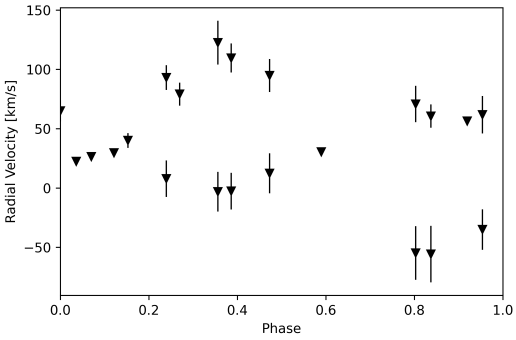

Fig. 9.26 Radial velocity curve for J183357 phase-folded with a period of 8.72 d.

not clear if the system truly is a binary. There appears to be a general trend with an extreme radial velocity amplitude of possibly $\sim$300 km s^{-1}, although this is dependent on a singular detection at phase $\sim$0.1. It is possible that this target is not a NCRGEB, but has been retained in the catalogue for exploration with binary component modelling.

1SWASPJ190114.91-380729.0

J190114, also known as TYC 7917-66-1 (Pojmanski, 2002), has a SuperWASP period of 10.96 d, although the photometric phase-folded light curve appears more convincing when folded at the ASAS-SN period of 11.09 d. The ASAS-SN classification is that of a rotational variable. The target was observed with both the 74″ and SALT which provides full phase coverage. The extracted radial velocity (Figure 9.25) shows no sign of strong line binary splitting, but does show periodic change on the same timescales as the photometric light curve, hence is kept as a NCRGEB candidate.

1SWASPJ183357.87+423725.2

J183357 has a period of 8.72 d in SuperWASP, and is also classified as an EW-type binary with a period of 8.72 d in ASAS-SN. It has also been identified as a Cepheid with a period

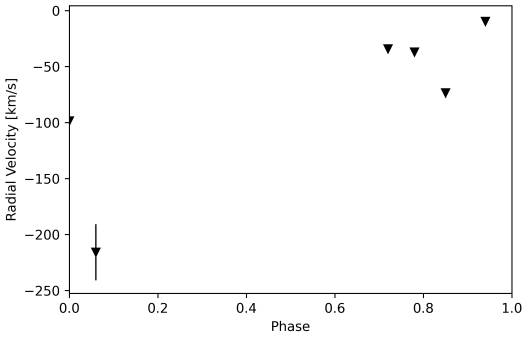

Fig. 9.27 Radial velocity curve for J165241 phase-folded with a period of 15.13 d.

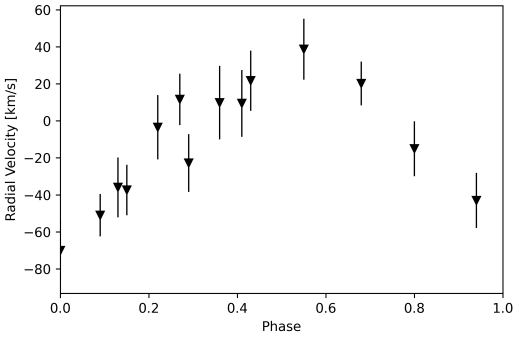

Fig. 9.28 Radial velocity curve for J154828 phase-folded with a period of 7.47 d.

of 4.38 d (Akerlof et al., 2000), although the phase-folded photometric light curve is more convincing when folded at the binary period.

The target was observed with the Liverpool Telescope, and is only one of very few NCRGEB candidates which shows clear binary splitting of strong lines which varies periodically. The radial velocity of each component was extracted (Figure 9.26), appeared to show one component with a radial velocity amplitude of almost 200 km s^{-1}, and the other with an amplitude of $\sim$75 km s^{-1}. J183357 is a strong NCRGEB candidate.

1SWASPJ165241.24+203224.7

J165241 was identified as having a period of only 0.88 d in SuperWASP, although classified as an EW-type binary with a period of 15.13 d in ASAS-SN, a Cepheid with a period of 7.57 d (Drake et al., 2014), half that of the ASAS-SN period. The SuperWASP photometric phase folded light curve appears to be convincing as a binary when folded at the ASAS-SN period, although are convincing also as a Cepheid folded at half the period.

The target was followed up using priority Z time on the Liverpool Telescope, gaining only 6 nights of observations, covering the extremes of the phase coverage. Whilst the radial velocity curve (Figure 9.27) does not provide a convincing binary curve, it has been retained in the sample so the variable type can be confirmed through component modelling.

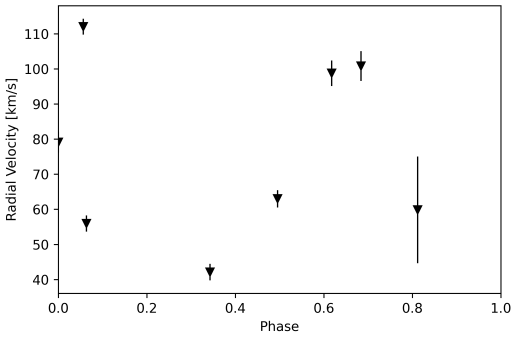

Fig. 9.29 Radial velocity curve for J132156 phase-folded with a period of 32.09 d.

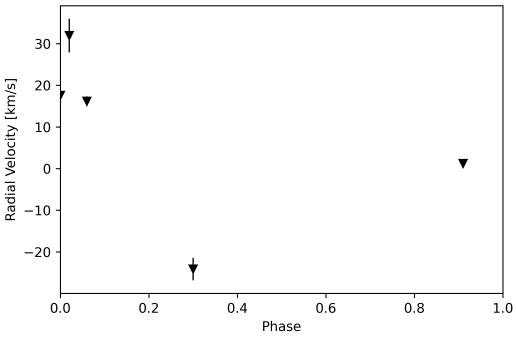

Fig. 9.30 Radial velocity curve for J093610 phase-folded with a period of 6.92 d.

1SWASPJ154828.29+201442.8

J154828 is an interesting system with a period of 7.47 d in SuperWASP. It has been identified as a candidate Cepheid with a period of 3.73 d (Pojmanski, 2002). ASAS-SN provides a classification of an EW-type binary with a period of 7.47 d. The extracted radial velocity curve (Figure 9.28) shows a variability in line with that of the binary system.

1SWASPJ132156.04-010742.8

J132156 has a SuperWASP period of 32.09 d, and an ASAS-SN classification of an EW-type binary with a period of 32.10 d. It has previously been identified a V Wirginis type variable (a type of Cepheid) with a period of 32.09 d (Pojmanski, 2002), however the phase-folded light curves are more convincing as a binary. J132156 was followed up over 8 nights using SALT, providing good phase coverage. The radial velocity curve (Figure 9.29) shows periodic variability, likely to be that of a binary system.

1SWASPJ093610.20-283847.2

J093610 has a SuperWASP period of 6.92 d, and has been identified as an EW-type binary also with a period of 6.92 d in ASAS-SN, although secondary eclipses appear to be extremely sharp. It was previously classified as a rotational variable by Drake et al. (2017) with a period

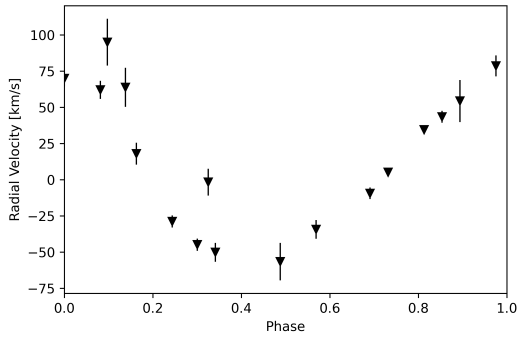

Fig. 9.31 Radial velocity curve for J035259 phase-folded with a period of 24.61 d.

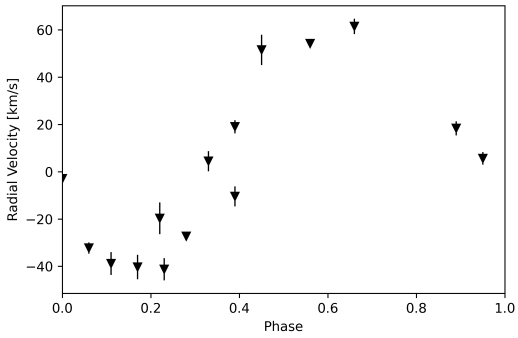

Fig. 9.32 Radial velocity curve for J003544 phase-folded with a period of 17.86 d.

of 6.92 d, however based on the SuperWASP and ASAS-SN light curves, this classification seems implausible. The target was followed up over only 5 night using SALT, although this provided a range of phase coverage. Although not immediately apparent, the radial velocity curve (Figure 9.30) is likely to be that of a binary system. Further follow-up would benefit J093610.

1SWASPJ035259.67+091717.1

J035259 has a SuperWASP period of 24.61 d, and has been identified as a both a WVir type system and since reclassified as an EB-type eclipsing binary system with a period of 24.6 d (Drake et al., 2014). J035259 was followed up spectroscopically over 14 nights using the Liverpool Telescope and 3 nights using the 74″, but showed no signs of line splitting. The extracted radial velocity curve (Figure 9.31) is clearly that of a binary system.

1SWASPJ003544.75+495450.0

J003544 has a SuperWASP period of 17.86 d, but has been detected as a rotational variable with a period of 8.93 d in ASAS-SN, half that of the SuperWASP period. The ASAS-SN light curve is less convincing as a rotational variable. J003544 was followed up spectroscopically

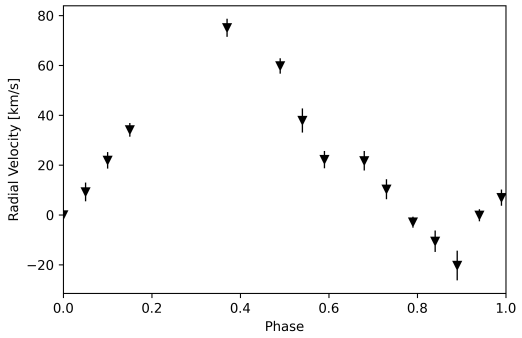

Fig. 9.33 Radial velocity curve for J002952 phase-folded with a period of 20.33 d.

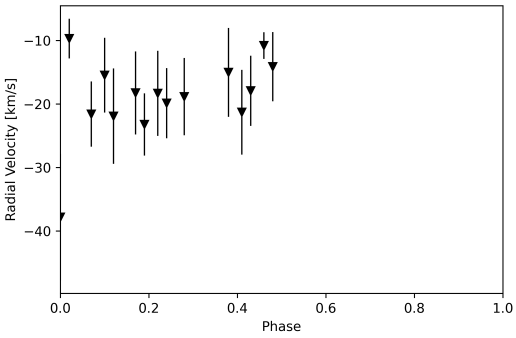

Fig. 9.34 Radial velocity curve for J001521 phase-folded with a period of 41.62 d.

over 15 nights using the Liverpool Telescope, but showed no signs of line splitting. The extracted radial velocity curve (Figure 9.32) is clearly that of a binary system.

1SWASPJ002952.96+475034.3

J002952, also known as V1038 Cas, is classified as an eclipsing binary of beta Lyrae type with a period ∼20.3 d (Kazarovets et al., 2011) and a SuperWASP period of 20.33 d. In ASAS-SN it is classified as a non-periodic variable. It was identified by citizen scientists through the SuperWASP Variable Stars project. It was followed up spectroscopically over 15 nights using the Liverpool Telescope, but showed no signs of line splitting. The extracted radial velocity curve (Figure 9.33) is clearly that of a binary system.

1SWASPJ001521.76+472055.2

At discovery in 2018, J001521, also known as TYC 3251-903-1, was a little known star of magnitude V∼11.3, which appeared to be an eclipsing contact binary with a period of 41.62 d. Since 2020, it has been classified as an EB-type eclipsing binary with a period of 41.2 d by ASAS-SN. This object was the first to be discovered during the initial set up of the SuperWASP Variable Stars Zooniverse project and was the one which started this path of research. In both SuperWASP and ASAS-SN, the target displays a clear binary light curve,

and a phase-fold at half the period ($\sim$20.6 d for ASAS-SN observations) can be convincing as a Cepheid.

J001521 was followed up photometrically and spectroscopically, using PIRATE, the WHT and the Liverpool Telescope. A single IR spectra from the WHT appeared to be that of a red giant with a binary component, but further spectroscopic follow-up over 15 nights with the Liverpool Telescope showed no sign of splitting of strong spectral lines. The extracted radial velocity curve (Figure 9.34) provides coverage of only half of the full phase, and further follow-up would be required to provide full phase coverage. The radial amplitude is unusually low in comparison to the other confirmed binaries. From this partial radial velocity curve, it is not possible to tell whether J001521 is a NCRGEB.

9.9 Discussion

In this section, I discuss the results of the spectroscopic follow-up and confirmation of 12 NCRGEB. The remainder of the 27 candidates are 15 non-NCRGEB consisting of Cepheids, rotational variables, and shell stars. These targets are examined and discussed in detail in Chapter 11, although they are briefly discussed here to provide context. An assessment of each candidate is listed in Table 9.8.

The results of the photometric follow-up using the $74''$, SALT, Liverpool Telescope, LCO, and WHT have reduced the number of candidate NCRGEB from 27 to 12. These candidates were identified photometrically, all of which appeared to show periodicity and maxima and minima similar to that of a contact binary system but with an extreme period. The spectroscopic follow-up allowed for the removal of non-binary systems, and the spectral typing, synthesis, and radial velocity extraction of candidate NCRGEB systems.

Radial velocity curves have been extracted for all candidates with a good coverage of the full phase curve, finding 12 NCRGEB. Additional confirmation that these systems are NCRGEB are provided through phase-folded line intensity and equivalent width plots.

WASP ID	Radial velocity assessment
1SWASPJ231800.38-031131.4	Binary
1SWASPJ204317.92-251850.0	Binary
1SWASPJ194733.51-471201.4	Cepheid
1SWASPJ194231.22-251605.5	Binary
1SWASPJ192628.96-233856.1	Shell
1SWASPJ192311.66-423244.5	Cepheid
1SWASPJ191910.42-414050.9	Cepheid
1SWASPJ190114.91-380729.0	Binary
1SWASPJ183357.87+423725.2	Binary
1SWASPJ165656.26-040414.3	Cepheid
1SWASPJ165241.24+203224.7	Binary
1SWASPJ154828.29+201442.8	Binary
1SWASPJ154607.55-191711.4	Unsure
1SWASPJ135703.85-474817.9	Cepheid
1SWASPJ132156.04-010742.8	Binary
1SWASPJ103327.40-304931.6	Shell
1SWASPJ093610.20-283847.2	Binary
1SWASPJ035259.67+091717.1	Binary
1SWASPJ022953.03+041420.9	Cepheid
1SWASPJ003544.75+495450.0	Binary
1SWASPJ003414.72-291038.4	Cepheid
1SWASPJ002952.96+475034.3	Binary
1SWASPJ002349.66+483114.5	Cepheid
1SWASPJ001545.50-622237.8	Cepheid
1SWASPJ001521.76+472055.2	Binary
1SWASPJ000927.89+014542.1	Cepheid
1SWASPJ000018.09+091923.9	Cepheid

Table 9.8 Assessment of the NCRGEB candidates following radial velocity follow-up.

Typically, the systems have a high radial velocity amplitude of $\sim$100–200 km s^{-1}. Of the 12 systems, 3 would benefit from more spectroscopic observations to provide fuller coverage of the phase curve, including 1SWASPJ165241.24, 1SWASPJ132156, and 1SWASPJ093610.

8 out of the 12 systems appear to be SB1 systems (where no binary line splitting is visible) due to blending of the spectra of the twin binary components. This is an issue which could cause over or under estimation of the radial velocity of the systems, however this does not appear to have reduced the accuracy of the radial velocity curves themselves. This problem is likely to be solved with higher resolution spectroscopy.

From radial velocity curves, it is immediately apparent that at least 10 targets are Cepheid variables or rotational variables, listed in Table 9.8. These targets display either no periodicity or periodicity which indicates that radial velocity detections are from the change in radius of the Cepheid. Interestingly, at least 2 targets are shell stars. Shell stars are stars which have extremely broad absorption lines and emission lines from the Balmer series, including Hα line profiles, which increase and decrease throughout a cycle. Such stars typically have high rotational velocities of 200–300 km s^{-1} and spectral types of O7.5-F5. As the Shell star rotate, the line profile changes dramatically, making them easy to distinguish from NCRGEB systems. For further discussion on this, see Chapter 11.

In Chapter 10, I model the 12 remaining NCRGEB systems using `PHOEBE`, a binary component modelling programme. `PHOEBE` takes inputs found during the process of spectral typing and synthesis, and radial velocity extraction, including photometric observations, radial velocity measurements, and temperatures.

9.10 Summary

Spectroscopic follow-up of all of the 27 candidate near-contact red giant eclipsing binaries has been completed, using SALT, the Liverpool Telescope, the 74″, LCO, and the WHT. Each candidate was observed at with a good coverage of the full orbital period. All spectroscopic

data have been reduced using a combination of automated pipelines specific to each telescope and instrument and routines in `PyRAF/IRAF`. Having done this, spectral typing and spectral synthesis has been completed for each candidate, allowing the spectral type to be identified, along with other parameters including metallicity, surface gravity, temperature, and more. This analysis feeds directly into modelling the binary components in `PHOEBE` and determining the evolutionary history and future of NCRGEB.

Through spectral typing and synthesis, all the targets have been found to be late-type giant systems with solar or near solar metallicity. Using strong lines including Hα and the Na doublet, Fourier cross-correlation has been completed and radial velocity plots have also been produced for all observed candidates. Where binaries appeared to be SB1s where SB2s were expected, a variety of methods were used, including an assessment of equivalent width, confirming the binary nature of the targets. Synthetic blended spectra have also been created, identifying that a higher resolution should be able to identify SB1s as SB2s, and at the observed resolution, blending of the components is common.

As a result of this analysis, the sample of 27 candidate near contact red giant eclipsing binaries has been narrowed down to 13 through photometric and spectroscopic follow-up. Intriguingly, the original target, 1SWASPJ001521 does not appear to show the expected radial velocity curve expected.

Chapter 10

Modelling Near Contact Red Giant Eclipsing Binaries

This chapter will focus on the modelling of the near-contact red giant eclipsing binaries. Only targets which have been confirmed as binaries through a combination of photometric (Chapter 8) and spectroscopic (Chapter 9) follow-up will be modelled. This chapter will include a summary of the modelling techniques used, the results of the modelling, and a discussion of the outputs.

The observationally confirmed NCRGEB are first modelled in `PHOEBE`, a program which models the components of the binary system. The purpose of this is to confirm whether the parameters identified through observational follow-up could actually produce a physically possible binary system. The second stage of modelling takes the form of evolutionary modelling using a combination of programs and models. The purpose of this is to explore the theory that NCRGEB are possible progenitors of red novae. The binary systems are evolved from ZAMS to explore their history and formation, and evolved forwards to understand the end of life of such binaries. Through this, I aim to answer questions such as *will these binary systems merge, and if so, on what timescale?*, and *are these systems likely to be changing on human-observable timescales?*, and *are NCRGEB actually progenitors of red novae?*

10.1 PHOEBE

To model the binary components of each confirmed NCRGEB, a binary star modelling program called PHOEBE (PHysics Of Eclipsing BinariEs) was used. PHOEBE is a graphical user interface which makes use of a recent version of the Wilson Devinney code (Prša and Zwitter, 2005), originally from the code of Wilson and Devinney (1971). PHOEBE takes inputs of multi-colour photometry and radial velocity curves based on spectroscopic observations, and a number of best guess input parameters, including an assumption about the type of binary system, i.e. detached, contact, or semi-contact system. Once this data have been input, PHOEBE finds an initial best fit to minimise the χ^2 value, i.e. the difference between the observed light curve and radial velocity curves and the synthesised versions, then a series of iterative fits are done to minimise χ^2. A good fit is found once the χ^2 value is minimised and does not change significantly when rerunning the fit.

To fit the NCRGEB components in PHOEBE, a combination of multi-colour photometry from different sets of observations was used. The initial input light curve was the SuperWASP V-band light curve, binned on every 100 data points (since PHOEBE struggles to run or even crashed with the full SuperWASP light curve). Where appropriate, only certain fields of SuperWASP data were used to improve signal.

Where available, V-band light curves from the ASAS-SN Catalogue of Variable Stars and Kepler were also used. Multi-colour photometry is important and allows for modelling the temperature of each binary component, so observations from PIRATE and LCO were used. For the radial velocity fits, the radial velocity curves from SALT, 74″, and LT were used. The radial velocity curve alone determines the semi-major axes and the sizes of the components, and the mass ratio is determined by both photometry and radial velocities. Input photometry and radial velocity curves take HJD inputs and PHOEBE phase-folds all data using the period input by the user.

WASP ID	Initial Assessment
1SWASPJ231800.38-031131.4	Binary
1SWASPJ204317.92-251850.0	Binary
1SWASPJ194231.22-251605.5	Binary
1SWASPJ190114.91-380729.0	Binary
1SWASPJ183357.87+423725.2	Binary
1SWASPJ154828.29+201442.8	Binary
1SWASPJ132156.04-010742.8	Binary
1SWASPJ093610.20-283847.2	Binary
1SWASPJ035259.67+091717.1	Binary
1SWASPJ003544.75+495450.0	Binary
1SWASPJ002952.96+475034.3	Binary
1SWASPJ001521.76+472055.2	Binary - low confidence

Table 10.1 List of NCRGEB candidates to be modelled in PHOEBE.

A set of initial best guess parameters were input. These include the assumption that the system is either a contact binary or a semi-detached binary (where both, or only one component overfills its Roche Lobe), temperature and surface gravity from spectral modelling, period from SuperWASP periodicity catalogue, colours from multi-colour photometry, etc. Whilst star spot coverage can be modelled, there is an absence of direct evidence for these, and as such, were not included in models. Techniques such as Doppler tomography would be required to confirm the presence of spots. The binaries modelled in PHOEBE are listed in Table 10.1 and results of the modelling are shown and commented on in Section 10.1.2.

10.1.1 Models of candidates

In this section, I detail the full models of light curves, radial velocity curves, binary component models, and best-fit parameters for each NCRGEB.

1SWASPJ231800.38-031131.4

Based on the photometric light curves of J231800, it appears to be a system with almost equal minima with one eclipse sharper and deeper than the other, hence the system is likely to be a near-contact system with components of significantly different radii.

To model this system in PHOEBE, it was assumed that the system was a semi-detached system with the primary star filling the Roche lobe. The period was set to 23.84 d (the SuperWASP period), and the starting HJD to 2456595.36. SuperWASP data were binned, but ASAS-SN, PIRATE, LCO, and Kepler data were not binned. Radial velocities were inputted from SALT and the 74″. All data sets were given in HJD, and were not converted to phases prior to modelling. The temperature for each component was set at 3980 K, as found from spectral typing and synthesis, and the angle of inclination, i, was set to 80°. The semi-major axis was estimated from the period as 40 $R_{\odot}$. Light curves alone provided enough information to determine good assumptions for the angle of inclination and the Kopal potentials. Using Kopal potentials, the binary filling factors can be calculated using the equation below from the PHOEBE manual[1]:

$$\mathscr{F} = \frac{\Omega - \Omega^{L_1}}{\Omega^{L_2}_{\text{crit}} - \Omega^{L_1}_{\text{crit}}}, \tag{10.1}$$

where Ω is the surface potential of the common envelope of the binary, and $\Omega^{L_2}_{\text{crit}}, \Omega^{L_2}_{\text{crit}}$ are the inner and outer Lagrangian surface potentials.

Using these assumptions, the radial velocities curves were first fitted for semi-major axis, a, inclination, i, and centre-of-mass velocity (kms^{-1}). The temperatures and surface potentials were optimised to fit the multicolour photometric data and constrain the mass ratio.

An initial best-fit was found manually for each system by minimising the χ^2 values for the SuperWASP, ASAS-SN, and PIRATE light curves and radial velocity curve. The radial velocity cure has excellent phase coverage, however has two data points which appear to be

[1]http://phoebe-project.org/static/legacy/docs/phoebe_manual.pdf

outliers at phase ∼0.8. These data points were taken on the first two nights of observing at the 74″ when the exposure time was too low and S/N too high. As such, these points were removed for modelling.

Using further χ^2 minimisation to reduced χ^2 to below 1, the best fit was obtained for J231800, shown in Fig 10.1. No spot fitting or third light source fitting was done due to the equal heights of the maxima, and lack of evidence for either phenomenon. The list of best-fit parameters can be found in Table 10.2. The best fit parameters indicate that 231800 is a semi-detached binary with the primary component filling the Roche lobe, comprised of 15.50 $R_\odot$ and 4.12 $R_\odot$ components, with a mass ratio, $q = M_2/M_1$ of 1.22.

The uncertainties on the many of the parameters are generated by PHOEBE and may be an underestimate. The errors on temperatures, $T_{1,2}$ were generated by spectral typing and synthesis. The errors on the component masses, $M_{1,2}$ were found using the formulae below, taken from the PHOEBE manual, and the same error analysis process was used for each of the binaries modelled:

$$\sigma_{M1} = M_1(3\frac{\sigma_a}{a} + 2\frac{\sigma_P}{P} + \frac{\sigma_q}{q+1}) \tag{10.2}$$

$$\sigma_{M2} = M_2(3\frac{\sigma_a}{a} + 2\frac{\sigma_P}{P} + \frac{\sigma_q}{q+1}) \tag{10.3}$$

1SWASPJ204317.92-251850.0

Based on the SuperWASP photometric light curves of J204317, it appears to be a system with slightly different depth minima, however the ASAS-SN, PIRATE, and LCO light curves show similar depth minima.

The system was modelled both as a near-contact (semi-detached) system with the primary star filling the Roche lobe, and a contact (double contact) system. The period was set to 4.92

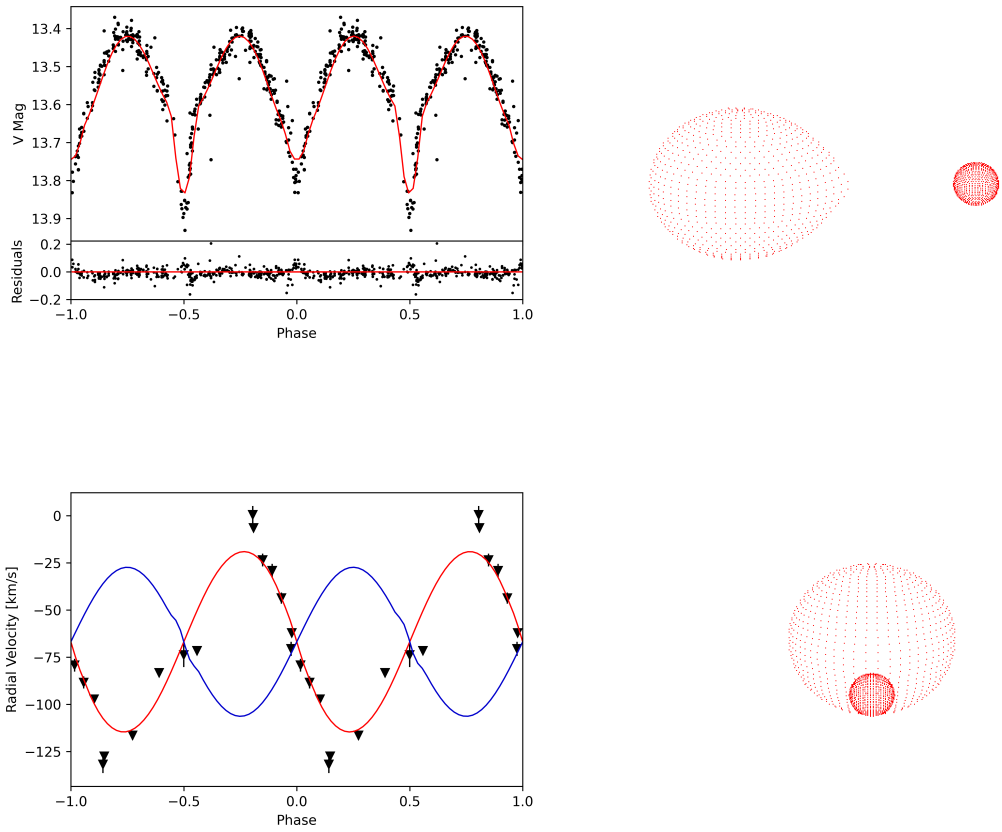

Fig. 10.1 Overview of J231800. **Top left:** SuperWASP V phase folded light curve fitted with PHOEBE model. **Top right:** Binary component model side view. **Bottom left:** Radial velocity curve fitted with PHOEBE model. **Bottom right:** Binary component model front view.

d (the SuperWASP period), and the starting HJD to 2458658.31. SuperWASP data were binned, but ASAS-SN, PIRATE, and LCO was not binned. Radial velocities were inputted from SALT and 74″. The temperature for both components were set at 4054 K, as found from spectral typing and synthesis, and multi-colour photometry from PIRATE and LCO was used to constrain temperatures. The SuperWASP light curve indicates that there may be a high angle of inclination i, with sharp minima, however the ASAS-SN, LCO, and PIRATE light curves do not appear to show as sharp a minima. The semi-major axis was estimated from the period as 15 $R_{\odot}$.

Parameter	Symbol	Model
Semi-major axis ($R_\odot$)	a	42.79 ± 0.92
Masses ($M_\odot$)	M_1	0.84 ± 0.08
	M_2	1.02 ± 0.10
Mass ratio	M_2/M_1	1.22 ± 0.06
COM velocity (km s^{-1})	V_0	-68.86 ± 0.70
Angle of inclination (deg)	i	75.56 ± 3.80
Radii ($R_\odot$)	R_1	15.50 ± 0.17
	R_2	4.12 ± 0.19
Temperature (K)	T_1	3973 ± 189
	T_2	4453 ± 284
Period (d)	P	23.84
Kopal potentials	Ω_1	4.10 ± 0.09
	Ω_1	3.54 ± 0.09
Filling factor	$\mathscr{F}$	0.98

Table 10.2 Binary component parameters for J231800.

J204317 was fitted in the same way as J231800, using initial parameters and χ^2 minimisation for both the semi-detached and the contact system. Again, no third light source or spot was fitted to either system. Both the semi-detached and contact systems produces a physically realistic systems, however the best-fitting contact system fails to fully fit the sharp minima of the secondary component. By contrast, the semi-detached system successfully fits the minima of the secondary and minima for all light curves. The full model is shown in Figure 10.2.

The output parameters for the contact system are listed in Table 10.3 with the errors on the parameters being generated by PHOEBE. The best fit parameters indicate that J204317 is a semi-detached system comprised of 5.49 $R_\odot$ and 6.38 $R_\odot$ components, with a mass ratio, $q = M_2/M_1$ of 0.46.

1SWASPJ194231.22-251605.5

Based on the photometric light curves of J194231, it appears to be a system with almost equal minima in the noisy SuperWASP light curve, but with different depth minima in the

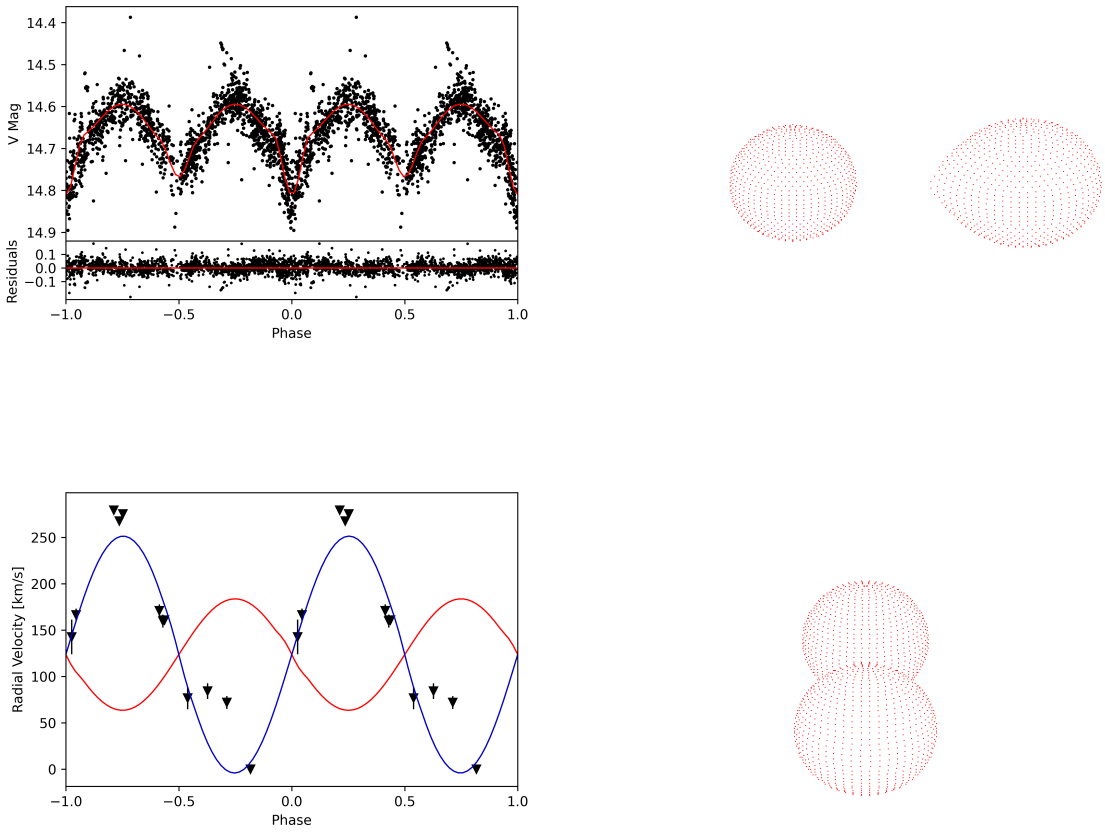

Fig. 10.2 Overview of J204317. **Top left:** SuperWASP V phase folded light curve fitted with `PHOEBE` model. **Top right:** Binary component model side view. **Bottom left:** Radial velocity curve fitted with `PHOEBE` model. **Bottom right:** Binary component model front view.

ASAS-SN light curve. From this, the system is likely to be either a contact or a semi-detached system, with different radii components and similar radii components respectively. The radial velocities extracted from SALT and the 74″ are inconclusive and appear not to be that of a binary system, however the light curves clearly show J194231 is a binary. This system is a best fit to the available radial velocity curve, however the actual system may significantly differ from the results listed below.

To model this system, it was assumed that the first system was a semi-detached system with the primary star filling the Roche lobe, and a second model for a contact system. The period was set to 23.18 d (the SuperWASP period), and the starting HJD to 2453862.72.

Parameter	Symbol	Model
Semi-major axis ($R_\odot$)	a	20.29 ± 0.19
Masses ($M_\odot$)	M_1	3.17 ± 0.12
	M_2	1.47 ± 0.06
Mass ratio	M_2/M_1	0.46 ± 0.01
COM velocity (km s^{-1})	V_0	123.67 ± 1.14
Angle of inclination (deg)	i	66.25 ± 1.23
Radii ($R_\odot$)	R_1	5.49 ± 0.07
	R_2	6.38 ± 0.19
Temperature (K)	T_1	4923 ± 249
	T_2	4595 ± 278
Period (d)	P	4.92
Kopal potentials	Ω_1	2.81 ± 0.10
	Ω_1	2.53 ± 0.07
Filling factor	$\mathscr{F}$	0.91

Table 10.3 Binary component parameters for J203417.

SuperWASP data were binned, but ASAS-SN and PIRATE data were not binned. Radial velocities were inputted from SALT and the 74″. The temperature for each component was set at 5145 K, and the sharp minima indicate a relatively high inclination i. The semi-major axis was estimated from the period as 55 $R_\odot$. The full model is shown in Figure 10.3.

J194231 was fitted as both a semi-detached and a contact system to identify the most physically realistic configuration. No third light source or spot was fitted. Both configurations proved to be physically realistic, however the semi-detached system with the secondary star filling the Roche lobe provides the best fitting and lowest χ^2 minimisation.

The output parameters are listed in Table 10.4 with the errors on the parameters being generated by PHOEBE. The best fit parameters indicate that J194231 is a semi-detached system comprised of 10.46 $R_\odot$ and 17.63 $R_\odot$ components, with a mass ratio, $q = M_2/M_1$ of 0.86. Due to the poor radial velocity curve, these parameters should be taken with extreme caution.

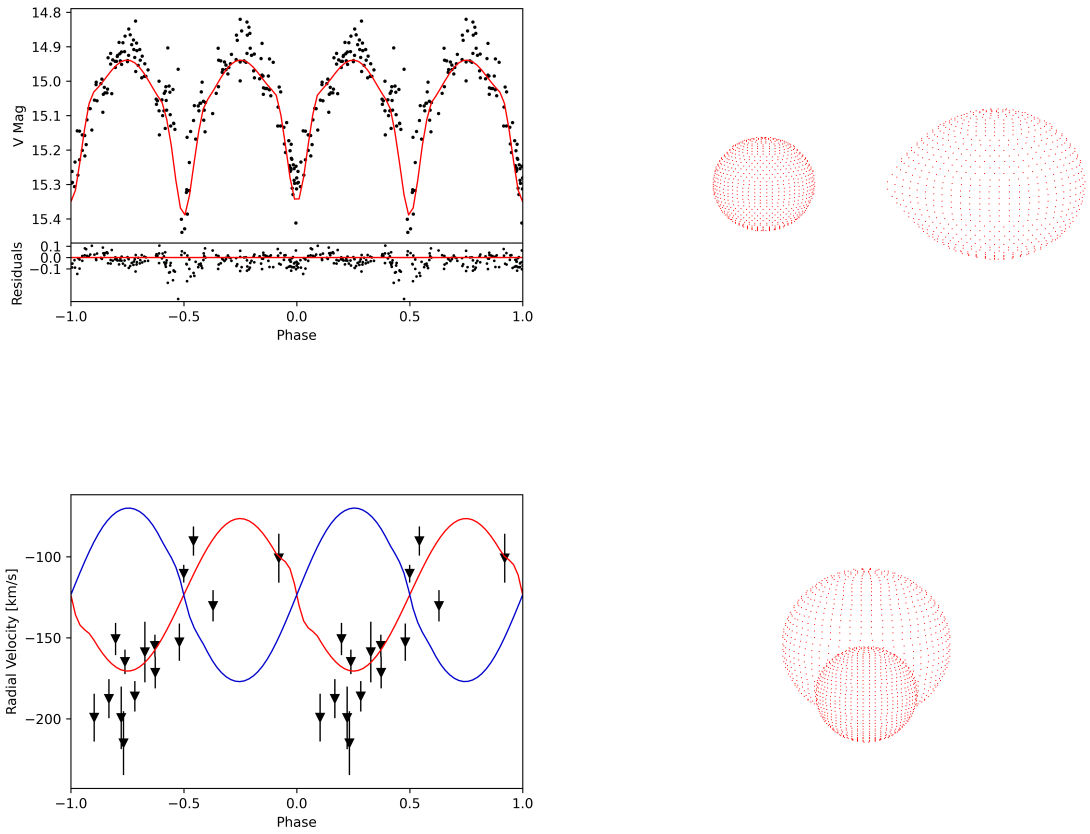

Fig. 10.3 Overview of J194231. **Top left:** SuperWASP V phase folded light curve fitted with PHOEBE model. **Top right:** Binary component model side view. **Bottom left:** Radial velocity curve fitted with PHOEBE model. **Bottom right:** Binary component model front view.

1SWASPJ190114.91-380729.0

Based on the photometric light curves of J190114, is a system with smoothly varying minima and sharper maxima. This indicates that the system is likely to be semi-detached and the primary component has a much smaller radius and eclipses only at the edge of the larger but less massive secondary, with a relatively high angle of inclination. For this target, the radial velocity curve provides full coverage but only component is visible.

To model this system, it was assumed that the system was a semi-detached system with the secondary star filling the Roche lobe and a smaller but more massive primary. The period was set to 11.09 d (the ASAS-SN period), and the starting HJD to 2456790.17. SuperWASP data

Parameter	Symbol	Model
Semi-major axis ($R_\odot$)	a	48.3 ± 0.49
Masses ($M_\odot$)	M_1	1.49 ± 0.06
	M_2	1.29 ± 0.05
Mass ratio	M_2/M_1	0.86 ± 0.02
COM velocity (km s^{-1})	V_0	-123.52 ± 0.32
Angle of inclination (deg)	i	79.34 ± 1.45
Radii ($R_\odot$)	R_1	10.46 ± 0.05
	R_2	17.63 ± 0.09
Temperature (K)	T_1	4950 ± 22
	T_2	5153 ± 25
Period (d)	P	23.18
Kopal potentials	Ω_1	3.52 ± 0.03
	Ω_1	3.04 ± 0.02
Filling factor	$\mathscr{F}$	0.63

Table 10.4 Binary component parameters for J194231.

were binned, but ASAS-SN data were not. There was no multi-colour photometry available, meaning that it is not possible to fully constraint the temperatures of the components. Radial velocities were inputted from the 74″. The temperature for each component was set at 5521 K, as found from spectral typing and synthesis. The light curve indicates that the system has a high angle of inclination i, initially modelled at 70°. The semi-major axis was estimated from the period as 30 $R_\odot$. The full model is shown in Figure 10.4.

J190114 was fit using initial parameters and χ^2 minimisation. Again, no third light source or spot was fitted. The output parameters are listed in Table 10.5 with the errors on the parameters being generated by PHOEBE. The best fit parameters indicate that J190114 is a semi-detached system comprised of 3.73 $R_\odot$ and 10.63 $R_\odot$ components, with a mass ratio, $q = M_2/M_1$ of 0.88.

1SWASPJ183357.87+423725.2

The SuperWASP photometric light curve of J183357 shows a system with marginally different depth and shaped minima, indicating that the system is likely to be a semi-detached system.

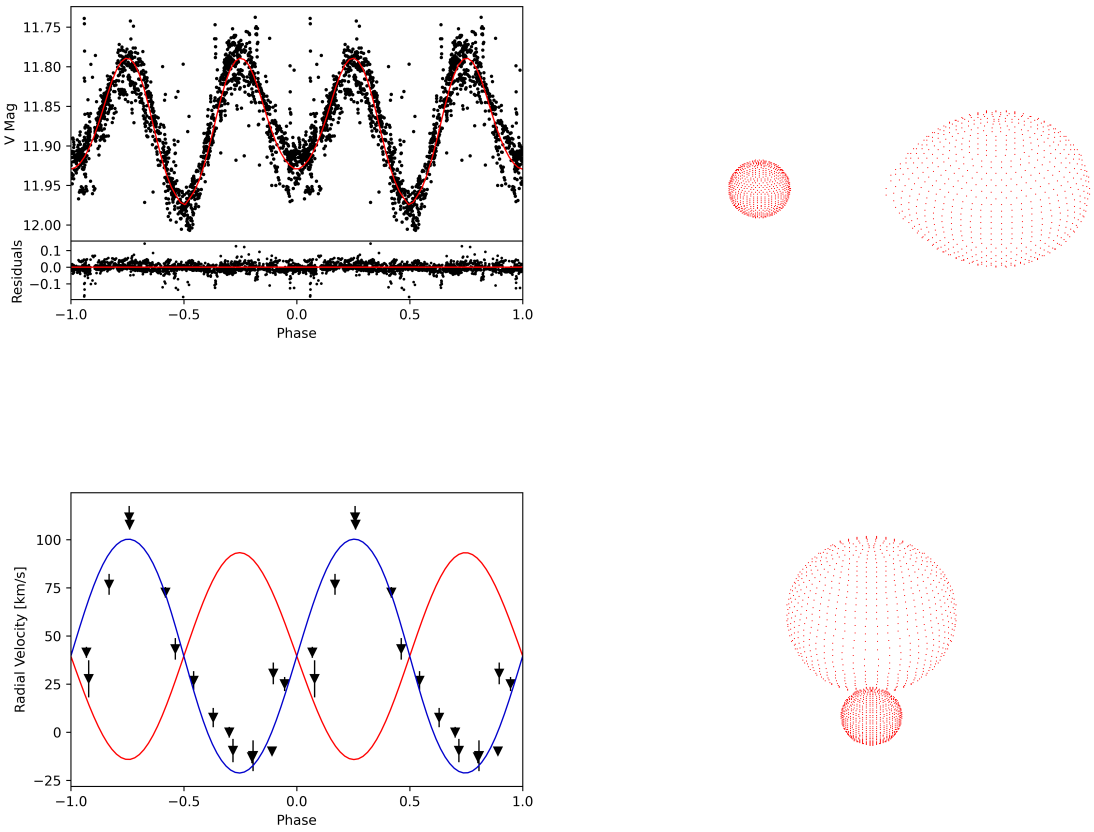

Fig. 10.4 Overview of J190114. **Top left:** SuperWASP V phase folded light curve fitted with PHOEBE model. **Top right:** Binary component model side view. **Bottom left:** Radial velocity curve fitted with PHOEBE model. **Bottom right:** Binary component model front view.

J183357 is the only one of the candidate NCRGEB which showed clear splitting of Hα emission and provided radial velocity curves for both binary components. Therefore, this system is likely to be the most accurately modelled system.

The system was modelled as a semi-detached system with the secondary star filling the Roche lobe. The period was set to 8.72 d (the SuperWASP period), and the starting HJD to 2453131.27. SuperWASP data were binned, but ASAS-SN, PIRATE, and LCO data were not. Radial velocities for both components were inputted from the Liverpool Telescope. The temperature for each component was set at 5529 K, as found from spectral typing and synthesis. The sharp minima indicates that the angle of inclination i, is only slightly less than

Parameter	Symbol	Model
Semi-major axis ($R_\odot$)	a	28.82 ± 0.18
Masses ($M_\odot$)	M_1	1.39 ± 0.04
	M_2	1.23 ± 0.03
Mass ratio	M_2/M_1	0.88 ± 0.01
COM velocity (km s^{-1})	V_0	39.55 ± 0.28
Angle of inclination (deg)	i	62.94 ± 0.69
Radii ($R_\odot$)	R_1	3.73 ± 0.02
	R_2	10.63 ± 0.02
Temperature (K)	T_1	3990 ± 10
	T_2	5721 ± 26
Period (d)	P	11.09
Kopal potentials	Ω_1	3.56 ± 0.01
	Ω_1	3.07 ± 0.02
Filling factor	$\mathscr{F}$	0.38

Table 10.5 Binary component parameters for J190114.

90°. The semi-major axis was estimated from the period as 20 $R_\odot$. The full model is shown in Figure 10.5.

J183357 was fit and optimised. Again, no third light source or spot was fitted. The output parameters are listed in Table 10.6 with the errors on the parameters being generated by PHOEBE. The best fit parameters indicate that J183357 is a low-mass-ratio semi-detached system comprised of 8.21 $R_\odot$ and 6.32 $R_\odot$ components, with a mass ratio, $q = M_2/M_1$ of 0.23.

1SWASPJ154828.29+201442.8

Based on the photometric light curves of J154828, it appears to be a system with equal minima and a triangular-like profile, hence this system is likely to be a near-contact or contact system with similar radii and temperature components.

To model this system, it was assumed that the system was either a semi-detached system with the primary star filling the Roche lobe or a contact system with both components filling their Roche lobes. Each type of system was modelled and the model which produced the

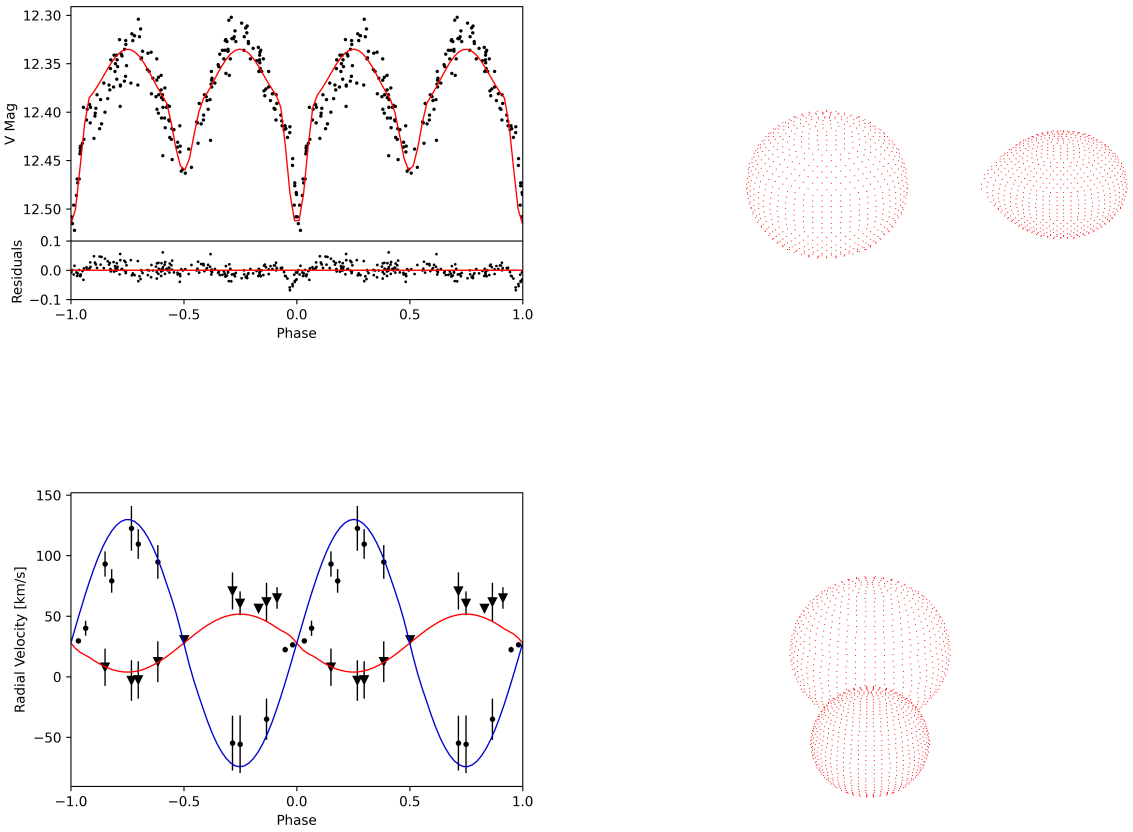

Fig. 10.5 Overview of J183357. **Top left:** SuperWASP V phase folded light curve fitted with PHOEBE model. **Top right:** Binary component model side view. **Bottom left:** Radial velocity curve fitted with PHOEBE model. **Bottom right:** Binary component model front view.

lowest χ^2 fit was chosen. The period was set to 7.47 d (the SuperWASP period), and the starting HJD to 2453854.00. SuperWASP data were binned, but ASAS-SN, PIRATE, and LCO data were not binned. The multicolour PIRATE and LCO light curves both provide sparse coverage, however were still used to constrain the temperatures of each component.

Radial velocities were inputted from the Liverpool Telescope. The temperature for each component was set at 4960 K, as found from spectral typing and synthesis. The smoothly varying minima implies that the angle of inclination, i, is significantly less than 90° so was set to 45°. The semi-major axis was estimated from the period as 20 $R_{\odot}$.

Parameter	Symbol	Model
Semi-major axis ($R_\odot$)	a	24.16 ± 0.82
Masses ($M_\odot$)	M_1	2.03 ± 0.22
	M_2	0.47 ± 0.05
Mass ratio	M_2/M_1	0.23 ± 0.00
COM velocity (km s^{-1})	V_0	27.76 ± 0.52
Angle of inclination (deg)	i	61.56 ± 0.08
Radii ($R_\odot$)	R_1	8.21 ± 0.29
	R_2	6.32 ± 0.22
Temperature (K)	T_1	5579 ± 38
	T_2	4983 ± 29
Period (d)	P	8.72
Kopal potentials	Ω_1	2.31 ± 0.02
	Ω_1	2.17 ± 0.03
Filling factor	$\mathscr{F}$	1.38

Table 10.6 Binary component parameters for J183357.

J154828 was fit using initial parameters and χ^2 minimisation. Again, no third light source or spot was fitted. Radial velocities were fitted as both contact and semi-detached systems, providing almost identical χ^2 values. Attempts to minimise χ^2 to decide between contact and semi-detached system were hampered by localised χ^2 minima. Similarly, fitting to the photometric light curves provided almost identical χ^2 values and provide only marginally better fits for the semi-detached system. The sparse coverage of the multicolour photometry meant that constraining temperatures of the components was hampered slightly, too. The full model is shown in Figure 10.6.

By a margin, the double contact system appears to be the best fit to the photometric light curves and radial velocity curve, however this classification should be used with caution. The output parameters are listed in Table 10.7 with the errors on the parameters being generated by PHOEBE. The best fit parameters indicate that 1SWASPJ154828 is comprised of 7.13 $R_\odot$ and 6.87 $R_\odot$ components, with a mass ratio, $q = M_2/M_1$ of 0.92.

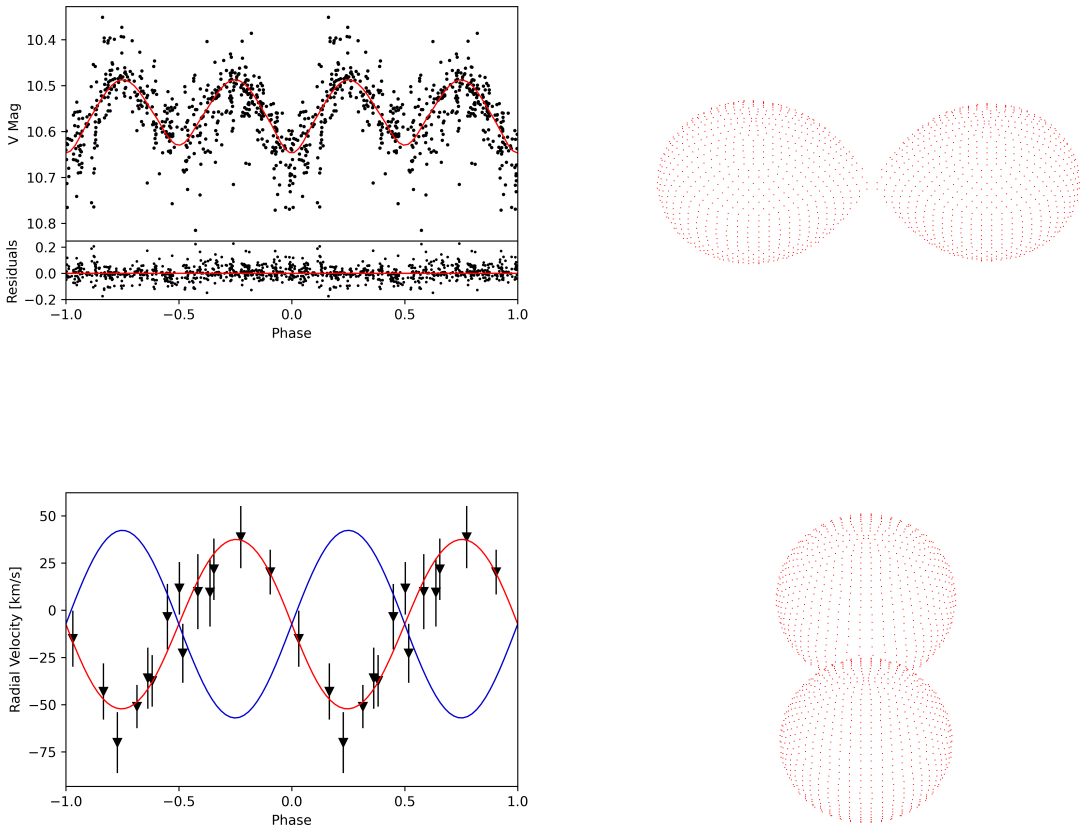

Fig. 10.6 Overview of J154828. **Top left:** SuperWASP V phase folded light curve fitted with PHOEBE model. **Top right:** Binary component model side view. **Bottom left:** Radial velocity curve fitted with PHOEBE model. **Bottom right:** Binary component model front view.

1SWASPJ132156.04-010742.8

J132156 is one of the best studied NCRGEB systems within this work, with photometric light curves from SuperWASP, ASAS-SN, Kepler, and BVR photometry from LCO. This system appears to have similar depth minima and maxima, implying components of similar size and temperature. The Kepler light curve indicates that the secondary must be smaller than the primary with a sharper decrease and increase in the eclipse. The extracted radial velocity curve does show significant variations on the same timescale as the SuperWASP period, however there are few data points which complicate the fitting process.

Parameter	Symbol	Model
Semi-major axis ($R_\odot$)	a	18.42 ± 0.36
Masses ($M_\odot$)	M_1	0.78 ± 0.08
	M_2	0.72 ± 0.07
Mass ratio	M_2/M_1	0.92 ± 0.07
COM velocity (km s^{-1})	V_0	-7.34 ± 0.68
Angle of inclination (deg)	i	51.01 ± 0.09
Radii ($R_\odot$)	R_1	7.13 ± 0.08
	R_2	6.87 ± 0.12
Temperature (K)	T_1	4581 ± 290
	T_2	4374 ± 186
Period (d)	P	7.47
Kopal potentials	Ω_1	3.63 ± 0.07
	Ω_1	3.12 ± 0.13
Filling factor	$\mathscr{F}$	1.11

Table 10.7 Binary component parameters for J154828.

This system was therefore assumed to be a semi-detached system with the primary star filling the Roche lobe. The period was set to 32.09 d (the SuperWASP period), and the starting HJD to 2453952.09. SuperWASP data were binned, but ASAS-SN, PIRATE and data were not. Radial velocities were inputted from SALT. The temperature for each component was set at 3980 K, as found from spectral typing and synthesis. The light curve indicates that the angle of inclination, i, is relatively high, and was initially set to 75°. The semi-major axis was estimated from the period as 50 $R_\odot$.

J132156 was fit in the same way, using initial parameters and χ^2 minimisation. No third light source or spot was fitted. The SuperWASP light curve contains significant noise, so the model was fitted primarily to the ASAS-SN light curve. The output parameters are listed in Table 10.8 with the errors on the parameters being generated by PHOEBE. The best fit parameters indicate that J132156 is a semi-detached binary with the primary star filling the Roche lobe, comprised of 16.06 $R_\odot$ and 12.09 $R_\odot$ components, with a mass ratio, $q = M_2/M_1$ of 1.07. Similarly, both components of the system are unusually low mass, which may be a

result of being able to constrain only one component through radial velocity measurements. The full model is shown in Figure 10.7.

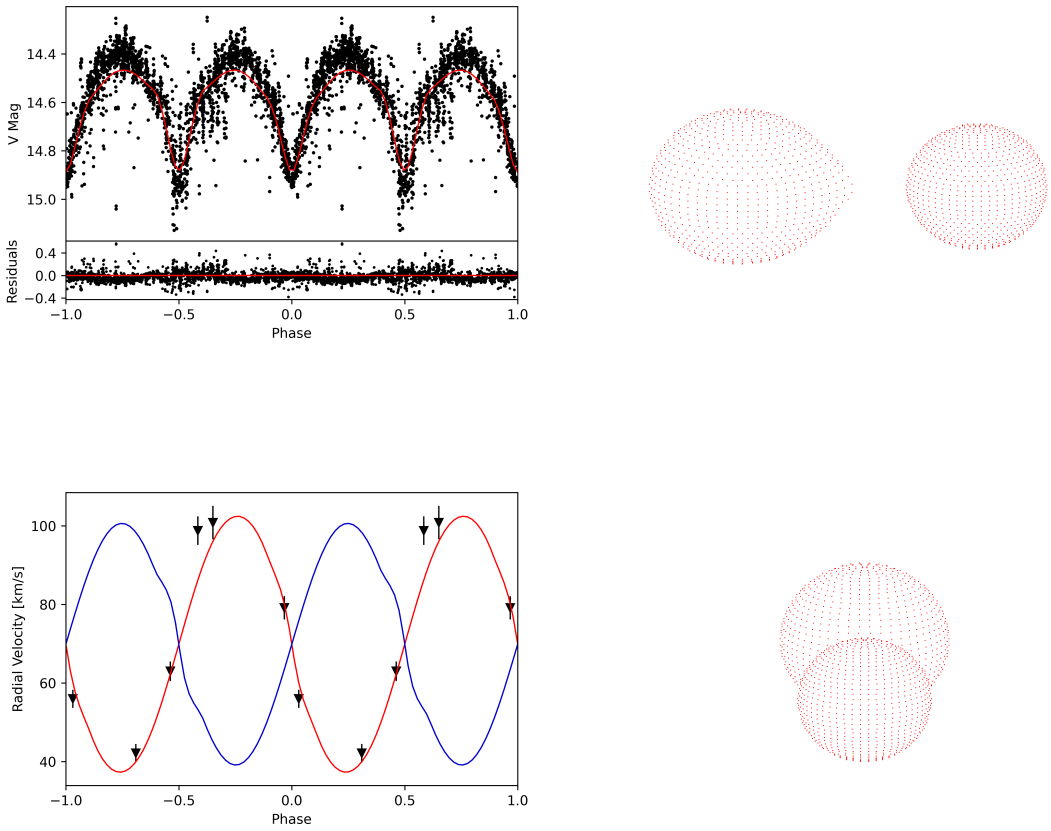

Fig. 10.7 Overview of J132156. **Top left:** SuperWASP V phase folded light curve fitted with `PHOEBE` model. **Top right:** Binary component model side view. **Bottom left:** Radial velocity curve fitted with `PHOEBE` model. **Bottom right:** Binary component model front view.

1SWASPJ093610.20-283847.2

J093610 is classified as rotator in VSX although the SuperWASP and ASAS-SN light curves show clear evidence of eclipses with a period of 4.92 d. Based on the photometric light curves, the target has one sharp, deep, eclipse, and a shallower eclipse, implying that the components differ slightly in radius and temperature. This system is likely to be semi-detached, however the modelled was severely hampered by the lack of good radial velocity follow-up.

Parameter	Symbol	Model
Semi-major axis ($R_\odot$)	a	42.92 ± 5.83
Masses ($M_\odot$)	M_1	0.50 ± 0.17
	M_2	0.53 ± 0.18
Mass ratio	M_2/M_1	1.07 ± 0.01
COM velocity (km s^{-1})	V_0	69.88 ± 2.44
Angle of inclination (deg)	i	74.28 ± 0.34
Radii ($R_\odot$)	R_1	16.06 ± 1.87
	R_2	12.09 ± 1.40
Temperature (K)	T_1	3646 ± 50
	T_2	3585 ± 42
Period (d)	P	32.10
Kopal potentials	Ω_1	3.86 ± 0.04
	Ω_1	3.31 ± 0.02
Filling factor	$\mathscr{F}$	0.84

Table 10.8 Binary component parameters for J132156.

To model this system, it was assumed that the system was a semi-detached system with the primary star filling the Roche lobe. The period was set to 4.92 d, and the starting HJD to 2466791.80. SuperWASP data were binned, but ASAS-SN and LCO data were not. The multicolour LCO data allows the temperature of the components to be constrained, however the coverage of the observations is low. Radial velocities were inputted from SALT, however the coverage is sparse and inconclusive. The lack of coverage means that constraining the masses of the components in the system is a challenge. The temperature for each component was set at 4320 K, as found from spectral typing and synthesis. Due to the sharp primary eclipse, the angle of inclination, i, was set at 70°. The semi-major axis was estimated from the period as 20 $R_\odot$.

J093610 was fit using initial parameters and χ^2 minimisation. Again, no third light source or spot was fitted, however the ASAS-SN light curve appears to show maxima with a difference of $\sim$0.025 Vmag. The output parameters are listed in Table 10.9 with the errors on the parameters being generated by PHOEBE. The best fit parameters indicate that J093610 is a semi-detached system comprised of 5.06 $R_\odot$ and 2.58 $R_\odot$ components, with a mass ratio,

$q = M_2/M_1$ of 0.97. Unusually, this system comprises extremely low mass components, close to the minimum mass limit for a red giant system. Similarly, the radii of the components are low for a red giant system. This is likely not to be a result of a physical configuration, but due to the lack of good radial velocity coverage, and the true masses and radii are likely to be significantly greater. The full model is shown in Figure 10.8.

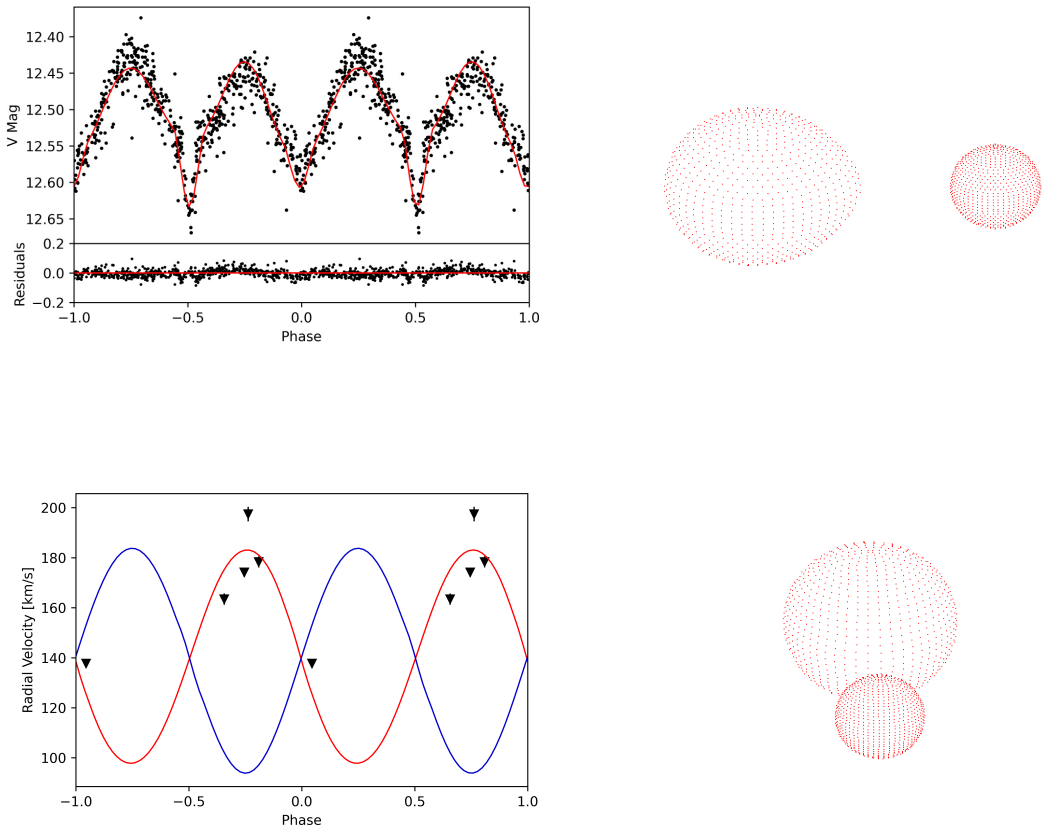

Fig. 10.8 Overview of J093610. **Top left:** SuperWASP V phase folded light curve fitted with PHOEBE model. **Top right:** Binary component model side view. **Bottom left:** Radial velocity curve fitted with PHOEBE model. **Bottom right:** Binary component model front view.

1SWASPJ035259.67+091717.1

J035259 is a system with near-equal minima and maxima, so this target was modelled as a near-contact system with similar temperature, with the primary star filling the Roche lobe.

Parameter	Symbol	Model
Semi-major axis ($R_\odot$)	a	13.43 ± 0.30
Masses ($M_\odot$)	M_1	0.35 ± 0.03
	M_2	0.33 ± 0.03
Mass ratio	M_2/M_1	0.97 ± 0.02
COM velocity (km s^{-1})	V_0	139.69 ± 0.17
Angle of inclination (deg)	i	64.81 ± 1.60
Radii ($R_\odot$)	R_1	5.06 ± 0.02
	R_2	2.57 ± 0.05
Temperature (K)	T_1	3872 ± 176
	T_2	4110 ± 265
Period (d)	P	4.92
Kopal potentials	Ω_1	3.75 ± 0.03
	Ω_1	3.17 ± 0.04
Filling factor	$\mathscr{F}$	1.07

Table 10.9 Binary component parameters for J093610.

The secondary eclipse is narrower than the primary, implying that the angle of inclination is relatively high and one component has a significantly smaller radius than the other.

The period was set to 24.10 d (the SuperWASP period), and the starting HJD to 2454162.31. SuperWASP data were binned, but ASAS-SN, PIRATE, and LCO data were not. PIRATE data have provided good multicolour phase coverage and LCO has provided good phase coverage in the B filter. Radial velocities were inputted from the Liverpool Telescope and the 74″, and provides excellent phase coverage. The temperature for each component was set at 3980 K, as found from spectral typing and synthesis. The angle of inclination, i, was set to 75°, and the semi-major axis was estimated from the period as 55 $R_\odot$.

J035259 was fit using the initial parameters and χ^2 minimisation. Again, no third light source or spot was fitted. The fit is generally good, although the B filter light curves show the greatest residuals. It is likely that the temperature of the secondary component could have fallen within a local χ^2 minima. The output parameters are listed in Table 10.10 with the errors on the parameters being generated by PHOEBE. The best fit parameters indicate that

J035259 is comprised of 25.45 $R_\odot$ and 14.72 $R_\odot$ components, with a mass ratio, $q = M_2/M_1$ of 1.03. The full model is shown in Figure 10.9.

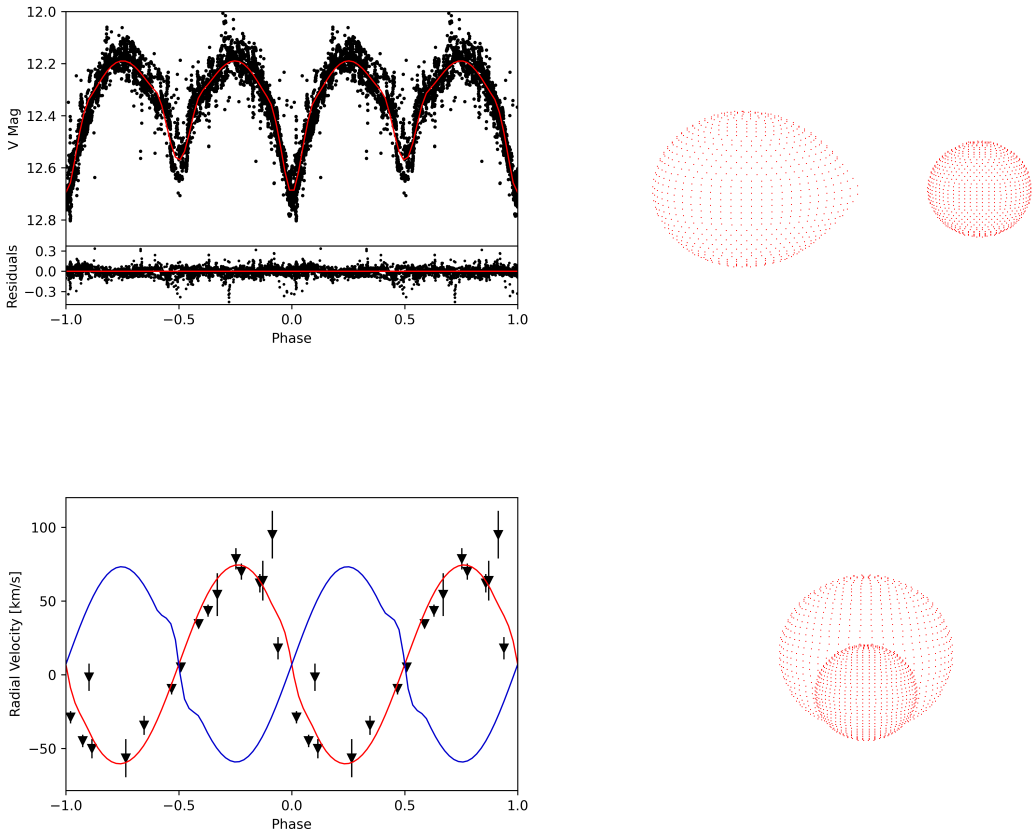

Fig. 10.9 Overview of J035259. **Top left:** SuperWASP V phase folded light curve fitted with `PHOEBE` model. **Top right:** Binary component model side view. **Bottom left:** Radial velocity curve fitted with `PHOEBE` model. **Bottom right:** Binary component model front view.

1SWASPJ003544.75+495450.0

J003544 is a system with a sharp eclipse and slightly deeper minima, which implies that it is either a system with different radii components or a system with a high angle of inclination.

To model this system, it was assumed that the system was a semi-detached system with the secondary star filling the Roche lobe. The period was set to 17.86 d, and the starting HJD to 2453225.80. SuperWASP data were binned, but PIRATE was not. There is no ASAS-SN

Parameter	Symbol	Model
Semi-major axis ($R_\odot$)	a	67.39 ± 1.46
Masses ($M_\odot$)	M_1	3.36 ± 0.23
	M_2	3.45 ± 0.23
Mass ratio	M_2/M_1	1.03 ± 0.01
COM velocity (km s^{-1})	V_0	7.03 ± 0.91
Angle of inclination (deg)	i	79.06 ± 0.11
Radii ($R_\odot$)	R_1	25.45 ± 0.55
	R_2	14.72 ± 0.32
Temperature (K)	T_1	3599 ± 5
	T_2	3484 ± 5
Period (d)	P	24.61
Kopal potentials	Ω_1	3.79 ± 0.03
	Ω_1	3.25 ± 0.03
Filling factor	$\mathscr{F}$	1.06

Table 10.10 Binary component parameters for J035259

data for this system, but the multicolour PIRATE data provides good phase coverage. Radial velocities were inputted from the Liverpool Telescope and similarly provide a good phase coverage. The temperature for each component was set at 4960 K, as found from spectral typing and synthesis. The angle of inclination, i, was estimated as 70°, and the semi-major axis was estimated from the period as 50 $R_\odot$.

J003544 was fit using initial parameters and χ^2 minimisation, and no third light source or spot was fitted. The output parameters are listed in Table 10.11 with the errors on the parameters being generated by PHOEBE. The best fit parameters indicate that J003544 is comprised of 14.81 $R_\odot$ and 21.09 $R_\odot$ components, with a mass ratio, $q = M_2/M_1$ of 1.13. Table 10.11 lists the parameters of the physically semi-detached system, however it is clear from the fitted light curve that fitting for the primary is not perfect. The full model is shown in Figure 10.10.

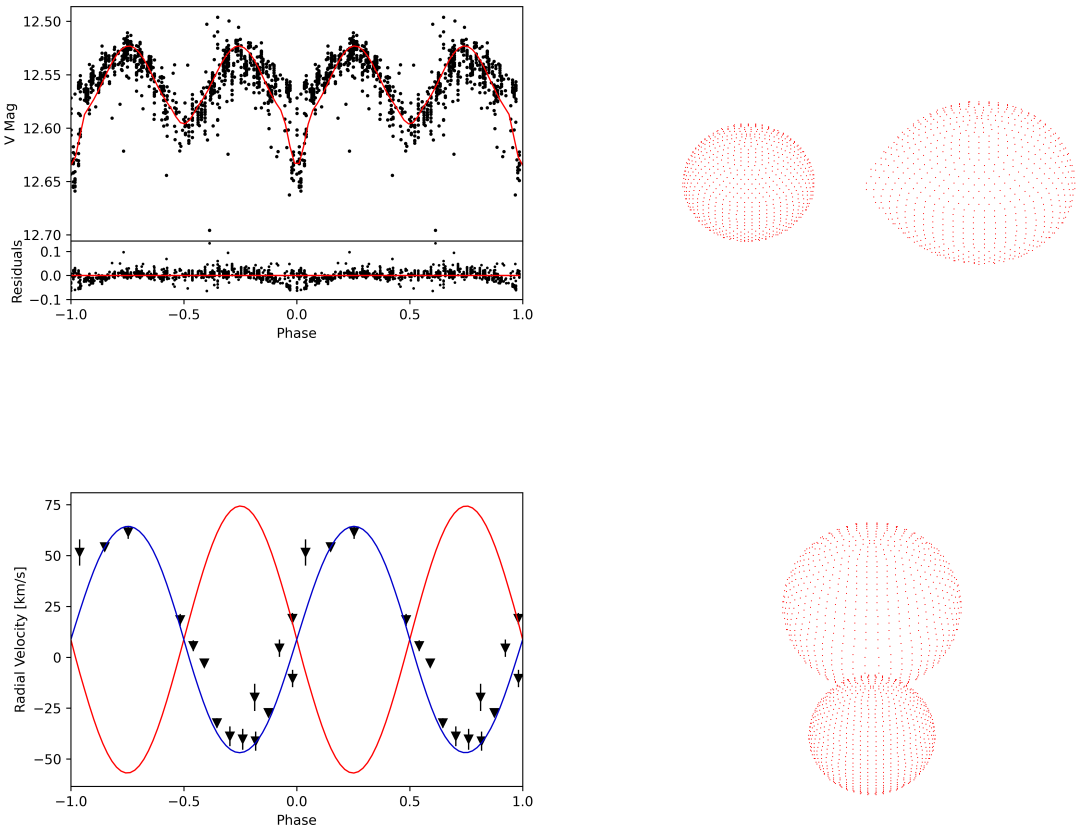

Fig. 10.10 Overview of J003544. **Top left:** SuperWASP V phase folded light curve fitted with PHOEBE model. **Top right:** Binary component model side view. **Bottom left:** Radial velocity curve fitted with PHOEBE model. **Bottom right:** Binary component model front view.

1SWASPJ002952.96+475034.3

Based on the photometric light curves of J002952, it appears to be a system with components of significantly different radius. The minima are smoothly varying which implies that a smaller component is only grazing the edge of the larger component, and the maxima are of an equal height. This system is possibly comprised of a giant and a sub-giant.

To model this system, similar to many other systems previously, it was assumed that the system was a semi-detached system with the primary star filling the Roche lobe. The period was set to 20.33 d, and the starting HJD to 2456621.00. SuperWASP data were binned, but

Parameter	Symbol	Model
Semi-major axis ($R_\odot$)	a	54.01 ± 0.09
Masses ($M_\odot$)	M_1	3.12 ± 0.04
	M_2	3.52 ± 0.04
Mass ratio	M_2/M_1	1.13 ± 0.01
COM velocity (km s^{-1})	V_0	8.73 ± 0.68
Angle of inclination (deg)	i	54.49 ± 1.68
Radii ($R_\odot$)	R_1	14.81 ± 0.07
	R_2	21.09 ± 0.09
Temperature (K)	T_1	4766 ± 16
	T_2	3907 ± 9
Period (d)	P	17.86
Kopal potentials	Ω_1	3.96 ± 0.02
	Ω_1	3.40 ± 0.01
Filling factor	$\mathscr{F}$	0.75

Table 10.11 Binary component parameters for J003544.

ASAS-SN and PIRATE was not. The ASAS-SN object was identified as a non-periodic variable, and the phase-folded light curve was noisy, to the data were not used in modelling. Radial velocities were inputted from the Liverpool Telescope and provide full phase coverage. The temperature for each component was set at 4810 K, as found from spectral typing and synthesis. The angle of inclination, i, was set to 70°. The semi-major axis was estimated from the period as 30 $R_\odot$.

Using initial parameters and χ^2 minimisation, J002952 was fit. No third light source or spot was fitted. The output parameters are listed in Table 10.12 with the errors on the parameters being generated by PHOEBE. The best fit parameters indicate that J002952 is a semi-detached system with the primary star filling its Roche lobe, comprised of 0.68 $R_\odot$ and 0.58 $R_\odot$ components, with a mass ratio, $q = M_2/M_1$ of 0.86. Again, this system has a relatively low mass, especially for the inflated primary, but it is not physically unrealistic. The full model is shown in Figure 10.11.

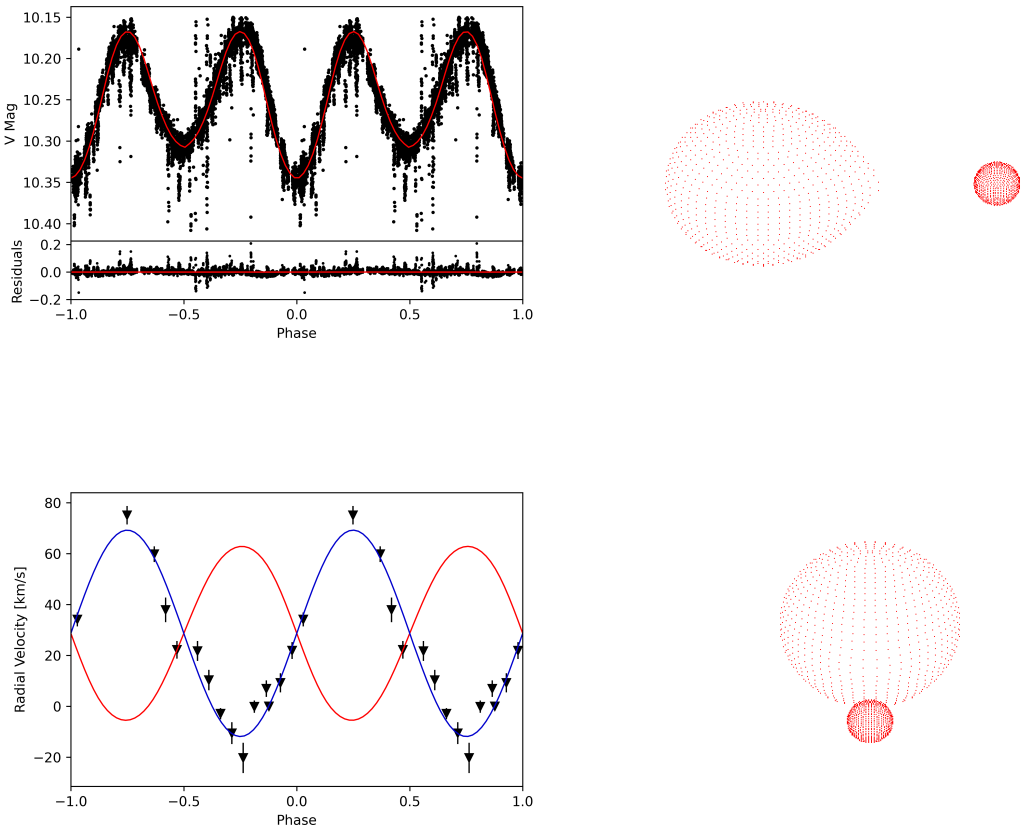

Fig. 10.11 Overview of J002952. **Top left:** SuperWASP V phase folded light curve fitted with PHOEBE model. **Top right:** Binary component model side view. **Bottom left:** Radial velocity curve fitted with PHOEBE model. **Bottom right:** Binary component model front view.

1SWASPJ001521.76+472055.2

J001521 was the target that started this path of research, and has the most convincing photometric light curves, but it has proved the most difficult to model. Based on the photometric light curves of J001521, it appears to be a system with semi-detached components, likely to be of a similar radii and temperature. The angle of inclination is likely to be high, since the minima are sharp but smooth. However, the extracted radial velocities were inconclusive and have complicated the modelling of the system.

Parameter	Symbol	Model
Semi-major axis ($R_\odot$)	a	33.83 ± 1.33
Masses ($M_\odot$)	M_1	0.68 ± 0.11
	M_2	0.58 ± 0.09
Mass ratio	M_2/M_1	0.86 ± 0.08
COM velocity (km s^{-1})	V_0	28.70 ± 0.17
Angle of inclination (deg)	i	64.07 ± 1.00
Radii ($R_\odot$)	R_1	13.30 ± 0.44
	R_2	3.32 ± 0.32
Temperature (K)	T_1	4863 ± 258
	T_2	4747 ± 242
Period (d)	P	20.33
Kopal potentials	Ω_1	3.52 ± 0.17
	Ω_1	3.04 ± 0.12
Filling factor	$\mathscr{F}$	1.15

Table 10.12 Binary component parameters for J002952.

To model this system, it was assumed that the system was a semi-detached system with the primary star filling the Roche lobe. The period was set to 41.20 d (the SuperWASP period), and the starting HJD to 2456640.21. As usual, the SuperWASP data were binned, but ASAS-SN and PIRATE data were not. Radial velocities were inputted from the Liverpool Telescope, however the phase coverage is poor and the radial velocity curve is such that the range of semi-major axis values is extremely wide. The temperature for each component was set at 4810 K, as found from spectral typing and synthesis. The angle of inclination, i, was set at 60°. The semi-major axis was estimated from the period as 55 $R_\odot$.

Assuming that the system was a semi-detached one, standard fitting was done using initial parameters and χ^2 minimisation. No third light source or spot was fitted. The first best fitting model for J001521 produced a physically unrealistic system with masses of each component being only $\sim$0.2 $M_\odot$, on the very low mass end of the range for a red giant star. Modelling for a range of semi-major axis values of $\sim$19–52 $R_\odot$ all minimise χ^2, indicating that the modelling may have been hampered by the presence of local χ^2 minima. The lowest value of $\sim$19 $R_\odot$ gives the most physically unrealistic mass value, with components of masses of

$\sim$0.03 $M_\odot$ and radii of $\sim$6 $R_\odot$, whilst the greatest value of $\sim$52 $R_\odot$ gives a more physically realistic components with masses of $\sim$0.6 $M_\odot$ and radii of $\sim$18 $R_\odot$. The full model is shown in Figure 10.12.

However, modelling the system as a contact system produced much better results which fit the radial velocity curve, although not necessarily more physically realistic, and with significant uncertainties. Modelling as a contact system with a low mass ratio and high semi-major axis produces components which are vastly inflated (up to $\sim$27 $R_\odot$ with only a mass of 0.9 $M_\odot$). Assuming such a system is real, it is unusual that only the less massive component was detected in the spectra. However, to achieve this model, the uncertainties on the system are almost are on the order of some of the values themselves, indicating that this really is a poor fit and J001521 is unlikely to be a true NCRGEB system.

Unfortunately, accurately modelling this system would require further spectroscopy of J001521, which is outside the time constraints of this research. Therefore, the output parameters for the best fitting model are listed in Table 10.13 with the errors on the parameters being generated by `PHOEBE`. The best fit parameters indicate that J001521 is a contact system comprised of 26.67 $R_\odot$ and 12.66 $R_\odot$ components, with a mass ratio, q=0.20. However, these parameters should be used with caution.

10.1.2 Discussion

The binary components of each of the 12 NCRGEB candidates have been modelled using `PHOEBE`. Through this modelling, I have confirmed that the 12 of the 27 systems originally identified as binaries are NCRGEB systems. For each NCRGEB model, star spots were not included due to a lack of direct evidence, however for certain objects where the maxima differ in height (e.g. J093610), the model could be improved by the inclusion of a spot.

It is also worth noting that despite best efforts, a number of the models are likely to be hampered by local χ^2 minima fitting, particularly those with poor radial velocity curves, in

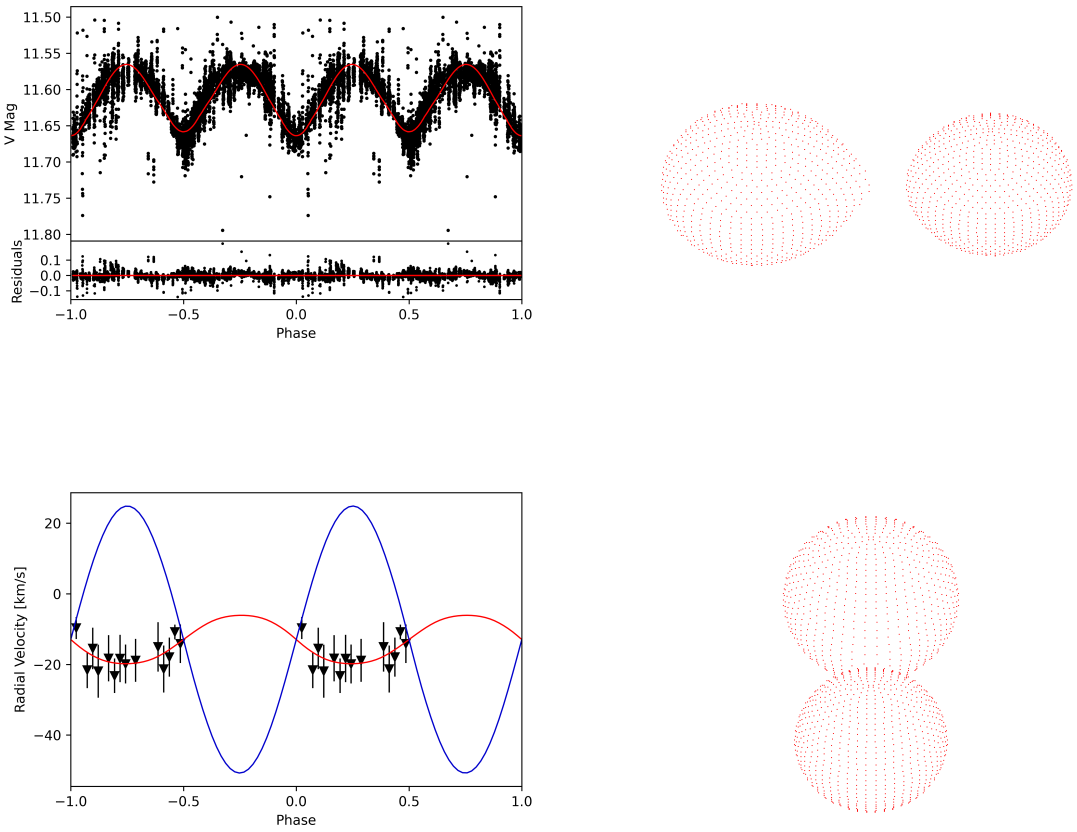

Fig. 10.12 Overview of J001521. **Top left:** SuperWASP V phase folded light curve fitted with PHOEBE model. **Top right:** Binary component model side view. **Bottom left:** Radial velocity curve fitted with PHOEBE model. **Bottom right:** Binary component model front view.

which the 'brute force' modelling finds the local minima rather than the global minima. The result of this is that the models found here may be "best estimates" rather than exact models, and some modelled parameters may differ from the true physical system. To fully counter this local minima issue and increase the reliability of the parameters, there are two options: either Markov chain Monte Carlo (MCMC) fitting could be used, or further photometric and spectroscopic observations could be taken, however both options now lie outside the timeframe of this work. Although completing a full MCMC analysis for each model was

Parameter	Symbol	Model
Semi-major axis ($R_\odot$)	a	50.79 ± 42.78
Masses ($M_\odot$)	M_1	0.87 ± 2.40
	M_2	0.17 ± 0.45
Mass ratio	M_2/M_1	0.20 ± 0.18
COM velocity (km s^{-1})	V_0	-12.95 ± 0.61
Angle of inclination (deg)	i	47.61 ± 24.19
Radii ($R_\odot$)	R_1	26.67 ± 2.92
	R_2	12.66 ± 2.46
Temperature (K)	T_1	5813 ± 351
	T_2	5637 ± 428
Period (d)	P	41.20
Kopal potentials	Ω_1	2.22 ± 0.40
	Ω_1	2.10 ± 0.29
Filling factor	$\mathscr{F}$	2.18

Table 10.13 Binary component parameters for J001521.

not possible, models which did appear to be obviously affected by minima were extensively tested and only the best fitting models are presented here.

What is the most interesting is that many of these binaries are low mass systems with high filling factors, with the least massive being comprised of components of only 0.17 $M_\odot$ and 0.87 $M_\odot$, but with inflated radii of 27 $R_\odot$ and 13$R_\odot$. Of the 12 NCRGEB, 5 are comprised of components with unusually low total masses: J002952 (1.26 $M_\odot$), J001521 (1.04 $M_\odot$), J093610 (0.68 $M_\odot$), J132156 (1.03 $M_\odot$), J154828 (1.5 $M_\odot$), whilst the remaining 7 are significantly more massive systems. Whilst these low mass systems are not all physically unrealistic, since red giants can have masses as low as 0.3 $M_\odot$ (and up to $\sim$8 $M_\odot$), it begs the question *are these systems massive enough to experience an energetic and explosive merger event, such as a red nova?*

The likely solution to the low mass component issue is not necessarily that the systems *are* low mass, but that they *appear* to be low mass. Of the 12 NCRGEB modelled, only 1 showed binary line splitting in the observed spectra due to the blending of the components in the spectra. The remaining 11 show periodic variations in line intensity and equivalent width

with the binary period, but without the binary line splitting, it was not possible to extract radial velocities for both components. This means that is has not been possible to constrain the masses of the unseen component, and this implies that the system mass is actually greater than what is modelled.

Of particular interest is J001521. Despite it being the binary system which started this path of research, the extracted radial velocity and subsequent model only barely provide evidence that this system is a NCRGEB. This system can be modelled as two low mass components with highly inflated radii. However, J001521 is unlikely to be a physically realistic model, and may be due to the lack of good quality spectra and subsequent radial velocity extraction. Instead, it is assumed that J001521, is actually a pulsating variable.

However, this modelling does not answer questions about the evolution and future of NCRGEB systems, and we do not yet understand how such systems form and what their end-of-life might look like. We cannot yet answer the question on whether NCRGEB are the progenitors of red novae. To do this, stellar and binary evolution modelling is needed, and the methods for angular momentum loss need to be understood more fully.

10.2 Angular momentum loss and the merger event

Angular momentum loss drives mergers, and this process can be measured by identifying period change within a binary system. Period change can occur through a number of different physical interactions which take place in contact and near-contact binary systems. In the case of giant binaries, and NCRGEB, period decrease might indicate a contact binary approaching merger, or a semi-detached binary experiencing unstable mass transfer which is likely to end with a merger event. Taking the V1309 Sco outburst contact binary progenitor as a baseline for red novae systems, the period decrease experienced by the binary would have been 0.3 s yr^{-1} about 130 years before the outburst and merger (Lohr et al., 2012). If any period change

for NCRGEB is detected with a similar order of magnitude, it is not unreasonable to assume that one or more of the NCRGEB may merge within decades or centuries.

In binary systems, mass loss is primarily driven by the mass transfer experienced in Roche-lobe overflow. As the photosphere of the primary expands to beyond the inner Lagrange point, it begins to exchange mass with the secondary, which in turn shifts the centre of mass towards the secondary. If the mass is transferred from the primary to the less massive secondary, conservation of angular momentum means that period decrease occurs. If the reverse happens, period increase occurs. Mass loss can also occur through stellar winds, which can cause period increase. In massive O-type stars, Sana et al. (2012) found that over 70% exchanged mass with their lower mass companion, and Kim et al. (2003) found that period change is common for short period contact binary systems, with 46% of binaries in Kreiner et al. (2001) showing evidence for this.

Based on the knowledge that contact and semi-detached systems commonly experience period change and mass loss, we therefore would expect these NCRGEB systems to also experience some form of period change and angular momentum loss. Given the extended envelopes of red giants, and the proximity of the binary components to one another, they ought to be interacting, at least for the closest systems.

Theoretical predictions of merger timescales can be made using known equations of angular momentum loss. The four main methods of angular momentum loss are mass transfer, gravitational wave radiation, tidal instabilities, and magnetic braking. For close systems, mass transfer is likely to be the main cause for period change and angular momentum loss. Mechanisms for unstable mass transfer and loss causing rapid period decrease and inspiralling for contact and near-contact binaries are discussed in Rasio (1995), Tylenda et al. (2011), and Jiang et al. (2012). Hilditch (2001) gives equations for period change from conservative and non-conservative mass transfer driven by, for example, magnetic braking or GWR, respectively, as:

$$\frac{\dot{P}}{P} = \frac{3\dot{M}_1(M_1 - M_2)}{M_1 M_2} \tag{10.4}$$

$$\frac{\dot{P}}{P} = 3\dot{M}_1 \left[\frac{(M_1 + M_2)}{M_1 M_2} \frac{d^2}{a^2} - \frac{M_2}{M_1(M_1 + M_2)} \right], \tag{10.5}$$

where $\dot{M}$=10^{-6} $M_\odot \mathrm{yr}^{-1}$, P_{orb} is the orbital period in days, M_1, M_2 are the masses of the components in solar units, a is the semi-major axis in solar radii, and d is the distance from the binary centre of mass to the Lagrange point L_2. These equations should be taken as best estimates, since the value of $\dot{M}$ is approximated as 10^{-6} $M_\odot \mathrm{yr}^{-1}$ for the sake of this work. This approximation is taken from Lohr (2015) and Hilditch (2001), who find $\dot{M}$=10^{-6}–10^{-7} $M_\odot \mathrm{yr}^{-1}$ for a range of contact binary systems, however it should be recognised that $\dot{M}$ will vary from system to system and depends on factors such as the dominant mechanism behind the angular momentum loss. The result of the best estimate value is that period change may be overestimated by a factor of 10 for some systems. In order to better constrain $\dot{M}$, the period change $\frac{\dot{P}}{P}$ would need to be known, or further evolutionary modelling would be required.

Gravitational wave radiation also causes angular momentum loss, but it likely contributes very little to overall angular momentum loss for the system. Following the method from Lohr (2015), the equations from Kolb (2010) and Hilditch (2001) can be combined to calculate the period change due to gravitational wave radiation for the system:

$$\frac{\dot{P}}{P} = 3\frac{\dot{J}}{J} = -1.27 \times 10^{-8} \mathrm{yr}^{-1} \frac{M_1 M_2}{(M_1 + M_2)^{1/3} M_\odot^{\frac{5}{3}}} \left(\frac{P_{\mathrm{orb}}}{h}\right)^{-8/3}, \tag{10.6}$$

where the terms are the same as above.

Tidal instabilities (e.g. Rasio (1995)) cause binaries to experience a merger on a relatively short timescale of only $t_D \sim 10^3 - 10^4$yr for an unstable contact W UMa system. For NCRGEB systems, especially the very near contact systems, tidal instabilities are likely to be a significant cause of orbital circularisation and merger.

Another method for period decrease and the removal of angular momentum from the binary system, is magnetic braking. This can be estimated using equations for angular momentum loss from Guinan and Bradstreet (1988), however, since this equation is only correct for detached systems where the magnetic fields are stronger, the values found are likely to be a significant overestimation for NCRGEB. The gyration constant, k^2, is taken as 0.1 (Bradstreet and Guinan, 1994), and the usual constants apply. It is possible that k^2 is an underestimate, since the gyration constant first decreases beyond ZAMS, and then increases to a maximum of 0.22 for the upturn of the Asymptotic Giant Branch (Schrijver and Zwaan, 2000) The equation for period change from magnetic braking is as follows:

$$\dot{P} \approx -1.1 \times 10^{-8} q^{-1} (1+q)^2 (M_1 + M_2)^{-\frac{5}{3}} k^2 (M_1 R_1^4 + M_2 R_2^4) P^{-\frac{7}{3}}, \qquad (10.7)$$

where P is the orbital period in days, q is the mass ratio, R_1, R_2 are the radii of the components in solar radii, k^2 is the gyration constant taken as 0.1, and the other terms are the same as above.

Taking the equations above, it is possible to estimate the timescales over which each form of angular momentum loss occurs, and deduce which form is likely to have the strongest influence on NCRGEB systems. The results of this estimation can be found in Table 10.14. J001521, despite being the most unlikely NCRGEB candidate, is included for continuity and comparison.

If we take into account that tidal instabilities operate over a timescale of $t_D \sim 10^3 - 10^4$yr, all other forms of mass transfer and period decrease actually appear to be contributing equally (or to within only an order or magnitude or two). We can make an estimate of merger time by simply taking the greatest contributor to period decrease and the current observed period (again, ignoring the effects of tidal instabilities). The greatest contributor is undoubtedly mass transfer, both conservative or non-conservative, with smaller contributions from magnetic braking and gravitational wave radiation. Since each system is a contact or semi-detached

system, this form of period decrease is to be expected. This estimate finds that a merger could be expected on the order of 0.005–29 Myr, roughly on similar timescales to the effects of tidal instabilities. Of course, this only takes into account one form of period decrease, and if we consider tidal instabilities, merger times for contact and semi-detached systems may be considerably shorter. Therefore, whilst these results provide a good estimate for merger time, further modelling will be able to provide analytic timescales for comparison.

WASP ID	Period (d)	M_1 ($M_\odot$)	M_2 ($M_\odot$)	q (M_2/M_1)	R_1 ($R_\odot$)	R_2 ($R_\odot$)	a ($R_\odot$)	Magnetic braking $\frac{\dot{P}}{P}$ (yr^{-1})	GWR $\frac{\dot{P}}{P}$ (yr^{-1})	Conservative $\frac{\dot{P}}{P}$ (yr^{-1})	Non-conservative $\frac{\dot{P}}{P}$ (yr^{-1})
1SWASPJ231800	23.84	0.84	1.02	1.21	15.50	4.12	42.79	-4.71×10^{-8}	-1.13×10^{-12}	-6.30×10^{-7}	-4.90×10^{-8}
1SWASPJ204317	4.92	3.17	1.47	0.46	5.49	6.38	20.29	-5.08×10^{-8}	-3.04×10^{-10}	1.09×10^{-6}	2.15×10^{-7}
1SWASPJ194231	23.18	1.49	1.29	0.87	10.46	17.63	48.30	-7.48×10^{-8}	-2.39×10^{-12}	3.12×10^{-7}	-1.75×10^{-7}
1SWASPJ190114	11.09	1.39	1.23	0.88	3.73	10.63	28.82	-5.16×10^{-8}	-1.54×10^{-11}	2.81×10^{-7}	1.44×10^{-7}
1SWASPJ183357	8.72	2.03	0.47	0.23	8.21	6.32	23.88	-9.98×10^{-8}	-1.66×10^{-11}	4.91×10^{-6}	9.27×10^{-7}
1SWASPJ154828	7.47	0.78	0.72	0.92	7.13	6.87	18.42	-7.44×10^{-8}	-1.75×10^{-11}	3.21×10^{-7}	-1.38×10^{-6}
1SWASPJ132156	32.09	0.50	0.53	1.06	16.06	12.09	53.13	-5.71×10^{-8}	-1.92×10^{-13}	-3.40×10^{-7}	-5.10×10^{-7}
1SWASPJ093610	6.92	0.35	0.33	0.97	5.06	2.57	13.43	-2.24×10^{-8}	-5.76×10^{-12}	5.19×10^{-7}	-8.65×10^{-7}
1SWASPJ035259	24.61	3.36	3.45	1.03	25.45	14.72	67.39	-1.61×10^{-7}	-9.10×10^{-12}	-2.33×10^{-8}	-1.65×10^{-7}
1SWASPJ003544	17.86	3.12	3.52	1.13	14.81	21.09	54.01	-1.91×10^{-7}	-2.04×10^{-11}	-1.09×10^{-7}	-3.06×10^{-7}
1SWASPJ002952	20.33	0.68	0.58	0.86	13.30	3.32	33.83	-5.70×10^{-8}	-9.04×10^{-13}	7.61×10^{-7}	4.50×10^{-7}
1SWASPJ001521	41.20	0.87	0.17	0.20	26.67	12.66	50.79	-5.63×10^{-7}	-5.49×10^{-14}	1.42×10^{-5}	5.10×10^{-7}

Table 10.14 Summary of expected timescales for angular momentum loss via magnetic braking, gravitational wave radiation, mass transfer, and tidal instabilities.

10.3 Evolutionary Modelling

Stellar evolution models allow astronomers to calculate stellar evolution tracks and map the evolution of internal and global stellar properties. The field of binary stars depends on highly accurate and detailed stellar evolution models to be able to determine formation mechanisms and end-of-life stellar processes. In order to characterise the evolution of NCRGEB and understand whether they may be the progenitors of red novae, binary evolution modelling is required.

To this end, a range of programmes were used to evolve the NCRGEB systems. `BiSEPS`, `BiSEC`, and `binary_c`, binary evolution models, were originally used to attempt to evolve the systems, however it was found that they could not provide the time steps necessary. In order to improve on the granularity of the model, `MESA`, a 1D stellar evolution code was used to build on the results from the three previous models, and investigate the evolution in more detail. In this section I briefly detail the relevant stellar evolution background, where necessary, and detail the modelling attempts made to characterise the evolutionary pathways of NCRGEB systems. I then discuss the results of this evolution, and note other programs which could be used to improve and build on the work done here.

10.3.1 Evolutionary modelling with `BiSEPS` and `BiSEC`

The Binary and Stellar Evolution Population Synthesis (`BiSEPS`) code (Willems & Kolb (Farmer et al. 2013; Willems and Kolb 2004; Willems et al. 2006, 2002) is a binary evolution tool. `BiSEPS` uses libraries of single and binary stellar models with different metallicities, created using simplified algorithms based on the analytical descriptions of binary and stellar evolution by Hurley et al. (2002).

Starting with a binary system with components of a given mass, `BiSEPS` can produce an evolutionary sequence of models from ZAMS to compact remnant. With the basis of the code being the Binary Star Evolution (BSE) models of Hurley et al. (2002), `BiSEPS` takes

a number of physical processes are taken into account, including Roche-lobe overflow and stellar winds (which causes mass transfer and mass loss), magnetic and gravitational braking (which decreases separation), tidal effects (which circularises the orbit).

Each sequence of evolutionary models contains physical parameters about the period, mass, radius, effective temperature, luminosity, metallicity, and the starting and ending age of the system over which each model is consistent. `BiSEPS` also outputs the mass transfer (if it has occurred) and the evolutionary status of each component over each time step. `BiSEPS` can also model single stars, but this is not relevant to the modelling for NCRGEB.

`BiSEPS` has previously been used to characterise the false positive rate of exoplanet transits from shallow eclipsing binaries in the early SuperWASP project Willems et al. (2006), but has since been used to detect asteroseismic binaries in Kepler data (Miglio et al., 2014) and PLATO (Rowden, 2019), and the effects of circumbinary discs on angular momentum loss (Willems et al., 2005), magnetic braking in post common envelope eclipsing binaries (Davis et al., 2010), and stellar population studies (Farmer et al., 2013) to name a few. Full details of how the `BiSEPS` code works can be found in the studies referenced here.

For the first attempt at modelling the binary evolution, `BiSEPS` was used (John Bray, private communications). A NCRGEB was selected for detailed analysis, the parameters are listed in Table 10.15, and the master list of models at Z=0.02 was searched for the best matching models, based on the radii and masses of each of the components, as well as the period and mass ratio. It was found that there was only one model that was close to matching the given parameters, with a period of 32.10 d and q=0.94, and this model was fully evolved using `BiSEPS`.

The closest matching model found that the system begins its evolution with solar mass main sequence components with an initial long period of $\sim$45 years which persists through much of the binary's life, lasting for an incredibly long $\sim$13.9 Gyr. As the binary components evolved to red giants and the separation increases, a common envelope develops and then,

	Observation NCRGEB	Start BiSEPS	Pre-inspiral BiSEPS	End-of-life BiSEPS	BiSEC
Time / Gyr	-	0	13.75	13.91	13.91
Period / d	32.10	16440.70	16557.44	16.51	16.50
R_1 / $R_\odot$	16.06	0.90	6.33	0.018	-
R_2 / $R_\odot$	12.09	0.90	6.02	0.019	-
a / $R_\odot$	42.92	3388.17	3400.16	2.66	-
M_1 / $M_\odot$	0.50	0.97	0.96	0.30	0.30
M_2 / $M_\odot$	0.53	0.97	0.96	0.26	0.26
q	0.94	1.00	1.00	0.88	0.88
$T_{\rm eff,1}$ / K	3646	5586	4654	23251	-
$T_{\rm eff,2}$ / K	3585	5585	4685	21924	-
Evolution	RG, RG	MS, MS	RG, RG	WD, WD	He WD, He WD
Formation	Semi-detached	Detached	Contact	Detached	Detached

Table 10.15 Input and output parameters of BiSEPS and BiSEC.

as expected, the period reduces rapidly during an in-spiralling event. In this model, the in-spiralling event takes 0.07 Gyr starting at ∼13.89 Gyr. Following a common envelope event, the remnants of the system are white dwarfs with masses ∼0.26–0.30 $M_\odot$, and radii of 0.018–0.019 $R_\odot$. The output of the model can be seen in Table 10.15. The graphical outputs are shown for period change (Figure 10.13 and Figure 10.14), mass (Figure 10.15 and Figure 10.16), and radius (Figure 10.17). Unfortunately, as can be seen from the figures, the time step for BiSEPS is too large, with only 36 timesteps, to give any granular data on the in-spiral and merger event.

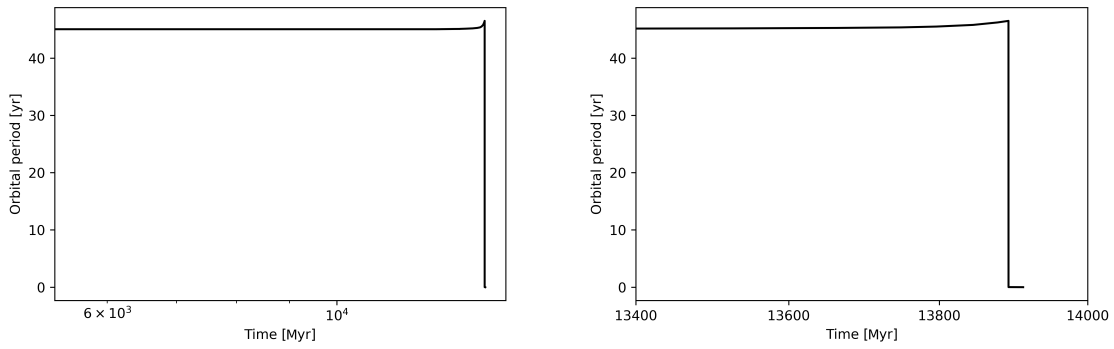

Fig. 10.13 **Left:** Full period-time plot from the NCRGEB BiSEPS model. **Right:** Partial period-time plot from the NCRGEB BiSEPS model.

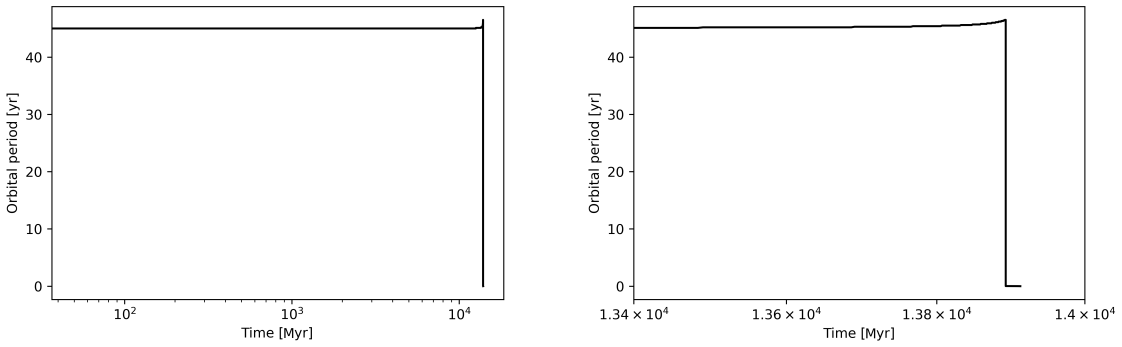

Fig. 10.14 **Left:** Full time-period plot from the NCRGEB BiSEC model. **Right:** Partial time-period plot from the NCRGEB BiSEC model.

In Table 10.15, a "pre-inspiral" evolved model produces a wide detached red giant system. This system contains two red giant components of a similar mass, temperature, and radius, albeit components with a higher mass and temperature and low radii and semi-major axis, and a significantly greater separation of $\sim$3400 $R_{\odot}$. Figure 10.17 shows that this system subsequently experiences significant inflation of the binary components (from $\sim$6 $R_{\odot}$ to $\sim$25 $R_{\odot}$), and then a common envelope and merger event in the next timestep $\sim$0.05 Gyr later. In the following 4 timesteps, $a < (R_1 + R_2)$, indicating that a merger begins to occur. In the 5th timestep, $\sim$0.1 Gyr after the "pre-inspiral" evolved model, the rapid in-spiralling event and significant mass loss occurs, with 70% of the system's mass being ejected, leaving white dwarf remnants.

In an attempt to improve on the time steps of BiSEPS, BiSEC was used. BiSEC (Binary Stellar Evolution Code) is a stellar evolution code that evolves a single system and utilises the BiSEPS stellar evolution routines, operating in much a similar way to BiSEPS and using an iteration of the same code. One of the main differences is that BiSEC provides the evolution of a binary rather than providing a searchable library and populations, and the outputs can differ slightly. To evolve a binary in BiSEC, it is simply a case in inputting the parameters of

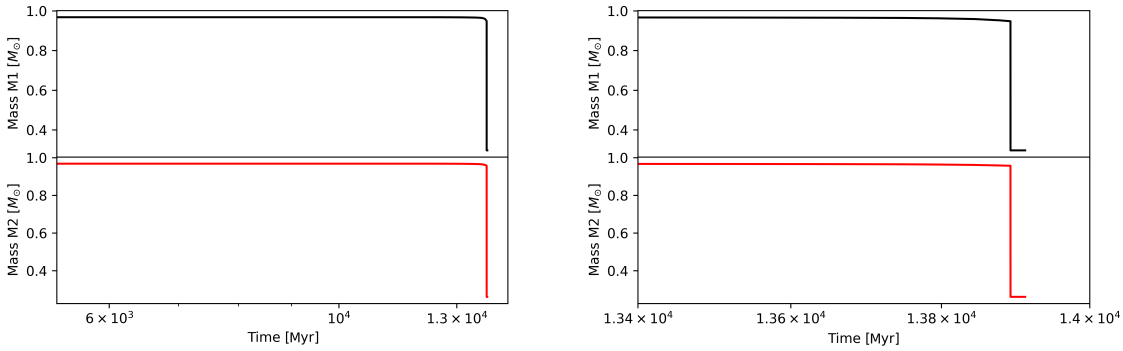

Fig. 10.15 **Left:** Full time-mass plot from the NCRGEB `BiSEPS` model. **Right:** Partial time-mass plot from the NCRGEB `BiSEPS` model.

the binary component and computing the evolutionary phases. By tracking back the `BiSEPS` model and running the original parameters through `BiSEC`, a more detailed time step can be achieved (Oleg Kozhura, private communications). In this model, `BiSEC` outputs period, mass, evolutionary status, and whether the system is detached or in contact.

The model was traced back and ran the original model parameters through the `BiSEC` code to give a more detailed evolution and merger event than `BiSEPS` could provide. However, whilst the finer time resolution was achieved, the inspiralling event happens on such a short timescale that no more detail could be achieved. As with `BiSEPS`, the system experiences significant mass loss at $\sim$13.89 Gyr, in which the period also experiences significant decrease from $\sim$46.5 yr to $\sim$5.9 d, shown in Figure 10.14, ending with a detached Helium white dwarf binary. Unfortunately, no more granularity can be achieved, despite the `BiSEC` model having 585 timesteps, and it appears that the `BiSEPS` and `BiSEC` time steps are both too coarse to provide any detailed information about the merger event for a NCRGEB.

Both `BiSEPS` and `BiSEC` also model the evolution over the incredibly long timescale of $\sim$13.9 Gyr, just longer than the age of our universe. If this timescale was to be believed, we should not have even yet observed NCRGEB, since they would have not yet had time to

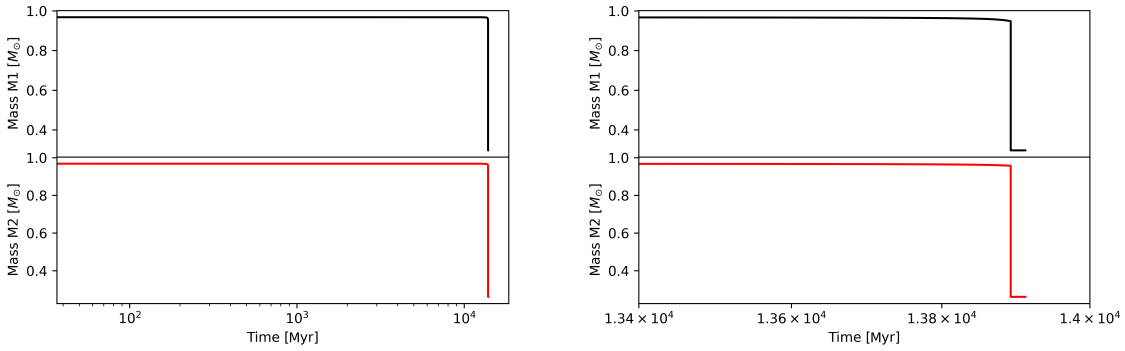

Fig. 10.16 **Left:** Full time-mass plot from the NCRGEB `BiSEC` model. **Right:** Partial time-mass plot from the NCRGEB `BiSEC` model.

evolve. For this evolutionary model to be correct, NCRGEB would have to be some of the oldest stars in the universe, a fact easily disproven by a simple comparison to the metal-poor stars which formed only 200 million years after the Big Bang (Howes et al., 2015). Further modelling will be required to provide a better constraint on the timescale of such binary evolutions. However, in the context of the evolution of two solar mass stars through the red giant phase, it is not a considerably unrealistic timescale.

To solve the timestep issue, a finer timestep or different modelling program are required. In any such program, the binary will need to again be evolved from ZAMS, since the internal structure of a star evolved from ZAMS will differ from that of a star modelled simply from the characteristics (e.g. mass and radius) we observe at its current evolutionary phase.

10.3.2 Evolutionary modelling with `binary_c`

The `binary_c` code (Izzard et al. 2006, 2009, 2018, 2004), similar to `BiSEPS` and `BiSEC`, is based on the Binary Star Evolution (BSE) code of Hurley et al. (2002), but operates as a C port of the code. `binary_c` models the evolution of binaries and single stellar structure, including the evolution of mass, luminosity, stellar radii, orbital period, and mass loss, and

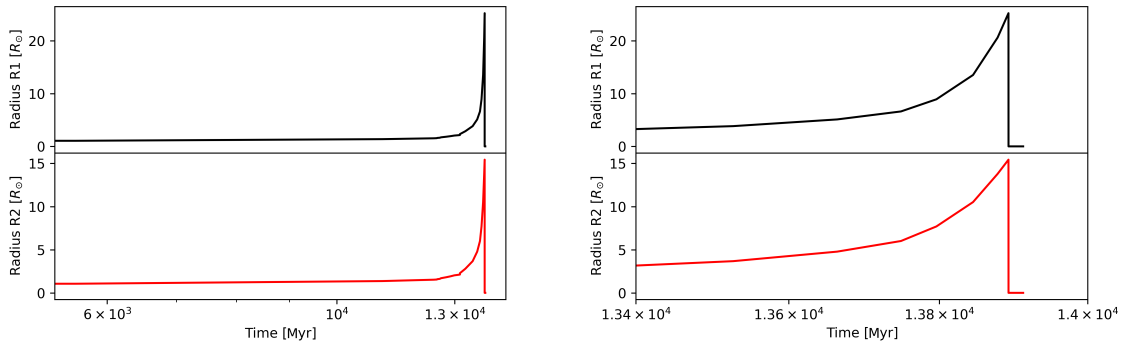

Fig. 10.17 **Left:** Full time-radii plot from the NCRGEB `BiSEC` model. **Right:** Partial time-radii plot from the NCRGEB `BiSEC` model.

the nucleosynthesis code within `binary_c`, *nucsyn* models the surface abundance of the stars. An example of the frontend to the `binary_c` code can be found as a simplified user interface, called `binary_c Online`[2].

For modelling the evolution of NCRGEB, `binary_c` was chosen for its ability to quickly model a range of required binary parameters to constrain the binary components. Modelling with `binary_c` was not intended to provide an in depth evolutionary model, but instead was used to constrain initial parameters for further modelling with `MESA`.

To model a simplified NCRGEB evolution, the standard `binary_c` parameters were used, and a grid search of the stellar masses and orbital period was performed in order to identify an evolutionary state most closely resembling the observations. As with `BiSEPS` and `BiSEC`, only two possible systems were identified, including a system with a period of 17.86 d and q=1.13. Of the two models, only one modelled through to completion without crashing the programme, so was chosen for this work. An example of one of the models generated with `binary_c` is described in Table 10.16. This model, whilst significantly more massive

[2]http://personal.ph.surrey.ac.uk/ ri0005/cgi-bin/binary5.cgi

	Observation NCRGEB	Start `binary_c`	Pre-inspiral `binary_c`	End-of-life `binary_c`
Time (Gyr)	-	0	3.07	3.20
Period (d)	17.86	17.87	15.21	-
R_1 / $R_\odot$	14.81	2.30	21.16	-
R_2 / $R_\odot$	21.09	2.30	21.26	-
a / $R_\odot$	54.01	53.67	47.55	-
M_1 / $M_\odot$	3.12	3.25	3.25	0.89
M_2 / $M_\odot$	3.52	3.25	3.25	0.00
q	1.13	1.00	1.00	-
$T_{\rm eff,1}$ / K	4766	-	-	-
$T_{\rm eff,2}$ / K	3907	-	-	-
Evolution	RG, RG	MS, MS	RG, RG	WD, massless remnant
Formation	Semi-detached	Detached	Contact	Carbon/Oxygen white dwarf

Table 10.16 Input and output parameters of `binary_c`.

than that found through the `BiSEPS` and `BiSEC` grid search, was chosen since it most closely aligned with the observations of of a NCRGEB, J003544, at the pre-CEE stage.

The `binary_c` model produces a binary of identical stars which evolve, as expected along the Hertzsprung Gap and the First Giant Branch. As the model reaches the "pre-inspiral" model of Table 10.16, the systems reach a contact stage in just 0.03 Myr from ZAMS. This is followed by a rapid period in which the secondary star merges into the primary, losing only 4% of the system's total mass. The primary then continues to evolve, expand, and lose mass as a Thermally Pulsing Asymptotic Giant Branch star (TP-AGB). After just 0.21 Myr from ZAMS, the star evolves to a Carbon/Oxygen white dwarf. The evolutionary track of the primary can be seen in Figure 10.18.

Unlike `BiSEPS` and `BiSEC`, `binary_c` was not able to replicate the extreme orbital period of $\sim$45 yrs, or systems with a mass of $\lesssim$1 $M_\odot$. Similarly however, the modelling found that a NCRGEB-type system could be achieved only through a binary with components of q=1, and a minimum component initial mass of 1.2$M_\odot$. This result is a logical one, since to achieve a NCRGEB, both components ought to have evolved at the same time and the same rate, therefore requiring almost the same initial mass at ZAMS. However, for `binary_c` to produce a system which resembles the observed NCRGEB systems, the q=1 requirement is a strict one, and even minute changes in q (e.g. q=0.99 or q=1.01) fail to replicate a system

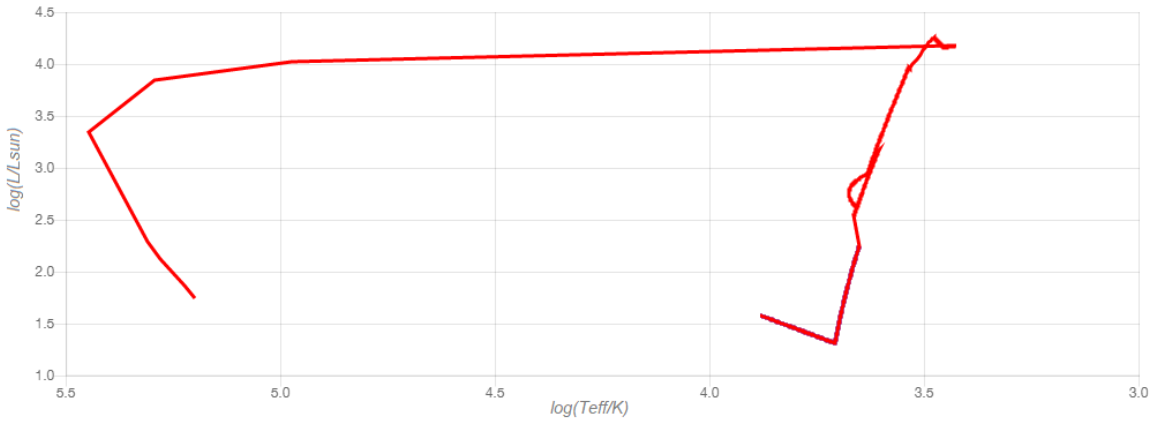

Fig. 10.18 The evolutionary track of the primary star modelled in `binary_c`.

where both components evolve into red giants on the same timescale. It is unclear as to whether this is a quirk of the software, or a physical requirement to create a NCRGEB. If it is the latter, it indicates that the formation of a NCRGEB must be extremely rare, and raises questions as to why the `PHOEBE` models show systems sometimes with significantly differing masses.

Interestingly, the CEE event in `binary_c` produces no significant mass ejection and only a single remnant, whereas `BiSEPS` and `BiSEC` find a significant mass ejection and produce binary Helium white dwarfs. Ideally, `binary_c` would be able to replicate the output, however the minimum initial mass of 1.2 $M_{\odot}$ limited the modelling. Modelling the same system as `BiSEPS` and `BiSEC`, just with a greater mass produce the same outcome as that seen in Table 10.16. It is unfortunate that a smaller timestep has not significantly increased the understanding of the NCRGEB evolution, so another modelling software must be used.

10.3.3 Evolutionary modelling with `MESA`

`MESA` (Modules for Experiments in Stellar Astrophysics)[3] is an open source one-dimensional stellar evolution code, written in Fortran (Paxton et al. 2011, 2015, 2018, 2019). `MESA`

[3]https://docs.mesastar.org/en/latest/index.html

combines a number of numerical and physics modules in order to simulate both single and binary evolution, from very low mass to very high mass systems. Using the stellar evolution module, `MESAstar`, the structure and composition of the system can be modelled simultaneously. As noted by Paxton et al. (2011) this allows for better control and granularity over known challenging phases of stellar evolution, including the He core flash in low-mass stars and advanced nuclear burning in massive stars. For more information about `MESA`, please refer to the papers noted above.

The advantage of `MESA` over `BiSEPS` and `BiSEC` lies primarily in the timestep control. `MESA` allows the user to specify timesteps either as a function of time alone, or as a function of change in envelope mass, binary separation, Roche-lobe, orbital angular momentum, orbital eccentricity, or more. `MESA` also allows for the evolutionary model to be stopped and started if the system reaches a set of parameters or a certain evolutionary phase. With this timestep control, `MESA` is well placed to model the merger and common envelope event in more detail, allowing for a better granularity during the rapid inspiralling event.

For this research, `MESA` release version 12778 and `SDK` version 20.3.1 was used. The first initial starting model for the NCRGEB was based on a `MESA` tutorial given by Selma de Mink[4], a model for the merger of a massive binary system. Whilst this model was valuable, the components were significantly more massive than those seen in a NCRGEB, and the evolution would not throw light on the end-of-life of a NCRGEB. The de Mink model was adapted in order to model low mass giants, taking into account lessons from a different, but very useful, `MESA` tutorial given by Aaron Drotter, titled *"how not to make Red Giants"*[5]. A third model was incorporated, based on results of Rawls (2016) and Li et al. (2017), in which both model red giant eclipsing binaries in Kepler. The binaries of Li et al. (2017) are similar to the NCRGEB in many respects, although the separation between the components is approximately 10–20 times the radii of the primary, and the companions

[4]https://zenodo.org/record/2603594#.YF5Cu6_7SUk
[5]https://zenodo.org/record/3374952#.YF5Cf6_7SUk

are dwarf stars. The binary of Rawls (2016) resembles NCRGEB more closely, with both components being red giants, although with a greater orbital period and separation. The main challenge with modelling NCRGEB, as a new configuration of binary, lies in that there appear to be no existing models against which these results can be compared. However, by drawing on previous expertise, it appears that the model generated (and detailed below) provide a physically realistic initial system, evolution, and end-of-life solution.

The initial binary model (Model 1) was chosen to align with the initial model chosen for `BiSEPS` and `BiSEC`, i.e. a wide detached binary system of solar mass stars with a multiple year period and a mass ratio of $q \sim 1$. A second system (Model 2) was also chosen in the same way to resemble that of the `binary_c` model. This system has more massive initial components, and a shorter period. Through this, it was possible to determine the most realistic evolutionary pathways for each binary. Only the best fitting evolutionary pathways are presented in this work.

Whilst the main aim of evolutionary modelling is to determine the end-of-life of NCRGEB systems, this cannot be achieved without a focus on determining the initial conditions of the binary system. The model for both binary systems modelled are almost identical, with the primary difference being the initial component masses and orbital periods, and varying the type of mass transfer accordingly. A system with non-conservative mass transfer will require a larger initial mass due to the significant mass lost in the mass transfer process. The model set up is described below as a singular model, and input parameters and differences are described where relevant.

The timestep was set to correspond to a change in the Roche Lobe gap of 0.02 change in $(R - R_L)/R_L$, a change in the orbital angular momentum of 0.002 kg m^2 s^{-1}, or 500 yr, whichever was smallest. The model was set to make 50 attempts to move to the next timestep, but if the next timestep could not be modelled in those 50 attempts, the entire model would fail.

To confirm the requirements for a mass ratio of q=1 seen in the BiSEPS, BiSEC, and binary_c models, q was varied between 0.8–1.2, since the majority (9 of the 12) of the NCRGEB systems modelled with PHOEBE find a q value within that parameter space. This constraint is also noted by Rawls (2016) who state that coeval stars on the Red Giant Branch must have components with masses of within 1% of one another in order to have reached the same evolutionary state in a relatively short time frame, whilst on the Horizontal Branch, the masses can differ more significantly due to the longer evolutionary lifetime.

The model takes into account magnetic braking, gravitational wave radiation, mass transfer mechanisms, and the accretor and donor were modelled as stars (not point masses). In MESA, mass loss via Roche-Lobe Overflow is only initiated when the star fills the Roche-Lobe, which causes mass loss to suddenly turn on. However the model of Kolb and Ritter (1990) (known as the Kolb model) predicts that there is a non-zero mass transfer from the extended stellar atmosphere, even if the star has not yet filled its Roche-lobe. This model is more realistic and numerically stable, producing a continually increasing amount of mass loss. For this reason, the Kolb model of mass transfer is used. For both models, metallicity was set to z=0.02, convective zone boundaries have an overshoot efficiency of f = 0.016 (Herwig, 2000), and the mixing-length parameter was set to α=2.5 to align to the small RBG stars modelled by Rawls (2016).

Model 1 aligns with the BiSEPS and BiSEC model, and Model 2 aligns with the binary_c model. For Model 1, the initial component masses were set to 1 $M_{\odot}$, q=1.00, and P=32.10 d. Full parameters, pre-inspiral, and end-of-life outcomes can be seen in Table 10.17. For Model 2, the initial component masses were set to 3.25 $M_{\odot}$ q=1.00, and P=17.86 d. Full parameters, pre-inspiral, and end-of-life outcomes can be seen in Table 10.18.

Modelling was constrained by the strict requirement that each component must have a mass of within 1% of the other. If the initial model did not fulfil this requirement, the more massive component would evolve to a red giant within a shorter time frame and reach its

	Observation NCRGEB	Start Model 1	Pre-inspiral Model 1: NC	End-of-life Model 1: NC	Pre-inspiral Model 1: C	End-of-life Model 1: C
Time (Gyr)	-	0.00	12.29	12.32	12.29	12.32
Period (d)	32.10	32.10	32.07	203.04	32.06	203.04
R_1 / $R_\odot$	16.06	0.89	15.82	0.03	19.88	0.03
R_2 / $R_\odot$	12.09	0.89	15.82	85.89	19.88	85.89
a / $R_\odot$	42.92	53.53	53.50	172.53	53.50	172.53
M_1 / $M_\odot$	0.50	1.00	1.00	0.35	1.00	0.35
M_2 / $M_\odot$	0.53	1.00	1.00	1.33	1.00	1.33
q	0.94	1.00	1.00	0.26	1.00	0.26
$T_{\mathrm{eff},1}$ / K	3646	5644	4278	24100	4173	24100
$T_{\mathrm{eff},2}$ / K	3585	5644	4278	3578	4173	3578
Evolution	RG, RG	MS, MS	RG, RG	WD, RG	RG, RG	WD, RG
Formation	SD	D	SD	D	SD	D

Table 10.17 Input and output parameters of Model 1 using MESA. C = conservative mass transfer; NC = non-conservative mass transfer. SD = semi-detached, D = detached.

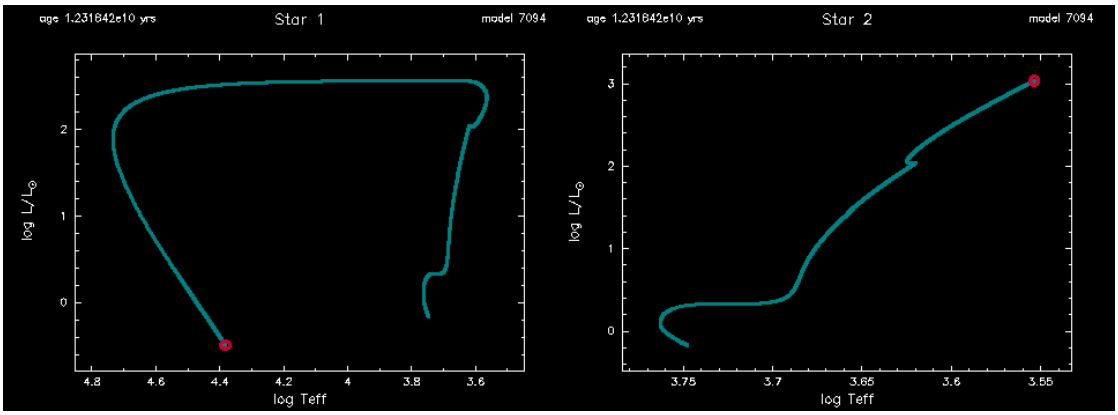

Fig. 10.19 MESA evolution of the stellar components of Model 1.

	Observation NCRGEB	Start Model 2	Pre-inspiral Model 2: NC	End-of-life Model 2: NC	Pre-inspiral Model 2: C	End-of-life Model 2: C
Time (Gyr)	-	0.00	0.26	0.32	0.26	0.32
Period (d)	17.86	17.90	17.90	140.20	17.90	140.20
R_1 / $R_\odot$	14.81	2.12	14.86	10.95	14.86	10.95
R_2 / $R_\odot$	21.09	2.12	14.86	67.89	14.86	67.89
a / $R_\odot$	54.01	54.00	53.72	81.91	53.72	81.91
M_1 / $M_\odot$	3.12	3.25	3.25	1.29	3.25	1.29
M_2 / $M_\odot$	3.52	3.25	3.25	4.23	3.25	4.23
q	1.13	1.00	1.00	3.30	1.00	3.30
$T_{\mathrm{eff},1}$ / K	4766	12910	4892	4715	4888	4715
$T_{\mathrm{eff},2}$ / K	3907	12910	4892	4179	4888	4179
Evolution	RG, RG	MS, MS	RG, RG	RG, RG	RG, RG	RG, RG
Formation	SD	D	SD	SD	SD	SD

Table 10.18 Input and output parameters of Model 2 using MESA. C = conservative mass transfer; NC = non-conservative mass transfer. SD = semi-detached, D = detached.

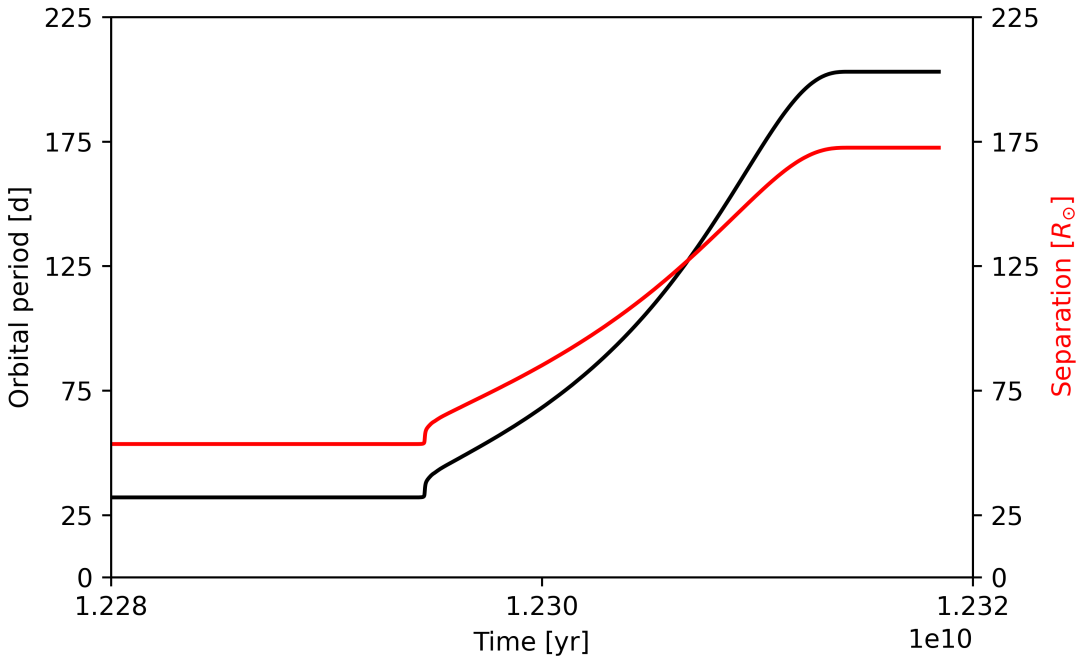

Fig. 10.20 MESA period-age plot from Model 1.

end of life before the other component. In terms of modelling, this meant the model would fail within ∼500 timesteps, rather than the ∼5,000 timesteps of a full model. Figure 10.19 shows the evolutionary tracks for Model 1, and Figure 10.22 shows the evolutionary tracks for Model 2.

For both models, with conservative and non-conservative mass loss, initial steps of each model are promising, with both components evolving, as expected, along the MS and to the RGB. In these initial stages, the primary difference between the conservative and the non-conservative model is negligible. In general, as the systems reach contact stage, for conservative mass loss, the orbital period decreases, the donor star experiences mass loss and the accretor experiences mass gain.

Both Model 1 with conservative mass transfer and Model 1 with non-conservative mass transfer show very similar initial and final evolutionary paths. The optimum initial period and mass were found to be 32.10 d and 1.0 $M_\odot$ respectively. Both components evolve to

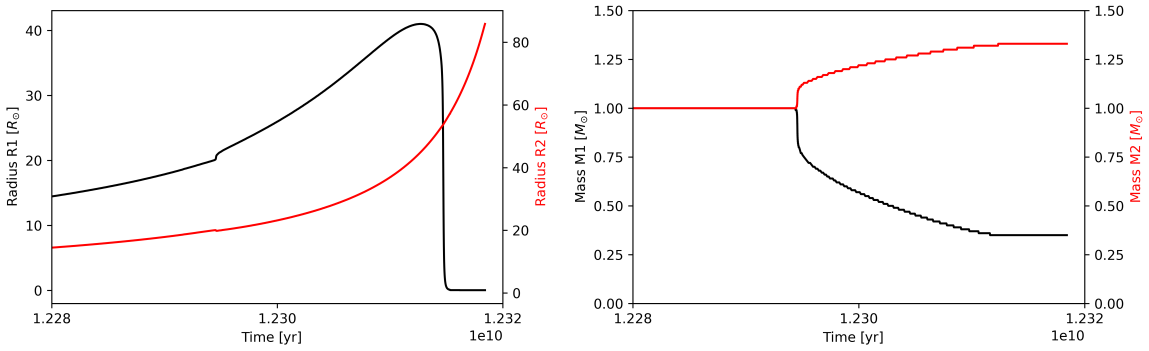

Fig. 10.21 **Left:** MESA radius-age plot from Model 1. **Right:** MESA mass-age plot from Model 1.

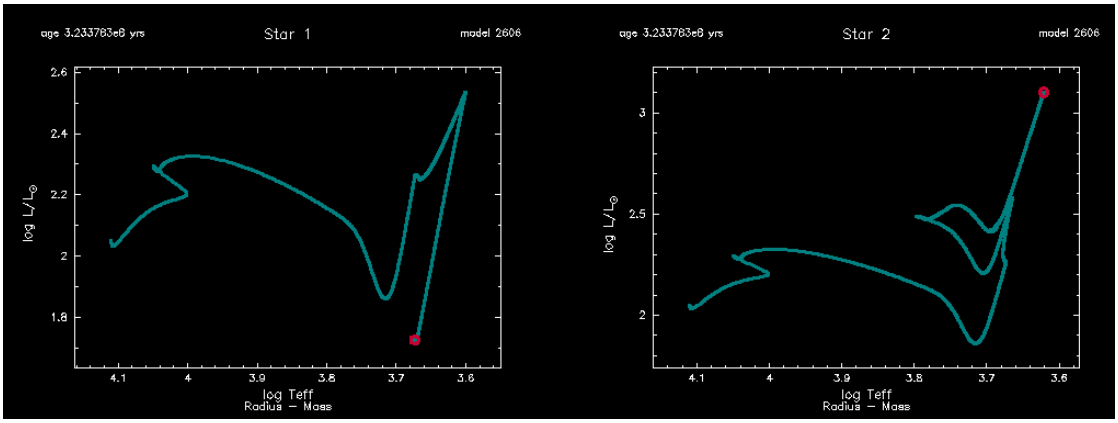

Fig. 10.22 MESA evolution of the stellar components of Model 2.

red giant systems, showing an inflated radius. The primary difference is that the model with non-conservative mass transfer shows greater inflation ($\sim$20 $M_\odot$) than that with conservative mass transfer ($\sim$16 $M_\odot$). Model 2, with greater initial masses and a lower initial orbital period experiences much the same path of evolution, albeit over a shorter timescale due to the higher initial masses. At the "pre-inspiral" of their evolution, the models are able to replicate the observed systems, to an extent.

The primary difference between Model 1 with conservative mass transfer and the observed system is that the radii of the binary components reaches a notably greater radius ($\sim 20R_\odot$)

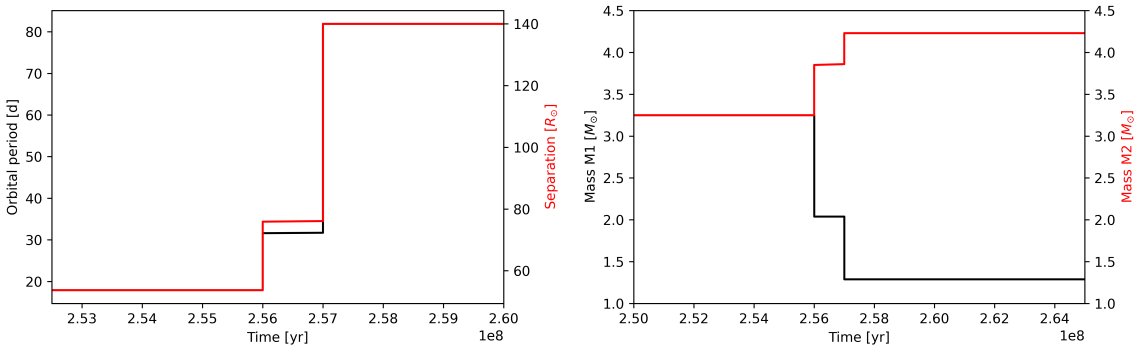

Fig. 10.23 **Left:** `MESA` period-age plot from Model 2. **Right:** `MESA` mass-age plot from Model 2.

before the system becomes contact and mass transfer occurs, compared to the observed system ($\sim 12-16R_\odot$) (even taking into account the difference in initial mass) and the system modelled in `BiSEPS` and `BiSEC` ($\sim 6R_\odot$). With non-conservative mass transfer, the radii are smaller ($\sim 16R_\odot$), aligning closely with the observed primary, but still greater than the secondary ($\sim 12R_\odot$). This model better replicates the observed system, with almost every parameter aligning with the observed system. This is replicated in Model 2. Despite the different starting parameters, again, we see the parameters of the non-conservative model aligning closely with the observed system, although unable to replicate the secondary. The model with conservative mass transfer shows a greatly inflated system.

However, this is where the similarities end between `MESA` and previous modelling. In `BiSEPS`, `BiSEC`, and `binary_c`, each model has shown a common envelope event, and a rapid inspiralling event (over ∼0.07 Gyr in `BiSEPS` and `BiSEC`, and ∼0.18 Gyr in `binary_c`) in which both stars experiences sudden mass loss and evolves to a white dwarf binary in a short period orbit, or one star experiences mass loss, and the other continues to evolve, eventually forming a white dwarf and a massless remnant.

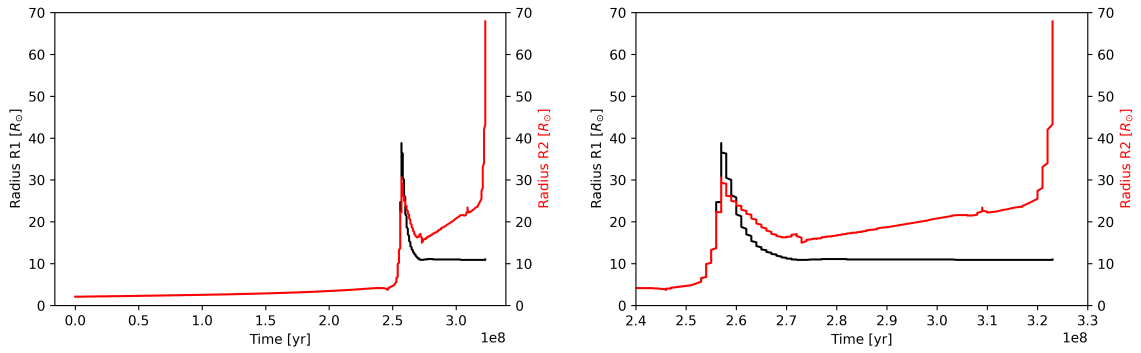

Fig. 10.24 **Left:** MESA radii-age plot from Model 2. **Right:** Zoom in of MESA radii-age plot from Model 2.

Similarly, each MESA model shows one star experiencing mass loss and the other, mass gain, however no inspiralling event occurs following the contact phase. Instead, every MESA model tested and described here shows the components of the binary actually increasing in orbital period and separation following the contact phase, as mass and angular momentum is transferred from one component to the other. For Model 1, the period increases from 32.10 d to 203 d over ∼0.01 Gyr, and for Model 2, the period increases from 17.90 d to 81.91 d over ∼0.001 Gyr.

10.4 Discussion

When NCRGEB were first discovered, we predicted that these binary systems would eventually merge and form red novae. This prediction was based on their rarity, assumed instability, and the fact of them being low temperature giant systems. Whilst photometric and spectroscopic follow-up has given valuable information about the systems as they currently exist, only evolutionary modelling has been able to determine the birth, evolution, and death of NCRGEB. In this section, I discuss the evolution and end-of-life of NCRGEB, and whether they could actually be ellipsoidal red giants instead.

10.4.1 The evolution of NCRGEB

Evolutionary modelling appears to show that we have caught these objects in a short-lived part of their life before they experience rapid instabilities and angular momentum loss, leading to a cataclysmic event. From `BiSEPS`, `BiSEC`, and `binary_c`, we know that a very rapid in-spiral and common envelope event occurs, however the coarse timestep does not allow any granular detail to be seen, and modelling with `BiSEPS` and `BiSEC` provides a significantly longer timescale of $\sim$14 billion years, nearing the age of the Universe. Whilst this timescale is long, it is not be unrealistic for the full birth-to-death evolution of a sub-solar mass red giant. Both `BiSEPS` and `BiSEC` predict that the NCRGEB modelled would form a Helium white dwarf binary, whilst `binary_c` produces a single white dwarf. Whilst `MESA` also models systems in which one component may become a white dwarf (albeit with the other component as an inflated red giant), these systems experience period and separation increase with mass and angular momentum transfer. This implies that the `MESA` models are not experiencing the common envelope event and sudden mass loss of other models, which may actually be down to the modelling set up rather than the physical reality of the evolution itself. The modelling set up and initial starting parameters are likely to be the main constraint on the modelling done here.

For each model, it is noticeable that the main difference between the model and the observed system, at the initial and "pre-inspiral" phases, is that the components of the model are identical, but the components of the observed systems are not. From this, we can infer that the only way a NCRGEB could form is from a q=1 binary (or to within 1%). This does not, however, imply the the mass ratio of the components must stay at q=1 for their entire evolution, a parameter displayed both in the evolutionary models and the component models. The models in particular appear to have mass ratios of near q=1. In fact, if we assume that q=1 holds until the components begin to experience Roche lobe overflow and mass transfer, then this implies that many of NCRGEB systems we see today have already

begun on their path of inspiral and merger. This has interesting implications for the binary parameters determined via PHOEBE earlier in this chapter, suggesting that J093610 (q=0.97), J035259 (q=1.03), and J132156 (q=1.06) have only just begun mass transfer. Whilst systems like J183357 (q=0.23) and J204317 (q=0.46) have low mass ratios, it does not necessarily rule these out as NCRGEBs, and may instead imply that these systems are well on their way through the inspiral phase. However, it may be more realistic to assume that these systems are not true NCRGEBs. J001521 has a very low mass ratio of q=0.20, but this is likely to be a result of poor data or not being a true NCRGEB, rather than an indication of merger.

As each model evolves and mass transfer takes place during the contact phase, the components begin to evolve separately from one another, and their radii, temperatures, and masses begin to differ. This implies that the systems observed have already begun the process of mass transfer, and are well on their way through the very short period of interaction seen in each model. In BiSEPS and BiSEC, this period lasts only $\sim$0.07 Gyr, in binary_c this lasts $\sim$0.18 Gyr, and in MESA, $\sim$0.001–0.01 Gyr. It is therefore highly likely that the binaries have been observed during an extremely short period of their lives, hence why they have not been recognised before.

We can compare these timescales to those estimated from the period change calculated in Table 10.14. From an assessment of various types of angular momentum loss, a merger of the components of NCRGEB might be expected on timescales of 0.005–29 Myr (or up to 0.03 Gyr), with mass transfer being the main driver of period change. For the NCRGEB with the shortest timescales, tidal instabilities may also become a dominant driver of period change. This aligns closely with the merger timescale found through all evolutionary modelling methods, confirming that a merger is the most likely scenario, and could occur in as little as 5,000 years (0.005 Myr). However, we should remember that since the value of $\dot{M}$ here is an assumption rather than a true value, the rate of period change may have been overestimated by a factor of 10, implying that some binaries may be merging on a longer timescale than

seen here. However, if we make the assumption that the common envelope event and mass ejection is the most likely evolutionary outcome, rather than the increased orbital period, it appears that these systems may be the progenitors of red novae. As a simplified exercise, we can compare the mass of the NCRGEB systems and the mass loss modelled to the mass lost in the V1309 Sco event.

An estimate by Stępień (2011) found that the giant progenitor of V1309 Sco was 1.1–1.3 $M_{\odot}$ and the ZAMS progenitor was 1.7–2.2 $M_{\odot}$. An estimate by Nandez et al. (2014) from the reconstruction of the light curve found that the mass of the outbursts of V1309 Sco constituted 0.02 and 0.04 $M_{\odot}$, and the original outburst constituted a mass loss of 0.05 $M_{\odot}$ (or $\sim$2% of the progenitor mass). We also know that the primary in the binary progenitor of V1309 Sco experienced a rapid change from an F-type giant to a late M-type giant in the few months post-outburst (Pejcha, 2014).

If we compare this to the models above, the mass loss found in NCRGEB is significantly greater than that of V1309 Sco. `BiSEPS` and `BiSEC` find a mass loss of $\sim$28%, `binary_c` finds 86%, `MESA` Model 1 finds $\sim$16%, and `MESA` Model 2 finds $\sim$15% mass loss. However, this mass loss takes into account the full evolution, which V1309 Sco had obviously not yet passed through. Unfortunately, the models showing mass loss through merger have no better time resolution, so the mass loss estimates given above may be an overestimate. Even so, the mass loss within these systems is an order of magnitude greater than that of V1309 Sco Stępień (2011), which may imply a more forceful ejection than experienced by a red novae.

10.4.2 Are NCRGEB the progenitors of red novae?

In this research, NCRGEB are thought to be a potential progenitor to red novae, however the evolutionary modelling is not robust enough to conclusively prove this. To provide conclusive evidence, either further modelling is required (for example, common envelope

event modelling and hydrodynamical simulations) or one of the NCRGEB would have to show strong proof of period change or experience a merger event.

One such method could be the use of a relatively new piece of software called Roche Lobe Overflow (`RLOF`) MacLeod et al. (2017a). This is a python package designed to solve point-mass orbit evolution equations for a binary star system undergoing Roche lobe overflow. By evolving the mass radius of the donor star, M_d and R_d respectively, separation, a, and mass of the accretor, M_a, `RLOF` solves the initial value problem for the coupled donor mass loss and orbit evolution. For more information on how `RLOF` works, see MacLeod and Loeb (2020). `RLOF` has been tested against the V1309 Sco progenitor and merger event and the famous red nova prediction, KIC 9832227 (Molnar et al., 2017) and proves that KIC 9832227 could not have merged with the same outcome. Using `RLOF` is therefore a useful method to determine whether any of the NCRGEB systems could follow similar pathways to KIC 9832227 or V1309 Sco. However it is now outside the time frame and scope of this research.

But without conclusive proof, we have to ask: *if the NCRGEB are not red novae progenitors, what are they progenitors of?* From this evolutionary modelling, the answer appears to be binary white dwarf systems, or double white dwarfs, which are fairly common end products of binary evolution (Marsh 1995; Toonen 2014).

We know that red novae are not closely related to standard novae, caused by explosions on the surface of a white dwarf. Should the modelling be correct and NCRGEB actually evolve to contain a white dwarf, the possibility of a red novae is almost certainly ruled out. However, although white dwarf binaries are obviously not red novae, these systems are interesting in and of themselves. Should these white dwarf binaries be eclipsing, they would act as valuable laboratories for constraining the component masses.

Statistically, the merger of Galactic white dwarf binaries should not be infrequent (Badenes and Maoz, 2012), and appear to be one of the main sources of background gravitational wave signals (Hermes et al. 2012; Nelemans et al. 2001; Rueda et al. 2019). Recent

work on the merger of white dwarf binaries has included WD J055134.612+413531.09, an unusual and exciting ultra-massive white dwarf formed by the merger of a close binary white dwarf (Hollands et al., 2020). It is possible that the binary white dwarfs created through the evolution of NCRGEB could be the progenitor of this rare type of system instead.

10.4.3 Are NCRGEB actually ellipsoidal red giants?

What has been apparent throughout this research is the similarities in the photometric light curves of NCRGEB and ellipsoidal red giants, originally studied by Wood (1999) and displayed in Figure 2.16 in Chapter 2. The light curves of both types of binaries appear to be that of contact or near contact eclipsing binaries but with long periods, which raises the question *"are NCRGEB actually ellipsoidal red giants?"*

Whilst the light curves appear similar, and at least one component in each type of system is a red giant, there are actually a number of distinct differences which indicate that NCRGEB are not simply ellipsoidal red giants. A study of 81 ellipsoidal red giant systems in the Large Magellanic Cloud by Nie et al. (2017) finds that these binaries are typically comprised of a red giant filling its Roche lobe and an unseen main-sequence companion, with extremely long periods of $\sim$70 d to $\sim$700 d, separations of $>$100 $R_{\odot}$, mass ratios of $q \sim$0.3, and eccentric orbits.

By contrast, NCRGEB have periods of $\sim$5 d to $\sim$32 d, separations of $\sim$13 $R_{\odot}$ to 70 $R_{\odot}$, and mass ratios closer to $q \sim$1. The spectroscopic follow-up also confirmed the presence of two components in each NCRGEB system, even if only through line broadening, whilst the main-sequence companion to ellipsoidal red giants is not visible in spectra Nie et al. (2017). This, compounded with the differences between evolutionary pathways from Nie et al. (2017) indicates that NCRGEB are not simply short period analogues of ellipsoidal red giant binaries, but are their own distinct system.

10.5 Summary

Having followed up 27 candidate NCRGEB with photometric and spectroscopic observations, I have confirmed that 12 are close giant binary systems through modelling their stellar components using `PHOEBE`. On average, NCRGEB are relatively low mass systems, with a high mass ratio, indicating that both stellar components are at similar stages in their evolution, and have formed and evolved on the same time frames. The mass of NCRGEB generally aligns with the total mass of the V1309 Sco progenitor system. The primary component is consistent with models of the progenitor, however the secondary is not.

The most interesting part of this work, to me, is that the original candidate NCRGEB, J001521, appears not to be a NCRGEB. Photometric follow-up shows that the light curve appears to be closer to a pulsating variable than an eclipsing binary, spectra show little to no radial velocity variability, and component modelling finds a physically unrealistic system. It is ironic that the candidate that lead me down this path of research has turned out not to be a NCRGEB.

By taking the models from `PHOEBE` as a starting point, I used a variety of programs to model the evolutionary pathways of the NCRGEB, from birth to death. I have found that NCRGEB can only form if the initial binary has a mass ratio of q=1 (or to within 1%), and the evolution each component goes through happens at the same rate. I have determined that the most likely reason for period decrease is not magnetic braking or GWR, but instead unstable mass transfer and angular momentum loss, which could lead to a merger.

Whilst `BiSEPS` and `BiSEC` could not provide the time steps needed, and provided a significantly longer lifetime prior to merger, these models provided a starting point for understanding the evolution, showing that the binaries experience a long period of stability followed by a common envelope event with significant mass ejection and rapid in-spiralling, resulting in the production of a white dwarf binary. Further modelling with `binary_c` provided a similar evolution and end-of-life, albeit with production of a single white dwarf

and a massless remnant. As seen with BiSEPS and BiSEC, binary_c would only evolve a system which appeared observationally similar to the NCRGEB with the stringent condition that q=1$\pm$0.01.

MESA provided an opportunity to model the binary evolution with more flexible initial parameters, and two models were explored, both with conservative and non-conservative mass transfer. The purpose of this was to identify if BiSEPS and BiSEC or binary_c provided the most realistic model, and to identify whether the evolution was affected by different forms of mass loss. Model 1 (aligned with BiSEPS and BiSEC) with conservative mass transfer evolved a system which appeared close to observations at the pre-inspiral point. However, this system shows no mass ejection or inspiralling, and instead shows an increase in orbital period and separation as mass and angular momentum transfer occurs. It is not clear which evolutionary scenario is the most realistic, since all produce binaries which are not dissimilar to what we observe now, however it is most likely that the rapid phase of period change, mass, and angular momentum transfer is true for any outcome.

Given that the NCRGEB appear to be experiencing period change with a likely merger on the timescale of megayears, it makes these objects less attractive for long-term monitoring campaigns. Obviously, it is highly unlikely that any object will merge on a human timescale, with the shortest timescale being on the order of $\sim$5,000 years, and the upper limit for merger being 0.03 Gyr. However long-term monitoring will be useful for understanding the rate of period change for this new type of binary. To this end, all NCRGEB systems have been placed in the *Lasair* (Smith et al., 2019) transient broker for long-term monitoring. The aim of *Lasair* is to ingest and present alerts from the public stream of the Zwicky Transient Facility (ZTF) data. If any of the NCRGEB systems monitored by ZTF experience a change in magnitude, whether it be brighter or fainter, an alert will be sent. This provides an early warning system for any merger or common-envelope events, should there be an unexpected change within the system. Alternatively, further theoretical work can be done to model

and understand the period change these NCRGEB systems may be facing. This might involve further O–C analysis using a longer baseline of data to constrain period change, or comparison to the period change experienced by V1309 Sco using the program `RLOF`.

The question remains: *are near contact red giant eclipsing binaries the progenitors of red novae?* and the answer has to be "we don't know!" From the follow-up and modelling, it appears that there is period decrease leading to a common envelope event, and this event causes significant mass loss within the system over a very short timescale. One model finds that a single star remains, one finds that a white dwarf binary remains, and one model finds no merger event at all. However, despite the common envelope event not being well understood, the possibility of NCRGEB being red novae progenitors is not out of the question. To fully understand the merger event though, either a merger event would need to be observed, or significant evolutionary and common envelope event modelling is required. I would recommend that additional observations also be taken, particularly in the view of characterising period change and the common envelope event.

Chapter 11

Discounted Near Contact Red Giant Eclipsing Binary Candidates

This chapter will cover the objects which were included as part of the photometric (Chapter 8) and spectroscopic (Chapter 9) follow-up but deemed not to be NCRGEB. The observational follow-up techniques have already been detailed, and no further modelling of stellar components or evolution were completed.

These non-NCRGEB objects include Cepheids and shell stars. Whilst they are not useful in the exploration of NCRGEB and potential red novae candidates, it is valuable to understand why these objects were originally included as NCRGEB candidates. In this brief chapter, I will explore the photometric light curves, spectra and spectral modelling, and radial velocity plots, where available. Using this data, I will explore why these objects were originally considered NCRGEB candidates, then discounted, and what lessons can be learned for future follow-up of similar candidates.

11.1 Discounted NCRGEB candidates

Of the 27 candidate NCRGEB, 14 were found to be either Cepheid variables, rotationally modulated stars, shell stars, or incorrectly observed targets. Below, each SuperWASP phase-folded light curve is displayed, and radial velocity curve where available. From the radial velocity plots, it is clear that many of the objects are not a binary, but instead are Cepheids. However, for many objects, they appear to either have no periodicity, or have error bars too large to determine a radial velocity curve. Radial velocity curves are also displayed folded at both the "binary period" and the "Cepheid period" if appropriate. For some objects, the phase coverage was too low to accurately determine whether it is a NCRGEB. Such objects would require further follow-up to provide a confirmation. Unfortunately, one target was mistakenly not observed spectroscopically, and this is detailed below.

1SWASPJ192628.96-233856.1

This object was identified by a cross match between SuperWASP and ASAS-SN, with periods of 28.54 d and 28.39 d respectively. It had previously been identified in ASAS-SN as a rotational variable with a period of 14.22 d (Jayasinghe et al., 2018) but has since been reclassified to an EW-type variable, although with a low ASAS-SN likelihood statistic of 0.17. Little else is known about this object. Visually assessing the full SuperWASP (Fig 11.2) and ASAS-SN light curves, it was not inconceivable that the object was a NCRGEB candidate, although the ASAS-SN light curve appeared to show a more triangular profile.

Despite this, J192628 was followed up both photometrically and spectroscopically. Only 9 full nights of PIRATE observations were possible, so no multi colour photometric light curve is available, however 13 nights of observations were made using the $74''$ providing good period coverage. Through spectral typing and synthesis, the target was found to be a K4-type star with T_{eff} $\sim$4080 K. The target shows some sign of radial velocity variations

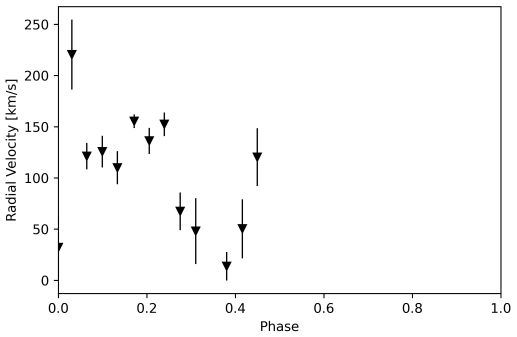

Fig. 11.1 Radial velocity curve for J192628 folded with a period of 28.54 d.

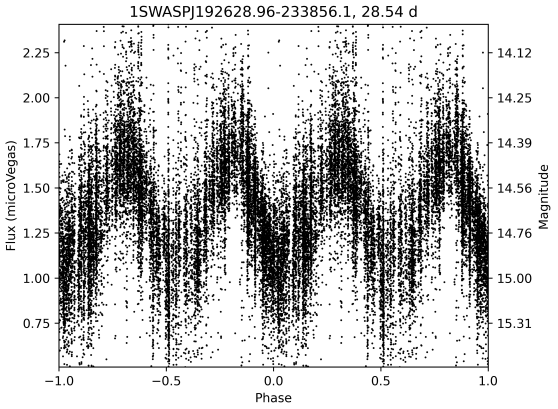

Fig. 11.2 SuperWASP light curve for J192628 phase-folded with a period of 28.54 d.

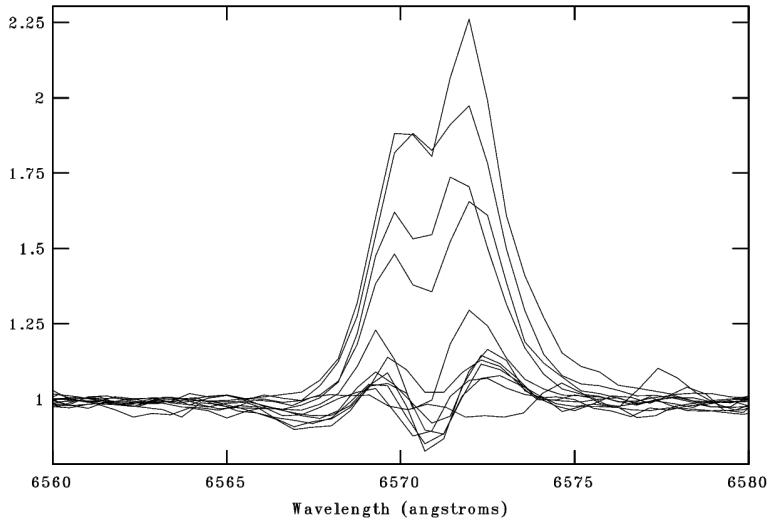

Fig. 11.3 The periodic rising, splitting, and falling of the Hα, characteristic of a shell star.

using the strong Na line, however, it does not display the curve expected for a binary at this period (Fig 11.1).

The spectra have a clear double Hα emission line which shows a periodic rise and fall, shown in Fig 11.3, characteristic of a shell star. It is not clear whether this object is a shell star with a decretion disc experiencing tidal warping (similar to Martin et al. (2011)), or a binary system with an accretion disc causing hydrogen emission. J192628 is therefore most likely not to be a NCRGEB and does not require further follow-up.

1SWASPJ192311.66-423244.5

This object was identified through a search of the SuperWASP archive and ASAS-SN Catalogue of Variable Stars. The SuperWASP object has a period of 16.64 d, while the ASAS-SN period is 16.62 d. In Drake et al. (2017), J192311 is classified as a rotational variable with a period of 8.32 d, exactly half the SuperWASP period, whereas the ASAS-SN Catalogue of Variable Stars identifies it as an EW-type binary albeit with a low likelihood statistic of 0.25. Little else is known about this star.

The SuperWASP phase-folded light curve (Fig 11.5) appears to be convincing folded at either binary or Cepheid periods, although it is possible that there is a slight asymmetry and smoothness to the minima, indicating a Cepheid or rotational variable type. No photometric follow-up was possible using PIRATE due to the declination of the target.

J192311 was followed up using the $74''$ telescope, gaining 12 nights of observations. Through spectral typing and synthesis, the target was found to be a K0-type star with $T_{eff} \sim$ 4810K. The spectra show no sign of binary splitting of absorption lines, and the extracted radial velocity curve (Fig 11.4) using Hα strong lines and the full spectrum is inconclusive, showing some signs of periodic variation, although not enough to provide evidence of being a NCRGEB. J192311 is highly unlikely to be a NCRGEB, and does not require further follow-up.

1SWASPJ191910.42-414050.9

This object was identified through a search of the SuperWASP archive and ASAS-SN Catalogue of Variable Stars. J191910 has a period of 16.60 d in SuperWASP and 16.62 d in ASAS-SN. Although this object is classified as a Cepheid of W Virginis type with a period of 16.61 d by Drake et al. (2017), ASAS-SN provides a classification of EW-type, albeit with a low likelihood statistic of 0.14. Despite the Cepheid classification, phase-folding at $\sim$16 d returns a light curve more like a binary than a Cepheid. Little else is known about this star.

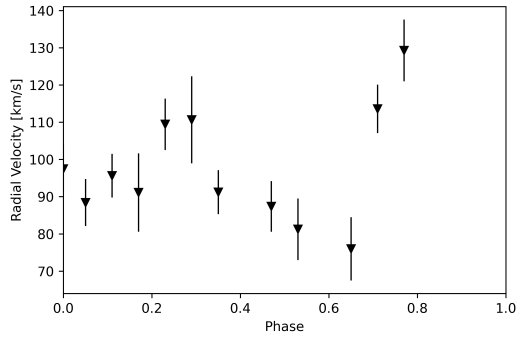

Fig. 11.4 Radial velocity curve for J192311 phase-folded with a period of 16.64 d.

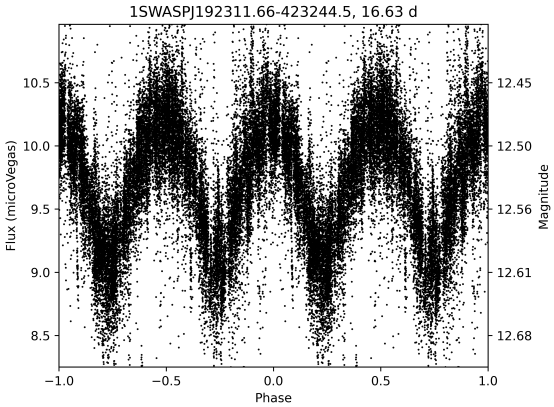

Fig. 11.5 SuperWASP light curve for J192311 phase-folded with a period of 16.64 d.

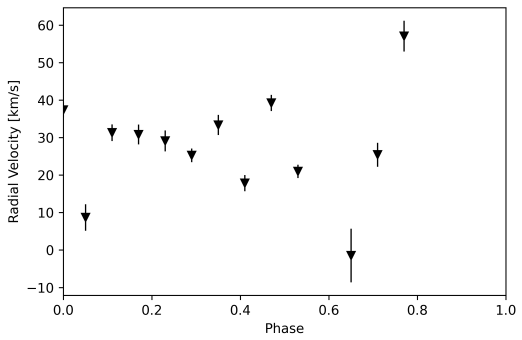

Fig. 11.6 Radial velocity curve for J191910 phase-folded with a period of 16.62 d.

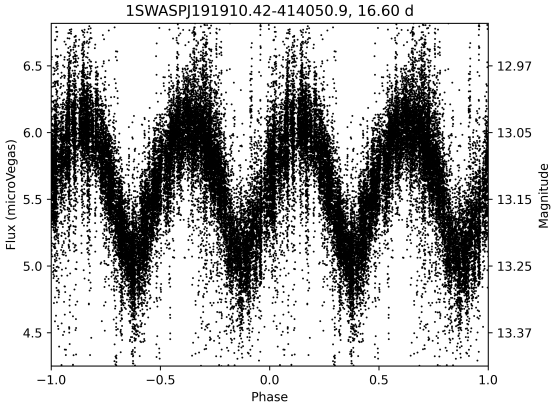

Fig. 11.7 SuperWASP light curve for J191910 phase-folded with a period of 16.62 d.

The SuperWASP phase-folded light curve (Fig 11.7) is a convincing example of a binary light curve, with equal depth minima. Unfortunately, no photometric follow-up was possible due to the declination of the target. Spectroscopic follow-up was done over 9 nights using the 74″. Through spectral typing and synthesis, the target was found to be a K4-type star with T_{eff} ∼4080 K. No binary line splitting was observed, and the extracted radial velocity curve using Hα and the full spectrum is inconclusive (Fig 11.6). There might feasibly be some periodic variability, however the radial velocity appears to be inconsistent across consecutive nights. For these reasons, J191910 was discounted as a NCRGEB.

1SWASPJ165656.26-040414.3

This object was identified by a cross match between SuperWASP and ASAS-SN, with a SuperWASP period of 15.68 d. This is the only object with a globular cluster in the field of view (Messier 10 or NGC 6254), complicating the follow-up efforts. The ASAS-SN counterpart, ASASSN-V J165655.96-040416.4, has a classification of EW-type binary with a period of 15.67 d, although it was originally classified as a Cepheid variable by Jayasinghe et al. (2018) with a period of 7.84 d, exactly half the SuperWASP period. J165656 has been studied significantly, and has consistently been classified as a Cepheid variable. From existing literature, this target appeared to be an unlikely NCRGEB candidate.

Both the SuperWASP (Fig 11.9) and ASAS-SN phase-folded light curves appear to be convincing EW-type binaries with equal depth minima, however the ASAS-SN plots appear to show a slight asymmetry. However, O–C analysis by Marcus Lohr found that the most likely type was a Cepheid variable (Marcus Lohr, private communications). Despite this, J165656 was followed up with PIRATE over $\sim$53 nights using BVRI filters.

J165656 was observed with the $74''$ and the Liverpool Telescope, gaining 24 nights of spectroscopy over 2 months, providing full cycle coverage. Through spectral typing and synthesis, the target was found to be a G8-type star with T_{eff} $\sim$4960 K. The spectra usually showed no line splitting, however every $\sim$8 d, J165656 appears to show split Hydrogen alpha emission, similar to that of a shell star. This is likely due to the presence of a disc. Attempting to find a radial velocity curve from the non-emission strong lines (Hα and the full spectrum) of the spectra is inconclusive (Fig 11.8). There is likely some periodic variability, however it is not obvious from the radial velocity curve.

Whilst every effort has been made to identify the correct object in follow-up, due to the large pixel scale of SuperWASP (and ASAS-SN), it is possible that the incorrect object was followed-up. However, every effort was made to identify and observe the correct object, and

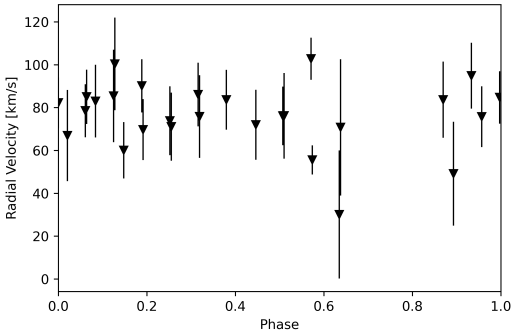

Fig. 11.8 Radial velocity curve for J165655 phase-folded with a period of 15.68 d.

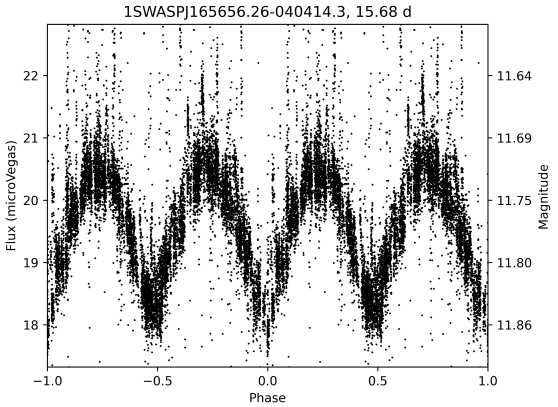

Fig. 11.9 SuperWASP light curve for J165655 phase-folded with a period of 15.68 d.

it is likely that this object is a Cepheid variable rather than a binary. J165656 is likely not to be a NCRGEB and does not require further follow-up.

1SWASPJ165241.24+203224.7

J165241 was identified by a cross match between SuperWASP and ASAS-SN, however the periods differed significantly. The SuperWASP period was identified as 0.88 d and the ASAS-SN period as 15.13 d. Whilst ASAS-SN classifies the target as an EW type binary, it has also been previously classified as CRTS J165241.2+203224, a faint (V$\sim$14) W Virginis (Type II) Cepheid with a period of 7.67 d and an amplitude of 0.15. Plotting the SuperWASP data at both the ASAS-SN and CRTS periods appears to give convincing light curves, however the Cepheid period provides a better fit to the data. O–C analysis showed that J165241 is showing a period of change of $\sim$12,000 s/year, although this is an unrealistic and highly unlikely to be a real result.

Despite the target being unlikely to be a NCRGEB, it was followed up with PIRATE and Priority Z time on the Liverpool Telescope, acquiring 6 spectra over 28 days. Through spectral typing and synthesis, the target was found to be a K0-type star with T_{eff} $\sim$4810 K.

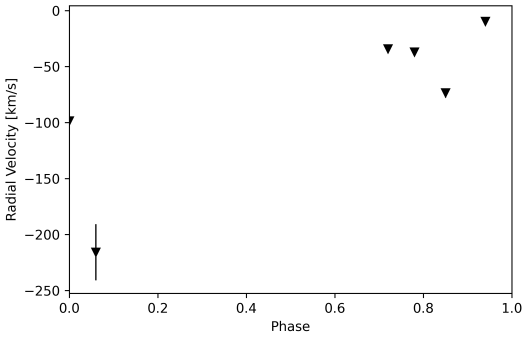

Fig. 11.10 Radial velocity curve for J165655 phase-folded with a period of 15.68 d.

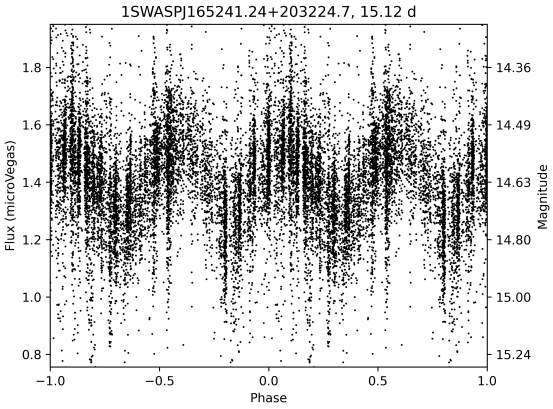

Fig. 11.11 SuperWASP light curve for J165241 phase-folded with a period of 15.68 d.

As expected, no binary line splitting was observed. Unfortunately, the extracted radial velocity data (from the Hα line and the full spectrum) provides an unconvincing radial velocity curve for a binary system, shown in Fig 11.10. Two extracted radial velocities appear to be at the extremes of radial velocity amplitudes, and it is unclear as to whether these are true radial velocities, or artefacts within the data.

Since J165241 appears to be a Cepheid with a period of 7.67 d from the photometric light curves, and the radial velocity curve is inconclusive, this target has been discounted as a NCRGEB and no further modelling was done.

1SWASPJ154607.55-191711.4

This object was identified by a cross match between SuperWASP and ASAS-SN with periods of 29.14 d and 29.26 d respectively. Despite the noisy SuperWASP light curve, the ASAS-SN light curve appeared to be much more convincing as a NCRGEB candidate. Pojmanski (2002) classified J154607 as a semiregular or miscellaneous variable with a period of 14.46 d, almost half that of the SuperWASP and ASAS-SN periods. SIMBAD provides a classification of a high proper motion star, and lists a close possible associated ROSAT X-ray source, 1RXS J154606.2-191714 just 19 arcseconds away. It is unclear if this source is related.

Breaking down the SuperWASP observations into "fields" shows a rapidly changing variable star which appears to look like a binary in some fields, but in others looks like a pulsating variable, shown in Fig. 11.12. The SuperWASP phase-folded light curve (Fig 11.14) is very noisy when viewed as a whole. Interestingly, the ASAS-SN light curve appears to be a very convincing binary with equal depth minima when folded at 29.26 d, however the light curve appeared to contain contamination. Photometric follow-up using LCO appeared to indicate that this contamination was a result of a non-varying source at $\sim$7 arcsecond distance from the target, however the ASAS-SN light curve appears to show that the contamination has the same period and magnitude as the target, hence contamination is unlikely to be from a nearby source. It is more likely that this contamination arises from the semiregular nature of J154607.

Despite this, follow-up was still completed, and 67 nights of multi colour photometric observations were made using PIRATE, providing good coverage of the light curve. Additionally, 12 nights of spectroscopic follow-up were done on the 74″, providing good period coverage. Through spectral typing and synthesis, the target was found to be a K4-type star with T_{eff} $\sim$4080 K. As expected, no binary line splitting was observed, and the resultant radial velocity curve from Hα and the full spectrum is characteristic of that of a pulsating variable (Fig 11.13). Through this follow-up, it is confirmed that J154607 is not a NCRGEB and does not require further follow-up.

1SWASPJ135703.85-474817.9

This object was identified by citizen scientist volunteers as a clear binary system with a period of 10.71 d. Similarly, the ASAS-SN light curve for ASASSN-V J135701.95-474810.0 has a period of 10.69 d and is a clear EB-type binary, although originally classified as an EA-type binary by Szczygieł et al. (2008). This period is typical of an EB-type system

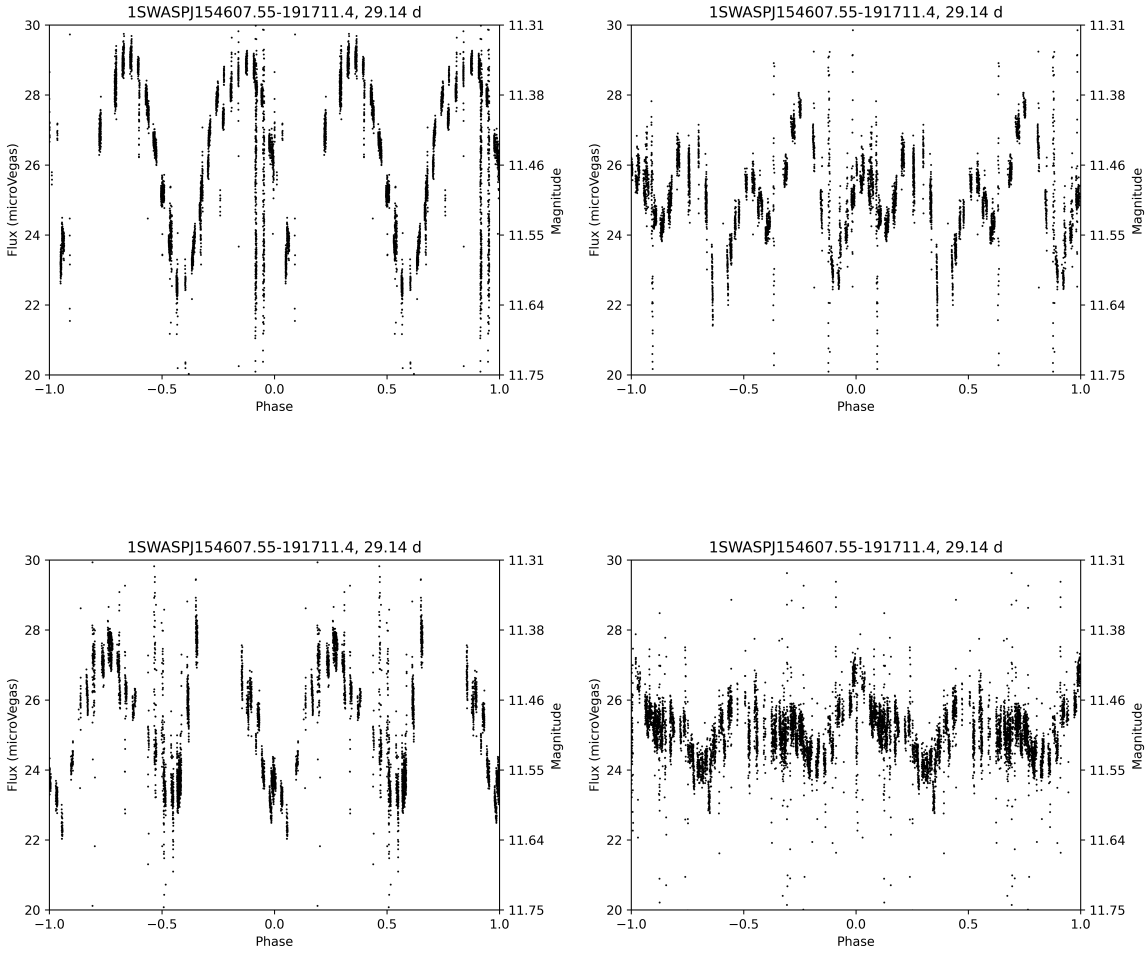

Fig. 11.12 J154607 phase-folded with a period of 29.14 d. Over the course of 8 years, the light curve of this target changes significantly.

with significantly different eclipse depths. In hindsight, it was clear that this star was not a candidate NCRGEB and the follow-up conducted was pointless.

The SuperWASP phase-folded light curve is a clear EB (Fig 11.16), however the ASAS-SN period of 10.69 d provides a better period than the SuperWASP one. J135703 was not observed with PIRATE due to declination constraints, nor with LCO due to timing constraints. It was, however, observed with the 74″ over 8 nights. Curiously, no binary splitting of absorption lines was seen, and it was difficult to extract a periodic radial velocity curve (Fig 11.16). The likely explanation for this is probably a case of mistaken identity.

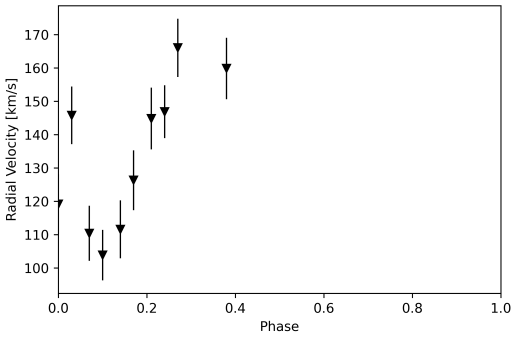

Fig. 11.13 Radial velocity curve for J154607 phase-folded with a period of 29.14 d.

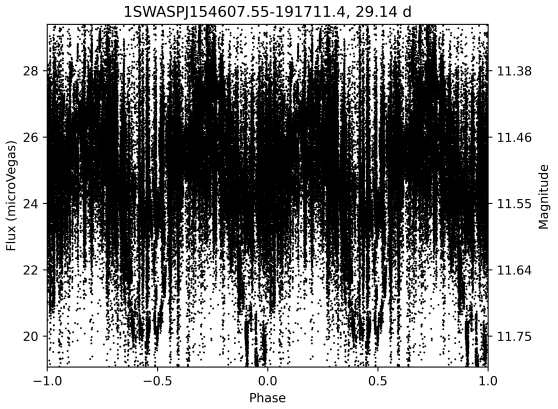

Fig. 11.14 SuperWASP light curve for J154607 phase-folded with a period of 29.14 d.

The exact coordinates for J135703 point toward a star of similar magnitude at a distance of 19 arcseconds from ASASSN-V J135701.95-474810.0, shown by the simulated finder chart displayed in Fig 11.17. The latter is most likely the true binary, whereas the SuperWASP object is a non-variable star, with the misclassification being due to the large pixel scale of SuperWASP possibly covering both stars within the aperture. Therefore, the non-variable star was observed spectroscopically. It is fortunate that this mistake was made only for a star which, based on its light curve, is very unlikely to be a NCRGEB. Through spectral typing and synthesis, the target was found to be a G8-type star with T_{eff} ∼4960 K. Despite this, it may be worth correctly following up this target spectroscopically for confirmation.

1SWASPJ103327.40-304931.6

This faint (V=15.6) stellar object was identified through a cross-match between the SuperWASP and ASAS-SN Catalogue of Variable Stars. Unusually, for this object, the SuperWASP and ASAS-SN periods differed significantly, periods of 0.90 d and 17.87 d respectively. The light curve lies just at the magnitude limit of SuperWASP, however it appears to be an EW-type binary (Fig 11.19). Similarly, the ASAS-SN light curve also appears to be that of

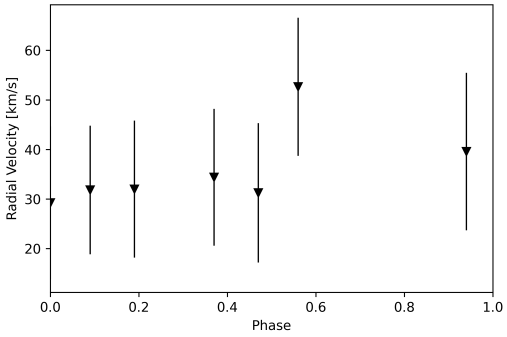

Fig. 11.15 Radial velocity curve for J135703 phase-folded with a period of 10.71 d.

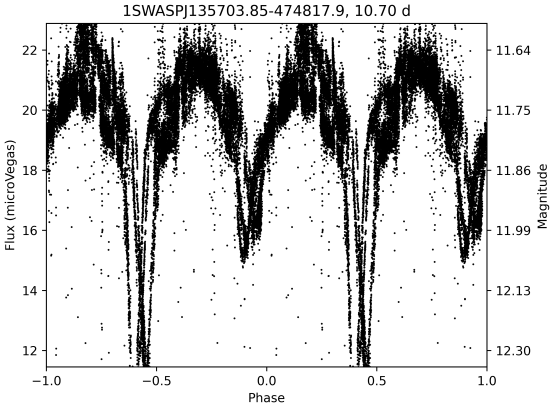

Fig. 11.16 SuperWASP light curve for J135703 phase-folded with a period of 10.71 d.

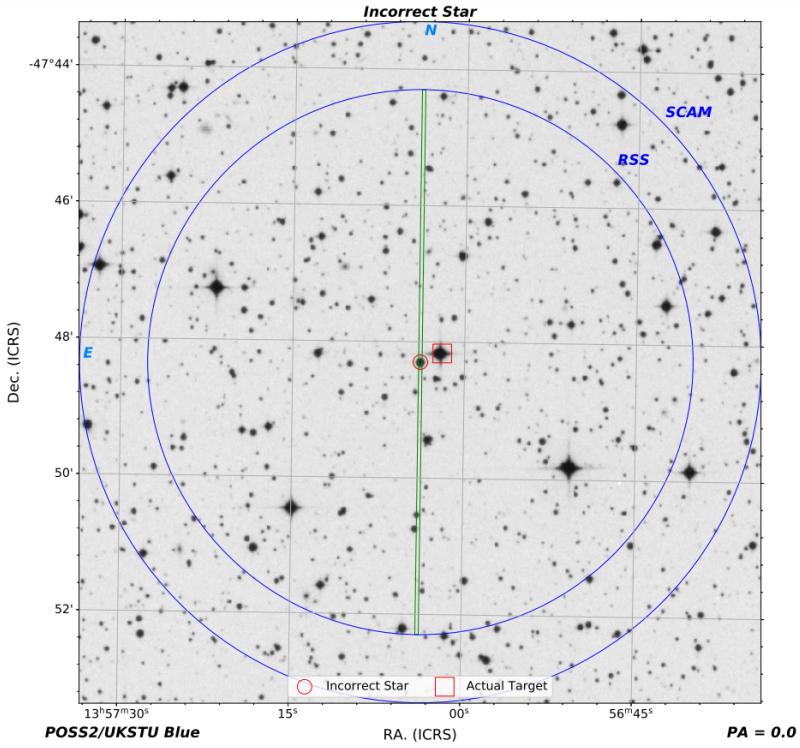

Fig. 11.17 Simulated finder chart created using *FinderChartWithAlignmentStar* (Dickinson, private communication). The finder chart indicates that the target star did not fall within the slit and its spectrum could not be extracted from observational data.

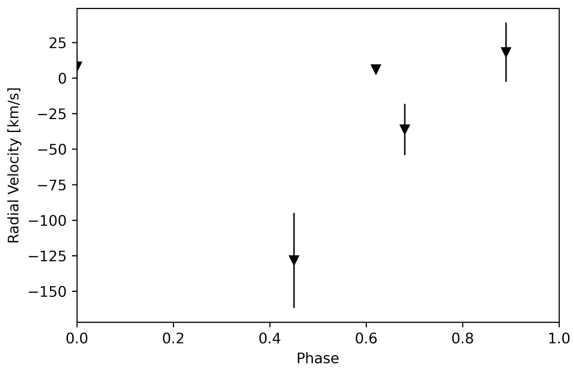

Fig. 11.18 Radial velocity curve for J103327 phase-folded with a period of 17.87 d.

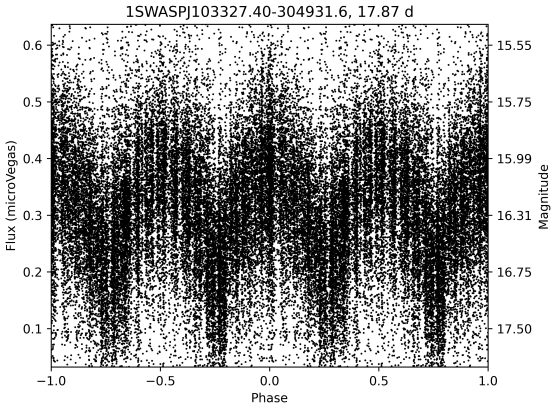

Fig. 11.19 SuperWASP light curve for J103327 phase-folded with a period of 17.87 d.

an EW-type binary, although it was originally classified as an EB-type binary (Drake et al., 2017).

J103327 was followed up using PIRATE, gaining 15 nights of BVRI photometry. An attempt was made to carry out BVR follow-up using LCO, however only 1 observation was successful. J103327 was followed up using SALT, covering only 5 nights of observations. Through spectral typing and synthesis, the target was found to be a K3-type star with T_{eff} ∼4320 K. Despite the low number of observations, the spectra are very odd, and emission and absorption lines change rapidly, especially the Na doublet and Hydrogen alpha lines. The radial velocity curve (Fig 11.18) shows no apparent real radial velocity variations, however the spectra have a clear split Hα which shows a periodic rise and fall, characteristic of a shell star. Due to the low number of spectra, it is not clear whether this object is a Be star with a decretion disc, or a binary system with an accretion disc causing hydrogen emission (Labadie-Bartz et al., 2017). J103327 is likely not to be a NCRGEB and does not require further follow-up.

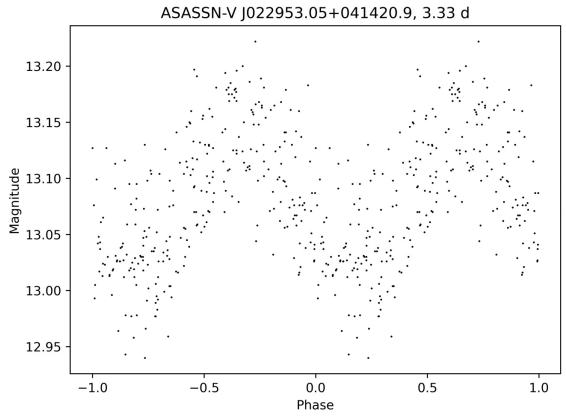

Fig. 11.20 ASAS-SN light curve for J022953 phase-folded with a period of 3.33 d.

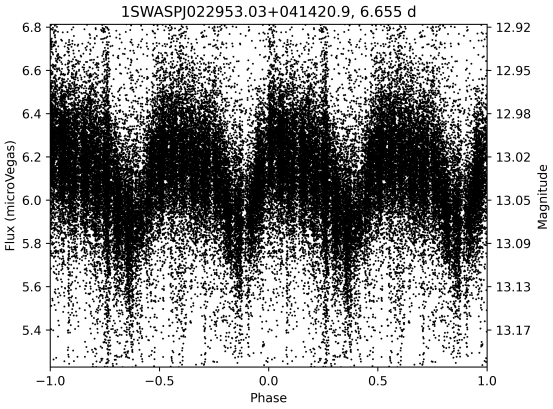

Fig. 11.21 SuperWASP light curve for J022953 phase-folded with a period of 6.66 d.

1SWASPJ022953.03+041420.9

This object was also identified by citizen scientist volunteers, with a period of 6.66 d. In the ASAS-SN Catalogue of Variable Stars, it was identified as ASASSN-V J022953.05+041420.9, a rotator with a period of 3.33 d. Little else is known about this target.

The SuperWASP phase-folded light curve (Fig 11.21) was fairly unconvincing, with an asymmetric profile and the ASAS-SN light curve (Fig 11.20) showing a triangular profile. Nonetheless, follow-up was attempted, and J022953 gained 15 nights of multi colour photometry with PIRATE, however this sparse follow-up did not provide much additional information.

J022953 was followed up spectroscopically with NRES on LCO, however it was not possible to extract spectra or radial velocities from the provided observations. From the light curve alone, J022953 was discounted as a NCRGEB and does not require further follow-up.

1SWASPJ003414.72-291038.4

This object was identified by citizen scientist volunteers, with a period of 11.32 d. At the time, it had no counterpart in the ASAS-SN Catalogue of Variable Stars, but has since been

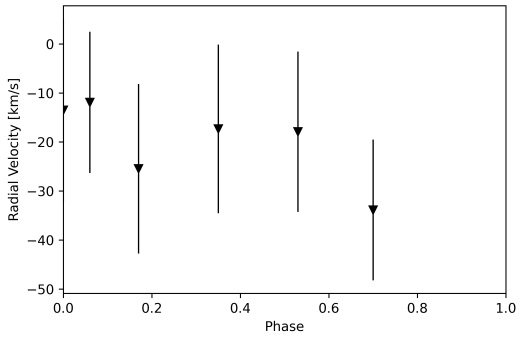

Fig. 11.22 Radial velocity curve for J003414 phase-folded with a period of 11.32 d.

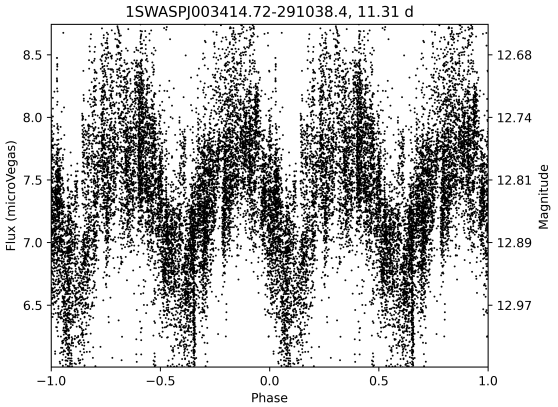

Fig. 11.23 SuperWASP light curve for J003414 phase-folded with a period of 11.32 d.

identified as ASASSN-V J003414.02-291116.3, a rotator with a period of 5.66 days, exactly half the period of the SuperWASP target. In VSX, multiple possible classifications exist for the target with a period of 5.65 d, including Cepheid, detached eclipsing binary, and ellipsoidal variable. Little else is known about J003414.

The phase-folded SuperWASP light curve (Fig 11.23) appeared to be a good contender for a NCRGEB, although the ASAS-SN light curve shows a more triangular profile. J003414 was followed up both photometrically and spectroscopically, using PIRATE and the 74″. However, only 5 nights of multi colour photometry with PIRATE was possible, due to scheduling constraints.

6 nights of spectroscopic follow-up were completed for J003414, however no characteristic binary line splitting was observed, and radial velocity extraction showed no periodic variation. Through spectral typing and synthesis, the target was found to be a G8-type star with T_{eff} ∼4960 K. The radial velocity curve (Fig 11.22) therefore shows that J003414 is not a NCRGEB and does not require further follow-up.

1SWASPJ002349.66+483114.5

J002349 was identified by citizen scientist volunteers, with a period of 17.14 d. It has an ASAS-SN counterpart, ASASSN-V J002349.64+483114.4, a rotationally modulated object with a period of 8.55 d, almost half that of the SuperWASP period. Interestingly, a ROSAT X-ray source, 1RXS J002348.8+483114 is almost coincident with this target, though similar to other targets, little else is known about it.

The phase-folded SuperWASP light curve was one of the less convincing NCRGEB candidates (Fig 11.25), with a slightly asymmetric triangular profile. From the outset, it was unlikely to be a successful candidate, however follow-up was still done. J002349 was observed with PIRATE for 2 weeks in BVRI filters, sparsely covering 2 periods. Photometric follow-up was hampered by the declination of the target, so the resultant light curve provides little extra information.

J002349 was observed with the Liverpool Telescope over 15 nights, however clear Hα absorption features were only visible for 1 night. For the remainder of the spectra, there appears to be a very faint Hα emission profile, or no detectable Hα emission or absorption at all. Through spectral typing and synthesis, the target was found to be a K3-type star with T_{eff} $\sim$4380 K. Radial velocities were extracted using the Ca line and appears to show some convincing periodic variability. J002349 is likely not to be a NCRGEB and does not require further follow-up.

1SWASPJ001545.50-622237.8

This object was identified by citizen scientist volunteers in the SuperWASP Variable Stars project part way through the 74″ observing run. The period of this object in SuperWASP is 91.03 d, the longest candidate NCRGEB. J001545 has a counterpart in the ASAS-SN Catalogue of Variable Stars, ASASSN-V J001545.47-622238.0, which is classified as a rotator with a period of 44.90 d. Little else is known about this target.

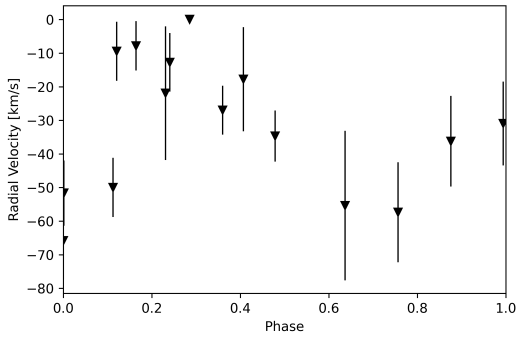

Fig. 11.24 Radial velocity curve for J002349 phase-folded with a period of 17.14 d.

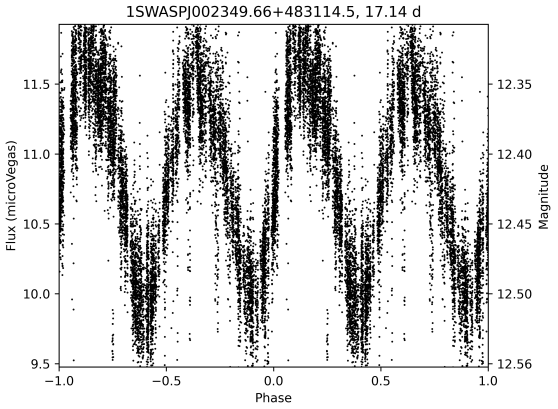

Fig. 11.25 SuperWASP light curve for J002349 phase-folded with a period of 17.14 d.

The SuperWASP phase-folded light curve (Fig 11.27) appears to be that of a NCRGEB, however, the unfolded light curve displays a more triangular profile, similar to that of a rotationally modulated star. Despite this, spectroscopic follow-up was done in order to confirm whether this system is a rotator or a binary. No photometric follow-up was possible, and J001545 was not observed with PIRATE or LCO due to the declination of the target.

J001545 was observed with the 74″ over 5 nights with a typical S/N∼15.8, although the final night provided unusable data. Through spectral typing and synthesis, the target was found to be a K5-type star with T_{eff} ∼3980 K. The target showed no signs of binary splitting of absorption lines, and despite radial velocity extraction, the radial velocity stayed constant showing no indication of a binary component and phase coverage was sparse (Fig 11.26). The radial velocity curve therefore shows that J001545 is not a binary and does not require further follow-up.

1SWASPJ000927.89+014542.1

This object was flagged by citizen scientist volunteers in the SuperWASP Variable Stars project. The SuperWASP period of this object is 32.72 d. J000927 has counterparts in the 2MASS, ASAS-SN and Gaia DR2 catalogues, but has no ASAS-SN variability detection. In

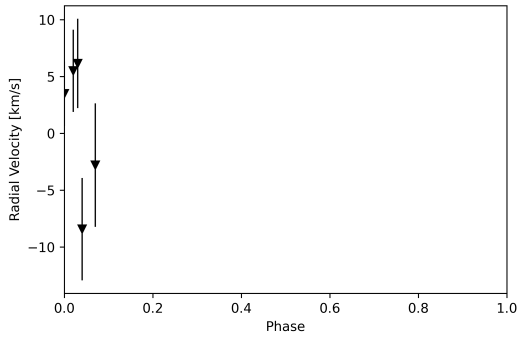

Fig. 11.26 Radial velocity curve for J001545 phase-folded with a period of 91.03 d.

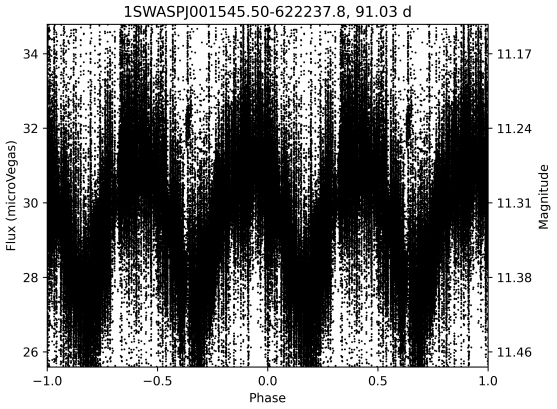

Fig. 11.27 SuperWASP light curve for J001545 phase-folded with a period of 91.03 d.

SIMBAD it is identified as a red giant star, and Price-Whelan et al. (2018) identify it as a likely evolved red giant with a companion, but could not determine any orbital properties. Since the start of the project, it has been identified in ZTF as ZTF J000927.88+014541.7, with a classification of a long period RS Canum Venaticorum-type (RS CVn) binary system with a gmag amplitude of 0.16 and a period of 16.71 d, just over half the SuperWASP period (Chen et al., 2020).

The SuperWASP light curve (Fig 11.29) appears to be a NCRGEB, although the faintness of the object makes it difficult to be sure. Despite this, follow-up observations were made on the 74″ and PIRATE. PIRATE was only able to make 8 nights of observations over 1 month, sparsely covering one full period, not enough to extract a multi-colour phase-folded light curve.

Although J000927 was observed with the 74″ for 9 nights, only 5 nights provided high quality data with a S/N∼25, whereas the poor quality data nights provided a S/N∼5–7. Through spectral typing and synthesis, the target was found to be a K5-type star with T_{eff} ∼4810 K. J000927 is a faint object with a magnitude of V = 14.15, requiring exposure times of ∼20 minutes. J000927 showed signs of splitting of spectral lines, as would be expected for a binary, and attempts were made to extract a radial velocity curve, however this

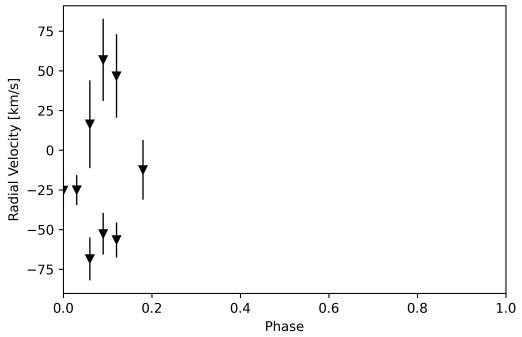

Fig. 11.28 Radial velocity curve for J000927 phase-folded with a period of 32.72 d..

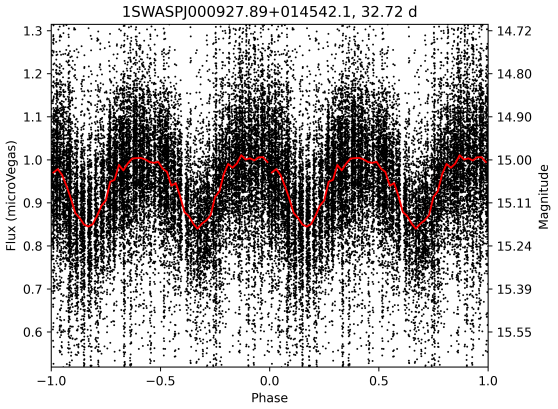

Fig. 11.29 SuperWASP light curve for J000927 phase-folded with a period of 32.72 d.

proved inconclusive (Fig 11.28). J000927 cannot be discounted as a candidate NCRGEB, however further photometric and spectroscopic follow-up using telescopes with a fainter magnitude limit would be required.

1SWASPJ000018.09+091923.9

J000018 was identified by citizen scientist volunteers in the SuperWASP Variable Stars project. The SuperWASP period of this object is 85.75 d, the second longest candidate NCRGEB. It is also known as TYC 594-495-1, ASAS 000018+0919.4, and UCAC4 497-000008, and was detected as a miscellaneous variable with a period of 43.07 d in ASAS (Pojmanski, 2002), and a rotator with a period of 869.28 d in the ASAS-SN Catalogue of Variable Stars.

The SuperWASP light curve appeared to be a NCRGEB, but also appeared to more closely resemble the light curve of a pulsating star with a period of 43.07 d. The phase-folded light curve from ASAS-SN equally shows the same, whether folded at the SuperWASP or ASAS-SN period, however since it was possible to carry out follow-up observations without significant extra time or cost, J000018 was followed up both photometrically and

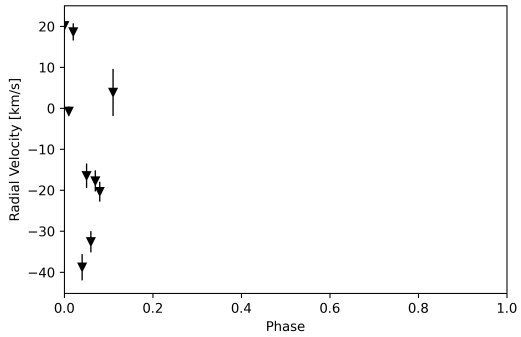

Fig. 11.30 Radial velocity curve for J000018 phase-folded with a period of 85.75 d.

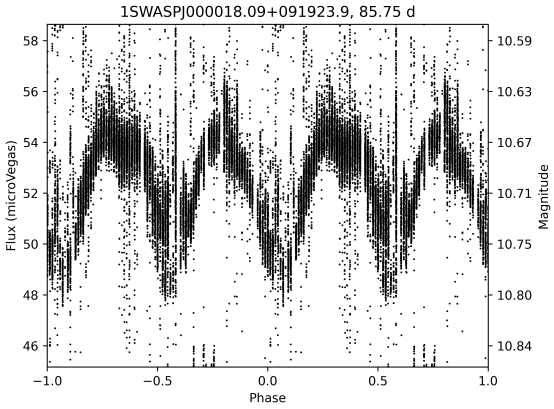

Fig. 11.31 SuperWASP light curve for J000018 phase-folded with a period of 85.75 d.

spectroscopically. J000018 was observed with PIRATE gaining ∼165 observations per filter over 3 months, equivalent to ∼41 nights.

J000018 was observed with the 74″ over 9 nights with a typical S/N∼21, giving usable spectra for each night. Through spectral typing and synthesis, the target was found to be a K4-type star with T_{eff} ∼4080 K. The radial velocity curve (Fig 11.30) does not appear to show a clear periodicity and the light curve itself appears to be closer to that of a Cepheid (Fig 11.31). J000018 is likely not to be a binary and does not require further follow-up.

11.2 Discussion and summary

In this short chapter, I summarised the observations of candidate NCRGEB which turned out to be other stellar variable types. Where possible, each candidate received multi-colour photometric and spectroscopic follow-up, as well as radial velocity extraction and spectral synthesis. Table 11.1 provides a summary of each target and the most likely variable type.

Unfortunately, 1 target, J135703 was incorrectly observed due to a mistake with the SuperWASP and ASAS-SN coordinates. Luckily, this target was unlikely to fit the NCRGEB criteria due to the distinct eclipse depth differences and did not warrant further follow-up.

Of the 14 discounted candidates, 3 appeared to be shell type stars with Hα emission. These types of systems can exist as either single stars or as binary systems, and it is likely that the systems detected here are binary systems due to line splitting of other strong lines and photometric light curves with clear eclipses. Whilst these stars are fascinating, they are not within the remit of this research and thus do not warrant further follow-up. Of these, 2 stars show extremes of Hα emission and absorption. J192628 almost exclusively shows double peaked Hα emission, but one on night, suddenly switches from emission to absorption and then returns to emission in the following observations. Conversely, J165655 shows almost exclusively absorption, but every $\sim$8 d, shows double peaked Hα emission. It is unclear as to the exact model for such extremes, however, they are likely to fall in the family of shell stars, stars with decretion discs, or stars with anisotropic discs which periodically display gaps. Similar systems are described by Rivinius et al. (2006) who find that the emission lines of the shell are not always detected in the spectrum. Unusually for shell stars (which are typically of spectral types O–F), these targets are late-type (K-type) stars, which is rare but not an unrealistic physical scenario (e.g. Danchi et al. 1994; de la Reza et al. 1997). However, this indicates that these may not be standard shell stars. Further follow-up would be required to fully understand these unusual objects.

The remainder of the targets appear to be either rotationally modulated stars, or Cepheid variables whose minima and maxima mimic eclipses when phase-folded at twice the period. Such targets were, from the photometric light curves alone, unlikely to be NCRGEB systems, however spectroscopic follow-up was done to confirm the variable type. Table 11.1 shows that the most common variable type confused with NCRGEB was rotational variables.

Whilst none of these stars necessarily warrant any specific follow-up or further study in the context of NCRGEB study, they can act as examples of what variable types can be confused with NCRGEB, acting as a warning for future work.

WASP ID	Period /d (binary)	Period /d (actual)	Variable type
1SWASPJ192628.96-233856.1	28.54	28.54	Shell
1SWASPJ192311.66-423244.5	16.64	8.32	Rotator
1SWASPJ191910.42-414050.9	16.60	16.60	Uncertain
1SWASPJ165656.26-040414.3	15.68	7.84	Shell
1SWASPJ165241.24+203224.7	15.13	7.57	Cepheid
1SWASPJ154607.55-191711.4	29.14	29.26	Semiregular
1SWASPJ135703.85-474817.9	10.71	10.69	EB binary
1SWASPJ103327.40-304931.6	0.90	17.87	Shell
1SWASPJ022953.03+041420.9	6.66	3.33	Rotator
1SWASPJ003414.72-291038.4	11.32	5.65	Rotator
1SWASPJ002349.66+483114.5	17.14	8.55	Rotator
1SWASPJ001545.50-622237.8	91.03	44.90	Rotator
1SWASPJ000927.89+014542.1	32.72	16.71	RS CVn
1SWASPJ000018.09+091923.9	85.75	43.07	Cepheid

Table 11.1 Summary of NCRGEB candidates discounted through photometric and spectroscopic follow-up. The majority of non-NCRGEB targets appear to be rotational variables.

Chapter 12

Classifying SuperWASP Variable Stars with Citizen Science

In this chapter, I begin to explore new ways of exploiting the vast SuperWASP archive: citizen science. There is a beauty in working with thousands of people across the world, all with the same goal of understanding the variable night sky, and I feel lucky to have had the opportunity to do so.

This chapter will introduce the SuperWASP Variable Stars Zooniverse project, a citizen science project which is aiming to classify $\sim$1.6 million phase-folded light curves of candidate stellar variables observed by the SuperWASP all sky survey with periods detected in the *SuperWASP periodicity catalogue*. The majority of this chapter was published in Thiemann et al. (2021).

Here, I will present the first analysis of results from the SuperWASP Variable Stars Zooniverse project, which, as of September 2020, contained $>$1 million classifications corresponding to $>$500,000 object-period combinations, provided by citizen-scientist volunteers. This chapter consists of an analysis of the accuracy of citizen-scientist volunteers in the classification of stellar variables, and the identification of previously unknown binaries, pulsators, and other preliminary findings on various unique and extreme stellar variables. I

also describe the future of the SuperWASP Variable Stars project as both a source of labelled data for machine learning and for further exploitation of the SuperWASP archive.

12.1 Introduction

Variable stars are key to investigating and testing stellar astrophysics, and the dynamics and structure of stellar systems. The detection, classification, and study of classes of variable stars is therefore an important pursuit. Typically, variable stars are detected through amplitude and period variations in their photometric light curve. Classifications of periodic variables based on their light curve are not always conclusive, but instead give a strong indication of variable type, and can be used to identify candidates for spectroscopic and photometric follow-up.

There have been previous attempts at using machine learning algorithms and Artificial Neural Networks (ANNs), often called Neural Networks (NN), to automate the classification of SuperWASP variable stars from the raw data, including Payne (2013), who made use of three NNs to process a range of parameters which defined the shape of the phase folded light curve. They processed over 4.3 million periods, giving $\sim$1.1 million preliminary classifications. However these NNs found only partial success, identifying 75% of light curves correctly. As an alternative to machine learning, the SuperWASP Variable Stars (SVS) Zooniverse[1] project is instead using citizen science to classify the 1.6 million folded light curves referred to above.

The SVS project was launched on 5th Sep 2018 and had engaged $\sim$4,500 volunteers at the time of this analysis in September 2020. This analysis acts as a preliminary look at the Zooniverse classifications, demonstrating that SVS can be used for both population studies and for identifying rare and unique variables. This analysis will guide how the project is developed as it gains more volunteer and machine learning classifications. The SuperWASP data used for SuperWASP Variable Stars was described in Chapter 3. and in Section 12.2 I

[1] www.zooniverse.org/projects/ajnorton/superwasp-variable-stars

describe the Zooniverse project itself. In Section 12.3 I summarise our results including the identification of new and unique stellar variables, and in Section 12.5 I draw conclusions and look to the future of the project.

12.2 Citizen science

The Zooniverse[2] (Lintott et al., 2008) is the world's most popular platform for "people-powered research", where a community of volunteers, or "citizen scientists", can participate in real scientific research through simple tasks such as analysing and categorising large data sets. This approach, using the "wisdom of the crowd", can be used to greatly improve the accuracy and speed with which data can be analysed and classified. Despite minimal training and subject matter expertise, Zooniverse volunteers have proven time and time again that non-experts can achieve a good level of accuracy, and can identify unusual objects that automated algorithms will often miss.

SVS launched on 5th September 2018, with the aim of classifying the output of the *SuperWASP Periodicity Catalogue* (Norton, 2018). The aim of SVS is threefold: to identify rare variable stars; to identify populations of variable stars in order to probe the extremes and trends of each population; and to facilitate the future development of a web portal in order to give researchers and the public access to the output of this project.

The SVS project was constructed using the Zooniverse project builder platform[3], creating a classification task, tutorial, and "Field Guide" which provides example light curves and guidance for classification. There is also an option for volunteers to report their findings in the "Talk" section, where they can discuss individual light curves, highlight unusual and rare ones, and identify which objects have already been detected in other databases.

[2] www.zooniverse.org/
[3] www.zooniverse.org/lab

The classification of variable stars can be difficult, with 211 variable star types and sub-types listed in the International Variable Star Index[4] (VSX) Watson et al. (2020). The noise level of the SuperWASP light curves often makes it difficult to distinguish between similar types of variables. However, to be successful, Zooniverse, projects must be accessible to non-subject matter experts. Volunteers are therefore asked to classify light curves into the following generic and overarching variable types:

- Pulsators: stars which display periodic changes in brightness due to changes in the star's size and luminosity as its outer layers expand and contract in a regular manner. This category includes RR Lyrae, δ Scuti, Cepheid variables, and Mira variables. Light curves are often asymmetric with a steeper rise and shallower fall in brightness.

- EA/EB: detached and semi-detached eclipsing binary systems which display periodic changes in brightness. This category includes Algol (EA) and Beta Lyrae (EB) eclipsing binaries. Two eclipses per cycle may be distinguished, often of different depth, with clear boundaries to the eclipses.

- EW: contact-eclipsing and near-contact eclipsing binary systems which display periodic changes in brightness. This category includes W Ursae Majoris (EW) type eclipsing binaries. Brightness variation is continuous and the eclipses are often of similar depth, resulting in half the orbital period often being identified instead of the true period.

- Rotators: stars which display rotational modulation in their light curve. This category includes single stars with significant star spots and stars with ellipsoidal modulation from close binaries that do not eclipse but instead are distorted into non-spherical (ellipsoidal) shapes by gravity due to their proximity. Brightness variations are typically quasi-sinusoidal.

[4]www.aavso.org/vsx/index.php

- Unknown: stars displaying some degree of periodicity but which do not fall into any previous category. This category might include semi-regular stars and long period variables.

- Junk: light curves which display no genuine periodicity, or apparent periodicity which is due only to data dropouts or remaining systematic artefacts.

To generate subjects for SVS (Norton, 2018), light curve data for objects with one or more potentially genuine periods listed in the *SuperWASP Periodicity Catalogue* were used. The data for each selected object were folded at each of its potential periods and then rendered to produce a set of one or more phase-folded light curve images. Each image displays the raw photometric data points, overlaid with the mean profile in 100 phase bins, an example of which is shown in Figure 12.1.

Volunteers are presented with a phase-folded light curve and tasked with classifying it into one of the following options: pulsator, EA/EB, EW, rotator, unknown, or junk, shown in Figure 12.1. If the volunteer chooses either EA/EB, EW, or pulsator, they are presented with a second question which asks them to choose whether the folding period is: correct period, half period, or wrong period. The classification task itself is essentially a pattern matching task.

Multiple classifications of each phase-folded light curve are collected, and the most common classification is taken as the true classification and "retire" it from the live project. Between 5th September 2018 – 23rd September 2019, each light curve required 7 classifications from separate volunteers to "retire" it, meaning that if a light curve received 4 or more of the same classification, the light curve would be assigned to the corresponding category. On 24th September 2019, a variable retirement rate was implemented using the Caesar[5] advanced retirement engine provided by the Zooniverse platform. As a result, a light curve is now retired if either the classification count reaches 7, the subject receives 4 of the same

[5]https://caesar.zooniverse.org/

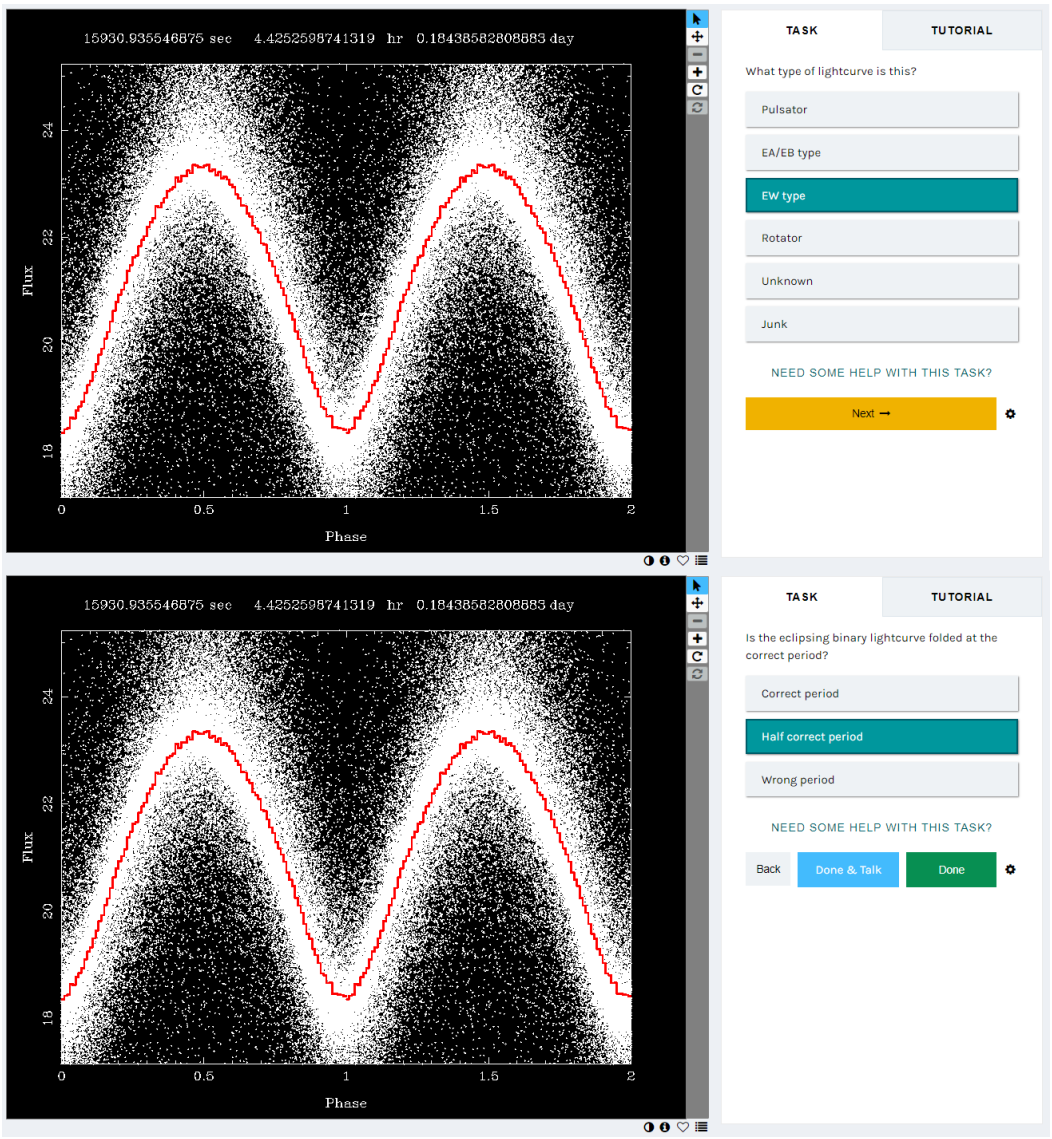

Fig. 12.1 **Upper panel:** Volunteers are first tasked with classifying each light curve as a generic variable type. This example shows an EW folded at half the correct period. **Lower panel:** If a volunteer chooses a classification of EA/EB, EW, or pulsator, they are asked to choose whether the period is correct or not.

classification, or if the subject receives 3 junk classifications, since junk light curves are typically easier to identify. Following the introduction of the variable retirement rate with Caesar, junk classified subjects are retired more quickly, so it would be expected that there is a higher relative frequency of junk in the output, with the number of junk classifications eventually plateauing as they are retired from the live project.

In the period immediately following the project launch, the subject images presented to volunteers were selected randomly from the full pool of 1.6 million light curves. Even if all 4,500 volunteers that had so far engaged with the project classified one subject per minute, the expected time for any particular subject to accrue 7 classifications is almost 40 hours. In reality, the initial retirement rate was ∼3,000 subjects per month on average. Accordingly, a subject batching strategy was adopted which reduced the available subject pool size to 288,000 light curves at any one time. Following this change, the retirement rate increased to ∼17,000 subjects per month, peaking at ∼43,711 retirements in October 2019.

Figure 12.2 shows the number of classifications and retirements during the first 2 years of SVS. The shallow increase shows pre-launch classifications from experts and beta testers. SVS was officially launched on 2nd September 2018, and since then has had a fairly consistent classification rate. Peaks of activity (such as being a "featured project") cause sudden rises in classifications. The change to a variable retirement limit and batching is clear in early 2019.

During peak times of activity (when SVS is promoted as a "featured project" on the Zooniverse front page), there is an average of ∼4,300 classifications per day, peaking at 11,442; outside of these intervals, there is an average of ∼1,100 classifications per day and a retirement rate of ∼5,000 per month. At this lower classification rate, it is estimated that it will take ∼4–5 years to complete each "live" set of 288,000 objects, or ∼25 years to complete the full set (∼15 years at a higher classification rate). By comparison, I classified ∼5,000 light curves in a day without working on other research activities. Considering these

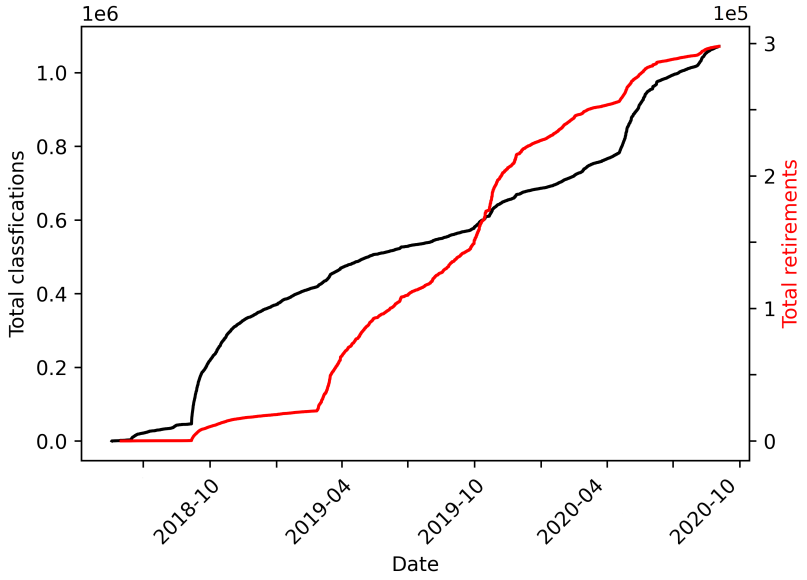

Fig. 12.2 The number of classifications (black) and retirements (red) over the first 2 years of the project.

timescales, machine learning will be vital to complete the classification of all 1.6 million phase-folded light curves within a reasonable time-frame.

The Gini coefficient is used to give a quantitative measure of the engagement of volunteers. The Gini coefficient ranges from 0 to 1, where 0 indicates that each volunteer contributes an equal number of classifications, and 1 indicates that there is an extreme difference in number of classifications from each volunteer. The mean Gini coefficient for SVS is found to be 0.92. By comparison, Spiers et al. (2019) finds that the mean Gini coefficient for astronomy projects on Zooniverse is 0.82, and Eisner et al. (2020) finds a similarly high Gini coefficient for *Planet Hunters TESS* of 0.94. Whilst a higher Gini coefficient does not necessarily indicate project "success", it does indicate that SVS has a large number of prolific classifiers, which is often desirable for citizen science projects. Loyal classifiers spend more time engaging with the project, and hence are likely to have a strong understanding of the project aims and classification methods and make fewer mistakes.

For the project age, SVS has fewer total volunteers than other general astronomy projects on the Zooniverse, but a comparable number of total volunteers to other non-astronomy

projects and variable star astronomy projects. A direct comparison is *Variable Star Zoo*[6] (classifying ∼60,000 light curves), a project which aims to classify variable stars in the VVV survey. *Variable Star Zoo* launched in July 2018 and has engaged with 5,305 volunteers to date, similar to SVS. Two upcoming variable star Zooniverse projects are *Zwicky Stellar Sleuths*[7], and *Citizen ASAS-SN*[8]. SVS will complement these projects, and the increase in variable star Zooniverse projects may increase volunteer interest in this branch of astronomy.

12.2.1 Data cleaning

The classifications used in this analysis were downloaded on 2nd September 2020, giving almost 2 years of classification data. Although there have been 1,071,345 classifications corresponding to over 568,739 unique object-period combinations, the majority of light curves have not yet received a sufficient number of classifications for retirement.

Classifications from SVS are exported as a CSV file from the Zooniverse site. Before data cleaning, the SVS classification export is stripped of non-essential data, including time of classification and username of Zooniverse volunteers. In addition to the primary science analysis, an in-depth assessment of classification reliability, including detection of "spam" classifications was performed. For this secondary analysis, the full SVS classification export was used as is.

The likely classification for each subject is decided by a custom written script. This script looks at all the classifications of the same Subject ID (or same SuperWASP ID and Period ID) and finds the most popular (or only) classification. If two (or more) classifications are equally popular, then the classification allocated is the first given classification from the following list: junk, pulsator, rotator, EW, EA/EB, unknown (ordered from most common to least common). The unfiltered SVS export has 1,071,345 rows corresponding to all classi-

[6]https://www.zooniverse.org/projects/ilacerna/variable-star-zoo
[7]https://www.zooniverse.org/projects/adamamiller/zwickys-stellar-sleuths
[8]https://www.zooniverse.org/projects/tharinduj/citizen-asas-sn

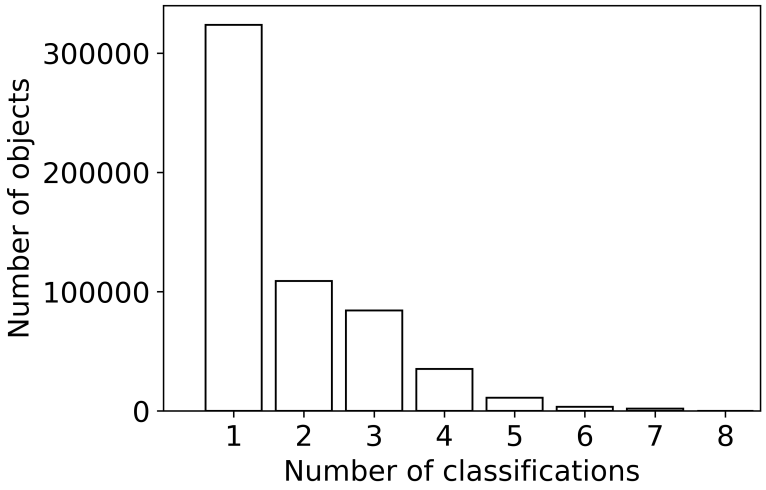

Fig. 12.3 A histogram of the number of classifications per SVS object.

fications made up to that time. After processing and removing duplicated rows, 1,025,750 light curve classifications remain. After finding the top classification for each subject, the output had 568,739 rows corresponding to unique object-period combinations. Figure 12.3 shows a histogram of the number of classifications per object. There are 5 objects with 9 classifications, 27 objects with 8 classifications, 1934 objects with 7 classifications, and 3510 objects with 6 classifications, 11,085 with 5 classifications, 35,298 with 4 classifications, 84,180 with 3 classifications, 109,034 with 2 classifications, 323,666 with 1 classification. At this stage, only 9% of objects (7% of non-junk objects) have received enough classifications for retirement.

Additional catalogues are cross-matched with the output to identify additional parameters such as distance, colour, and previous classifications. This includes a 10 arcsecond spatial cross-match with Gaia-DR2 and the Gaia-DR2 Bailer-Jones distance catalogue (Bailer-Jones et al. 2018; Gaia Collaboration 2018), a 10 arcsecond cross-match with NOMAD (Zacharias et al., 2004), and a 2 arcminute cross-match to VSX (Watson et al., 2020).

Light curves with fewer than 4 classifications are removed, and any remaining duplicates (both spatial and WASP ID) are retained, since these are plausibly multi-periodic or multi-

	Full	EA/EB	EW	Pulsator	Rotator	Unknown	Junk
Classifications	568739	29882	36328	25730	56582	41541	378,671
$N_{class} \geq 4$	13390	2425	3187	1777	4402	1599	N/A
$N_{class} \geq 4$, $P_{correct}$	11322	1629	2672	1020	4402	1599	N/A
In Gaia-DR2	10213	792	2599	1000	4275	1547	N/A
In VSX	5,283	665	1528	579	1939	572	N/A
Payne and/or Greer	314	259	44	11	N/A	N/A	N/A

Table 12.1 Breakdown of the first 1 million classifications corresponding to 568,739 unique object-period combinations, and the results of positional cross-matches to the Gaia-DR2 and Bailer-Jones et al. (2018) catalogue, VSX, and SuperWASP catalogues of binaries Payne (2013) and pulsators Greer et al. (2017).

classification objects. An initial visual assessment of unrealistic periods is completed, but at this stage, objects with such periods are not removed since these are plausibly extreme period objects which may be of interest. Table 12.1 shows a breakdown of the cleaned data set.

12.2.2 Classification reliability

A total of 7,478 volunteers made 1,071,345 classifications. SVS has ∼4,500 registered volunteers, indicating that ∼3000 volunteers engaged with the project but did not register on the Zooniverse platform. Registered volunteers made 93.9% of classification, and 6.1% of classifications (65,398) were made by unregistered or anonymous volunteers, making ∼20 classification each on average. Fig 12.4 shows the distribution of classifications made per volunteer. Just over half (52.6%) of volunteers made 10 or fewer classifications, 36.0% made 11–100, 9.6% made 101–1000, and 1.6% made over 1,000. 18 (0.2%) "super-classifiers" made more than 10,000 classifications. Any classifications made by an anonymous volunteer over different days will be counted as multiple volunteers' inputs.

To estimate the classification reliability, SVS classifications are compared existing variable classifications, such as VSX classifications or Gaia-DR2 variable types. Figure 12.5 shows the confusion matrix for volunteer classifications compared to VSX classifications. While the SVS classification accuracy is high for binaries and pulsators, with ∼89% of EA/EBs, ∼71% of EWs, and ∼78% of pulsators being correctly classified, rotators are a

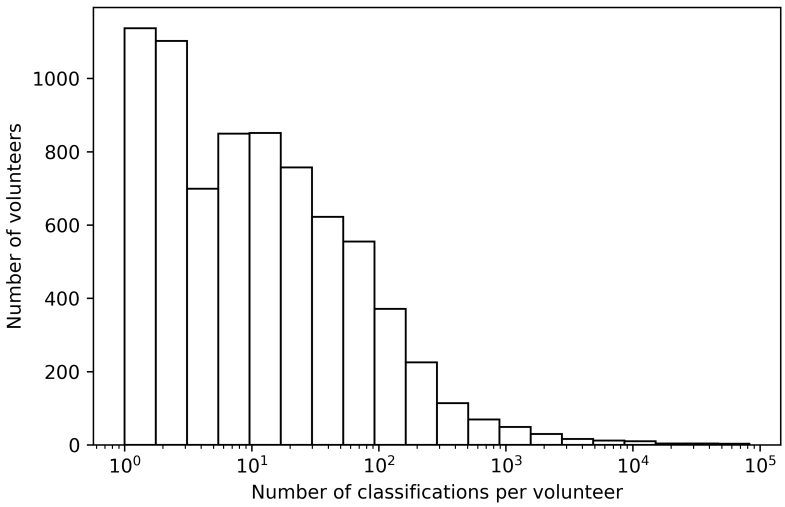

Fig. 12.4 The number of classifications per volunteer.

more challenging variable type with only ∼9% of rotator classifications being "correct". The category of unknown easily categorised, but separating SVS classified objects into their corresponding classes from the VSX catalogue gives ∼24% semi-regular variables, ∼23% miscellaneous variables, and ∼15% long period variables. Overall, a classification accuracy of 60% for all variable types is found, excluding junk.

Too few SVS variables have a Gaia-DR2 variability component to undertake a similar full assessment, using the *Gaia-DR2 variability results* catalogue containing 363,369 classifications of pulsators from Cepheids to Mira variables. Only 1 EA/EB and 8 EW type SVS variables are classified as pulsating stars in Gaia-DR2. Of the 273 pulsators (27% of 1020 identified) in *Gaia-DR2 variability results*, 9 are classified as Type I or II Cepheids, 9 are Mira variables, 17 are δ Scuti stars, and 238 are RR Lyrae stars. 81 rotators and 47 unknown variables are classified as pulsators in *Gaia-DR2 variability results*.

This assessment gives a rudimentary estimate on the probability that different classes of variables are classified correctly. When combined with the *SuperWASP periodicity catalogue* likelihood statistics, it can be used to provide a good idea of the correct period and variability type. It is most likely that incorrect classifications arise from two causes. Some variable types,

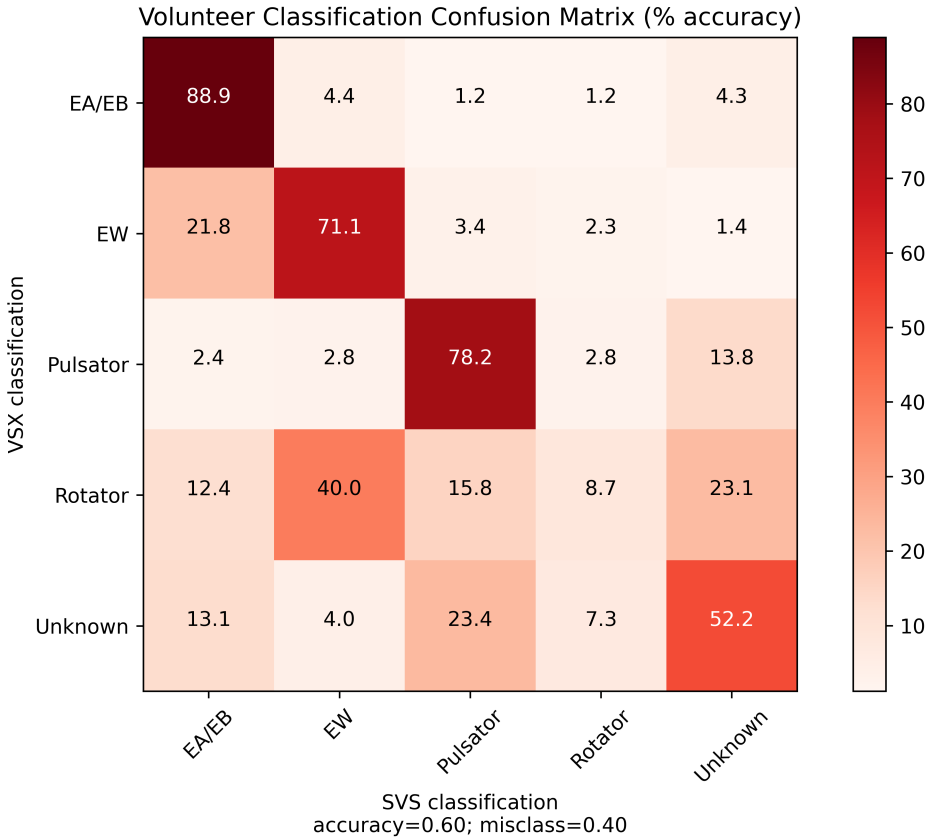

Fig. 12.5 The confusion matrix for volunteer classifications compared to VSX classifications.

especially EA/EB, can appear to be another variable type when folded at the wrong period. It is therefore important that there is a robust method of identifying the true period of an object which may have multiple detected periods, see Section 12.3.3. The other dominant cause of incorrect classifications will mostly likely be human error, and non-specialists may miss some of the nuances of a light curve that indicate a certain variability type. But a cohort of non-specialist volunteers is by no means a bad thing, since the combination of people-power and multiple classifications means that an accurate consensus is usually reached. Feedback from citizen-scientist volunteers also suggests that confusion can arise from the overlaid binned red line, especially in instances where the binned line appears to show a different variable type from the actual data, due to data drop-outs or spikes. At this stage of the project, it is not possible to remove or edit this binned line, but it is something to be aware of in the analysis of the resultant classifications, and use of labelled data in machine learning. Other issues may arise if volunteers skip the training available to them through the Zooniverse interface, forget the training, or find the training is not written in their first language.

While highly unlikely, it is also possible that bots, spamming, or deliberate sabotage can influence the results. There are no in-built protections against this on the Zooniverse platform, so the only way of identifying "spam" classifications is by checking for a high number of classifications by the same user within an unrealistically short time-frame. All classifications were checked for a single user making multiple classifications per second and none were found. It is not possible to check this for users who are not logged in, so unexpected spikes in classifications ($>$100 classifications in $<$1 minute) were searched for. Only one spike in activity matching these parameters was detected by a single user, and their classifications were visually assessed and verified as non-spam.

Volunteer weightings have not yet been implemented in the classification pipeline, but will be an important part of the CNN, and will be used to improve classification reliability. Two simple methods of calculating weightings were trialled: identifying overlap of classifications

with "expert" or author classifications, and overlap with VSX classifications. With 6 possible variable types, a suitable number of classifications is needed for each variable type to calculate weightings. Unfortunately the overlap with "expert" classifications is too low to provide a conclusive weighting. Assessing against VSX, only those have made $>$100 classifications of each variable type were taken, of which only 15 have an overlap of $>$100 with VSX, which also provides an inconclusive weighting system. Alternative methods will be explored in future work, for example through the use of individual volunteer confusion matrices, see Section 12.4.1.

12.3 Results

In this next section, I outline the results of the analysis of citizen scientist-classified light curves, including the discovery of new variable objects, and the hunt for multiply periodic and rare stellar variables.

12.3.1 Overview

Volunteer classifications indicate that this first analysis consists primarily of junk classifications (66.6% of all classifications), which are discarded. The remainder of the classifications are made up of EA/EB (5.3%), EW (6.4%), pulsators (4.5%), rotators (9.9%), and unknown (7.3%). As previously identified, the classification accuracy of rotators is low so the true proportion will be lower than this figure indicates. Figure 12.6 shows the distribution of V band magnitudes ranging from approximately 8$\geq$V$\geq$15, with a number of fainter sources. Figure 12.7 shows the distribution of distances of these typically near-by stellar variables. Each variable type has a similar distribution, with the exception of pulsators, showing a peak in distance at $\sim$4800 pc, with a fainter average V magnitude of $\sim$13.8, likely due to a greater number of more distant stellar variables of this type.

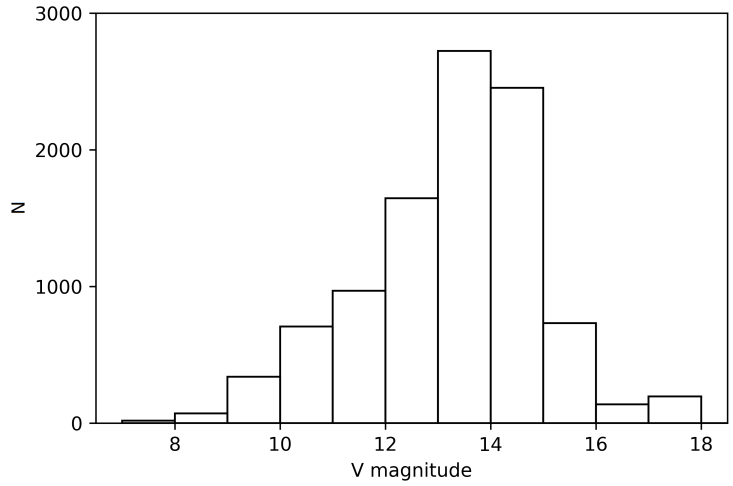

Fig. 12.6 The distribution of NOMAD V magnitude of SVS stars with a variable type classification and correct period classification ranges between 8≥V≥18.

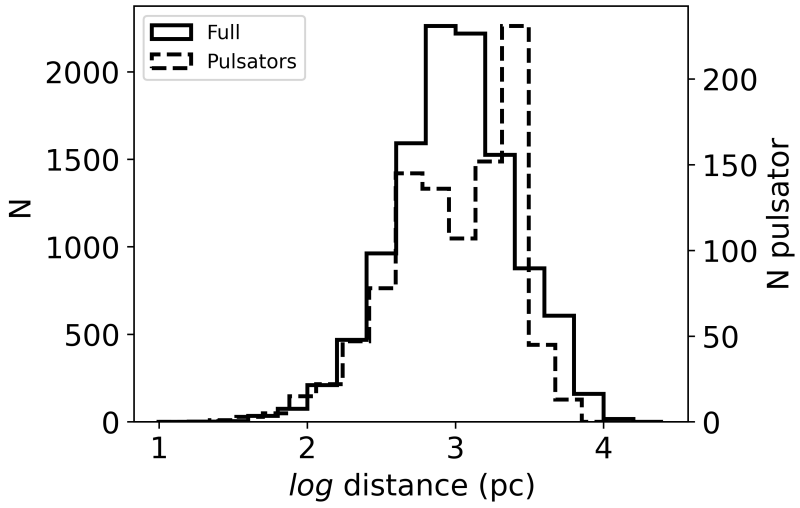

Fig. 12.7 The distance (pc) distribution of SVS stars with a variable type classification and correct period classification. The full data set is shown in the solid line, while the pulsators are shown by the dashed line.

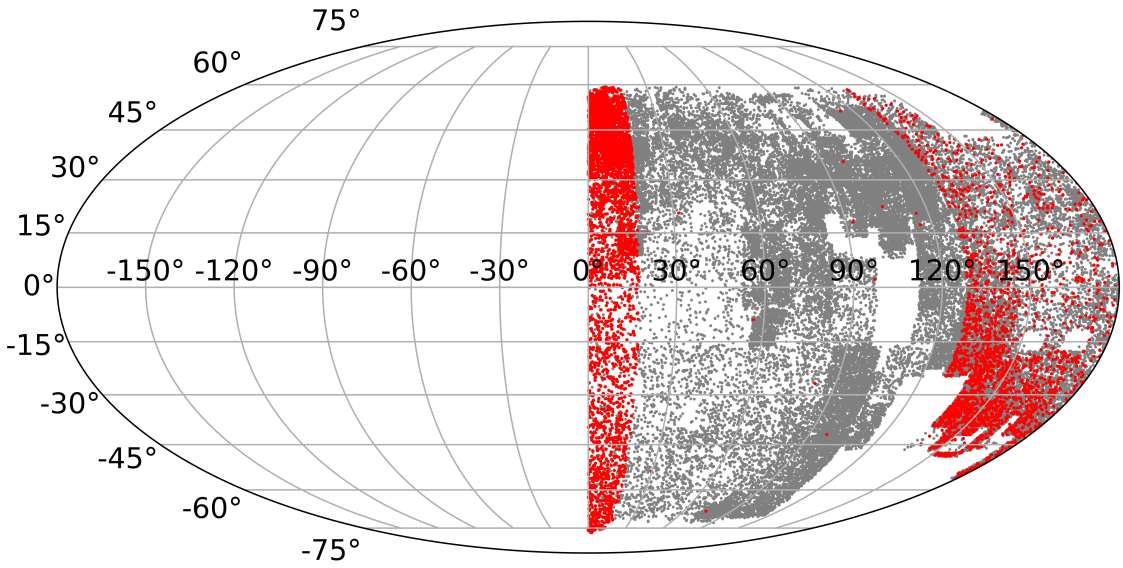

Fig. 12.8 Map of SVS classifications. Red points indicate objects which have been retired from the live queue, grey points indicate objects which have received too few classifications for retirement.

The spatial distribution of the 568,739 unique object-period combinations is shown as a sky density plot in Figure 12.8. The classifications are not evenly distributed, since typically only a few degrees of sky are available for classification at any one time, and SuperWASP could not resolve objects in the dense regions of the Galactic Plane.

The effects of interstellar extinction and reddening on magnitudes, colours, and variable classification have not yet been accounted for. Jayasinghe et al. (2018) make use of the reddening-free Wesenheit magnitudes (e.g. Lebzelter et al. 2018; Madore 1982), with Gaia DR2 and 2MASS passbands to improve variability classification for ASAS-SN, but do not account for the effects of extinction in colours. Future research might aim to complete an analysis of the effect of both in future analyses of SVS classifications, making use of either the reddening-free Wesenheit magnitudes, the calculation of stellar extinction using the Binary and Stellar Evolution and Population Synthesis (BiSEPS) (Willems and Kolb, 2002) implementation of extinction given by Drimmel et al. (2003), or Gaia-DR2 reddening values and distances. Unlike ASAS-SN, magnitude and passband data does not feed into an

Type	EA/EB	EW	Pulsator	Rotator	Unknown
Number	192	40	69	1,365	894

Table 12.2 Previously unidentified stellar variables by variable type.

automated classification pipeline, and our initial machine learning classification algorithm will not incorporate this data (Section 12.4.1). It is expected that reddening would not be the cause of reclassification of the overarching variable types, however, for specific subsets of variable types (e.g. RR Lyrae stars), extinction correction may be necessary.

12.3.2 New variable objects

SVS is expected to classify many known stellar variables, and identify several previously unknown stellar variables. Previously known variables are identified by a 2 arcminute cross-match with the VSX catalogue (retrieved on 20 October 2020), which contains classifications of 2,105,377 variable stars from surveys including OGLE (Udalski, 2003b), ASAS (Rucinski, 2006), ASAS-SN (Jayasinghe et al. 2018; Kochanek et al. 2017; Shappee et al. 2014), ROTSE (Akerlof et al., 2003), NSVS (Wozniak et al., 2003), ZTF (Bellm et al., 2019). A secondary cross-match is performed with catalogues from Payne (2013) containing 12,884 EAs, 5,226 EBs, and 2,875 EWs, and Greer et al. (2017) containing 4,963 RR Lyrae stars.

To select potentially new variable stars, objects with a known classification and period are removed; objects that are flagged as variable, but which have no classification or period, are not removed. All new stellar variables were assessed by eye to verify the classification type and correctness of the period. Duplicated objects were removed and objects were reclassified as required. The subset of remaining rotator and unknown objects may still contain binaries and pulsators at the incorrect period, despite best efforts to identify them. Through this process, 2,560 unique candidate new variables remain, shown in Table 12.2. In this table, it is clear that there are significantly more variables classified as rotator or unknown. Stars classified as rotators are unlikely to be true rotators and may be binaries and pulsators folded

WASP ID	Type	Period (days)	B mag	V mag	R mag	Other ID
1SWASPJ000005.14-755731.3	EA/EB	4.30	13.33		12.53	
1SWASPJ000026.84+393855.6	EA/EB	3.59	11.84	11.18	10.74	TYC 2785-314-1
1SWASPJ000028.05+041248.4	EA/EB	4.69	13.49	12.76	12.97	
1SWASPJ000039.60-191306.0	EA/EB	6.76	13.74	13.77	13.68	
1SWASPJ000047.05+353443.1	EW	1.22	10.11	10.03	9.98	TYC 2267-94-1
1SWASPJ000054.70+544425.6	EA/EB	3.19	14.09		12.06	
1SWASPJ000057.42-544520.1	EA/EB	0.75	11.36	10.95	10.68	HD 224822
1SWASPJ000059.84+094404.5	EA/EB	0.65	14.38	13.83	14.20	
1SWASPJ000105.41-622920.6	EA/EB	1.48	10.22	9.84	9.59	CD-63 1632
1SWASPJ000132.23-051917.6	Pulsator	1.62	13.48	13.23	13.73	PHL 627
1SWASPJ000132.66-091513.7	EA/EB	4.19	13.64	13.30	13.06	
1SWASPJ000145.10+501843.4	EA/EB	1.69	13.75	13.17	12.89	
1SWASPJ000149.26+061830.8	EA/EB	0.32	13.48	13.02	13.26	
1SWASPJ000149.45-363918.1	Pulsator	0.64	12.44	11.91	11.55	TYC 6995-236-1
1SWASPJ000203.48-214746.0	EA/EB	0.86	14.02	14.02	14.17	
1SWASPJ000315.40+495750.8	EA/EB	3.65	12.71	11.96	11.47	TYC 3254-1505-1
1SWASPJ000323.81+325049.7	EA/EB	8.25	14.90		14.43	
1SWASPJ000343.16+465244.0	Pulsator	1.31	12.87	11.82	11.14	1RXS J000343.6+465256
1SWASPJ000353.60+043503.0	EW	0.28	15.07	14.57	14.92	
1SWASPJ000410.77-525122.4	EW	0.24	15.78	14.99	10.70	

Table 12.3 Sample from 301 previously unidentified stellar variables and related characteristics, not including rotators and unknown variables.

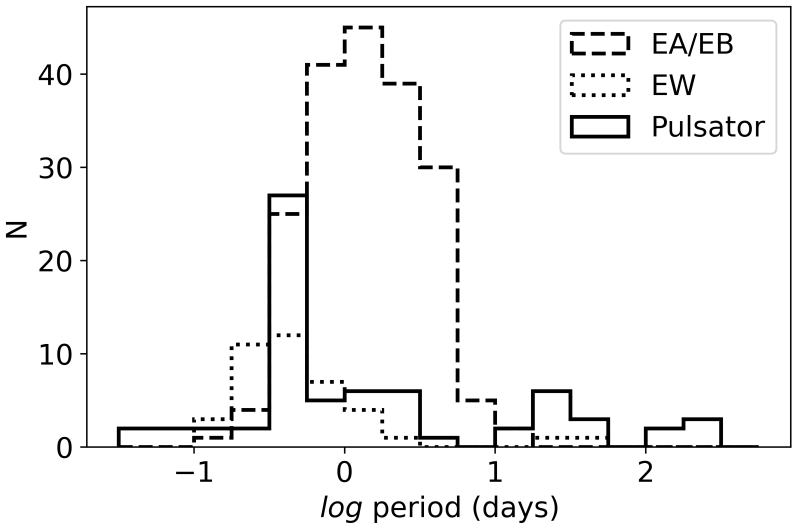

Fig. 12.9 The distribution of period of newly identified stellar variables (EA/EB, EW, and pulsator) by variable type. EA/EBs are shown by the dashed line; EWs by the dotted line; pulsators by the solid line.

at the wrong period, and unknown variables are likely to be junk, semi-regular or long period variables.

Using this approach, 301 previously unknown variable stars were identified, not including rotators and unknown variables, a selection of which are shown in Table 12.3, with a period distribution shown in Figure 12.9. The periods of each object have been assessed to correct for mis-classifications; whilst they have been corrected as much as possible, some periods remain best guesses. The table of 301 new pulsators and binaries can be found on Zenodo[9] and in Appendix C. Of particular interest are a short period cutoff eclipsing binary (with two SuperWASP IDs: 1SWASPJ004003.56+501501.9 and J004008.54+501455.6), new δ Scuti stars (Section 12.3.4), and binaries displaying the O'Connell effect. Based on the low classification accuracy of rotators, new variables classified as rotators or unknown may not have the correct classification.

Excluding rotators and unknown variables, these new variables are typically bright (V$\sim$13) stars. It is likely that these objects have not been detected due to either surveys not

[9]http://doi.org/10.5281/zenodo.4439383

yet having enough epochs to provide a variability classification (e.g. ASAS-SN), focus on the Galactic Plane or specific fields (e.g. Kepler, OGLE), or can only observe one hemisphere (ZTF). Assuming that 66% of the 1.6 million light curves in SVS are junk, it is estimated that on completion of SVS, ∼5,000 new EA/EB, EW, and pulsating stellar variables could be identified.

12.3.3 Multiple periods and multiple classifications

Stars displaying two or more real periodic modulations in their light curve are of great interest, and multiply periodic systems can act as stellar laboratories. Particular targets of interest are pulsating stars in eclipsing binary systems. A search identified 1,202 multi-periodic systems, including 229 EA/EBs, 362 EWs, 100 pulsators, 441 rotators, and 70 unknowns. A visual inspection revealed that none are convincing multi-periodic systems, but instead are objects with aliases of the true period. Initially, 1SWASPJ004859.70+172328.1 appeared to have multiple correct EA/EB classifications. Further investigation found this object has a true period of 3.11 d, discounting the alias periods. However, this object has previously been identified as an eclipseless rotator (with a period of 3.11 d), but the SuperWASP light curves show a clear primary eclipse and shallow secondary eclipse, shown in Figure 12.10. While the primary eclipse depth remains constant, the out of eclipse light curve changes significantly over the 8 years of observation, possibly due to a tidally locked star spot on one of the stellar components.

Multi-classification systems are also of great interest, and the SVS data set was searched for subjects that have the same WASP ID but have multiple different, but by consensus "correct" period classifications. This search found 1,563 systems with 2 or more classifications, shown in Table 12.4. The classifications with the greatest overlap appear to be EA/EB and EW, and rotators with other classifications, likely due to the low classification accuracy of rotators, and the high number of alias period light curves per rotator object. Based on

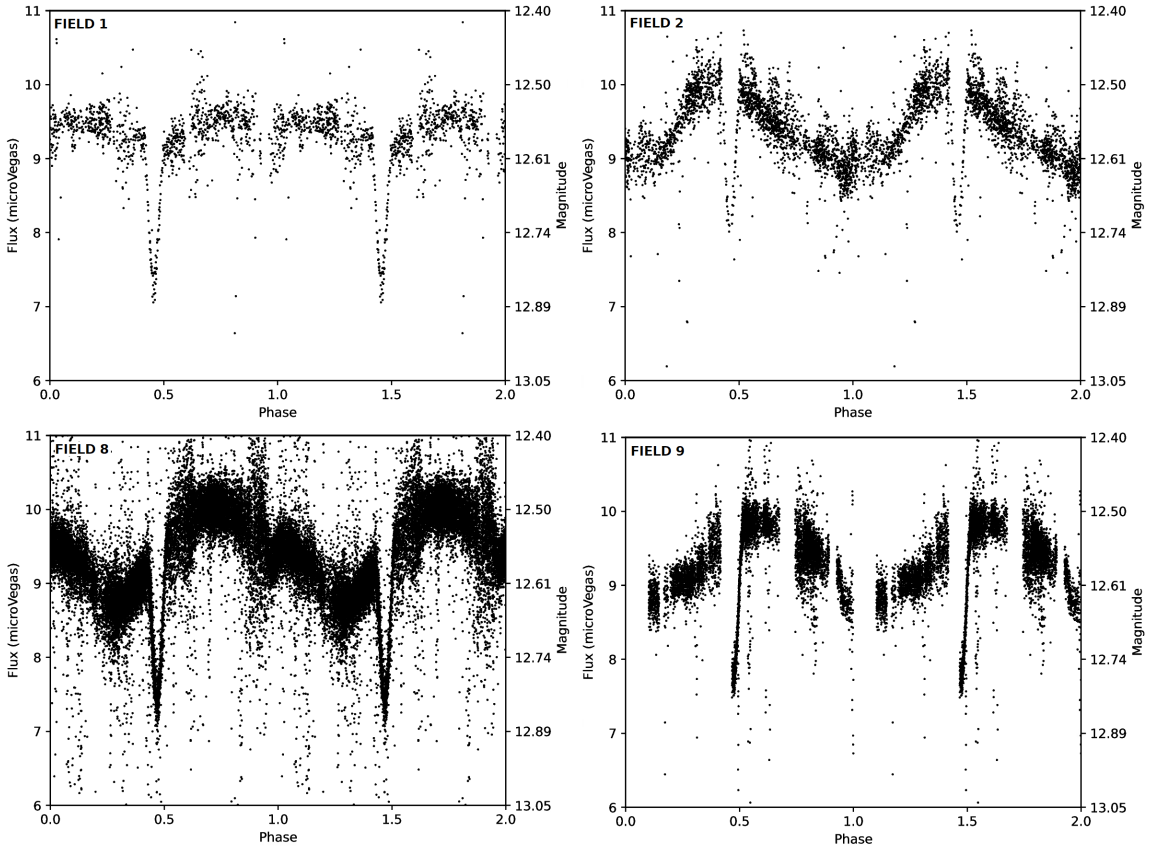

Fig. 12.10 1SWASPJ004859.70+172328.1, an object with multiple EA/EB classifications, with a true period of 3.11 d. The midpoint of each frame is as follows: field 1 (August 2004), field 2 (August 2006), field 8 (October 2011), field 9 (December 2012).

	EA/EB	EW	Rotator	Pulsator	Unknown
EA/EB	-	246	128	5	75
EW	246	-	716	16	46
Rotator	128	716	-	99	202
Pulsator	5	16	99	-	30
Unknown	75	46	202	30	-

Table 12.4 The number of light curves with multiple classifications per classification type.

the low classification accuracy of rotators, it can be assumed that any multi-classification object in which one classification is rotator or unknown can be discounted as a true multiple classification.

Each of our candidate multi-classification systems were verified by eye (excluding rotators and unknown variables), ultimately yielding only apparently 1 real multi-classification system, 1SWASPJ000220.66-292933.8, shown in Figure 12.11. This object has both an EW and pulsator classification and SuperWASP periods of 3.15 d and 1.46 d respectively. On inspection, the EW classified light curve appears to be that of a RS Canum Venaticorum (RS CVn) binary. This object has a candidate RS CVn classification, with a period of 6.29 d or an eclipseless RS CVn classification with a period of 3.14 d in VSX. This object appears to have experienced significant surface spot coverage evolution over the 7 years of observations, and even hints at an eclipse in field 2.

Another object of particular interest was one which appeared to be a δ Scuti star in an eclipsing binary (1SWASPJ004811.15+473719.1), however this was found to be two separate systems, a binary (1SWASPJ004810.36+473747.7) and a δ Scuti star (1SWASPJ004811.15+473719.1), spatially separated by 30 arcseconds, shown in Fig 12.12.

12.3.4 Extreme variables

A valuable aspect of large catalogues of variable stars can be the identification of extremes of each class, i.e. those with extremely long or short periods, or extremely high or low amplitudes. SVS has the opportunity to increase the sample size of short period contact

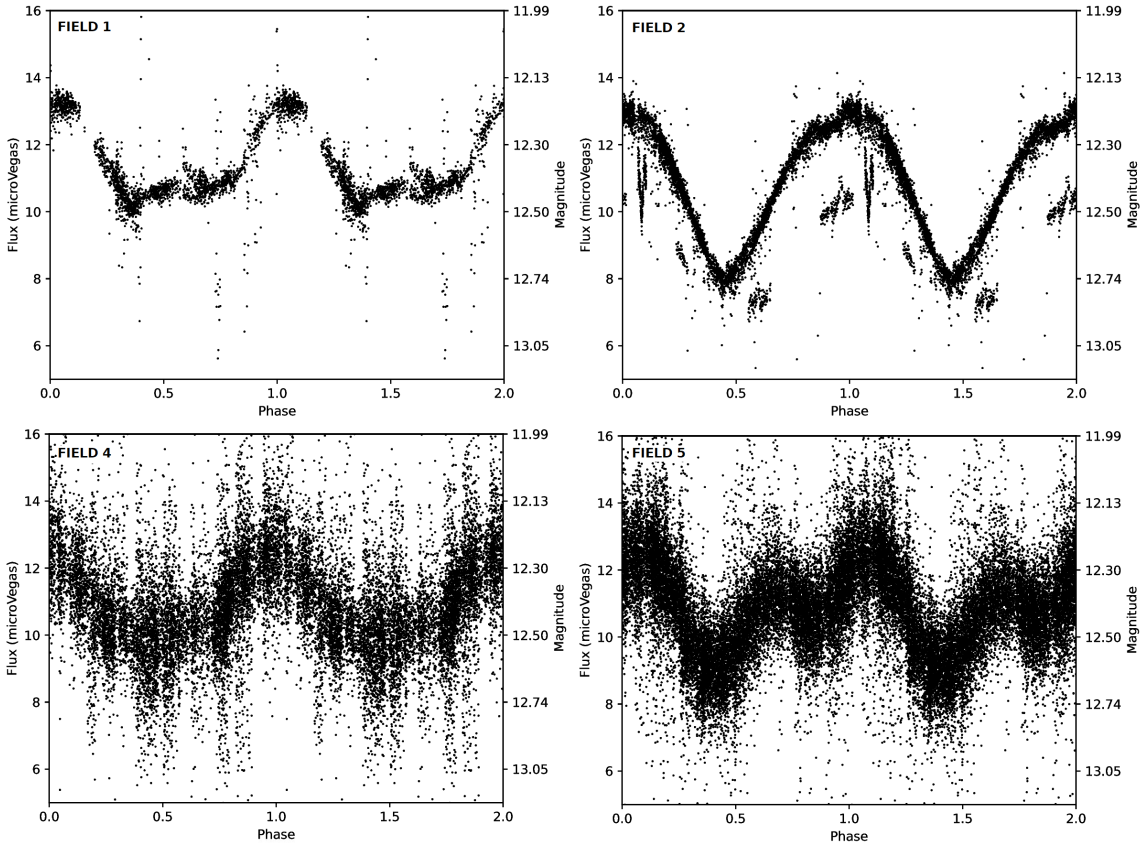

Fig. 12.11 The light curve of 1SWASPJ000220.66-292933.8, classified by volunteers both as an EW with a period of 3.15 d and a pulsator with a period of 1.46 d. The midpoint of each frame is as follows: field 1 (September 2006), field 2 (September 2007), field 4 (August 2012), field 5 (September 2013).

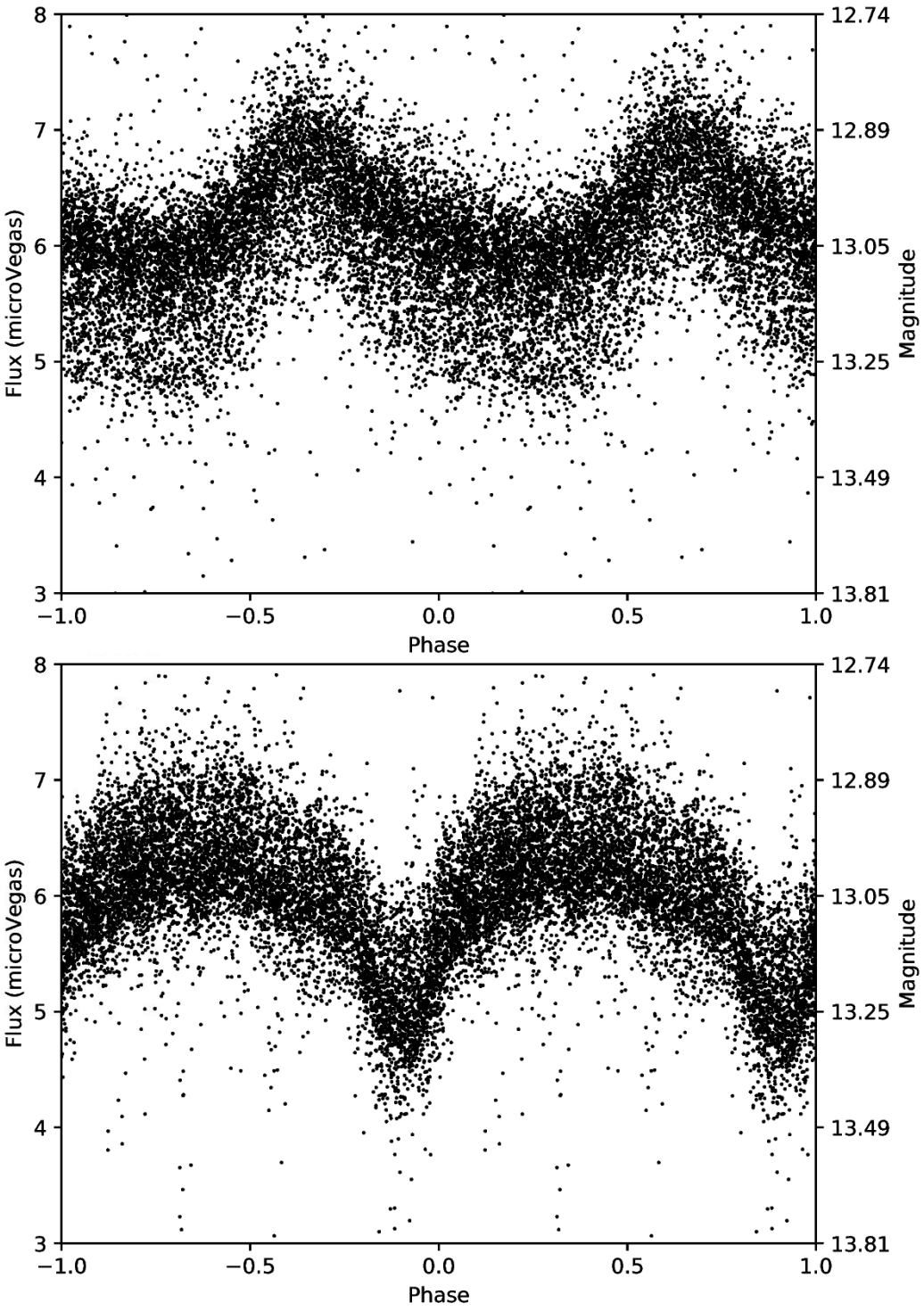

Fig. 12.12 **Upper:** The δ Scuti star 1SWASPJ004811.15+473719.1 with a period of 1.9 hours. **Lower:** The EW-type eclipsing binary 1SWASPJ004810.36+473747.7 with a period of 18.7 hours (0.78 d). These objects were classified as the singular object 1SWASPJ004811.15+473719.1 with both an EW and a δ Scuti star in the same photometric aperture.

binaries, as well as identifying, for example, unusually long period contact binaries. For the full SVS data set, there are two peaks, at $\sim$0.3 days where we might expect to find short period binaries and aliases of binaries, and short period pulsators, and $\sim$30 days where we might expect to find semi-regular stars, currently classified as unknown.

The extremes of each variable type were explored using the following criteria as standard definitions of periods, and visually inspect light curves at the extremes of each period:

- EA/EB: 0.3 d$\leq P \leq$10 d (e.g. Stepien (1995))
- EW: 0.22 d$\leq P \leq$1 d (e.g. Rucinski (1992))
- Pulsator: 0.3 d$\leq P \leq$8 d (e.g. Breger 1979; Drake et al. 2014; Leavitt and Pickering 1912; Matsunaga et al. 2006)
- Rotator: P$\geq$0.5 d (periods range from hours to months (e.g. Nielsen et al. (2013))
- Unknown: N/A (semi-regular P $\geq$10 d) (e.g. Soszyński et al. (2009))

The class of pulsators has the widest range of possible periods, including δ Scuti ($\sim<$0.3d), RR Lyrae (0.44–0.82 d), Cepheid (with periods of weeks to months), Mira (P$\geq$100 d), and W Virginis (0.8 d$\leq P \leq$35 d). A lower limit of P$\leq$0.3d was chosen to allow for the identification of candidate δ Scuti and High Amplitude δ Scuti stars (HADS).

Objects that appear to be long-period examples of near-contact eclipsing binary stars were identified, with orbital periods of up to a month or more. These objects became the subject of the follow-up campaign detailed in Chapters 6–11. SVS volunteers identified $\sim$10 candidates, with an example of one of these systems identified in SVS is shown in Figure 12.13.

A new eclipsing binary (with both SuperWASP IDs: 1SWASPJ004003.56+501501.9 and 1SWASPJ004008.54+501455.6) has been identified with a period of $\sim$0.23 days near the short-period cutoff of $\sim$0.22 days, shown in Figure 12.14. Such stars are of importance in the study of the evolution and structure of close binary systems.

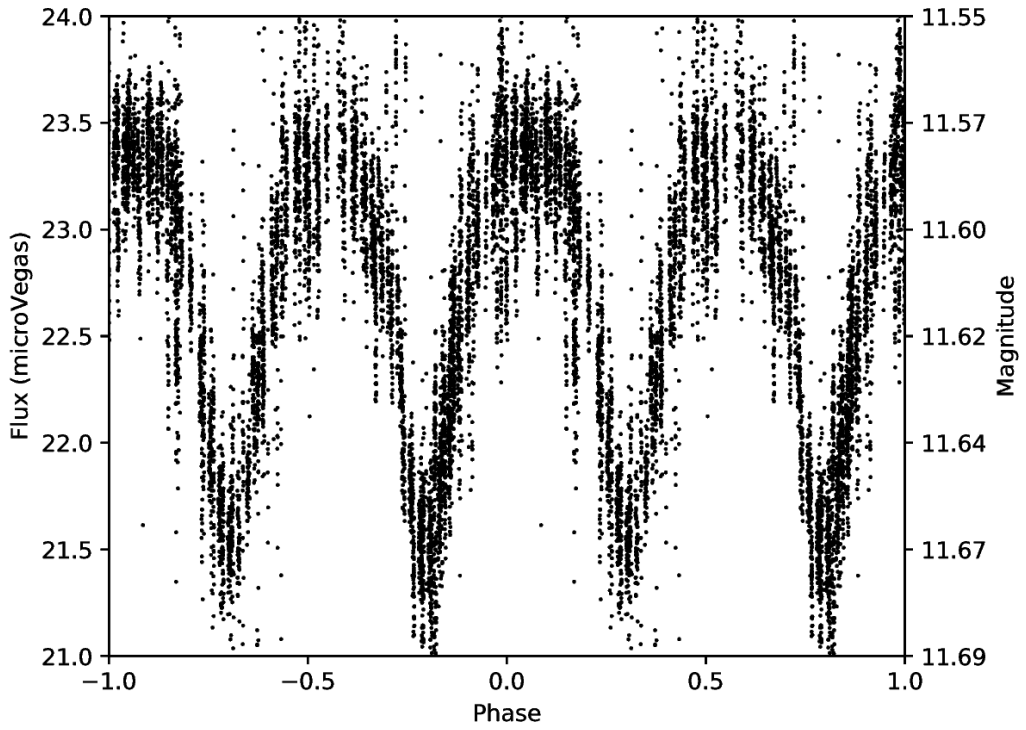

Fig. 12.13 The first classification of a candidate near contact red giant eclipsing binary, 1SWASPJ000927.89+014542.1, with a period of 41.62 d.

12.4 Discussion

Although it is disappointing not to find many new multi-periodic or multi-classification systems at this stage, this analysis method can be applied to future analyses, especially for the identification of variables with evolving star spots. With a greater number of classifications, it is expected that a significant number of extremely short and long period pulsators would be identified, including δ Scuti stars and Mira variables. Individual pulsator sub-types are not identified by citizen scientist volunteers, so would require the further visual inspection of each each pulsator light curve after making cuts using additional period, colour, and luminosity data. Exploration of the project should identify more extreme binaries, including near-contact red giant eclipsing binaries, and binaries near the short-period cutoff. It is evident that if some form of machine learning is implemented, there may still be the need

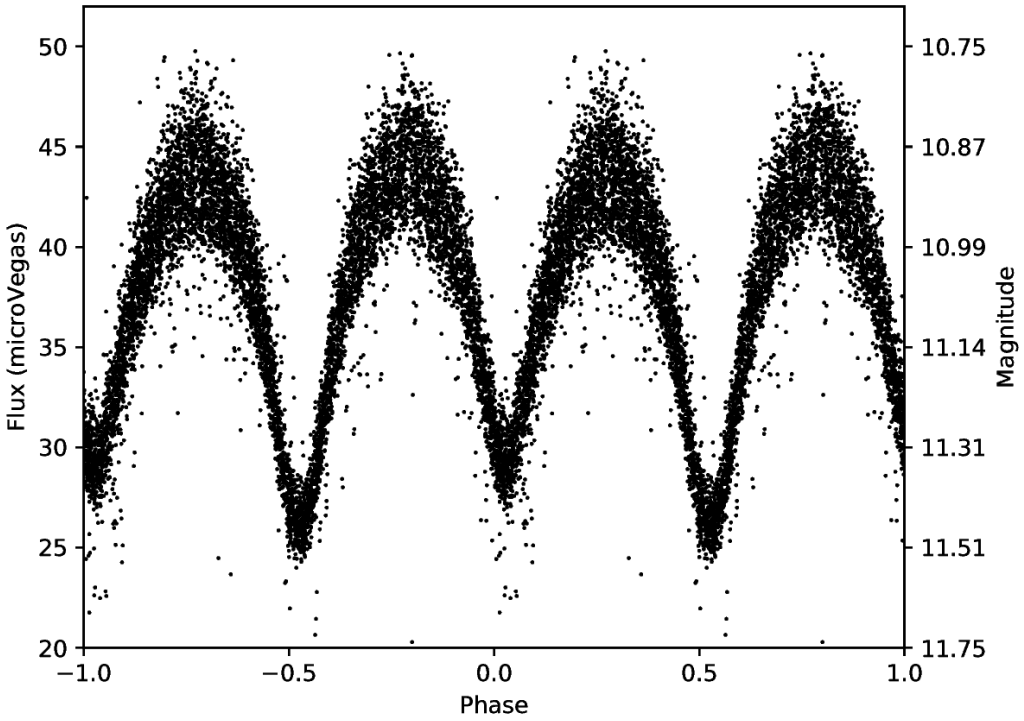

Fig. 12.14 A newly identified EW type binary (both 1SWASPJ004003.56+501501.9 and 1SWASPJ004008.54+501455.6) with a period of 0.23 d, close to the short-period cutoff.

for some level of human interaction with multi-periodic and multi-classification systems to identify false positives.

It is currently not possible to estimate whether volunteer classifications have been biased. There is no identifying data on the image of each light curve, in an attempt to keep the classification task to a pattern matching exercise only. However, following the project launch, it was realised that some metadata for each light curve was visible to volunteers in the form of the SuperWASP ID. For volunteers who notice this, the ID gives information on the RA and Declination of each SuperWASP object, and hence the exact object itself. Subsequently, some users have used this ID to cross-match the light curve to existing classifications and surveys, using this knowledge to make a decision on the classification type. There is not a way of identifying who has made use of this method and whether it can bias the results. Volunteer feedback has indicated that use of cross-matching has improved their knowledge

of stellar variables and classification accuracy, and they value being able to investigate the light curves in more depth.

To that end, as of November 2020, the SuperWASP Variable Stars team added links to external catalogues (CERiT, ASAS-SN, and Simbad) to the metadata which is visible only after a classification has been completed. It is not intended to be a tool to influence classifications, but it has been developed in order to allow interested volunteers to engage with the project further.

12.4.1 The future of SuperWASP Variable Stars

To successfully complete all classifications in SVS and make the results public, there are a number of new additions and improvements that can be made, including implementing machine learning techniques and building a platform through which the results can be accessed.

The Need for Machine Learning

At the current classification rate it will take at least 15 years to classify all 1.6 million light curves in SVS. To this extent, a novel method for classifying these phase-folded light curves is being developed by a colleague, in order to speed up the classification process. This new method will involved the training of a Convolutional Neural Network (CNN) on the same *images* of phase-folded light curves as those presented to SVS volunteers. This will make use of the >1 million volunteer-generated classifications, or labels, to train the CNNs. An initial CNN using volunteer-generated labels will be run, then expert classified light curves will be used to calculate further volunteer confusion matrices, deriving *fuzzy* labels and weighting classifications to improve reliability. A custom Zooniverse project will be implemented to allow for expert bulk classification of CNN predictions, and retrain the CNN using expert classifications.

There is also the scope to use volunteer comments from the "Talk" forum section of SVS. It is possible for a volunteer to create a discussion page for each light curve, where they might "tag" or comment on it, giving a further classification type (i.e. while the SVS classification might be pulsator, a volunteer might comment "RR Lyrae" which indicates that the light curve is a pulsator sub-type). This forum potentially holds another significant source of labelled data which may be explored in future work.

A New User Interface

One of the key aims of SVS is to make the classified *SuperWASP periodicity catalogue* light curves publicly available and to create the first catalogue of variable stars in the SuperWASP archive. Colleagues have begun work on a new user interface (UI), similar to WASP-DR1[10] and the ASAS-SN Catalogue of Variable Stars[11].

This (UI) will take the form of a web portal, which will allow a user to easily and quickly search the classified light curves using a number of different parameters, including RA and Declination with a search radius, magnitude or flux, period, and variable type. A search of this UI will not only provide SuperWASP data and classifications, but also an automated cross-match to other catalogues, for example: SIMBAD, ASAS-SN, and VSX. Having selected an object, the user will be able to dynamically work with the data or download a FITS or CSV file. The dynamic interface will allow the user to fold the light curve at a different period, re-scale the plot, or convert between magnitude and flux, and more. This new UI will be updated with new SVS classifications or reclassifications every 6 months following its launch.

[10]https://wasp.cerit-sc.cz/form
[11]https://asas-sn.osu.edu/variables

12.5 Conclusions

I presented the preliminary results of the first analysis of the SuperWASP Variable Stars Zooniverse project, which consists of 1,025,750 classifications corresponding to 568,739 unique object-period combinations. Over 4,500 registered volunteers had engaged with the project between September 2018 and September 2020. By May 2021, the number of registered volunteers engaged with the project has risen to ∼9,000.

Each SuperWASP light curve has been classified by between 4 and 7 volunteers, classifying it as a broad type of stellar variable. I find that the majority (66.6%) of classifications are junk and are therefore discarded, but the remainder (33.4%) of the classifications corresponding to EA/EB, EW, pulsator, rotator, and unknown, are valuable for population studies and studies of unique stellar variables. I identified that variables with a rotational modulation are the most inconsistently classified by volunteers, with only ∼9% of rotators being correctly classified, compared to ∼89% of EA/EB type binaries. I would caution that the classification of rotator should not be relied upon until there is a more reliable method of classification for this variable type.

As a result of SVS, 301 new variable stars have been identified. Extrapolating to the wider data set, I would expect that ∼5,000 new variable stars could be identified on completion of this project. I have identified extreme period variables, including long period contact binaries, and eclipsing contact binaries near the short-period cutoff, and δ Scuti stars. This project has the potential to expand the catalogue of δ Scuti stars in eclipsing binaries, and discover the first Cepheids in eclipsing binaries (if they exist), as well as to identify multi-periodic Cepheids and RR Lyrae stars. The high number of false-positive multiply periodic and multi-classification light curves identified by volunteers indicates that an expert must complete the final stage of classification by eye for the most extreme and unusual light curves.

This analysis is not conclusive, but it demonstrates that SVS is successful in its aims of identifying unique and extreme variables, and identifying populations of stellar variables for

further study. This analysis and methods will guide the project in future analyses of volunteer and machine learning classifications. Future work on SVS includes working on using citizen scientist classified data to train CNNs to speed up the classification process, however humans are still skilled at picking out the rare and unique objects, and generating labelled data. Both volunteer classified light curves and CNN classified light curves will feed into a new public user interface which is currently under development.

Chapter 13

Conclusions and Future Work

Having explored various aspects of variability in the SuperWASP all-sky survey, I will now conclude the project. In this chapter, I will provide a summary of the previous chapters and the key findings from each, grouped into the three key areas of research: the rotation-activity relation, the discovery and follow-up of near contact red giant eclipsing binaries, and the SuperWASP Variable Stars citizen science project. I will also discuss areas for improvement and further work that these key areas could benefit from.

Project outline

This research project had a primary aim of investigating variable stars in the SuperWASP all-sky survey. The recent reanalysis by Norton (2018) detected 1,569,061 candidate periods in 767,199 unique objects, which make up the *SuperWASP periodicity catalogue*, a catalogue of long-baseline and high-cadence SuperWASP data. Although the focus was varied, from stellar variability as a whole to investigating different types of variability, the theme throughout remained the question of how best to exploit the *SuperWASP periodicity catalogue*, alongside other stellar archives, to identify trends in stellar variability and to discover unique stellar variables.

Keeping this in mind, the first aspect of investigation focused on identifying trends in SuperWASP and ASAS-SN rotational variables, the second on the serendipitous discovery

of a near contact red giant eclipsing binary, and the third on the creation and analysis of the SuperWASP Variable Stars citizen science project, in which over 300 new stellar variables were identified.

Characterising the rotation-activity relation

The original aim for this work was to update and add to research done by Norton et al. (2007), in which SuperWASP rotationally modulated stars were cross-matched with ROSAT X-ray sources. At the time, only the first few years of SuperWASP data were available, and no distance data were available to assess the bolometric luminosity and flux of the sources. With the advent of the Gaia survey, distance data were available, and the measurement of X-ray activity was improved through the use of the XMM-Newton survey.

Through the cross-match of SuperWASP and XMM-DR4, 16,827 rotationally modulated objects with a coincident X-ray detection were identified. Of these, 581 were identified as late-type main sequence stars which satisfied all the criteria. For a cross-match between ASAS-SN and XMM-DR4, a similar number were found, and both catalogues were used to characterise the rotation-activity relation, the results of which were published in Thiemann et al. (2020).

Three regimes (the unsaturated, saturated, and supersaturated) were characterised, and this work may have found the most convincing evidence for the supersaturated regime in main sequence stars to date. What also sets this work apart from other studies of the same topic is the use of only photometrically defined periods. Although this means that the uncertainty on the fit of the unsaturated regime is greater than other methods using different activity indicators, the value of $\beta = -1.84 \pm 0.18$ found for SuperWASP aligns with the canonical values of $\beta = -2$. Intriguingly, when ASAS-SN photometrically defined periods were used, the same fit could not be found. Since ASAS-SN periods and classifications are classified through an automated process, whereas SuperWASP targets were identified by eye, it may

have been an indication that humans are still highly successful at classifying rotational stellar variables.

Identification and characterisation of near contact red giant eclipsing binaries

The bulk of the research came quite by chance, through the serendipitous discovery of J001521, a previously unknown star which appeared to be a contact binary system with a period of $\sim$42 days, far greater than the classical period of $<$1 day. Through a cross-match of the SuperWASP periodicity catalogue and the ASAS-SN Catalogue of Variable Stars, a further 16 candidate binaries were identified. Citizen scientists increased the number of candidates by 10 in the year following, bringing the total to 27. Due to the long periods, likely unstable systems, and late-type components, these NCRGEB were postulated to be progenitors of the rare transient, red novae. Similar contact red giant systems with periods of hundreds of days were thought to have been observed by Wood et al. (1999) but were instead found to be ellipsoidal variables. The NCRGEB in this research have many of the same characteristics as the ellipsoidal red giants, but with shorter periods and two giant components.

Following the discovery, a successful campaign of photometric and spectroscopic follow-up was carried out. Northern and mid-latitude candidates were observed photometrically in BVRI over 2 years using The Open University's PIRATE telescope, and schools were engaged to observe southern candidates in BVR using the Las Cumbres Observatory network of telescopes. The Liverpool Telescope was used to take spectroscopy of northern candidates, and southern candidates were observed using SALT and an in-person 2-week observing run at the 74$''$ telescope.

Radial velocities for each candidate were extracted from the observed spectra, and by combining radial velocity curves and phase-folded photometric light curves, the 27 candidates were whittled down to 12 convincing binaries. The remaining 12 were modelled using `PHOEBE`, to characterise the components of each binary. This modelling found that the

average NCRGEB has a total mass of $\sim$3 $M_{\odot}$ (ranging from 0.2–3.5 $M_{\odot}$), a semi-major axis of 38 $R_{\odot}$ (ranging from 24–67 $R_{\odot}$), temperatures of $\sim$4600 K (ranging from 3600–5800 K), and components with radii of 10–13 $R_{\odot}$ (ranging from 3–25 $R_{\odot}$).

The remaining 15 candidates were not subject to any further follow-up, although their variability type was estimated. These failed NCRGEB candidates included shell stars, Cepheid variables, and rotationally modulated stars. The knowledge of which types of stellar variables can be confused with genuine NCRGEB will be valuable for future researchers, given, for example, the presence of Hα emission is likely to be evidence of a shell star rather than a binary.

Modelling of the evolution of near contact red giant eclipsing binaries

The parameters from `PHOEBE` were used as a starting point for identifying period change and estimating timescales over which a merger event might occur. The first attempt at characterising period change was through `ah3`, a period change programme written by Lohr (2015). Unfortunately, this programme was designed for less noisy SuperWASP light curves for binaries with periods $<$5 days, hence the period change for NCRGEB was discarded. A more successful attempt was made using `PHOEBE` parameters and a number of known equations for binary angular momentum loss, including conservative and non-conservative mass transfer, magnetic braking, gravitational wave radiation, and tidal circularisation. This provided an estimate of a merger on timescales of just 5,000 years to 29 Myr (0.03 Gyr).

A number of binary and stellar evolutionary models were then used to understand the formation and end-of-life of NCRGEB, their merger event and the timescales, and whether they could be the progenitors of red novae. Three methods, `BiSEPS`, `BiSEC`, and `binary_c` constrained the initial mass ratio to within 1% of $q = 1$, but differed on the initial orbital period and timescales, with the former two programmes finding an initial period of $\sim$45 yrs, and `binary_c` finding an initial period of close to the orbital period currently observed. All three programmes find that NCRGEB experience a rapid phase of inspiralling and mass

loss during a common envelope event, quickly ending their life as either a single or binary white dwarf over the course of ∼0.07 Gyr. MESA, the fourth modelling programme finds similarities and differences. Like `binary_c`, it finds an initial orbital period close to the observed orbital period to be acceptable. It also finds that an initial mass ratio to within 1% of q=1 is required. However, whilst MESA models experience mass loss, they do not experience inspiralling. Instead, both components continue to evolve and experience an sudden increase in orbital period and separation over the course of ∼0.18 Gyr. Although we cannot say for sure what the common envelope event and end-of-life looks like for NCRGEB, there is an alignment between the merger timescales.

We cannot say for certain that these binaries are the progenitors of red novae, but the process of discovery, follow-up, and modelling has been a fascinating one. If future work confirms that they are the progenitors, then this work will be valuable for future characterisation of red novae, and the long term monitoring through projects such as ZTF and ASAS-SN will be gold mines for future researchers.

Citizen science with SuperWASP Variable Stars

Much of the previous research in this thesis has operated through cross-matching, classification by eye, and serendipitous discoveries, however it is clear that to efficiently exploit the SuperWASP periodicity catalogue, a better option was required. Since machine learning had previously been explored, with some success, an alternative option was to use citizen science, hence SuperWASP Variable Stars Zooniverse project was created. In this project, citizen scientists are asked to classify phase-folded light curves as one of 4 variable types, something unknown, or junk, with the aim of identifying large populations of the same type of stellar variable and identifying rare and extreme stellar variables. A third benefit became apparent not long after the project was founded: by creating a large catalogue of labelled images, the outputs of SuperWASP Variable Stars could be used for machine learning to classify the full SuperWASP periodicity catalogue of ∼1.6 million phase-folded light curves.

An analysis of the first >1 million classifications (corresponding to >500,000 object-period combinations) was completed as part of this work and published in Thiemann et al. (2021). The aim was to understand the accuracy of classifications provided by citizen scientists, identify any new discoveries which may have been made in the first 2 years of the project running, and provide a proof-of-concept that the outputs of the project will be valuable for further research.

By comparing citizen scientist classifications to known classifications in VSX, it was found that volunteer classified light curves have a ∼89% accuracy for detached and semidetached eclipsing binaries, ∼78% for pulsators, ∼71% for contact eclipsing binaries, and then a sudden drop to only ∼9% of rotationally modulated variables. We are yet to understand quite why rotationally modulated stars are so difficult to classify.

Stars displaying two or more real periodic modulations in their light curve are of great interest, and multiply periodic systems can act as stellar laboratories. Targets displaying one or both of these features are expected to be found in the SuperWASP Variable Stars project, however although promising initial signs of these types of variables were found, none were conclusively identified. Instead, volunteers had identified systems undergoing significant variability change over the course of the SuperWASP observations, typically due to tidally locked star-spots. Through the remainder of the project, real systems are expected to be found.

A number of new and extreme stellar variables were identified by citizen-scientist volunteers, including 1SWASPJ004003.56+501501.9, a new eclipsing binary with a period of ∼0.23 d, close to the short period binary cut-off of ∼0.22 d, and 1SWASPJ001521.76+472055.2, the original near contact red giant eclipsing binary, with a period of 41.62 d. In addition to this, 301 stars were identified as variable for the first time, including 192 detached and semidetached eclipsing binaries, 40 contact eclipsing binaries, and 69 pulsating stars. It is

estimated that ∼5,000 more could be identified throughout the remainder of the SuperWASP Variable Stars project.

As a result of this initial analysis, the groundwork has been laid for future work. Already, work has already begun on identifying new ways to exploit the SuperWASP archive for the study of stellar variability. A colleague, Adam McMaster, is in the process of developing a website through which the public and other astronomers can access the results of SuperWASP Variable Stars, and another colleague, Hugh Dickinson, is making use of the same SuperWASP data set to create a new Zooniverse project, *SuperWASP: Black Hole Hunters*. In this, the aim of the project is to search for distinctive but rare signatures of gravitational microlensing caused by non-accreting black holes in stellar binary systems. This new project will show short segments of light curves that contain a significant (but mysterious) peak to volunteers, and they will be asked whether the mysterious peak appears to be that of a microlensing event. Within these two projects alone, it demonstrates that there remains a huge archive of SuperWASP data for future exploitation.

Recommendations for future work

In terms of improvements to the rotation-activity relation, an increase in sample size would both reduce the uncertainty on the fit of the unsaturated regime, and provide more convincing evidence for the extremes of the relationship. A larger data set of rotational variables might be taken from the results of the SuperWASP Variable Stars Zooniverse project, provided there is a solution to increasing the accuracy of volunteer classified rotational variables.

Moving away from the citizen science and the machine learning that can come from SuperWASP Variable Stars, there is still significant work to be done around fully understanding the unique and new near contact red giant eclipsing binaries. Through this research, I have identified, characterised, and modelled the components and evolution of these binaries, but further work needs to be done to fully understand the final stages of evolution of such

systems, and provide a conclusive answer to *"are near contact red giant eclipsing binaries the progenitors of red novae?"*

Nearly all near contact red giant eclipsing binary models would benefit from better radial velocity phase coverage to constrain the component models, with the exception of J183357. The spectroscopic follow-up conducted in this work found convincing evidence of binary line splitting in the spectrum for only 1 or the 12 binaries, and higher resolution spectroscopy should be able to disentangle the two components in the spectra. Although the equivalent widths and intensities of strong lines (predominantly Hα) were used to confirm the systems were binaries, radial velocity extraction was not possible via this route. Improving spectroscopic resolution would improve the constraint on the masses of each component, which in turn, would improve merger timescale calculations and evolutionary modelling.

Similarly, a number of candidates, including J194231, J132156, and J093610 would benefit from better multi-colour photometric phase coverage. Whilst these systems have been confirmed to be binaries and spectral typing and synthesis has confirmed the spectral type of each target as a whole, the temperatures of each individual component could be constrained in `PHOEBE` by having better BVRI photometry. Improved photometric coverage could also be combined with techniques such as Doppler tomography to model the presence of large star spots, which are thought to be present on J093610.

Since this research has focused primarily on exploiting data archives and observational follow-up, the logical next step should therefore lie in modelling the common envelope event, inspiralling, and post-merger form of NCRGEB using parameters identified through this research. Due to time constraints, such work has so far been limited, but it would provide more conclusive proof as to whether NCRGEB are the progenitors of red novae. As identified in Chapter 10, programmes such as `RLOF` (MacLeod et al., 2017a) would confirm whether the period change within NCRGEB systems aligns with that seen prior to the V1309 Sco merger event. If I could start a new piece of research using SuperWASP data, I would start by using

RLOF on the entire SuperWASP archive to catch previously unknown binaries undergoing period decrease to find twins of V1309 Sco.

To further understand the mysteries of near contact red giant eclipsing binaries, I would suggest that a number of other routes be explored. This could include population synthesis models such as BiSEPS, BiSEC, or COMPAS (Howitt et al., 2020) to identify how common such systems are, and numerically modelling the energy and mass lost from the system during the common envelope event to provide direct comparisons to V1309 Sco and similar such events (Howitt et al., 2020). Since a merger event is predicted to happen on timescales too distant for us to observe, modelling is the only way we might be able to understand NCRGEB. Despite this, monitoring of the 12 NCRGEB continues through the ZTF *Lasair* transient broker, just in case.

Conclusions

The story of the SuperWASP project is not yet over; there is so much more out there to be discovered. For this reason, I have to quote my colleague and friend, Joe, who remarked in his thesis that SuperWASP, despite not being a new data set, is full of possibilities Cooper (2020). A few years down the line, this remains true. SuperWASP still holds many secrets, including yet undiscovered exoplanets, new types of stellar variables, gravitational microlensing events, and more. Using the SuperWASP archive has been a fantastic and invigourating journey of discovery, from investigating populations of rotational variables, to engaging the public with astronomy, and the serendipitous discovery of a new type of binary. With the new online portal to SuperWASP data and the inclusion of machine learning, there is so much more to come. Therefore, in a time when funding for new telescopes and missions is tight, the exploitation of historical archives is one of the most efficient uses of data and funding, and the field of astronomy can only benefit from exploiting the SuperWASP archive further.

References

Abbott, B., Abbott, R., Abbott, T., Acernese, F., Ackley, K., Adams, C., Adams, T., Addesso, P., Adhikari, R., Adya, V., and et al. (2017). Gw170817: Observation of gravitational waves from a binary neutron star inspiral. *Physical Review Letters*, 119(16).

Acosta-Pulido, J., Ballesteros, E., Barreto, M., Correa, S., Delgado, J. M., Dominguez-Tagle, C., Hernandez, E., Lopez, R., Manchado, A., Manescau, A., Moreno, H., Prada, F., Redondo, P., Sanchez, V., and Tenegi, F. (2002). LIRIS: A Long-Slit Intermediate Resolution Infrared Sectrograph for the WHT. *The Newsletter of the Isaac Newton Group of Telescopes*, 6:22–24.

Adams, S., Kochanek, C. S., Dong, S., and Wagner, R. M. (2015). ATel 7468: Spitzer Observations of the 2015 M31 Stellar Merger. *The Astronomer's Telegram*, 7468:1.

Akerlof, C., Amrose, S., Balsano, R., Bloch, J., Casperson, D., Fletcher, S., Gisler, G., Hills, J., Kehoe, R., Lee, B., Marshall, S., McKay, T., Pawl, A., Schaefer, J., Szymanski, J., and Wren, J. (2000). ROTSE All-Sky Surveys for Variable Stars. I. Test Fields. AJ, 119(4):1901–1913.

Akerlof, C. W., Kehoe, R. L., McKay, T. A., Rykoff, E. S., Smith, D. A., Casperson, D. E., McGowan, K. E., Vestrand, W. T., Wozniak, P. R., Wren, J. A., Ashley, M. C. B., Phillips, M. A., Marshall, S. L., Epps, H. W., and Schier, J. A. (2003). The ROTSE-III Robotic Telescope System. PASP, 115(803):132–140.

Alpaslan, M. (2009). A quick guide to FXCOR. *arXiv e-prints*, page arXiv:0912.4755.

Andrae, R., Fouesneau, M., Creevey, O., Ordenovic, C., Mary, N., Burlacu, A., Chaoul, L., Jean-Antoine-Piccolo, A., Kordopatis, G., Korn, A., Lebreton, Y., Panem, C., Pichon, B., Thévenin, F., Walmsley, G., and Bailer-Jones, C. A. L. (2018). Gaia Data Release 2. First stellar parameters from Apsis. A&A, 616:A8.

Argiroffi, C., Caramazza, M., Micela, G., Sciortino, S., Moraux, E., Bouvier, J., and Flaccomio, E. (2016). Supersaturation and activity-rotation relation in PMS stars: the young cluster h persei. *Astronomy & Astrophysics*, 589:A113.

Arkhypov, O. V., Khodachenko, M. L., Lammer, H., Güdel, M., Lüftinger, T., and Johnstone, C. P. (2018). Starspot variability as an x-ray radiation proxy. *Monthly Notices of the Royal Astronomical Society*, 476(1):1224–1233.

Audard, M., Gudel, M., Drake, J. J., and Kashyap, V. L. (2000). Extreme-ultraviolet flare activity in late-type stars. *The Astrophysical Journal*, 541(1):396–409.

Badenes, C. and Maoz, D. (2012). The Merger Rate of Binary White Dwarfs in the Galactic Disk. ApJ, 749(1):L11.

Bailer-Jones, C. A. L., Rybizki, J., Fouesneau, M., Mantelet, G., and Andrae, R. (2018). Estimating Distance from Parallaxes. IV. Distances to 1.33 Billion Stars in Gaia Data Release 2. AJ, 156:58.

Barnes, S. A. (2007). Ages for Illustrative Field Stars Using Gyrochronology: Viability, Limitations, and Errors. ApJ, 669(2):1167–1189.

Barnsley, R. M., Smith, R. J., and Steele, I. A. (2012). A fully automated data reduction pipeline for the FRODOSpec integral field spectrograph. *Astronomische Nachrichten*, 333(2):101–117.

Barsukova, E. A., Goranskij, V. P., Valeev, A. F., and Zharova, A. V. (2014). Evolution of red Nova V4332 Sagittarii remnant. *Astrophysical Bulletin*, 69(1):67–81.

Bayless, A. J., Robinson, E. L., Mason, P. A., and Robertson, P. (2011). The Optical Orbital Light Curve of the Low-Mass x-Ray Binary v1408 Aquilae (= 4u 1957115). *The Astrophysical Journal*, 730(1):43.

Bellm, E. C., Kulkarni, S. R., Graham, M. J., Dekany, R., Smith, R. M., Riddle, R., Masci, F. J., Helou, G., Prince, T. A., Adams, S. M., Barbarino, C., Barlow, T., Bauer, J., Beck, R., Belicki, J., Biswas, R., Blagorodnova, N., Bodewits, D., Bolin, B., Brinnel, V., Brooke, T., Bue, B., Bulla, M., Burruss, R., Cenko, S. B., Chang, C.-K., Connolly, A., Coughlin, M., Cromer, J., Cunningham, V., De, K., Delacroix, A., Desai, V., Duev, D. A., Eadie, G., Farnham, T. L., Feeney, M., Feindt, U., Flynn, D., Franckowiak, A., Frederick, S., Fremling, C., Gal-Yam, A., Gezari, S., Giomi, M., Goldstein, D. A., Golkhou, V. Z., Goobar, A., Groom, S., Hacopians, E., Hale, D., Henning, J., Ho, A. Y. Q., Hover, D., Howell, J., Hung, T., Huppenkothen, D., Imel, D., Ip, W.-H., Ivezić, Ž., Jackson, E., Jones, L., Juric, M., Kasliwal, M. M., Kaspi, S., Kaye, S., Kelley, M. S. P., Kowalski, M., Kramer, E., Kupfer, T., Landry, W., Laher, R. R., Lee, C.-D., Lin, H. W., Lin, Z.-Y., Lunnan, R., Giomi, M., Mahabal, A., Mao, P., Miller, A. A., Monkewitz, S., Murphy, P., Ngeow, C.-C., Nordin, J., Nugent, P., Ofek, E., Patterson, M. T., Penprase, B., Porter, M., Rauch, L., Rebbapragada, U., Reiley, D., Rigault, M., Rodriguez, H., van Roestel, J., Rusholme, B., van Santen, J., Schulze, S., Shupe, D. L., Singer, L. P., Soumagnac, M. T., Stein, R., Surace, J., Sollerman, J., Szkody, P., Taddia, F., Terek, S., Van Sistine, A., van Velzen, S., Vestrand, W. T., Walters, R., Ward, C., Ye, Q.-Z., Yu, P.-C., Yan, L., and Zolkower, J. (2019). The Zwicky Transient Facility: System Overview, Performance, and First Results. PASP, 131(995):018002.

Benbakoura, M., Gaulme, P., McKeever, J., Sekaran, S., Beck, P. G., Spada, F., Jackiewicz, J., Mathis, S., Mathur, S., Tkachenko, A., and García, R. A. (2021). Spectroscopic and seismic analysis of red giants in eclipsing binaries discovered by Kepler. A&A, 648:A113.

Benson, R. S. (1970). *Evolution of Early-Type Close Binary Systems.* PhD thesis, University of California, Berkeley.

Berger, E., Soderberg, A. M., Chevalier, R. A., Fransson, C., Foley, R. J., Leonard, D. C., Debes, J. H., Diamond-Stanic, A. M., Dupree, A. K., Ivans, I. I., Simmerer, J., Thompson,

I. B., and Tremonti, C. A. (2009). An Intermediate Luminosity Transient in NGC 300: The Eruption of a Dust-Enshrouded Massive Star. ApJ, 699(2):1850–1865.

Bertin, E. and Arnouts, S. (1996). SExtractor: Software for source extraction. A&AS, 117:393–404.

Bertout, C. (1989). T tauri stars: Wild as dust. *Annual Review of Astronomy and Astrophysics*, 27(1):351–395.

Blagorodnova, N., Klencki, J., Pejcha, O., Vreeswijk, P. M., Bond, H. E., Burdge, K. B., De, K., Fremling, C., Gehrz, R. D., Jencson, J. E., Kasliwal, M. M., Kupfer, T., Lau, R. M., Masci, F. J., and Rich, M. R. (2021). The luminous red nova AT 2018bwo in NGC 45 and its binary yellow supergiant progenitor. *arXiv e-prints*, page arXiv:2102.05662.

Blagorodnova, N., Kotak, R., Polshaw, J., Kasliwal, M. M., Cao, Y., Cody, A. M., Doran, G. B., Elias-Rosa, N., Fraser, M., Fremling, C., Gonzalez-Fernandez, C., Harmanen, J., Jencson, J., Kankare, E., Kudritzki, R. P., Kulkarni, S. R., Magnier, E., Manulis, I., Masci, F. J., Mattila, S., Nugent, P., Ochner, P., Pastorello, A., Reynolds, T., Smith, K., Sollerman, J., Taddia, F., Terreran, G., Tomasella, L., Turatto, M., Vreeswijk, P. M., Wozniak, P., and Zaggia, S. (2017). Common Envelope Ejection for a Luminous Red Nova in M101. ApJ, 834(2):107.

Blanco-Cuaresma, S., Soubiran, C., Heiter, U., and Jofré, P. (2014). iSpec: Stellar atmospheric parameters and chemical abundances.

Bond, H. E., Bedin, L. R., Bonanos, A. Z., Humphreys, R. M., Monard, L. A. G. B., Prieto, J. L., and Walter, F. M. (2009). The 2008 Luminous Optical Transient in the Nearby Galaxy NGC 300. ApJ, 695(2):L154–L158.

Bond, H. E., Henden, A., Levay, Z. G., Panagia, N., Sparks, W. B., Starrfield, S., Wagner, R. M., Corradi, R. L. M., and Munari, U. (2003). An energetic stellar outburst accompanied by circumstellar light echoes. Nature, 422(6930):405–408.

Bond, H. E. and Siegel, M. H. (2006). Hubble Space Telescope Imaging of the Outburst Site of M31 RV. AJ, 131(2):984–989.

Bradstreet, D. H. and Guinan, E. F. (1994). Stellar Mergers and Acquisitions: The Formation and Evolution of W Ursae Majoris Binaries. In Shafter, A. W., editor, *Interacting Binary Stars*, volume 56 of *Astronomical Society of the Pacific Conference Series*, page 228.

Brandenburg, A. and Giampapa, M. S. (2018). Enhanced Stellar Activity for Slow Antisolar Differential Rotation? ApJ, 855:L22.

Brandenburg, A., Käpylä, P. J., and Korpi, M. J. (2011). From convective to stellar dynamos. In Brummell, N. H., Brun, A. S., Miesch, M. S., and Ponty, Y., editors, *Astrophysical Dynamics: From Stars to Galaxies*, volume 271 of *IAU Symposium*, pages 279–287.

Breger, M. (1979). Delta Scuti and related stars. PASP, 91:5–26.

Brown, N. J., Waagen, E. O., Scovil, C., Nelson, P., Oksanen, A., Solonen, J., and Price, A. (2002). Peculiar variable in Monoceros. IAU Circ., 7785:1.

Brown, T. M., Baliber, N., Bianco, F. B., Bowman, M., Burleson, B., Conway, P., Crellin, M., Depagne, É., De Vera, J., Dilday, B., Dragomir, D., Dubberley, M., Eastman, J. D., Elphick, M., Falarski, M., Foale, S., Ford, M., Fulton, B. J., Garza, J., Gomez, E. L., Graham, M., Greene, R., Haldeman, B., Hawkins, E., Haworth, B., Haynes, R., Hidas, M., Hjelstrom, A. E., Howell, D. A., Hygelund, J., Lister, T. A., Lobdill, R., Martinez, J., Mullins, D. S., Norbury, M., Parrent, J., Paulson, R., Petry, D. L., Pickles, A., Posner, V., Rosing, W. E., Ross, R., Sand, D. J., Saunders, E. S., Shobbrook, J., Shporer, A., Street, R. A., Thomas, D., Tsapras, Y., Tufts, J. R., Valenti, S., Vander Horst, K., Walker, Z., White, G., and Willis, M. (2013). Las Cumbres Observatory Global Telescope Network. PASP, 125(931):1031.

Bruton, D., Linenschmidt, R., and Schmude, R. W., J. (1996). Watching β Lyrae Evolve. *International Amateur-Professional Photoelectric Photometry Communications*, 63:51.

Buckley, D. A. H., Swart, G. P., and Meiring, J. G. (2006). Completion and commissioning of the Southern African Large Telescope. In Stepp, L. M., editor, *Society of Photo-Optical Instrumentation Engineers (SPIE) Conference Series*, volume 6267 of *Society of Photo-Optical Instrumentation Engineers (SPIE) Conference Series*, page 62670Z.

Burgh, E. B., Nordsieck, K. H., Kobulnicky, H. A., Williams, T. B., O'Donoghue, D., Smith, M. P., and Percival, J. W. (2003). Prime Focus Imaging Spectrograph for the Southern African Large Telescope: optical design. In Iye, M. and Moorwood, A. F. M., editors, *Instrument Design and Performance for Optical/Infrared Ground-based Telescopes*, volume 4841 of *Society of Photo-Optical Instrumentation Engineers (SPIE) Conference Series*, pages 1463–1471.

Cai, Y. Z., Pastorello, A., Fraser, M., Prentice, S. J., Reynolds, T. M., Cappellaro, E., Benetti, S., Morales-Garoffolo, A., Reguitti, A., Elias-Rosa, N., Brennan, S., Callis, E., Cannizzaro, G., Fiore, A., Gromadzki, M., Galindo-Guil, F. J., Gall, C., Heikkilä, T., Mason, E., Moran, S., Onori, F., Sagués Carracedo, A., and Valerin, G. (2019). The transitional gap transient AT 2018hso: new insights into the luminous red nova phenomenon. A&A, 632:L6.

Caramazza, M., Flaccomio, E., Micela, G., Reale, F., Wolk, S. J., and Feigelson, E. D. (2007). X-ray flares in Orion low-mass stars. A&A, 471:645–654.

Charbonneau, P. (2014). Solar dynamo theory. *Annual Review of Astronomy and Astrophysics*, 52(1):251–290.

Charbonneau, P., Christensen-Dalsgaard, J., Henning, R., Larsen, R. M., Schou, J., Thompson, M. J., and Tomczyk, S. (1999). Helioseismic Constraints on the Structure of the Solar Tachocline. *apj*, 527:445–460.

Chen, X., Wang, S., Deng, L., de Grijs, R., Yang, M., and Tian, H. (2020). The Zwicky Transient Facility Catalog of Periodic Variable Stars. ApJS, 249(1):18.

Chornock, R., Bhirombhakdi, K., Katebi, R., Blanchard, P., Nicholl, M., and Berger, E. (2016). Spectroscopic classification of two superluminous supernovae. *The Astronomer's Telegram*, 8790:1.

Clayton, G. C. (2012). What are the r coronae borealis stars?

Collins, K. A., Kielkopf, J. F., Stassun, K. G., and Hessman, F. V. (2017). Astroimagej: Image processing and photometric extraction for ultra-precise astronomical light curves. *The Astronomical Journal*, 153(2):77.

Collins, K. A., Kielkopf, J. F., Stassun, K. G., and Hessman, F. V. (2017). AstroImageJ: Image Processing and Photometric Extraction for Ultra-precise Astronomical Light Curves. AJ, 153(2):77.

Cooper, J. (2020). Disrupted exoplanet systems in the superwasp archive.

Covey, K. R., Ivezić, Ž., Schlegel, D., Finkbeiner, D., Padmanabhan, N., Lupton, R. H., Agüeros, M. A., Bochanski, J. J., Hawley, S. L., West, A. A., Seth, A., Kimball, A., Gogarten, S. M., Claire, M., Haggard, D., Kaib, N., Schneider, D. P., and Sesar, B. (2007). Stellar SEDs from 0.3 to 2.5 μm: Tracing the Stellar Locus and Searching for Color Outliers in the SDSS and 2MASS. AJ, 134(6):2398–2417.

Cox, A. N. (2000). *Allen's astrophysical quantities*.

Crause, L. A., Carter, D., Daniels, A., Evans, G., Fourie, P., Gilbank, D., Hendricks, M., Koorts, W., Lategan, D., Loubser, E., Mouries, S., O'Connor, J. E., O'Donoghue, D. E., Potter, S., Sass, C., Sickafoose, A. A., Stoffels, J., Swanevelder, P., Titus, K., van Gend, C., Visser, M., and Worters, H. L. (2016). SpUpNIC (Spectrograph Upgrade: Newly Improved Cassegrain) on the South African Astronomical Observatory's 74-inch telescope. In Evans, C. J., Simard, L., and Takami, H., editors, *Ground-based and Airborne Instrumentation for Astronomy VI*, volume 9908 of *Society of Photo-Optical Instrumentation Engineers (SPIE) Conference Series*, page 990827.

Crawford, S. M., Still, M., Schellart, P., Balona, L., Buckley, D. A. H., Dugmore, G., Gulbis, A. A. S., Kniazev, A., Kotze, M., Loaring, N., Nordsieck, K. H., Pickering, T. E., Potter, S., Romero Colmenero, E., Vaisanen, P., Williams, T., and Zietsman, E. (2010). PySALT: the SALT science pipeline. In Silva, D. R., Peck, A. B., and Soifer, B. T., editors, *Observatory Operations: Strategies, Processes, and Systems III*, volume 7737 of *Society of Photo-Optical Instrumentation Engineers (SPIE) Conference Series*, page 773725.

Czesla, S. and Schmitt, J. H. H. M. (2007). Are magnetic hot stars intrinsic X-ray sources? *aap*, 465:493–499.

Danchi, W., Bester, M., Degiacomi, C., Greenhill, L., and Townes, C. (1994). Characteristics of dust shells around 13 late-type stars. *The Astronomical Journal*, 107:1469–1513.

Darnley, M. J., Bode, M. F., Kerins, E., Newsam, A. M., An, J., Baillon, P., Belokurov, V., Novati, S. C., Carr, B. J., Crézé, M., and et al. (2006). Classical novae from the point–agape microlensing survey of m31 – ii. rate and statistical characteristics of the nova population. *Monthly Notices of the Royal Astronomical Society*, 369(1):257–271.

Davies, S. R. (1990). An improved test for periodicity. MNRAS, 244:93–95.

Davis, P. J., Kolb, U., and Willems, B. (2010). A comprehensive population synthesis study of post-common envelope binaries. MNRAS, 403(1):179–195.

de la Reza, R., Drake, N. A., da Silva, L., Torres, C. A. O., and Martin, E. L. (1997). On a Rapid Lithium Enrichment and Depletion of K Giant Stars. ApJ, 482(1):L77–L80.

Desidera, S., Chauvin, G., Bonavita, M., Messina, S., LeCoroller, H., Schmidt, T., Gratton, R., Lazzoni, C., Meyer, M., Schlieder, J., Cheetham, A., Hagelberg, J., Bonnefoy, M., Feldt, M., Lagrange, A.-M., Langlois, M., Vigan, A., Tan, T. G., Hambsch, F. J., Millward, M., Alcala, J., Benatti, S., Brandner, W., Carson, J., Covino, E., Delorme, P., D'Orazi, V., Janson, M., Rigliaco, E., Beuzit, J. L., Biller, B., Boccaletti, A., Dominik, C., Cantalloube, F., Fontaniv, C., Galicher, R., Henning, T., Lagadec, E., Ligi, R., Maire, A.-L., Menard, F., Mesa, D., Muller, A., Samland, M., Schmid, H. M., Sissa, E., Turatto, M., Udry, S., Asensio-Torres, A. Z. R., Kopytova, T., Rickman, E., Abe, L., Antichi, J., Baruffolo, A., Baudoz, P., Baudrand, J., Blanchard, P., Bazzon, A., Buey, T., Carbillet, M., Carle, M., Charton, J., Cascone, E., Claudi, R., Costille, A., Deboulbe, A., De Caprio, V., Dohlen, K., Fantinel, D., Feautrier, P., Fusco, T., Gigan, P., Giro, E., Gisler, D., Gluck, L., Hubin, N., Hugot, E., Jaquet, M., Kasper, M., Madec, F., Magnard, Y., Martinez, P., Maurel, D., Le Mignant, D., Moller-Nilsson, O., Llored, M., Moulin, T., Origne, A., Pavlov, A., Perret, D., Petit, C., Pragt, J., Puget, P., Rabou, P., Ramon, J., Rigal, F., Rochat, S., Roelfsema, R., Rousset, G., Roux, A., Salasnich, B., Sauvage, J. F., Sevin, A., Soenke, C., Stadler, E., Suarez, M., Weber, L., and Wildi, F. (2021). The SPHERE infrared survey for exoplanets (SHINE)- I Sample definition and target characterization. *arXiv e-prints*, page arXiv:2103.04366.

Dong, S., Kochanek, C. S., Adams, S., and Prieto, J. L. (2015). The Probable M31 Stellar Merger: Identification and Variability of the Likely Progenitor System. *The Astronomer's Telegram*, 7173:1.

Douglas, S. T., Agüeros, M. A., Covey, K. R., Bowsher, E. C., Bochanski, J. J., Cargile, P. A., Kraus, A., Law, N. M., Lemonias, J. J., Arce, H. G., Fierroz, D. F., and Kundert, A. (2014). The factory and the beehive. ii. activity and rotation in praesepe and the hyades. *The Astrophysical Journal*, 795(2):161.

Drake, A. J., Djorgovski, S. G., Catelan, M., Graham, M. J., Mahabal, A. A., Larson, S., Christensen, E., Torrealba, G., Beshore, E., McNaught, R. H., Garradd, G., Belokurov, V., and Koposov, S. E. (2017). The Catalina Surveys Southern periodic variable star catalogue. MNRAS, 469(3):3688–3712.

Drake, A. J., Graham, M. J., Djorgovski, S. G., Catelan, M., Mahabal, A. A., Torrealba, G., García-Álvarez, D., Donalek, C., Prieto, J. L., Williams, R., Larson, S., Christen sen, E., Belokurov, V., Koposov, S. E., Beshore, E., Boattini, A., Gibbs, A., Hill, R., Kowalski, R., Johnson, J., and Shelly, F. (2014). The Catalina Surveys Periodic Variable Star Catalog. ApJS, 213(1):9.

Drimmel, R., Cabrera-Lavers, A., and López-Corredoira, M. (2003). A three-dimensional Galactic extinction model. A&A, 409:205–215.

Duerbeck, H. W. (1996). *W UMa type variables*, page 183.

Duquennoy, A. and Mayor, M. (1991). *How Many Single Stars Among Solar Type Stars?*, volume 390, pages 39–43.

Duvall, Jr., T., Dziembowski, W., Goode, P., Gough, D., Harvey, J., and Leibacher, J. (1984). Internal rotation of the sun. *nat*, 310:22–25.

E. Baiada, A. . F. B., editor (1995). *Museo della Specola: catalogo italiano - ingles*. Bologna University Press.

Eggleton, P. (2006). *Evolutionary Processes in Binary and Multiple Stars*.

Eisner, N. L., Barragán, O., Lintott, C., Aigrain, S., Nicholson, B., Boyajian, T. S., Howell, S. B., Johnston, C., Lakeland, B., Miller, G., McMaster, A., Parviainen, H., Safron, E. J., Schwamb, M. E., Trouille, L., Vaughan, S., Zicher, N., Allen, C., Allen, S., Bouslog, M., Johnson, C., Simon, M. N., Wolfenbarger, Z., Baeten, E. M. L., Bundy, D. M., and Hoffman, T. (2020). Planet Hunters TESS II: Findings from the first two years of TESS. *arXiv e-prints*, page arXiv:2011.13944.

Evans, N. R., Berdnikov, L., Gorynya, N., Rastorguev, A., and Eaton, J. (2011). The Orbit of the Cepheid V350 Sgr Revisited. AJ, 142(3):87.

Eyer, L. and Mowlavi, N. (2008). Variable stars across the observational hr diagram. *Journal of Physics: Conference Series*, 118:012010.

Falcón-Barroso, J., Sánchez-Blázquez, P., Vazdekis, A., Ricciardelli, E., Cardiel, N., Cenarro, A. J., Gorgas, J., and Peletier, R. F. (2011). An updated MILES stellar library and stellar population models. A&A, 532:A95.

Fang, X.-S., Zhao, G., Zhao, J.-K., and Kumar, Y. B. (2018). Stellar activity with LAMOST – II. chromospheric activity in open clusters. *Monthly Notices of the Royal Astronomical Society*, 476(1):908–926.

Farmer, R., Kolb, U., and Norton, A. J. (2013). The true stellar parameters of the Kepler target list. MNRAS, 433(2):1133–1145.

Flaccomio, E., Micela, G., Sciortino, S., Feigelson, E. D., Herbst, W., Favata, F., Harnden, Jr., F. R., and Vrtilek, S. D. (2005). Rotational Modulation of X-Ray Emission in Orion Nebula Young Stars. *apjs*, 160:450–468.

Flannery, B. P. (1977). Mass Transfer Effects in Binary Star Evolution. In Papagiannis, M. D., editor, *Eighth Texas Symposium on Relativistic Astrophysics*, volume 302, page 36.

Foreman-Mackey, D., Hogg, D. W., Lang, D., and Goodman, J. (2013). emcee: The MCMC Hammer. PASP, 125(925):306.

Frasca, A., Biazzo, K., Catalano, S., Marilli, E., Messina, S., and Rodonò, M. (2005). Measuring starspot temperature from line-depth ratios. *http://dx.doi.org/10.1051/0004-6361:20041373*.

Gaia Collaboration (2016). The Gaia mission. A&A, 595:A1.

Gaia Collaboration (2018). Gaia Data Release 2. Summary of the contents and survey properties. A&A, 616:A1.

Gaia-ESO Survey Team (2012). The Gaia-ESO Public Spectroscopic Survey. *The Messenger*, 147:25–31.

Gaspani, A. (1998). Who Discovered Mira Ceti? (The first variabilist was a Celt man who lived in Libenice. In Dusek, J. and Zejda, M., editors, *29th Conference on Variable Star Research*, page 94.

Gastine, T., Yadav, R. K., Morin, J., Reiners, A., and Wicht, J. (2014). From solar-like to antisolar differential rotation in cool stars. MNRAS, 438(1):L76–L80.

Gaulme, P. (2013). Testing Asteroseismology with Red Giants in Eclipsing Binary and Multiple-star Systems. In Shibahashi, H. and Lynas-Gray, A. E., editors, *Progress in Physics of the Sun and Stars: A New Era in Helio- and Asteroseismology*, volume 479 of *Astronomical Society of the Pacific Conference Series*, page 185.

Gaulme, P., Jackiewicz, J., Appourchaux, T., and Mosser, B. (2014). Surface Activity and Oscillation Amplitudes of Red Giants in Eclipsing Binaries. ApJ, 785(1):5.

Gaulme, P., McKeever, J., Rawls, M. L., Jackiewicz, J., Mosser, B., and Guzik, J. A. (2013). Red Giants in Eclipsing Binary and Multiple-star Systems: Modeling and Asteroseismic Analysis of 70 Candidates from Kepler Data. ApJ, 767(1):82.

Gautschy, A. and Saio, H. (1996). Stellar pulsations across the hr diagram: Part ii. *Annual Review of Astronomy and Astrophysics*, 34(1):551–606.

Gershberg, R. E. and Shakhovskaia, N. I. (1983). Characteristics of activity energetics of the UV cet-type flare stars. Ap&SS, 95(2):235–253.

Gilman, P. A. (1983). Dynamically consistent nonlinear dynamos driven by convection in a rotating spherical shell. II - dynamos with cycles and strong feedbacks. *The Astrophysical Journal Supplement Series*, 53:243.

Glass, I. S. (1989). The Story of the Radcliffe Telescope. QJRAS, 30:33–58.

Goodricke, J. (1784). On the Periods of the Changes of Light in the Star Algol. In a Letter from John Goodricke, Esq. to the Rev. Anthony Shepherd, D. D. F. R. S. Professor of Astronomy at Cambridge. *Philosophical Transactions of the Royal Society of London Series I*, 74:287–292.

Goranskij, V. P., Barsukova, E. A., Valeev, A. F., Tsvetkov, D. Y., Volkov, I. M., Metlov, V. G., and Zharova, A. V. (2016). SN2015bh in NGC 2770: LBV core collapse in merging of binary system components. *Astrophysical Bulletin*, 71(4):422–435.

Goranskij, V. P., Metlova, N. V., Shugarov, S. Y., Zharova, A. V., Barsukova, E. A., and Kroll, P. (2007). Historical Light Curves of Peculiar Red Novae V838 Mon and V4332 Sgr. In Corradi, R. L. M. and Munari, U., editors, *The Nature of V838 Mon and its Light Echo*, volume 363 of *Astronomical Society of the Pacific Conference Series*, page 214.

Gray, R. O. and Corbally, C. J. (1994). The Calibration of MK Spectral Classes Using Spectral Synthesis. I. The Effective Temperature Calibration of Dwarf Stars. AJ, 107:742.

Greer, P. A., Payne, S. G., Norton, A. J., Maxted, P. F. L., Smalley, B., West, R. G., Wheatley, P. J., and Kolb, U. C. (2017). The SuperWASP catalogue of 4963 RR Lyr stars: identification of 983 Blazhko effect candidates. A&A, 607:A11.

Gregory, S. G. (2016). The long-term evolution of stellar activity. *Proceedings of the International Astronomical Union*, 12(S328):252–263.

Gregory, S. G., Adams, F. C., and Davies, C. L. (2016). The coronal evolution of pre-main-sequence stars. *ArXiv e-prints*.

Guillochon, J., Parrent, J., Kelley, L. Z., and Margutti, R. (2017). An Open Catalog for Supernova Data. ApJ, 835(1):64.

Guinan, E. F. and Bradstreet, D. H. (1988). Kinematic Clues to the Origin and Evolution of Low Mass Contact Binaries. In Dupree, A. K. and Lago, M. T. V. T., editors, *Formation and Evolution of Low Mass Stars*, volume 241 of *NATO Advanced Study Institute (ASI) Series C*, page 345.

Gustafsson, B., Edvardsson, B., Eriksson, K., Jørgensen, U. G., Nordlund, Å., and Plez, B. (2008). A grid of MARCS model atmospheres for late-type stars. I. Methods and general properties. A&A, 486(3):951–970.

Hall, D. S. and Duerbeck, H. W. (1996). *Eclipsing binary systems.*, pages 168–187.

Han, Z. (1995). *Applications of binary evolution*. PhD thesis, University of Cambridge.

Hekker, S., De Ridder, J., Baudin, F., Barban, C., Carrier, F., Hatzes, A. P., Kallinger, T., and Weiss, W. W. (2010). Red Giants observed with CoRoT. *arXiv e-prints*, page arXiv:1001.4543.

Henden, A. A., Levine, S., Terrell, D., and Welch, D. L. (2015). APASS - The Latest Data Release. In *American Astronomical Society Meeting Abstracts #225*, volume 225 of *American Astronomical Society Meeting Abstracts*, page 336.16.

Hermes, J. J., Kilic, M., Brown, W. R., Winget, D. E., Allende Prieto, C., Gianninas, A., Mukadam, A. S., Cabrera-Lavers, A., and Kenyon, S. J. (2012). Rapid Orbital Decay in the 12.75-minute Binary White Dwarf J0651+2844. ApJ, 757(2):L21.

Herwig, F. (2000). The evolution of AGB stars with convective overshoot. A&A, 360:952–968.

Hilditch, R. W. (2001). *An Introduction to Close Binary Stars*.

Hoffleit, D. (1993). *Women in the history of variable star astronomy*.

Hoffleit, D. (1997). History of the Discovery of Mira Stars. *Journal of the American Association of Variable Star Observers (JAAVSO)*, 25(2):115–136.

Hollands, M. A., Tremblay, P. E., Gänsicke, B. T., Camisassa, M. E., Koester, D., Aungwerojwit, A., Chote, P., Córsico, A. H., Dhillon, V. S., Gentile-Fusillo, N. P., Hoskin, M. J., Izquierdo, P., Marsh, T. R., and Steeghs, D. (2020). An ultra-massive white dwarf with a mixed hydrogen-carbon atmosphere as a likely merger remnant. *Nature Astronomy*, 4:663–669.

Holmes, S., Kolb, U., Haswell, C. A., Burwitz, V., Lucas, R. J., Rodriguez, J., Rolfe, S. M., Rostron, J., and Barker, J. (2011). PIRATE: A Remotely Operable Telescope Facility for Research and Education. PASP, 123(908):1177.

Howerton, S., Drake, A. J., Djorgovski, S. G., Mahabal, A., Graham, M. J., Williams, R., Prieto, J. L., Catelan, M., Beshore, E. C., Larson, S. M., Christensen, E., Vinko, J., Wheeler, J. C., Chatzopoulos, E., Marion, G. H., Caldwell, J., Taubenberger, S., Pastorello, A., Elias-Rosa, N., Benetti, S., and Bufano, F. (2011). Psn J10523453+2256052 in NGC 3437. *Central Bureau Electronic Telegrams*, 2637:1.

Howes, L. M., Casey, A. R., Asplund, M., Keller, S. C., Yong, D., Nataf, D. M., Poleski, R., Lind, K., Kobayashi, C., Owen, C. I., and et al. (2015). Extremely metal-poor stars from the cosmic dawn in the bulge of the milky way. *Nature*, 527(7579):484–487.

Howitt, G., Stevenson, S., Vigna-Gómez, A., Justham, S., Ivanova, N., Woods, T. E., Neijssel, C. J., and Mandel, I. (2020). Luminous Red Novae: population models and future prospects. MNRAS, 492(3):3229–3240.

Huemmerich, S. and Bernhard, K. (2012). New Eclipsing Binaries in the OGLE-II Database (Part 1). The Carina Galactic Disk Fields. *Peremennye Zvezdy Prilozhenie*, 12(11):11.

Hurley, J. R., Tout, C. A., and Pols, O. R. (2002). Evolution of binary stars and the effect of tides on binary populations. *Monthly Notices of the Royal Astronomical Society*, 329(4):897–928.

Husser, T. O., Wende-von Berg, S., Dreizler, S., Homeier, D., Reiners, A., Barman, T., and Hauschildt, P. H. (2013). A new extensive library of PHOENIX stellar atmospheres and synthetic spectra. A&A, 553:A6.

Iaconi, R. and De Marco, O. (2019). Speaking with one voice: simulations and observations discuss the common envelope parameter. *Monthly Notices of the Royal Astronomical Society*, 490(2):2550–2566.

Iben, Icko, J. and Livio, M. (1993). Common Envelopes in Binary Star Evolution. PASP, 105:1373.

Ivanova, N. (2016). Common envelope: progress and transients. *Proceedings of the International Astronomical Union*, 12(S329):199–206.

Ivanova, N., Justham, S., Chen, X., De Marco, O., Fryer, C. L., Gaburov, E., Ge, H., Glebbeek, E., Han, Z., Li, X. D., Lu, G., Marsh, T., Podsiadlowski, P., Potter, A., Soker, N., Taam, R., Tauris, T. M., van den Heuvel, E. P. J., and Webbink, R. F. (2013). Common envelope evolution: where we stand and how we can move forward. A&A Rev., 21:59.

Ivezić, Ž., Kahn, S. M., Tyson, J. A., et al. (2019). LSST: From Science Drivers to Reference Design and Anticipated Data Products. ApJ, 873(2):111.

Izzard, R. G., Dray, L. M., Karakas, A. I., Lugaro, M., and Tout, C. A. (2006). Population nucleosynthesis in single and binary stars. I. Model. A&A, 460(2):565–572.

Izzard, R. G., Glebbeek, E., Stancliffe, R. J., and Pols, O. R. (2009). Population synthesis of binary carbon-enhanced metal-poor stars. A&A, 508(3):1359–1374.

Izzard, R. G., Preece, H., Jofre, P., Halabi, G. M., Masseron, T., and Tout, C. A. (2018). Binary stars in the Galactic thick disc. MNRAS, 473(3):2984–2999.

Izzard, R. G., Tout, C. A., Karakas, A. I., and Pols, O. R. (2004). A new synthetic model for asymptotic giant branch stars. MNRAS, 350(2):407–426.

Jardine, M. (2004). Coronal stripping in supersaturated stars. *Astronomy & Astrophysics*, 414(1):L5–L8.

Jardine, M. and Unruh, Y. C. (1999). Coronal emission and dynamo saturation. *Astronomy & Astrophysics*, 346:883–891.

Jayasinghe, T., Kochanek, C. S., Stanek, K. Z., Shappee, B. J., Holoien, T. W. S., Thompson, T. A., Prieto, J. L., Dong, S., Pawlak, M., Shields, J. V., Pojmanski, G., Otero, S., Britt, C. A., and Will, D. (2018). The ASAS-SN catalogue of variable stars I: The Serendipitous Survey. MNRAS, 477(3):3145–3163.

Jayasinghe, T., Stanek, K. Z., Kochanek, C. S., Shappee, B. J., Holoien, T. W. S., Thompson, T. A., Prieto, J. L., Dong, S., Pawlak, M., Pejcha, O., Shields, J. V., Pojmanski, G., Otero, S., Hurst, N., Britt, C. A., and Will, D. (2019). The ASAS-SN catalogue of variable stars III: variables in the southern TESS continuous viewing zone. MNRAS, 485(1):961–971.

Jayasinghe, T., Stanek, K. Z., Kochanek, C. S., Shappee, B. J., Holoien, T. W. S., Thompson, T. A., Prieto, J. L., Dong, S., and Stevens, D. J. (2018). Asas-sn identification of a detached eclipsing binary system with a ~ 7.3 year period.

Jeffries, R. D., Jackson, R. J., Briggs, K. R., Evans, P. A., and Pye, J. P. (2011). Investigating coronal saturation and supersaturation in fast-rotating M-dwarf stars. MNRAS, 411:2099–2112.

Jencson, J. E., Adams, S. M., Bond, H. E., van Dyk, S. D., Kasliwal, M. M., Bally, J., Blagorodnova, N., De, K., Fremling, C., Yao, Y., Fruchter, A., Rubin, D., Barbarino, C., Sollerman, J., Miller, A. A., Hicks, E. K. S., Malkan, M. A., Andreoni, I., Bellm, E. C., Buchheim, R., Dekany, R., Feeney, M., Frederick, S., Gal-Yam, A., Gehrz, R. D., Giomi, M., Graham, M. J., Green, W., Hale, D., Hankins, M. J., Hanson, M., Helou, G., Ho, A. Y. Q., Hung, T., Jurić, M., Kendurkar, M. R., Kulkarni, S. R., Lau, R. M., Masci, F. J., Neill, J. D., Quin, K., Riddle, R. L., Rusholme, B., Sims, F., Smith, N., Smith, R. M., Soumagnac, M. T., Tachibana, Y., Tinyanont, S., Walters, R., Watson, S., and Williams, R. E. (2019). Discovery of an intermediate-luminosity red transient in m51 and its likely dust-obscured, infrared-variable progenitor. *The Astrophysical Journal*, 880(2):L20.

Jiang, D., Han, Z., Ge, H., Yang, L., and Li, L. (2012). The short-period limit of contact binaries. MNRAS, 421(4):2769–2773.

Jordan, R., Kobulnicky, H., Molnar, L. A., and McLane, J. (2019). Detecting a Third Body in KIC9832227. In *American Astronomical Society Meeting Abstracts #233*, volume 233 of *American Astronomical Society Meeting Abstracts*, page 464.04.

Kahraman Aliçavuș, F., Soydugan, E., Smalley, B., and Kubát, J. (2017). Eclipsing binary stars with a δ Scuti component. MNRAS, 470(1):915–931.

Kamiński, T., Schmidt, M., and Tylenda, R. (2010). V4332 Sagittarii: a circumstellar disc obscuring the main object. A&A, 522:A75.

Kamiński, T., Menten, K. M., Tylenda, R., Hajduk, M., Patel, N. A., and Kraus, A. (2015). Nuclear ashes and outflow in the eruptive star nova vul 1670. *Nature*, 520(7547):322–324.

Kankare, E., Kotak, R., Pastorello, A., Fraser, M., Mattila, S., Smartt, S. J., Bruce, A., Chambers, K. C., Elias-Rosa, N., Flewelling, H., Fremling, C., Harmanen, J., Huber, M., Jerkstrand, A., Kangas, T., Kuncarayakti, H., Magee, M., Magnier, E., Polshaw, J., Smith, K. W., Sollerman, J., and Tomasella, L. (2015). On the triple peaks of SNHunt248 in NGC 5806. A&A, 581:L4.

Karak, B. B., Käpylä, P. J., Käpylä, M. J., Brandenburg, A., Olspert, N., and Pelt, J. (2015). Magnetically controlled stellar differential rotation near the transition from solar to anti-solar profiles. A&A, 576:A26.

Kashi, A., Michaelis, A. M., and Feigin, L. (2019). ASASSN-13db 2014-2017 Eruption as an Intermediate Luminosity Optical Transient. *Galaxies*, 8(1):2.

Kasliwal, M. M. (2011). *Bridging the gap : elusive explosions in the local universe*. PhD thesis, California Institute of Technology.

Kasliwal, M. M., Kulkarni, S. R., Arcavi, I., Quimby, R. M., Ofek, E. O., Nugent, P., Jacobsen, J., Gal-Yam, A., Green, Y., Yaron, O., Fox, D. B., Howell, J. L., Cenko, S. B., Kleiser, I., Bloom, J. S., Miller, A., Li, W., Filippenko, A. V., Starr, D., Poznanski, D., Law, N. M., Helou, G., Frail, D. A., Neill, J. D., Forster, K., Martin, D. C., Tendulkar, S. P., Gehrels, N., Kennea, J., Sullivan, M., Bildsten, L., Dekany, R., Rahmer, G., Hale, D., Smith, R., Zolkower, J., Velur, V., Walters, R., Henning, J., Bui, K., McKenna, D., and Blake, C. (2011). PTF 10fqs: A Luminous Red Nova in the Spiral Galaxy Messier 99. ApJ, 730(2):134.

Kazarovets, E. V., Samus, N. N., Durlevich, O. V., Kireeva, N. N., and Pastukhova, E. N. (2011). The 80th Name-List of Variable Stars. Part I - RA 0h to 6h. *Information Bulletin on Variable Stars*, 5969:1.

Kesseli, A., West, A. A., Harrison, B., Veyette, M., and Feldman, D. (2017). PyHammer: An Automatic and Visual Suite for Spectral Typing Stars. In *American Astronomical Society Meeting Abstracts #229*, volume 229 of *American Astronomical Society Meeting Abstracts*, page 240.35.

Kesseli, A. Y., West, A. A., Veyette, M., Harrison, B., Feldman, D., and Bochanski, J. J. (2017). An empirical template library of stellar spectra for a wide range of spectral classes, luminosity classes, and metallicities using sdss boss spectra. *The Astrophysical Journal Supplement Series*, 230(2):16.

Kővári, Z., Strassmeier, K. G., Carroll, T. A., Oláh, K., Kriskovics, L., Kővári, E., Kovács, O., Vida, K., Granzer, T., and Weber, M. (2017). Antisolar differential rotation with surface lithium enrichment on the single K-giant V1192 Orionis. A&A, 606:A42.

Kim, C. H., Kreiner, J. M., and Nha, L. S. (2003). *Statistics of times of minimum light of 1140 eclipsing binary stars*, volume 298, page Li.

Kimeswenger, S. (2007). V838 Mon, V4332 Sgr, ... and Relatives in our Galaxy? In Corradi, R. L. M. and Munari, U., editors, *The Nature of V838 Mon and its Light Echo*, volume 363 of *Astronomical Society of the Pacific Conference Series*, page 197.

Kobulnicky, H. A., Nordsieck, K. H., Burgh, E. B., Smith, M. P., Percival, J. W., Williams, T. B., and O'Donoghue, D. (2003). Prime focus imaging spectrograph for the Southern African large telescope: operational modes. In Iye, M. and Moorwood, A. F. M., editors, *Instrument Design and Performance for Optical/Infrared Ground-based Telescopes*, volume 4841 of *Society of Photo-Optical Instrumentation Engineers (SPIE) Conference Series*, pages 1634–1644.

Kochanek, C. S., Adams, S. M., and Belczynski, K. (2014). Stellar mergers are common. MNRAS, 443(2):1319–1328.

Kochanek, C. S., Shappee, B. J., Stanek, K. Z., Holoien, T. W. S., Thompson, T. A., Prieto, J. L., Dong, S., Shields, J. V., Will, D., Britt, C., Perzanowski, D., and Pojmański, G. (2017). The All-Sky Automated Survey for Supernovae (ASAS-SN) Light Curve Server v1.0. PASP, 129(980):104502.

Kolb, U. (2010). *Extreme Environment Astrophysics*. Cambridge University Press, Cambridge.

Kolb, U., Brodeur, M., Braithwaite, N., and Minocha, S. (2018). A robotic telescope for university-level distance teaching. *Robotic Telescope, Student Research and Education Proceedings*, 1(1):127–136.

Kolb, U., Brodeur, M., Braithwaite, N., and Minocha, S. (2018). A robotic telescope for university-level distance teaching.

Kolb, U. and Ritter, H. (1990). A comparative study of the evolution of a close binary using a standard and an improved technique for computing mass transfer. A&A, 236:385–392.

Korzennik, S. G. and Eff-Darwich, A. (2011). The rotation rate and its evolution derived from improved mode fitting and inversion methodology. *Journal of Physics: Conference Series*, 271(1):012067.

Kraft, R. P. (1967). Studies of stellar rotation. v. the dependence of rotation on age among solar-type stars. *The Astrophysical Journal*, 150:551.

Kreiner, J. M., Kim, C.-H., and Nha, I.-S. (2001). *An Atlas of O-C Diagrams of Eclipsing Binary Stars*.

Kulkarni, S. R., Ofek, E. O., Rau, A., Cenko, S. B., Soderberg, A. M., Fox, D. B., Gal-Yam, A., Capak, P. L., Moon, D. S., Li, W., Filippenko, A. V., Egami, E., Kartaltepe, J., and Sanders, D. B. (2007). An unusually brilliant transient in the galaxy M85. Nature, 447(7143):458–460.

Kurtenkov, A. (2017). Searching for twins of the V1309 Sco progenitor system: a selection of long-period contact binaries. *Bulgarian Astronomical Journal*, 26:26.

Kurucz, R. L. (2005). ATLAS12, SYNTHE, ATLAS9, WIDTH9, et cetera. *Memorie della Societa Astronomica Italiana Supplementi*, 8:14.

Kurucz, R. L. (2014). *How to Build a Model of the Atmosphere and Spectrum*, pages 25–37.

L. Gilliland, R. (1985). Relation of chromospheric activity to convection, rotation, and pre-main-sequence evolution. 300:339–347.

Labadie-Bartz, J., Pepper, J., McSwain, M. V., Bjorkman, J. E., Bjorkman, K. S., Lund, M. B., Rodriguez, J. E., Stassun, K. G., Stevens, D. J., James, D. J., Kuhn, R. B., Siverd, R. J., and Beatty, T. G. (2017). Photometric variability of the be star population. *The Astronomical Journal*, 153(6):252.

Lada, C. J. (2006). Stellar Multiplicity and the Initial Mass Function: Most Stars Are Single. ApJ, 640(1):L63–L66.

Lai, D., Rasio, F. A., and Shapiro, S. L. (1993). Hydrodynamic Instability and Coalescence of Close Binary Systems. ApJ, 406:L63.

Landin, N. R., Mendes, L. T. S., and Vaz, L. P. R. (2010). Theoretical values of convective turnover times and rossby numbers for solar-like, pre-main sequence stars. *Astronomy and Astrophysics*, 510:A46.

Lasker, B. M., Lattanzi, M. G., McLean, B. J., Bucciarelli, B., Drimmel, R., Garcia, J., Greene, G., Guglielmetti, F., Hanley, C., Hawkins, G., Laidler, V. G., Loomis, C., Meakes, M., Mignani, R., Morbidelli, R., Morrison, J., Pannunzio, R., Rosenberg, A., Sarasso, M., Smart, R. L., Spagna, A., Sturch, C. R., Volpicelli, A., White, R. L., Wolfe, D., and Zacchei, A. (2008). The Second-Generation Guide Star Catalog: Description and Properties. AJ, 136(2):735–766.

Leavitt, H. S. (1908). 1777 variables in the Magellanic Clouds. *Annals of Harvard College Observatory*, 60:87–108.3.

Leavitt, H. S. and Pickering, E. C. (1912). Periods of 25 Variable Stars in the Small Magellanic Cloud. *Harvard College Observatory Circular*, 173:1–3.

Lebzelter, T., Mowlavi, N., Marigo, P., Pastorelli, G., Trabucchi, M., Wood, P. R., and Lecoeur-Taïbi, I. (2018). A new method to identify subclasses among AGB stars using Gaia and 2MASS photometry. A&A, 616:L13.

Li, T., Bedding, T. R., Huber, D., Ball, W. H., Stello, D., Murphy, S. J., and Bland-Hawthorn, J. (2017). Modelling Kepler red giants in eclipsing binaries: calibrating the mixing-length parameter with asteroseismology. *Monthly Notices of the Royal Astronomical Society*, 475(1):981–998.

Lintott, C. J., Schawinski, K., Slosar, A., Land, K., Bamford, S., Thomas, D., Raddick, M. J., Nichol, R. C., Szalay, A., Andreescu, D., Murray, P., and Vandenberg, J. (2008). Galaxy Zoo: morphologies derived from visual inspection of galaxies from the Sloan Digital Sky Survey. MNRAS, 389(3):1179–1189.

Lipunov, V. M., Blinnikov, S., Gorbovskoy, E., Tutukov, A., Baklanov, P., Krushinski, V., Tiurina, N., Balanutsa, P., Kuznetsov, A., Kornilov, V., Gorbunov, I., Shumkov, V., Vladimirov, V., Gress, O., Budnev, N. M., Ivanov, K., Tlatov, A., Gabovich, A., Yurkov, V., Sergienko, Y., and Zalozhnykh, I. (2017). MASTER OT J004207.99+405501.1/M31LRN 2015 luminous red nova in M31: discovery, light curve, hydrodynamics and evolution. *Monthly Notices of the Royal Astronomical Society*, 470(2):2339–2350.

Livio, M. and Soker, N. (1988). The Common Envelope Phase in the Evolution of Binary Stars. ApJ, 329:764.

Lohr, M. (2015). Eclipsing binaries and period changes in the superwasp archive.

Lohr, M. E., Norton, A. J., Anderson, D. R., Collier Cameron, A., Faedi, F., Haswell, C. A., Hellier, C., Hodgkin, S. T., Horne, K., Kolb, U. C., Maxted, P. F. L., Pollacco, D., Skillen, I., Smalley, B., West, R. G., and Wheatley, P. J. (2014). Period and amplitude variations in post-common-envelope eclipsing binaries observed with SuperWASP. A&A, 566:A128.

Lohr, M. E., Norton, A. J., Gillen, E., Busuttil, R., Kolb, U. C., Aigrain, S., McQuillan, A., Hodgkin, S. T., and González, E. (2015a). The doubly eclipsing quintuple low-mass star system 1SWASP J093010.78+533859.5. A&A, 578:A103.

Lohr, M. E., Norton, A. J., Kolb, U. C., Anderson, D. R., Faedi, F., and West, R. G. (2012). Period decrease in three SuperWASP eclipsing binary candidates near the short-period limit. A&A, 542:A124.

Lohr, M. E., Norton, A. J., Kolb, U. C., Maxted, P. F. L., Todd, I., and West, R. G. (2013). Period and period change measurements for 143 SuperWASP eclipsing binary candidates near the short-period limit and discovery of a doubly eclipsing quadruple system. A&A, 549:A86.

Lohr, M. E., Norton, A. J., Payne, S. G., West, R. G., and Wheatley, P. J. (2015b). Orbital period changes and the higher-order multiplicity fraction amongst SuperWASP eclipsing binaries. A&A, 578:A136.

Lombardi, J. C., J., Holtzman, W., Dooley, K. L., Gearity, K., Kalogera, V., and Rasio, F. A. (2011). Twin Binaries: Studies of Stability, Mass Transfer, and Coalescence. ApJ, 737(2):49.

Lucy, L. B. and White, R. L. (1980). X-ray emission from the winds of hot stars. *apj*, 241:300–305.

Luri, X., Brown, A. G. A., Sarro, L. M., Arenou, F., Bailer-Jones, C. A. L., Castro-Ginard, A., de Bruijne, J., Prusti, T., Babusiaux, C., and Delgado, H. E. (2018). Gaia Data Release 2: using Gaia parallaxes. *ArXiv e-prints*.

MacLeod, M., Antoni, A., Murguia-Berthier, A., Macias, P., and Ramirez-Ruiz, E. (2017a). Common Envelope Wind Tunnel: Coefficients of Drag and Accretion in a Simplified Context for Studying Flows around Objects Embedded within Stellar Envelopes. ApJ, 838(1):56.

MacLeod, M. and Loeb, A. (2020). Runaway Coalescence of Pre-common-envelope Stellar Binaries. ApJ, 893(2):106.

MacLeod, M., Macias, P., Ramirez-Ruiz, E., Grindlay, J., Batta, A., and Montes, G. (2017b). Lessons from the Onset of a Common Envelope Episode: the Remarkable M31 2015 Luminous Red Nova Outburst. ApJ, 835(2):282.

Madore, B. F. (1982). The period-luminosity relation. IV. Intrinsic relations and reddenings for the Large Magellanic Cloud Cepheids. ApJ, 253:575–579.

Madore, B. F. and Freedman, W. L. (1985). The search, discovery and use of cepheid variables as distance indicators : past procedures and future strategies. AJ, 90:1104–1112.

Magill, L., Kotak, R., Fraser, M., Smartt, S., Ochner, P., Pastorello, A., Benetti, S., and Harutunyan, A. (2011). PSN J12304185+4137498 in NGC 4490. *Central Bureau Electronic Telegrams*, 2789:2.

Mamajek, E. E., Torres, G., Prsa, A., Harmanec, P., Asplund, M., Bennett, P. D., Capitaine, N., Christensen-Dalsgaard, J., Depagne, E., Folkner, W. M., Haberreiter, M., Hekker, S., Hilton, J. L., Kostov, V., Kurtz, D. W., Laskar, J., Mason, B. D., Milone, E. F., Montgomery, M. M., Richards, M. T., Schou, J., and Stewart, S. G. (2015). IAU 2015 Resolution B2 on Recommended Zero Points for the Absolute and Apparent Bolometric Magnitude Scales. *ArXiv e-prints*.

Marsden, S. C., Carter, B. D., and Donati, J. F. (2009). The chromospheric emission of solar-type stars in the young open clusters IC 2391 and IC 2602. MNRAS, 399(2):888–905.

Marsh, T. R. (1995). The discovery of a short-period double-degenerate binary star. MNRAS, 275(1):L1–L5.

Marsh, T. R. (2014). PAMELA: Optimal extraction code for long-slit CCD spectroscopy.

Martin, R. G., Pringle, J. E., Tout, C. A., and Lubow, S. H. (2011). Tidal warping and precession of Be star decretion discs. MNRAS, 416(4):2827–2839.

Martini, P., Wagner, R. M., Tomaney, A., Rich, R. M., della Valle, M., and Hauschildt, P. H. (1999). Nova Sagittarii 1994 1 (V4332 Sagittarii): The Discovery and Evolution of an Unusual Luminous Red Variable Star. AJ, 118(2):1034–1042.

Mason, E., Diaz, M., Williams, R. E., Preston, G., and Bensby, T. (2010). The peculiar nova V1309 Scorpii/nova Scorpii 2008. A candidate twin of V838 Monocerotis. A&A, 516:A108.

Matsunaga, N., Fukushi, H., Nakada, Y., Tanabé, T., Feast, M. W., Menzies, J. W., Ita, Y., Nishiyama, S., Baba, D., Naoi, T., Nakaya, H., Kawadu, T., Ishihara, A., and Kato, D. (2006). The period-luminosity relation for type II Cepheids in globular clusters. MNRAS, 370(4):1979–1990.

Mauerhan, J. C., Van Dyk, S. D., Graham, M. L., Zheng, W., Clubb, K. I., Filippenko, A. V., Valenti, S., Brown, P., Smith, N., Howell, D. A., and Arcavi, I. (2015). SN Hunt 248: a super-Eddington outburst from a massive cool hypergiant. MNRAS, 447(2):1922–1934.

Mauerhan, J. C., Van Dyk, S. D., Johansson, J., Fox, O. D., Filippenko, A. V., and Graham, M. L. (2018). The dusty aftermath of SN Hunt 248: merger-burst remnant? MNRAS, 473(3):3765–3775.

Mayall, M. W. (1949). Six novae, one with a late-type spectrum. AJ, 54:R191.

McCully, C., Volgenau, N. H., Harbeck, D.-R., Lister, T. A., Saunders, E. S., Turner, M. L., Siiverd, R. J., and Bowman, M. (2018). Real-time processing of the imaging data from the network of Las Cumbres Observatory Telescopes using BANZAI. In Guzman, J. C. and Ibsen, J., editors, *Software and Cyberinfrastructure for Astronomy V*, volume 10707

of *Society of Photo-Optical Instrumentation Engineers (SPIE) Conference Series*, page 107070K.

Metcalfe, T. S. and Egeland, R. (2019). Understanding the Limitations of Gyrochronology for Old Field Stars. ApJ, 871:39.

Metcalfe, T. S. and van Saders, J. (2017). Magnetic evolution and the disappearance of sun-like activity cycles. *Solar Physics*, 292(9).

Metzger, B. D. (2017). Kilonovae. *Living Reviews in Relativity*, 20(1).

Metzger, B. D., Martínez-Pinedo, G., Darbha, S., Quataert, E., Arcones, A., Kasen, D., Thomas, R., Nugent, P., Panov, I. V., and Zinner, N. T. (2010). Electromagnetic counterparts of compact object mergers powered by the radioactive decay of r-process nuclei. *Monthly Notices of the Royal Astronomical Society*, 406(4):2650–2662.

Metzger, B. D. and Pejcha, O. (2017). Shock-powered light curves of luminous red novae as signatures of pre-dynamical mass-loss in stellar mergers. MNRAS, 471(3):3200–3211.

Micela, G., Sciortino, S., Serio, S., Vaiana, G. S., Bookbinder, J., Golub, L., F. R., J. H., and Rosner, R. (1985). Einstein x-ray survey of the pleiades - the dependence of x-ray emission on stellar age. *The Astrophysical Journal*, 292:172.

Miglio, A., Chaplin, W. J., Farmer, R., Kolb, U., Girardi, L., Elsworth, Y., Appourchaux, T., and Handberg, R. (2014). Prospects for Detecting Asteroseismic Binaries in Kepler Data. ApJ, 784(1):L3.

Mohanty, S. and Basri, G. (2003). Rotation and activity in mid-m to l field dwarfs. *The Astrophysical Journal*, 583(1):451.

Molnar, L. A., Van Noord, D. M., Kinemuchi, K., Smolinski, J. P., Alexander, C. E., Cook, E. M., Jang, B., Kobulnicky, H. A., Spedden, C. J., and Steenwyk, S. D. (2017). Prediction of a Red Nova Outburst in KIC 9832227. ApJ, 840(1):1.

Monet, D. G., Levine, S. E., Canzian, B., Ables, H. D., Bird, A. R., Dahn, C. C., Guetter, H. H., Harris, H. C., Henden, A. A., Leggett, S. K., Levison, H. F., Luginbuhl, C. B., Martini, J., Monet, A. K. B., Munn, J. A., Pier, J. R., Rhodes, A. R., Riepe, B., Sell, S., Stone, R. C., Vrba, F. J., Walker, R. L., Westerhout, G., Brucato, R. J., Reid, I. N., Schoening, W., Hartley, M., Read, M. A., and Tritton, S. B. (2003). The USNO-B Catalog. AJ, 125(2):984–993.

Montanari, G., editor (1671). *Sopra la sparizione d'alcune stelle et altre novità celesti*. G. B. Capponi, ed., Prose de' signori Accademici Gelati di Bologna.

Morales-Rueda, L., Carter, D., Steele, I. A., Charles, P. A., and Worswick, S. (2004). The Liverpool Telescope Spectrograph: FRODOSpec. *Astronomische Nachrichten*, 325(3):215–215.

Morrell, M. (2021). Monitoring the Variable Stellar Universe. PhD thesis, Open University.

Mould, J., Graham, J., Matthews, K., Soifer, B. T., and Phinney, E. S. (1989). Infrared Images of the Nucleus of M31. ApJ, 339:L21.

Muirhead, P. S., Kesseli, A., Han, E., and Veyette, M. (2019). Are Exoplanets Orbiting M Dwarfs Extreme? In *AAS/Division for Extreme Solar Systems Abstracts*, volume 51 of *AAS/Division for Extreme Solar Systems Abstracts*, page 502.01.

Munari, U., Henden, A., Kiyota, S., Laney, D., Marang, F., Zwitter, T., Corradi, R. L. M., Desidera, S., Marrese, P. M., Giro, E., Boschi, F., and Schwartz, M. B. (2002). The mysterious eruption of V838 Mon. A&A, 389:L51–L56.

Nakano, S., Nishiyama, K., Kabashima, F., Sakurai, Y., Jacques, C., Pimentel, E., Chekhovich, D., Korotkiy, S., Kryachko, T., and Samus, N. N. (2008). V1309 Scorpii = Nova Scorpii 2008. IAU Circ., 8972:1.

Nakar, E. and Sari, R. (2010). Early Supernovae Light Curves Following the Shock Breakout. ApJ, 725(1):904–921.

Nandez, J. L. A. and Ivanova, N. (2016). Common envelope events with low-mass giants: understanding the energy budget. MNRAS, 460(4):3992–4002.

Nandez, J. L. A., Ivanova, N., and Lombardi, J. C., J. (2014). V1309 Sco—Understanding a Merger. ApJ, 786(1):39.

Nataf, D. M., Gould, A., and Pinsonneault, M. H. (2012). Detached red giant eclipsing binary twins: Rosetta stones to the galactic bulge.

Nelemans, G., Yungelson, L. R., and Portegies Zwart, S. F. (2001). The gravitational wave signal from the Galactic disk population of binaries containing two compact objects. A&A, 375:890–898.

Newton, E. R., Irwin, J., Charbonneau, D., Berlind, P., Calkins, M. L., and Mink, J. (2017). The h-emission of nearby m dwarfs and its relation to stellar rotation. *The Astrophysical Journal*, 834(1):85.

Nicholl, M., Blanchard, P. K., Berger, E., Chornock, R., Margutti, R., Gomez, S., Lunnan, R., Miller, A. A., Fong, W.-f., Terreran, G., Vigna-Gómez, A., Bhirombhakdi, K., Bieryla, A., Challis, P., Laher, R. R., Masci, F. J., and Paterson, K. (2020). An extremely energetic supernova from a very massive star in a dense medium. *Nature Astronomy*, 4:893–899.

Nicholls, C. P., Melis, C., Soszynski, I., Udalski, A., Szymanski, M. K., Kubiak, M., Pietrzynski, G., Poleski, R., Ulaczyk, K., Wyrzykowski, L., Kozlowski, S., and Pietrukowicz, P. (2013). The dusty aftermath of the V1309 Sco binary merger. MNRAS, 431:L33–L37.

Nie, J. D., Wood, P. R., and Nicholls, C. P. (2017). The orbital nature of 81 ellipsoidal red giant binaries in the large magellanic cloud. *The Astrophysical Journal*, 835(2):209.

Nielsen, M. B., Gizon, L., Schunker, H., and Karoff, C. (2013). Rotation periods of 12 000 main-sequence Kepler stars: Dependence on stellar spectral type and comparison with v sin i observations. A&A, 557:L10.

Norton, A. J. (2018). A Zooniverse Project to Classify Periodic Variable Stars from SuperWASP. *Research Notes of the American Astronomical Society*, 2(4):216.

Norton, A. J., Lohr, M. E., Smalley, B., Wheatley, P. J., and West, R. G. (2016). SuperWASP discovery and SALT confirmation of a semi-detached eclipsing binary that contains a δ Scuti star. A&A, 587:A54.

Norton, A. J., Wheatley, P. J., West, R. G., Haswell, C. A., Street, R. A., Collier Cameron, A., Christian, D. J., Clarkson, W. I., Enoch, B., Gallaway, M., Hellier, C., Horne, K., Irwin, J., Kane, S. R., Lister, T. A., Nicholas, J. P., Parley, N., Pollacco, D., Ryans, R., Skillen, I., and Wilson, D. M. (2007). New periodic variable stars coincident with ROSAT sources discovered using SuperWASP. A&A, 467(2):785–905.

Noyes, R. W., Hartmann, L. W., Baliunas, S. L., Duncan, D. K., and Vaughan, A. H. (1984). Rotation, convection, and magnetic activity in lower main-sequence stars. *The Astrophysical Journal*, 279:763.

Ochsenbein, F., Bauer, P., and Marcout, J. (2000). The VizieR database of astronomical catalogues. A&AS, 143:23–32.

O'Connell, D. J. K. (1951). The so-called periastron effect in close eclipsing binaries ; New variable stars (fifth list). *Publications of the Riverview College Observatory*, 2(6):85–100.

Owocki, S. P., Castor, J. I., and Rybicki, G. B. (1988). Time-dependent models of radiatively driven stellar winds. I - Nonlinear evolution of instabilities for a pure absorption model. *apj*, 335:914–930.

Özdarcan, O., Carroll, T. A., Künstler, A., Strassmeier, K. G., Evren, S., Weber, M., and Granzer, T. (2016). Time-series Doppler imaging of the red giant HD 208472. Active longitudes and differential rotation. A&A, 593:A123.

Paczynski, B. (1976). Common Envelope Binaries. In Eggleton, P., Mitton, S., and Whelan, J., editors, *Structure and Evolution of Close Binary Systems*, volume 73, page 75.

Pallavicini, R., Golub, L., Rosner, R., Vaiana, G. S., Ayres, T., and Linsky, J. L. (1981). Relations among stellar x-ray emission observed from einstein, stellar rotation and bolometric luminosity. *The Astrophysical Journal*, 248:279.

Parker, E. (1955). Hydromagnetic Dynamo Models. *apj*, 122:293.

Parkin, E. R., Pittard, J. M., Hoare, M. G., Wright, N. J., and Drake, J. J. (2009). The interactions of winds from massive young stellar objects: X-ray emission, dynamics and cavity evolution. MNRAS, 400:629–645.

Pastorello, A., Della Valle, M., Smartt, S. J., Zampieri, L., Benetti, S., Cappellaro, E., Mazzali, P. A., Patat, F., Spiro, S., Turatto, M., and Valenti, S. (2007). A very faint core-collapse supernova in M85. Nature, 449(7164):1–2.

Pastorello, A., Fraser, M., Valerin, G., Reguitti, A., Itagaki, K., Ochner, P., Williams, S. C., Jones, D., Munday, J., Smartt, S. J., Smith, K. W., Srivastav, S., Elias-Rosa, N., Kankare, E., Karamehmetoglu, E., Lundqvist, P., Mazzali, P. A., Munari, U., Stritzinger, M. D., Tomasella, L., Anderson, J. P., Chambers, K. C., and Rest, A. (2021a). Forbidden hugs in pandemic times. I. Luminous red nova AT 2019zhd, a new merger in M 31. A&A, 646:A119.

Pastorello, A., Mason, E., Taubenberger, S., Fraser, M., Cortini, G., Tomasella, L., Botticella, M. T., Elias-Rosa, N., Kotak, R., Smartt, S. J., Benetti, S., Cappellaro, E., Turatto, M., Tartaglia, L., Djorgovski, S. G., Drake, A. J., Berton, M., Briganti, F., Brimacombe, J., Bufano, F., Cai, Y. Z., Chen, S., Christensen, E. J., Ciabattari, F., Congiu, E., Dimai, A., Inserra, C., Kankare, E., Magill, L., Maguire, K., Martinelli, F., Morales-Garoffolo, A., Ochner, P., Pignata, G., Reguitti, A., Sollerman, J., Spiro, S., Terreran, G., and Wright, D. E. (2019). Luminous red novae: Stellar mergers or giant eruptions? A&A, 630:A75.

Pastorello, A., Valerin, G., Fraser, M., Elias-Rosa, N., Valenti, S., Reguitti, A., Mazzali, P. A., Amaro, R. C., Andrews, J. E., Dong, Y., Jencson, J., Lundquist, M., Reichart, D. E., Sand, D. J., Wyatt, S., Smartt, S. J., Smith, K. W., Srivastav, S., Cai, Y. Z., Cappellaro, E., Holmbo, S., Fiore, A., Jones, D., Kankare, E., Karamehmetoglu, E., Lundqvist, P., Morales-Garoffolo, A., Reynolds, T. M., Stritzinger, M. D., Williams, S. C., Chambers, K. C., de Boer, T. J. L., Huber, M. E., Rest, A., and Wainscoat, R. (2021b). Forbidden hugs in pandemic times. II. The luminous red nova variety: AT 2020hat and AT 2020kog. A&A, 647:A93.

Paxton, B., Bildsten, L., Dotter, A., Herwig, F., Lesaffre, P., and Timmes, F. (2011). Modules for Experiments in Stellar Astrophysics (MESA). ApJS, 192(1):3.

Paxton, B., Marchant, P., Schwab, J., Bauer, E. B., Bildsten, L., Cantiello, M., Dessart, L., Farmer, R., Hu, H., Langer, N., Townsend, R. H. D., Townsley, D. M., and Timmes, F. X. (2015). Modules for Experiments in Stellar Astrophysics (MESA): Binaries, Pulsations, and Explosions. ApJS, 220(1):15.

Paxton, B., Schwab, J., Bauer, E. B., Bildsten, L., Blinnikov, S., Duffell, P., Farmer, R., Goldberg, J. A., Marchant, P., Sorokina, E., Thoul, A., Townsend, R. H. D., and Timmes, F. X. (2018). Modules for Experiments in Stellar Astrophysics (MESA): Convective Boundaries, Element Diffusion, and Massive Star Explosions. ApJS, 234(2):34.

Paxton, B., Smolec, R., Schwab, J., Gautschy, A., Bildsten, L., Cantiello, M., Dotter, A., Farmer, R., Goldberg, J. A., Jermyn, A. S., Kanbur, S. M., Marchant, P., Thoul, A., Townsend, R. H. D., Wolf, W. M., Zhang, M., and Timmes, F. X. (2019). Modules for Experiments in Stellar Astrophysics (MESA): Pulsating Variable Stars, Rotation, Convective Boundaries, and Energy Conservation. ApJS, 243(1):10.

Payne, S. G. (2013). The identification and classification of variability in stellar sources observed with superwasp. The Open University.

Pejcha, O. (2014). Burying a Binary: Dynamical Mass Loss and a Continuous Optically thick Outflow Explain the Candidate Stellar Merger V1309 Scorpii. ApJ, 788(1):22.

Percy, J. R. (2007). *Understanding Variable Stars*. Cambridge University Press.

Peres, G., Orlando, S., Reale, F., Rosner, R., and Hudson, H. (2000). The Sun as an X-Ray Star. II. Using theYohkoh/Soft X-Ray Telescope-derived Solar Emission Measure versus Temperature to Interpret Stellar X-Ray Observations. ApJ, 528(1):537–551.

Pietrukowicz, P., Soszyński, I., Udalski, A., Szymański, M. K., Wyrzykowski, Ł., Poleski, R., Kozłowski, S., Skowron, J., Mróz, P., Pawlak, M., and Ulaczyk, K. (2017). Searching for Potential Mergers among 22 500 Eclipsing Binary Stars in the OGLE-III Galactic Bulge Fields. Acta Astron., 67(2):115–130.

Pineda, J., Youngblood, A., and France, K. (2020). Far Ultraviolet M-dwarf Evolution Survey: Rotation-Activity-Age Correlations Across the High-Energy Spectrum. In *American Astronomical Society Meeting Abstracts #235*, volume 235 of *American Astronomical Society Meeting Abstracts*, page 273.18.

Pizzolato, N., Maggio, A., Micela, G., Sciortino, S., and Ventura, P. (2003). The stellar activity-rotation relationship revisited: Dependence of saturated and non-saturated x-ray emission regimes on stellar mass for late-type dwarfs. *Astronomy & Astrophysics*, 397(1):147–157.

Plez, B. (2012). Turbospectrum: Code for spectral synthesis.

Podsiadlowski, P. (2001). Common-Envelope Evolution and Stellar Mergers. In Podsiadlowski, P., Rappaport, S., King, A. R., D'Antona, F., and Burderi, L., editors, *Evolution of Binary and Multiple Star Systems*, volume 229 of *Astronomical Society of the Pacific Conference Series*, page 239.

Pojmanski, G. (2002). The All Sky Automated Survey. Catalog of Variable Stars. I. 0 h - 6 hQuarter of the Southern Hemisphere. Acta Astron., 52:397–427.

Pollacco, D. L., Skillen, I., Collier Cameron, A., Christian, D. J., Hellier, C., Irwin, J., Lister, T. A., Street, R. A., West, R. G., Anderson, D. R., Clarkson, W. I., Deeg, H., Enoch, B., Evans, A., Fitzsimmons, A., Haswell, C. A., Hodgkin, S., Horne, K., Kane, S. R., Keenan, F. P., Maxted, P. F. L., Norton, A. J., Osborne, J., Parley, N. R., Ryans, R. S. I., Smalley, B., Wheatley, P. J., and Wilson, D. M. (2006). The WASP Project and the SuperWASP Cameras. *pasp*, 118:1407–1418.

Poppenhaeger, K. (2018). How planets affect cool stars. In *20th Cambridge Workshop on Cool Stars, Stellar Systems and the Sun*, Cambridge Workshop on Cool Stars, Stellar Systems, and the Sun, page 34.

Porceddu, S., Jetsu, L., Markkanen, T., and Toivari-Viitala, J. (2008). Evidence of periodicity in ancient egyptian calendars of lucky and unlucky days. *Cambridge Archaeological Journal*, 18(3):327–339.

Powell, B. P., Kostov, V. B., Rappaport, S. A., Borkovits, T., Zasche, P., Tokovinin, A., Kruse, E., Latham, D. W., Montet, B. T., Jensen, E. L. N., and et al. (2021). Tic 168789840: A sextuply eclipsing sextuple star system. *The Astronomical Journal*, 161(4):162.

Prša, A. and Zwitter, T. (2005). A computational guide to physics of eclipsing binaries. i. demonstrations and perspectives. *The Astrophysical Journal*, 628(1):426–438.

Preibisch, T. and Feigelson, E. D. (2005). The evolution of x-ray emission in young stars. *The Astrophysical Journal Supplement Series*, 160(2):390–400.

Price-Whelan, A. M., Hogg, D. W., Rix, H.-W., Lee, N. D., Majewski, S. R., Nidever, D. L., Troup, N., Fernández-Trincado, J. G., García-Hernández, D. A., Longa-Peña, P., Nitschelm, C., Sobeck, J., and Zamora, O. (2018). Binary companions of evolved stars in APOGEE DR14: Search method and catalog of $\sim$5000 companions. *The Astronomical Journal*, 156(1):18.

Prieto, J. L., Sellgren, K., Thompson, T. A., and Kochanek, C. S. (2009). A Spitzer/IRS Spectrum of the 2008 Luminous Transient in NGC 300: Connection to Proto-Planetary Nebulae. *The Astrophysical Journal*, 705(2):1425–1432.

Raetz, S., Stelzer, B., and Scholz, A. (2020). The rotation-activity relation of M dwarfs: From K2 to TESS and PLATO. *Astronomische Nachrichten*, 341(5):519–556.

Randich, S. (1998). Supersaturation in X-ray Emission of Cluster Stars. In Donahue, R. A. and Bookbinder, J. A., editors, *Cool Stars, Stellar Systems, and the Sun*, volume 154 of *Astronomical Society of the Pacific Conference Series*, page 501.

Randich, S., Schmitt, J. H. M. M., Prosser, C. F., and Stauffer, J. R. (1996). The X-ray properties of the young open cluster around α Persei. *Astronomy & Astrophysics*, 305:785.

Rasio, F. A. (1995). The Minimum Mass Ratio of W Ursae Majoris Binaries. ApJ, 444:L41.

Rau, A., Kulkarni, S. R., Ofek, E. O., and Yan, L. (2007). Spitzer Observations of the New Luminous Red Nova M85 OT2006-1. ApJ, 659(2):1536–1540.

Rawls, M. L. (2016). *Red Giants in Eclipsing Binaries as a Benchmark for Asteroseismology*. PhD thesis, New Mexico State University.

Rawls, M. L., Gaulme, P., McKeever, J., Jackiewicz, J., Orosz, J. A., Corsaro, E., Beck, P. G., Mosser, B., Latham, D. W., and Latham, C. A. (2016). KIC 9246715: The Double Red Giant Eclipsing Binary with Odd Oscillations. ApJ, 818(2):108.

Reiners, A., Basri, G., and Browning, M. (2009). EVIDENCE FOR MAGNETIC FLUX SATURATION IN RAPIDLY ROTATING m STARS. *The Astrophysical Journal*, 692(1):538–545.

Reiners, A., Schüssler, M., and Passegger, V. M. (2014). Generalized investigation of the rotation-activity relation: Favouring rotation period instead of rossby number. *The Astrophysical Journal*, 794(2):144.

Reipurth, B. (1990). Fu-Orionis Eruptions and Early Stellar Evolution. In Mirzoian, L. V., Pettersen, B. R., and Tsvetkov, M. K., editors, *Flare Stars in Star Clusters, Associations and the Solar Vicinity*, volume 137, page 229.

Rich, R. M., Mould, J., Picard, A., Frogel, J. A., and Davies, R. (1988). Detection of Late Type Giants in the Nuclear Bulge of M31. In *Bulletin of the American Astronomical Society*, volume 20, page 1097.

Ridpath, I., editor (2018). *Star Tales*. Lutterworth Press.

Rivinius, T., Štefl, S., and Baade, D. (2006). Bright Be-shell stars. A&A, 459(1):137–145.

Roberts, D. H., Lehar, J., and Dreher, J. W. (1987). Time series analysis with CLEAN. I. Derivation of a spectrum. AJ, 93:968–989.

Rodgers, A. W. (1957). Radius Variation and Population Type of Cepheid Variables. *Monthly Notices of the Royal Astronomical Society*, 117(1):85–94.

Rosen, S. R., Webb, N. A., Watson, M. G., Ballet, J., Barret, D., Braito, V., Carrera, F. J., Ceballos, M. T., Coriat, M., Della Ceca, R., Denkinson, G., Esquej, P., Farrell, S. A., Freyberg, M., Gris'e, F., Guillout, P., Heil, L., Koliopanos, F., Law-Green, D., Lamer, G., Lin, D., Martino, R., Michel, L., Motch, C., Nebot Gomez-Moran, A., Page, C. G., Page, K., Page, M., Pakull, M. W., Pye, J., Read, A., Rodriguez, P., Sakano, M., Saxton, R., Schwope, A., Scott, A. E., Sturm, R., Traulsen, I., Yershov, V., and Zolotukhin, I. (2016). The XMM-Newton serendipitous survey. VII. The third XMM-Newton serendipitous source catalogue. *aap*, 590:A1.

Roulston, B. R., Green, P. J., and Kesseli, A. Y. (2020). Classifying single stars and spectroscopic binaries using optical stellar templates. *The Astrophysical Journal Supplement Series*, 249(2):34.

Rowden, P. M. (2019). *False Positives and Shallow Eclipsing Binaries in Transiting Exoplanet Surveys*. PhD thesis, The Open University.

Rucinski, S. M. (1992). Can Full Convection Explain the Observed Short-Period Limit of the W UMa-Type Binaries? AJ, 103:960.

Rucinski, S. M. (1998). Contact Binaries of the Galactic Disk: Comparison of the Baade's Window and Open Cluster Samples. AJ, 116(6):2998–3017.

Rucinski, S. M. (2006). Luminosity function of contact binaries based on the All Sky Automated Survey (ASAS). MNRAS, 368(3):1319–1322.

Rudy, R. J., Lynch, D. K., Russell, R. W., Sitko, M., Woodward, C. E., and Aspin, C. (2008). V1309 Scorpii. IAU Circ., 8997:2.

Rueda, J., Ruffini, R., Wang, Y., Bianco, C., Blanco-Iglesias, J., Karlica, M., Lorén-Aguilar, P., Moradi, R., and Sahakyan, N. (2019). Electromagnetic emission of white dwarf binary mergers. *Journal of Cosmology and Astroparticle Physics*, 2019(03):044–044.

Ryan, S. G. and Norton, A. J. (2010a). *Stellar Evolution and Nucleosynthesis*. Cambridge University Press, Cambridge. Course reader for Open University course S382 Astrophysics.

Ryan, S. G. and Norton, A. J. (2010b). *Stellar Evolution and Nucleosynthesis*. Cambridge University Press, Cambridge. Course reader for Open University course S382 Astrophysics.

Saad, S., Hamdy, M., and Abolazm, M. (2012). An overview investigation of be/shell stars. *NRIAG Journal of Astronomy and Geophysics*, 1(2):97–105.

Samec, R., Caton, D., Robb, R., and Faulkner, D. R. (2018). V1187 Herculis, the Most Extreme Mass Ratio Solar-type Binary Known. *Research Notes of the American Astronomical Society*, 2(1):13.

Samus, N. N., Kazarovets, E. V., Durlevich, O. V., Kireeva, N. N., and Pastukhova, E. N. (2017). General catalogue of variable stars: Version GCVS 5.1. *Astronomy Reports*, 61:80–88.

Sana, H., de Mink, S. E., de Koter, A., Langer, N., Evans, C. J., Gieles, M., Gosset, E., Izzard, R. G., Le Bouquin, J. B., and Schneider, F. R. N. (2012). Binary Interaction Dominates the Evolution of Massive Stars. *Science*, 337(6093):444.

Sánchez-Blázquez, P., Peletier, R. F., Jiménez-Vicente, J., Cardiel, N., Cenarro, A. J., Falcón-Barroso, J., Gorgas, J., Selam, S., and Vazdekis, A. (2006). Medium-resolution Isaac Newton Telescope library of empirical spectra. MNRAS, 371(2):703–718.

Sarotsakulchai, T., Qian, S. B., Soonthornthum, B., Zhou, X., Zhang, J., Reichart, D. E., Haislip, J. B., Kouprianov, V. V., and Poshyachinda, S. (2018). TY Pup: A Low-mass-ratio and Deep Contact Binary as a Progenitor Candidate of Luminous Red Novae. AJ, 156(5):199.

Schrijver, C. J. and Zwaan, C. (2000). *Solar and Stellar Magnetic Activity*.

Shappee, B. J., Prieto, J. L., Grupe, D., Kochanek, C. S., Stanek, K. Z., De Rosa, G., Mathur, S., Zu, Y., Peterson, B. M., Pogge, R. W., Komossa, S., Im, M., Jencson, J., Holoien, T. W. S., Basu, U., Beacom, J. F., Szczygieł, D. M., Brimacombe, J., Adams, S., Campillay, A., Choi, C., Contreras, C., Dietrich, M., Dubberley, M., Elphick, M., Foale, S., Giustini, M., Gonzalez, C., Hawkins, E., Howell, D. A., Hsiao, E. Y., Koss, M., Leighly, K. M., Morrell, N., Mudd, D., Mullins, D., Nugent, J. M., Parrent, J., Phillips, M. M., Pojmanski, G., Rosing, W., Ross, R., Sand, D., Terndrup, D. M., Valenti, S., Walker, Z., and Yoon, Y. (2014). The Man behind the Curtain: X-Rays Drive the UV through NIR Variability in the 2013 Active Galactic Nucleus Outburst in NGC 2617. ApJ, 788(1):48.

Shara, M. M., Moffat, A. F. J., and Webbink, R. F. (1985). Unraveling the oldest and faintest recovered nova : CK Vulpeculae (1670). ApJ, 294:271–285.

Shu, F. H., Lubow, S. H., and Anderson, L. (1979). On the structure of contact binaries. III. Mass and energy flow. ApJ, 229:223–241.

Silaj, J., Jones, C. E., Sigut, T. A. A., and Tycner, C. (2014). The h Profile of be Shell Stars. *The Astrophysical Journal*, 795(1):82.

Siverd, R., Brown, T., Henderson, T., Hygelund, J., Barnes, S., de Vera, J., Eastman, J., Kirby, A., Smith, C., Taylor, B., Tufts, J., and van Eyken, J. (2018). NRES: The Network of Robotic Echelle Spectrographs. In *American Astronomical Society Meeting Abstracts #231*, volume 231 of *American Astronomical Society Meeting Abstracts*, page 152.24.

Skrutskie, M. F., Cutri, R. M., Stiening, R., Weinberg, M. D., Schneider, S., Carpenter, J. M., Beichman, C., Capps, R., Chester, T., Elias, J., Huchra, J., Liebert, J., Lonsdale, C., Monet, D. G., Price, S., Seitzer, P., Jarrett, T., Kirkpatrick, J. D., Gizis, J. E., Howard, E., Evans, T., Fowler, J., Fullmer, L., Hurt, R., Light, R., Kopan, E. L., Marsh, K. A., McCallon, H. L., Tam, R., Van Dyk, S., and Wheelock, S. (2006). The Two Micron All Sky Survey (2MASS). AJ, 131(2):1163–1183.

Skumanich, A. (1972). Time Scales for CA II Emission Decay, Rotational Braking, and Lithium Depletion. *apj*, 171:565.

Slettebak, A. (1982). Spectral types and rotational velocities of the brighter Be stars and A-F type shell stars. ApJS, 50:55–83.

Smart, P. K. . T., editor (1986). *Short Guide to Modern Star Names and Their Derivations*. Otto Harrassowitz.

Smith, K. W., Williams, R. D., Young, D. R., Ibsen, A., Smartt, S. J., Lawrence, A., Morris, D., Voutsinas, S., and Nicholl, M. (2019). Lasair: The Transient Alert Broker for LSST:UK. *Research Notes of the American Astronomical Society*, 3(1):26.

Smith, N., Andrews, J. E., Van Dyk, S. D., Mauerhan, J. C., Kasliwal, M. M., Bond, H. E., Filippenko, A. V., Clubb, K. I., Graham, M. L., Perley, D. A., Jencson, J., Bally, J., Ubeda, L., and Sabbi, E. (2016). Massive star mergers and the recent transient in NGC 4490: a more massive cousin of V838 Mon and V1309 Sco. MNRAS, 458(1):950–962.

Sneden, C., Bean, J., Ivans, I., Lucatello, S., and Sobeck, J. (2012). MOOG: LTE line analysis and spectrum synthesis.

Socia, Q. J., Welsh, W. F., Short, D. R., Orosz, J. A., Angione, R. J., Windmiller, G., Caldwell, D. A., and Batalha, N. M. (2018). KIC 9832227: Using Vulcan Data to Negate the 2022 Red Nova Merger Prediction. ApJ, 864(2):L32.

Soderblom, D. R., Stauffer, J. R., Hudon, J. D., and Jones, B. F. (1993). Rotation and chromospheric emission among f, g, and k dwarfs of the pleiades. *The Astrophysical Journal Supplement Series*, 85:315.

Soker, N. and Tylenda, R. (2003). Main-Sequence Stellar Eruption Model for V838 Monocerotis. ApJ, 582(2):L105–L108.

Sokolovsky, K. V. and Lebedev, A. A. (2017). Vast: a variability search toolkit.

Sokolovsky, K. V. and Lebedev, A. A. (2018). VaST: A variability search toolkit. *Astronomy and Computing*, 22:28–47.

Solanki, S., editor (2018). *Living Reviews in Solar Physics*. Springer.

Soszynski, I., Udalski, A., Kubiak, M., Szymanski, M., Pietrzynski, G., Zebrun, K., Szewczyk, O., Wyrzykowski, L., and Dziembowski, W. (2005). The optical gravitational lensing experiment. ellipsoidal variability of red giants in the large magellanic cloud. *Acta Astronomica -Warsaw and Cracow-*, 54.

Soszynski, I., Udalski, A., Kubiak, M., Szymanski, M. K., Pietrzynski, G., Zebrun, K., Szewczyk, O., Wyrzykowski, L., and Dziembowski, W. A. (2004). The Optical Gravitational Lensing Experiment. Ellipsoidal Variability of Red Giants in the Large Magellanic Cloud. Acta Astron., 54:347–362.

Soszyński, I., Udalski, A., Szymański, M. K., Kubiak, M., Pietrzyński, G., Wyrzykowski, Ł., Szewczyk, O., Ulaczyk, K., and Poleski, R. (2009). The Optical Gravitational Lensing Experiment. The OGLE-III Catalog of Variable Stars. IV. Long-Period Variables in the Large Magellanic Cloud. Acta Astron., 59(3):239–253.

Spada, F., Demarque, P., Kim, Y.-C., and Sills, A. (2013). The Radius Discrepancy in Low-mass Stars: Single versus Binaries. *apj*, 776:87.

Spiegel, E. and Zahn, J.-P. (1992). The solar tachocline. *aap*, 265:106–114.

Spiers, H., Swanson, A., Fortson, L., Simmons, B., Trouille, L., Blickhan, S., and Lintott, C. (2019). Population synthesis of wide binary millisecond pulsars. *Journal of Science Communication*, 18.

Staab, D. (2018). Enshrouded exoplanetary systems.

Stępień, K. (2011). Evolution of the progenitor binary of V1309 Scorpii before merger. A&A, 531:A18.

Stępień, K., Schmitt, J. H. M. M., and Voges, W. (2001). ROSAT all-sky survey of W Ursae Majoris stars and the problem of supersaturation. A&A, 370:157–169.

Steele, I. A., Smith, R. J., Rees, P. C., Baker, I. P., Bates, S. D., Bode, M. F., Bowman, M. K., Carter, D., Etherton, J., Ford, M. J., Fraser, S. N., Gomboc, A., Lett, R. D. J., Mansfield, A. G., Marchant, J. M., Medrano-Cerda, G. A., Mottram, C. J., Raback, D., Scott, A. B., Tomlinson, M. D., and Zamanov, R. (2004). The Liverpool Telescope: performance and first results. In Oschmann, Jacobus M., J., editor, *Ground-based Telescopes*, volume 5489 of *Society of Photo-Optical Instrumentation Engineers (SPIE) Conference Series*, pages 679–692.

Stelzer, B., Damasso, M., Scholz, A., and Matt, S. P. (2016). A path towards understanding the rotation-activity relation of M dwarfs with K2 mission, X-ray and UV data. MNRAS, 463(2):1844–1864.

Stepien, K. (1994). Applicability of the Rossby number in activity-rotation relations for dwarfs and giants. *Astronomy & Astrophysics*, 292:191–207.

Stepien, K. (1995). Loss of angular momentum of cool close binaries and formation of contact systems. MNRAS, 274(4):1019–1028.

Sterken, C. (2005). The O-C Diagram: Basic Procedures. In Sterken, C., editor, *The Light-Time Effect in Astrophysics: Causes and cures of the O-C diagram*, volume 335 of *Astronomical Society of the Pacific Conference Series*, page 3.

Sterken, C. and Jaschek, C. (1996). *Light Curves of Variable Stars, A Pictorial Atlas*.

Strassmeier, K. G., Kratzwald, L., and Weber, M. (2003). Doppler imaging of stellar surface structure. XX. The rapidly-rotating single K2-giant HD 31993 = V1192 Orionis. A&A, 408:1103–1113.

Stritzinger, M. D., Taddia, F., Fraser, M., Tauris, T. M., Contreras, C., Drybye, S., Galbany, L., Holmbo, S., Morrell, N., Pastorello, A., Phillips, M. M., Pignata, G., Tartaglia, L., Suntzeff, N. B., Anais, J., Ashall, C., Baron, E., Burns, C. R., Hoeflich, P., Hsiao, E. Y., Karamehmetoglu, E., Moriya, T. J., Bock, G., Campillay, A., Castellón, S., Inserra, C., González, C., Marples, P., Parker, S., Reichart, D., Torres-Robledo, S., and Young, D. R. (2020). The Carnegie Supernova Project II. Observations of the luminous red nova AT 2014ej. A&A, 639:A104.

Struve, O. (1931). On the Origin of Bright Lines in Spectra of Stars of Class B. ApJ, 73:94.

Sybilski, P. W., Pawłaszek, R., Kozłowski, S. K., Konacki, M., Ratajczak, M., and Hełminiak, K. G. (2014). Software for autonomous astronomical observatories: challenges and opportunities in the age of big data. In Chiozzi, G. and Radziwill, N. M., editors, *Software and Cyberinfrastructure for Astronomy III*, volume 9152 of *Society of Photo-Optical Instrumentation Engineers (SPIE) Conference Series*, page 91521C.

Szczygieł, D. M., Socrates, A., Paczyński, B., Pojmański, G., and Pilecki, B. (2008). Coronal Activity from the ASAS Eclipsing Binaries. Acta Astron., 58:405.

Szymanski, M. K. (2005). The Optical Gravitational Lensing Experiment. Internet Access to the OGLE Photometry Data Set: OGLE-II BVI maps and I-band data. Acta Astron., 55:43–57.

Tauris, T. M. and van den Heuvel, E. P. J. (2006). *Formation and evolution of compact stellar X-ray sources*, page 623–666. Cambridge Astrophysics. Cambridge University Press.

Terrell, D. (2001). Eclipsing Binary Stars: Past, Present, and Future. *Journal of the American Association of Variable Star Observers (JAAVSO)*, 30(1):1.

Testa, P. (2010). X-ray emission processes in stars and their immediate environment. *Proceedings of the National Academy of Science*, 107:7158–7163.

Testa, P., Saar, S. H., and Drake, J. J. (2015). Stellar activity and coronal heating: an overview of recent results. *Philosophical Transactions of the Royal Society A: Mathematical, Physical and Engineering Sciences*, 373(2042):20140259–20140259.

Thiemann, H. B., Norton, A. J., Dickinson, H. J., McMaster, A., and Kolb, U. C. (2021). SuperWASP variable stars: classifying light curves using citizen science. MNRAS, 502(1):1299–1311.

Thiemann, H. B., Norton, A. J., and Kolb, U. C. (2020). The stellar rotation-activity relation for a sample of SuperWASP and ASAS-SN field stars. PASA, 37:e042.

Thompson, T. A., Prieto, J. L., Stanek, K. Z., Kistler, M. D., Beacom, J. F., and Kochanek, C. S. (2009). A New Class of Luminous Transients and a First Census of their Massive Stellar Progenitors. ApJ, 705(2):1364–1384.

Tody, D. (1986). The IRAF Data Reduction and Analysis System. In Crawford, D. L., editor, *Instrumentation in astronomy VI*, volume 627 of *Society of Photo-Optical Instrumentation Engineers (SPIE) Conference Series*, page 733.

Tonry, J. and Davis, M. (1979). A survey of galaxy redshifts. I. Data reduction techniques. AJ, 84:1511–1525.

Toonen, S. (2014). The progenitors of supernovae Type Ia. In de Grijs, R., editor, *Binary Systems, their Evolution and Environments*, page 26.

Tylenda, R., Górny, S. K., Kamiński, T., and Schmidt, M. (2015). VLT/UVES spectroscopy of V4332 Sagittarii in 2005: The best view on a decade-old stellar-merger remnant. A&A, 578:A75.

Tylenda, R., Hajduk, M., Kamiński, T., Udalski, A., Soszyński, I., Szymański, M. K., Kubiak, M., Pietrzyński, G., Poleski, R., Wyrzykowski, Ł., and Ulaczyk, K. (2011). V1309 Scorpii: merger of a contact binary. A&A, 528:A114.

Tylenda, R. and Kamiński, T. (2016). Evolution of the stellar-merger red nova V1309 Scorpii: Spectral energy distribution analysis. A&A, 592:A134.

Tylenda, R., Kamiński, T., and Mehner, A. (2019). Elemental abundances in the remnant of the ancient eruption of CK Vulpeculae. A&A, 628:A124.

Tylenda, R., Kamiński, T., Udalski, A., Soszyński, I., Poleski, R., Szymański, M. K., Kubiak, M., Pietrzyński, G., Kozłowski, S., Pietrukowicz, P., Ulaczyk, K., and Wyrzykowski, Ł. (2013). OGLE-2002-BLG-360: from a gravitational microlensing candidate to an overlooked red transient. A&A, 555:A16.

Tylenda, R. and Soker, N. (2006). Eruptions of the V838 Mon type: stellar merger versus nuclear outburst models. A&A, 451(1):223–236.

Tylenda, R., Soker, N., and Szczerba, R. (2005). On the progenitor of V838 Monocerotis. A&A, 441(3):1099–1109.

Udalski, A. (2003a). The Optical Gravitational Lensing Experiment. Real Time Data Analysis Systems in the OGLE-III Survey. Acta Astron., 53:291–305.

Udalski, A. (2003b). The Optical Gravitational Lensing Experiment. Real Time Data Analysis Systems in the OGLE-III Survey. Acta Astron., 53:291–305.

Vaiana, G., Cassinelli, J., Fabbiano, G., Giacconi, R., Golub, L., Gorenstein, P., Haisch, B., Harnden, Jr., F., Johnson, H., Linsky, J., Maxson, C., Mewe, R., Rosner, R., Seward, F., Topka, K., and Zwaan, C. (1981). Results from an extensive Einstein stellar survey. *apj*, 245:163–182.

Valenti, J. A. and Piskunov, N. (2012). SME: Spectroscopy Made Easy.

van Dokkum, P. G. (2001). Cosmic-Ray Rejection by Laplacian Edge Detection. PASP, 113(789):1420–1427.

Van Dyk, S. D., Peng, C. Y., King, J. Y., Filippenko, A. V., Treffers, R. R., Li, W., and Richmond, M. W. (2000). SN 1997bs in M66: Another Extragalactic η Carinae Analog? PASP, 112(778):1532–1541.

van Saders, J. L., Ceillier, T., Metcalfe, T. S., Silva Aguirre, V., Pinsonneault, M. H., García, R. A., Mathur, S., and Davies, G. R. (2016). Weakened magnetic braking as the origin of anomalously rapid rotation in old field stars. Nature, 529(7585):181–184.

Vidotto, A. A. (2017). Stellar Coronal and Wind Models: Impact on Exoplanets. *ArXiv e-prints*.

Vidotto, A. A., Gregory, S. G., Jardine, M., Donati, J. F., Petit, P., Morin, J., Folsom, C. P., Bouvier, J., Cameron, A. C., Hussain, G., Marsden, S., Waite, I. A., Fares, R., Jeffers, S., and do Nascimento, J. D. (2014). Stellar magnetism: empirical trends with age and rotation. *Monthly Notices of the Royal Astronomical Society*, 441(3):2361–2374.

Vilhu, O. (1984). The nature of magnetic activity in lower main sequence stars. *Astronomy & Astrophysics*, 133:117–126.

Wadhwa, S. S., De Horta, A., Filipović, M. D., Tothill, N. F. H., Arbutina, B., Petrović, J., and Djurašević, G. (2021). ZZ Piscis Austrinus (ZZ PsA): a bright red nova progenitor and the instability mass ratio of contact binary stars. MNRAS, 501(1):229–235.

Wagner, R. M., Starrfield, S. G., Wilber, A., Kochanek, C. S., Dong, S., Prieto, J. L., and Adams, S. (2015). The Probable M31 Stellar Merger Now Has a Late K or Early M Spectrum. *The Astronomer's Telegram*, 7208:1.

Walter, F. M. and Bowyer, S. (1981). On the coronae of rapidly rotating stars. i - the relation between rotation and coronal activity in RS CVn systems. *The Astrophysical Journal*, 245:671.

Warner, B. (2003). *Cataclysmic Variable Stars*.

Watson, C., Henden, A. A., and Price, A. (2020). VizieR Online Data Catalog: AAVSO International Variable Star Index VSX (Watson+, 2006-2014). *VizieR Online Data Catalog*, page B/vsx.

Wegner, W. (1994). Intrinsic colour indices of OB supergiants, giants and dwarfs in the UBVRIJHKLM system. MNRAS, 270:229–234.

Weiss, N. O. (2005). Linear and nonlinear dynamos. *Astronomische Nachrichten*, 326:157–165.

West, A. A., Weisenburger, K. L., Irwin, J., Berta-Thompson, Z. K., Charbonneau, D., Dittmann, J., and Pineda, J. S. (2015). An activity-rotation relationship and kinematic analysis of nearby mid-to-late-type m dwarfs. *The Astrophysical Journal*, 812(1):3.

Wilk, S. R. (1996). Mythological Evidence for Ancient Observations of Variable Stars. *Journal of the American Association of Variable Star Observers (JAAVSO)*, 24(2):129–133.

Willems, B. and Kolb, U. (2002). Population synthesis of wide binary millisecond pulsars. MNRAS, 337(3):1004–1016.

Willems, B. and Kolb, U. (2004). Detached white dwarf main-sequence star binaries. A&A, 419:1057–1076.

Willems, B., Kolb, U., and Justham, S. (2006). Eclipsing binaries in extrasolar planet transit surveys: the case of SuperWASP. MNRAS, 367(3):1103–1112.

Willems, B., Kolb, U., Sandquist, E. L., Taam, R. E., and Dubus, G. (2005). Angular Momentum Losses and the Orbital Period Distribution of Cataclysmic Variables below the Period Gap: Effects of Circumbinary Disks. ApJ, 635(2):1263–1280.

Willems, B., Mundin, R. P., and Kolb, U. (2002). BiSEPS: A new binary population synthesis code. In Gänsicke, B. T., Beuermann, K., and Reinsch, K., editors, *The Physics of Cataclysmic Variables and Related Objects*, volume 261 of *Astronomical Society of the Pacific Conference Series*, page 303.

Williams, S. C., Darnley, M. J., Bode, M. F., and Steele, I. A. (2015). A luminous red nova in m31 and its progenitor system. *The Astrophysical Journal*, 805(2):L18.

Wilson, O. C. (1966). Stellar convection zones, chromospheres, and rotation. *The Astrophysical Journal*, 144:695.

Wilson, R. E. and Devinney, E. J. (1971). Realization of Accurate Close-Binary Light Curves: Application to MR Cygni. ApJ, 166:605.

Wood, P. R. (2000). Variable red giants in the lmc: Pulsating stars and binaries? *Publications of the Astronomical Society of Australia*, 17(1):18–21.

Wood, P. R. (2007). Variable Red Giant Stars. In Kang, Y. W., Lee, H. W., Leung, K. C., and Cheng, K. S., editors, *The Seventh Pacific Rim Conference on Stellar Astrophysics*, volume 362 of *Astronomical Society of the Pacific Conference Series*, page 234.

Wood, P. R., Alcock, C., Allsman, R. A., Alves, D., Axelrod, T. S., Becker, A. C., Bennett, D. P., Cook, K. H., Drake, A. J., Freeman, K. C., Griest, K., King, L. J., Lehner, M. J., Marshall, S. L., Minniti, D., Peterson, B. A., Pratt, M. R., Quinn, P. J., Stubbs, C. W., Sutherland, W., Tomaney, A., Vandehei, T., and Welch, D. L. (1999). MACHO observations of LMC red giants: Mira and semi-regular pulsators, and contact and semi-detached binaries. In Le Bertre, T., Lebre, A., and Waelkens, C., editors, *Asymptotic Giant Branch Stars*, volume 191, page 151.

Wozniak, P. R., Vestrand, W. T., McGowan, K. E., Kinemuchi, K., and ROTSE Collaboration (2003). Northern Sky Variability Survey (NSVS). In *American Astronomical Society Meeting Abstracts*, volume 203 of *American Astronomical Society Meeting Abstracts*, page 57.03.

Wright, N. J. and Drake, J. J. (2016). Solar-type dynamo behaviour in fully convective stars without a tachocline. *Nature*, 535(7613):526–528.

Wright, N. J., Drake, J. J., Mamajek, E. E., and Henry, G. W. (2011). The stellar activity-rotation relationship and the evolution of stellar dynamos. *The Astrophysical Journal*, 743(1):48.

Wright, N. J., Newton, E. R., Williams, P. K. G., Drake, J. J., and Yadav, R. K. (2018). The stellar rotation-activity relationship in fully convective M dwarfs. MNRAS, 479:2351–2360.

Yungel'Son, L. R. (1973). Evolution of a Close Binary with Mass Loss from the System. Soviet Ast., 16:864.

Zacharias, N., Monet, D. G., Levine, S. E., Urban, S. E., Gaume, R., and Wycoff, G. L. (2004). The Naval Observatory Merged Astrometric Dataset (NOMAD). In *American Astronomical Society Meeting Abstracts*, volume 205 of *American Astronomical Society Meeting Abstracts*, page 48.15.

Appendix A

The full catalogue of the rotation-activity relation

This appendix contains the full catalogues of X-ray visible unique objects displaying rotational modulation in their photometric variability, first SuperWASP, then ASAS-SN.

Table A.1 G- to M-type SuperWASP objects from the full catalogue containing 900 X-ray visible unique objects displaying rotational modulation in their photometric variability.

XMM ID	WASP ID	SpT	Period [d]	V [mag]	V-K	Distance [pc]	F_x [10^{-14}] [erg/cm^2/s]	log Ro	log R_x			
4XMM J023732.1-522331	1SWASPJ023732.16-522332.5	K5V	14.51	0.13	46.08	4.32E+29	4.08E+28	2.90	5.42E-03	2.71E-04	2.43E-04	2.34E-05
4XMM J122942.4+015524	1SWASPJ122942.46+015525.0	K0V	12.78	2.22	66.59	7.36E+30	6.05E+28	1.95	1.66E-01	8.28E-03	7.59E-04	3.82E-05
4XMM J213531.0-011254	1SWASPJ213530.98-011254.0	K2V	10.07	9.84	6.22	3.11E+28	4.47E+27	2.20	6.35E-01	3.17E-02	2.23E-05	3.21E-06
4XMM J053929.3-695710	1SWASPJ053929.31-695710.8	G3V	11.13	18.53	54.77	1.80E+30	7.24E+28	1.52	1.77E+00	8.87E-02	5.48E-05	2.66E-06
4XMM J045217.7-421428	1SWASPJ045217.73-421428.7	G8V	10.87	12.62	12.21	7.37E+28	6.91E+27	1.77	1.04E+00	5.21E-02	3.52E-05	3.31E-06
4XMM J092834.3-060345	1SWASPJ092834.32-060345.8	G2V	13.45	0.16	67.26	2.64E+30	4.81E+28	1.46	1.57E-02	7.87E-04	5.57E-04	2.28E-05
4XMM J153158.9+324825	1SWASPJ153158.99+324825.8	K8V	13.55	2.21	17.72	1.05E+30	2.40E+28	3.43	7.02E-02	3.51E-03	1.16E-03	2.83E-05
4XMM J055902.8-382450	1SWASPJ055902.84-382451.8	G3V	10.59	3.54	14.44	2.00E+29	5.43E+27	1.49	3.43E-01	1.71E-02	5.39E-05	1.50E-06
4XMM J190222.1-365540	1SWASPJ190222.21-365540.5	M1V	13.93	4.09	15.36	7.80E+29	8.80E+27	3.96	9.59E-02	4.80E-03	1.25E-03	1.92E-05
4XMM J043558.9+223835	1SWASPJ043558.93+223835.1	M2V	12.03	1.93	15.82	1.98E+30	2.38E+28	4.28	3.76E-02	1.88E-03	3.92E-04	7.25E-06
4XMM J032807.4-311826	1SWASPJ032807.62-311826.7	K3.5V	10.78	21.14	5.27	4.77E+28	6.14E+27	2.61	1.08E+00	5.41E-02	7.93E-05	1.02E-05
4XMM J170320.6+454059	1SWASPJ170320.62+454059.5	G2V	10.15	5.61	11.02	9.84E+28	5.17E+27	1.46	5.55E-01	2.77E-02	2.93E-05	1.55E-06
4XMM J152242.5-381815	1SWASPJ152242.51-381813.6	K0V	12.83	0.14	35.46	7.78E+29	2.34E+28	1.92	1.07E-02	5.36E-04	2.39E-04	9.54E-06
4XMM J034403.5+243015	1SWASPJ034403.55+243015.2	K0.5V	10.93	1.48	13.50	1.99E+30	1.58E+28	1.98	1.08E-01	5.42E-03	7.08E-04	1.18E-05
4XMM J003823.9+401250	1SWASPJ003823.99+401250.2	K2V	12.40	4.66	92.82	2.37E+31	2.57E+29	2.15	3.10E-01	1.55E-02	8.16E-04	8.94E-05
4XMM J053406.8+100100	1SWASPJ053406.87+100101.0	K1.5V	11.67	3.74	39.93	5.65E+30	1.09E+29	2.10	2.56E-01	1.28E-02	5.06E-04	1.94E-05
4XMM J082253.0+160755	1SWASPJ082253.08+160755.4	K0.5V	13.23	0.58	33.74	2.26E+30	1.00E+29	1.97	4.26E-02	2.13E-03	1.20E-03	6.10E-05
4XMM J193216.6-264022	1SWASPJ193216.59-264022.7	K1.5V	12.19	0.16	31.85	9.77E+29	3.40E+28	2.11	1.08E-02	5.39E-04	2.16E-04	8.82E-06
4XMM J053936.5-024216	1SWASPJ053936.54-024217.2	K2V	9.99	12.50	35.58	5.65E+30	1.57E+29	2.17	8.21E-01	4.11E-02	1.50E-04	1.36E-05
4XMM J021442.0-061635	1SWASPJ021442.07-061635.7	K3V	12.48	18.97	56.72	7.57E+30	2.31E+29	2.44	1.07E+00	5.33E-02	7.25E-04	3.99E-05
4XMM J053044.9-044411	1SWASPJ053044.90-044411.5	K6.5V	12.52	3.76	12.88	3.88E+29	4.92E+27	3.31	1.28E-01	6.42E-03	3.60E-04	6.42E-06
4XMM J051653.8-682108	1SWASPJ051653.77-682109.1	K6.5V	11.91	16.82	4.53	7.34E+27	3.26E+26	3.25	5.92E-01	2.96E-02	3.02E-05	1.35E-06
4XMM J144502.4+020203	1SWASPJ144502.54+020204.3	K3V	13.87	0.13	36.98	4.71E+29	9.18E+27	2.43	7.54E-03	3.77E-04	3.23E-04	8.93E-06
4XMM J205815.2+170843	1SWASPJ205815.27+170844.2	M1V	13.31	0.14	13.12	7.57E+29	1.06E+28	4.04	3.23E-03	1.62E-04	8.53E-04	1.87E-05
4XMM J063117.5-282407	1SWASPJ063117.64-282408.7	K5.5V	14.18	0.66	31.89	8.54E+29	5.91E+28	3.01	2.67E-02	1.34E-03	7.67E-04	5.39E-05
4XMM J051121.3+042524	1SWASPJ051121.27+042523.8	G7V	12.80	0.67	40.04	2.61E+30	1.21E+29	1.71	5.75E-02	2.88E-03	8.89E-04	5.24E-05
4XMM J104916.9-395939	1SWASPJ104916.86-395939.8	G7V	13.94	3.70	138.85	2.20E+31	1.09E+30	1.69	3.21E-01	1.61E-02	1.69E-03	1.16E-04
4XMM J054709.0-701702	1SWASPJ054711.62-701832.3	K5V	15.44	3.88	273.23	1.21E+31	9.76E+29	-0.18	9.85E-01	4.93E-02	4.71E-04	3.94E-04
4XMM J222918.1+203454	1SWASPJ222918.12+203455.2	K2.5V	12.90	4.12	39.86	1.00E+30	5.88E+28	2.30	2.51E-01	1.26E-02	3.19E-04	1.98E-05
4XMM J163211.6-244021	1SWASPJ163211.81-244021.8	M4.5V	13.47	1.56	13.82	1.78E+30	2.89E+28	5.68	1.36E-02	6.78E-04	4.86E-04	5.37E-05
4XMM J054232.2-083850	1SWASPJ054232.23-083850.3	K8V	12.59	0.24	10.96	2.31E+29	4.29E+27	3.42	7.79E-03	3.89E-04	2.84E-04	5.66E-06
4XMM J054143.7-680915	1SWASPJ054143.75-680913.1	G7V	12.92	0.55	126.57	2.75E+30	3.26E+29	1.70	4.77E-02	2.39E-03	7.84E-05	1.03E-05
4XMM J223238.7-201149	1SWASPJ223238.51-201147.9	G8V	13.93	0.13	36.33	3.54E+29	4.31E+28	1.74	1.13E-02	5.63E-04	3.26E-04	1.28E-04
4XMM J161302.7-225745	1SWASPJ161302.72-225745.9	K6.5V	11.42	2.10	13.96	2.83E+30	3.70E+28	3.27	7.36E-02	3.68E-03	8.09E-04	1.53E-05
4XMM J075821.1+373314	1SWASPJ075820.93+373315.3	G9V	12.65	0.17	42.76	1.03E+30	1.14E+29	1.86	1.33E-02	6.63E-04	1.90E-04	5.01E-05
4XMM J023507.6+034357	1SWASPJ023507.59+034356.7	K1.5V	12.38	4.23	7.88	2.95E+28	2.16E+27	2.10	2.90E-01	1.45E-02	1.19E-04	8.80E-06
4XMM J064147.7+093409	1SWASPJ064147.80+093409.7	K4.5V	14.66	16.69	71.32	1.79E+30	1.34E+29	2.85	7.42E-01	3.71E-02	6.49E-04	5.57E-05
4XMM J164051.8+464105	1SWASPJ164051.86+464105.4	K4V	12.99	1.79	27.49	1.70E+30	4.92E+28	2.68	8.74E-02	4.37E-03	7.80E-04	5.81E-04
4XMM J001321.2+054505	1SWASPJ001321.26+054505.8	G8V	11.63	13.39	62.56	1.02E+30	6.81E+28	1.73	1.13E+00	5.67E-02	6.18E-05	5.79E-06
4XMM J022413.5+274136	1SWASPJ022413.54+274136.1	K2.5V	11.72	0.16	32.26	1.24E+30	1.59E+29	2.28	9.61E-03	4.81E-04	1.75E-04	3.96E-05
4XMM J054048.0-080557	1SWASPJ054048.18-080559.0	K6.5V	12.18	1.87	9.83	3.03E+29	9.14E+27	3.27	6.53E-02	3.27E-03	3.49E-04	7.10E-05
4XMM J071752.4-595031	1SWASPJ071752.40-595031.7	K3V	12.49	4.51	46.25	7.36E+30	3.77E+29	2.44	2.53E-01	1.26E-02	8.24E-04	4.43E-05
4XMM J153954.3-243913	1SWASPJ153954.23-243911.2	K3.5V	12.35	9.74	54.45	8.80E+30	8.20E+29	2.53	5.21E-01	2.60E-02	5.98E-04	6.20E-05
4XMM J205703.1+171622	1SWASPJ205703.09+171622.0	K3.5V	13.71	11.49	88.90	5.27E+30	1.71E+29	2.58	5.95E-01	2.97E-02	5.49E-04	3.63E-05
4XMM J000234.8-300525	1SWASPJ000234.82-300525.3	K4.5V	13.81	0.71	23.25	5.46E+29	1.40E+28	2.78	3.25E-02	1.63E-03	7.23E-04	2.37E-05
4XMM J094101.6+044940	1SWASPJ094101.68+044940.4	G8V	12.01	8.17	27.61	1.09E+29	1.15E+28	1.75	6.85E-01	3.42E-02	2.90E-05	3.23E-06
4XMM J045255.8-700921	1SWASPJ045255.52-700919.3	K3.5V	14.77	0.55	37.77	1.65E+30	1.25E+29	2.61	2.81E-02	1.40E-03	2.20E-03	1.68E-04

4XMM J090247.5+004023	1SWASPJ090247.60+004024.2	G3V	11.60	3.34	21.58	2.17E+29	2.29E+28	1.50	3.23E-01	1.62E-02	6.59E-05	7.08E-06
4XMM J191755.7+442449	1SWASPJ191755.71+442449.5	G9V	10.79	13.95	17.45	5.16E+28	6.05E+27	1.90	1.07E+00	5.36E-02	1.04E-05	1.23E-06
4XMM J043356.3-612916	1SWASPJ043356.50-612916.5	K0.5V	10.57	3.39	9.29	9.51E+29	1.29E+28	1.98	2.48E-01	1.24E-02	5.20E-04	7.30E-06
4XMM J192411.6-425300	1SWASPJ192411.64-425300.1	G8V	9.93	8.46	10.81	1.20E+29	1.50E+28	1.72	7.22E-01	3.61E-02	2.78E-05	3.49E-06
4XMM J212558.6+223845	1SWASPJ212558.71+223845.3	K3.5V	13.68	8.26	110.21	1.73E+31	9.82E+29	2.64	4.14E-01	2.07E-02	1.07E-03	8.30E-05
4XMM J154447.1-381139	1SWASPJ154447.12-381140.6	K6.5V	11.45	3.18	12.76	1.50E+30	3.17E+28	3.29	1.10E-01	5.48E-03	5.10E-04	1.60E-05
4XMM J172612.1+021827	1SWASPJ172615.68+021925.1	G8V	14.25	0.38	64.40	1.50E+31	6.36E+29	1.76	3.17E-02	1.59E-03	1.33E-02	9.00E-04
4XMM J011858.9-341427	1SWASPJ011858.94-341428.5	K1V	12.98	15.78	68.63	7.94E+30	1.18E+29	2.06	1.10E+00	5.51E-02	7.80E-04	3.65E-05
4XMM J060651.1-340929	1SWASPJ060651.04-340930.1	K4V	13.03	4.96	106.60	7.30E+30	7.29E+29	2.65	2.47E-01	1.24E-02	3.77E-04	4.20E-05
4XMM J161329.3-231107	1SWASPJ161329.29-231107.4	K6.5V	11.61	3.11	13.82	1.61E+30	2.79E+28	3.25	1.10E-01	5.50E-03	5.60E-04	1.19E-05
4XMM J032814.9+300119	1SWASPJ032814.96+300119.1	G8V	11.61	0.16	22.64	6.59E+29	3.65E+28	1.78	1.28E-02	6.40E-04	1.73E-04	1.11E-05
4XMM J094955.1-251933	1SWASPJ094955.16-251933.8	K3V	13.93	1.72	24.83	4.01E+29	3.46E+28	2.42	9.77E-02	4.89E-03	6.25E-04	5.47E-05
4XMM J191856.4+463844	1SWASPJ191856.32+463843.1	G4V	10.79	11.10	15.66	8.49E+28	8.00E+27	1.54	1.05E+00	5.24E-02	2.30E-05	2.27E-06
4XMM J053656.1-670006	1SWASPJ053656.61-670006.1	K3V	12.68	0.14	28.12	8.22E+29	7.72E+28	2.46	7.86E-03	3.93E-04	2.98E-04	2.86E-05
4XMM J020930.9+342421	1SWASPJ020930.99+342421.0	K2V	13.08	3.85	129.04	2.06E+31	9.67E+29	2.14	2.58E-01	1.29E-02	6.72E-04	9.06E-05
4XMM J042041.1-483736	1SWASPJ042041.16-483735.7	K5.5V	13.98	0.38	37.53	1.17E+30	7.02E+28	3.04	1.52E-02	7.58E-04	6.10E-04	3.75E-05
4XMM J083951.9+322633	1SWASPJ083951.96+322633.7	K3V	13.22	0.63	27.24	1.68E+30	1.21E+29	2.44	3.54E-02	1.77E-03	1.03E-03	7.51E-05
4XMM J122751.1+333843	1SWASPJ122751.20+333843.4	K7V	12.04	10.87	7.49	1.10E+29	2.43E+27	3.36	3.59E-01	1.80E-02	1.83E-04	4.45E-06
4XMM J190646.5+440145	1SWASPJ190646.59+440146.0	K2.5V	13.23	6.99	120.06	5.03E+31	5.45E+29	2.26	4.36E-01	2.18E-02	1.90E-03	9.23E-05
4XMM J145704.3-430018	1SWASPJ145704.32-430018.7	G8V	11.22	4.21	52.14	2.10E+31	2.69E+29	1.73	3.57E-01	1.78E-02	7.41E-04	5.41E-05
4XMM J030846.5+485946	1SWASPJ030846.52+485946.5	K5V	12.67	0.14	25.76	4.30E+29	3.25E+28	2.94	5.76E-03	2.88E-04	1.45E-04	1.11E-05
4XMM J141142.0-310423	1SWASPJ141141.98-310425.8	G0V	13.88	3.19	54.80	5.63E+29	5.41E+28	1.38	3.31E-01	1.65E-02	2.50E-04	2.66E-05
4XMM J032240.3-365917	1SWASPJ032246.95-370025.9	G3V	11.84	0.36	43.99	3.48E+29	5.32E+28	1.48	3.50E-02	1.75E-03	3.18E-05	4.90E-06
4XMM J134514.9-000047	1SWASPJ134514.97-000047.8	K2V	11.77	9.24	54.97	1.15E+31	6.15E+29	2.19	6.00E-01	3.00E-02	6.21E-04	4.79E-05
4XMM J022319.5+472720	1SWASPJ022319.50+472722.1	G4V	11.45	3.16	18.33	3.63E+29	3.94E+28	1.53	3.00E-01	1.50E-02	1.32E-04	1.44E-05
4XMM J034322.4+242910	1SWASPJ034322.39+242910.6	K1V	12.58	4.49	23.60	3.43E+29	3.16E+28	2.08	3.11E-01	1.56E-02	1.82E-04	1.72E-05
4XMM J062408.2-425935	1SWASPJ062408.16-425936.6	M1V	12.52	10.28	10.95	4.73E+29	1.42E+28	3.98	2.38E-01	1.19E-02	3.71E-04	1.48E-05
4XMM J052000.3+061303	1SWASPJ052000.29+061303.6	K4V	11.84	3.51	9.72	7.63E+29	1.71E+28	2.71	1.70E-01	8.49E-03	9.12E-04	2.21E-05
4XMM J084130.6+185219	1SWASPJ084130.69+185218.6	K3.5V	12.88	2.41	18.26	1.22E+30	4.80E+28	2.59	1.25E-01	6.24E-03	1.25E-03	5.61E-05
4XMM J173329.2+502425	1SWASPJ173329.20+502425.1	K4V	13.83	2.92	34.14	3.72E+29	2.98E+28	2.65	1.45E-01	7.27E-03	2.35E-04	1.91E-05
4XMM J055420.0+014256	1SWASPJ055420.05+014255.9	M2.5V	14.03	10.45	33.21	9.59E+29	2.83E+28	4.37	1.93E-01	9.66E-03	2.91E-04	1.05E-05
4XMM J222551.7+171030	1SWASPJ222551.67+171030.6	K8V	14.80	12.81	115.43	8.43E+30	3.00E+29	3.44	4.05E-01	2.03E-02	1.54E-03	1.89E-04
4XMM J163338.3+402509	1SWASPJ163338.35+402509.5	K5V	15.18	0.57	38.61	8.02E+29	3.95E+28	2.95	2.40E-02	1.20E-03	1.25E-03	6.38E-05
4XMM J034638.7+245734	1SWASPJ034638.77+245734.7	G4V	10.39	2.32	13.63	2.72E+29	9.97E+27	1.56	2.17E-01	1.09E-02	6.40E-05	2.52E-06
4XMM J030816.4+490050	1SWASPJ030816.46+490051.0	K4V	12.50	1.73	24.83	2.26E+30	7.57E+28	2.72	8.32E-02	4.16E-03	7.77E-04	2.90E-05
4XMM J053932.5-023943	1SWASPJ053932.58-023943.9	M0.5V	13.85	6.90	39.53	2.37E+30	8.15E+28	3.93	1.64E-01	8.22E-03	6.77E-04	3.82E-05
4XMM J231830.9+425539	1SWASPJ231830.97+425541.4	K0V	13.32	0.17	49.21	1.33E+30	9.85E+28	1.94	1.29E-02	6.43E-04	3.83E-04	3.03E-05
4XMM J142937.3-375337	1SWASPJ142937.36-375337.1	K4.5V	12.90	2.30	19.62	4.59E+29	4.17E+28	2.81	1.05E-01	5.24E-03	3.44E-04	3.14E-05
4XMM J053539.6-042513	1SWASPJ053539.56-042513.2	K4V	12.92	11.86	36.50	2.34E+30	1.06E+29	2.71	5.71E-01	2.86E-02	6.86E-04	3.86E-05
4XMM J053821.3-685032	1SWASPJ053821.22-685033.4	K2.5V	11.60	5.74	24.39	2.21E+29	1.25E+28	2.22	3.66E-01	1.83E-02	4.30E-05	2.51E-06
4XMM J044009.2+253532	1SWASPJ044009.15+253533.1	K6.5V	10.81	5.61	4.42	4.39E+29	4.66E+27	3.24	1.98E-01	9.92E-03	6.89E-04	7.93E-06
4XMM J015636.6+285643	1SWASPJ015636.65+285643.7	K3.5V	12.94	5.27	22.16	6.72E+29	3.02E+28	2.63	2.65E-01	1.32E-02	5.17E-04	2.60E-05
4XMM J024614.4-205011	1SWASPJ024622.47-205004.5	G8V	14.70	0.18	177.96	1.05E+32	6.18E+30	1.81	1.41E-02	7.07E-04	8.90E-03	1.08E-03
4XMM J033939.5+152954	1SWASPJ033939.49+152954.9	K2V	11.82	4.37	15.54	2.98E+29	2.28E+28	2.16	2.90E-01	1.45E-02	1.79E-04	1.50E-05
4XMM J192029.1+464508	1SWASPJ192028.79+464509.9	G8V	11.76	5.40	24.57	1.08E+29	2.44E+28	1.72	4.60E-01	2.30E-02	2.85E-05	6.41E-06
4XMM J183430.6+324548	1SWASPJ183430.66+324548.3	G0V	13.19	0.19	80.17	1.21E+30	9.50E+28	1.36	2.00E-02	9.99E-04	1.20E-04	9.99E-06
4XMM J054445.5-681207	1SWASPJ054449.18-681229.9	K1.5V	12.53	0.39	17.43	4.26E+28	1.24E+28	2.13	2.60E-02	1.30E-03	4.00E-05	1.17E-05
4XMM J161551.4-055234	1SWASPJ161558.12-055234.2	G4V	10.69	0.61	23.68	3.96E+28	6.88E+27	1.59	5.60E-02	2.80E-03	4.08E-06	7.33E-07
4XMM J025700.4+055415	1SWASPJ025702.21+055338.2	G0V	13.56	0.35	141.66	2.22E+30	4.03E+29	1.34	3.72E-02	1.86E-03	1.96E-04	3.92E-05
4XMM J164800.5+270308	1SWASPJ164755.42+270243.6	G0V	13.61	0.25	74.29	4.95E+29	1.03E+29	1.37	2.60E-02	1.30E-03	8.68E-05	1.83E-05
4XMM J151642.6-004850	1SWASPJ151642.89-004850.7	K0V	14.34	0.17	111.84	4.46E+30	2.45E+29	1.93	1.27E-02	6.33E-04	8.20E-04	8.66E-05
4XMM J221448.1+004245	1SWASPJ221448.12+004245.0	K2.5V	12.98	8.24	117.26	5.88E+30	1.01E+30	2.31	4.99E-01	2.50E-02	3.39E-04	6.78E-05
4XMM J051027.1-671449	1SWASPJ051029.13-671342.2	K0V	13.70	1.97	50.14	8.71E+29	9.17E+28	1.94	1.48E-01	7.40E-03	3.07E-04	3.28E-05
4XMM J234658.8-545308	1SWASPJ234658.71-545309.7	K3.5V	13.94	0.14	37.70	5.37E+29	5.18E+28	2.62	7.13E-03	3.56E-04	3.21E-04	3.12E-05

4XMM J163911.2-205919	1SWASPJ163911.29-205918.4	K2.5V	14.23	0.17	73.70	7.18E+29	8.65E+28	2.21	1.12E-02	5.59E-04	1.84E-04	2.36E-05
4XMM J051147.5+043632	1SWASPJ051147.60+043632.3	G4V	12.83	0.19	60.46	3.09E+30	4.51E+29	1.59	1.75E-02	8.75E-04	5.36E-04	8.44E-05
4XMM J052451.6+425211	1SWASPJ052447.29+425212.0	K5V	13.06	0.05	13.34	1.11E+28	2.09E+27	2.96	1.98E-03	9.91E-05	1.90E-05	3.57E-06
4XMM J182436.4+303344	1SWASPJ182436.39+303343.8	K2V	11.52	9.01	11.12	2.44E+28	1.59E+27	2.15	6.00E-01	3.00E-02	2.10E-05	1.37E-06
4XMM J180724.9+292928	1SWASPJ180724.82+292927.5	G0V	13.48	0.18	84.45	1.21E+30	2.50E+29	1.34	1.87E-02	9.33E-04	1.58E-04	3.29E-05
4XMM J005305.0+394730	1SWASPJ005310.20+394834.0	G7V	13.00	25.88	51.32	2.61E+29	5.99E+28	1.68	2.26E+00	1.13E-01	5.81E-05	1.35E-05
4XMM J053924.6-701428	1SWASPJ053929.93-701408.0	K1.5V	14.84	0.25	180.22	3.72E+30	3.76E+29	2.12	1.69E-02	8.43E-04	2.78E-04	2.62E-04
4XMM J133342.3+503803	1SWASPJ133342.30+503802.8	K1.5V	12.78	7.56	34.55	1.82E+29	1.44E+28	2.11	5.13E-01	2.56E-02	5.37E-05	4.38E-06
4XMM J165836.2+375821	1SWASPJ165836.29+375820.9	G9V	8.67	10.24	4.37	2.21E+28	3.27E+27	1.83	8.18E-01	4.09E-02	9.42E-06	1.39E-06
4XMM J052641.4+431027	1SWASPJ052631.82+430933.0	G9V	13.12	2.26	128.57	9.93E+30	1.95E+30	1.87	1.76E-01	8.81E-03	3.04E-04	7.19E-05
4XMM J194214.2-103210	1SWASPJ194210.97-103153.4	K2V	13.50	0.22	47.54	4.89E+29	1.49E+29	2.16	1.45E-02	7.24E-04	1.76E-04	5.42E-05
4XMM J115319.8-464242	1SWASPJ115319.82-464241.6	G9V	13.76	0.19	84.86	1.86E+30	1.91E+29	1.88	1.46E-02	7.31E-04	2.77E-04	3.03E-05
4XMM J090827.4+011306	1SWASPJ090827.32+011304.0	G8V	14.16	0.79	46.95	5.28E+30	9.00E+29	1.80	6.41E-02	3.20E-03	3.86E-03	6.68E-04
4XMM J090926.7-092725	1SWASPJ090926.75-092725.1	G4V	13.26	0.32	69.58	3.57E+30	2.21E+29	1.54	3.07E-02	1.53E-03	5.71E-04	3.93E-05
4XMM J135119.3-333341	1SWASPJ135119.49-333341.8	G9V	15.49	0.13	108.01	1.03E+30	2.75E+29	1.85	1.07E-02	5.33E-04	4.56E-04	1.31E-04
4XMM J052752.4-392956	1SWASPJ052752.40-392956.8	K4V	14.29	13.89	97.53	1.02E+31	1.00E+30	2.73	6.63E-01	3.31E-02	1.25E-03	1.27E-04
4XMM J213740.0-424907	1SWASPJ213740.12-424907.1	G0V	13.41	0.65	73.21	5.03E+30	1.10E+30	1.37	6.71E-02	3.36E-03	7.29E-04	1.65E-04
4XMM J075156.1+421221	1SWASPJ075156.16+421219.4	G4V	11.91	5.77	19.43	8.92E+28	2.29E+28	1.57	5.34E-01	2.67E-02	4.15E-05	1.07E-05
4XMM J123601.6-400445	1SWASPJ123601.63-400444.9	K1.5V	15.32	0.14	67.02	7.27E+29	4.92E+28	2.10	9.52E-03	4.76E-04	8.55E-04	7.78E-05
4XMM J134131.0-294750	1SWASPJ134139.29-294750.2	G9V	14.57	0.33	69.76	8.73E+29	2.17E+29	1.88	2.58E-02	1.29E-03	3.80E-04	9.58E-05
4XMM J164803.9+270528	1SWASPJ164759.54+270450.5	G8V	12.93	0.25	63.79	3.55E+29	8.46E+28	1.82	2.01E-02	1.00E-03	4.20E-05	1.03E-05
4XMM J100447.4-063225	1SWASPJ100449.28-063314.5	G4V	14.61	0.17	107.61	4.33E+30	6.47E+29	1.60	1.52E-02	7.62E-04	1.13E-03	3.41E-04
4XMM J002847.8+345355	1SWASPJ002841.59+345358.9	G2V	14.73	27.94	104.25	4.81E+29	1.56E+29	1.47	2.75E+00	1.38E-01	1.79E-04	6.01E-05
4XMM J215911.6+182305	1SWASPJ215911.27+182301.7	G8V	12.99	0.29	34.08	2.22E+29	2.79E+28	1.79	2.33E-02	1.16E-03	9.57E-05	1.22E-05
4XMM J043454.5+240512	1SWASPJ043456.17+240543.5	M2V	13.68	0.65	22.73	2.16E+28	4.25E+27	4.24	1.30E-02	6.48E-04	9.51E-06	1.88E-06
4XMM J174831.4+451757	1SWASPJ174831.47+451757.9	G9V	13.33	7.23	62.27	2.76E+30	4.71E+29	1.89	5.58E-01	2.79E-02	4.84E-04	8.32E-05
4XMM J064058.1-255239	1SWASPJ064058.09-255240.8	K4.5V	13.42	4.00	68.38	2.46E+30	2.63E+29	2.87	1.76E-01	8.80E-03	2.73E-04	6.90E-05
4XMM J184746.4+454456	1SWASPJ184746.32+454455.6	G7V	14.90	0.17	121.53	2.35E+30	1.72E+29	1.71	1.49E-02	7.45E-04	4.55E-04	4.02E-05
4XMM J234205.4-550235	1SWASPJ234205.47-550236.3	K2V	14.69	0.15	67.42	1.02E+30	1.03E+29	2.14	1.02E-02	5.11E-04	4.42E-04	4.64E-05
4XMM J173358.2+490521	1SWASPJ173358.15+490521.7	G8V	12.45	12.32	23.34	3.55E+28	7.21E+27	1.74	1.03E+00	5.17E-02	1.91E-05	3.89E-06
4XMM J050613.1-681214	1SWASPJ050559.20-681201.3	G4V	13.73	7.39	73.19	7.03E+29	6.39E+28	1.55	6.92E-01	3.46E-02	1.28E-04	1.22E-05
4XMM J105712.3+070044	1SWASPJ105711.41+070052.8	G9V	13.34	0.06	40.23	7.88E+28	2.61E+28	1.91	4.72E-03	2.36E-04	3.40E-05	1.13E-05
4XMM J200859.6-610015	1SWASPJ200858.81-610017.0	K1V	14.94	0.33	80.18	7.60E+27	1.54E+28	2.09	2.25E-02	1.13E-03	3.04E-06	6.15E-06
4XMM J191659.6+411912	1SWASPJ191659.63+411913.2	K0V	12.75	7.61	20.48	2.95E+28	4.97E+27	1.96	5.65E-01	2.83E-02	2.58E-05	4.36E-06
4XMM J120738.4-524414	1SWASPJ120738.51-524414.4	G9V	11.29	16.99	11.80	2.98E+28	3.08E+27	1.91	1.30E+00	6.48E-02	2.03E-05	2.10E-06
4XMM J173827.8+585353	1SWASPJ173827.82+585352.7	G2V	12.17	10.42	55.83	6.68E+29	1.26E+29	1.47	1.03E+00	5.13E-02	5.07E-05	9.62E-06
4XMM J164116.6+384917	1SWASPJ164115.75+385002.7	K1.5V	14.73	0.33	35.91	2.83E+29	3.93E+28	2.13	2.21E-02	1.10E-03	4.79E-04	6.68E-05
4XMM J053837.0-663030	1SWASPJ053836.72-663027.0	K2.5V	16.44	2.02	523.99	1.86E+31	4.00E+30	2.24	1.28E-01	6.39E-03	6.91E-04	3.21E-04
4XMM J230754.1-020817	1SWASPJ230754.16-020817.1	K3.5V	13.41	6.01	50.07	2.79E+30	1.90E+29	2.53	3.22E-01	1.61E-02	6.84E-04	4.97E-05
4XMM J161412.3-221913	1SWASPJ161406.40-221806.0	K0V	13.69	0.62	66.01	1.62E+30	1.18E+29	1.92	4.69E-02	2.35E-03	3.37E-04	3.89E-05
4XMM J054743.3-695603	1SWASPJ054757.22-695515.7	K2.5V	14.31	0.26	42.00	1.15E+28	1.47E+28	2.23	1.66E-02	8.31E-04	9.45E-06	1.21E-05
4XMM J231820.5-442212	1SWASPJ231820.43-442211.8	K3.5V	13.62	0.13	113.57	2.50E+30	1.02E+29	2.57	6.57E-03	3.28E-04	1.30E-04	1.72E-04
4XMM J201354.0-414615	1SWASPJ201357.11-414648.9	K4V	13.36	0.19	28.04	6.01E+28	1.41E+28	2.70	9.17E-03	4.58E-04	3.69E-05	8.66E-06
4XMM J161407.3-221731	1SWASPJ161407.32-221732.0	M2V	13.20	0.62	14.62	1.08E+30	3.24E+28	4.23	1.24E-02	6.22E-04	7.25E-04	2.55E-05
4XMM J093329.3+054625	1SWASPJ093329.05+054625.9	K0.5V	12.56	5.11	73.19	1.92E+31	1.64E+30	1.97	3.76E-01	1.88E-02	1.36E-03	1.47E-04
4XMM J053004.5+113455	1SWASPJ053005.75+113625.9	G2V	13.14	0.06	93.38	6.28E+29	1.12E+29	1.44	5.64E-03	2.82E-04	4.83E-05	1.02E-05
4XMM J162358.0+262927	1SWASPJ162358.17+262926.9	G3V	13.62	0.19	87.81	1.69E+30	5.76E+29	1.52	1.86E-02	9.28E-04	2.11E-04	7.21E-05
4XMM J195952.2+593322	1SWASPJ195952.57+593322.6	G2V	12.76	4.43	40.55	2.95E+29	9.69E+28	1.45	4.41E-01	2.21E-02	7.24E-05	2.38E-05
4XMM J182652.1+301505	1SWASPJ182651.81+301504.6	K0V	11.13	13.02	11.75	1.19E+28	2.98E+27	1.96	9.67E-01	4.83E-02	6.95E-06	2.73E-06
4XMM J184112.0+622053	1SWASPJ184112.05+622053.7	G8V	12.50	6.51	25.47	1.32E+29	1.31E+28	1.76	5.40E-01	2.70E-02	6.11E-05	6.09E-06
4XMM J213524.8-572016	1SWASPJ213524.74-572017.1	G3V	13.38	5.40	80.59	3.29E+30	8.67E+29	1.49	5.24E-01	2.62E-02	3.51E-04	9.35E-05
4XMM J080843.7+400200	1SWASPJ080843.94+400202.2	G7V	13.01	0.20	65.28	2.79E+30	6.16E+29	1.68	1.75E-02	8.77E-04	3.22E-04	7.37E-05
4XMM J051108.1+163456	1SWASPJ051102.94+163335.3	G3V	12.28	0.58	58.74	4.08E+29	5.29E+28	1.51	5.53E-02	2.77E-03	3.17E-05	4.43E-06
4XMM J115441.5-423710	1SWASPJ115441.58-423709.9	K5V	13.61	22.86	108.04	6.69E+30	8.09E+29	2.97	9.45E-01	4.73E-02	3.87E-04	5.30E-05

4XMM J200838.1-610054	1SWASPJ200838.24-610054.8	K0V	14.42	0.20	95.58	8.10E+29	8.09E+28	1.92	1.48E-02	7.40E-04	1.47E-04	2.39E-04
4XMM J020953.8+342309	1SWASPJ020957.38+342412.6	K4V	13.91	0.40	19.93	8.60E+28	1.51E+28	2.69	1.97E-02	9.83E-04	1.77E-04	3.11E-05
4XMM J052133.1-673137	1SWASPJ052141.24-673011.2	G9V	12.53	19.55	20.97	5.61E+28	1.22E+28	1.86	1.54E+00	7.69E-02	3.77E-05	8.24E-06
4XMM J224451.1+280829	1SWASPJ224451.16+280830.9	K4V	13.78	0.58	29.89	7.01E+29	5.58E+28	2.69	2.81E-02	1.41E-03	6.26E-04	5.05E-05
4XMM J163306.7+412239	1SWASPJ163306.69+412239.1	G2V	11.49	4.03	21.08	2.21E+29	2.95E+28	1.45	4.00E-01	2.00E-02	6.41E-05	8.59E-06
4XMM J002914.0+345133	1SWASPJ002918.85+345102.9	K1V	12.83	27.83	41.83	3.42E+29	3.99E+28	2.06	1.95E+00	9.76E-02	1.16E-04	1.49E-05
4XMM J050952.5-690410	1SWASPJ050943.77-690409.3	K1.5V	13.75	0.51	154.62	1.02E+30	2.10E+29	0.05	1.13E-01	5.67E-03	3.72E-05	3.42E-05
4XMM J044910.5+060244	1SWASPJ044910.64+060243.8	G9V	12.06	10.49	22.68	7.61E+28	1.24E+28	1.89	8.11E-01	4.06E-02	3.01E-05	4.95E-06
4XMM J062415.8-430228	1SWASPJ062408.17-430217.9	K5.5V	12.76	13.36	10.98	2.07E+28	4.00E+27	3.01	5.41E-01	2.71E-02	3.80E-05	7.35E-06
4XMM J161617.0+073333	1SWASPJ161617.14+073334.4	K0.5V	11.65	28.75	39.99	2.11E+29	6.56E+28	1.97	2.13E+00	1.06E-01	1.82E-05	5.68E-06
4XMM J134326.9-482041	1SWASPJ134327.42-482039.7	K0V	13.70	0.16	71.47	5.26E+29	1.85E+29	1.94	1.21E-02	6.07E-04	9.46E-05	3.37E-05
4XMM J022216.2-031036	1SWASPJ022215.35-031031.8	K3.5V	13.89	0.20	20.74	1.44E+28	5.58E+27	2.58	1.05E-02	5.25E-04	2.90E-05	1.13E-05
4XMM J191553.4+492412	1SWASPJ191553.60+492411.9	G3V	11.24	8.98	38.40	5.57E+29	6.47E+28	1.49	8.72E-01	4.36E-02	3.84E-05	4.51E-06
4XMM J223925.3+032044	1SWASPJ223925.47+032035.7	G8V	10.45	1.77	15.51	1.96E+30	1.77E+29	1.74	1.49E-01	7.46E-03	4.06E-04	3.85E-05
4XMM J034902.4+231607	1SWASPJ034902.32+231509.0	K2V	11.85	6.15	13.99	2.11E+28	4.78E+27	2.16	4.06E-01	2.03E-02	1.57E-05	3.55E-06
4XMM J151640.5-004920	1SWASPJ151640.54-004919.3	G8V	14.31	0.17	96.10	1.48E+30	1.65E+29	1.79	1.37E-02	6.85E-04	3.56E-04	4.63E-05
4XMM J131004.3-350942	1SWASPJ131004.32-350942.0	K3.5V	14.52	9.93	203.46	1.37E+31	2.26E+30	2.63	5.01E-01	2.51E-02	5.37E-04	1.35E-04
4XMM J093301.4-173600	1SWASPJ093301.68-173601.6	K3.5V	14.86	8.56	125.43	5.00E+30	1.18E+30	2.55	4.52E-01	2.26E-02	6.47E-04	1.62E-04
4XMM J221635.0-163158	1SWASPJ221635.09-163158.1	K2.5V	14.94	0.60	48.59	2.80E+30	3.34E+29	2.24	3.81E-02	1.91E-03	3.20E-03	3.97E-04
4XMM J154940.4-321227	1SWASPJ154940.53-321226.9	G8V	12.52	0.20	55.04	1.12E+30	1.18E+29	1.72	1.72E-02	8.59E-04	1.13E-04	1.30E-05
4XMM J061726.9-573708	1SWASPJ061725.15-573658.1	G3V	13.46	0.16	65.64	1.28E+30	4.65E+29	1.50	1.54E-02	7.70E-04	2.26E-04	8.22E-05
4XMM J134022.0-002410	1SWASPJ134022.18-002410.7	K4.5V	12.79	22.90	11.75	6.90E+27	2.68E+27	2.80	1.04E+00	5.23E-02	1.32E-05	5.13E-06
4XMM J063532.8+353556	1SWASPJ063532.66+353552.5	G8V	12.13	7.80	29.16	8.22E+28	3.57E+28	1.81	6.30E-01	3.15E-02	2.09E-05	9.10E-06
4XMM J215108.2-072639	1SWASPJ215108.33-072640.7	G9V	13.98	0.16	73.15	9.88E+29	1.29E+29	1.86	1.29E-02	6.44E-04	2.70E-04	3.86E-05
4XMM J204010.1-003828	1SWASPJ204010.58-003809.2	K3V	13.00	10.22	16.05	2.33E+27	3.16E+27	2.43	5.77E-01	2.89E-02	3.50E-06	4.74E-06

Table A.2 G- to M-type ASAS-SN objects from the full catalogue containing 900 X-ray visible unique objects displaying rotational modulation in their photometric variability.

XMM ID	ASAS-SN ID	SpT	Period [d]	V [mag]	V-K	Distance [pc]	F_x [10^{-14}] [erg/cm^2/s]	logRo	logR_x			
4XMM J021802.8+625416	ASASSN-V J021803.03+625418.1	K4.5V	0.55	14.26	2.84	24.31	2.33E+29	2.75E+28	2.53E-02	1.26E-03	4.06E-04	4.90E-05
4XMM J033735.1+170515	ASASSN-V J033735.10+170516.0	K6.5V	0.46	13.57	3.32	15.81	1.44E+29	1.18E+28	1.59E-02	7.98E-04	2.34E-04	1.93E-05
4XMM J080838.3-472818	ASASSN-V J080838.36-472818.4	K5V	0.86	13.94	2.91	34.28	2.53E+30	3.91E+28	3.73E-02	1.87E-03	1.65E-03	3.47E-05
4XMM J131204.1-342026	ASASSN-V J131204.08-342026.2	K6.5V	0.72	15.34	3.24	25.45	4.24E+29	1.52E+28	2.47E-02	1.24E-03	1.34E-03	3.83E-04
4XMM J172038.0-250535	ASASSN-V J172037.86-250537.2	K5V	2.39	12.19	2.95	14.54	1.24E+30	8.91E+28	1.04E-01	5.20E-03	8.18E-04	5.98E-05
4XMM J191212.3+100142	ASASSN-V J191212.28+100141.1	M2.5V	1.55	15.14	4.36	6.61	6.67E+28	1.89E+27	2.77E-02	1.38E-03	1.18E-03	3.45E-05
4XMM J145657.3+221312	ASASSN-V J145657.71+221315.3	K3.5V	3.42	15.39	2.55	187.44	2.05E+31	9.13E+29	1.77E-01	8.85E-03	2.06E-03	3.46E-04
4XMM J191152.6+090423	ASASSN-V J191152.63+090422.9	M2V	22.69	13.53	4.28	87.83	1.54E+31	1.74E+29	4.53E-01	2.26E-02	5.72E-04	4.47E-05
4XMM J053517.8-044452	ASASSN-V J053517.85-044452.5	M2V	5.66	14.07	4.25	39.98	1.42E+30	1.05E+29	1.13E-01	5.64E-03	3.65E-04	2.82E-05
4XMM J034703.6+240935	ASASSN-V J034703.58+240935.0	K7V	0.30	14.44	3.32	13.44	1.96E+29	5.88E+27	1.02E-02	5.09E-04	9.29E-04	2.98E-05
4XMM J064102.4+093458	ASASSN-V J064102.54+093455.8	K2V	1.98	14.28	2.20	71.01	2.56E+30	1.34E+29	1.33E-01	6.65E-03	8.77E-04	5.89E-05
4XMM J082507.6+294705	ASASSN-V J082507.69+294706.1	K5.5V	1.18	15.62	3.08	36.70	5.46E+29	5.65E+28	4.71E-02	2.36E-03	1.68E-03	1.80E-04
4XMM J064127.1+093506	ASASSN-V J064127.09+093506.1	K2.5V	1.54	13.94	2.31	70.93	4.34E+30	1.72E+29	9.55E-02	4.78E-03	1.06E-03	6.92E-05
4XMM J031331.7-223658	ASASSN-V J031331.73-223656.8	K4V	5.36	15.38	2.71	177.06	7.01E+30	4.91E+29	2.55E-01	1.27E-02	7.77E-04	1.50E-04
4XMM J115835.2-791317	ASASSN-V J115834.35-791317.8	M3V	2.10	12.99	4.55	17.95	2.47E+30	7.88E+28	3.40E-02	1.70E-03	6.76E-04	3.29E-05
4XMM J053601.8-051736	ASASSN-V J053601.86-051736.6	K9V	41.00	13.29	3.55	37.01	2.71E+30	6.62E+28	1.19E+00	5.97E-02	6.28E-04	2.38E-05
4XMM J053529.0-054948	ASASSN-V J053529.01-054948.6	K6.5V	5.24	13.87	3.25	31.69	2.99E+30	5.92E+28	1.81E-01	9.05E-03	1.83E-03	5.99E-05
4XMM J053456.8-051133	ASASSN-V J053456.81-051133.1	K4.5V	3.98	12.98	2.80	37.17	2.94E+30	4.70E+28	1.84E-01	9.19E-03	8.12E-04	2.97E-05
4XMM J074559.0-375841	ASASSN-V J074558.98-375842.1	K0.5V	2.33	13.68	1.98	36.48	7.71E+29	3.59E+28	1.71E-01	8.56E-03	4.92E-04	2.38E-05

4XMM J155757.9+350511	ASASSN-V J155757.96+350513.9	K1V	0.66	13.66	2.08	93.16	1.16E+31	1.51E+30	4.76E-02	2.38E-03	1.15E-03	1.52E-04
4XMM J053506.1-054531	ASASSN-V J053506.15-054531.2	K8V	8.30	15.00	3.42	36.52	1.46E+30	5.07E+28	2.56E-01	1.28E-02	1.77E-03	7.40E-05
4XMM J190235.9+424830	ASASSN-V J190236.12+424831.7	G8V	12.60	12.17	1.78	56.60	3.54E+30	1.28E+29	1.04E+00	5.22E-02	2.54E-04	1.09E-05
4XMM J053450.6-043532	ASASSN-V J053450.64-043533.2	K6.5V	3.77	13.97	3.27	38.82	1.91E+30	8.42E+28	1.30E-01	6.51E-03	9.27E-04	5.45E-05
4XMM J064822.9-441145	ASASSN-V J064822.98-441145.5	K1V	0.69	11.48	2.09	16.48	2.08E+30	1.03E+28	4.92E-02	2.46E-03	8.20E-04	1.51E-05
4XMM J034008.5+412846	ASASSN-V J034008.44+412847.0	K3V	13.70	13.15	2.45	65.84	3.01E+30	2.18E+29	7.97E-01	3.99E-02	3.01E-04	2.61E-05
4XMM J053447.5-054630	ASASSN-V J053447.58-054630.6	M2V	11.42	16.01	4.25	47.49	3.13E+30	8.78E+28	2.28E-01	1.14E-02	3.40E-03	1.36E-03
4XMM J203407.1-355323	ASASSN-V J203407.17-355323.4	K3V	8.96	11.43	2.43	42.43	1.39E+31	2.92E+29	5.21E-01	2.61E-02	7.93E-04	7.01E-05
4XMM J225315.8+623526	ASASSN-V J225315.79+623526.3	M3.5V	1.56	15.64	4.92	82.64	1.54E+31	5.73E+29	2.01E-02	1.00E-03	1.78E-03	1.20E-04
4XMM J190502.8+421745	ASASSN-V J190502.83+421745.1	G4V	4.81	11.18	1.55	16.55	1.39E+29	1.10E+28	4.34E-01	2.17E-02	4.64E-05	3.70E-06
4XMM J164104.7-453647	ASASSN-V J164104.83-453647.6	K3.5V	1.17	13.98	2.51	31.00	1.24E+30	2.72E+28	6.05E-02	3.03E-03	1.13E-03	3.43E-05
4XMM J140413.3-412749	ASASSN-V J140413.31-412749.6	K1.5V	0.59	13.60	2.10	21.86	1.10E+30	6.56E+27	4.09E-02	2.04E-03	1.71E-03	3.05E-05
4XMM J053807.8-023131	ASASSN-V J053807.82-023130.9	K5.5V	3.20	12.80	3.08	39.80	5.99E+30	8.22E+28	1.28E-01	6.40E-03	1.20E-03	4.00E-05
4XMM J053427.7-053155	ASASSN-V J053427.70-053155.3	K9V	3.35	12.19	3.56	39.64	1.40E+31	7.20E+28	9.76E-02	4.88E-03	1.03E-03	3.26E-05
4XMM J053447.6-054351	ASASSN-V J053447.64-054350.8	K4.5V	1.31	13.05	2.81	37.85	2.74E+30	4.62E+28	6.06E-02	3.03E-03	7.63E-04	2.65E-05
4XMM J181048.8-212150	ASASSN-V J181048.90-212150.2	G8V	0.80	13.10	1.79	57.38	6.12E+30	1.85E+29	6.62E-02	3.31E-03	1.21E-03	7.48E-05
4XMM J144103.6+534105	ASASSN-V J144103.68+534105.4	K2.5V	1.10	13.50	2.25	81.92	3.55E+30	3.19E+29	6.82E-02	3.41E-03	3.50E-04	3.23E-05
4XMM J034425.5+321229	ASASSN-V J034425.57+321230.0	M3.5V	8.38	16.19	4.85	33.27	5.22E+29	2.67E+28	1.08E-01	5.40E-03	6.29E-04	4.88E-05
4XMM J164346.2-543524	ASASSN-V J164346.27-543523.1	K5V	5.17	14.30	2.98	169.45	2.33E+31	9.53E+29	2.25E-01	1.13E-02	7.69E-04	9.74E-05
4XMM J161438.8-252459	ASASSN-V J161438.76-252500.1	M3.5V	7.13	13.66	4.92	13.23	1.00E+30	2.23E+28	9.18E-02	4.59E-03	7.03E-04	3.32E-05
4XMM J180451.9+095940	ASASSN-V J180451.86+095942.2	K5V	6.01	14.82	2.88	93.06	5.64E+30	4.32E+29	2.62E-01	1.31E-02	1.68E-03	1.56E-04
4XMM J171110.7-232720	ASASSN-V J171110.74-232719.9	K2.5V	10.89	13.68	2.22	102.19	7.54E+30	4.19E+29	6.74E-01	3.37E-02	6.19E-04	5.47E-05
4XMM J053513.3-050920	ASASSN-V J053513.30-050921.8	M1.5V	1.11	15.37	4.15	39.15	1.56E+30	2.61E+28	2.37E-02	1.19E-03	1.44E-03	9.70E-05
4XMM J053411.0-062225	ASASSN-V J053411.10-062225.8	K7V	7.72	14.60	3.32	38.05	1.42E+30	4.54E+28	2.60E-01	1.30E-02	1.19E-03	4.62E-05
4XMM J133207.0-314037	ASASSN-V J133206.99-314037.5	K1V	0.87	13.24	2.07	22.70	2.21E+29	9.40E+27	6.24E-02	3.12E-03	2.54E-04	1.13E-05
4XMM J053101.4+103332	ASASSN-V J053101.40+103331.9	K3.5V	5.16	13.88	2.55	39.00	1.96E+30	6.42E+28	2.67E-01	1.34E-02	1.12E-03	8.47E-05
4XMM J063350.6+062041	ASASSN-V J063350.52+062041.2	K2V	1.49	14.18	2.19	183.58	2.40E+31	1.65E+30	1.00E-01	5.01E-03	1.55E-03	2.36E-04
4XMM J111356.6+124757	ASASSN-V J111356.67+124758.3	G9V	1.11	13.76	1.83	71.21	2.21E+30	1.05E+29	8.73E-02	4.37E-03	4.80E-04	3.48E-04
4XMM J183539.5+440152	ASASSN-V J183539.34+440153.5	K7V	7.63	15.39	1.27	240.92	1.37E+31	1.01E+30	2.57E-01	1.29E-02	5.21E-04	7.62E-05
4XMM J184143.0+053436	ASASSN-V J184142.99+053435.6	K4V	0.50	13.55	2.71	24.51	8.51E+29	5.83E+28	2.37E-02	1.19E-03	8.25E-04	5.74E-05
4XMM J072513.6-074819	ASASSN-V J072513.66-074819.2	K3V	2.64	13.77	2.45	151.15	3.11E+31	8.35E+29	1.54E-01	7.68E-03	1.61E-03	1.26E-04
4XMM J053440.1-045839	ASASSN-V J053440.13-045839.8	K9V	2.35	14.49	3.54	40.67	1.98E+30	8.01E+28	6.85E-02	3.43E-03	1.18E-03	2.07E-04
4XMM J205154.4+445433	ASASSN-V J205154.50+445434.1	K4V	1.40	14.76	2.69	47.69	1.06E+30	8.04E+28	6.66E-02	3.33E-03	9.02E-04	7.11E-05
4XMM J080226.4-462516	ASASSN-V J080226.41-462516.6	K1V	3.92	13.31	2.05	41.99	1.89E+30	9.57E+28	2.81E-01	1.40E-02	6.96E-04	3.78E-05
4XMM J053523.4-060125	ASASSN-V J053523.49-060125.1	M1V	4.00	15.46	4.01	42.41	3.36E+30	6.51E+28	9.05E-02	4.53E-03	3.28E-03	2.61E-04
4XMM J053436.0-054215	ASASSN-V J053436.09-054215.3	M1V	8.50	15.19	3.96	38.95	1.33E+30	2.57E+28	1.93E-01	9.63E-03	1.17E-03	3.52E-05
4XMM J042923.2-030146	ASASSN-V J042923.22-030146.4	G8V	10.47	13.67	1.76	140.62	1.06E+31	3.46E+29	8.67E-01	4.34E-02	1.68E-03	1.33E-04
4XMM J053755.5-065718	ASASSN-V J053755.65-065718.1	M1V	7.06	14.32	4.00	40.38	5.34E+30	1.94E+29	1.60E-01	7.99E-03	1.91E-03	3.63E-04
4XMM J185743.3+443555	ASASSN-V J185743.25+443555.8	K2V	18.96	12.88	2.15	117.25	9.40E+30	5.03E+29	1.27E+00	6.37E-02	2.78E-04	2.46E-05
4XMM J053610.3-051945	ASASSN-V J053610.49-051944.9	K8V	6.07	13.81	3.40	39.54	2.57E+30	1.33E+29	1.87E-01	9.34E-03	9.04E-04	5.00E-05
4XMM J191447.5-213212	ASASSN-V J191447.48-213212.6	K3.5V	5.88	12.63	2.51	104.82	1.41E+31	5.83E+29	3.05E-01	1.52E-02	4.37E-04	4.47E-05
4XMM J020841.2+351243	ASASSN-V J020841.29+351243.6	K5V	4.17	14.97	2.92	27.02	2.48E+29	1.33E+28	1.82E-01	9.10E-03	6.61E-04	3.70E-05
4XMM J053445.5-043607	ASASSN-V J053445.55-043607.7	K9V	2.79	14.51	3.57	39.21	1.29E+30	7.51E+28	8.11E-02	4.06E-03	8.63E-04	5.25E-05
4XMM J191222.0+100147	ASASSN-V J191222.39+100149.0	K3.5V	44.78	14.69	2.64	139.49	3.60E+30	3.63E+29	2.32E+00	1.16E-01	4.66E-04	6.86E-05
4XMM J190127.6+043953	ASASSN-V J190127.70+043953.2	K4.5V	6.97	14.23	2.83	21.51	2.44E+29	2.57E+28	3.22E-01	1.61E-02	5.64E-04	5.97E-05
4XMM J125945.8-593158	ASASSN-V J125945.87-593158.3	M1.5V	10.19	14.37	4.15	11.72	2.93E+29	1.27E+28	2.18E-01	1.09E-02	9.70E-04	4.30E-05
4XMM J153524.7+731443	ASASSN-V J153524.25+731442.7	K2.5V	8.44	13.68	2.30	84.20	4.38E+30	4.27E+29	5.22E-01	2.61E-02	4.78E-04	4.82E-05
4XMM J115414.0+521921	ASASSN-V J115414.12+521921.4	K0V	2.11	14.58	1.95	36.18	6.41E+29	3.86E+28	1.57E-01	7.85E-03	9.28E-04	5.76E-05
4XMM J053838.4-023455	ASASSN-V J053838.52-023455.2	K7V	13.89	12.23	3.39	40.85	1.65E+31	1.31E+29	4.68E-01	2.34E-02	1.49E-03	4.72E-05
4XMM J080823.0-355232	ASASSN-V J080822.92-355233.9	K7V	10.28	14.41	3.33	102.30	5.97E+30	4.14E+29	3.46E-01	1.73E-02	5.12E-04	4.03E-05
4XMM J200522.0+354212	ASASSN-V J200522.03+354211.4	K4V	8.75	14.31	2.71	115.03	8.56E+30	3.66E+29	4.16E-01	2.08E-02	7.94E-04	4.58E-05
4XMM J034112.0-050914	ASASSN-V J034112.02-050914.5	K3.5V	5.12	12.08	2.58	13.12	3.65E+29	1.63E+28	2.65E-01	1.33E-02	3.27E-04	1.50E-05
4XMM J054218.1-075850	ASASSN-V J054218.16-075850.1	M3V	7.71	16.23	4.53	44.18	7.50E+29	3.51E+28	1.25E-01	6.25E-03	8.04E-04	4.66E-05
4XMM J111950.9+142321	ASASSN-V J111950.95+142321.9	K4.5V	4.76	14.78	2.88	94.38	5.60E+30	3.36E+29	2.20E-01	1.10E-02	1.26E-03	1.10E-04

4XMM J054053.9-020302	ASASSN-V J054053.96-020301.8	K1.5V	1.25	11.34	2.09	36.82	1.25E+31	7.13E+28	8.72E-02	4.36E-03	1.15E-03	3.75E-05
4XMM J084431.9-784631	ASASSN-V J084431.95-784631.3	M2V	20.10	12.54	4.28	9.79	4.30E+29	9.10E+27	4.01E-01	2.01E-02	3.47E-04	7.66E-06
4XMM J134807.0-625450	ASASSN-V J134806.94-625450.3	K5V	5.30	13.99	2.99	67.98	1.07E+31	2.43E+29	2.31E-01	1.15E-02	1.76E-03	6.12E-05
4XMM J052951.5+114030	ASASSN-V J052951.62+114031.6	M1V	3.24	14.87	3.97	47.21	4.23E+30	1.70E+29	7.34E-02	3.67E-03	1.71E-03	1.57E-04
4XMM J053441.5-042431	ASASSN-V J053441.52-042431.9	K3.5V	4.85	12.93	2.60	40.16	2.02E+30	1.58E+29	2.51E-01	1.26E-02	5.59E-04	4.66E-05
4XMM J053536.8-061631	ASASSN-V J053536.84-061631.0	K9V	5.74	14.79	3.54	36.65	1.10E+30	4.50E+28	1.67E-01	8.36E-03	1.03E-03	4.60E-05
4XMM J053610.4-062001	ASASSN-V J053610.44-062001.5	K5.5V	4.96	14.14	3.07	38.08	2.23E+30	4.45E+28	1.98E-01	9.91E-03	1.48E-03	4.05E-05
4XMM J033202.1-270251	ASASSN-V J033202.12-270251.9	K5.5V	0.66	12.54	3.06	14.35	1.11E+30	2.06E+28	2.64E-02	1.32E-03	1.01E-03	2.43E-05
4XMM J053742.7-064016	ASASSN-V J053742.79-064016.1	K5.5V	3.74	13.31	3.04	37.62	1.93E+30	3.61E+28	1.49E-01	7.46E-03	5.97E-04	2.14E-05
4XMM J054338.8-095625	ASASSN-V J054338.78-095627.6	K7V	3.14	14.36	3.33	45.07	2.17E+30	1.45E+29	1.06E-01	5.30E-03	1.07E-03	7.55E-05
4XMM J011648.3-002104	ASASSN-V J011648.31-002103.5	K2.5V	25.10	11.63	2.23	60.99	1.09E+31	3.30E+29	1.55E+00	7.77E-02	4.51E-04	2.97E-05
4XMM J011226.8+152751	ASASSN-V J011226.86+152752.4	K5.5V	1.16	14.65	3.06	24.94	1.22E+30	5.47E+28	4.63E-02	2.32E-03	3.54E-03	1.71E-04
4XMM J054217.6-080343	ASASSN-V J054217.66-080342.6	K9V	0.35	14.97	3.54	32.72	9.11E+29	3.05E+28	1.02E-02	5.10E-04	1.18E-03	5.19E-05
4XMM J212543.6+200605	ASASSN-V J212543.56+200605.1	K2V	13.68	11.74	2.17	49.77	1.18E+31	3.10E+29	9.19E-01	4.59E-02	7.61E-04	7.25E-05
4XMM J220603.1-500911	ASASSN-V J220603.13-500911.6	K1V	17.46	14.89	2.08	178.94	7.63E+30	8.34E+29	1.25E+00	6.25E-02	5.89E-04	8.41E-05
4XMM J053805.4-065314	ASASSN-V J053805.49-065314.8	K7V	3.49	13.84	3.38	38.64	3.34E+30	9.38E+28	1.18E-01	5.89E-03	1.30E-03	2.43E-04
4XMM J171633.4+422512	ASASSN-V J171633.56+422513.2	K4V	10.68	13.94	2.75	78.63	8.94E+30	3.31E+29	5.08E-01	2.54E-02	1.16E-03	5.06E-05
4XMM J192410.5+420742	ASASSN-V J192410.41+420741.8	K4V	12.80	14.57	2.67	200.20	1.01E+32	1.99E+30	6.08E-01	3.04E-02	3.83E-03	2.83E-04
4XMM J063047.3-560753	ASASSN-V J063047.34-560753.5	K5.5V	8.11	13.82	1.14	70.40	7.09E+30	1.49E+29	3.24E-01	1.62E-02	8.72E-04	2.62E-05
4XMM J080125.8-461049	ASASSN-V J080125.80-461049.1	G9V	3.07	13.40	1.85	45.88	1.17E+30	9.56E+28	2.41E-01	1.20E-02	4.14E-04	3.44E-05
4XMM J183312.1-341507	ASASSN-V J183312.04-341506.9	K4V	26.99	13.90	2.73	116.06	4.29E+30	3.65E+29	1.28E+00	6.41E-02	7.65E-04	8.26E-05
4XMM J210416.7-073638	ASASSN-V J210416.68-073638.6	K5V	4.04	15.01	2.95	128.35	1.16E+31	9.32E+29	1.76E-01	8.81E-03	2.02E-03	2.59E-04
4XMM J132650.3-223628	ASASSN-V J132650.37-223628.6	K5V	4.27	14.12	2.89	15.04	2.67E+29	1.43E+28	1.86E-01	9.30E-03	9.93E-04	6.44E-05
4XMM J231548.7+014321	ASASSN-V J231548.77+014321.6	K6.5V	0.78	14.13	3.29	18.41	4.66E+29	1.04E+28	2.69E-02	1.35E-03	9.72E-04	2.41E-05
4XMM J000228.1-300442	ASASSN-V J000228.21-300443.4	K5V	5.46	13.02	2.89	24.66	4.67E+29	1.44E+28	2.38E-01	1.19E-02	2.45E-04	1.16E-05
4XMM J090439.4+554638	ASASSN-V J090439.42+554638.4	K4V	0.50	12.71	2.66	20.88	1.63E+30	8.56E+28	2.37E-02	1.19E-03	9.42E-04	5.17E-05
4XMM J053557.4-043909	ASASSN-V J053557.50-043909.3	K9V	11.34	14.81	3.53	40.18	1.42E+30	9.06E+28	3.30E-01	1.65E-02	1.21E-03	8.65E-05
4XMM J034741.3+235818	ASASSN-V J034741.44+235819.0	K5V	0.48	13.50	2.97	13.55	2.56E+29	1.01E+28	2.11E-02	1.05E-03	6.43E-04	2.63E-05
4XMM J141237.9+542648	ASASSN-V J141237.93+542648.4	K3.5V	2.49	14.01	2.61	36.58	1.80E+30	1.46E+29	1.29E-01	6.47E-03	1.25E-03	1.03E-04
4XMM J163923.4-643555	ASASSN-V J163923.28-643554.9	K2V	0.75	14.62	2.19	124.71	2.30E+31	8.99E+29	5.07E-02	2.54E-03	2.74E-03	2.09E-04
4XMM J053710.7-064540	ASASSN-V J053710.81-064540.9	M1.5V	9.79	15.19	4.15	39.30	2.29E+30	5.49E+28	2.09E-01	1.05E-02	1.70E-03	1.62E-04
4XMM J194659.3+205624	ASASSN-V J194659.31+205624.4	K5.5V	6.83	14.43	3.05	101.00	1.96E+31	7.78E+29	2.73E-01	1.36E-02	2.49E-03	1.48E-04
4XMM J034810.9+233025	ASASSN-V J034810.98+233025.3	K5.5V	7.69	14.36	3.03	13.57	1.40E+29	5.20E+27	3.07E-01	1.54E-02	7.27E-04	2.81E-05
4XMM J053403.0-053657	ASASSN-V J053403.00-053657.3	M3V	2.65	13.69	4.56	39.96	4.76E+30	4.00E+28	4.29E-02	2.15E-03	6.18E-04	1.52E-05
4XMM J064025.4+094825	ASASSN-V J064025.47+094825.9	K4V	3.15	14.97	2.64	70.08	1.47E+30	8.25E+28	1.49E-01	7.47E-03	7.61E-04	6.76E-05
4XMM J191806.2+143359	ASASSN-V J191806.40+143359.5	K4.5V	2.04	14.69	2.87	45.79	1.24E+30	1.21E+29	9.44E-02	4.72E-03	9.86E-04	1.00E-04
4XMM J163035.5-243417	ASASSN-V J163035.64-243419.0	M3.5V	0.88	12.66	4.92	13.20	1.41E+30	2.20E+28	1.14E-02	5.68E-04	4.06E-04	1.10E-05
4XMM J074943.5-461901	ASASSN-V J074943.50-461901.8	K5.5V	3.23	13.52	3.00	42.05	2.04E+30	6.52E+28	1.29E-01	6.45E-03	5.28E-04	7.48E-05
4XMM J084512.6-503318	ASASSN-V J084512.61-503318.2	K1V	3.41	13.87	2.05	35.61	9.06E+29	5.78E+28	2.44E-01	1.22E-02	7.30E-04	4.78E-05
4XMM J053540.6-043327	ASASSN-V J053540.70-043327.4	M0.5V	6.87	15.85	3.95	35.91	6.02E+29	4.26E+28	1.73E-01	8.64E-03	1.25E-03	9.52E-05
4XMM J205256.5+312051	ASASSN-V J205256.25+312052.4	K5V	9.33	15.09	2.99	147.09	8.81E+30	1.41E+30	4.07E-01	2.03E-02	8.93E-04	1.59E-04
4XMM J142912.0+474056	ASASSN-V J142912.15+474056.4	G9V	20.14	14.31	1.88	112.89	8.67E+30	5.28E+29	1.58E+00	7.91E-02	1.07E-03	7.98E-05
4XMM J064055.5+093721	ASASSN-V J064055.43+093723.7	K6.5V	1.90	15.71	3.28	74.03	4.07E+30	2.07E+29	6.56E-02	3.28E-03	2.70E-03	2.22E-04
4XMM J164858.4+344839	ASASSN-V J164858.55+344838.2	K1.5V	0.50	14.06	2.13	46.47	6.80E+29	4.46E+28	3.48E-02	1.74E-03	3.83E-04	2.59E-05
4XMM J053639.8+090715	ASASSN-V J053639.86+090716.4	K4V	0.77	12.36	2.69	39.62	6.51E+30	5.14E+29	3.64E-02	1.82E-03	8.85E-04	7.39E-05
4XMM J084756.7-785453	ASASSN-V J084756.73-785452.9	M3.5V	1.25	13.14	4.89	9.54	1.28E+30	1.89E+28	1.62E-02	8.08E-04	1.06E-03	2.06E-05
4XMM J063903.8+100038	ASASSN-V J063903.87+100037.1	K7V	1.47	15.87	3.36	72.35	1.60E+31	3.28E+29	4.95E-02	2.48E-03	2.78E-02	1.60E-03
4XMM J045635.3+543505	ASASSN-V J045635.17+543506.1	K5.5V	0.69	15.13	3.02	33.53	6.73E+29	6.41E+28	2.74E-02	1.37E-03	1.17E-03	1.16E-04
4XMM J173253.9-371214	ASASSN-V J173253.85-371209.9	K5.5V	1.38	11.82	3.02	13.06	1.32E+30	2.45E+28	5.52E-02	2.76E-03	7.01E-04	1.66E-05
4XMM J054310.7-083150	ASASSN-V J054310.72-083150.1	K6.5V	1.76	13.23	3.27	41.90	3.78E+30	7.20E+28	6.06E-02	3.03E-03	7.41E-04	2.62E-05
4XMM J064021.0+093631	ASASSN-V J064021.01+093632.0	K1V	1.48	13.42	2.05	70.20	8.04E+30	2.36E+29	1.06E-01	5.28E-03	1.31E-03	5.56E-05
4XMM J085513.4-453306	ASASSN-V J085513.40-453307.1	G0V	1.00	13.21	1.38	48.83	7.31E+29	6.57E+28	9.96E-02	4.98E-03	2.49E-04	2.30E-05
4XMM J150230.9-413229	ASASSN-V J150231.02-413228.1	G9V	5.19	14.61	1.90	38.75	3.90E+29	4.12E+28	4.07E-01	2.04E-02	5.29E-04	5.86E-05
4XMM J190037.0-245901	ASASSN-V J190036.94-245900.6	K4.5V	9.99	14.95	2.83	137.77	1.43E+31	1.42E+30	4.62E-01	2.31E-02	2.07E-03	3.51E-04

4XMM J034737.9+232805	ASASSN-V J034737.76+232805.2	K4.5V	8.33	13.67	2.82	13.75	1.23E+29	4.66E+27	3.85E-01	1.93E-02	3.78E-04	1.47E-05
4XMM J154038.2-342136	ASASSN-V J154038.22-342136.7	M3.5V	0.52	14.14	4.98	10.98	5.16E+29	1.24E+28	6.74E-03	3.37E-04	8.10E-04	2.98E-05
4XMM J104916.1+325313	ASASSN-V J104916.14+325313.6	K2V	2.64	14.08	2.13	37.93	1.14E+30	7.65E+28	1.77E-01	8.87E-03	9.66E-04	6.82E-05
4XMM J054111.0-093352	ASASSN-V J054111.07-093352.7	K7V	1.76	14.24	3.36	45.26	3.56E+30	8.54E+28	5.93E-02	2.97E-03	1.48E-03	6.23E-05
4XMM J113411.8-701940	ASASSN-V J113411.87-701939.1	K4V	3.15	14.16	2.67	29.04	4.01E+29	1.67E+28	1.50E-01	7.49E-03	4.51E-04	1.93E-05
4XMM J072856.0+333816	ASASSN-V J072856.11+333816.1	K2.5V	3.36	13.07	2.20	25.80	9.55E+29	2.62E+28	2.08E-01	1.04E-02	6.40E-04	2.11E-05
4XMM J080859.9-492258	ASASSN-V J080900.04-492257.8	K2V	2.69	13.05	2.18	37.26	2.28E+30	5.43E+28	1.80E-01	9.02E-03	7.95E-04	2.23E-05
4XMM J064132.0+100023	ASASSN-V J064132.00+100024.3	K3.5V	4.78	15.41	2.57	67.79	2.16E+30	2.59E+29	2.47E-01	1.24E-02	1.97E-03	2.57E-04
4XMM J005414.1-351713	ASASSN-V J005414.09-351712.6	K4V	3.40	13.74	2.68	20.38	4.73E+29	3.87E+28	1.62E-01	8.09E-03	7.55E-04	6.23E-05
4XMM J073129.6-465848	ASASSN-V J073129.63-465848.6	K4V	6.88	11.89	2.71	42.09	1.94E+31	3.27E+29	3.27E-01	1.63E-02	1.46E-03	3.52E-05
4XMM J053702.7-010508	ASASSN-V J053702.73-010507.5	K4V	2.57	13.04	2.70	36.26	2.12E+30	2.08E+29	1.22E-01	6.11E-03	8.70E-04	8.84E-05
4XMM J034351.2+321309	ASASSN-V J034351.24+321309.2	K6.5V	0.79	12.98	3.28	33.93	4.94E+30	9.70E+28	2.72E-02	1.36E-03	1.03E-03	4.18E-05
4XMM J171011.8+641204	ASASSN-V J171011.89+641204.4	K5V	3.71	13.32	2.98	83.03	2.51E+31	4.39E+29	1.62E-01	8.08E-03	1.54E-03	4.70E-05
4XMM J181859.7+143308	ASASSN-V J181859.92+143307.3	K2V	0.68	13.93	2.16	82.64	6.61E+30	5.73E+29	4.56E-02	2.28E-03	1.20E-03	1.17E-04
4XMM J042208.1+191520	ASASSN-V J042208.27+191521.8	M2V	5.12	12.91	4.22	3.58	1.30E+29	2.78E+27	1.02E-01	5.10E-03	1.09E-03	2.36E-05
4XMM J163433.0-575957	ASASSN-V J163433.26-575957.4	G3V	2.76	13.41	1.52	44.51	6.38E+29	5.14E+28	2.53E-01	1.26E-02	2.27E-04	1.90E-05
4XMM J080127.2-494021	ASASSN-V J080127.27-494021.5	K2.5V	0.88	13.30	2.25	42.28	1.84E+30	1.77E+29	5.45E-02	2.72E-03	6.40E-04	6.18E-05
4XMM J202321.6+380006	ASASSN-V J202321.70+380006.6	K5.5V	3.20	11.93	3.07	39.28	1.56E+31	2.84E+29	1.28E-01	6.40E-03	1.23E-03	3.42E-05
4XMM J172020.2-411106	ASASSN-V J172020.31-411107.6	K9V	16.17	14.32	3.55	90.86	1.06E+31	4.33E+29	4.71E-01	2.35E-02	8.46E-04	5.36E-05
4XMM J054133.1-012340	ASASSN-V J054133.22-012340.2	K4.5V	0.75	14.97	2.83	34.94	8.50E+29	7.14E+28	3.49E-02	1.74E-03	1.92E-03	1.66E-04
4XMM J064107.2+095830	ASASSN-V J064107.25+095831.1	K4.5V	2.59	15.40	2.87	70.71	2.24E+30	1.48E+29	1.20E-01	5.99E-03	1.63E-03	1.45E-04
4XMM J203255.6+440305	ASASSN-V J203255.70+440305.5	G9V	5.06	14.25	1.84	40.93	2.76E+29	3.91E+28	3.97E-01	1.99E-02	2.67E-04	3.80E-05
4XMM J053546.5-042612	ASASSN-V J053546.57-042612.7	K9V	9.00	14.96	3.57	39.31	1.11E+30	8.16E+28	2.62E-01	1.31E-02	1.14E-03	8.86E-05
4XMM J042318.2-275912	ASASSN-V J042318.14-275910.3	K6.5V	1.26	14.35	3.26	174.85	1.78E+31	2.48E+30	4.34E-02	2.17E-03	5.73E-04	4.48E-04
4XMM J133148.0-314059	ASASSN-V J133148.01-314059.0	K0V	11.06	14.23	1.93	140.17	4.40E+30	3.46E+29	8.23E-01	4.12E-02	3.83E-04	4.69E-05
4XMM J134955.0-132658	ASASSN-V J134955.00-132658.1	K3.5V	2.51	14.13	2.54	32.10	4.81E+29	3.05E+28	1.30E-01	6.49E-03	5.27E-04	3.57E-05
4XMM J192953.8+500240	ASASSN-V J192953.80+500240.8	K5V	3.19	15.22	2.89	153.64	8.16E+30	7.54E+29	1.39E-01	6.96E-03	8.32E-04	9.11E-05
4XMM J152436.5-381758	ASASSN-V J152436.33-381758.7	K4.5V	3.91	15.30	2.80	216.39	6.57E+30	8.49E+29	1.81E-01	9.04E-03	3.77E-04	8.83E-05
4XMM J075720.5-610417	ASASSN-V J075720.51-610417.1	K0.5V	9.96	12.84	1.97	61.47	3.67E+30	2.53E+29	7.31E-01	3.66E-02	3.77E-04	2.78E-05
4XMM J012106.0+195953	ASASSN-V J012106.02+195952.8	K3.5V	1.33	15.38	2.54	142.70	7.26E+30	1.26E+30	6.87E-02	3.43E-03	2.59E-03	5.32E-04
4XMM J044056.3-531412	ASASSN-V J044056.45-531413.1	G9V	5.92	13.48	1.86	168.96	1.50E+31	7.23E+29	4.64E-01	2.32E-02	4.15E-04	8.57E-05
4XMM J110430.0+360017	ASASSN-V J110430.09+360017.5	K2V	3.91	14.05	2.19	45.52	7.45E+29	6.50E+28	2.62E-01	1.31E-02	4.21E-04	3.94E-05
4XMM J122255.1-614442	ASASSN-V J122255.14-614441.0	G9V	21.83	14.38	1.90	180.49	1.11E+31	1.59E+30	1.71E+00	8.57E-02	5.57E-04	5.34E-04
4XMM J064031.5+094823	ASASSN-V J064031.60+094822.4	K3V	4.19	14.59	2.43	73.31	2.29E+29	5.13E+28	2.44E-01	1.22E-02	8.83E-05	2.04E-05
4XMM J160416.3+324042	ASASSN-V J160416.29+324041.8	K4V	6.73	15.49	2.77	75.77	1.55E+30	1.35E+29	3.20E-01	1.60E-02	8.97E-04	2.90E-04
4XMM J070419.2-112507	ASASSN-V J070419.26-112507.3	K2.5V	1.62	14.86	2.28	116.27	1.91E+31	5.99E+29	9.99E-02	5.00E-03	4.44E-03	4.15E-04
4XMM J030654.5-775740	ASASSN-V J030654.80-775740.6	K4.5V	3.18	15.36	2.78	141.89	5.57E+30	4.74E+29	1.47E-01	7.36E-03	7.64E-04	8.76E-05
4XMM J080550.2-281011	ASASSN-V J080550.32-281011.2	K4V	4.20	14.93	2.73	192.73	6.20E+30	1.08E+30	2.00E-01	9.98E-03	3.76E-04	8.00E-05
4XMM J035017.8-502950	ASASSN-V J035017.98-502949.8	K6.5V	0.42	14.42	3.26	25.28	4.67E+29	4.88E+28	1.45E-02	7.25E-04	6.74E-04	7.16E-05
4XMM J123018.2+211630	ASASSN-V J123018.12+211631.7	G3V	13.52	14.36	1.48	154.21	5.43E+30	6.25E+29	1.24E+00	6.20E-02	4.16E-04	6.64E-05
4XMM J020656.2-044905	ASASSN-V J020656.27-044906.1	G9V	6.01	14.83	1.87	62.00	3.28E+29	6.70E+28	4.71E-01	2.36E-02	2.99E-04	6.61E-05
4XMM J104814.0-583052	ASASSN-V J104814.19-583052.5	K3.5V	0.75	13.67	2.57	19.60	2.56E+29	2.07E+28	3.90E-02	1.95E-03	4.59E-04	3.71E-05
4XMM J173519.5-333532	ASASSN-V J173519.56-333530.1	G8V	0.79	11.72	1.75	43.06	9.32E+28	1.73E+28	6.57E-02	3.29E-03	7.84E-06	1.48E-06
4XMM J211836.5-072357	ASASSN-V J211836.61-072357.4	K2.5V	0.70	14.88	2.27	44.01	6.79E+29	4.17E+28	4.36E-02	2.18E-03	8.99E-04	6.22E-05
4XMM J070500.3-113742	ASASSN-V J070500.33-113741.8	K5V	1.27	15.47	2.94	111.65	3.54E+30	2.82E+29	5.53E-02	2.77E-03	1.10E-03	1.20E-04
4XMM J103908.9-051710	ASASSN-V J103908.89-051711.4	K4.5V	0.41	14.51	2.82	17.48	1.92E+29	1.96E+28	1.87E-02	9.38E-04	8.30E-04	8.53E-05
4XMM J004154.9+413332	ASASSN-V J004154.90+413332.3	K4V	7.71	15.81	2.76	164.18	9.22E+30	2.88E+29	3.66E-01	1.83E-02	1.82E-03	3.78E-04
4XMM J192240.3+612519	ASASSN-V J192240.49+612523.1	K0.5V	10.98	15.25	1.97	292.09	2.49E+31	4.22E+30	8.06E-01	4.03E-02	1.04E-03	2.18E-04
4XMM J140957.8-423321	ASASSN-V J140957.84-423321.6	K3.5V	3.74	11.81	2.53	14.21	1.11E+30	1.02E+29	1.94E-01	9.70E-03	6.59E-04	6.07E-05
4XMM J082129.7-393237	ASASSN-V J082129.57-393237.2	K1V	1.81	14.86	2.09	63.78	9.66E+29	2.09E+29	1.29E-01	6.48E-03	6.09E-04	1.32E-04
4XMM J091456.1-622039	ASASSN-V J091456.08-622039.2	K0.5V	1.89	15.25	1.98	50.72	7.35E+29	8.25E+28	1.39E-01	6.95E-03	1.04E-03	1.20E-04
4XMM J053632.9-012333	ASASSN-V J053633.01-012333.3	K5V	4.91	13.07	2.98	34.58	1.76E+30	1.65E+29	2.14E-01	1.07E-02	6.51E-04	6.38E-05
4XMM J114145.8+102158	ASASSN-V J114145.83+102159.8	K0V	6.59	13.42	1.93	98.92	7.80E+30	7.50E+29	4.90E-01	2.45E-02	6.77E-04	7.86E-05
4XMM J233446.6-532049	ASASSN-V J233446.42-532049.8	K0V	4.56	14.44	1.94	64.73	9.33E+29	1.68E+29	3.40E-01	1.70E-02	3.74E-04	6.82E-05

4XMM J053511.9-053154	ASASSN-V J053511.89-053155.3	M3V	3.07	13.88	4.54	39.70	2.07E+30	3.96E+28	4.98E-02	2.49E-03	3.22E-04	1.38E-05
4XMM J073340.2+314107	ASASSN-V J073340.10+314110.4	K3.5V	0.84	14.69	2.57	44.40	1.05E+30	2.41E+29	4.35E-02	2.17E-03	9.75E-04	2.25E-04
4XMM J225702.8-214445	ASASSN-V J225702.93-214445.0	K2.5V	8.79	14.16	2.25	31.66	1.77E+29	2.42E+28	5.44E-01	2.72E-02	2.19E-04	3.02E-05
4XMM J090659.6+052633	ASASSN-V J090659.71+052633.5	K5.5V	2.09	14.21	3.08	18.82	2.79E+29	1.85E+28	8.33E-02	4.17E-03	6.88E-04	4.68E-05
4XMM J180650.7-344448	ASASSN-V J180650.68-344449.2	K2.5V	5.63	13.60	2.31	82.81	1.12E+31	1.03E+30	3.48E-01	1.74E-02	1.21E-03	1.25E-04
4XMM J213711.9-205102	ASASSN-V J213711.91-205102.7	K4.5V	3.70	14.24	2.83	104.52	7.52E+30	7.52E+29	1.71E-01	8.55E-03	7.78E-04	1.01E-04
4XMM J054057.0-020001	ASASSN-V J054057.00-020001.2	K1.5V	12.58	12.00	2.11	36.92	5.31E+29	3.45E+28	8.77E-01	4.39E-02	9.02E-05	6.62E-06
4XMM J184219.9-321726	ASASSN-V J184219.90-321727.0	K2V	0.67	14.69	2.20	42.39	7.97E+29	1.36E+29	4.51E-02	2.26E-03	3.50E-03	6.06E-04
4XMM J220805.7+454806	ASASSN-V J220805.56+454805.3	K3.5V	0.79	14.66	2.56	43.83	1.08E+30	1.14E+29	4.10E-02	2.05E-03	1.04E-03	1.14E-04
4XMM J181420.9-574513	ASASSN-V J181421.11-574510.5	K3.5V	9.39	16.15	2.63	211.11	2.89E+30	7.53E+29	4.86E-01	2.43E-02	4.41E-04	1.99E-04
4XMM J090339.7-362055	ASASSN-V J090339.21-362055.9	K0V	11.18	14.07	1.94	34.97	1.77E+28	1.27E+28	8.32E-01	4.16E-02	2.02E-05	1.45E-05
4XMM J220446.5+024142	ASASSN-V J220446.53+024142.6	G8V	1.87	14.00	1.78	42.96	1.59E+30	2.48E+29	1.55E-01	7.75E-03	1.37E-03	2.18E-04
4XMM J180222.4-295757	ASASSN-V J180222.32-295759.4	K1.5V	11.07	13.19	2.13	86.38	2.63E+30	2.87E+29	7.72E-01	3.86E-02	1.92E-04	2.36E-05
4XMM J141103.5-424021	ASASSN-V J141103.51-424020.9	K1.5V	3.72	14.73	2.12	43.54	7.18E+29	9.02E+28	2.59E-01	1.30E-02	8.15E-04	1.07E-04
4XMM J163900.5-642333	ASASSN-V J163900.72-642332.1	K4.5V	21.43	15.11	2.81	187.07	6.57E+30	1.43E+30	9.91E-01	4.95E-02	4.12E-04	1.03E-04
4XMM J203449.9+382430	ASASSN-V J203449.99+382429.9	K5V	2.58	16.24	2.93	91.61	1.02E+30	1.52E+29	1.13E-01	5.63E-03	9.18E-04	1.48E-04
4XMM J233714.1+461538	ASASSN-V J233713.98+461539.3	K4V	0.91	14.21	2.69	45.08	1.11E+30	1.22E+29	4.34E-02	2.17E-03	7.13E-04	7.98E-05
4XMM J023000.7-042536	ASASSN-V J023000.79-042536.7	K8V	1.07	13.68	3.47	12.66	8.58E+29	1.59E+28	3.30E-02	1.65E-03	2.14E-03	6.68E-05
4XMM J090441.9-490746	ASASSN-V J090441.95-490748.0	G2V	3.33	13.77	1.48	46.27	4.74E+29	8.71E+28	3.10E-01	1.55E-02	2.37E-04	4.37E-05
4XMM J161845.8-592453	ASASSN-V J161845.87-592454.3	K4V	19.80	14.43	2.73	132.97	4.63E+30	1.06E+30	9.41E-01	4.70E-02	3.24E-04	7.84E-05
4XMM J075913.3-604024	ASASSN-V J075913.36-604023.6	G7V	4.20	13.54	1.70	40.97	1.21E+29	1.53E+28	3.59E-01	1.80E-02	5.62E-05	7.14E-06
4XMM J084622.8-503430	ASASSN-V J084622.74-503430.9	K5V	7.87	14.83	2.97	158.53	5.24E+30	1.14E+30	3.43E-01	1.72E-02	3.53E-04	8.19E-05
4XMM J162814.5+404615	ASASSN-V J162814.43+404614.2	K3.5V	1.20	14.82	2.59	37.60	5.61E+29	9.78E+28	6.21E-02	3.11E-03	8.09E-04	1.42E-04
4XMM J171449.4-392941	ASASSN-V J171449.47-392939.7	K2.5V	3.07	14.06	2.23	48.46	8.12E+29	6.31E+28	1.90E-01	9.50E-03	3.66E-04	3.14E-05
4XMM J190822.1-204458	ASASSN-V J190822.58-204500.2	K2V	5.48	14.11	2.18	174.79	1.08E+31	2.02E+30	3.68E-01	1.84E-02	5.21E-04	1.25E-04
4XMM J025805.9+125446	ASASSN-V J025806.02+125446.9	K5.5V	1.16	14.47	3.08	27.19	2.55E+29	2.85E+28	4.65E-02	2.33E-03	4.23E-04	4.84E-05
4XMM J115525.7-631403	ASASSN-V J115526.01-631403.9	K0.5V	3.42	13.19	1.96	65.17	1.05E+30	3.52E+29	2.51E-01	1.26E-02	1.34E-04	4.97E-05
4XMM J204608.2-312612	ASASSN-V J204608.37-312612.8	K4V	6.39	14.39	2.67	43.91	3.77E+29	6.16E+28	3.04E-01	1.52E-02	2.91E-04	6.80E-05
4XMM J190205.0+425637	ASASSN-V J190205.08+425637.2	K4V	4.14	15.69	2.68	242.26	1.61E+31	1.94E+30	1.97E-01	9.85E-03	1.12E-03	1.98E-04
4XMM J053338.5-242306	ASASSN-V J053338.63-242305.1	G8V	4.03	13.74	1.73	51.91	2.83E+29	5.91E+28	3.34E-01	1.67E-02	1.07E-04	2.25E-05
4XMM J053528.9+093521	ASASSN-V J053528.97+093520.9	K3.5V	15.31	14.73	2.56	40.77	2.79E+29	5.76E+28	7.93E-01	3.97E-02	3.45E-04	7.18E-05
4XMM J102333.8-471317	ASASSN-V J102333.90-471322.6	K4V	8.59	13.76	2.71	113.26	7.16E+30	9.57E+29	4.08E-01	2.04E-02	4.13E-04	5.89E-05
4XMM J221444.5-005114	ASASSN-V J221444.42-005113.9	K4.5V	14.95	15.53	2.78	144.86	9.89E+30	1.78E+30	6.91E-01	3.45E-02	4.35E-03	1.10E-03
4XMM J073402.0+435149	ASASSN-V J073402.45+435151.6	K0.5V	1.57	14.29	1.98	44.01	4.14E+30	4.02E+29	1.15E-01	5.75E-03	3.13E-03	3.13E-04
4XMM J104256.9-690708	ASASSN-V J104256.71-690707.6	K5V	3.16	14.10	2.88	41.54	2.29E+30	2.15E+29	1.37E-01	6.88E-03	1.09E-03	1.03E-04
4XMM J151903.1+062533	ASASSN-V J151903.04+062534.5	K2.5V	5.14	14.09	2.26	41.25	4.91E+29	1.32E+29	3.18E-01	1.59E-02	3.48E-04	9.37E-05
4XMM J214254.9+434151	ASASSN-V J214254.89+434150.9	K7V	7.20	14.89	3.32	160.23	7.03E+30	5.74E+29	2.43E-01	1.21E-02	4.08E-04	4.54E-05
4XMM J053631.4-064114	ASASSN-V J053631.52-064113.5	M0.5V	8.72	16.05	3.91	37.84	5.08E+29	5.52E+28	2.19E-01	1.09E-02	1.09E-03	1.27E-04
4XMM J063720.3-192418	ASASSN-V J063720.36-192416.3	K6.5V	0.31	13.61	3.24	22.09	3.94E+29	8.20E+28	1.06E-02	5.30E-04	3.70E-04	7.71E-05
4XMM J033046.8+435159	ASASSN-V J033046.92+435157.6	K5V	5.22	15.08	2.98	266.72	4.23E+31	4.35E+30	2.27E-01	1.14E-02	1.19E-03	3.12E-04
4XMM J121106.1+671449	ASASSN-V J121106.38+671456.2	K1.5V	24.00	14.15	2.09	142.47	5.58E+30	1.84E+30	1.67E+00	8.37E-02	3.38E-04	1.13E-04

Appendix B

Light curves of all near contact red giant eclipsing binary candidates

This appendix contains the phase-folded and unfolded SuperWASP and ASAS-SN light curves for all 27 near contact red giant eclipsing binary candidates, where available.

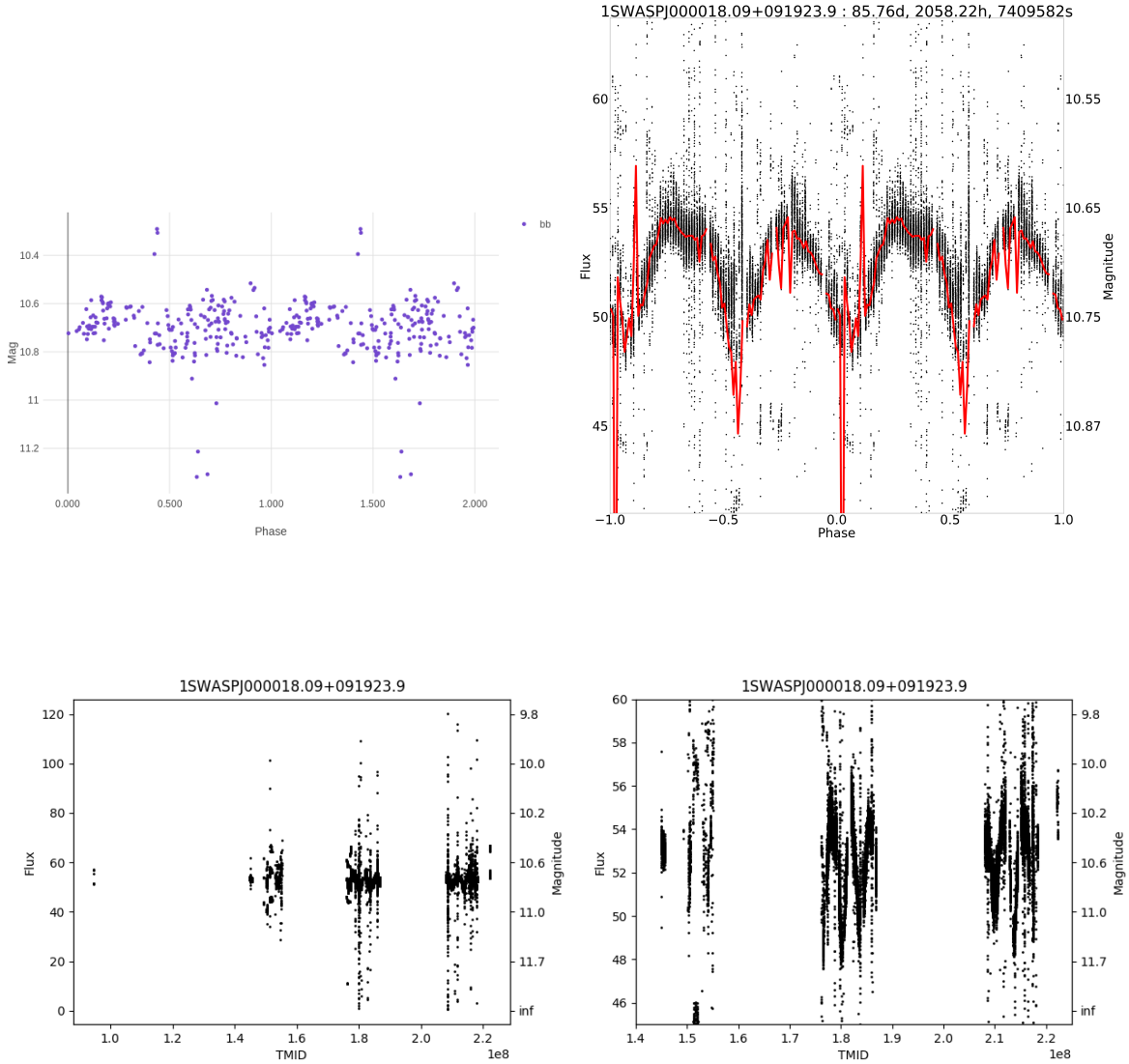

Fig. B.1 Phase-folded light curves for J000018. **Top left:** phase-folded ASAS-SN; **top right:** phase-folded SuperWASP; **bottom left:** unfolded SuperWASP; **bottom right:** zoom in of unfolded SuperWASP.

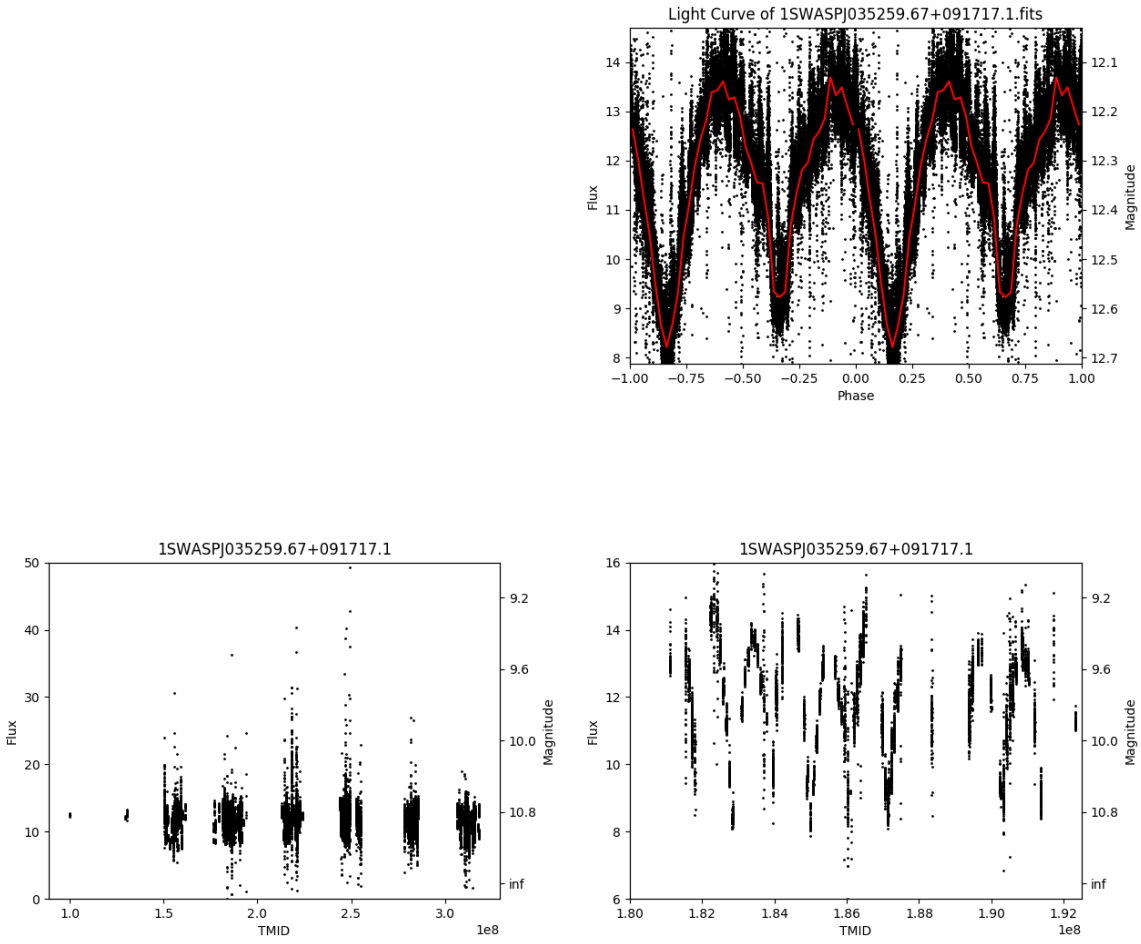

Fig. B.2 Phase-folded light curves for J000927. **top right:** phase-folded SuperWASP; **bottom left:** unfolded SuperWASP; **bottom right:** zoom in of unfolded SuperWASP.

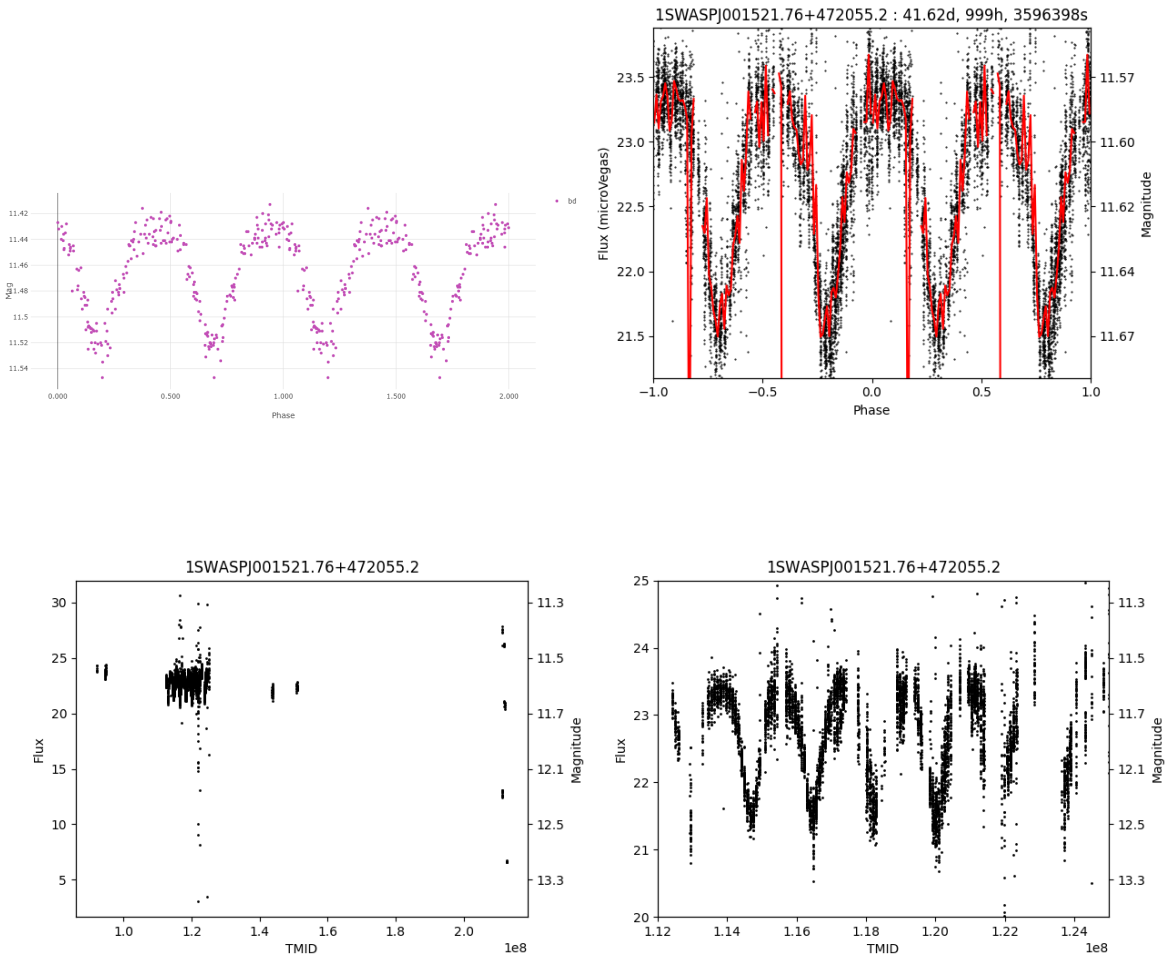

Fig. B.3 Phase-folded light curves for J001521. **Top left:** phase-folded ASAS-SN; **top right:** phase-folded SuperWASP; **bottom left:** unfolded SuperWASP; **bottom right:** zoom in of unfolded SuperWASP.

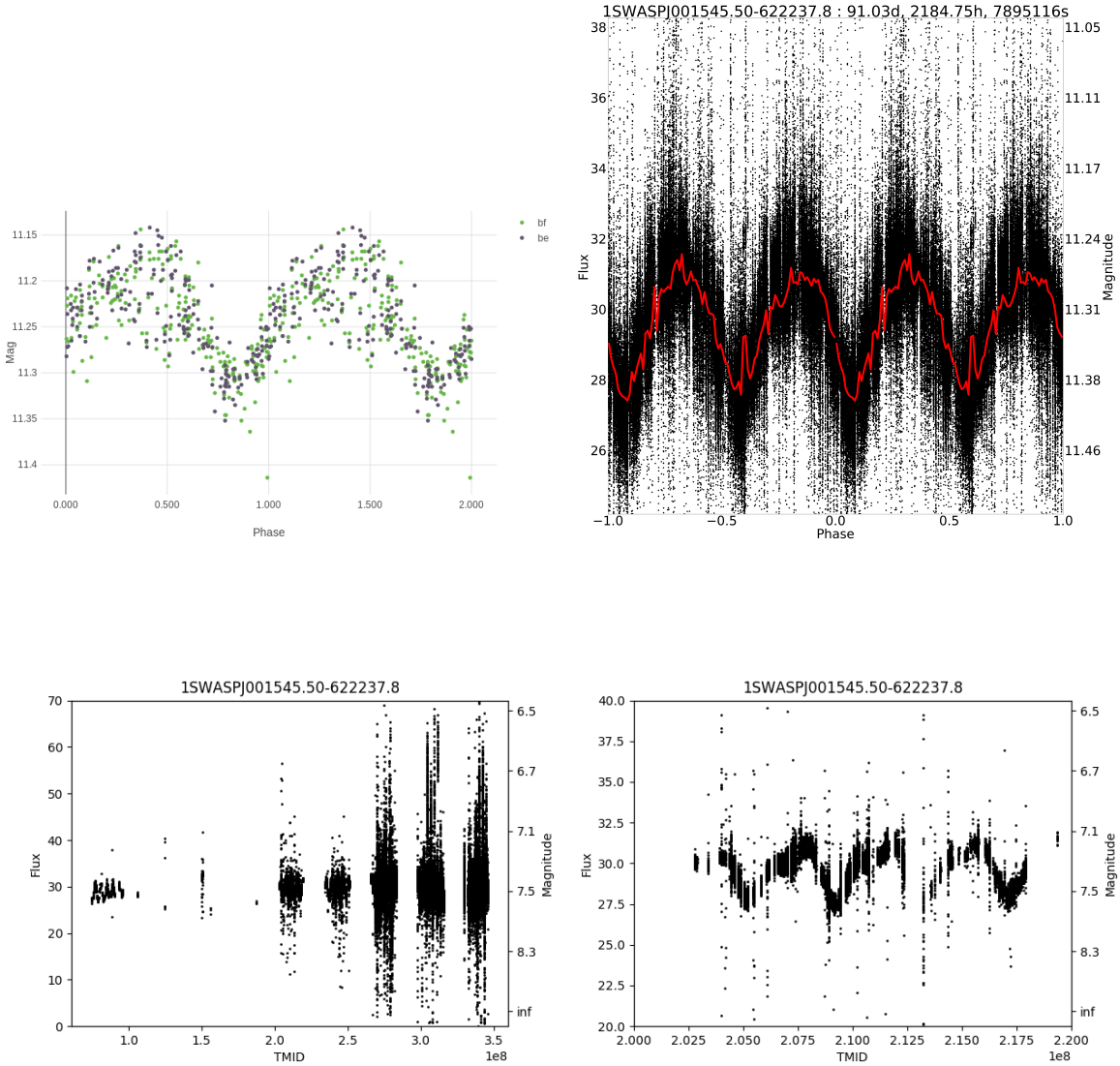

Fig. B.4 Phase-folded light curves for J001545. **Top left:** phase-folded ASAS-SN; **top right:** phase-folded SuperWASP; **bottom left:** unfolded SuperWASP; **bottom right:** zoom in of unfolded SuperWASP.

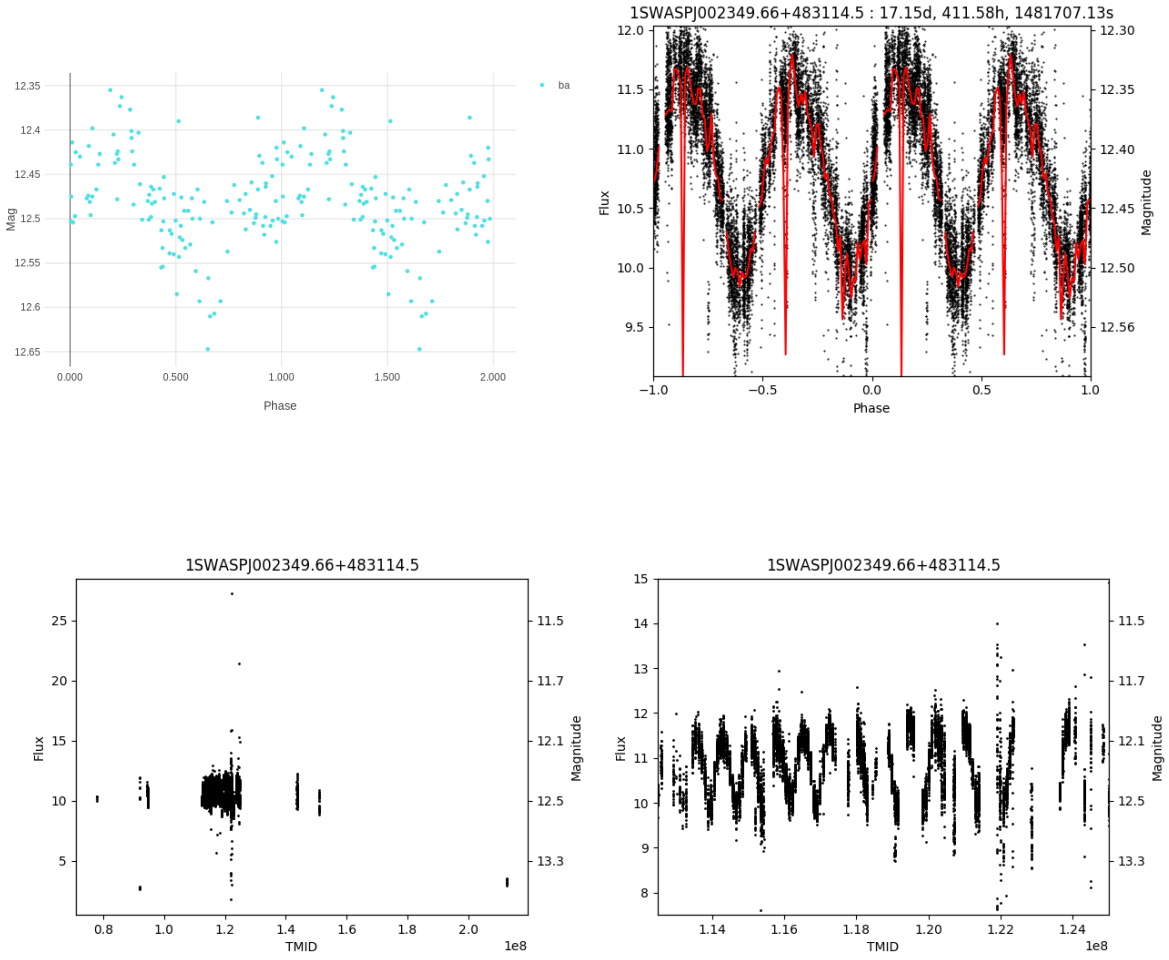

Fig. B.5 Phase-folded light curves for J002349. **Top left:** phase-folded ASAS-SN; **top right:** phase-folded SuperWASP; **bottom left:** unfolded SuperWASP; **bottom right:** zoom in of unfolded SuperWASP.

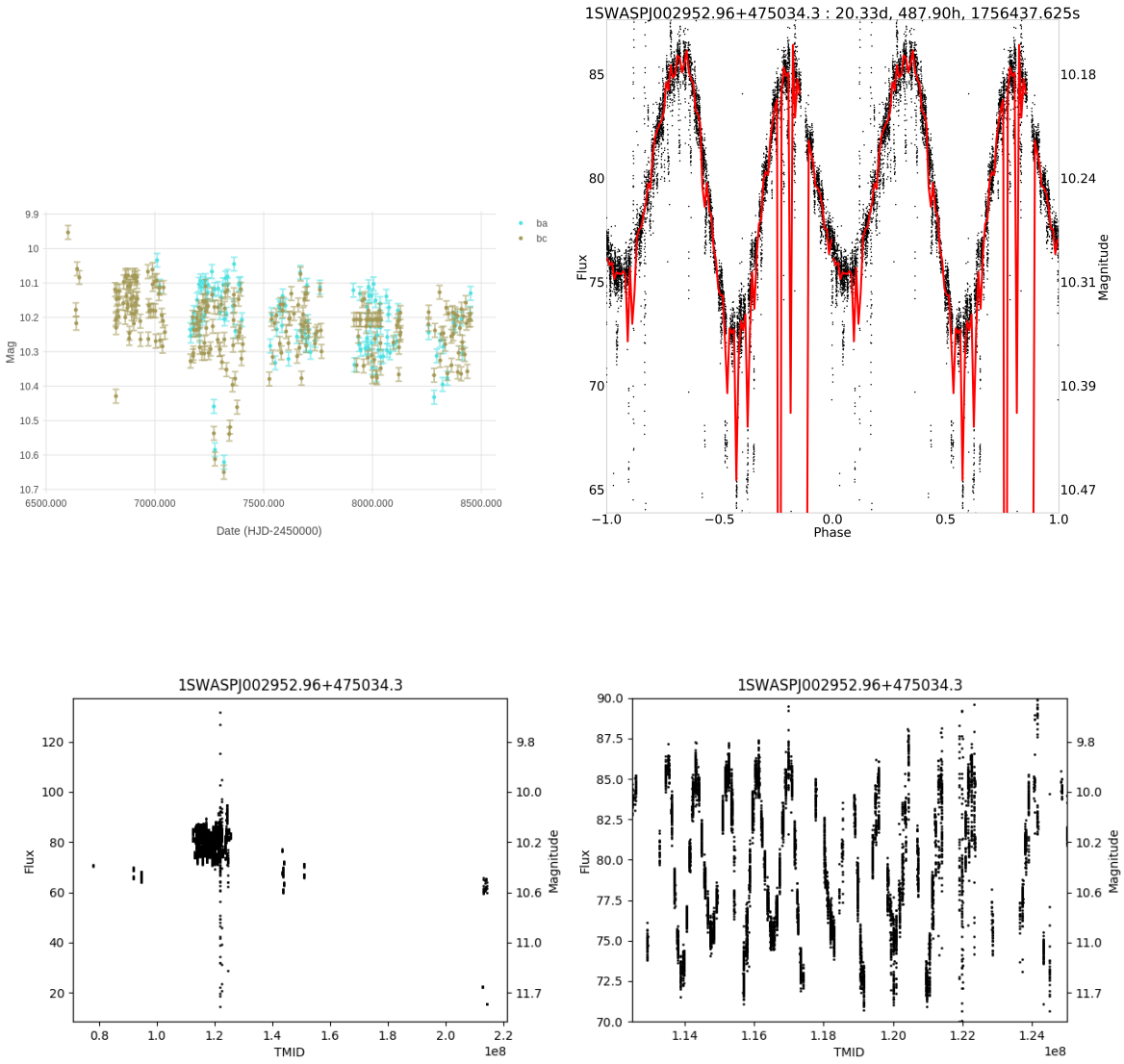

Fig. B.6 Phase-folded light curves for J002952. **Top left:** phase-folded ASAS-SN; **top right:** phase-folded SuperWASP; **bottom left:** unfolded SuperWASP; **bottom right:** zoom in of unfolded SuperWASP.

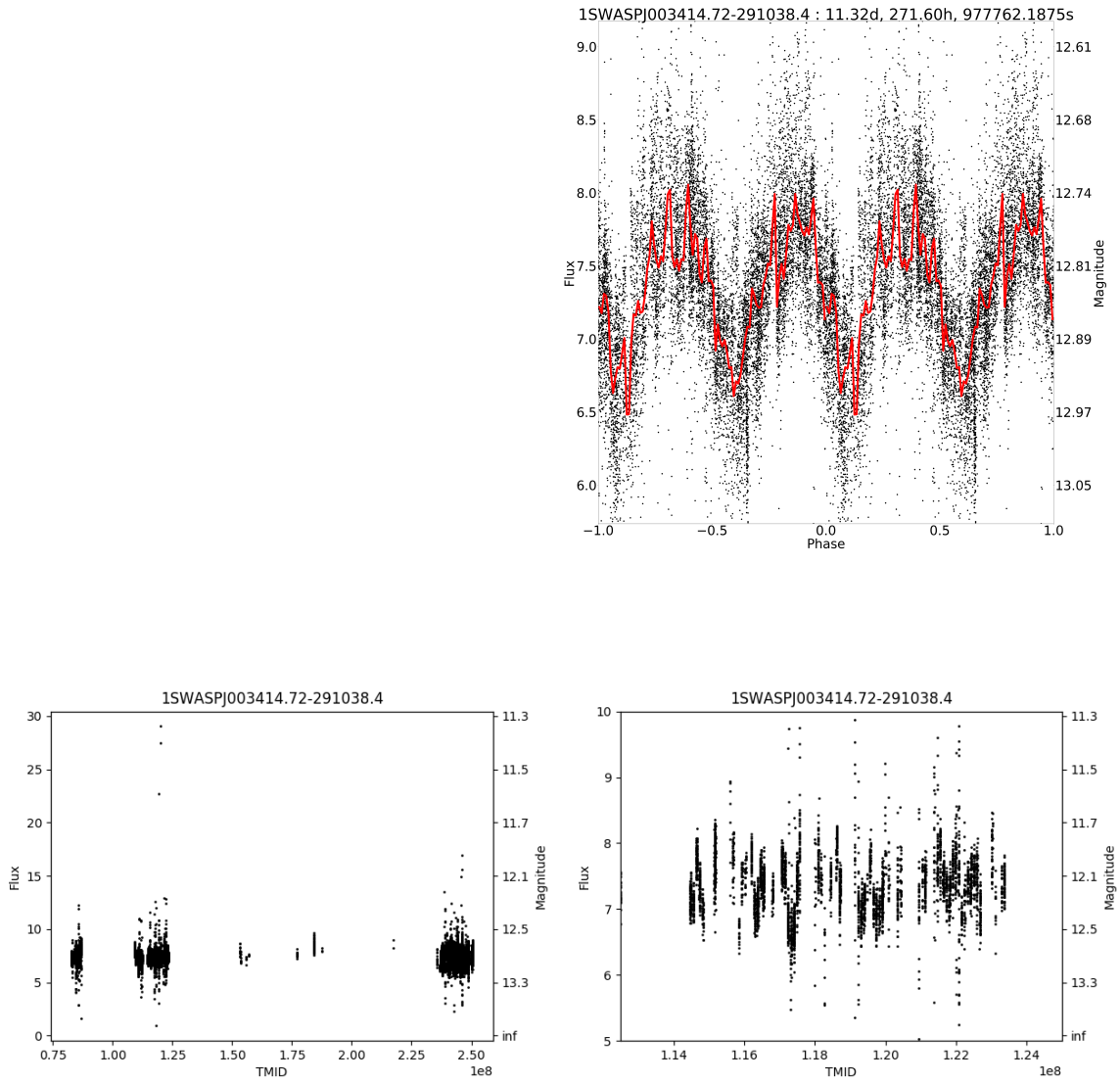

Fig. B.7 Phase-folded light curves for J003414. **top right:** phase-folded SuperWASP; **bottom left:** unfolded SuperWASP; **bottom right:** zoom in of unfolded SuperWASP.

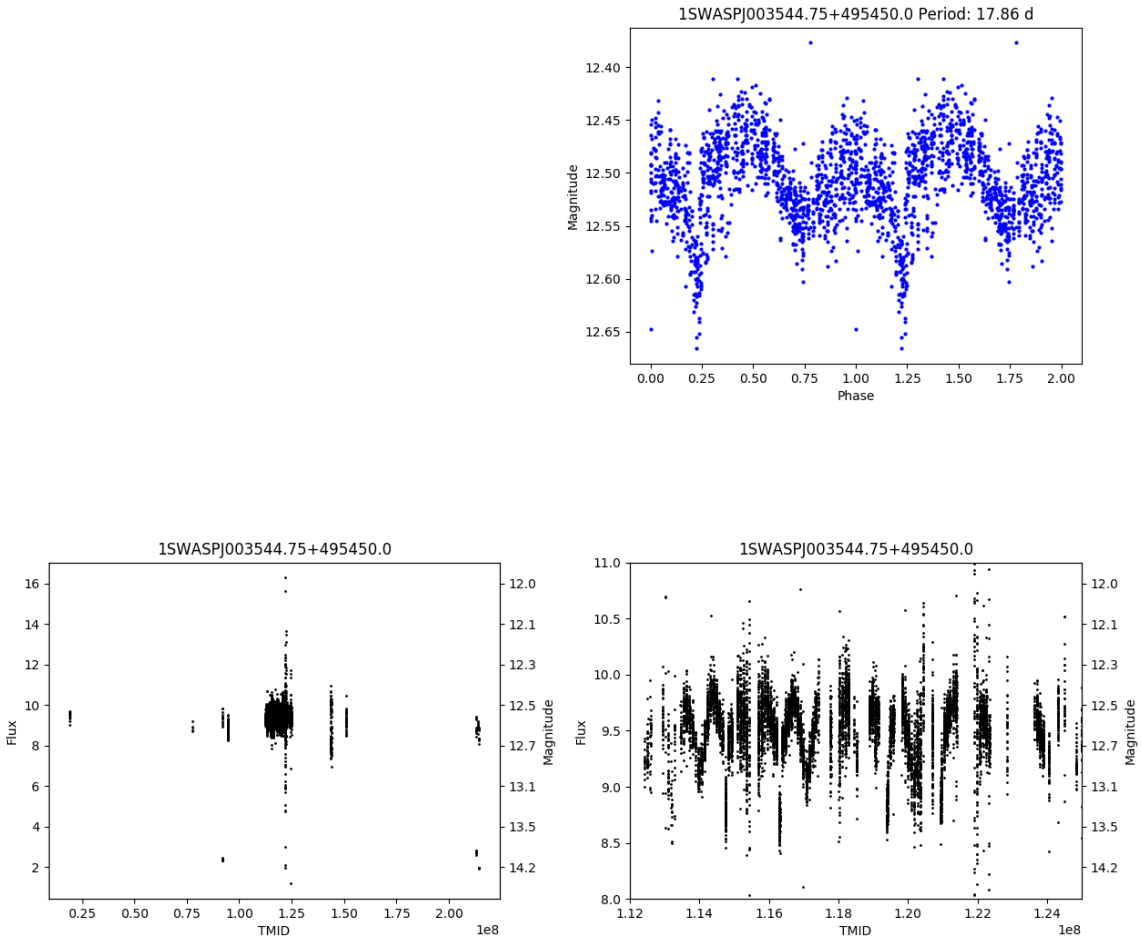

Fig. B.8 Phase-folded light curves for J003544. **top right:** phase-folded SuperWASP; **bottom left:** unfolded SuperWASP; **bottom right:** zoom in of unfolded SuperWASP.

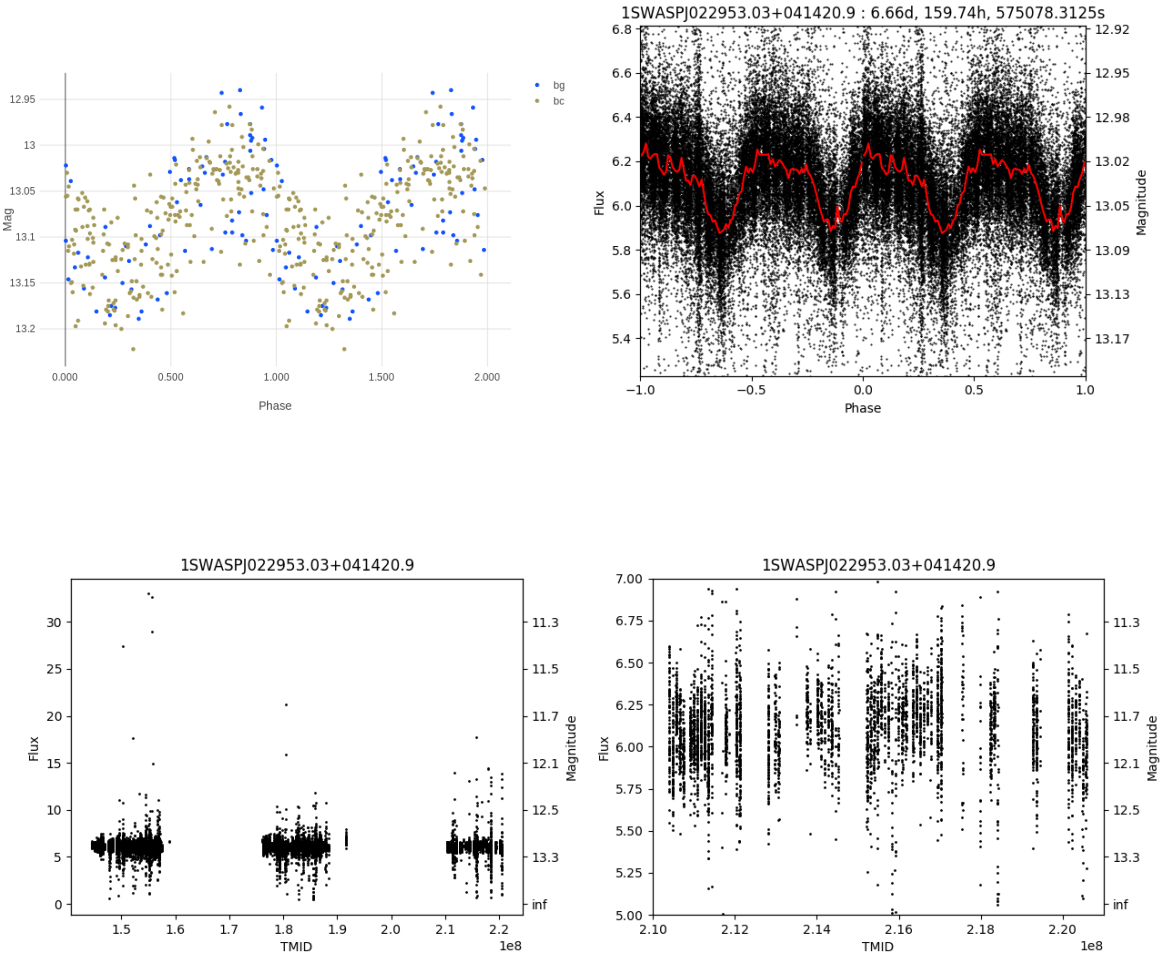

Fig. B.9 Phase-folded light curves for J022953. **Top left:** phase-folded ASAS-SN; **top right:** phase-folded SuperWASP; **bottom left:** unfolded SuperWASP; **bottom right:** zoom in of unfolded SuperWASP.

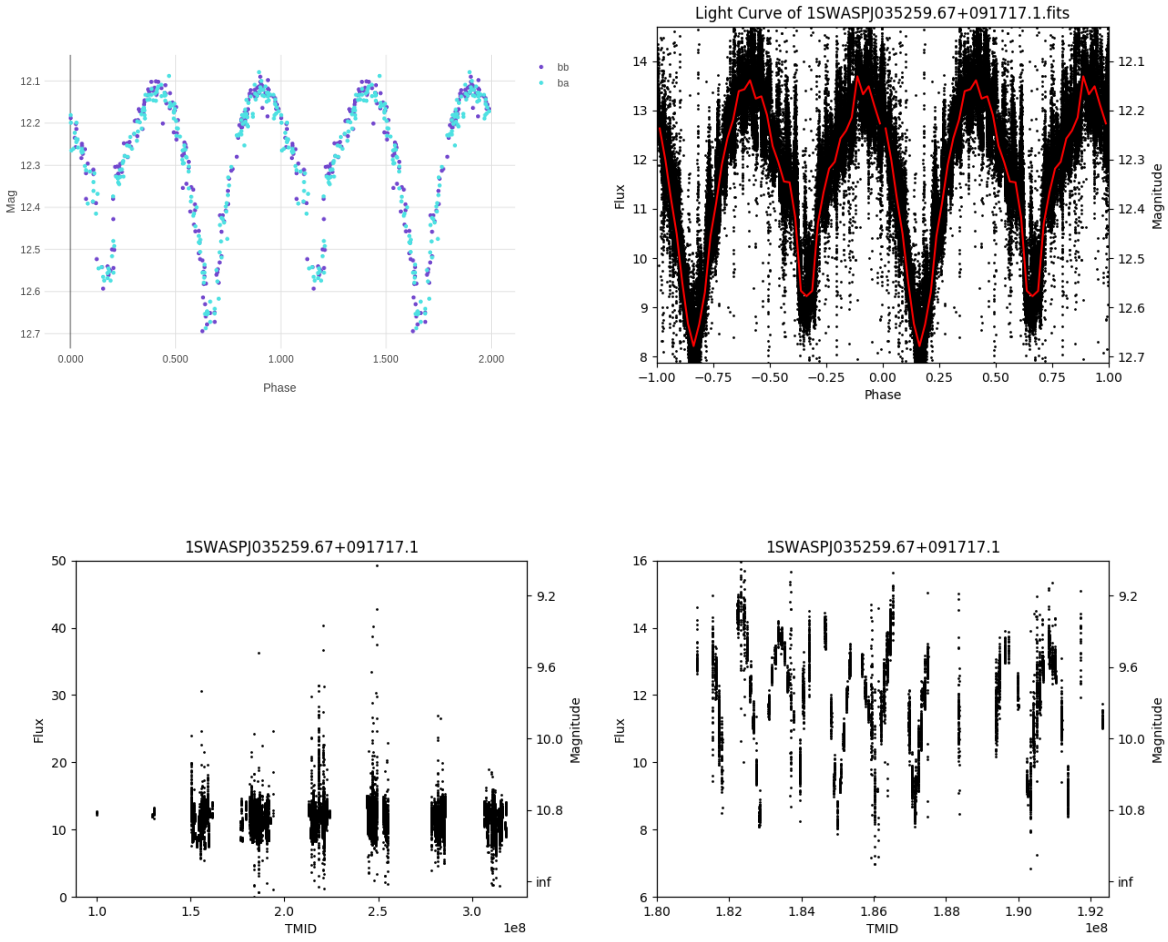

Fig. B.10 Phase-folded light curves for J035259. **Top left:** phase-folded ASAS-SN; **top right:** phase-folded SuperWASP; **bottom left:** unfolded SuperWASP; **bottom right:** zoom in of unfolded SuperWASP.

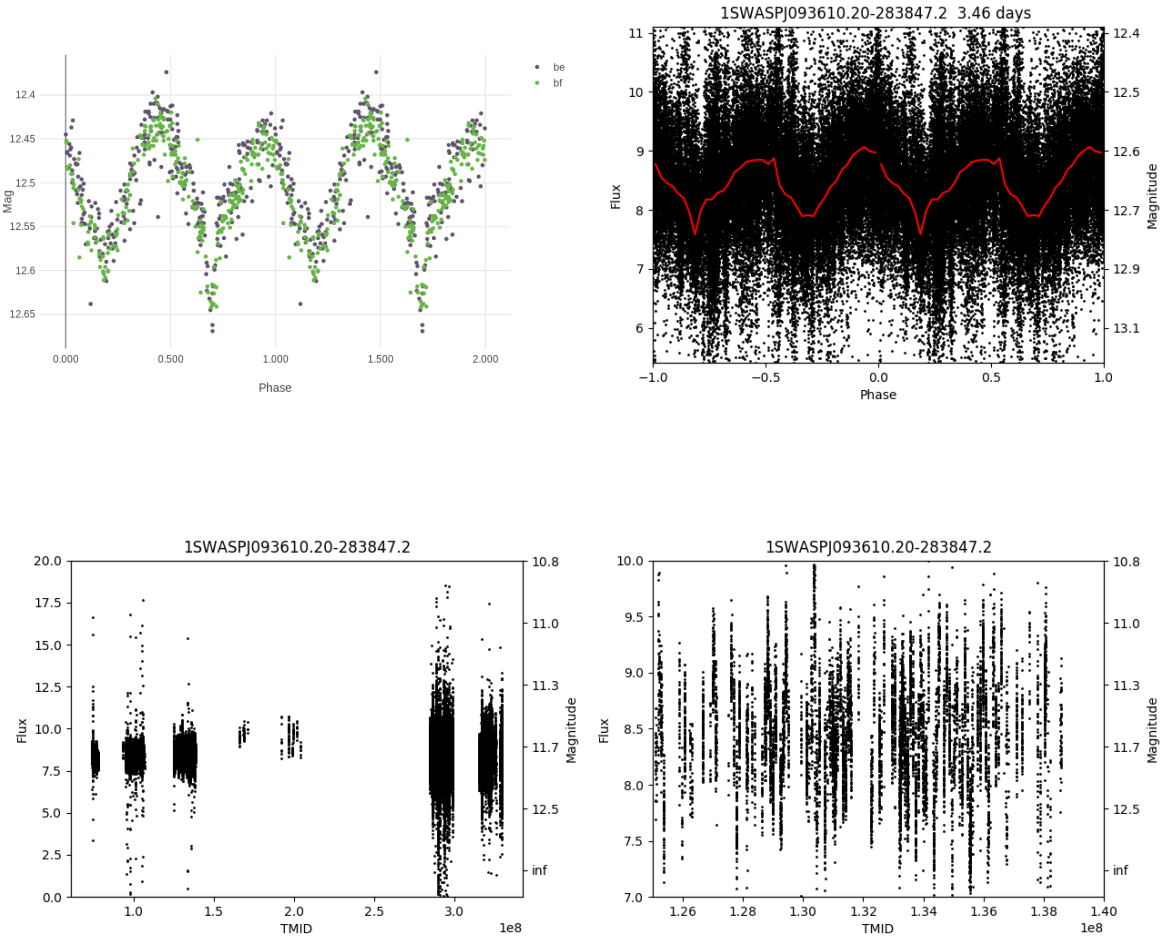

Fig. B.11 Phase-folded light curves for J093610. **Top left:** phase-folded ASAS-SN; **top right:** phase-folded SuperWASP; **bottom left:** unfolded SuperWASP; **bottom right:** zoom in of unfolded SuperWASP.

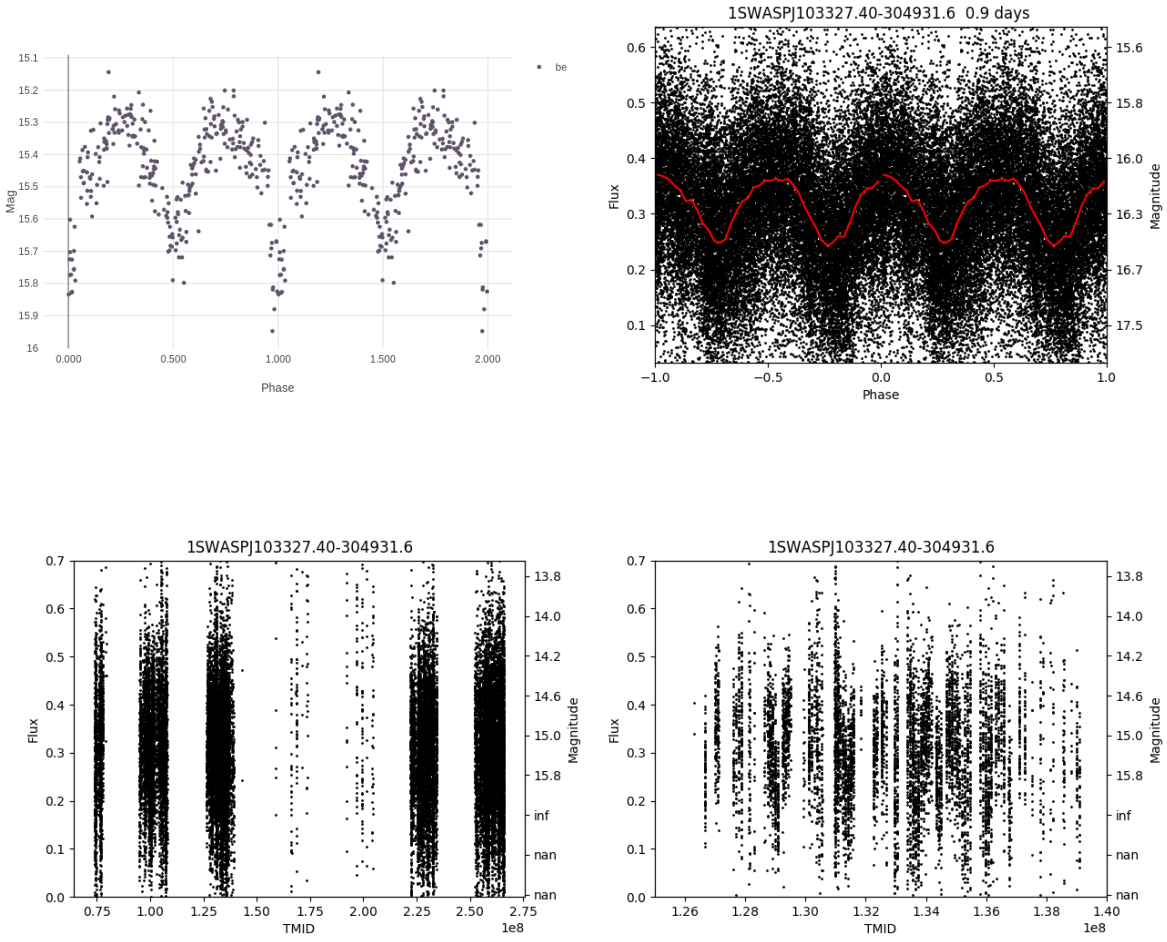

Fig. B.12 Phase-folded light curves for J103327. **Top left:** phase-folded ASAS-SN; **top right:** phase-folded SuperWASP; **bottom left:** unfolded SuperWASP; **bottom right:** zoom in of unfolded SuperWASP.

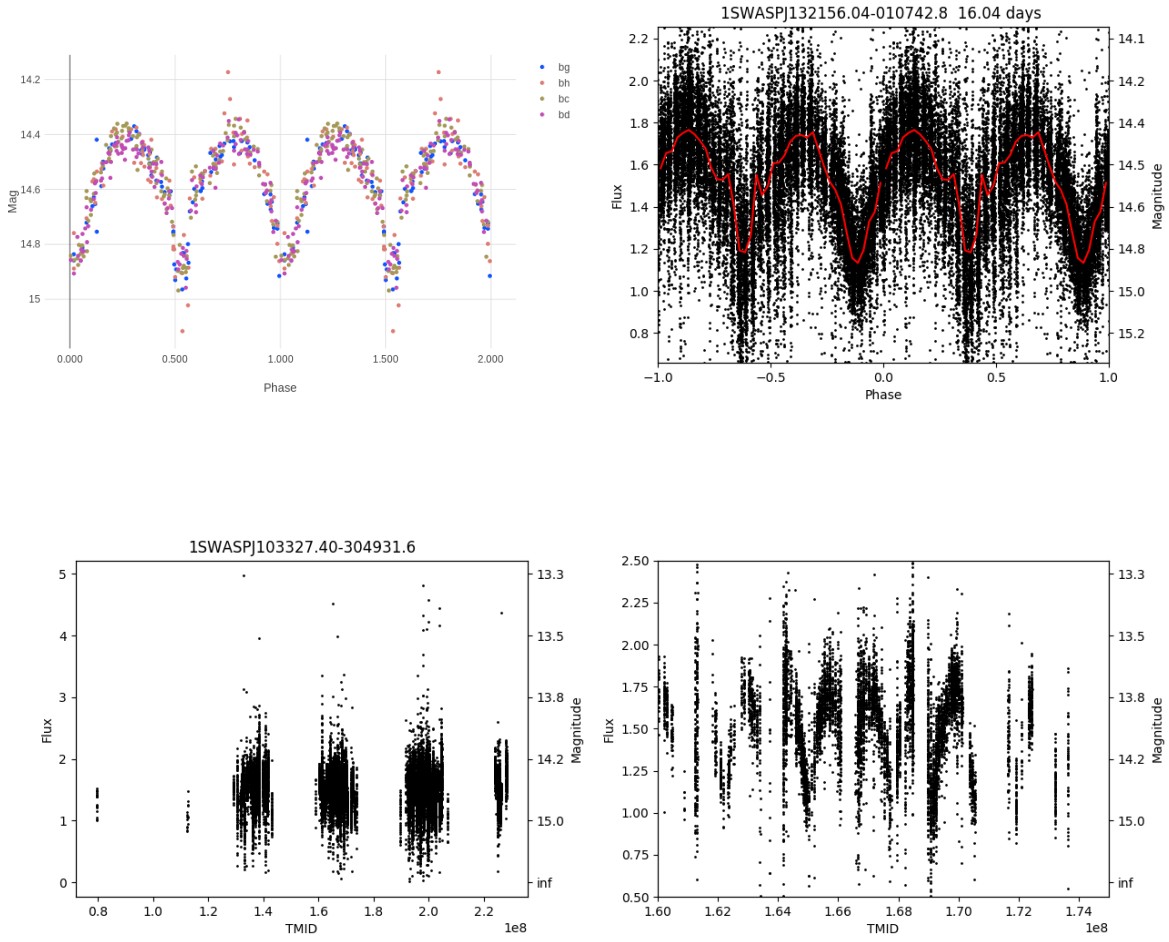

Fig. B.13 Phase-folded light curves for J132156. **Top left:** phase-folded ASAS-SN; **top right:** phase-folded SuperWASP; **bottom left:** unfolded SuperWASP; **bottom right:** zoom in of unfolded SuperWASP.

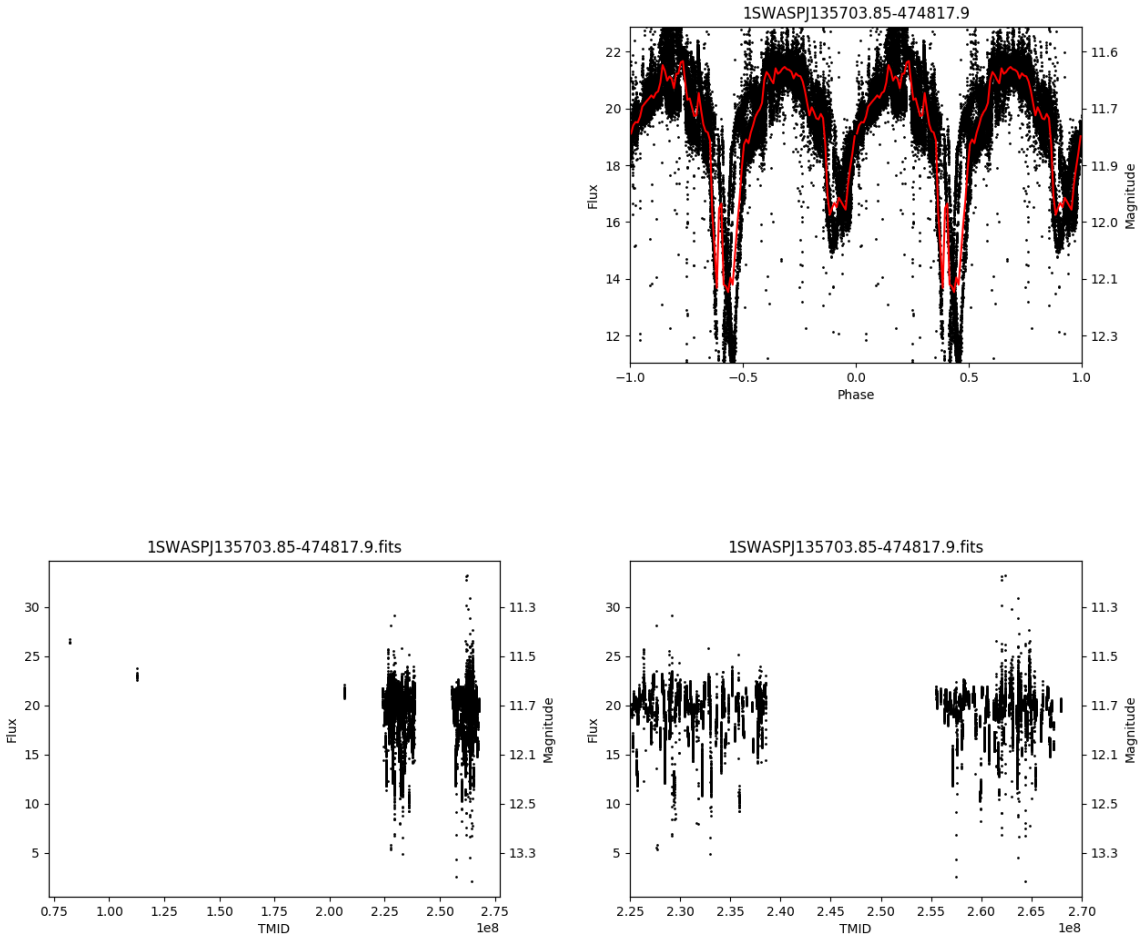

Fig. B.14 Phase-folded light curves for J135703. **Top left:** phase-folded ASAS-SN; **top right:** phase-folded SuperWASP; **bottom left:** unfolded SuperWASP; **bottom right:** zoom in of unfolded SuperWASP.

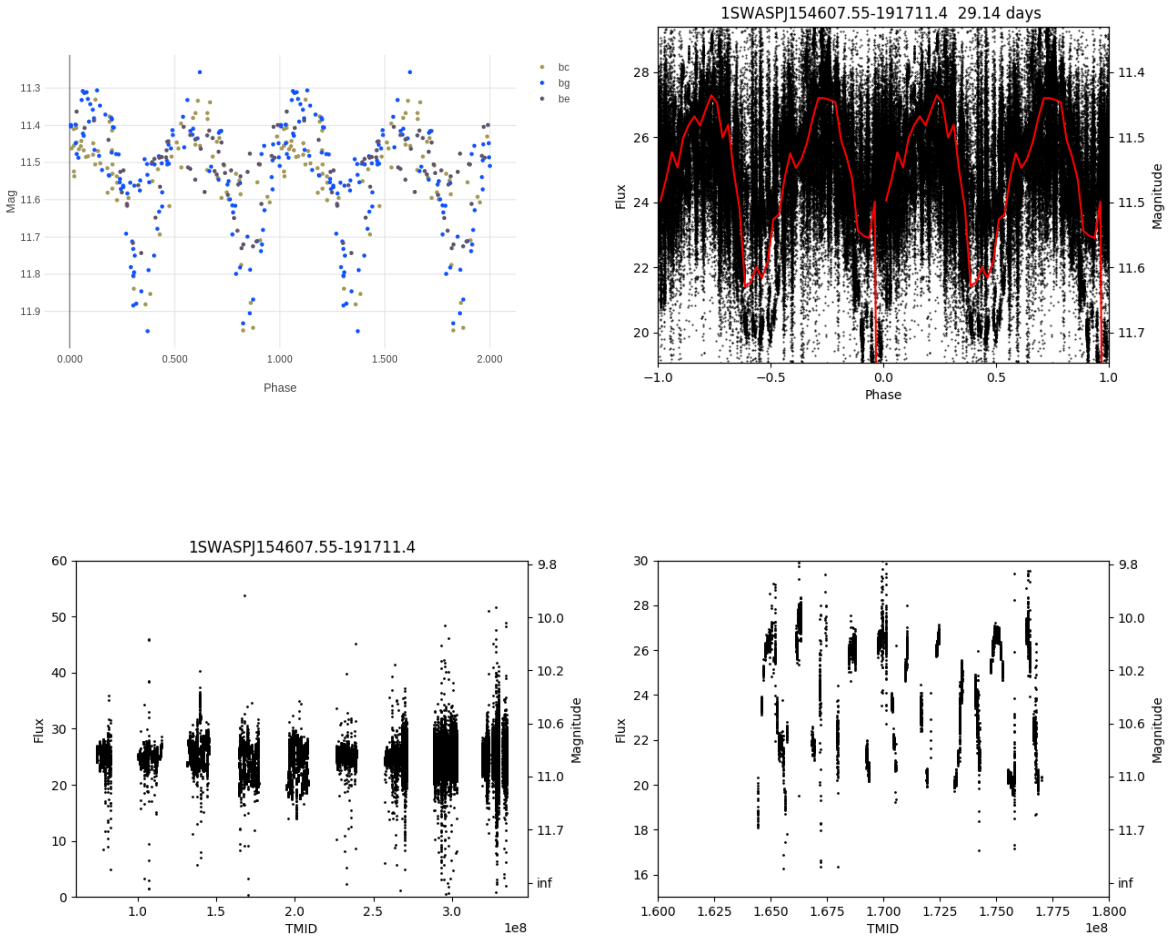

Fig. B.15 Phase-folded light curves for J154607. **Top left:** phase-folded ASAS-SN; **top right:** phase-folded SuperWASP; **bottom left:** unfolded SuperWASP; **bottom right:** zoom in of unfolded SuperWASP.

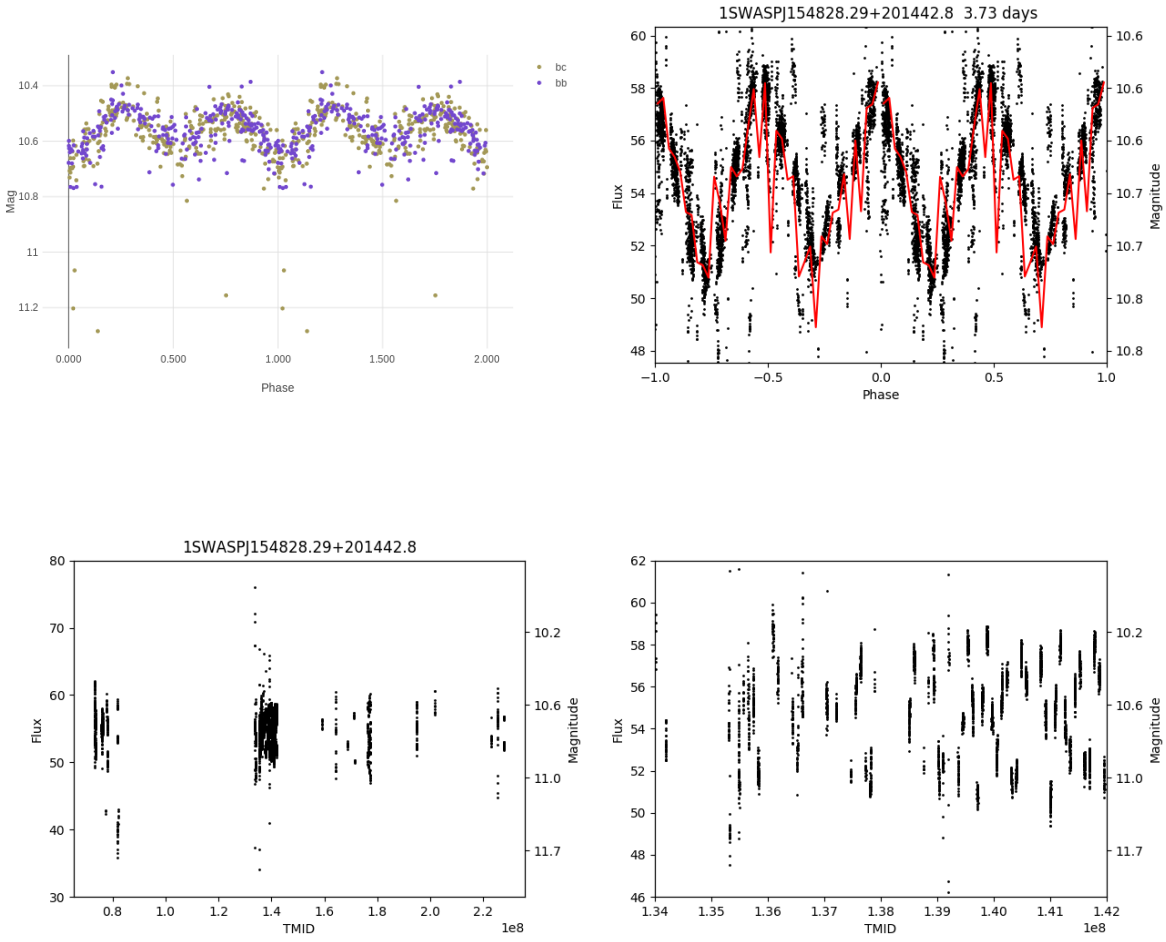

Fig. B.16 Phase-folded light curves for J154828. **Top left:** phase-folded ASAS-SN; **top right:** phase-folded SuperWASP; **bottom left:** unfolded SuperWASP; **bottom right:** zoom in of unfolded SuperWASP.

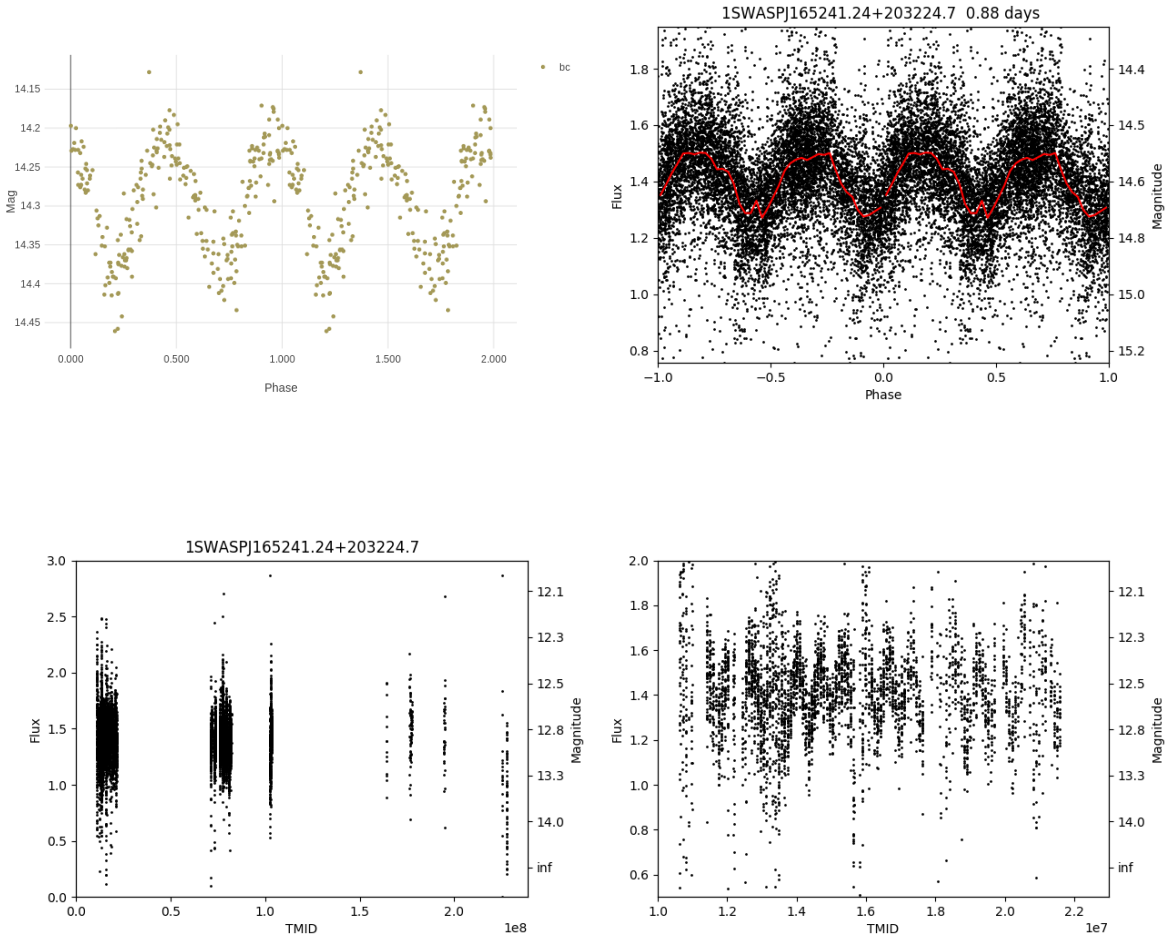

Fig. B.17 Phase-folded light curves for J165241. **Top left:** phase-folded ASAS-SN; **top right:** phase-folded SuperWASP; **bottom left:** unfolded SuperWASP; **bottom right:** zoom in of unfolded SuperWASP.

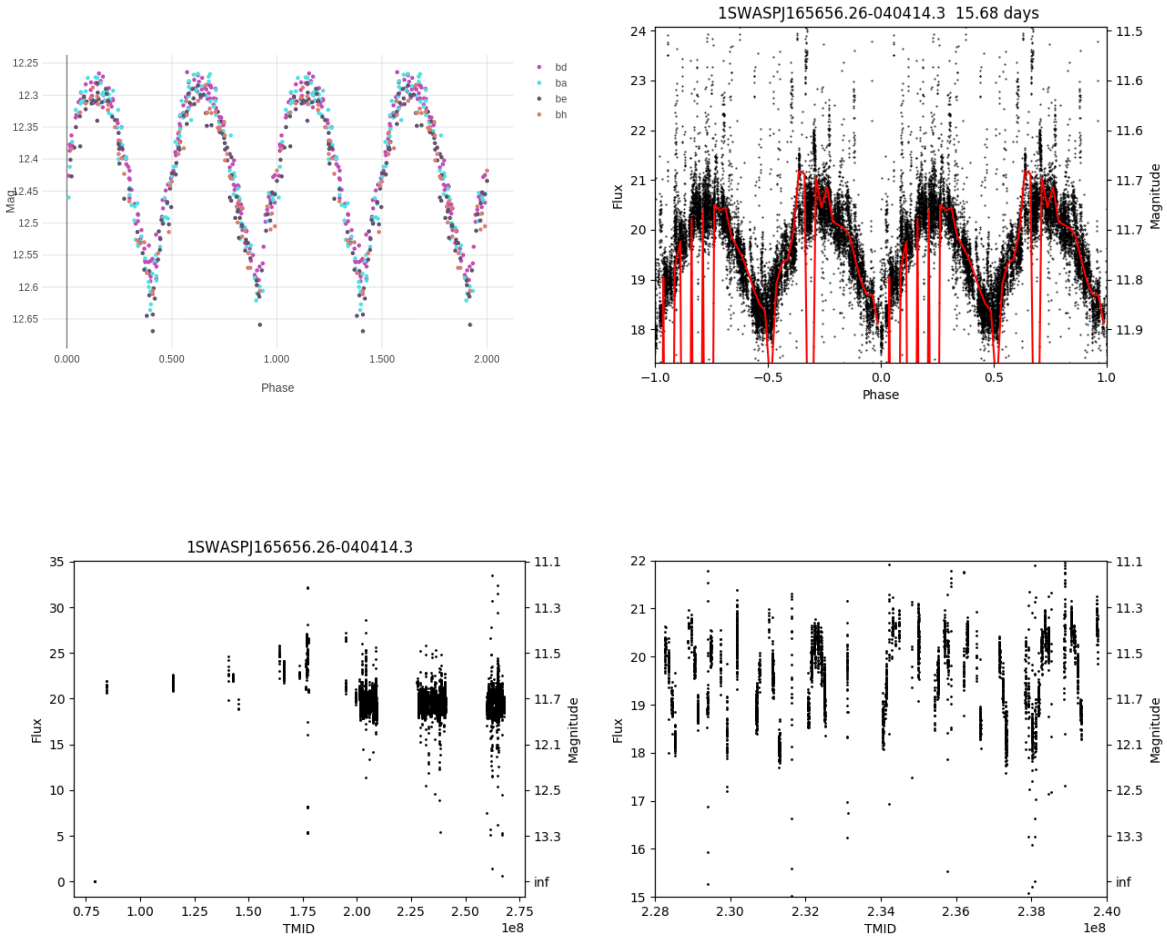

Fig. B.18 Phase-folded light curves for J165656. **Top left:** phase-folded ASAS-SN; **top right:** phase-folded SuperWASP; **bottom left:** unfolded SuperWASP; **bottom right:** zoom in of unfolded SuperWASP.

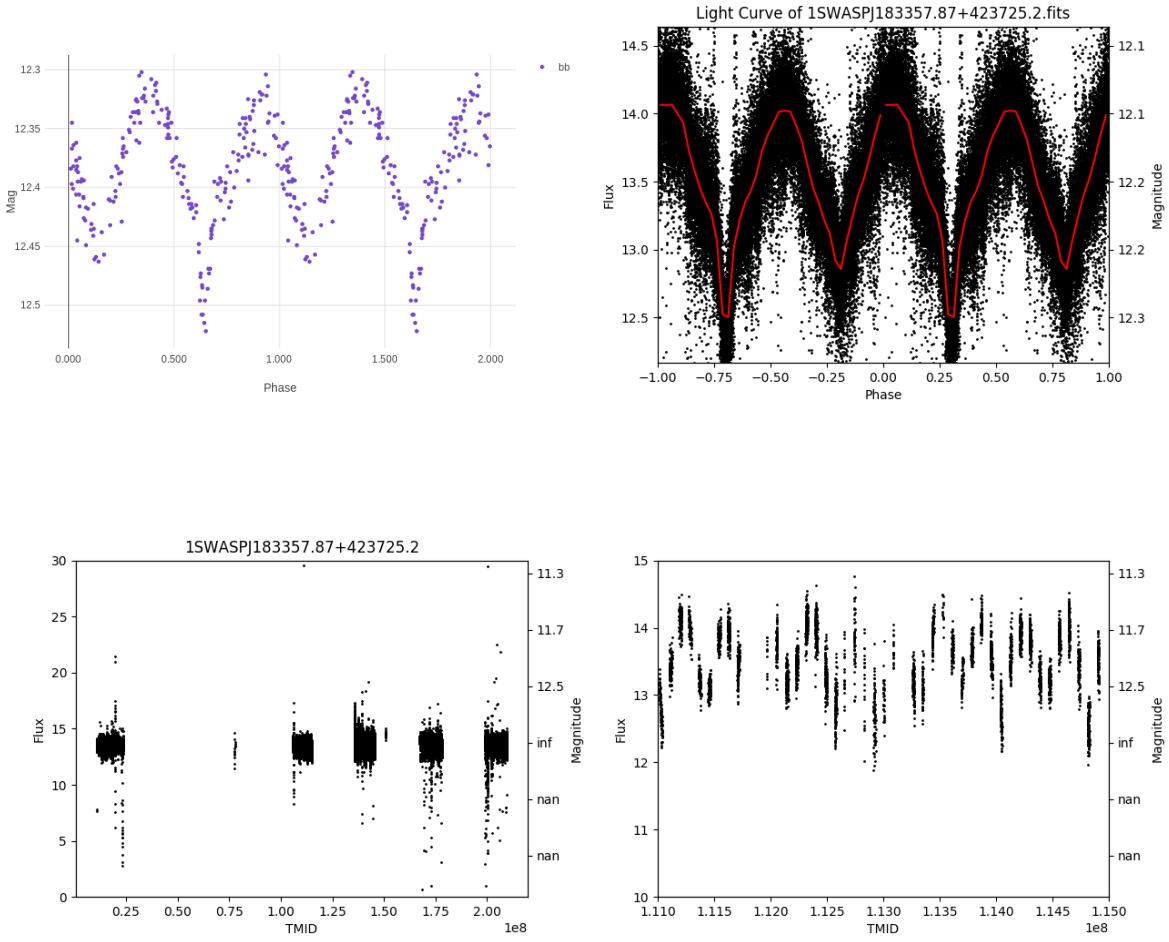

Fig. B.19 Phase-folded light curves for J183357. **Top left:** phase-folded ASAS-SN; **top right:** phase-folded SuperWASP; **bottom left:** unfolded SuperWASP; **bottom right:** zoom in of unfolded SuperWASP.

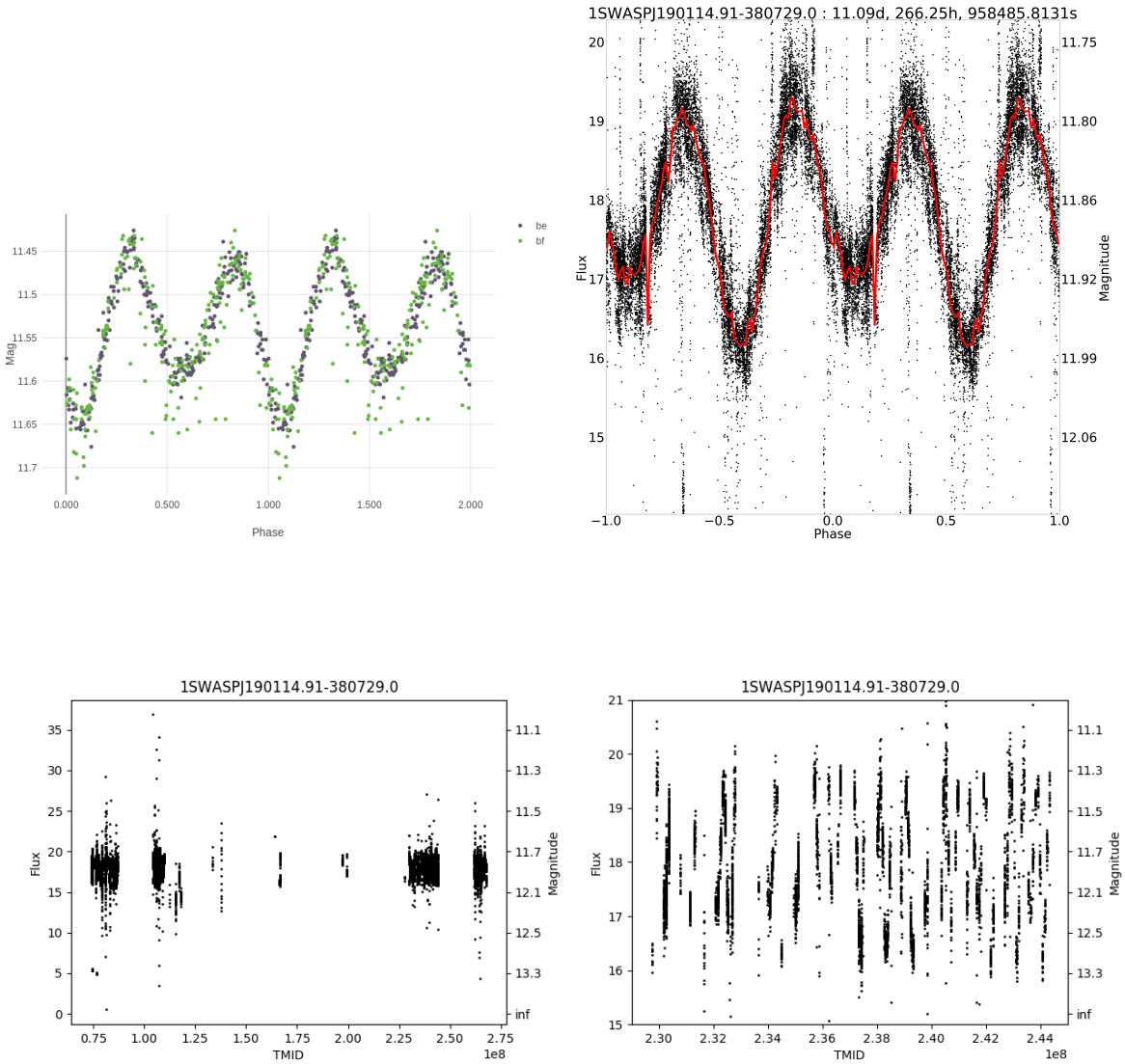

Fig. B.20 Phase-folded light curves for J190114. **Top left:** phase-folded ASAS-SN; **top right:** phase-folded SuperWASP; **bottom left:** unfolded SuperWASP; **bottom right:** zoom in of unfolded SuperWASP.

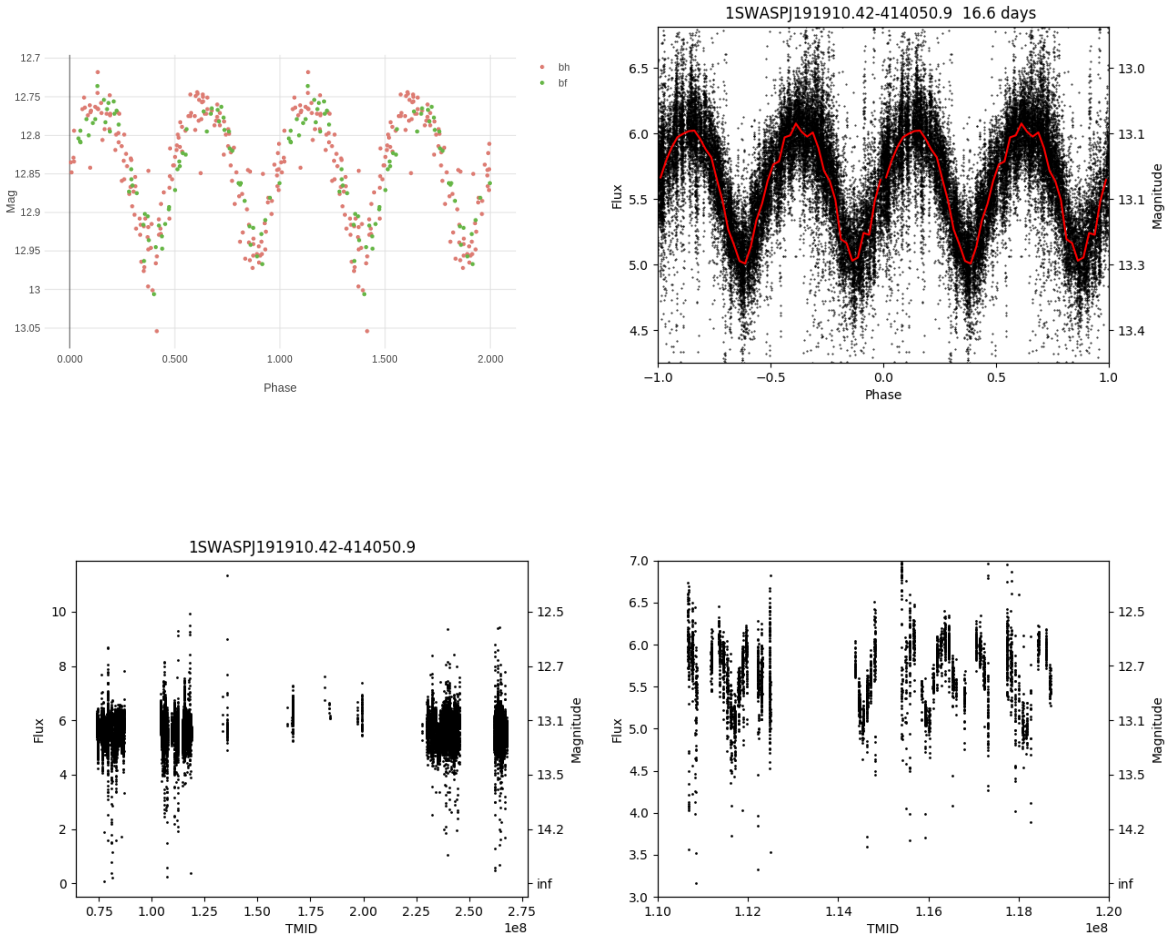

Fig. B.21 Phase-folded light curves for J191910. **Top left:** phase-folded ASAS-SN; **top right:** phase-folded SuperWASP; **bottom left:** unfolded SuperWASP; **bottom right:** zoom in of unfolded SuperWASP.

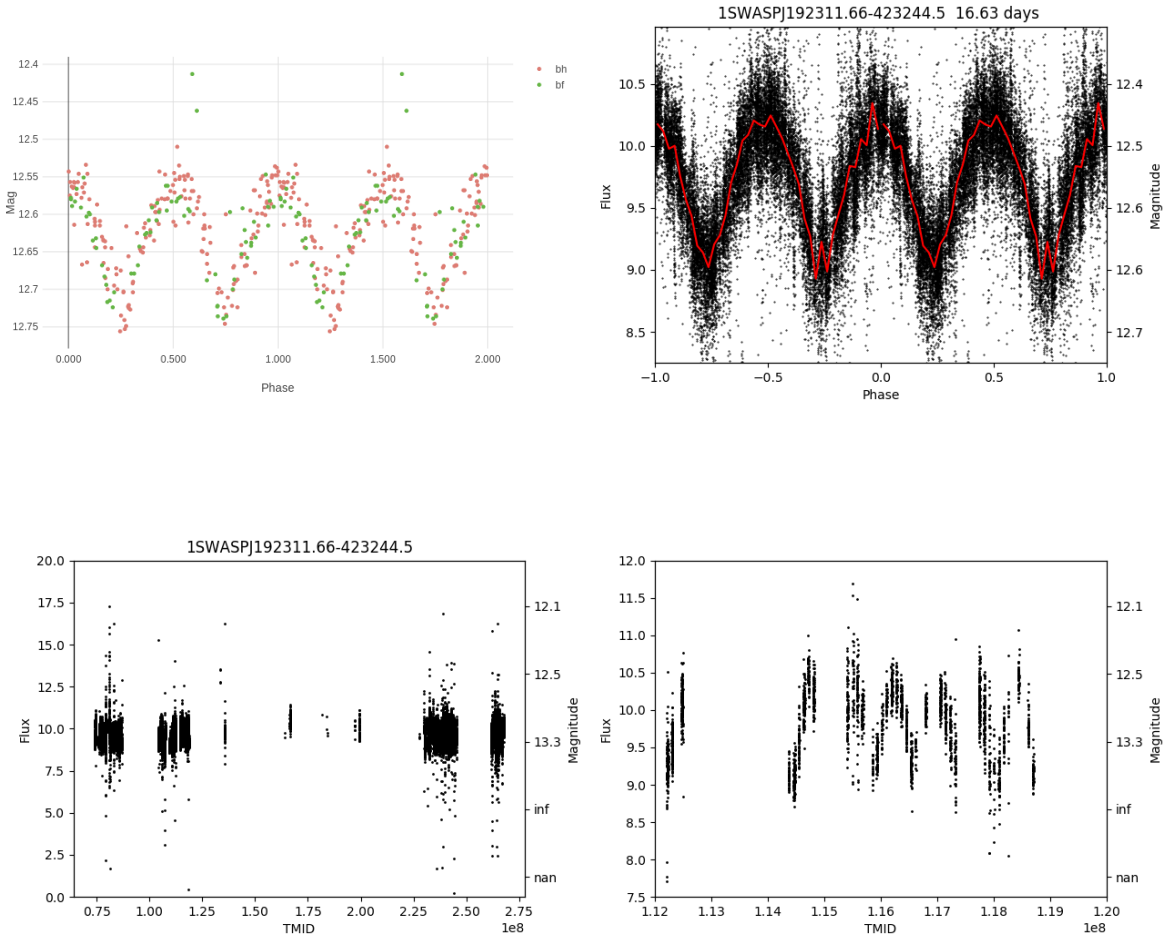

Fig. B.22 Phase-folded light curves for J192311. **Top left:** phase-folded ASAS-SN; **top right:** phase-folded SuperWASP; **bottom left:** unfolded SuperWASP; **bottom right:** zoom in of unfolded SuperWASP.

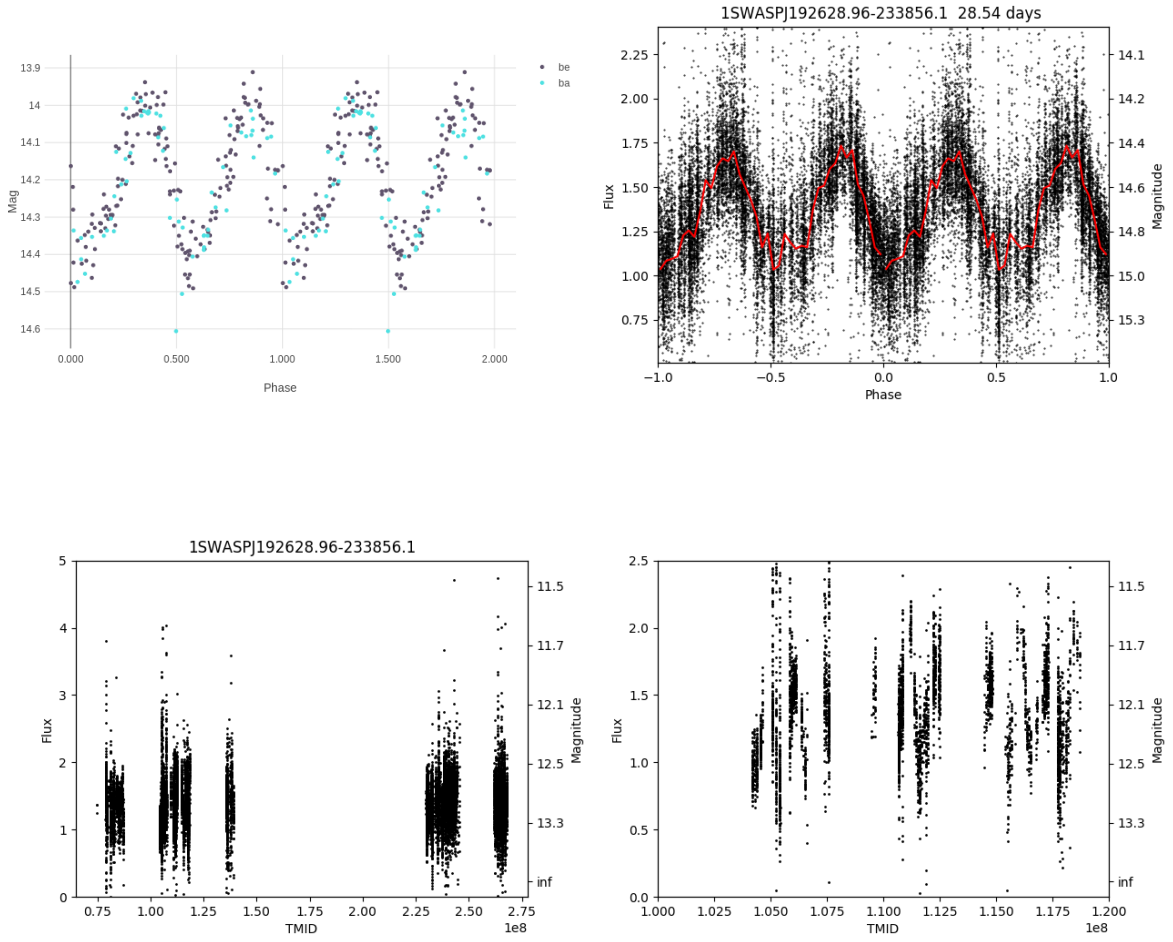

Fig. B.23 Phase-folded light curves for J192628. **Top left:** phase-folded ASAS-SN; **top right:** phase-folded SuperWASP; **bottom left:** unfolded SuperWASP; **bottom right:** zoom in of unfolded SuperWASP.

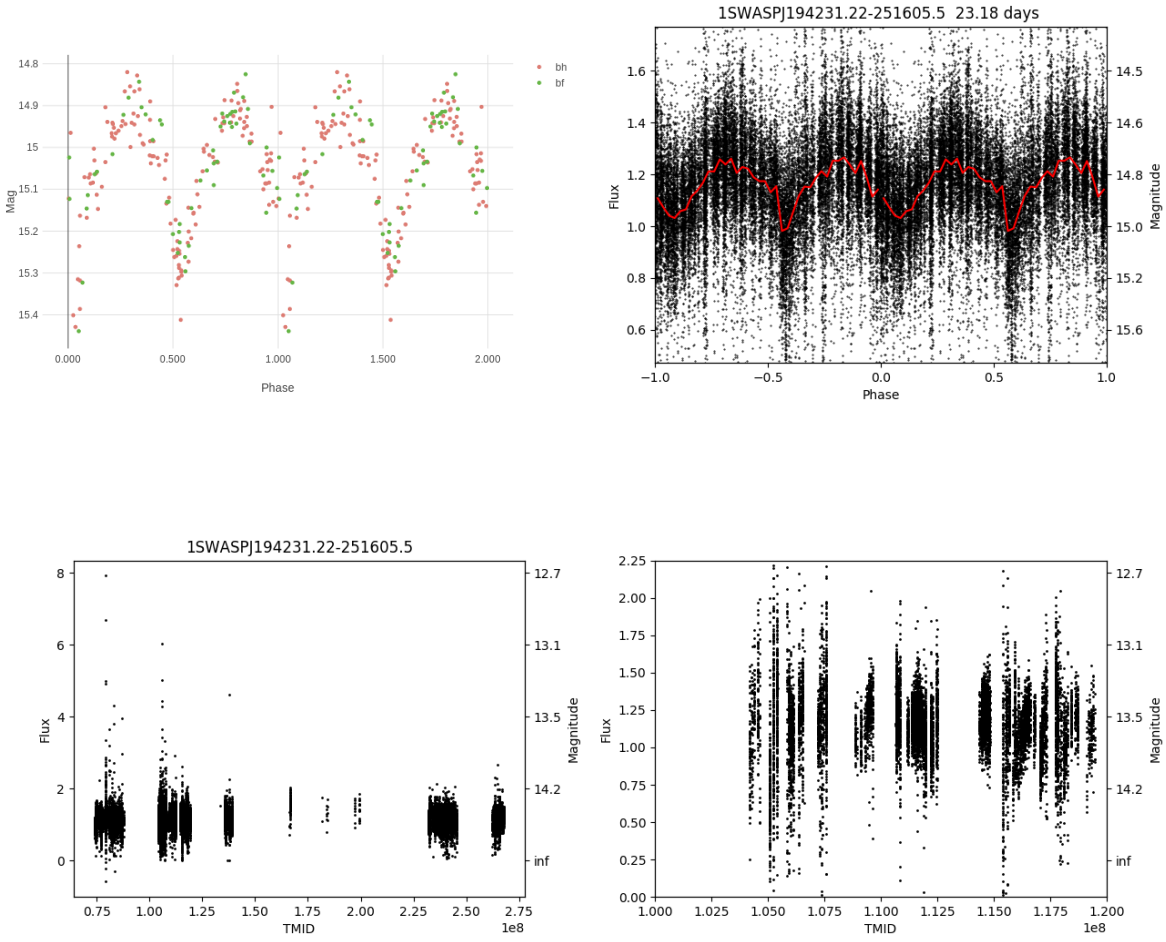

Fig. B.24 Phase-folded light curves for J194231. **Top left:** phase-folded ASAS-SN; **top right:** phase-folded SuperWASP; **bottom left:** unfolded SuperWASP; **bottom right:** zoom in of unfolded SuperWASP.

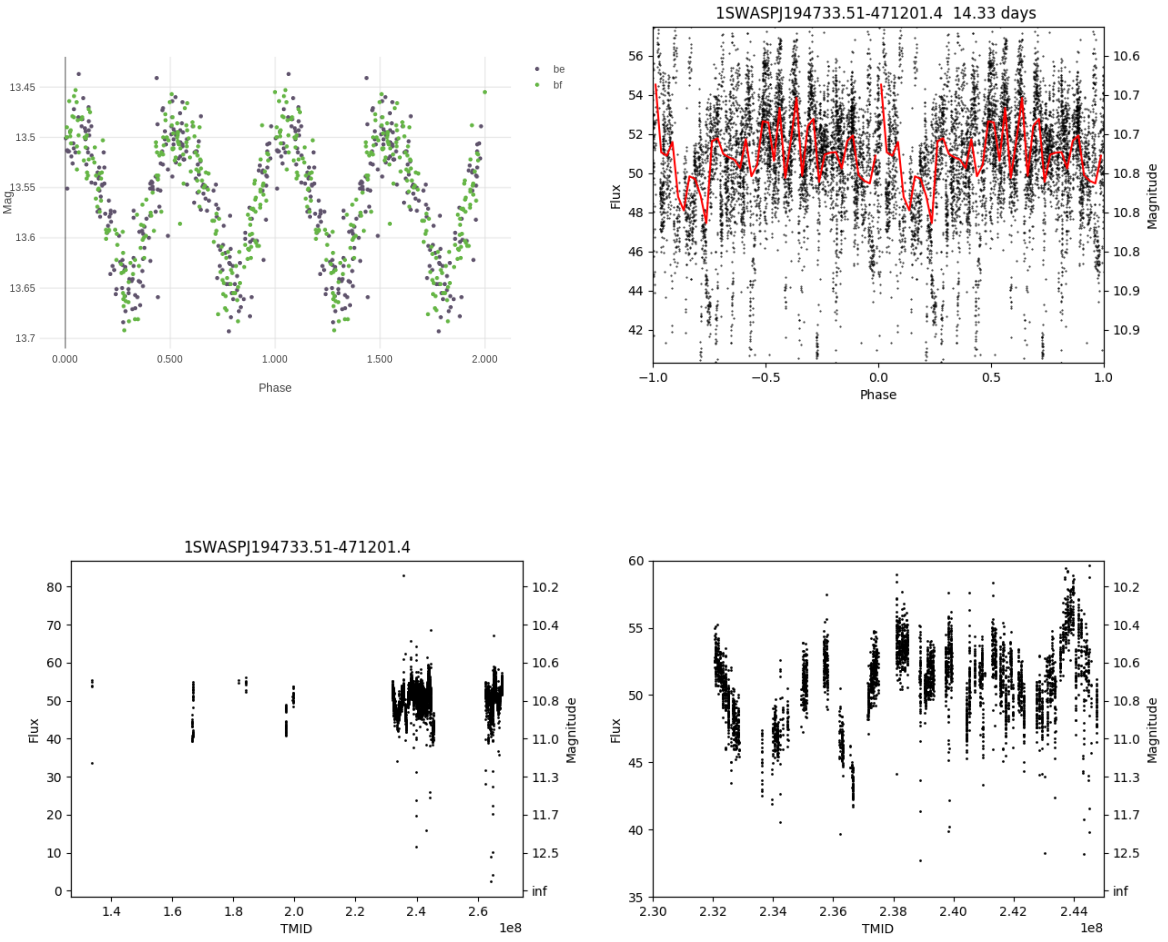

Fig. B.25 Phase-folded light curves for J194733. **Top left:** phase-folded ASAS-SN; **top right:** phase-folded SuperWASP; **bottom left:** unfolded SuperWASP; **bottom right:** zoom in of unfolded SuperWASP.

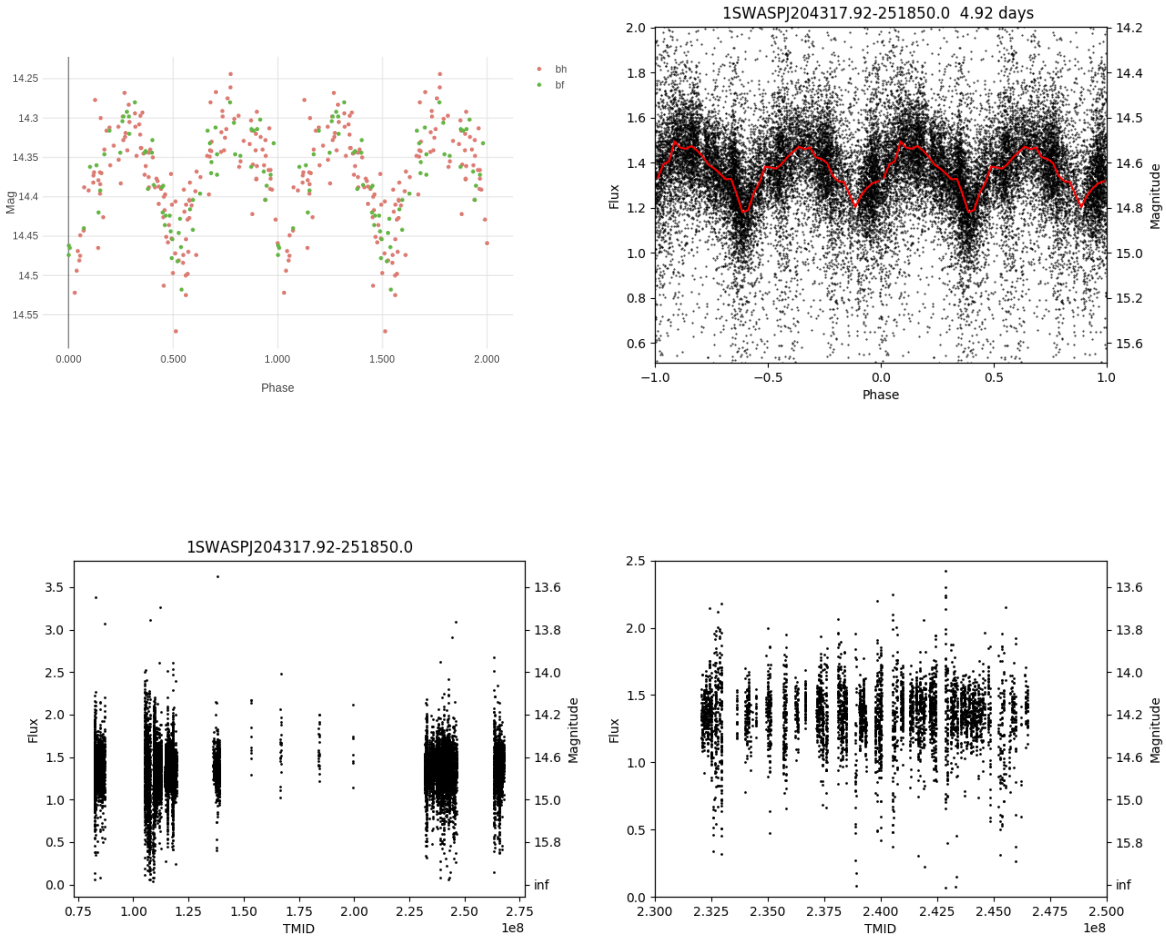

Fig. B.26 Phase-folded light curves for J204317. **Top left:** phase-folded ASAS-SN; **top right:** phase-folded SuperWASP; **bottom left:** unfolded SuperWASP; **bottom right:** zoom in of unfolded SuperWASP.

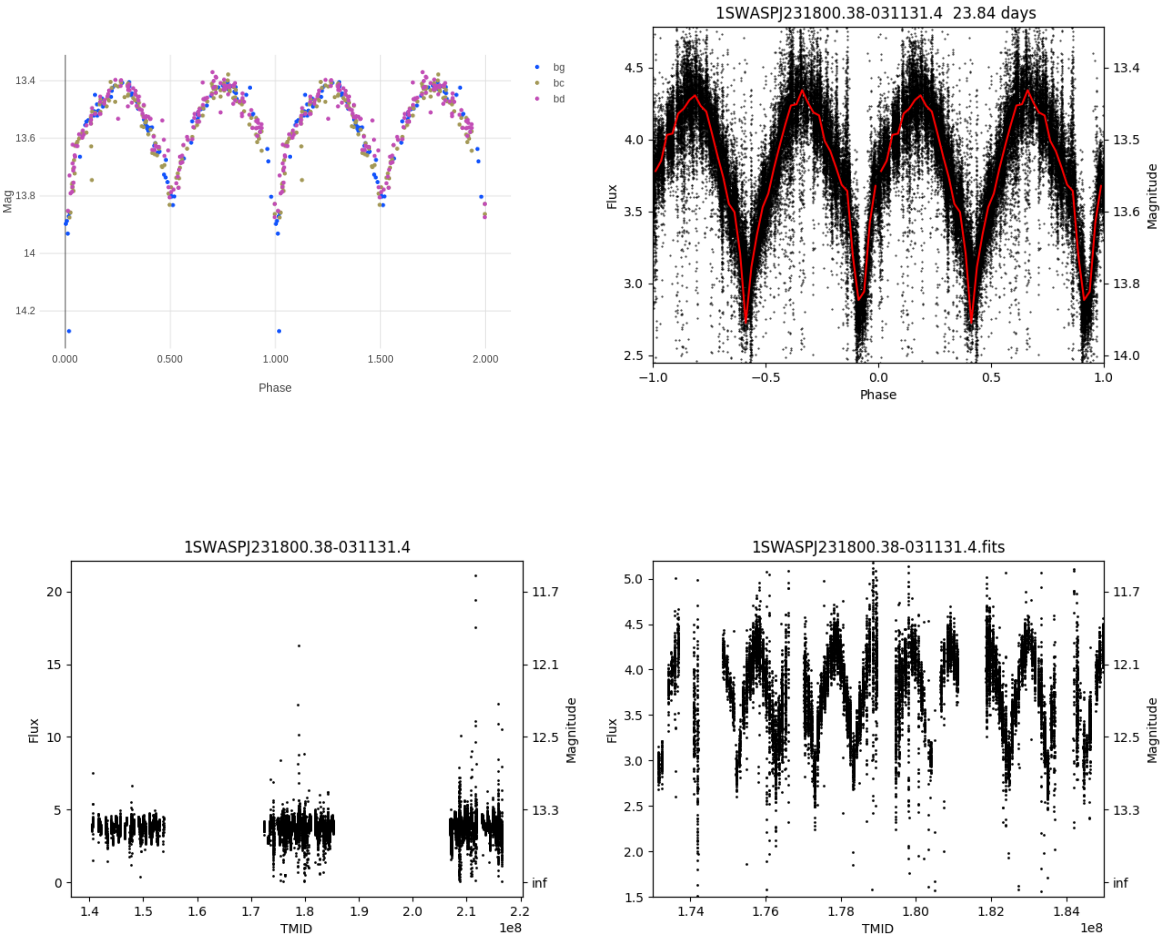

Fig. B.27 Phase-folded light curves for J231800. **Top left:** phase-folded ASAS-SN; **top right:** phase-folded SuperWASP; **bottom left:** unfolded SuperWASP; **bottom right:** zoom in of unfolded SuperWASP.

Appendix C

Catalogue of new variables detected in SuperWASP Variable Stars

This appendix contains the full list of 201 newly identified stellar variables (pulsating variables, EA/EB and EW binaries) discovered in the first analysis of the SuperWASP Variable Stars Zooniverse project, ordered by SuperWASP ID.

Table C.1 301 previously unidentified stellar variables and related characteristics, not including rotators and unknown variables.

WASP_ID	Type	Period (days)	Period (seconds)
1SWASPJ000005.14-755731.3	EA/EB	4.30	3.72E+05
1SWASPJ000026.84+393855.6	EA/EB	3.59	3.10E+05
1SWASPJ000028.05+041248.4	EA/EB	4.69	4.05E+05
1SWASPJ000039.60-191306.0	EA/EB	6.76	5.84E+05
1SWASPJ000047.05+353443.1	EW	1.32	1.14E+05
1SWASPJ000054.70+544425.6	EA/EB	3.19	2.76E+05
1SWASPJ000057.42-544520.1	EA/EB	0.75	6.46E+04
1SWASPJ000059.84+094404.5	EA/EB	0.65	5.60E+04
1SWASPJ000105.41-622920.6	EA/EB	1.48	1.28E+05
1SWASPJ000132.23-051917.6	Pulsator	1.62	1.40E+05
1SWASPJ000132.66-091513.7	EA/EB	4.19	3.62E+05
1SWASPJ000145.10+501843.4	EA/EB	1.69	1.46E+05
1SWASPJ000149.26+061830.8	EA/EB	0.32	2.74E+04
1SWASPJ000149.45-363918.1	Pulsator	0.64	5.51E+04
1SWASPJ000203.48-214746.0	EA/EB	0.86	7.40E+04

1SWASPJ000315.40+495750.8	EA/EB	3.65	3.16E+05
1SWASPJ000323.81+325049.7	EA/EB	8.25	7.12E+05
1SWASPJ000343.16+465244.0	Pulsator	1.31	1.14E+05
1SWASPJ000353.60+043503.0	EW	0.30	2.59E+04
1SWASPJ000410.77-525122.4	EW	0.26	2.27E+04
1SWASPJ000434.72+342311.5	EA/EB	0.43	3.70E+04
1SWASPJ000439.12+443453.0	EA/EB	1.36	1.18E+05
1SWASPJ000443.02+475901.9	EW	0.64	5.50E+04
1SWASPJ000446.15+493644.0	EW	0.24	2.03E+04
1SWASPJ000504.06-220948.2	EA/EB	0.68	5.87E+04
1SWASPJ000510.93+333421.0	Pulsator	1.45	1.26E+05
1SWASPJ000522.14+025726.1	Pulsator	0.05	4.03E+03
1SWASPJ000540.33+272357.4	EA/EB	4.78	4.13E+05
1SWASPJ000549.48+462125.1	Pulsator	0.07	6.42E+03
1SWASPJ000558.92+363258.2	EA/EB	3.12	2.70E+05
1SWASPJ000633.43+332436.9	EA/EB	4.95	4.28E+05
1SWASPJ000659.49+515953.2	EA/EB	3.08	2.66E+05
1SWASPJ000705.08+335534.4	EW	0.35	3.06E+04
1SWASPJ000713.95+165424.7	EA/EB	1.24	1.07E+05
1SWASPJ000739.24+501725.4	EA/EB	1.55	1.34E+05
1SWASPJ000756.46+221309.8	EA/EB	0.40	3.45E+04
1SWASPJ000756.60-313821.6	EA/EB	0.32	2.74E+04
1SWASPJ000806.22+525252.1	EA/EB	1.60	1.38E+05
1SWASPJ000819.89+340646.0	EA/EB	0.80	6.92E+04
1SWASPJ000855.88+364633.9	EA/EB	10.02	8.66E+05
1SWASPJ000857.98+240227.6	Pulsator	1.32	1.14E+05
1SWASPJ000908.70+495550.8	EA/EB	2.14	1.85E+05
1SWASPJ000941.67-132901.5	EA/EB	1.37	1.19E+05
1SWASPJ000948.77+300653.9	EW	0.30	2.59E+04
1SWASPJ001002.40+540322.9	EW	0.31	2.70E+04
1SWASPJ001003.28+470444.3	Pulsator	41.27	3.57E+06
1SWASPJ001005.09+412814.3	Pulsator	17.05	1.47E+06
1SWASPJ001012.19-091244.2	EW	0.29	2.51E+04
1SWASPJ001041.63+464047.6	Pulsator	2.07	1.79E+05
1SWASPJ001048.95-683249.9	EA/EB	1.85	1.60E+05
1SWASPJ001049.71+050754.9	EA/EB	0.37	3.23E+04
1SWASPJ001111.06+533306.6	EW	0.39	3.35E+04
1SWASPJ001314.61+230843.5	EW	0.38	3.31E+04
1SWASPJ001328.35+350823.7	EW	0.70	6.04E+04
1SWASPJ001413.24+252135.1	Pulsator	0.64	5.53E+04
1SWASPJ001436.99+470216.6	EA/EB	1.79	1.54E+05
1SWASPJ001525.74-623944.0	Pulsator	0.34	2.94E+04
1SWASPJ001615.38+455440.0	EW	2.98	2.57E+05

1SWASPJ001644.30+570829.7	EA/EB	1.28	1.11E+05
1SWASPJ001659.68+473548.1	Pulsator	0.76	6.55E+04
1SWASPJ001724.08+521532.4	EA/EB	3.03	2.62E+05
1SWASPJ001739.55+430504.1	EA/EB	1.20	1.03E+05
1SWASPJ001747.11-580049.3	Pulsator	21.02	1.82E+06
1SWASPJ001750.78+491047.9	EA/EB	0.90	7.78E+04
1SWASPJ001826.12-632838.9	Pulsator	2.34	2.03E+05
1SWASPJ001828.85+430336.4	EW	0.37	3.23E+04
1SWASPJ001856.70+134125.5	EW	0.27	2.31E+04
1SWASPJ001912.30+542846.2	EA/EB	0.79	6.86E+04
1SWASPJ001913.92+153916.2	EA/EB	1.17	1.01E+05
1SWASPJ002005.03+505958.1	EW	0.63	5.46E+04
1SWASPJ002005.70+375502.5	EA/EB	3.06	2.64E+05
1SWASPJ002029.87+250826.0	EA/EB	2.26	1.95E+05
1SWASPJ002037.33+475500.5	EA/EB	0.82	7.08E+04
1SWASPJ002038.90-321900.8	EA/EB	0.78	6.71E+04
1SWASPJ002052.37+402625.8	Pulsator	0.65	5.66E+04
1SWASPJ002104.46-575625.6	EW	0.23	2.00E+04
1SWASPJ002205.48+060556.2	Pulsator	21.75	1.88E+06
1SWASPJ002223.88-183127.7	Pulsator	198.16	1.71E+07
1SWASPJ002234.18-715532.3	Pulsator	0.45	3.89E+04
1SWASPJ002240.00+495816.8	EA/EB	3.56	3.07E+05
1SWASPJ002241.47+410837.5	Pulsator	0.34	2.98E+04
1SWASPJ002250.33-614124.0	Pulsator	145.00	1.25E+07
1SWASPJ002254.33+410623.3	Pulsator	0.34	2.98E+04
1SWASPJ002254.40+404852.1	Pulsator	0.34	2.91E+04
1SWASPJ002307.49+304926.9	EA/EB	3.14	2.71E+05
1SWASPJ002307.81+375255.3	EW	0.35	3.03E+04
1SWASPJ002334.22+410837.3	Pulsator	0.34	2.98E+04
1SWASPJ002439.04+410950.7	Pulsator	0.34	2.98E+04
1SWASPJ002505.68+482554.8	EA/EB	2.80	2.42E+05
1SWASPJ002517.03+431557.2	EA/EB	2.97	2.56E+05
1SWASPJ002538.78-212203.1	Pulsator	2.95	2.55E+05
1SWASPJ002540.29-174855.0	EW	0.47	4.08E+04
1SWASPJ002544.11+411112.6	Pulsator	0.34	2.98E+04
1SWASPJ002552.75+454445.3	EA/EB	0.86	7.40E+04
1SWASPJ002621.25+540634.9	Pulsator	26.68	2.31E+06
1SWASPJ002634.89-654536.0	Pulsator	20.74	1.79E+06
1SWASPJ002647.57+411205.3	Pulsator	0.34	2.98E+04
1SWASPJ002652.32+395609.6	EA/EB	0.53	4.60E+04
1SWASPJ002657.92-584532.6	EW	0.35	3.04E+04
1SWASPJ002818.41+242821.5	EA/EB	0.40	3.44E+04
1SWASPJ002847.00+421321.6	EA/EB	2.16	1.86E+05

1SWASPJ002848.63+475137.0	EA/EB	4.32	3.73E+05
1SWASPJ002904.08+395028.5	EA/EB	3.00	2.59E+05
1SWASPJ002906.93+411234.3	Pulsator	0.34	2.94E+04
1SWASPJ002956.42+363539.5	Pulsator	3.19	2.76E+05
1SWASPJ002956.77+405114.5	Pulsator	0.34	2.91E+04
1SWASPJ003004.11+411321.3	Pulsator	0.26	2.21E+04
1SWASPJ003018.30+492723.2	EA/EB	1.85	1.60E+05
1SWASPJ003028.33+463543.3	Pulsator	41.49	3.58E+06
1SWASPJ003031.68+422814.2	EA/EB	3.28	2.83E+05
1SWASPJ003033.29+411323.6	Pulsator	0.34	2.98E+04
1SWASPJ003043.39+411637.0	Pulsator	0.33	2.84E+04
1SWASPJ003106.81+405158.5	Pulsator	0.34	2.94E+04
1SWASPJ003118.90+481140.0	EA/EB	1.85	1.59E+05
1SWASPJ003127.20-101720.3	EW	0.30	2.61E+04
1SWASPJ003131.64+475827.0	Pulsator	16.24	1.40E+06
1SWASPJ003146.20+365216.2	EA/EB	1.32	1.14E+05
1SWASPJ003223.45+393052.2	EA/EB	1.24	1.07E+05
1SWASPJ003235.89+092024.7	EA/EB	0.80	6.91E+04
1SWASPJ003255.14+373130.5	EA/EB	4.07	3.52E+05
1SWASPJ003300.46+515950.3	EA/EB	16.77	1.45E+06
1SWASPJ003303.68+411542.1	Pulsator	0.34	2.98E+04
1SWASPJ003337.56+411602.4	Pulsator	0.26	2.21E+04
1SWASPJ003410.22-374940.8	Pulsator	43.59	3.77E+06
1SWASPJ003424.14-730934.6	Pulsator	0.35	2.98E+04
1SWASPJ003424.41+400355.5	EW	0.35	3.02E+04
1SWASPJ003424.97+405313.1	Pulsator	0.34	2.94E+04
1SWASPJ003432.99+411606.5	Pulsator	0.34	2.98E+04
1SWASPJ003505.62+535756.5	EW	41.00	3.54E+06
1SWASPJ003508.52-572314.3	Pulsator	1.85	1.60E+05
1SWASPJ003521.60-344123.5	EA/EB	5.08	4.39E+05
1SWASPJ003544.75+495450.0	EW	17.86	1.54E+06
1SWASPJ003714.67+474032.4	EA/EB	3.35	2.89E+05
1SWASPJ003724.38+454806.4	EW	0.92	7.97E+04
1SWASPJ003725.32+411721.4	Pulsator	0.34	2.98E+04
1SWASPJ003741.77+503924.9	EA/EB	2.84	2.45E+05
1SWASPJ003835.87-143121.1	EA/EB	0.65	5.62E+04
1SWASPJ004003.56+501501.9	EW	0.23	2.02E+04
1SWASPJ004006.87-674948.5	Pulsator	134.21	1.16E+07
1SWASPJ004011.67+455218.6	EA/EB	2.77	2.39E+05
1SWASPJ004026.80+345035.6	EA/EB	1.70	1.47E+05
1SWASPJ004127.43+220717.1	EA/EB	5.71	4.93E+05
1SWASPJ004143.34+572716.3	EA/EB	0.77	6.70E+04
1SWASPJ004144.21+515043.8	EA/EB	1.85	1.60E+05

1SWASPJ004217.42+472136.9	EA/EB	1.72	1.49E+05
1SWASPJ004242.03-163857.5	EA/EB	0.63	5.43E+04
1SWASPJ004314.56+344142.3	EA/EB	0.70	6.01E+04
1SWASPJ004432.61+195559.4	EA/EB	2.33	2.01E+05
1SWASPJ004458.95-411520.4	EA/EB	1.51	1.30E+05
1SWASPJ004512.20+400551.0	Pulsator	0.34	2.91E+04
1SWASPJ004518.12+372946.1	Pulsator	211.81	1.83E+07
1SWASPJ004527.74+210427.9	EA/EB	1.66	1.44E+05
1SWASPJ004611.58+384900.4	EA/EB	0.69	5.94E+04
1SWASPJ004623.86+061534.7	Pulsator	17.93	1.55E+06
1SWASPJ004650.03+370113.1	Pulsator	212.93	1.84E+07
1SWASPJ004712.92+395132.6	Pulsator	0.34	2.91E+04
1SWASPJ004730.50+052310.7	EA/EB	0.40	3.47E+04
1SWASPJ004731.94+513216.0	EA/EB	1.20	1.04E+05
1SWASPJ004800.26+410257.4	Pulsator	0.34	2.91E+04
1SWASPJ004804.21+202258.8	EA/EB	1.22	1.05E+05
1SWASPJ004816.69+284330.1	EA/EB	7.26	6.27E+05
1SWASPJ004839.71-631659.3	EA/EB	2.11	1.82E+05
1SWASPJ004844.10+024126.1	EA/EB	3.85	3.33E+05
1SWASPJ004857.63+373209.3	EA/EB	1.33	1.15E+05
1SWASPJ004859.70+172328.1	EA/EB	3.11	2.69E+05
1SWASPJ004941.97+275304.3	EW	0.13	1.13E+04
1SWASPJ004942.46+085804.0	EA/EB	1.50	1.30E+05
1SWASPJ005008.02+340209.3	Pulsator	0.34	2.91E+04
1SWASPJ005009.85+405411.4	Pulsator	0.34	2.91E+04
1SWASPJ005025.05+294723.0	EA/EB	0.35	3.04E+04
1SWASPJ005027.46+152903.0	EA/EB	1.47	1.27E+05
1SWASPJ005033.34+163921.9	EA/EB	1.64	1.41E+05
1SWASPJ005100.15+502736.9	EA/EB	2.15	1.86E+05
1SWASPJ005107.84+214352.7	EA/EB	0.29	2.54E+04
1SWASPJ005113.24+284027.7	EA/EB	0.61	5.28E+04
1SWASPJ005148.24+354310.9	EA/EB	0.61	5.30E+04
1SWASPJ005202.56-675337.2	EA/EB	0.28	2.41E+04
1SWASPJ005204.76+393828.2	Pulsator	0.34	2.91E+04
1SWASPJ005211.03+264121.9	Pulsator	1.58	1.36E+05
1SWASPJ005223.31+373755.4	Pulsator	0.08	7.00E+03
1SWASPJ005245.64-174450.6	EW	0.40	3.46E+04
1SWASPJ005316.14+443843.8	EW	1.52	1.31E+05
1SWASPJ005338.98+045305.9	EW	0.36	3.11E+04
1SWASPJ005401.45+503532.4	Pulsator	0.13	1.15E+04
1SWASPJ005404.18+532315.0	Pulsator	2.71	2.34E+05
1SWASPJ005421.55+391320.4	EA/EB	4.58	3.96E+05
1SWASPJ005454.74+324445.5	Pulsator	24.53	2.12E+06

1SWASPJ005458.28+381339.5	EA/EB	0.45	3.89E+04
1SWASPJ005500.35+183956.2	EA/EB	0.61	5.28E+04
1SWASPJ005510.25+402055.3	EA/EB	1.68	1.45E+05
1SWASPJ005520.99-590854.8	Pulsator	0.05	4.09E+03
1SWASPJ005523.92+361535.5	EA/EB	0.67	5.82E+04
1SWASPJ005552.34+500946.9	EA/EB	1.39	1.20E+05
1SWASPJ005558.63-023316.7	Pulsator	2.85	2.46E+05
1SWASPJ005630.60+391345.6	Pulsator	0.34	2.91E+04
1SWASPJ005633.04-555021.2	EW	0.30	2.62E+04
1SWASPJ005658.75+280616.3	EA/EB	1.21	1.05E+05
1SWASPJ005701.83+421123.9	EA/EB	1.70	1.47E+05
1SWASPJ005702.31-384348.1	EW	0.14	1.19E+04
1SWASPJ005710.89+171715.1	EA/EB	2.79	2.41E+05
1SWASPJ005728.43+280654.6	EA/EB	2.50	2.16E+05
1SWASPJ005759.30+202351.3	Pulsator	0.73	6.35E+04
1SWASPJ005805.85+533921.5	Pulsator	0.38	3.29E+04
1SWASPJ005810.22+350309.2	EW	0.52	4.52E+04
1SWASPJ005811.98-130122.1	EA/EB	0.74	6.36E+04
1SWASPJ005818.26+204348.0	EA/EB	0.44	3.81E+04
1SWASPJ005824.28+085011.9	Pulsator	1.65	1.43E+05
1SWASPJ005826.50+411546.2	Pulsator	0.10	9.02E+03
1SWASPJ005847.66+320606.8	EA/EB	0.68	5.91E+04
1SWASPJ005848.37+464137.0	EW	0.71	6.12E+04
1SWASPJ010045.96-050755.2	EA/EB	0.40	3.44E+04
1SWASPJ010311.33-084632.7	EA/EB	0.64	5.54E+04
1SWASPJ010655.61+500428.9	EA/EB	3.22	2.78E+05
1SWASPJ010748.49+420427.7	EA/EB	4.54	3.92E+05
1SWASPJ010757.74+091023.9	EA/EB	1.50	1.29E+05
1SWASPJ010809.25+334224.7	EA/EB	1.31	1.13E+05
1SWASPJ010829.07+114318.5	EA/EB	0.27	2.36E+04
1SWASPJ065312.18+270453.5	EA/EB	2.11	1.82E+05
1SWASPJ083356.41-175557.4	EA/EB	1.48	1.28E+05
1SWASPJ083533.50-210111.2	EA/EB	2.63	2.27E+05
1SWASPJ083619.61+384108.5	EA/EB	0.61	5.23E+04
1SWASPJ083630.67+275632.4	EA/EB	0.67	5.75E+04
1SWASPJ083652.43+255212.4	EA/EB	0.34	2.95E+04
1SWASPJ083811.72+414058.3	EA/EB	0.69	5.99E+04
1SWASPJ084219.88-101720.8	EA/EB	5.63	4.87E+05
1SWASPJ084338.10-150513.3	EA/EB	1.69	1.46E+05
1SWASPJ084345.54+384833.7	EA/EB	4.70	4.06E+05
1SWASPJ084800.36-091334.0	EA/EB	1.19	1.03E+05
1SWASPJ084810.73+031645.8	EA/EB	4.51	3.89E+05
1SWASPJ084907.38+345812.8	EA/EB	1.98	1.71E+05

1SWASPJ085038.53-195713.3	EA/EB	2.03	1.76E+05
1SWASPJ085052.75+154435.9	EA/EB	0.34	2.95E+04
1SWASPJ085235.51-233338.4	EA/EB	3.10	2.68E+05
1SWASPJ085244.09+294225.7	EA/EB	0.34	2.95E+04
1SWASPJ085322.17+380729.0	EA/EB	1.60	1.39E+05
1SWASPJ085342.32+262956.3	EA/EB	1.53	1.32E+05
1SWASPJ085435.86+254334.8	EA/EB	0.34	2.95E+04
1SWASPJ085500.15+300513.7	EA/EB	0.34	2.95E+04
1SWASPJ085926.14+405814.8	EA/EB	5.03	4.34E+05
1SWASPJ090021.68+225217.2	EA/EB	0.34	2.95E+04
1SWASPJ090541.27-135446.2	EA/EB	4.51	3.89E+05
1SWASPJ090623.07-074533.0	EA/EB	0.61	5.28E+04
1SWASPJ090846.99-154857.3	EA/EB	0.62	5.35E+04
1SWASPJ091126.99-335445.4	EA/EB	1.40	1.21E+05
1SWASPJ091150.02+000716.9	EA/EB	0.73	6.35E+04
1SWASPJ091207.93+294036.4	EA/EB	1.19	1.03E+05
1SWASPJ091554.38-184932.1	EA/EB	0.42	3.60E+04
1SWASPJ091707.26-193228.1	EA/EB	0.68	5.88E+04
1SWASPJ091915.51-270213.2	EA/EB	0.34	2.98E+04
1SWASPJ092053.80-321719.4	EA/EB	1.27	1.10E+05
1SWASPJ092227.22-324454.7	EA/EB	1.47	1.27E+05
1SWASPJ092424.92-175341.3	EA/EB	0.87	7.54E+04
1SWASPJ092616.74-201040.3	EA/EB	3.49	3.02E+05
1SWASPJ092801.06-193346.3	EA/EB	0.70	6.01E+04
1SWASPJ092831.89-114822.5	EW	0.65	5.57E+04
1SWASPJ092949.61-195015.1	EA/EB	1.25	1.08E+05
1SWASPJ093504.19-143656.9	EA/EB	0.38	3.28E+04
1SWASPJ094035.69+040718.4	EA/EB	0.42	3.60E+04
1SWASPJ094234.01+092238.4	EA/EB	0.34	2.96E+04
1SWASPJ094410.62-450420.5	EA/EB	0.16	1.39E+04
1SWASPJ094800.86-450838.5	EA/EB	0.61	5.29E+04
1SWASPJ095126.68-221135.9	EA/EB	0.28	2.40E+04
1SWASPJ095916.38-411524.2	EA/EB	1.07	9.25E+04
1SWASPJ100214.08-190601.6	EA/EB	0.63	5.46E+04
1SWASPJ101149.62-075748.0	EA/EB	3.18	2.74E+05
1SWASPJ101709.12-251821.8	EA/EB	4.12	3.56E+05
1SWASPJ101736.82-201054.9	EA/EB	1.22	1.05E+05
1SWASPJ101741.04-474224.1	EA/EB	3.14	2.71E+05
1SWASPJ102429.37-321525.4	EA/EB	1.28	1.11E+05
1SWASPJ103053.95-334833.0	EA/EB	1.48	1.28E+05
1SWASPJ103653.62+310553.0	EA/EB	0.34	2.94E+04
1SWASPJ103859.31-323234.3	EA/EB	2.44	2.10E+05
1SWASPJ104459.09-383455.0	EA/EB	3.00	2.59E+05

1SWASPJ104813.37-444012.2	EA/EB	1.56	1.34E+05
1SWASPJ105200.65-131909.6	EA/EB	4.11	3.55E+05
1SWASPJ110422.96+014252.6	EA/EB	0.69	5.97E+04
1SWASPJ110636.12-454443.1	EA/EB	2.99	2.58E+05
1SWASPJ110740.70-181004.3	EA/EB	3.83	3.30E+05
1SWASPJ111312.97-190623.5	EA/EB	0.78	6.72E+04
1SWASPJ111405.08+224415.7	EA/EB	0.80	6.92E+04
1SWASPJ112440.86+303734.9	EA/EB	0.75	6.51E+04
1SWASPJ112651.37-382455.3	EW	1.53	1.32E+05
1SWASPJ113009.30-192701.5	EA/EB	0.61	5.28E+04
1SWASPJ113251.01+055829.8	EA/EB	4.86	4.20E+05
1SWASPJ113330.07+140951.8	EA/EB	2.14	1.85E+05
1SWASPJ115731.69+370947.5	EA/EB	1.37	1.18E+05
1SWASPJ115748.13-482630.9	EW	0.15	1.30E+04
1SWASPJ121319.42-382428.7	EA/EB	2.93	2.53E+05
1SWASPJ122258.47+071422.3	EA/EB	4.50	3.89E+05
1SWASPJ122336.55-180722.1	EA/EB	4.65	4.02E+05
1SWASPJ122834.81+323437.8	EA/EB	1.70	1.47E+05
1SWASPJ123301.44-254546.3	EA/EB	1.90	1.64E+05
1SWASPJ124304.15-345636.1	EA/EB	0.38	3.29E+04
1SWASPJ124628.66-134751.5	EW	0.32	2.75E+04
1SWASPJ125507.71+493839.3	EA/EB	2.71	2.34E+05
1SWASPJ130017.13-544001.4	EA/EB	3.11	2.68E+05
1SWASPJ130312.66-083628.0	EW	0.77	6.65E+04
1SWASPJ132620.26-221811.1	EW	1.69	1.46E+05
1SWASPJ132958.24-092101.1	EA/EB	0.85	7.36E+04
1SWASPJ135745.98-313544.9	EA/EB	0.75	6.45E+04
1SWASPJ142956.01+233722.5	EA/EB	3.09	2.67E+05